frontiers | Research Topics

Metabolism of herbs/ natural products and pharmacodynamic or toxic mechanisms

Edited by
Qi Wang, Bingyou Yang, Longlong Si and Shuai Ji

Published in
Frontiers in Pharmacology

ISSN 1664-8714
ISBN 978-2-83251-631-7
DOI 10.3389/978-2-83251-631-7

About Frontiers

Frontiers is more than just an open access publisher of scholarly articles: it is a pioneering approach to the world of academia, radically improving the way scholarly research is managed. The grand vision of Frontiers is a world where all people have an equal opportunity to seek, share and generate knowledge. Frontiers provides immediate and permanent online open access to all its publications, but this alone is not enough to realize our grand goals.

Frontiers journal series

The Frontiers journal series is a multi-tier and interdisciplinary set of open-access, online journals, promising a paradigm shift from the current review, selection and dissemination processes in academic publishing. All Frontiers journals are driven by researchers for researchers; therefore, they constitute a service to the scholarly community. At the same time, the *Frontiers journal series* operates on a revolutionary invention, the tiered publishing system, initially addressing specific communities of scholars, and gradually climbing up to broader public understanding, thus serving the interests of the lay society, too.

Dedication to quality

Each Frontiers article is a landmark of the highest quality, thanks to genuinely collaborative interactions between authors and review editors, who include some of the world's best academicians. Research must be certified by peers before entering a stream of knowledge that may eventually reach the public - and shape society; therefore, Frontiers only applies the most rigorous and unbiased reviews. Frontiers revolutionizes research publishing by freely delivering the most outstanding research, evaluated with no bias from both the academic and social point of view. By applying the most advanced information technologies, Frontiers is catapulting scholarly publishing into a new generation.

What are Frontiers Research Topics?

Frontiers Research Topics are very popular trademarks of the *Frontiers journals series*: they are collections of at least ten articles, all centered on a particular subject. With their unique mix of varied contributions from Original Research to Review Articles, Frontiers Research Topics unify the most influential researchers, the latest key findings and historical advances in a hot research area.

Find out more on how to host your own Frontiers Research Topic or contribute to one as an author by contacting the Frontiers editorial office: frontiersin.org/about/contact

Metabolism of herbs/natural products and pharmacodynamic or toxic mechanisms

Topic editors

Qi Wang — Harbin Medical University, China
Bingyou Yang — Heilongjiang University of Chinese Medicine, China
Longlong Si — Harvard University, United States
Shuai Ji — Xuzhou Medical University, China

Citation

Wang, Q., Yang, B., Si, L., Ji, S., eds. (2023). *Metabolism of herbs/natural products and pharmacodynamic or toxic mechanisms*. Lausanne: Frontiers Media SA.
doi: 10.3389/978-2-83251-631-7

Table of contents

frontiers in Pharmacology

ORIGINAL RESEARCH
published: 09 March 2022
doi: 10.3389/fphar.2022.828449

Surface-Enhanced Raman Spectroscopy Analysis of *Astragalus* Saponins and Identification of Metabolites After Oral Administration in Rats by Ultrahigh-Performance Liquid Chromatography/Quadrupole Time-of-Flight Mass Spectrometry Analysis

Shengnan Kong[1†], Shan Ou[2†], Yan Liu[1†], Minzhen Xie[2], Ting Mei[2], Yingshuo Zhang[2], Jincheng Zhang[2], Qi Wang[2] and Bingyou Yang[1]**

[1]Key Laboratory of Basic and Application Research of Beiyao (Heilongjiang University of Chinese Medicine), Ministry of Education, Heilongjiang University of Chinese Medicine, Ministry of Education, Harbin, China, [2]Department of Medicinal Chemistry and Natural Medicine Chemistry, College of Pharmacy, Harbin Medical University, Harbin, China

OPEN ACCESS

Edited by:
Jian-Bo Wan,
University of Macau, China

Reviewed by:
Feng-Qing Yang,
Chongqing University, China
Pei Luo,
Macau University of Science and Technology, Macao SAR, China

***Correspondence:**
Qi Wang
mydearmumu@163.com
Bingyou Yang
ybywater@163.com

[†]These authors share first authorship

Specialty section:
This article was submitted to Ethnopharmacology, a section of the journal Frontiers in Pharmacology

Received: 03 December 2021
Accepted: 24 January 2022
Published: 09 March 2022

Citation:
Kong S, Ou S, Liu Y, Xie M, Mei T, Zhang Y, Zhang J, Wang Q and Yang B (2022) Surface-Enhanced Raman Spectroscopy Analysis of Astragalus Saponins and Identification of Metabolites After Oral Administration in Rats by Ultrahigh-Performance Liquid Chromatography/Quadrupole Time-of-Flight Mass Spectrometry Analysis. Front. Pharmacol. 13:828449. doi: 10.3389/fphar.2022.828449

Astragalus mongholicus Bunge (Fabaceae) is an ancient Chinese herbal medicine, and *Astragalus* saponins are the main active components, which have a wide range of biological activities, such as immunomodulation, antioxidation, and neuroprotection. In this study, silver nanoparticles obtained by sodium borohydride reduction were used as the enhanced substrate to detect astragaloside I (1), astragaloside II (2), astragaloside III (3), astragaloside IV (4), isoastragaloside I (5), and isoastragaloside II (6) in the phloem, xylem, and cork by surface-enhanced Raman spectroscopy (SERS). In the SERS spectrum of *Astragalus* slices, the characteristic peaks were observed at 562, 671, 732, 801, 836, 950, 1,026, 1,391, and 1,584 cm^{-1}, among which 950 cm^{-1} and 1,391 cm^{-1} were strong SERS signals. Subsequently, the metabolites of the six kinds of *Astragalus* saponins were identified by UPLC/ESI/Q-TOF-MS. Totally, 80, 89, and 90 metabolites were identified in rat plasma, urine, and feces, respectively. The metabolism of saponins mainly involves dehydration, deacetylation, dihydroxylation, dexylose reaction, deglycosylation, methylation, deacetylation, and glycol dehydration. Ten metabolites (1-M2, 1-M11, 2-M3, 2-M12, 3-M14, 4-M9, 5-M2, 5-M17, 6-M3, and 6-M12) were identified by comparison with reference standards. Interestingly, *Astragalus* saponins 1, 2, 5, and 6 were deacetylated to form astragaloside IV (4), which has been reported to have good pharmacological neuroprotective, liver protective, anticancer, and antidiabetic effects. Six kinds of active *Astragalus* saponins from different parts of *Astragalus mongholicus* were identified by SERS spectroscopy. Six kinds of active *Astragalus* saponins from different parts of *Astragalus mongholicus* were identified by SERS spectrum, and the metabolites were characterized by UPLC/ESI/Q-TOF-MS,

which not only provided a new method for the identification of traditional Chinese medicine but also provided a theoretical basis for the study of the pharmacodynamic substance basis of *Astragalus mongholicus* saponins.

Keywords: astragali radix, surface-enhanced Raman spectroscopy, metabolite identification, Astragalus saponins, astragaloside IV

1 INTRODUCTION

Astragalus mongholicus Bunge is an ancient Chinese herbal medicine used as an essential ingredient in over 200 Chinese herbal formulas prescribed to treat different diseases in China and other Asian countries (Yuan et al., 2012; Sun et al., 2019). Pharmacological studies have shown that their saponins, flavonoids, and polysaccharide phytochemicals have interesting bioactivities, such as antioxidant, anti-inflammatory, immunomodulatory, antiviral, and antitumor activities (Liu et al., 2017). According to the Chinese Pharmacopeia (2020 version), astragaloside saponins (especially astragaloside IV) possess interesting pharmacological activities, and they are used as quality assessment markers for *Astragalus mongholicus* Bunge. At present, more than 40 triterpenoid saponins have been obtained from *Astragalus mongholicus* Bunge and its related plants (Lee et al., 2017a; Song et al., 2007).

Because *Astragalus mongholicus* Bunge has many pharmacological effects, the current research focuses on the pharmacological substance basis of *Astragalus mongholicus*, mainly including the identification and content determination of flavonoids and saponins in *Astragalus mongholicus* (Zhang et al., 2018; Mei et al., 2020). At the same time, the quality of *Astragalus mongholicus* was also determined by diffuse reflectance mid-infrared transform spectroscopy (Yang et al., 2020). In addition, several researchers have studied the pharmacokinetic characteristics of its active components and metabolites in different crude extracts (Liu et al., 2015; Shi et al., 2015). Among them, astragaloside IV has been studied for neuroprotection, liver protection, anticancer, and antidiabetes and has also been studied extensively in terms of the pharmacokinetics of rats and dogs (Cheng et al., 2016; Lee et al., 2017b; Zhang et al., 2020; Zhang et al., 2007; Zhang et al., 2005). However, *Astragalus* saponins have similar structures and more isomers, making them difficult to identify. Many potential active saponins in *Astragalus* mongholicus Bunge have not been studied.

Therefore, it is of great significance to develop a rapid and effective modern detection method for *Astragalus* saponins in chemical studies and the study of their metabolism *in vivo*. This study used SERS to detect interesting astragaloside saponins (astragaloside I (1), astragaloside II (2), astragaloside III (3), astragaloside IV (4), isoastragaloside I (5), and isoastragaloside II (6)), identify metabolites, and determine the metabolic profile of them in rat biosamples by UPLC/ESI/Q-TOF-MS to provide a fundamental basis for further pharmacology research and clinical applications of these phytochemicals.

MATERIALS AND METHODS

Chemicals and Reagents

Compound astragaloside I (1), astragaloside II (2), astragaloside III (3), astragaloside IV (4), isoastragaloside I (5), isoastragaloside II (6), and cycloastragenol were all purchased from Chengdu Monster Biological Technology Co., Ltd., and their purity was above 98%. Heparin sodium was purchased from Beijing Xinyoubo Biotechnology Co., Ltd. (**Figure 1**). *Astragalus mongholicus* Bunge was purchased from Heilongjiang Zhongxin Co., Ltd. Sodium borohydride and silver nitrate were purchased from Aladdin. All other reagents were of analytical grade.

Preparation of *Astragalus mongholicus* Bunge Sample and SERS Spectrum Detection

The phloem, xylem, and cork of *Astragalus mongholicus* Bunge were extracted with 0.5 g powder and 1 ml chromatographic methanol for ultrasonic extraction for 30 min. Centrifuge for 15 min at 6,000 rpm, and take the supernatant. The six *Astragalus* saponins were 1 mg, and 100 μl of chromatographic methanol was added to each and dissolved by ultrasound. 10 μl of silver nanoparticles (Ag@BO) reduced by centrifuged sodium borohydride was added into a 1.5 ml centrifuge tube; then, the sample (2 μl) was added into the centrifuge tube, mixed, and shaken well. After that, 5 μl of sodium borohydride solution was added, shaken, and mixed, and a small amount of mixed sample was absorbed by 0.5 mm capillary for Raman detection. Raman instruments are manufactured by Wetic (Germany). Raman detection parameters are as follows: laser wavelength 633 nm, grating 600, scanning time 10 s/time, laser power 10 mW, and cumulative scanning times once. All Raman signal data in this article have no other smoothing operation except for base operation.

Animals and Drug Administration

Sixteen male Sprague Dawley rats (220–250 g) were purchased from the Experimental Animal Center of the Second Affiliated Hospital of Harbin Medical University. The laboratory animal facilities and procedures have been approved by the Animal Care and Use Committee of Harbin Medical University. All procedures are strictly implemented following the National Institute of Health Guidelines for the Care and Use of Laboratory Animals (Institute for Laboratory Animal Resources, 1996). Rats were fed in a metabolic cage with a temperature of 25°C, humidity of 60 ± 5%, 12 h dark-light cycle, free drinking water, and normal feed for three consecutive days. Rats fasted for 12 h

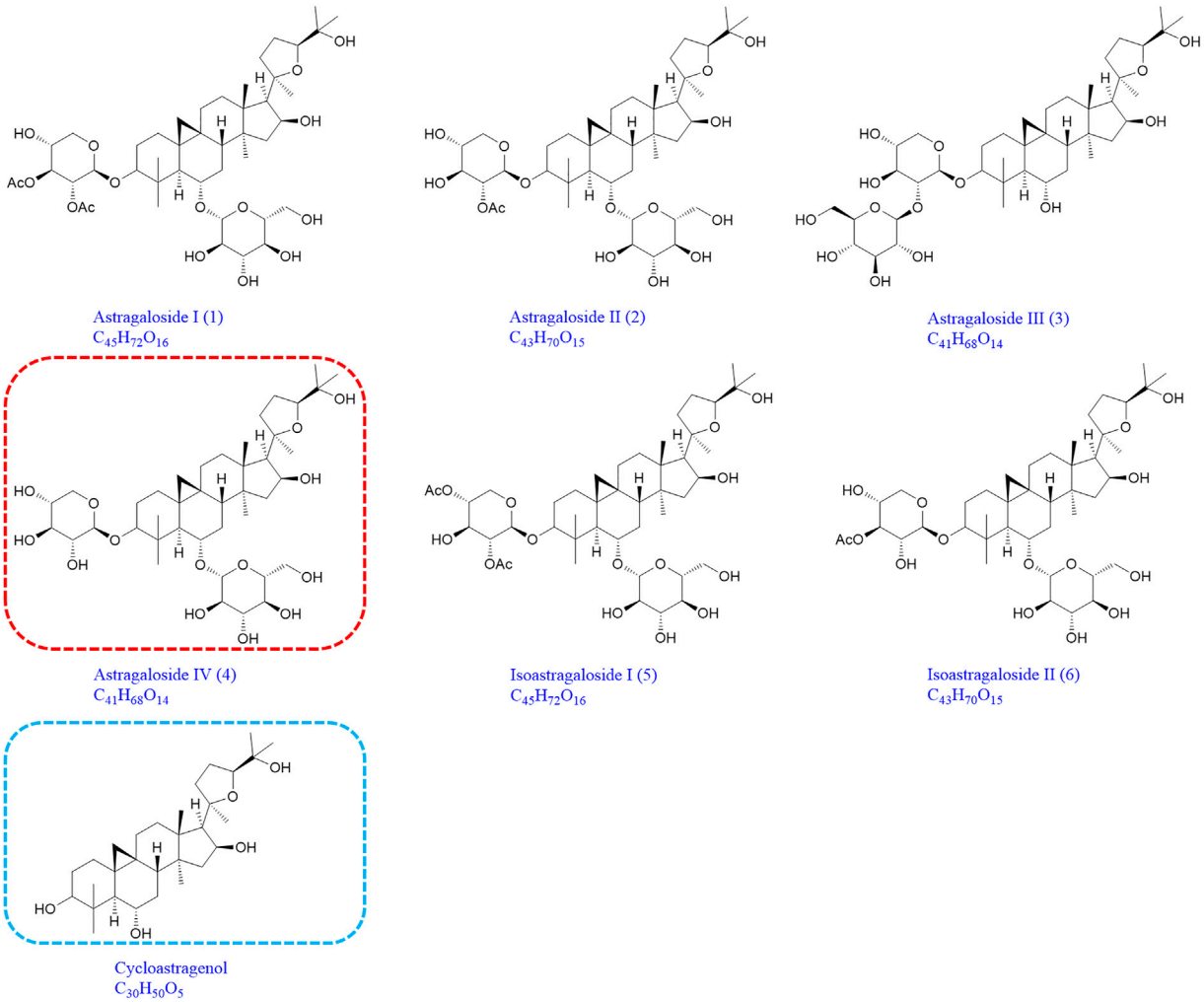

FIGURE 1 | Chemical structures of astragaloside I (1), astragaloside II (2), astragaloside III (3), astragaloside IV (4), isoastragaloside I (5), isoastragaloside II (6), and cycloastragenol (the same as 1-M12, 2-M14, 3-M9, 4-M11, 5-M17, and 6-M12).

before the experiment. Seven compounds were suspended in 1% sodium carboxymethyl cellulose to obtain suspension (2 mg/ml for each compound). Rats (n = 2) were orally given 40 mg/kg, while the control group was orally given the same amount of normal saline (Wang et al., 2014).

Preparation of Plasma, Urine, and Fecal Samples

0.5 ml of ocular vein blood was collected from rats in each treatment group at 0.5, 1, 2, 4, 6, and 8 h after administration and was centrifuged at 3,000 rpm for 10 min. Plasma samples were collected from the supernatant, combined with plasma, and stored in a −20°C refrigerator for cryopreservation. Urine was collected within 24 h and stored in a refrigerator at −20°C. The feces of rats within 24 h after oral administration were collected and air-dried naturally.

1 ml of plasma was taken, and four times the volume of methanol-acetonitrile (2:1) precipitated protein was added. The precipitated protein was vortexed for 5 min and centrifuged at 13,500 rpm for 5 min, and the supernatant was taken out and rotated-dried at 37°C. 2 ml of urine was extracted and purified on an activated solid-phase extraction column (OASIS HLB 6 CC). Purification process is as follows: first eluting with 3 ml of water, then eluting with 3 ml of 5% methanol-water, and finally eluting with 5 ml of methanol. The methanol eluted parts were collected, decompressed in water at 37°C, rotated, and dried. The dry feces were ground into powder, and 1.0 g was extracted with 20 ml methanol for 30 min by ultrasonic extraction. After extraction, the supernatant was centrifugally extracted, rotated, and dried at 37°C under reduced pressure. All samples were redissolved with 200 µl methanol and filtered through a 0.45 µm filter. Triple TOF® 5,600+ LC/MS/MS analysis (Xia et al., 2019).

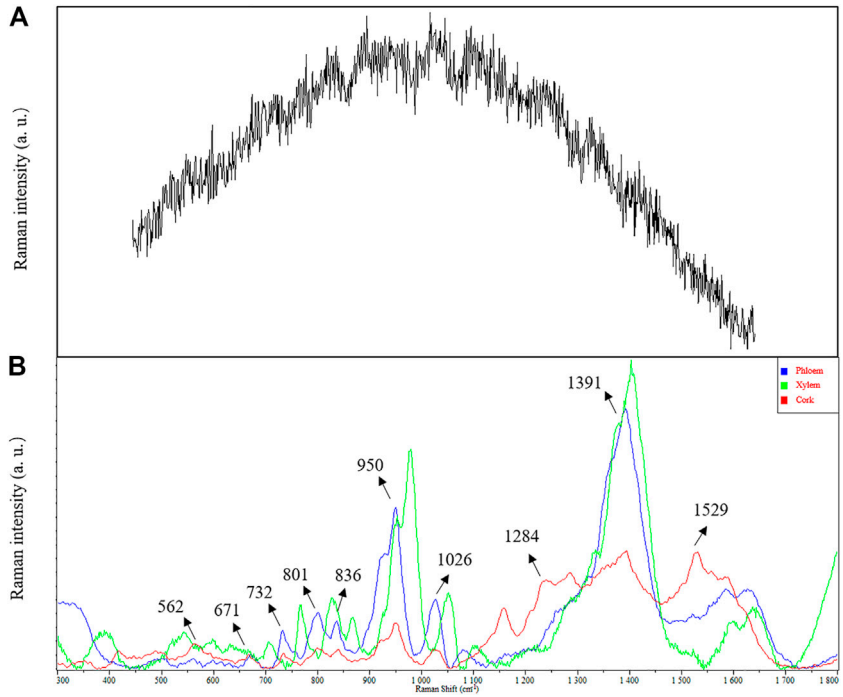

FIGURE 2 | Comparison in SERS and conventional Raman spectra of *Astragalus mongholicus* Bunge. **(A)** conventional Raman spectra. **(B)** SERS.

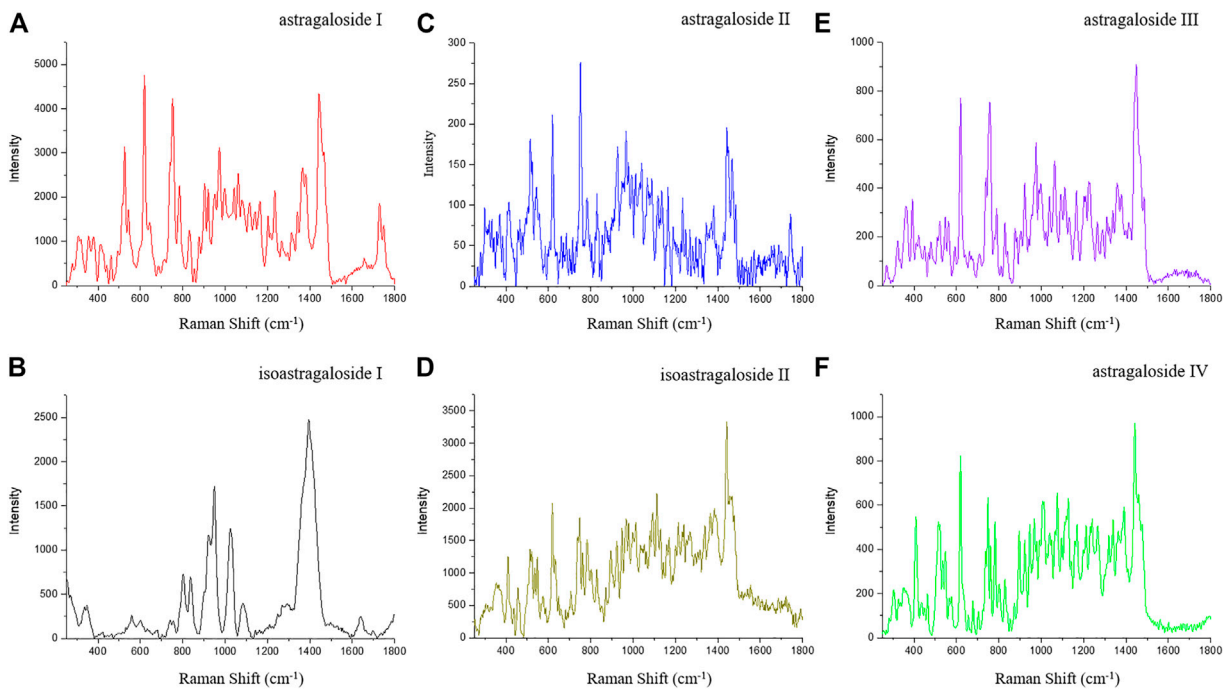

FIGURE 3 | SERS of astragaloside I **(A)**, isoastragaloside I **(B)**, astragaloside II **(C)**, isoastragaloside II **(D)**, astragaloside III **(E)**, and astragaloside IV **(F)**.

UPLC/ESI/Q-TOF-MS Analysis

An AB SCIEX Triple TOF 5600 was used for chromatographic separation. An ACQUITYUPLC CSHTM Phenyl-Hexyl (2.1 mm × 178,100 mm, 1.7 μm; Waters) was utilized for chromatographic separation. The mobile phase consisted of water (A) containing 0.1% (v/v) formic acid and acetonitrile

(B) at a flow rate of 0.4 ml/min. The pressure limit is 15,000 psi. The linear gradient elution program was set as follows: 0–3 min, 3–30% B; 3–23 min, 30–50% B; and 23–35 min, 50–100% B. 5 μl of sample aliquot was injected onto the column, with the column temperature maintained at 35 °C. The MS full scan range was 150–1,200 m/z, and the production scan range was 80–1,000 m/z. The optimized parameters were as follows: capillary voltage, 5.5 kV; declustering potential, 80 V; and collision energy, 35 V. High-purity nitrogen (N2) and high-purity argon (Ar) were separately used as the desolvation and collision gas, respectively. The flow rate of cone gas (N2) was 0.8 L/min. The desolvation and source temperatures were 450 and 100°C, respectively. All data obtained in positive ion mode were acquired and processed by Analyst® TF (V1.6) software (Xu et al., 2018).

RESULTS AND DISCUSSION

Comparison in SRSE and Conventional Raman Spectra of *Astragalus mongholicus* Bunge

In conventional Raman spectrum detection, the Raman effect is very weak due to strong fluorescence background interference (**Figure 2A**). SERS technology effectively quenched the fluorescence, and higher sensitivity was obtained by adsorbing the analyte to the plasma nanoparticles while significantly enhancing the Raman spectral signal (**Figure 2B**). Compared with conventional Raman spectroscopy, when noble metal nanoparticles were used, the conventional surface-enhanced Raman spectroscopy (SERS) enhanced factor was 10^6~10^8 (Albrecht et al., 1977; Jeanmaire and Van Duyne, 1977; Gu et al., 2018). Therefore, SERS has become an interesting method for biological analysis of *Astragalus* and its saponins due to its excellent selectivity and high sensitivity (Stiles et al., 2008; Cialla-May et al., 2017).

SERS Characterization of *Astragalus* Saponins

Astragalus saponins (astragalosides I–IV and isoastragalosides I-II) have similar structures. Although they have characteristic Raman peaks at 732, 801, 836, 950, and 1,026 cm^{-1}, there are significant differences (**Figure 3D**). Compared with the strong Raman signal peak of 1,442 cm^{-1} of other *Astragalus* saponins, the strong Raman signal of isoastragaloside I was 1,391 cm^{-1} (**Figure 3B**). Astragaloside I (**Figures 3A**) and astragaloside II (**Figure 3c**) were 619 cm^{-1} and 715 cm^{-1}, respectively, and 1,391 cm^{-1} was the second strong signal. Astragaloside IV also had a Raman peak of 1,391 cm^{-1} (**Figure 3F**), but the response was very low. The strongest peak of astragaloside III shifted to the right, forming a peak of 1,448 cm^{-1} (**Figure 3E**).

SERS Characterization of *Astragalus mongholicus* Bunge

Obvious Raman characteristic peaks could be observed at 562, 671, 732, 801, 836, 950, 1,026, 1,391, and 1,584 cm^{-1}. 950 and 1,391 cm^{-1} were strong Raman signals, indicating the fingerprint characteristics of biochemical substances in *Astragalus mongholicus* Bunge. Due to the interaction between compounds, the Raman characteristic peaks of a compound in the prepared slices are offset from those of a single compound measured by Raman spectra. The characteristic Raman frequencies of astragaloside saponins (astragalosides I–IV and isoastragalosides I-II) were consistent with those of *Astragalus* saponins at 732, 801, 836, 950, and 1,026 cm^{-1} in *Astragalus mongholicus* Bunge Raman spectrum, indicating that *Astragalus* saponins were contained in *Astragalus* slices (**Figures 2B**). The peak of 1026 cm^{-1} also indicated that the contents of glycogen, amylopectin, amylose, glucuronic acid, and medium glucosamine were consistent with the known biochemical components of *Astragalus mongholicus* Bunge, such as protein, amino acid, starch, and polysaccharide. Compared with phloem and xylem, the Raman peak of 1284 cm^{-1} indicated that the cork of *Astragalus mongholicus* Bunge may contain N-acetylglucose, Deuterium N-acetylglucose, glycogen, cyclohexyl amylose, and maltose. The peak of 1529 cm^{-1} exhibits tertiary nitroalkanes, which are opposed to NO_2 stretching. The signal intensity showed that xylem > phloem > cork.

Characteristic Fragments of Saponins in *Astragalus mongholicus* Bunge

Compound 1 astragaloside I had an $[M + H]^+$ peak at *m/z* 869.4880 (−2.19 ppm), and an *m/z* 671.4162 ($[M + H\text{-Glu-}2{*}H_2O]^+$) fragment ion was formed after the removal of glucose (162 Da) and two molecules of water (36 Da). *m/z* 473.3731, *m/z* 437.3422, and *m/z* 419.3312 were formed by continuous dehydration after aglycone formation, and *m/z* 395.3014 was formed by the loss of 84 Da ($C_4H_4O_2$) based on *m/z* 437.3422 (**Figure 4A**). The $[M + Na]^+$ peak of compound 2 was at *m/z* 849.4619 (0.82 ppm). In the positive ion mode, aglycones were formed with continuous water loss to produce fragments of *m/z* 455.3516, *m/z* 437.3413, and *m/z* 419.3315. In addition, after the aglycones lost two molecules of water, the five-member ring connected to C-17 lost 100 Da ($C_5H_8O_2$) to form fragments of *m/z* 355.2631 and C-17 residue *m/z* 143.1061 ($[C_8H_{15}O_2]^+$) (**Figure 4B**). Compound 3 astragaloside III had an $[M + H]^+$ peak at *m/z* 785.4654 (−4.20 ppm). In tandem mass spectrometry, fragments of *m/z* 587.3915, *m/z* 455.3503, *m/z* 437.3397, *m/z* 419.3296, *m/z* 355.2618, and *m/z* 143.1054 were generated (**Figure 4C**). High-resolution mass spectrometry showed that compound 4 astragaloside IV had an $[M + Na]^+$ ion peak at *m/z* 807.4512 (0.62 ppm) in positive ion mode. In MS/MS, without glucose (162 Da) and two molecules of water (36 Da), *m/z* 587.3957 ($[M + H\text{-Glu-}2 \times H_2O]^+$) was formed. In addition, under the condition of aglycone formation, four molecules of water were successively removed to form *m/z* 473.3636, *m/z* 455.3526, *m/z* 437.3422, *m/z* 419.3318, and the C-17 residue *m/z* 143.1067 ($[C_8H_{15}O_2]^+$) (**Figure 4D**). Compound 5 isoastragaloside I had an $[M + H]^+$ peak at *m/z* 869.4871 (−3.22 ppm). The molecules generated fragments of *m/z* 671.4144, *m/z* 455.3515, *m/z* 437.3410, *m/z* 419.3303, and *m/z* 143.1059 in the secondary mass spectrometry (**Figure 4E**).

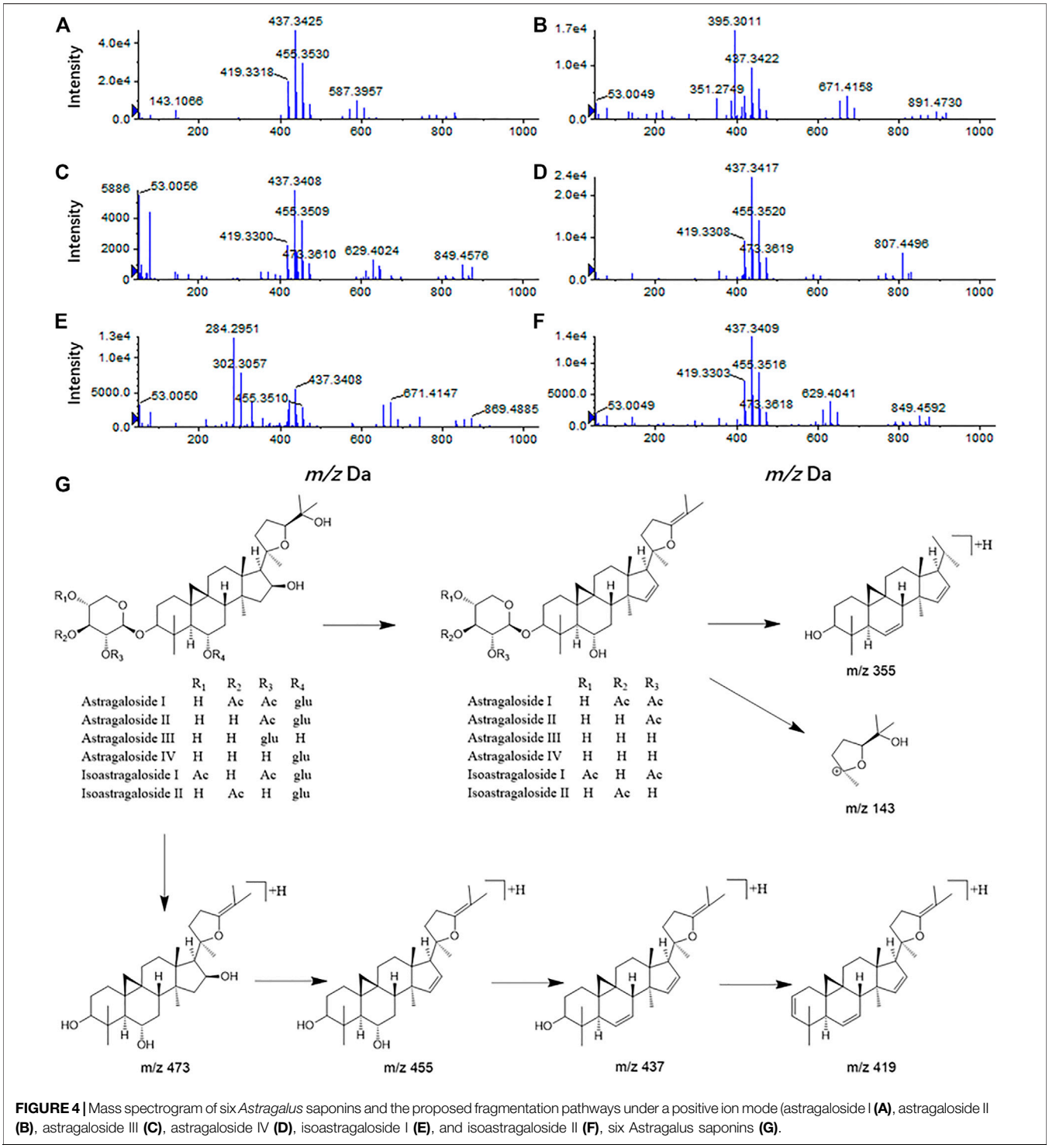

FIGURE 4 | Mass spectrogram of six *Astragalus* saponins and the proposed fragmentation pathways under a positive ion mode (astragaloside I **(A)**, astragaloside II **(B)**, astragaloside III **(C)**, astragaloside IV **(D)**, isoastragaloside I **(E)**, and isoastragaloside II **(F)**, six Astragalus saponins **(G)**.

Compound 6 isoastragaloside II had an $[M + Na]^+$ peak at *m/z* 827.4785 (−0.97 ppm). Fragments of *m/z* 629.4043, *m/z* 473.3619, *m/z* 455.3515, *m/z* 437.3412, *m/z* 419.3305, and *m/z* 355.2826 were produced (**Figure 4F**). Compound 6 was present in large quantities in feces.

Therefore, based on the above analysis of secondary fragments of *Astragalus* saponins compounds in mass spectrometry, *Astragalus* saponins compounds can produce fragments of glucose (162 Da) and two water molecules (36 Da) in mass spectrometry. Based on lysis into aglycones, the fragments of

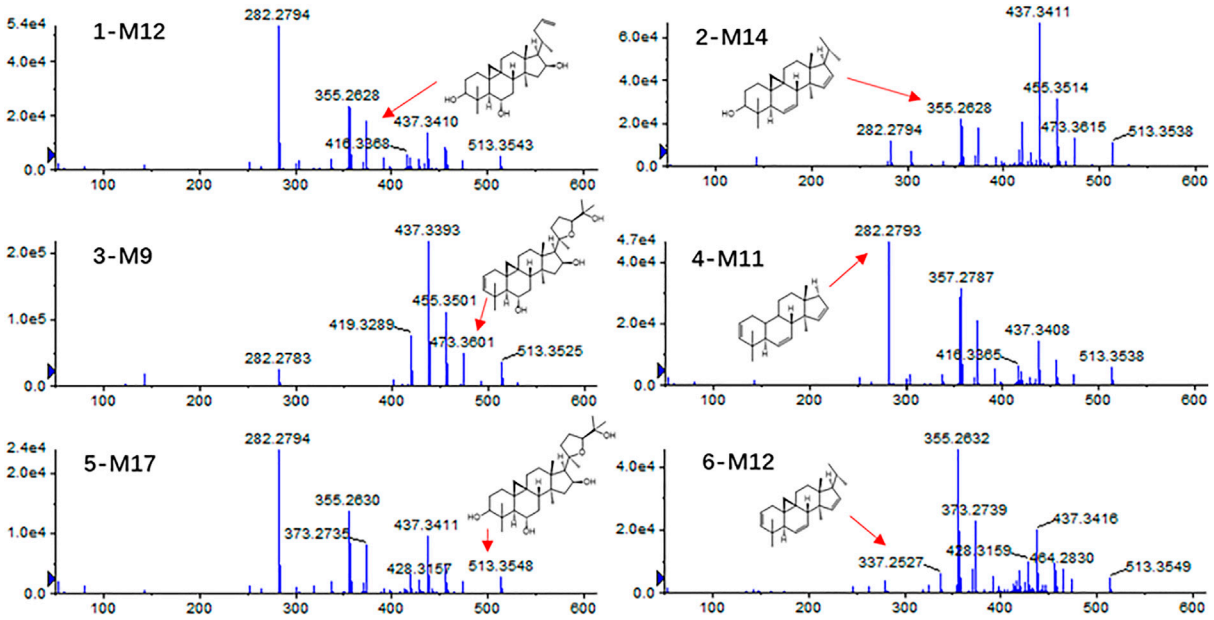

FIGURE 5 | Tandem mass spectra for 1-M12, 2-M14, 3-M9, 4-M11, 5-M17, and 6-M12.

m/z 473, *m/z* 455, *m/z* 437, *m/z* 419, and the aglycones were dehydrated continuously. After the loss of two molecules of water, the five-membered ring connected to C-17 lost 100 Da ($C_5H_8O_2$) to form *m/z* 355 and the C-17 residues *m/z* 143.1061 ($[C_8H_{15}O_2]^+$) (**Figure 4G**).

Metabolite Identification of *Astragalus* Saponins

After oral administration of astragalosides I–IV and isoastragalosides I-II, compound 1 was not detected in the plasma, but it was abundant in feces. A total of 17 metabolites (1-M1 to 1-M17) were detected, among which 11 were detected in plasma and 15 in the urine and feces. In addition, compound 2 produces 18 metabolites (2-M1 to 2-M18) by desiccation, dehydration, dihydroxylation, methylation, and gluconic acid reactions, 11 of which are in the plasma and 17 of which are found in the urine and feces. Additionally, a total of 13 (3-M1 to 3-M13) metabolites with a high content were detected in the plasma, urine, and feces of rats under positive ion mode. In contrast, a total of 14 astragaloside IV-related metabolites (4-M1 to 4-M14) were detected in the rat biosamples. Among them, 4-M4 to 4-M7 were mainly detected in feces, while the remaining metabolites were identified in plasma, urine, and feces. Additionally, twenty-one metabolites (5-M1 to 5-M21) were produced in the blood, urine, and feces of rats after oral administration of isoastragaloside I. All metabolites were present in the plasma, 5-M17 was absent from the urine, and 5-M13 and 5-M14 were absent from the feces. A total of 16 (6-M1 to 6-M16) metabolites were detected in positive ion mode after oral administration of compound 6. There were 14 metabolites in the plasma and urine. Except for 6-M3, all of the other metabolites were present in feces (**Figure 5**).

Astragalosides II–IV and isoastragalosides I-II can cause continuous dehydration, such as metabolites 2-M1 (*m/z* 809.4675, −.48 ppm), 3-M1 (*m/z* 767.4582, −4.56 ppm), 4-M1 (*m/z* 767.4594, 1.56 ppm), 5-M4 (*m/z* 851.4793, −1.41 ppm), 6-M1 (*m/z* 809.4687, −1.73 ppm) identified as the dehydration products of *Astragalus* saponins. The six kinds of *Astragalus* saponins not only underwent deglucosylation and continuous dehydration, but also underwent dexylose reaction, deglucosylation, and continuous dehydration reactions. Furthermore, the metabolites (1-M12, 2-M14, 3-M9, 4-M11, 5-M17, and 6-M12) produced by deglycosylation of six astragalus saponins were the same (**Figure 5**). Except for astragaloside III, all the other saponins caused dexylose reaction, and continuous dehydration reactions occurred. Additionally, the deacetylation of astragalosides I-II and isoastragalosides I-II occurs due to the presence of acetyl groups.

The metabolite 1-M11 (*m/z* 679.405, −1.03 ppm) formed by methylation after deglycosylation of compound 1.1-M16 was a $[M + Na]^+$ peak at *m/z* 501.332 (−4.99 ppm), suggesting that 1-M16 was a metabolite formed by acetylation and tri-dehydration along with the deglucosylation and dexylosylation of 1.1-M17 was determined to be $C_{31}H_{46}O_2$ and produced *m/z* 455.3258, *m/z* 373.2740, *m/z* 355.2630, and *m/z* 318.3008 fragment ions. Hence, it was identified as a tri-dehydration and methylation product of the aglycone moiety of 1. However, 2-M16, molecular formula $C_{38}H_{58}O_{10}$, is a dehydration, deglucosylation, dexylosylation methylation, and glucoaldehydation product of 2. Additionally, 3-M8 was a $[M + H]^+$ peak at *m/z* 807.4493 (−4.71 ppm), suggesting that 3-M8 was a metabolite formed by glucoaldehydation and methylation along with deglycosylation and dehydration of 3. The molecular formula of 3-M13 was $C_{31}H_{52}O_4$ (*m/z* 511.3728). It is a dehydroxylated and methylated metabolite after aglycones formed by the removal of two sugars

TABLE 1 | Characterization of *in vivo* metabolites of eggplant green calyx compounds 1–6 by UPLC/ESI/Q-TOF-MS.

No.	RT (min)	Formula	Ion condition	Theoretical (m/z)	Experimental (m/Z)	Error ($x10^{-6}$)	MS/MS Fragment	Transformations	*p*	u	f
1	16.29	$C_{45}H_{72}O_{16}$	Na	891.4718	891.473	1.35	671.4162,473.3731,437.3422, 419.3312,395.3014	Prototype		a	b
1-M1	11.33	$C_{43}H_{70}O_{15}$	H	827.4793	827.4787	–0.73	629.4055,473.3630,455.3529,437. 3422,419.3314,143.1064	Deacetylation	c	c	c
[d]1-M2	8.92	$C_{41}H_{68}O_{14}$	Na	807.4507	807.4506	–0.12	455.3525,437.3422,355.2635, 297.1854,149.0231	Double-deacetylation	c	c	
1-M3	16.42	$C_{43}H_{70}O_{14}$	Na	833.4663	833.4679	1.92	437.3422,419.3313,395.3011,351. 2747,201.1849,133.0856	Deacetylation/dehydroxylation		c	c
1-M4	11.30	$C_{36}H_{60}O_{10}$	Na	675.4084	675.4075	–1.33	629.4054,473.2629,455.3526,437. 3421,419.3313,143.1066	Double-deacetylation/ dexylose reaction	c	c	c
1-M5	11.38	$C_{36}H_{58}O_9$	H	635.4159	635.4167	1.26	629.4055,473.3632,455.3526,437. 3423,419.3313,143.1066	Deacetylation/dexylose reaction/ dehydration	c	c	a
1-M6	11.32	$C_{36}H_{56}O_8$	H	617.4053	617.404	2.11	473.3629,455.3517,437.3419, 419.3304,143.1063	Double-deacetylation/ dexylcosylation/ double-dehydration	c	c	c
1-M7	11.30	$C_{36}H_{54}O_7$	H	599.3948	599.3939	-1.50	473.3629,455.3526,437.3421, 419.3313,143.1066	Double-deacetylation/ dexylcosylation/tri-dehydration	c	c	c
1-M8	16.37	$C_{39}H_{60}O_{10}$	H	689.4265	689.4268	0.44	473.3627,437.3422,419.3310,395.3011, 351.2749,217.0704	Deglucosylation/dehydration		a	c
1-M9	16.31	$C_{39}H_{58}O_9$	H	671.4159	671.4151	–1.19	473.3625,455.3524,437.3420,419. 3314,395.3012,217.0705	Deglucosylation/double- dehydration		a	a
1-M10	16.34	$C_{39}H_{56}O_8$	H	653.4053	653.4057	0.61	473.3631,437.3420,419.3312,395. 3013,351.2749,133.0856	Deglucosylation/tri-dehydration		a	c
1-M11	26.94	$C_{37}H_{58}O_{11}$	H	679.4057	679.405	–1.03	635.3782,547.3257,397.3845,299.2014,149.0234	Deglucosylation/double- demethylation	c	a	
[d]1-M12	15.97	$C_{30}H_{50}O_5$	Na	513.3556	513.3544	–2.34	457.3419,373.2737,355.2632,337. 2524,282.2796,159.1162	Double-deacetylation/ dexylcosylation/deglucosylation	a	a	c
1-M13	11.36	$C_{30}H_{48}O_4$	H	473.3631	473.3632	0.21	455.3527,437.3423,419.3314, 175.0598,143.1065	Deglucosylation/double- deacetylation/ dexylcosylation/ dehydration	a	a	a
1-M14	11.28	$C_{30}H_{46}O_3$	H	455.3525	455.3529	0.88	437.3422,419.3313,285.0760, 175.0600,143.1065	Deglucosylation/double- deacetylation/ dexylcosylation/ double-dehydration	a	a	a
1-M15	11.25	$C_{30}H_{44}O_2$	H	437.342	437.342	0.00	419.2212,285.0758,175.0594,143.1062	Double-deacetylation/ dexylcosylation/ deglucosylation/tri-dehydration	b	a	a
1-M16	10.56	$C_{32}H_{46}O_3$	Na	501.3345	501.332	–4.99	473.3262,391.2841,373.2737,355.2631	Double-deacetylation/ dexylcosylation/ deglucosylation/tri-dehydration/ acetylation			b
1-M17	8.34	$C_{31}H_{46}O_2$	Na	473.3396	473.3372	–5.07	455.3258,373.2740,355.2630,318.3008	Double-deacetylation/ dexylcosylation/ deglucosylation/tri-dehydration/ methylation			b

(Continued on following page)

TABLE 1 | (*Continued*) Characterization of *in vivo* metabolites of eggplant green calyx compounds 1–6 by UPLC/ESI/Q-TOF-MS.

No.	RT (min)	Formula	Ion condition	Theoretical (m/z)	Experimental (m/Z)	Error ($x10^{-6}$)	MS/MS Fragment	Transformations	*p*	u	f
2	11.35	$C_{43}H_{70}O_{15}$	Na	849.4612	849.4619	0.82	473.3622,455.3516,437.3413, 419.3315,355.2631,143.1061	Prototype	c	a	b
2-M1	11.33	$C_{43}H_{68}O_{14}$	H	809.4687	809.4675	−1.48	635,4,176,611.3944,473.3626, 455.3519,437.3410, 419.3306,401.3192,297.2240,143.1057	Dehydration		c	c
2-M2	19.95	$C_{43}H_{66}O_{13}$	H	791.4582	791.4588	0.76	655.2749,629.4038,537.2873,437.3411,419.3308, 373.2735,355.2633,317.2475,143.1060	Double-dehydration		c	c
[d]2-M3	8.98	$C_{41}H_{68}O_{14}$	H	785.4687	785.4677	−1.27	587.3940,473.3620,455.3520,437.3413,419.3306, 373.2736,355.2631,337.2524,143.1061	Deacetylation		a	a
2-M4	12.92	$C_{41}H_{68}O_{13}$	Na	791.4558	791.4575	2.15	473.3362,455.3514,437. 3414,373.2736,355.2635,143.1060	Deacetylation/dehydroxylation		c	c
2-M5	11.16	$C_{36}H_{60}O_{10}$	Na	675.4084	675.4073	−1.63	635.4174,599.3935,473.3622,455.3519, 437.3413,419,3,306,401.3202,143.1059	Deacetylation/dexylcosylation	c	c	a
2-M6	11.25	$C_{36}H_{58}O_9$	H	635.4159	635.4177	2.83	473.3619,455.3513437.3412,419.3303,143.1060	Deacetylation/dexylcosylation/ dehydration		c	a
2-M7	11.21	$C_{36}H_{56}O_8$	H	617.4053	617.4039	−2.27	473.3617,455.3518,437,3,413,373. 2735,355.2630,143.1062	Deacetylation/dexylcosylation/ double-dehydration	c	c	a
2-M8	11.33	$C_{36}H_{54}O_7$	H	599.3948	599.3927	−3.50	473.3618,455.3520,437. 3415,419.3307,143.1067	Deacetylation/dexylcosylation/ tri-dehydration	c	a	a
2-M9	12.95	$C_{37}H_{58}O_9$	H	647.4159	647.4131	−4.32	629.4038,537.2873,437.3411,419. 3308,373.2735, 355.2633,317.2475	Deglucosylation/dehydration		a	a
2-M10	11.38	$C_{37}H_{56}O_8$	H	629.4053	629.404	−2.07	473.3624,455.3519,437.3409,373. 2732,355.2631,337.2532,143.1042	Deglucosylation/double-dehydration	c	a	a
2-M11	12.95	$C_{37}H_{54}O_7$	H	611.3948	611.3936	−1.96	455.3511,437.3411, 373.2735,355.2633,317.2475	Deglucosylation/tri-dehydration		a	a
2-M12	11.44	$C_{35}H_{58}O_9$	Na	645.3979	645.3957	−3.41	629.4030,473. 3611,455.3511,437.3407, 419.3300,297.2208,240.2323,175.0598	Deacetylation/deglucose	c	c	
2-M13	12.98	$C_{35}H_{58}O_8$	Na	629.4029	629.4044	2.38	557.3788,455.3506,437.3411,373. 2735,355.2632,317.2476,219.1738	Deacetylation/dehydroxylation/ deglucosylation	c		a
[d]2-M14	15.97	$C_{30}H_{50}O_5$	Na	513.3556	513.3537	−3.70	473.3611,455.3511,437.3408,419.3304, 355.2628,282.2795,143.1065	Deacetylation/dexylcosylation/ deglucosylation	c	c	a
2-M15	11.18	$C_{30}H_{48}O_4$	H	473.3631	473.3618	−2.75	455.3519,437.3414,419. 3309,401.3197,143.1059	Deglucosylation/deacetylation/ dexylcosylation/dehydration	a	a	a
2-M16	11.13	$C_{38}H_{58}O_{10}$	H	675.4108	675.4071	−5.48	473.3620,455.3520,437.3403,419. 3308,401.3198,143.1058	Deglucosylation/deacetylation/ dexylcosylation/dehydration/ glucoaldehydation/methylation	c	c	a
2-M17	11.21	$C_{30}H_{46}O_3$	H	455.3525	455.3517	−1.76	437.3412,419.3307,401.3195143.1058	Deglucosylation/deacetylation/ dexylcosylation/double-dehydration	a	a	b
2-M18	11.23	$C_{30}H_{44}O_2$	H	437.342	437.3413	−1.60	419.3307,389.2679,371. 2577,353.2470,143.1061	Deacetylation/dexylcosylation/ deglucosylation/tri-dehydration	b	b	b
3	9.27	$C_{41}H_{68}O_{14}$	Na	807.4507	807.4496	−4.20	587.3915,455.3503,437.3397, 419.3296,355.2618,143.1054	Prototype	a	a	a
3-M1	9.32	$C_{41}H_{66}O_{13}$	H	767.4582	767.4547	−4.56	587.3912,473.3604,455.3503,437.3399,419. 3292,373.2723,355.2618,2143.1054	Dehydration	c	a	a

(Continued on following page)

TABLE 1 | (*Continued*) Characterization of *in vivo* metabolites of eggplant green calyx compounds 1–6 by UPLC/ESI/Q-TOF-MS.

No.	RT (min)	Formula	Ion condition	Theoretical (m/z)	Experimental (m/Z)	Error ($x10^{-6}$)	MS/MS Fragment	Transformations	*p*	u	f
3-M2	9.35	$C_{41}H_{64}O_{12}$	H	749.4476	749.4435	−5.47	587.3918,455.3505,437.3399,419.3292,373.2721,355.2612,143.1054	Double-dehydration	c	c	a
3-M3	9.24	$C_{41}H_{62}O_{11}$	H	731.437	731.4339	−4.24	587.3918,473.3606,455.3502,437.3397,419.3291,373.2723,355.2618,337.2515,143.1054	Tri-dehydration	c	c	c
3-M4	9.21	$C_{35}H_{58}O_9$	H	623.4159	623.4142	−2.73	587.3939,473.3620,455.3518,437.3412,419.3305,143.1063	Deglucosylation	c	c	
3-M5	9.19	$C_{35}H_{56}O_8$	H	605.4053	605.4016	−6.11	473.3606,455.3502,437.3395,419.3291,371.2565,143.1056	Deglucosylation/dehydration	c	a	a
3-M6	9.15	$C_{35}H_{54}O_7$	H	587.3948	587.3936	−2.04	473.3620,455.3518,437.3411,419.3306,245.0474	Deglucosylation/double-dehydration	c	a	
3-M7	9.23	$C_{35}H_{52}O_6$	H	569.3842	569.3829	−2.28	473.3621,455.3517,437.3413,419.3307,143.1060	Deglucosylation/tri-dehydration	c	c	
3-M8	9.17	$C_{43}H_{66}O_{14}$	H	807.4531	807.4493	−4.71	473.3626,455.3521,437.3416,419.3307,355.2631,143.1065	Deglucosylation/dehydration/glucoaldehydation/methylation	a	c	a
[d]3-M9	15.98	$C_{30}H_{50}O5$	Na	513.3556	513.3551	−3.05	473.3620,455.3518,437.3412,419.3308,143.1061	Dexylcosylation/deglucosylation	c	c	a
3-M10	11.30	$C_{30}H_{48}O_4$	H	473.3631	473.3607	−5.07	455.3504,437.3398,419.3293,373.2724,355.2618,143.1054	Deglucosylation/dexylcosylation/dehydration	a	a	b
3-M11	11.19	$C_{30}H_{46}O_3$	H	455.3525	455.3503	−4.83	437.3399,419.3293,282.2781,373.2723,355.2617,143.1054	Deglucosylation/dexylcosylation/double-dehydration	a	b	b
3-M12	11.25	$C_{33}H_{44}O_2$	H	437.342	437.3401	−4.34	389.2671,371.2569,355.2622,331.2263	Dexylcosylation/deglucosylation/tri-dehydration	b	b	b
3-M13	8.73	$C_{31}H_{52}O_4$	Na	511.3763	511.3728	−6.84	448.3055,430.2952,412.2847,363.3271,355.2635,219.1741	Dexylcosylation/deglucosylation/dehydroxylation/methylation	a		c
4	9.08	$C_{41}H_{68}O_{14}$	Na	807.4507	807.4512	0.62	587.3957,473.3636,455.3526,437.3422,419.3318,143.1067	Prototype	a	a	a
4-M1	9.24	$C_{41}H_{66}O_{13}$	H	767.4582	767.4594	1.56	587.3956,569.3856,473.3636,455.3530,437.3424,419.3319,373.2750,355.2635	Dehydration	c	c	a
4-M2	8.90	$C_{41}H_{64}O_{12}$	H	749.4476	749.448	0.53	587.3953,569.3842,473.3633,455.3529,437.3423,419.3320,373.2743,355.2638	Double-dehydration	c	c	a
4-M3	8.98	$C_{41}H_{62}O_{11}$	H	731.437	731.437	0.00	473.3637,455.3529,437.3425,419.3319,401.3207,297.2217,143.1068	Tri-dehydration	c	c	c
4-M4	11.17	$C_{36}H_{60}O_{10}$	Na	675.4081	675.4061	0.30	473.3614,455.3514,437.3408,419.3302,371.2575,143.1063	Dexylcosylation			a
4-M5	11.23	$C_{36}H_{58}O_9$	H	635.4159	635.4151	1.26	455.3527,437.3423,419.3314,355.2640,143.1062	Dexylcosylation/dehydration			a
4-M6	11.14	$C_{36}H_{56}O_8$	H	617.4053	617.4035	2.92	473.3634,455.3530,437.3425,419.3320,143.1065	Dexylcosylation/double-dehydration			a
4-M7	11.20	$C_{36}H_{54}O_7$	H	599.3948	599.3935	2.17	473.3636,455.3531,437.3425,419.3317,355.2641,143.1067	Dexylcosylation/tri-dehydration			a
4-M8	9.17	$C_{35}H_{56}O_8$	H	605.4053	605.4035	−2.97	587.3937,569.3828,473.3618,455.3515,437.3409,419.3303,373.2735,355.2627	Deglucosylation/dehydration	a	a	a

(Continued on following page)

TABLE 1 | (*Continued*) Characterization of *in vivo* metabolites of eggplant green calyx compounds 1–6 by UPLC/ESI/Q-TOF-MS.

No.	RT (min)	Formula	Ion condition	Theoretical (m/z)	Experimental (m/Z)	Error ($x10^{-6}$)	MS/MS Fragment	Transformations	*p*	u	f
4-M9	8.96	$C_{35}H_{54}O_7$	H	587.3948	587.3933	−2.55	455.3515,437.3410,419.3302,389.2681, 373.2735,355.2628,335.2365	Deglucosylation/double-dehydration	a	a	b
4-M10	9.00	$C_{35}H_{52}O_6$	H	569.3842	569.385	1.41	473.3632,455.3531,437. 3426,419.3317,143.1068	Deglucosylation/tri-dehydration	a	a	a
[d]4-M11	15.96	$C_{30}H_{50}O_5$	Na	513.3556	513.3538	−3.51	455.3510,437.3408,416. 3365,357.2787,282.2793	Dexylcosylation/deglucose	a	a	a
4-M12	9.19	$C_{30}H_{48}O_4$	H	473.3631	473.3635	0.85	455.3531,437.3424,419.3316,389. 2685,355.2645,143.1067	Deglucosylation/ dexylcosylation/dehydration	a	a	a
4-M13	9.36	$C_{30}H_{46}O_3$	H	455.3525	455.3516	−1.98	437.3410,389.2683,373.2735, 355.2630,335.2365,271.1691	Deglucosylation/ dexylcosylation/double-dehydration	b	b	b
4-M14	9.06	$C_{30}H_{44}O_2$	H	437.342	437.3425	1.14	419.3320,355.2640,341. 1055,245.0479,143.1068	Dexylcosylation/ deglucosylation/tri-dehydration	b	b	b
5	17.77	$C_{45}H_{72}O_{16}$	H	869.4899	869.4871	−3.22	671.4144,455.3515,437. 3410,419.3303,143.1059	Prototype	a	a	a
5-M1	14.29	$C_{43}H_{70}O_{15}$	Na	849.4612	849.46	−1.41	647.4132,611.3921,473.3593,437 .3404,357.2786,318.3001,161.1317	Deacetylation	c	c	c
[d]5-M2	9.09	$C_{41}H_{68}O_{14}$	Na	807.4507	807.4496	−1.36	767.4565,617.4022,587.3934,473.3614455.3514,437. 3408,419.3301,355.2625,297.2207,143.1058	Double-deacetylation	c	c	a
5-M3	17.86	$C_{43}H_{70}O_{14}$	Na	833.4663	833.4667	0.48	741.4411,689.4251,671.4145,455.3514,437.3411	Deacetylation/dehydroxylation	c	a	c
5-M4	17.72	$C_{45}H_{70}O_{15}$	H	851.4793	851.4781	−1.41	741.4411,689.4251, 671.4145,455.3514,437. 3411,330.3005,302.3056,284.2951	Dehydration	c	a	c
5-M5	17.88	$C_{45}H_{66}O_{13}$	H	815.4582	815.4584	0.25	741.4411,689.4251,671.4145,455.3514,437.3411, 330.3005,302.3056,284.2951	Tri-dehydration	c	c	c
5-M6	11.13	$C_{36}H_{60}O_{10}$	Na	675.4084	675.4067	−2.52	473.3616,455.3517,437.3411,419.3302,143.1061	Double-deacetylation/ dexylcosylation	c	c	a
5-M7	11.31	$C_{36}H_{58}O_9$	H	635.4159	635.4151	−1.26	473.3615,455.3515,437.3410, 419.3302,355.2622,143.1061	Double-deacetylation/ dexylcosylation/dehydration	c	a	a
5-M8	11.34	$C_{36}H_{56}O_8$	H	617.4053	617.4044	−1.46	473.3619,455.3516,437.3410. 419.3304,401.3195,143.1062	Double-deacetylation/ dexylcosylation/double-dehydration	c	c	a
5-M9	11.18	$C_{36}H_{54}O_7$	H	599.3948	599.3924	−4.00	473.3617,455.3515, 437.3409,419.3304,143.1062	Double-deacetylation/ dexylcosylation/tri-dehydration	c	c	a
5-M10	17.75	$C_{39}H_{60}O_{10}$	H	689.4265	689.4247	−2.61	671.4145,437.3410,355.2628,330. 3001,302.3054,284.2947,217.0698	Deglucosylation/dehydration	c	c	c
5-M11	17.80	$C_{39}H_{58}O_9$	H	671.4159	671.4145	−2.09	653.4039,455.3514,437.3411,330. 3005,302.3056,284.2951,284.2951,217.0697	Deglucosylation/double-dehydration	a	a	a
5-M12	17.83	$C_{39}H_{56}O_8$	H	653.4053	653.404	−1.99	455.3510,437.3408,419.3303,355.2627, 330.3005,302.3057,284.2951,217.0698	Deglucosylation/tri-dehydration	a	a	a
5-M13	14.97	$C_{37}H_{60}O_{10}$	Na	687.4084	687.4063	−3.05	566.3233,460.2692,415.2111,318.3001,267.1221	Deacetylation/deglucosylation	c	c	
5-M14	15.02	$C_{35}H_{58}O_9$	Na	645.3979	645.3979	0.00	503.1080,429.0882,318.3008,219.1739	double-deacetylation/ deglucosylation	c	c	
5-M15	11.42	$C_{43}H_{70}O_{15}$	Na	849.4612	849.4589	−2.71	698.4831,639.4035,473.3615,455.2519,437. 3411,419.3304,373.2726,143.1060	Double-deacetylation/ deglucosylation/ glucoaldehydation/double-methylation	c	c	c

(Continued on following page)

TABLE 1 | (*Continued*) Characterization of *in vivo* metabolites of eggplant green calyx compounds 1–6 by UPLC/ESI/Q-TOF-MS.

No.	RT (min)	Formula	Ion condition	Theoretical (m/z)	Experimental (m/Z)	Error ($x10^{-6}$)	MS/MS Fragment	Transformations	*p*	u	f
5-M16	17.81	$C_{37}H_{60}O_9$	Na	671.4135	671.4149	2.09	635.3962,455.3518, 437.3411,419.3307,217.0701	Deacetylation/ dehydroxylation/ deglucosylation	a	a	a
[d]5-M17	15.97	$C_{30}H_{50}O_5$	Na	513.3556	513.3539	−3.31	455.3517,437.3411,419.3303,373. 3736,355.2628,337.2528,143.1059	Double-deacetylation/ dexylcosylation/deglucosylation	c		a
5-M18	11.26	$C_{30}H_{48}O_4$	H	473.3631	473.3613	−3.80	455.3518,437.3412,419.3305,401.3198, 353.2467,175.0593,143.1061	Deglucosylation/ double-deacetylation/ dexylcosylation/ dehydration	c	a	a
5-M19	11.20	$C_{30}H_{46}O_3$	H	455.3525	455.3516	−1.98	437.3410,419.3303,401.3196,371. 2577,355.2570,143.1059	Deglucosylation/ double-deacetylation/ dexylcosylation/ double-dehydration	a	a	b
5-M20	11.15	$C_{30}H_{44}O_2$	H	437.342	437.341	−2.29	419.3302,401.3196,297.3306,143.1061	Double-deacetylation/ dexylcosylation/ deglucosylation/tri-dehydration	a	a	b
5-M21	8.40	$C_{31}H_{46}O_2$	Na	473.3396	473.3364	−6.76	413.3042,371.2574,355. 2629,318.3006	Double-deacetylation/ dexylcosylation/ deglucosylation/tri-dehydration/ methylation	a	c	c
6	11.34	$C_{43}H_{70}O_{15}$	Na	849.4612	849.4592	−0.97	629.4043,473. 3619,455.3515, 437.3412,419.3305, 355.2826	Prototype	c	c	a
6-M1	12.90	$C_{43}H_{68}O_{14}$	H	809.4687	809.4673	−1.73	629.4045,473.3621, 455.3518,437.3412,419. 3309,401.3197,297. 2210,143.1062	Dehydration	c	c	a
6-M2	11.58	$C_{43}H_{66}O_{13}$	H	791.4582	791.457	−1.52	473.3621,455.3520,437,3414,419,3,307, 371.2581,317.2477,143.1063	Double-dehydration		c	a
[d]6-M3	8.93	$C_{41}H_{68}O_{14}$	Na	807.4507	807.4487	−2.48	587.3937,473. 3622,455.3515,437. 3412,419.3306, 355.2628,143.1058	Deacetylation	c	c	
6-M4	11.42	$C_{41}H_{68}O_{13}$	Na	791.4558	791.4567	1.14	647.4149,629.4047,611.3941, 473.3622,455.3521,437.3416, 419.3308,355.2631, 175.0594,143.1062	Deacetylation/dehydroxylation	c	c	a
6-M5	11.15	$C_{36}H_{60}O_{10}$	Na	675.4084	675.4071	−1.92	635.4183,480.3137,455.3516, 437.3408,419.3306	Deacetylation/dexylcosylation	c	c	a
6-M6	11.17	$C_{36}H_{58}O_9$	H	635.4159	635.4179	3.15	455.3514,437.3407,419. 3305,335.2379,143.1061	Deacetylation/dexylcosylation/ dehydration	c	c	a
6-M7	11.12	$C_{36}H_{56}O_8$	H	617.4053	617.4046	−1.13	534.3410,498.2881, 473.3619,455.3519,437. 3409,419.3307,389. 2684,335.2572,143.1061	Deacetylation/dexylcosylation/ double-dehydration	c	c	a
6-M8	11.31	$C_{37}H_{58}O_9$	H	647.4159	647.4153	−0.93		Deglucosylation/dehydration	a	a	a

(Continued on following page)

TABLE 1 | (*Continued*) Characterization of *in vivo* metabolites of eggplant green calyx compounds 1–6 by UPLC/ESI/Q-TOF-MS.

No.	RT (min)	Formula	Ion condition	Theoretical (m/z)	Experimental (m/Z)	Error ($x10^{-6}$)	MS/MS Fragment	Transformations	p	u	f
							629.4047,611.3940,473.3618,455.3512, 437.3414, 419.3308,373.2731, 355.2630,175.0596,143.1060				
6-M9	11.39	$C_{37}H_{56}O_8$	H	629.4053	629.4047	–0.95	473.3622,455.3520,437.3414, 419.3308,355.2628,175.0591,143.1060	Deglucosylation/double-dehydration	[a]	[a]	[a]
6-M10	11.28	$C_{37}H_{54}O_7$	H	611.3948	611.3939	–1.47	473.3621,455. 3519,437.3413,419. 3307,371.2579,355. 2631,175.0594,143.1062	Deglucosylation/tri-dehydration	[a]	[a]	[a]
6-M11	11.36	$C_{35}H_{58}O_8$	Na	629.4029	629.4044	2.38	473.3620,455.3519,437.3413,419. 3308,355.2624, 175.0591,143.1059	Deacetylation/dehydroxylation/ deglucosylation	[a]	[a]	[a]
[d]6-M12	15.99	$C_{30}H_{50}O_5$	Na	513.3556	513.3549	–1.36	455.3518,437.3416,373.2739, 355.2632,337.2527	Deacetylation/dexylcosylation/ deglucosylation	[c]		[a]
6-M13	11.25	$C_{30}H_{48}O_4$	H	473.3631	473.3622	–1.90	455.3519,437.3413,419.3307, 401.3197,297. 2210,143.1061	Deglucosylation/deacetylation/ dexylcosylation/dehydration	[a]	[a]	[b]
6-M14	11.23	$C_{30}H_{46}O_3$	H	455.3525	455.3518	–1.54	437.3414,419.3309,401. 3194,297.2208,143.1062	Deglucosylation/deacetylation/ dexylcosylation/double-dehydration	[a]	[b]	[b]
6-M15	11.21	$C_{30}H_{44}O_2$	H	437.342	437.3414	–1.37	419.3307,401.3202,297.2213,143.1056	Deacetylation/dexylcosylation/ deglucosylation/tri-dehydration	[b]	[b]	[b]
6-M16	6.70	$C_{32}H_{48}O_4$	Na	519.345	519.3431	–3.66	389.2686,371.2579,333.2425	Deglucosylation/deacetylation/ dexylcosylation/double-dehydration/Acetylation			[b]

[d]*Identified by comparing with reference standards.*
[b]*Detected at the highest abundance.*
[a]*detected at comparatively high abundance.*
[c]*detected at detected at low abundance (+++>++>+).*
p *plasma; u: urine; f: feces.*

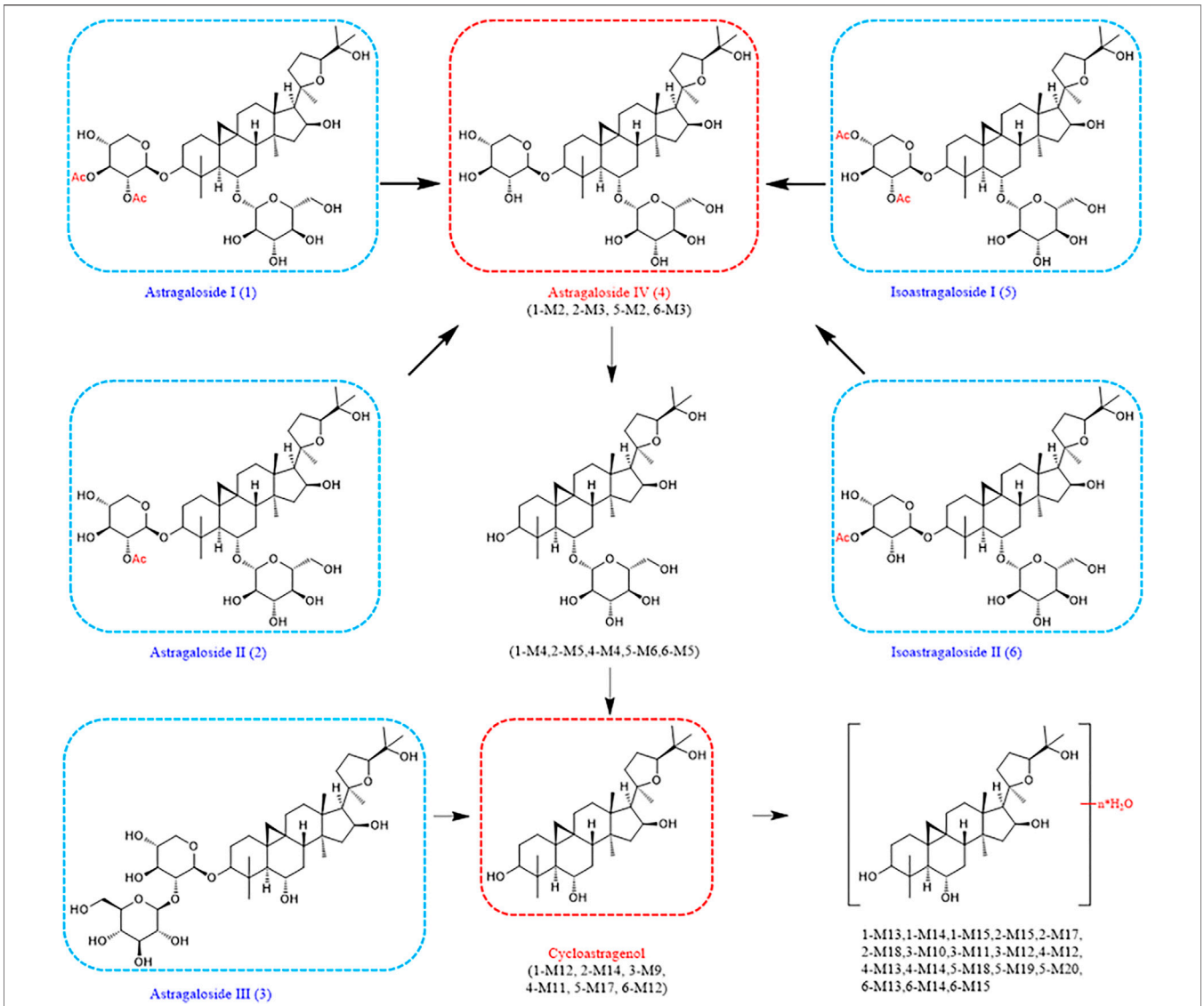

FIGURE 6 | Metabolic pathways of compounds 1–6 in *Astragalus mongholicus* Bunge.

from compound 3. In contrast, the $[M + Na]^+$ peak of 5-M15 at *m/z* 849.4589 (−2.71 ppm) indicated five deacetylation, deglycosylation, methylation, and glucoaldehydation derivatives. 5-M21 was shown to be $C_{31}H_{46}O_2$ (*m/z* 473.3364) and it is a five deacetylation, deglycosylation, dexylose reaction, dehydration, and methylation derivatives. 6-M16 was confirmed as $C_{32}H_{48}O_4$, which is an acetylated derivative after compound 6 aglycones dehydration products (**Table. 1**).

Metabolic Pathways of Compounds 1–6 in *Astragalus mongholicus* Bunge

Astragalus saponins 1–6 could not easily be used as a prototype component in plasma after oral administration, but they had a higher content in feces (Fu et al., 2019). This may be related to the physical and chemical properties of saponins, such as their high molecular weight, high hydrogen bondability, polymer flexibility, and poor membrane permeability, leading to a decrease in their bioavailability (Gao et al., 2012; Yu et al., 2012). Among the phase I metabolites, a relatively large number of dehydration products can be observed in biological samples, all of which are formed by the dehydration of hydroxyl groups at the 3, 6, and 16 positions, which is consistent with our previous findings (Cheng and Wei, 2014; Chen et al., 2018; Lü et al., 2019). Compounds 1, 2, 5, and 6 also had diacetyl metabolites in their biological samples due to the presence of one or two acetyl substitutions on glucose. In addition, compounds 1, 2, and 5 had glycolaldehyde and methylation and acetylation of compound 6, which are all unique metabolic forms but have not been reported previously (Wan et al., 2016; Chen et al., 2019; Li et al., 2021).

In identifying metabolites of astragaloside IV, 12 new dehydration products were added compared with the

previously known ones (Cheng and Wei, 2014). Other pharmacological activities of *Astragalus* saponins have been less studied, all of which were the first metabolites studied here. Interestingly, these six *Astragalus* saponins all underwent deglycosylation and dexylose reaction reactions in the body to form the same aglycones that then underwent dehydration. More importantly, astragalosides I-II and isoastragalosides I-II can form astragaloside IV, which has increased activity after removing the acetyl group (**Figure 6**). This leads us to speculate that astragalosides I-II and isoastragalosides I-II may have the same potential anti-inflammatory, antifibrotic, antioxidative stress, antiasthma, antidiabetes, immunoregulation, and cardioprotective effects as astragaloside IV (Li et al., 2017).

CONCLUSION

In this study, silver nanoparticles obtained by sodium borohydride reduction were first used as the enhanced substrate to detect astragaloside I (1), astragaloside II (2), astragaloside III (3), astragaloside IV, (4) isoastragaloside I (5), and isoastragaloside II (6) in the phloem, xylem, and cork, by SERS. The Raman signal and mass spectrometry decomposition of the detection results were analyzed. In the SERS spectrum of astragalus slices, the characteristic peaks were observed at 562, 671, 732, 801, 836, 950, 1,026, 1,391, and 1,584 cm^{-1}, among which 950 cm^{-1} and 1,391 cm^{-1} were strong SERS signals. The SERS peak locations obtained could be attributed to biochemical substances such as *Astragalus* saponin, glucose, and acetamide. The technology of SERS can be used as a new, quick, and effective detection method for biochemical analysis, quality control, and discrimination of decocting pieces of *Astragalus mongholicus* Bunge or other Chinese medicine. UPLC/ESI/QTOF-MS was used to detect six representative *Astragalus* saponins in biological samples after the oral administration of *Astragalus mongholicus* Bunge to rats. Their metabolites were identified, and their metabolic pathways and transformation formed *in vivo* were summarized. The metabolism of *Astragalus* saponins 1–6 mainly involved dehydration, deacetylation, dihydroxylation, deglycosylation, methylation, deacetylation, and glycol dehydration reactions. Ten metabolites were identified by comparison with reference standards. According to earlier studies, this is the first study on the metabolism of these *Astragalus* saponins. The most valuable is that astragalosides I-II and isoastragalosides I-II can form astragaloside IV with better activity after removing acetyl groups. This study is of great significance for applying SERS spectroscopy in the identification of TCM and predicting the metabolism of other saponins with similar structures in *Astragalus mongholicus* Bunge, which can promote the systematic study of multi-component metabolism and clinical efficacy of the *Astragalus mongholicus* Bunge.

DATA AVAILABILITY STATEMENT

The original contributions presented in the study are included in the article/Supplementary Material, Further inquiries can be directed to the corresponding authors.

ETHICS STATEMENT

The animal study was reviewed and approved by the Animal Care and Use Committee of Harbin Medical University.

AUTHOR CONTRIBUTIONS

QW, BY, SK, and YL participated in the research design. SK, SO, YL, TM, YZ, JZ, and MX conducted the experiments. QW, SK, and YL performed data analysis. QW, SK, SO, YL, MX, and JZ contributed to the writing of the manuscript.

FUNDING

This work was supported by the National Natural Science Foundation of China (Grant no. 82003919), Excellent Young Talents Funding of Natural Science Foundation of Heilongjiang Province in 2020 (Grant no. YQ 2020H008), Starting fund for postdoctoral of Heilongjiang Province (Grant no. LBH-Q19049), and Heilongjiang Touyan Innovation Team Program.

ACKNOWLEDGMENTS

The authors acknowledge the contributions of specific colleagues, institutions, or agencies that were very beneficial.

REFERENCES

Albrecht, M. G., Creighton, J. A., and Chem, J. A. (1977). Anomalously Intense Raman Spectra of Pyridine at a Silver Electrode. *J. Am. Chem. Soc.* 99, 5215–5217. doi:10.1021/ja00457a071

Chen, M. Y., Shao, L., Zhang, W., Wang, C. Z., Zhou, H. H., Huang, W. H., et al. (2018). Metabolic Analysis of Panax Notoginseng Saponins with Gut Microbiota-Mediated Biotransformation by HPLC-DAD-Q-TOF-MS/MS. *J. Pharm. Biomed. Anal.* 150, 199–207. doi:10.1016/j.jpba.2017.12.011

Chen, X., Xu, L., Guo, S., Wang, Z., Jiang, L., Wang, F., et al. (2019). Profiling and Comparison of the Metabolites of Diosmetin and Diosmin in Rat Urine, Plasma and Feces Using UHPLC-LTQ-Orbitrap MSn. *J. Chromatogr. B Analyt Technol. Biomed. Life Sci.* 1124, 58–71. doi:10.1016/j.jchromb.2019.05.030

Cheng, X., Wei, B., Sun, L., Hu, X., Liang, J., and Chen, Y. (2016). Astragaloside I Stimulates Osteoblast Differentiation through the Wnt/β-Catenin Signaling Pathway. *Phytother Res.* 30, 1680–1688. doi:10.1002/ptr.5674

Cheng, X. D., and Wei, M. G. (2014). Profiling the Metabolism of Astragaloside IV by Ultra Performance Liquid Chromatography Coupled with Quadrupole/time-Of-Flight Mass Spectrometry. *Molecules* 19, 18881–18896. doi:10.3390/molecules191118881

Cialla-May, D., Zheng, X. S., Weber, K., and Popp, J. (2017). Recent Progress in Surface-Enhanced Raman Spectroscopy for Biological and Biomedical Applications: from Cells to Clinics. *Chem. Soc. Rev.* 46, 3945–3961. doi:10.1039/c7cs00172j

Fu, J., Wu, H., Wu, H., Deng, R., and Li, F. (2019). Chemical and Metabolic Analysis of Achyranthes Bidentate Saponins with Intestinal Microflora-Mediated Biotransformation by Ultra-performance Liquid Chromatography-Quadrupole Time-Of-Flight Mass Spectrometry Coupled with Metabolism Platform. *J. Pharm. Biomed. Anal.* 170, 305–320. doi:10.1016/j.jpba.2019.03.041

Gao, S., Basu, S., Yang, Z., Deb, A., and Hu, M. (2012). Bioavailability Challenges Associated with Development of Saponins as Therapeutic and Chemopreventive Agents. *Curr. Drug Targets* 13, 1885–1899. doi:10.2174/138945012804545498

Gu, X., Trujillo, M. J., Olson, J. E., and Camden, J. P. (2018). SERS Sensors: Recent Developments and a Generalized Classification Scheme Based on the Signal Origin, Annual Review of Analytical Chemistry. *Annu. Rev. Anal. Chem. (Palo Alto Calif.* 11, 147–169. doi:10.1146/annurev-anchem-061417-125724

Jeanmaire, D. L., and Van Duyne, R. P. (1977). Surface Raman Spectroelectrochemistry. *J. Electroanalytical Chem. Interfacial Electrochemistry* 84, 1–20. doi:10.1016/S0022-0728(77)80224-6

Lee, S. M., Jeong, J. S., Kwon, H. J., and Hong, S. P. (2017a). Quantification of Isoflavonoids and Triterpene Saponins in Astragali Radix, the Root of Astragalus Mongholicus, via Reverse-phase High-Performance Liquid Chromatography Coupled with Integrated Pulsed Amperometric Detection. *J. Chromatogr. B Analyt Technol. Biomed. Life Sci.* 1070, 76–81. doi:10.1016/j.jchromb.2017.10.046

Lee, S. Y., Tsai, W. C., Lin, J. C., Ahmetaj-Shala, B., Huang, S. F., Chang, W. L., et al. (2017b). Astragaloside II Promotes Intestinal Epithelial Repair by Enhancing L-Arginine Uptake and Activating the mTOR Pathway. *Sci. Rep.* 7, 12302. doi:10.1038/s41598-017-12435-y

Li, C. X., Liang, J., Song, Y., Chai, J. H., Kuang, H. X., and Xia, Y. G. (2021). Structural Characterization of the Metabolites of Orally Ingested Hederasaponin B, a Natural Saponin that Is Isolated from Acanthopanax Senticosus Leaves by Liquid Chromatography-Mass Spectrometry. *J. Pharm. Biomed. Anal.* 197, 113929. doi:10.1016/j.jpba.2021.113929

Li, L., Hou, X., Xu, R., Liu, C., and Tu, M. (2017). Research Review on the Pharmacological Effects of Astragaloside IV. *Fundam. Clin. Pharmacol.* 31, 17–36. doi:10.1111/fcp.12232

Liu, M., Li, P., Zeng, X., Wu, H., Su, W., and He, J. (2015). Identification and Pharmacokinetics of Multiple Potential Bioactive Constituents after Oral Administration of Radix Astragali on Cyclophosphamide-Induced Immunosuppression in Balb/c Mice. *Int. J. Mol. Sci.* 16, 5047–5071. doi:10.3390/ijms16035047

Liu, P., Zhao, H., and Luo, Y. (2017). Anti-Aging Implications of Astragalus Mongholicus (Huangqi): A Well-Known Chinese Tonic. *Aging Dis.* 8, 868–886. doi:10.14336/AD.2017.0816

Lü, S., Zhao, S., Zhao, M., Guo, Y., Li, G., Yang, B., et al. (2019). Systematic Screening and Characterization of Prototype Constituents and Metabolites of Triterpenoid Saponins of Caulopphyllum Robustum Maxim Using UPLC-LTQ Orbitrap MS after Oral Administration in Rats. *J. Pharm. Biomed. Anal.* 168, 75–82. doi:10.1016/j.jpba.2019.02.005

Mei, X., Wang, Y., Liu, Z., Wang, S., Dong, F., Wang, Z., et al. (2020). The Chemical Transformations for Radix Astragali via Different Alkaline Wash Conditions by Quantitative and Qualitative Analyses. *J. Pharm. Biomed. Anal.* 185, 185113164. doi:10.1016/j.jpba.2020.113164

Shi, J., Zheng, L., Lin, Z., Hou, C., Liu, W., Yan, T., et al. (2015). Study of Pharmacokinetic Profiles and Characteristics of Active Components and Their Metabolites in Rat Plasma Following Oral Administration of the Water Extract of Astragalus Mongholicus Bunge Using UPLC-MS/MS. *J. Ethnopharmacol* 169, 183–194. doi:10.1016/j.jep.2015.04.019

Song, J. Z., Mo, S. F., Yip, Y. K., Qiao, C. F., Han, Q. B., and Xu, H. X. (2007). Development of Microwave Assisted Extraction for the Simultaneous Determination of Isoflavonoids and Saponins in Radix Astragali by High Performance Liquid Chromatography. *J. Sep. Sci.* 30, 819–824. doi:10.1002/jssc.200600340

Stiles, P. L., Dieringer, J. A., and Shah, X. (2008). Duyne. Surface-Enhanced Raman Spectroscopy. *Annu. Rev. Anal. Chem.* 1, 601–626. doi:10.1007/s00216-009-2864-z10.1146/annurev.anchem.1.031207.112814

Sun, W. X., Zhang, Z. F., Xie, J., He, Y., Cheng, Y., Ding, L. S., et al. (2019). Determination of an Astragaloside IV Derivative LS-102 in Plasma by Ultra-performance Liquid Chromatography Tandem Mass Spectrometry in Dog Plasma and its Application in a Pharmacokinetic Study. *Phytomedicine* 53, 243–251. doi:10.1016/j.phymed.2018.09.019

Wan, J. Y., Wang, C. Z., Liu, Z., Zhang, Q. H., Musch, M. W., Bissonnette, M., et al. (2016). Determination of American Ginseng Saponins and Their Metabolites in Human Plasma, Urine and Feces Samples by Liquid Chromatography Coupled with Quadrupole Time-Of-Flight Mass Spectrometry. *J. Chromatogr. B Analyt Technol. Biomed. Life Sci.* 1015-1016, 62–73. doi:10.1016/j.jchromb.2016.02.008

Wang, Q., Qiao, X., Qian, Y., Liu, C. F., Yang, Y. F., Ji, S., et al. (2014). Metabolites Identification of Glycyrin and Glycyrol, Bioactive Coumarins from Licorice. *J. Chromatogr. B Analyt Technol. Biomed. Life Sci.* 983-984, 39–46. doi:10.1016/j.jchromb.2014.12.028

Xia, C., Liu, Y., Qi, H., Niu, L., Zhu, Y., Lu, W., et al. (2019). Characterization of the Metabolic Fate of Datura Metal Seed Extract and its Main Constituents in Rats. *Front. Pharmacol.* 28 (10), 571. doi:10.1016/j.jchromb.2014.12.02810.3389/fphar.2019.00571

Xu, S., Liu, Y., Xiang, L., Zhou, F., Li, H., Su, Y., et al. (2018). Metabolites Identification of Bioactive Compounds Daturataturin A, Daturametelin I, N-Trans-Feruloyltyramine, and Cannabisin F from the Seeds of Datura Metal in Rats. *Front. Pharmacol.* 9 (9), 731. doi:10.3389/fphar.2018.00731

Yang, J., Yin, C., Miao, X., Meng, X., Liu, Z., and Hu, L. (2020). Rapid Discrimination of Adulteration in Radix Astragali Combining Diffuse Reflectance Mid-infrared Fourier Transform Spectroscopy with Chemometrics. *Spectrochim Acta A. Mol. Biomol. Spectrosc.* 5 (248), 119251. doi:10.1016/j.saa.2020.119251

Yu, K., Chen, F., and Li, C. (2012). Absorption, Disposition, and Pharmacokinetics of Saponins from Chinese Medicinal Herbs: what Do We Know and what Do We Need to Know More? *Curr. Drug Metab.* 13, 577–598. doi:10.2174/1389200211209050577

Yuan, Y. M., Gao, J. W., Shi, Z., Huang, P., Lu, Y. S., Yao, M. C., et al. (2012). Herb-drug Pharmacokinetic Interaction between Radix Astragali and Pioglitazone in Rats. *J. Ethnopharmacol* 144, 300–304. doi:10.1016/j.jep.2012.09.012

Zhang, J., Xu, W., Wang, P., Huang, J., Bai, J. Q., Huang, Z. H., et al. (2018). Chemical Analysis and Multi-Component Determination in Chinese Medicine Preparation Bupi Yishen Formula Using Ultra-high Performance Liquid Chromatography with Linear Ion Trap-Orbitrap Mass Spectrometry and Triple-Quadrupole Tandem Mass Spectrometry. *Front. Pharmacol.* 8 (9), 568. doi:10.3389/fphar.2018.00568

Zhang, J., Wu, C., Gao, L., Du, G., and Qin, X. (2020). Astragaloside IV Derived from Astragalus Mongholicus: A Research Review on the Pharmacological Effects. *Adv. Pharmacol.* 87, 89–112. doi:10.1016/bs.apha.2019.08.002

Zhang, Q., Zhu, L. L., Chen, G. G., and Du, Y. (2007). Pharmacokinetics of Astragaloside Iv in Beagle Dogs. *Eur. J. Drug Metab. Pharmacokinet.* 32, 75–79. doi:10.1007/BF03190995

Zhang, W., Zhang, C., Liu, R., Li, H., Zhang, J., Mao, C., et al. (2005). Quantitative Determination of Astragaloside IV, a Natural Product with Cardioprotective Activity, in Plasma, Urine and Other Biological Samples by HPLC Coupled with Tandem Mass Spectrometry. *J. Chromatogr. B Analyt Technol. Biomed. Life Sci.* 822, 170–177. doi:10.1016/j.jchromb.2005.05.034

Conflict of Interest: The authors declare that the research was conducted in the absence of any commercial or financial relationships that could be construed as a potential conflict of interest.

Publisher's Note: All claims expressed in this article are solely those of the authors and do not necessarily represent those of their affiliated organizations or those of the publisher, the editors, and the reviewers. Any product that may be evaluated in this article, or claim that may be made by its manufacturer, is not guaranteed or endorsed by the publisher.

frontiers in Pharmacology

ORIGINAL RESEARCH
published: 21 March 2022
doi: 10.3389/fphar.2022.842720

Stewed Rhubarb Decoction Ameliorates Adenine-Induced Chronic Renal Failure in Mice by Regulating Gut Microbiota Dysbiosis

Rui Wang[1,2†], *Baifei Hu*[1†], *Cheng Ye*[3], *Zhigang Zhang*[1], *Mingzhu Yin*[1], *Qiushi Cao*[1], *Yuanming Ba*[2,4*] and *Hongtao Liu*[1*]

[1]College of Basic Medical Sciences, Hubei University of Chinese Medicine, Wuhan, China, [2]Nephrology Department, Hubei Provincial Hospital of Traditional Chinese Medicine, Wuhan, China, [3]Technology Center of Wuhan Customs, Wuhan, China, [4]Nephrology Department, Hubei Provincial Traditional Chinese Medicine Research Institute, Wuhan, China

OPEN ACCESS

Edited by:
Shuai Ji,
Xuzhou Medical University, China

Reviewed by:
Wei Liu,
Shanghai University of Traditional Chinese Medicine, China
Chenyang Lu,
Ningbo University, China

***Correspondence:**
Yuanming Ba
bayuanming@126.com
Hongtao Liu
hongtaoliu@hbtcm.edu.cn

[†]These authors have contributed equally to this work.

Specialty section:
This article was submitted to Ethnopharmacology, a section of the journal Frontiers in Pharmacology

Received: 24 December 2021
Accepted: 28 February 2022
Published: 21 March 2022

Citation:
Wang R, Hu B, Ye C, Zhang Z, Yin M, Cao Q, Ba Y and Liu H (2022) Stewed Rhubarb Decoction Ameliorates Adenine-Induced Chronic Renal Failure in Mice by Regulating Gut Microbiota Dysbiosis. Front. Pharmacol. 13:842720. doi: 10.3389/fphar.2022.842720

This study aimed to investigate the protective effect of *Stewed Rhubarb* (*SR*) decoction on chronic renal failure (CRF) through the regulation of gut microbiota. Using a CRF mouse model induced by a 0.2% adenine diet, we proved that *SR* decoction (2.0 g crude SR/kg) significantly reduced the levels of urea and creatinine in plasma of CRF mice, accompanied by the improvement of renal fibrosis and tubular atrophy, amelioration of inflammation, and inhibition of aquaporins damage. Also, SR decoction alleviated gut barrier damage, indicative of the elevated mRNA expression of intestinal mucins and tight junctions. By 16S rDNA sequencing, SR decoction reshaped the imbalanced gut microbiota in CRF mice by statistically reversing the abundance changes of a wide range of intestinal bacteria at family and genus levels, which further led to balance in the production of intestinal metabolites, including short-chain fatty acids (acetic acid, propionic acid, and valeric acid), indole, and bile acids (TUDCA and CDCA). Inversely, SR decoction failed to repress the occurrence of CRF in mice with gut microbiota depletion, confirming the essential role of gut microbiota in SR decoction-initiated protection against CRF. In summary, SR decoction can improve adenine-induced CRF in mice by remolding the structure of destructed gut microbiota community. Our findings shed light on the clinical application of SR decoction in nephropathy treatment.

Keywords: gut microbiota, intestinal metabolites, renal fibrosis, stewed rhubarb, chronic renal failure (CRF)

Abbreviation: *SR, Stewed Rhubarb*; CRF, chronic renal failure; DHA, 2,8-dihydroxyadenine; TCM, Traditional Chinese Medicine ; RT-PCR, real-time quantitative PCR; H&E, hematoxylin and eosin; PAS, Periodic acid Schiff; HPLC, High Performance Liquid Chromatography; Rg, Rhein-8-O-β-D-glucopyranoside; *Il-1β*, interleukin 1β; Tlr4, Toll-like receptor 4; *Col1a1*, Collagen alpha-1(I); *Nlrp3*, NOD-like receptor pyrin domain containing 3; *Tnf-α*, tumor necrosis factor-α; AQP, aquaporin; *Ang4*, Angiogenin 4; *Muc*, mucin; SCFAs, Short-chain fatty acids; BAs, bile acids; CA, cholic acid; TCA, taurocholic acid; CDCA, chenodeoxycholic acid; TCDCA, taurochenodeoxycholic acid; DCA, deoxycholic acid; T-α-MCA, tauro-α-murocholic acid; T-β-MCA, tauro-β-murocholic acid; TDCA, Taurodeoxycholic acid; TUDCA, taurourso-deoxycholic acid; UCDCA, Ursodeoxycholic acid; Abx, antibiotic mixture; BCA, bicinchoninic acid.

INTRODUCTION

Chronic renal failure (CRF) is a progressive renal parenchymal injury resulting renal atrophy and a reduction in glomerular filtration rate. The characteristics of CRF are retention of metabolites, renal fibrosis, and imbalance of fluid, electrolyte, and acid-base (Ammirati, 2020). Meanwhile, CRF is often accompanied by multiple complications, such as hypertension, nausea, and neurological disorders (Wang et al., 2016). According to statistics, the incidence rate of chronic kidney disease is 9.1%, and there are currently 697.5 million cases worldwide (GBD Chronic Kidney Disease Collaboration, 2020; Li et al., 2021). The major interventions of CRF are dialysis and kidney transplantation. However, both treatments cause a huge financial burden and usually have adverse effects, like gastrointestinal reactions, kidney transplant rejection, and dialysis complications (Wang et al., 2016).

Adenine is a purine nucleobase, which plays a vital role in the biochemical and physiological functions of cells (Dos Santos et al., 2019). Under physiological conditions, xanthine oxidase catalyzes adenine to 2, 8-dihydroxyadenine (DHA) in the liver, and DHA is finally excreted from urine (Wyngaarden and Dunn, 1957). However, the over-produced DHA will form crystals and deposit in renal tubules or interstitial tissues due to its poor solubility under the pH value of urine, leading to kidney damage (Dos Santos et al., 2019). Now, adenine is widely used to establish the experimental model of chronic renal failure (CRF) in rodents. For example, C57BL/6 mice are often fed with a 0.2% adenine diet to induce the CRF model (Mishima et al., 2015). The primary pathology of the CRF model is renal fibrosis, related to the abnormal changes of several signal pathways, such as TGF-β1/Smad, MAPK signaling, and GSK-3β/β-Catenin (Ma and Meng, 2019; Schunk et al., 2021; Zhou et al., 2021). Noticeably, GSK-3β/β-Catenin is pivotal for the formation of renal fibrosis. The phosphorylation of GSK-3β (ser9) can inhibit its enzymatic activity and suppress the degradation of β-catenin, which causes epithelial-mesenchymal transformation, renal fibrosis, and tight junction destruction characterized by the down-regulation of E-cadherin (Sun et al., 2016).

Gut microbiota interacts with various organs to maintain host health. It was shown that kidney damage is at least partly due to the dysbiosis of intestinal flora. For example, the increase of *Clostridium* and *Lactobacillales* accelerated tubular atrophy and dilatation, interstitial fibrosis, and inflammatory cell infiltration in the kidney (Chen et al., 2019). In clinical trials, the ratio of Firmicutes to Bacteroidetes and α-diversity of intestinal flora was elevated in CRF patients (Jiang et al., 2016; Chen et al., 2019). Further, the disrupted homeostasis among gut microbiota led to bacterial translocation, systemic inflammation, and subsequent renal fibrosis (Miyazaki-Anzai et al., 2021). In addition, the metabolites of gut microbiota play pivotal roles in the occurrence of CRF. In previous studies, the accumulation of uremic toxins (gut microbiota-derived metabolites) caused endothelial cell damage and microvascular injury in the kidney, followed by aggravated tubulointerstitial fibrosis (Koizumi et al., 2014; Giordano et al., 2021). In contrast, as the metabolites of intestinal flora, short-chain fatty acids (SCFAs) significantly improved renal function by reducing the production of reactive oxygen species and apoptotic cells (Wang et al., 2019). By inhibiting the biotransformation reaction of bile acids (BAs) through gut microbiota, circulating BAs were decreased, accompanied by the relief of vascular calcification and atherosclerosis in CRF (Miyazaki-Anzai et al., 2021). It seems that gut microbiota and their metabolites should be potential regulatory targets in treating CRF.

Stewed Rhubarb (*SR*), a processed product of *Rhubarb*, has been used as a herbal medicine for thousands of years. *SR* was first recorded in "*Treatise on Febrile Diseases*", in which *SR* was obtained by steaming raw *Rhubarb* with glutinous rice wine until it turned black (Zhu et al., 2016). *SR* has a milder purgative effect than raw *Rhubarb*, making it possible for long-term medication without significant side effects to the intestine (Yao et al., 2012). Traditional Chinese Medicine (TCM) theory believes that *SR* has pharmacological effects of defecating, relieving heat, and promoting blood circulation (Zhuang et al., 2020). These effects are attributed to multiple natural active ingredients from *SR*, including Rhein, Emodin, Aloe Emodin, Physcion, and Chrysophanol for their anti-bacterial, anti-fibrotic, and anti-inflammatory efficacy (Cao et al., 2017). So far, *SR* has been widely used to treat acute pancreatitis, constipation, and chronic renal failure (CRF) (Zhang et al., 2017; Zhang et al., 2018).

In most cases, Chinese herbal medicines are orally administered and thus will interact with gastrointestinal bacteria before exerting their pharmacological activities (Liu et al., 2020). This gives them more opportunities to affect intestinal flora and its metabolites, thus showing unique advantages in disease treatment. This study hypothesizes that SR decoction can ameliorate CRF by suppressing the imbalanced gut microbiota and their metabolite changes. Based on an adenine-induced CRF mouse model, we investigated the protective effect of SR decoction on the damage to mouse kidneys. We also examined the improvement of SR decoction on the change of intestinal flora structure and alteration of microbial metabolite profiles in CRF mice. Further, a germ-depletion mouse experiment was designed to assess the effect of SR decoction on CRF via gut microbiota modulation.

MATERIALS AND METHODS

Reagents

Stewed Rhubarb (*Polygonaceae*; *Rhei Radix et Rhizoma*) (*SR*) is the dried root and rhizome of *Rheum palmatum* L. And *SR* was purchased from Hubei Tianji Chinese Medicine Decoction Company (Wuhan, China) with the batch number 202005018. Sodium butyrate, sodium acetate anhydrous, sodium propionate, valeric acid, adenine hydrochloride, Metronidazole, Ampicillin, Neomycin sulfate, Gentamycin sulfate, Gallic acid, Aloe-emodin, Chrysophanol, Physcion, Rhein, and Emodin were obtained from Aladdin (Shanghai, China). Rhein-8-O-β-D-glucopyranoside was purchased from YuanyeBio Co., Ltd. (Shanghai, China). Indole, cholic acid (CA), taurocholic acid (TCA), chenodeoxycholic acid (CDCA), taurochenodeoxycholic acid (TCDCA), deoxycholic

acid (DCA), Taurodeoxycholic acid (TDCA), tauroursodeoxycholic acid (TUDCA), and Ursodeoxycholic acid (UCDCA) were obtained from Sigma (St. Louis, MO, United States). Tauro-α-murocholic acid (T-α-MCA) and tauro-β-murocholicacid (T-β-MCA) were purchased from TRC (Toronto, Canada). Primary antibodies against phosphorylation-GSK-3β (ser 9) and GSK-3β were obtained from Cell Signaling Technology Inc. (Beverly, MA, United States). Other antibodies, including β-Catenin, E-Cadherin, and β-actin, were separately purchased from Proteintech Group, Inc. (Wuhan, China), Abcam (Cambridge, MA, United States), and Santa Cruz Biotechnology (Santa Cruz, CA, United States).

Water Extracts Preparation and Compositional Identification of SR Decoction

The preparation of SR decoction referred to the regulation of "*Treatise on Febrile Diseases*". In brief, the drug–solvent ratio was 1:8, that is, 30 g of *SR* species (*Rheum palmatum L*; 202005018, Hubei Tianji Chinese Medicine Decoction Company, Wuhan, China) was added into 240 ml of boiling water and extracted for 10 min. Next, the SR decoction was concentrated to 150 ml, and the crude drug content of SR decoction was 200 mg/ml. After that, a part of SR decoction was dried in a vacuum drier to calculate the extraction rate, and the ratio of SR decoction powder to raw herbs was 7.31%. Based on the above, a 2 g crude SR/kg was equivalent of 146.2 mg/kg SR powder in this study. The dose conformed to the concentration range (100–200 mg/kg *in vivo* studies of extracts) (Heinrich et al., 2020). The experimental dose was obtained by a preliminary experiment (**Supplementary Table S1**).

To analyze the composition of SR decoction, we conducted High-Performance Liquid Chromatography (HPLC) analysis on a Waters-system (Waters Corp, Milford, United States) with an Agilent Eclipse XDB C18 column (250 × 4.6 mm, 5 μm). The flow rate was 1.0 ml/min, and the mobile phase was composed of 0.2% acetic acid v/v (A) and acetonitrile (B). The gradient elution with a flow rate of 1.0 ml/min was as follows: 5–12% B at 0–10 min, 12%–26% B at 10–28 min, 26%–38% B at 28–53 min, 38%–42% B at 53–70 min, 42%–47% B at 70–80 min, 47%–51% B at 80–88 min, 51%–71% B at 88–110 min. The injection volume was 20 μL, and the column temperature was set to 35°C. The mass spectrometry analysis was performed in both positive and negative ion modes in a range of 100–1100 Da. The optimized parameters of the ESI source were set as follows: drying gas (N_2) flow rate, 10.0 L/min; drying gas temperature, 350°C; nebulizer pressure, 30 psig; fragmentor, 80, 135, 175, 225, 300, and 375 V; capillary voltage, −3,500 or 4000 V. The mass spectrometer was set in multiple reaction monitoring modes for quantification of selected ions.

Animal Experiment

Male C57BL/6 mice (Six-week-old, 20 ± 2 g) were purchased from Hubei Center for disease Control and Prevention (Wuhan, China). Mice were adaptively housed for 1 week with 12 h light/dark cycle (55 ± 5% humidity, 23 ± 2°C) and free access to food and water. After that, mice were randomly divided into four groups (n = 9): 1) Ctrl group, fed with normal chow diet and administered with saline by gavage for 2 weeks; 2) CRF group, fed with 0.2% adenine diet (w/w) and administered with saline by gavage for 2 weeks; 3) SR group, fed with normal chow diet and administered with SR decoction (2.0 g crude SR/kg) for 2 weeks by gavage; 4) CRF + SR group, fed with 0.2% adenine diet (w/w) and administered with *SR* decoction (2.0 g/kg) by gavage for 2 weeks. Animal diet was bought from Chunzhilong Experimental Animal Co., Ltd. (Wuhan, China). During the animal experiment, the body weight, diet intake, and water drinking of mice were monitored. At the end of the experiment, fresh feces were collected from each mouse. Then, all mice were euthanized with the collection of the kidney, colon, cecum contents, and plasma. Colon length was measured, and the kidney tissues were photographed. All samples were stored at −80°C for further experiment.

For the antibiotic experiment, male C57BL/6 mice were randomly divided into four groups (n = 9): 1) Ctrl group, given distilled water for 4 weeks and then fed with normal chow diet plus saline by gavage for another 2 weeks; 2) CRF group, give distilled water for 4 weeks and then fed with 0.2% adenine diet (w/w) plus saline by gavage for another 2 weeks; 3) CRF + AB group, given antibiotic mixture (Abx, 1.0 mg/ml ampicillin, 1.0 mg/ml neomycin, 0.5 mg/ml vancomycin, and 0.5 mg/ml metronidazole in distilled water) for 4 weeks and then fed with 0.2% adenine diet (w/w) plus saline by gavage for another 2 weeks; 4) CRF + AB+ SR group, given Abx for 4 weeks and then fed with 0.2% adenine diet (w/w) plus *SR* decoction (2.0 g/kg) by gavage for another 2 weeks. Four weeks after the start of the animal experiment, mouse fecal samples were collected, and the DNA was extracted for the detection of bacterial content by RT-qPCR. At the end of the experiment, all mice were euthanized, and the tissues were collected as those mentioned above.

The animal experiments were performed according to the Animal Care and Use Committee of the animal facility at the Hubei University of Chinese Medicine.

Creatinine and Urea Analysis

Creatinine Colorimetric Assay Kit and Urea Colorimetric Assay Kit were separately used to detect the levels of creatinine and urea in plasma according to the manufacturer's instructions (Elabscience Biotechnology Co., Ltd., Wuhan, China).

RNA Extraction and Real-Time Quantitative PCR

Based on the manufacturer's protocol, total RNA of kidney and colon tissues was extracted using Trizol reagent and reversely transcribed to cDNA with a first-strand cDNA synthesis kit (Allmeek Co., Ltd., Beijing, China). The relative mRNA levels of target genes were measured by RT-qPCR using a SYBR QPCR mixture (Allmeek Co., Ltd., Beijing, China) at the ABI 7500 Real-Time Fluorescence Quantitative PCR instrument. The primer

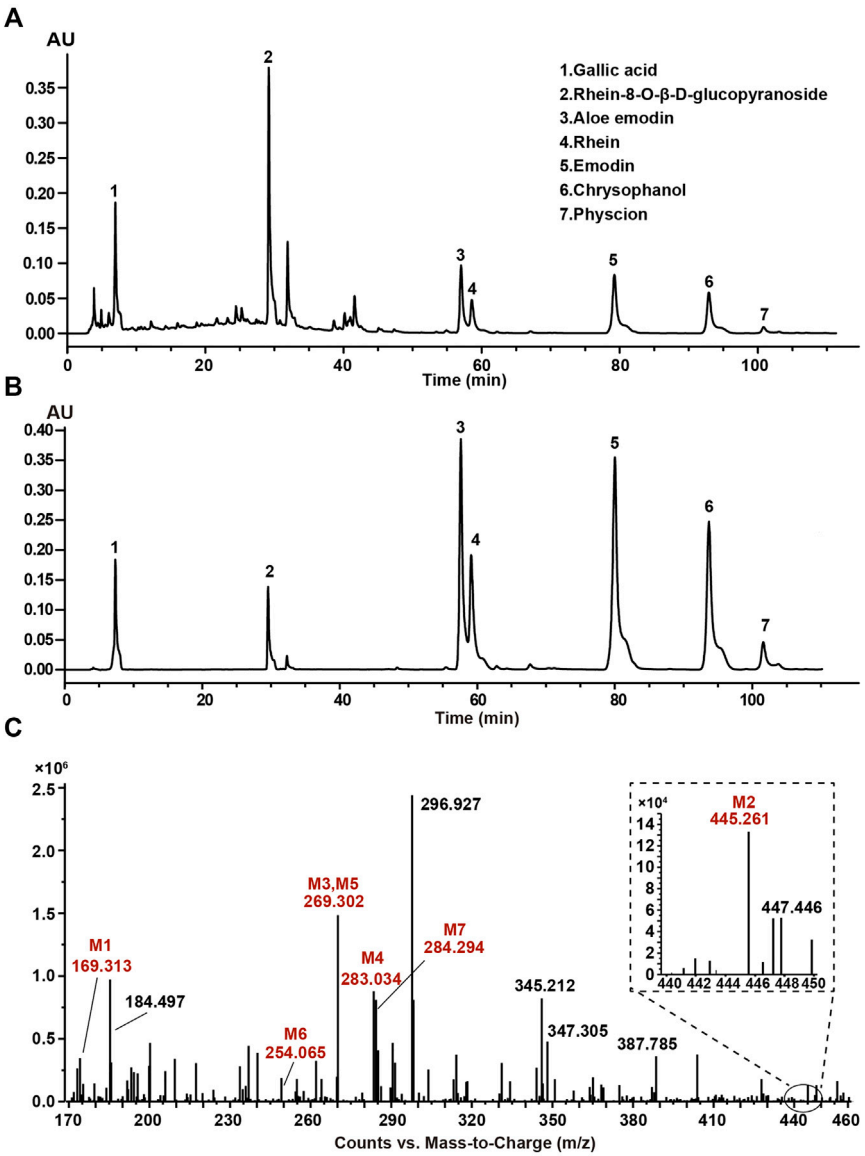

FIGURE 1 | Composition analysis of SR decoction by high-performance liquid chromatography (HPLC) and mass spectrometry. **(A)** HPLC analysis of SR decoction. **(B)** HPLC analysis of related standards. Peak 1, Gallic acid; Peak 2, Rhein-8-O-β-D-glucopyranoside; Peak 3, Aloe emodin; Peak 4, Rhein; Peak 5, Emodin; Peak 6, Chrysophanol; Peak 7, Physcion. **(C)** MS spectra of SR decoction by mass spectrometry. M1, Gallic acid; M2, Rhein-8-O-β-D-glucopyranoside; M3, Aloe emodin; M4, Rhein; M5, Emodin; M6, Chrysophanol; M7, Physcion.

sequences were listed in **Supplementary Tables S2, S3**. The thermal cycle condition was as follows: pre-denaturing at 95°C for 10 min; 40 cycles of denaturation at 95°C for 10 s, annealing/extension at 60°C for 30 s. Target gene expressions were normalized against that of β-actin, and fold changes were calculated using a $2^{(-\Delta\Delta CT)}$ method.

Histological Analysis

Kidney and colon tissues were fixed with 4% paraformaldehyde, dehydrated, paraffin-embedded, and cut into 5 μm-thick sections. After the deparaffinization using xylene and seriously diluted ethanol, sections were stained with hematoxylin and eosin (H&E). Besides, Periodic Acid-Schiff (PAS) Staining Kit (Solaibao Co., Ltd., Beijing, China) and MASSON Staining Kit (Heart Biological Co., Ltd., Xian, China) were used to evaluate the levels of glomerulosclerosis and renal fibrosis, respectively. Alcian blue staining was performed to evaluate the acidic mucin expression in colon tissues following the manufacturer's instruction (Vectorlabs, Beijing, China). Glycosylated mucin expression in colon tissues was stained using Wheat Germ Agglutinin (WGA)-FITC (Sigma, St. Louis, MO, United States). Images were acquired by a Leica DFC310 FX digital camera connected to a Leica DMI4000B light microscope (Wetzlar, Germany).

TABLE 1 | Typical MS data of major compounds in SR decoction.

Peak no	Name	Formula	Molecular mass	Measured [M-H]$^-$ (m/z)	Fragment ions
M1	Gallic acid	$C_7H_6O_5$	170	169.010	124.9
M2	Rg	$C_{21}H_{18}O_{11}$	446	445.261	240.1, 284.0
M3	Aloe emodin	$C_{15}H_{10}O_5$	270	269.302	239.2
M4	Rhein	$C_{15}H_8O_6$	284	283.034	239.0
M5	Emodin	$C_{15}H_{10}O_5$	270	269.302	225.0
M6	Chrysophanol	$C_{15}H_{10}O_4$	254	254.093	209.7, 225.3
M7	Physcion	$C_{15}H_8O_6$	284	284.294	211.7, 239.4, 268.7

Quantification of Intestinal Metabolites in Feces

To quantify the levels of BAs in feces, we homogenized 50 mg of fecal samples with 1 ml of water-methanol-formic acid solution (25:74:1, V/V/V) containing d_5-CA and d_4-TCA as internal standards at a final concentration of 0.2 μg/ml. To determine the contents of SCFAs, we homogenized 50 mg of fecal sample with 1 ml of 50% (V/V) methanol-aqueous solution (containing 0.2% HCl). To detect the level of indole, we homogenized 25 mg of fecal sample with 1 ml of pre-cooled methanol. All samples were used for GC-MS or LC-MS analysis. The detailed analytical information was indicated in **Supplementary Methods**.

16S rDNA Gene Sequencing

The total mouse fecal genome was extracted, and intestinal flora was detected by sequencing the V3-V4 region of 16S rDNA on the Illumina MiSeq platform (Illumina, San Diego, CA, United States). The metagenomic DNA from mouse colonic contents was obtained using a FastDNA™ SPIN Kit (MP Biomedicals, CA, United States). The V3-V4 variable region was amplified using barcoded primers. The PCR product was detected by 1% agarose gel electrophoresis and purified with Agencourt AMPure XP Nucleic acid purification kit. The amplicons were then pooled in paired-end sequence on an Illumina MiSeq platform (Illumina, Journal Pre-proof 9 San Diego, CA, United States) by Beijing Allwegene Tech (Beijing, China) following the standard protocols. The detailed analytical information was indicated in **Supplementary Methods**.

Western Blot

Total protein was extracted from kidney tissues using RIPA buffer (Beyotime, Shanghai, China) supplemented with a protease inhibitor cocktail (Merck, Darmstadt, Germany). Then, protein concentrations were determined using a bicinchoninic acid (BCA) protein assay kit (Beyotime, Shanghai, China). Protein samples were separated on sodium dodecyl sulfate polyacrylamide gel electrophoresis (SDS-PAGE) gels and transferred to polyvinylidene difluoride (PVDF) membranes. After blocking with 5% skim milk in Tris-buffered saline tween-20 (TBST) for 1 h, the membranes were separately incubated with primary antibodies at 4°C overnight, including E-Cadherin, β-Catenin, p-GSK-3β (ser 9), GSK-3β, and β-actin. After the wash with TBST, membranes were incubated with secondary antibody conjugated with horseradish peroxidase (HRP) for 1.5 h. Finally, protein signals were visualized using an ECL Protein Detection kit.

Statistical Analysis

Data were presented as mean ± SD. The difference between the two groups was analyzed using an unpaired two-tailed Student's *t*-test. Differences among multiple groups were assessed using a one-way ANOVA and Bonferroni post-hoc analysis. And $p < 0.05$ was considered statistically significant. Regular analysis was carried out using GraphPad Prism (Version 8.0.1, GraphPad Software Inc., CA, United States).

RESULTS

Component Identification of SR Decoction by HPLC and MS

The typical HPLC chromatogram of SR decoction (**Figure 1A**) was mainly composed of seven components as compared to related standards (**Figure 1B**): Peak 1, Gallic acid; Peak 2, Rhein-8-O-β-D-glucopyranoside; Peak 3, Aloe emodin; Peak 4, Rhein; Peak 5, Emodin; Peak 6, Chrysophanol; Peak 7, Physcion. Further, these components were confirmed and quantified by mass spectrometry analysis, as shown in **Figure 1C** and **Table 1**, **Supplementary Figure S1**, and **Supplementary Table S4**.

SR Decoction Improved Physiochemical Parameters of CRF Mice

The schematic diagram of animal experimental was indicated in **Figure 2A**. In brief, mice were fed with a 0.2% adenine diet to induce CRF, and then SR decoction was used to interfere with CRF for 2 weeks. Results show that the body weight of CRF mice was gradually decreased (**Figure 2B**). After the treatment of SR decoction, the weight loss of CRF mice was notably inhibited ($p < 0.05$, *vs.* CRF group) (**Figures 2B,C**). The water drinking of CRF mice was also significantly reduced after the intervention of SR decoction ($p < 0.05$, *vs.* CRF group) (**Figure 2D**). As indicated in **Supplementary Figure S2**, the diet intake was significantly decreased in mice of the CRF group compared to the Ctrl group ($p < 0.01$), but there was no

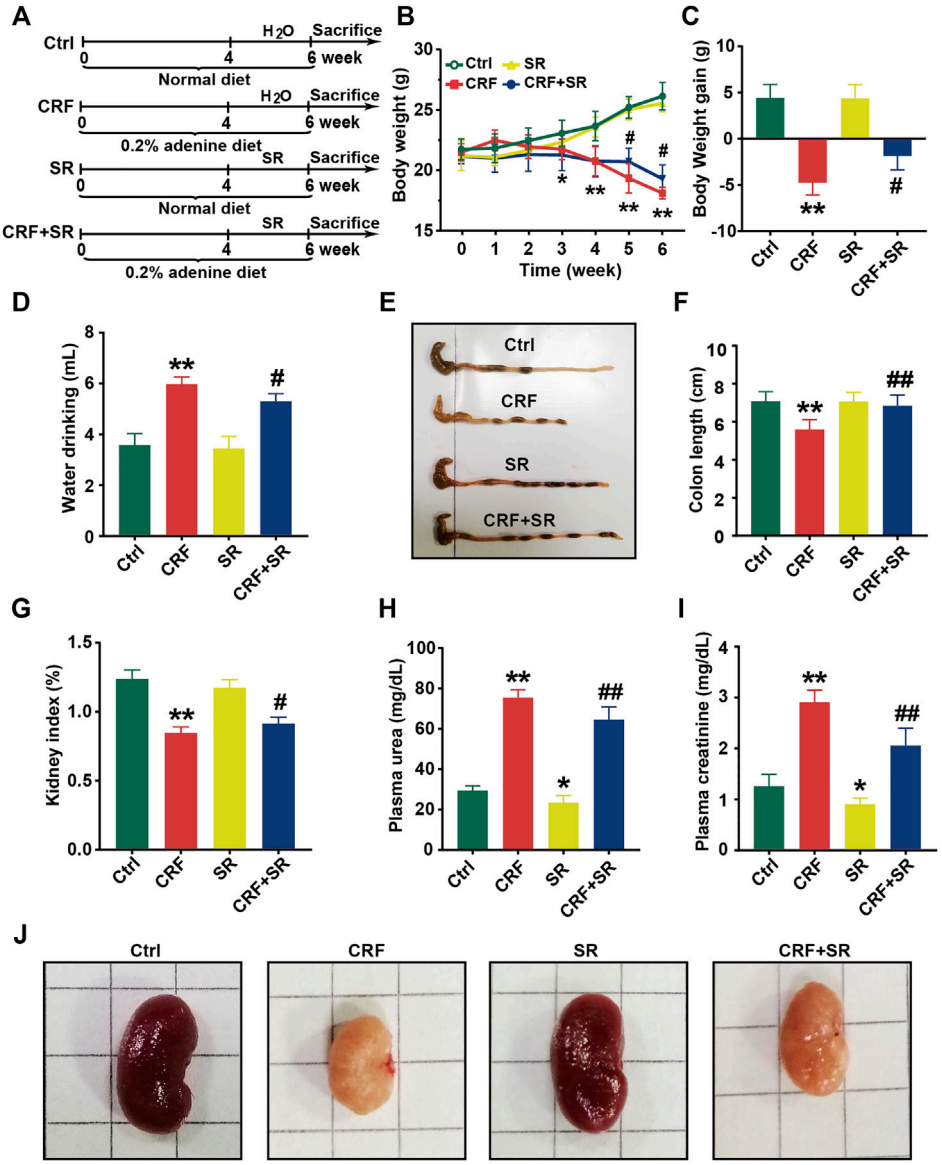

FIGURE 2 | Improvement of physiochemical parameters in adenine-induced CRF mice by SR decoction. **(A)** Experimental schematic diagram. **(B)** Growth curve. **(C)** Body weight gain. **(D)** Water drinking. **(E)** Macroscopic observation of colon. **(F)** Measurement of colon length. **(G)** Kidney index. **(H)** Level of plasma urea. **(I)** Leve of plasma creatinine. **(J)** Macroscopic observation of kidney. Data were presented as mean ± SD (n = 8). $^{*}p < 0.05$, $^{**}p < 0.01$ *vs.* Ctrl group; $^{\#}p < 0.05$, $^{\#\#}p < 0.01$ *vs.* CRF group.

difference between the CRF group and CRF + SR group. Meanwhile, the colon length was shortened in CRF mice but corrected by SR decoction treatment ($p < 0.05$, *vs.* CRF group) (**Figures 2E,F**). In comparison with the CRF group, the decreased kidney index was partly reversed in the CRF + SR group ($p < 0.05$) (**Figure 2G**). Additionally, SR decoction suppressed the increase in levels of urea and creatinine of CRF mice ($p < 0.05$, *vs.* CRF group) (**Figures 2H,I**). Noticeably, SR decoction also decreased the levels of plasma urea and creatinine in the control mice ($p < 0.05$, SR group *vs.* Ctrl group) (**Figures 2H,I**). Finally, the kidney morphology of CRF mice was characterized by apparent shrinkage and paleness, which were improved by SR decoction treatment (**Figure 2J**).

SR Decoction Suppressed Fibrosis, Inflammation, and Reduction of Aquaporins in Kidney Tissues of CRF Mice

In **Figure 3A**, renal glomerular sclerosis was observed in CRF mice by HE staining, with characteristics of vacuolization and atrophy of renal tubules. Compared to the Ctrl group, PAS staining of renal tissues manifested thickening of the glomerular basement membrane and renal tubule in mice of

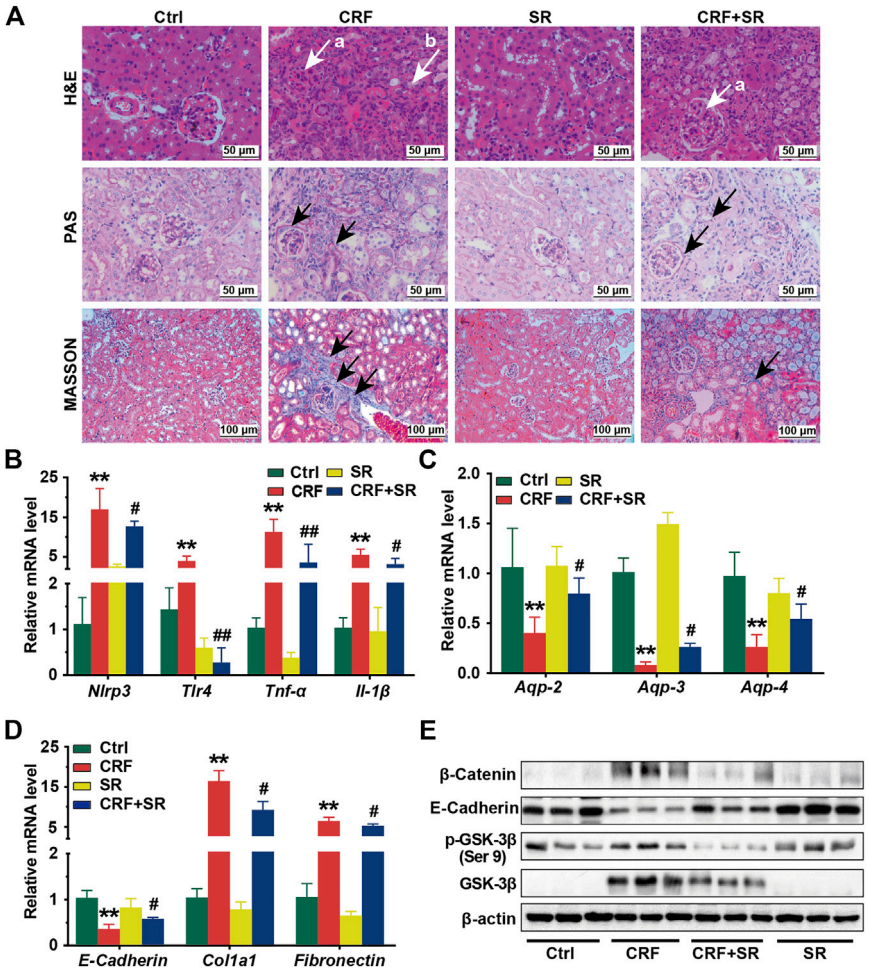

FIGURE 3 | Reversal of inflammatory responses, fibrosis, reduced aquaporins in kidney tissues of CRF mice by SR decoction. **(A)** Morphological changes of kidney tissues among four experimental groups by H&E staining (400 ×, "a" indicates glomerulosclerosis and "b" indicates tubular atrophy), PAS staining (400 ×, arrows indicate lesions), and MASSON staining (200 ×, arrows indicate collagen fiber). **(B)** Expressions of proinflammatory cytokines, including *Nlrp3*, *Tlr-4*, *Tnf-α*, and *Il-1β* at mRNA levels. **(C)** Expressions of aquaporins, including *Aqp-2*, *Aqp-3*, and *Aqp-4* at mRNA levels. **(D)** Expressions of renal fibrosis-related molecules, including *E-Cadherin*, *Col1a1*, and *Fibronectin* at mRNA levels. **(E)** Expressions of renal fibrosis signaling pathway-related regulators, including β-Catenin, E-Cadherin, p-GSK-3β (ser 9), and GSK-3β at protein levels by Western blot. Data were presented as mean ± SD. $^{*}p < 0.05$, $^{**}p < 0.01$ *vs.* Ctrl group; $^{\#}p < 0.05$, $^{\#\#}p < 0.01$ *vs.* CRF group.

the CRF group (**Figure 3A**). By MASSON staining, mice of the CRF group displayed band-like interstitial fibrosis and collagen fiber proliferation (**Figure 3A**). In contrast, SR decoction treatment ameliorated the above pathological changes in kidney tissues of CRF mice (**Figure 3A**).

To further explore the protective effect of SR decoction on kidney injuries of CRF mice, the mRNA expressions of associated regulators were analyzed by RT-qPCR. As shown in **Figures 3B,C**, we observed the increased expressions of proinflammatory cytokines (*Nlrp3*, *Tlr-4*, *Tnf-α*, and *Il-1β*) ($p < 0.01$, *vs.* Ctrl group) and reduced expressions of aquaporins (*Aqp-2*, *Aqp-3*, and *Aqp-4*) at mRNA levels in CRF mice kidneys ($p < 0.01$, *vs.* Ctrl group), and these changes significantly blocked by SR decoction ($p < 0.05$ or 0.01, *vs.* CRF group). Also, we detected abnormal mRNA expressions of fibrosis-related molecules in kidney tissues of CRF mice, as indicated by the down-regulation of *E-Cadherin* and up-regulation of *Col1a1* and *Fibronectin* ($p < 0.01$, *vs.* Ctrl group), which were statistically reversed by SR decoction ($p < 0.05$, *vs.* CRF group) (**Figure 3D**).

To gain more insight into the effect of SR decoction on the renal fibrosis signaling pathway, we examined the protein expressions of β-catenin-related transduction signals in kidneys by western blot analysis. Among these molecules, the E-Cadherin expression was reduced, but the levels of β-Catenin, p-GSK-3β (ser 9), and GSK-3β were increased in CRF mice (**Figure 3E**). On the contrary, SR decoction treatment remarkably inhibited the protein changes of the above regulators or kinases in CRF mice (**Figure 3E**).

SR Decoction Protected Gut Barrier Against Damage in CRF Mice

Since the colon length was shortened in CRF mice (**Figures 2E,F**), we exploited the effect of SR decoction on damage to the

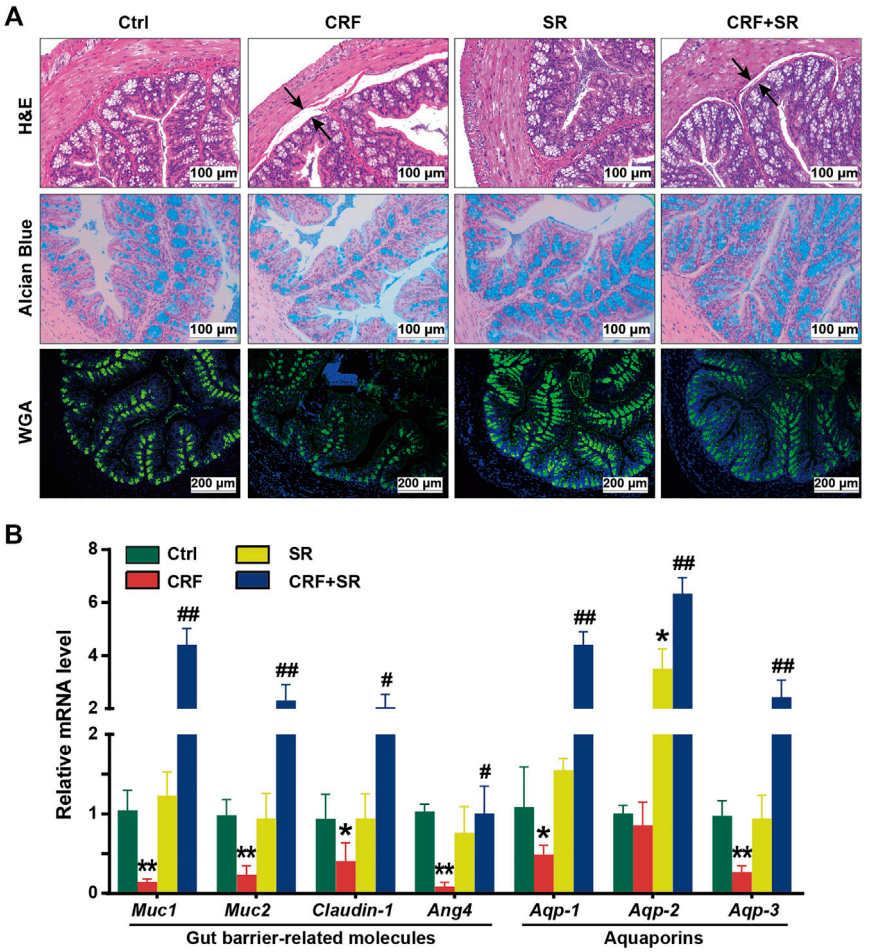

FIGURE 4 | Protection of gut barrier damage in colon of CRF mice by SR decoction. **(A)** Morphology of colon tissues by using H&E staining (200 ×), Alcian blue staining (200 ×), and WGA-FITC staining (100 ×). Black arrows, indicating intestinal edema. **(B)** Expressions of gut barrier-related molecules and aquaporins in colon tissues at mRNA level by RT-qPCR. Data were presented as mean ± SD (n = 6). $^{*}p < 0.05$, $^{**}p < 0.01$ *vs.* Ctrl group; $^{\#}p < 0.05$, $^{\#\#}p < 0.01$ *vs.* CRF group.

gut barrier of adenine diet-fed mice. As illustrated in **Figure 4A**, H&E staining shows an intestinal edema change between the muscular layer and mucous layers in CRF mice with thinned muscularis in the colon, and SR decoction treatment corrected these pathological changes. By WGA-FITC staining and Alcian blue staining, we found the reduced content of intestinal glycoprotein mucins in colon tissues of the CRF group, which was significantly restored by SR decoction (**Figure 4A**). In consistence with morphological changes, the mRNA expressions of key regulators related to the gut barrier (*Muc1*, *Muc2*, *Claudin-1*, and *Ang4*) were remarkably lowered in colon tissues of CRF mice ($p < 0.05$, *vs.* Ctrl group) but modified after SR decoction intervention ($p < 0.05$ or 0.01, *vs.* CRF group) (**Figure 4B**). In consideration of the intestinal edema in CRF mice, the mRNA levels of aquaporins in colon tissues were measured among experimental groups. As indicated in **Figure 4B**, SR decoction entirely reversed the decrease of *Aqp-1*, *Aqp-2*, and *Aqp-3* levels in CRF mice ($p < 0.01$, *vs.* CRF group).

SR Decoction Regulated Production of Gut Microbiota Metabolites in CRF Mice

CRF tends to cause intestinal endotoxin accumulation, thus we quantified the contents of gut microbiota metabolites in fecal samples among four experimental groups by LC/GC-MS analysis. As shown in **Figure 5A**, the level of acetic acid was increased in the feces of CRF mice but remarkably decreased after *SR* decoction treatment ($p < 0.05$, *vs.* CRF group). In contrast, the fecal levels of propionic acid and valeric acid in CRF mice were reduced, whereas SR decoction statistically reversed these changes ($p < 0.05$ or 0.01, *vs.* CRF group). Notably, the contents of four SCFAs were also increased in control mice with SR decoction treatment (**Figure 5A**).

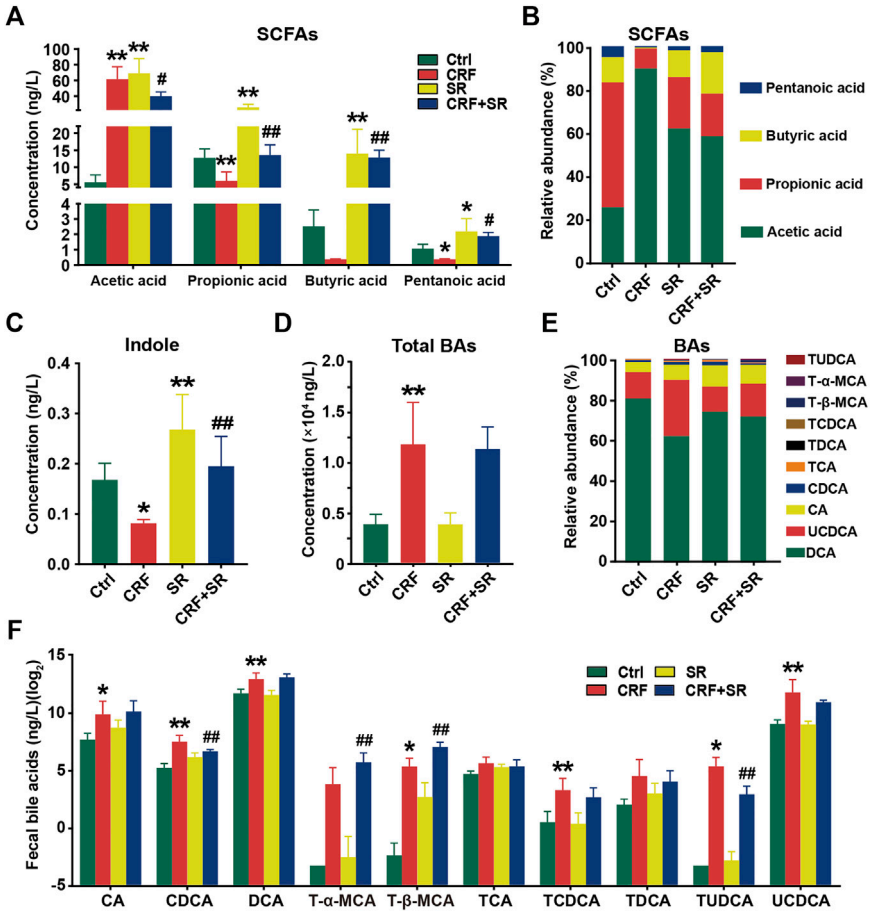

FIGURE 5 | Regulatory effect of SR decoction on production of gut microbiota metabolites in CRF mice. **(A)** SCFAs contents in feces. **(B)** Relative abundances of individual SCFAs in feces. **(C)** Content of indole content in feces. **(D)** Contents of total BAs in feces. **(E)** Relative abundances of individual BAs in feces. **(F)** Quantification of individual BAs. Data were presented as mean ± SD (n = 6). $^{*}p < 0.05$, $^{**}p < 0.01$ *vs.* Ctrl group; $^{\#}p < 0.05$, $^{\#\#}p < 0.01$ *vs.* CRF group.

Consistently, the relative proportions of four SCFAs in feces were changed as indicated by the increased abundance of acetic acid and decreased abundance of pentanoic acid in CRF mice, which were markedly curbed by SR decoction (**Figure 5B**). Meanwhile, SR decoction suppressed the reduction of fecal indole in CRF mice ($p < 0.01$, *vs.* CRF group) (**Figure 5C**).

Compared to the Ctrl group, the total BAs in feces were significantly increased in CRF mice ($p < 0.01$) (**Figure 5D**). Although SR decoction failed to block the increment of total BAs in CRF mice, it inhibited the changed proportions of several individual BAs, like UCDCA and CA (**Figures 5D,E**). Next, we determined the absolute contents of individual BAs in feces among experimental groups (**Figure 5F**). Except for T-α-MCA, TCA, and TDCA, the levels of other BAs were elevated in the feces of the CRF group ($p < 0.05$ or 0.01, *vs.* Ctrl group). Among them, the contents of TUDCA and CDCA were statistically reduced after SR decoction intervention ($p < 0.01$, *vs.* CRF group), while the contents of T-α-MCA and T-β-MCA were further promoted by SR decoction ($p < 0.01$, *vs.* CRF group) (**Figure 5F**).

SR Decoction Ameliorated Gut Microbiota Dysbiosis in CRF Mice

Gut microbiota plays a vital role in producing intestinal metabolites and the maintenance of gut barrier integrity (Akchurin and Kaskel, 2015). Hence, the 16S rDNA sequencing was conducted to assay the intestinal flora in feces using an Illumina MiSeq platform. A total of 1,765,681 raw sequence reads were obtained, and 2,548 operational taxonomic units (OTUs) were yielded after the exclusion of ineligible OTUs (**Supplementary Table S5**). Alpha diversity was calculated by a Shannon index, which represented the richness of gut microbiota. It was shown that SR decoction reversed the up-regulation of bacterial richness in CRF mice ($p < 0.05$, *vs.* CRF group) (**Figure 6A**). The primary component analysis (PCA) and non-metric multidimensional scaling

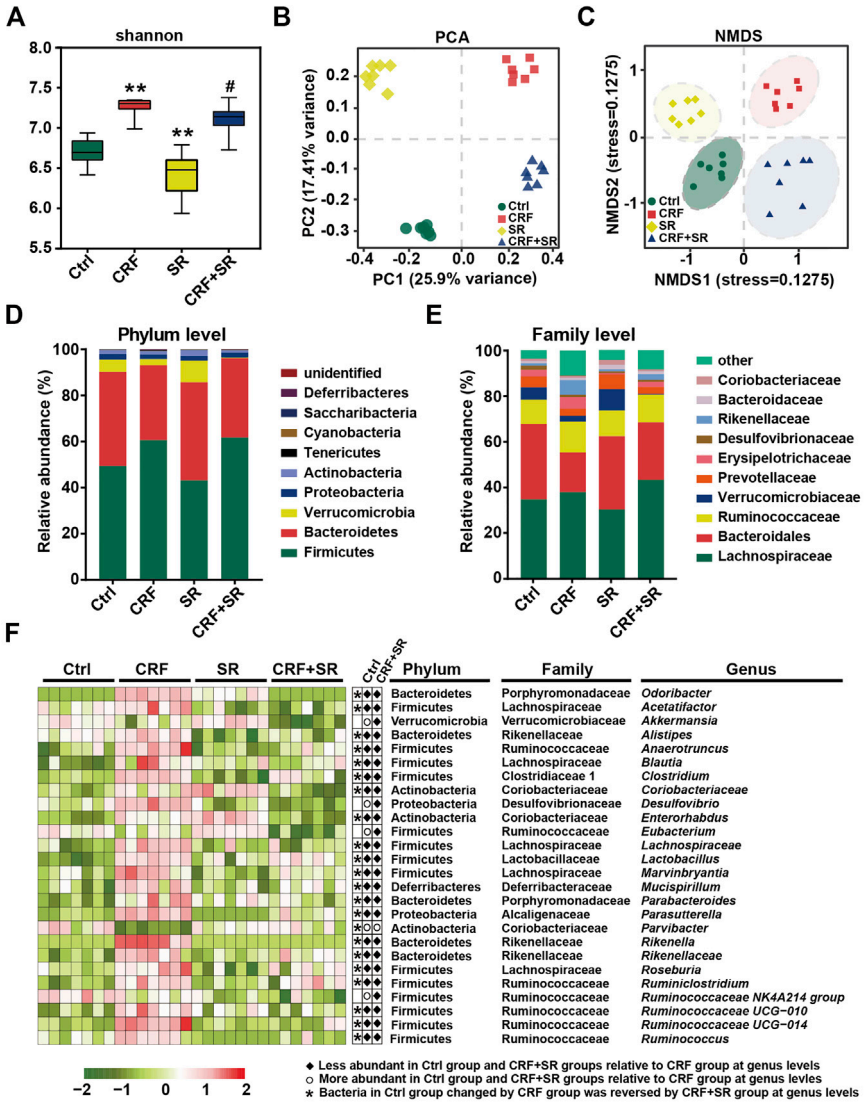

FIGURE 6 | Amelioration of gut microbiota dysbiosis in CRF mice by SR decoction. **(A)** Shannon's diversity index. **(B)** Principal component analysis (PCA). **(C)** Non-metric multidimensional scaling (NMDS). **(D)** Relative abundances at phylum levels. **(E)** Relative abundances at family levels. **(F)** Relative abundances of representative bacteria at genus levels. $^{*}p < 0.05$, $^{**}p < 0.01$ *vs*. Ctrl group; $^{\#}p < 0.05$, $^{\#\#}p < 0.01$ *vs*. CRF group.

(NMDS) plot revealed four distinct clusters, suggesting the different structure of gut microbiota among four experimental groups (**Figures 6B,C**).

We performed a taxonomic analysis to quantify the relative abundances of gut microbiota among four experimental groups. At phylum levels, Firmicutes, Bacteroidetes, Verrucobacteria, Proteobacteria, and Actinobacteria were the dominant ones in fecal samples. As compared to the Ctrl group, the abundances of Firmicutes and Tenericutes phylum were up-regulated, while the contents of Verrucomicrobia and Bacteroidetes phyla were down-regulated in the CRF group (**Figure 6D**). SR decoction did not affect these phylum changes of CRF mice. However, it reversed the increase of Bacteroidaceae and the decrease of Rikenellaceae and Erysipelotrichaceae at family levels in the CRF group (**Figure 6E**). As indicated by the heat map analysis (**Figure 6F**), the abundances of a series of bacteria were significantly altered in the CRF group at genus levels. Among them, the content of *Parvibacter* was promoted after SR decoction treatment. In contrast, some other bacteria were decreased in abundances, including *Odoribacter*, *Acetatifactor*, *Alistipes*, *Anaerotruncus*, *Blautia*, *Clostridium*, *Desulfovibrio*, *Enterococcus*, *Lachnospiraceae*, *Marvinbryantia*, *Rikenellaceae*, *Rikenella*, *Ruminiclostridium*, and *Roseburia* ($p < 0.05$, *vs.* CRF group).

By the LEfSe analysis, we compared the characteristic bacteria taxa among four experimental groups at distinct classification levels ("p_," phylum; "o_," order; "c_," class, "f_," family, "g_," genus, and "s_," species). As illustrated in **Figure 7A**, seven bacterial taxa were identified in the Ctrl group, which were significantly different from those of the other three

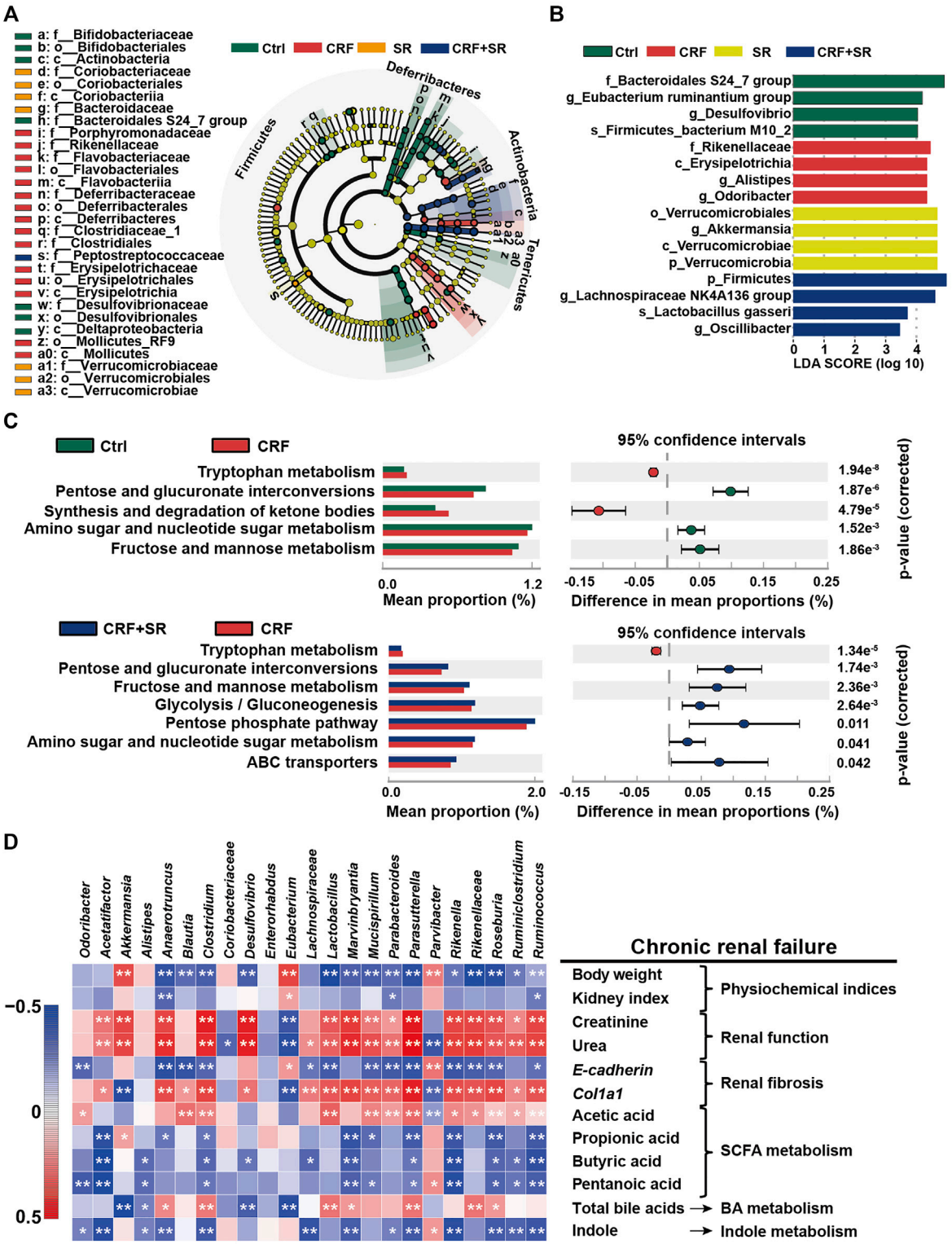

FIGURE 7 | Impact of SR decoction on characteristic taxa and bacterial metabolism in CRF mice, and correlation between gut microbiota dysbiosis and SRF occurrence. **(A)** Identification of characteristic taxa among four experimental groups by linear discriminant analysis (LDA) effect size (LEfSe). **(B)** Presentation of characteristic taxa using LDA with a threshold score >3.0. Bar length of LDA represents the impact of characteristic taxa in individual groups. **(C)** Functional prediction of Kyoto Encyclopedia of Genes and Genomes (KEGG) pathways by Phylogenetic investigation of communities by reconstruction of unobserved states (PICRUSt) analysis. **(D)** Spearman's correlation analysis between physiochemical indexes and 23 genera with the greatest changes in abundance among four experimental groups. The colors ranged from blue (negative correlation) to dark red (positive correlation), and significant correlations (n = 7) were marked by $*p < 0.05$, $**p < 0.01$.

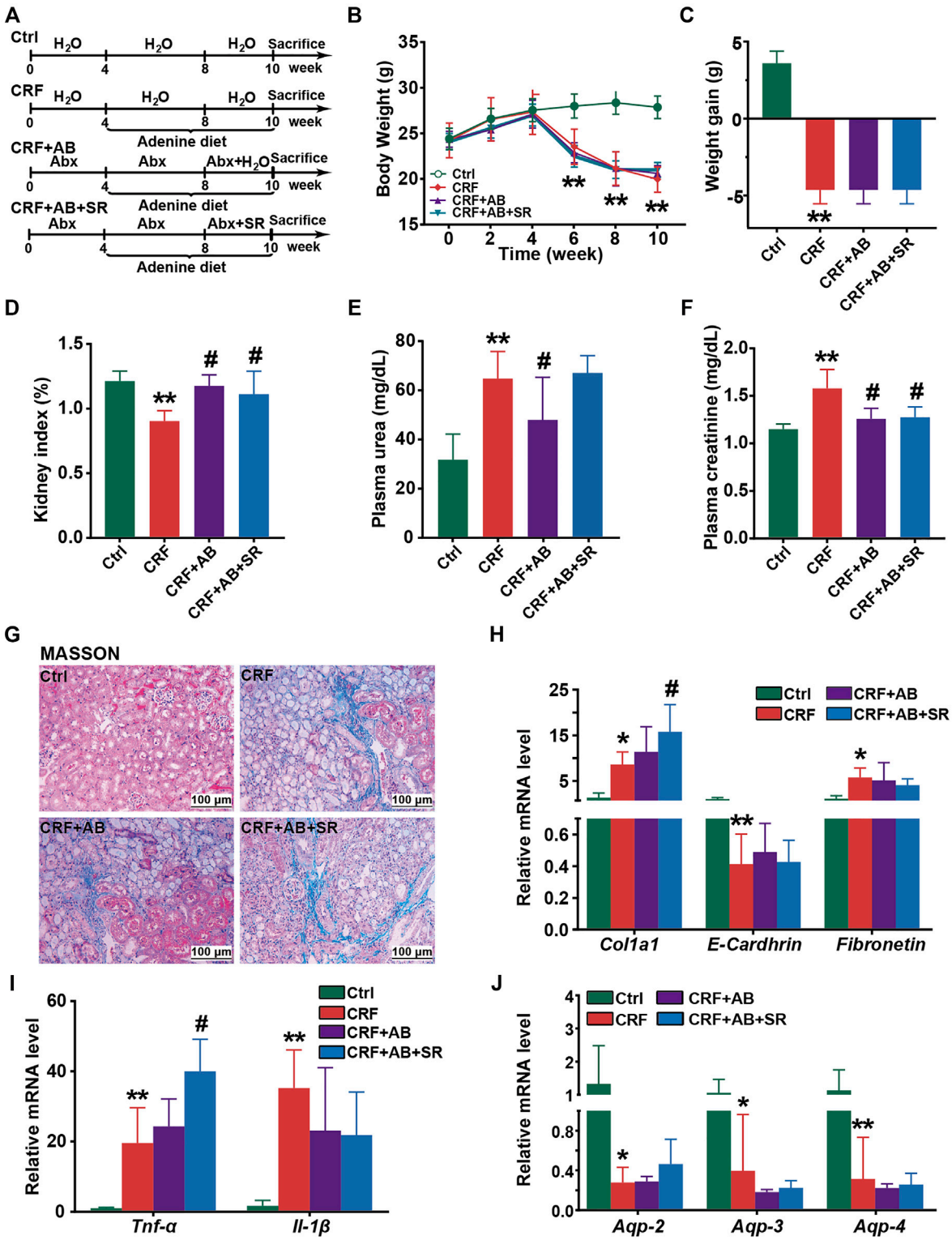

FIGURE 8 | Effect of SR decoction on CRF in mice with gut microbiota depletion. **(A)** Experimental schematic diagram. **(B)** Growth curve. **(C)** Body weight gain. **(D)** Kidney index. **(E)** Level of plasma urea. **(F)** Level of plasma creatinine. **(G)** MASSON staining of kidney tissues (200 ×). **(H)** Expression of renal fibrosis biomarkers in kidney tissues at mRNA levels, including *E-Cadherin*, *Col1a1*, and *Fibronectin*. **(I)** Expression of proinflammatory cytokines in kidney tissues at mRNA levels, including *Tnf-α* and *Il-1β*. **(J)** Expression of aquaporins in kidney tissues, including *Aqp-2*, *Aqp-3*, and *Aqp-4*. Data were represented as mean ± SD (n = 6). $^{*}p < 0.05$, $^{**}p < 0.01$ *vs*. Ctrl group; $^{\#}p < 0.05$, $^{\#\#}p < 0.01$ *vs*. CRF group.

experimental groups in abundance. Seven typical taxa belonged to the CRF group, and fifteen taxa were detected in the SR group. Additionally, Pptostreptococcaceae was the characteristic family in the CRF + SR group. Further, the taxa with the most remarkable differences in abundance were listed using linear discriminant analysis (LDA): 1) f_Bacteroidales S24_7 group, g_Eubacterium ruminantium group, g_Desulfovibrio, and s_Firmicutes bacterium M10_2 for the Ctrl group; 2) f_Rikenellaceae, c_Erysipelotrichia, g_Alistipes, and g_Odoribacter for the CRF group; 3) o_Verrucomicrobiales, g_Akkermansia, c_Verrucomicrobiae, and p_Verrucomicrobia for the SR group; 4) p_Firmicutes, g_Lachnospiraceae NK4A136 group, s_Lactobacillus gasseri, and g_Oscillibacter for the CRF + SR group (**Figure 7B**).

SR Decoction Affected Metabolic Pathways of Intestinal Bacteria in CRF Mice

The PICRUST analysis was employed to assess the impact of SR decoction on metabolic pathways of gut microbiota in CRF mice. Based on 141 Kyoto Encyclopedia of Genes and Genomes (KEGG) pathways, seven evidently changed ones were screened for comparison among four experimental groups (**Figure 7C**). Compared to the Ctrl group, there were five pathways found to be affected in the CRF group ($p < 0.01$). Among them, the metabolic activity of two pathways was upregulated, including Tryptophan metabolism and synthesis/degradation of ketone bodies; three pathways were downregulated, including pentose and glucuronate interconversions, amino sugar and nucleotide sugar metabolism, and fructose and mannose metabolism. Conversely, most of these altered pathways were recovered after SR decoction treatment ($p < 0.01$ or 0.05, *vs.* CRF group) (**Figure 7C**).

Correlation Between Bacterial Abundances and CRF-Related Indicators

To explore the association between gut microbiota dysbiosis and CRF occurrence, we calculated Spearman's correlation coefficient between physiochemical indexes and 23 genera with the greatest changes in abundance among four experimental groups. As illustrated in **Figure 7D**, 17 bacteria (*Anaerotruncus*, *Blautia*, *Clostridium*, etc.) were negatively correlated with body weight, kidney index, E-cadherin level, and metabolism of SCFA and indole, while positively related to renal function, Col1a1, and acetic acid levels, and BA metabolism. By contrast, totally different correlations were observed between the other six genera and physiochemical parameters of CRF mice, such as *Akkermansia*, *Alistipes*, and *Coriobacteriaceae*, etc.

SR Decoction Failed to Alleviate CRF in Mice With Gut Microbiota Depletion

To examine whether gut microbiota played a vital role in protecting of SR decoction against CRF, we fed mice with adenine diet, adenine diet + AB, or adenine diet + AB+ SR decoction (2.0 g crude SR/kg) (**Figure 8A**). After AB treatment for 4 weeks, the intestinal bacteria of mice were almost depleted, as indicated by the undetectable abundances of major phyla in comparison with those of the Ctrl and CRF group (**Supplementary Figure S3A**). As suggested in **Figure 8**, most of the deteriorated physiochemical parameters in the CRF group were not improved in either the CRF + AB group or the CRF + AB+ SR group, including the growth curve (**Figure 8B**), weight gain (**Figure 8C**), renal fibrosis (**Figures 8G,H**) and inflammation (**Figure 8I**), aquaporins destruction in kidneys (**Figure 8J**), and other related detection indexes (**Supplementary Figures S3B–S3F**). As compared to the CRF group, the change of kidney index and levels of urea and creatinine in plasma were statistically suppressed in mice of the CRF + AB group due to the depletion of gut microbiota ($p < 0.05$) (**Figures 8D–F**). However, SR decoction treatment failed to further strengthen the AB-initiated protective effect (**Figures 8D–F**). Meanwhile, SR decoction also did not rescue the intestinal damage to CRF mice, as can be seen by the worsened colonic structure in the CRF + AB + SR group (**Supplementary Figure S4**). The above results imply that SR decoction had no alleviating effect on the occurrence of CRF in mice with gut microbiota depletion.

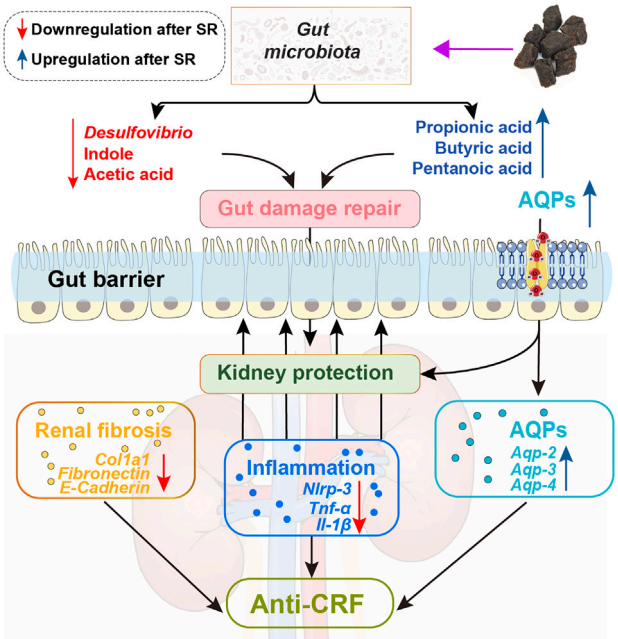

FIGURE 9 | Schematic diagram showing how SR decoction improved CRF. Red arrows, decreased changes after SR decoction treatment. Blue arrows, increased changes after SR decoction treatment.

DISCUSSION

As a recognized model drug, adenine degenerates renal tubule and interstitium that causes the occurrence of CRF, characterized by the inhibited excretion of nitrogen compounds, like Creatinine and Urea

(Claramunt et al., 2015). Creatinine is the metabolic end product of creatine and phosphocreatine, and urea is synthesized from ammonia in the liver (Baum et al., 1975; Jones and Brunett, 1975). Both metabolites are transported to the kidney for excretion through glomerular filtration, while impairment of the glomerulus will lead to the accumulation of toxic metabolites followed by the occurrence of CRF. In this study, we found that the levels of creatinine and urea in plasma were significantly increased in mice feeding with a 0.2% adenine diet (**Figures 2H–J**), accompanied by the abnormal changes of related physiochemical parameters (**Figures 2**, **3A**). On the contrary, these typical pathological features of CRF were statistically ameliorated by SR decoction. Since there was no difference in diet intake between the CRF group and CRF + SR group, the alleviated symptoms in the CRF + SR group were not due to less adenine intake (**Supplementary Figure S2**). This may be attributed to an active ingredient of *Rhubarb*, i.e., Emodin. Emodin is reported to increase glomerular filtration by inhibiting glomerular podocyte apoptosis and endoplasmic reticulum stress (Tian et al., 2018).

CRF is characterized by renal fibrosis, chronic inflammation, and fluid metabolism disorder. In CRF patients, increased nitrogenous substances may contribute to systemic inflammation via the increment of pro-inflammatory cytokines, like *Nlrp3, Tlr4, Il-1β*, and *Tnf-α* (Komada and Muruve, 2019; Ebert et al., 2020). Previously, SR decoction was demonstrated to have an inhibitory effect on inflammation both *in vitro* and *in vivo* (Ye et al., 2019; Ji et al., 2020). Similarly, we found that SR decoction could suppress the activation of *Nlrp3* and decrease the mRNA levels of *Il-1β* and *Tnf-α* (**Figure 3B**). Aquaporin is mainly expressed in the kidney and intestine (Esteva-Font et al., 2012). Aquaporins are divided into several subtypes and play different roles in the progression of CRF. Among them, AQP-1 and AQP-3 are responsible for toxin transport like urea and ammonia, and renal tubule injury will cause decreased expressions of both aquaporins followed by delayed toxin elimination (Litman et al., 2009; Hua et al., 2019). AQP-2 not only reabsorbs water but can alleviate renal inflammation in CRF, and AQP-4 is vital for the transport of water and electrolytes (Kong et al., 2020). In the study, SR decoction significantly inhibited the downregulation of these AQPs in CRF mice, suggesting its pivotal role in the maintenance of water and toxin transport (**Figure 3C**). In addition, SR decoction has a therapeutic effect on renal fibrosis by partly reversing the expression changes of major biomarkers in the kidney, such as E-Cadherin, Col1a1, and Fibronectin (**Figures 3D,E**). E-Cadherin is an important adhesion molecule to maintain the polarity between renal tubular epithelial cells (Black et al., 2019). Col1a1 and Fibronectin can promote fibroblast differentiation, and their over-production often causes excessive fiber deposition in the kidney (Mack and Yanagita, 2015; Huang et al., 2020). In the study, SR decoction reduced the mRNA levels of *Col1a1* and *Fibronectin* in kidney tissues of CRF mice, implying its efficacy in the treatment of renal fibrosis (**Figure 3D**). Further, SR decoction reduced the protein levels of p-GSK-3β (ser 9), GSK-3β, and β-Catenin (**Figure 3E**). We presume that SR decoction ameliorated renal fibrosis dependent on a blockade of the GSK-3β/β-Catenin signaling pathway.

Notably, SR decoction displayed a protective effect on the intestinal damage of CRF mice (**Figures 2**, **4**), and the action mechanisms may be multifactorial. On the one hand, since urea-derived ammonia and ammonium hydroxide directly damage the intestinal epithelial barrier (Huang et al., 2020), a reduced level of urea by SR decoction might benefit the gut barrier integrity in CRF mice (**Figure 2H**). On the other hand, the progression of CRF is accompanied by the dominance of pathogenic intestinal bacteria, leading to gut barrier corrosion (Meijers et al., 2019). Hence, the anti-bacterial effect of SR decoction makes it possible to prevent the intestine from damage (Xiang et al., 2020). Meanwhile, aquaporins play a major role in the progression of edema. The downregulation of aquaporins in the colon will deteriorate the water transport of mucosa cells and result in intestinal edema (Pelagalli et al., 2016). After SR decoction intervention, we observed significantly increased expressions of *Aqp-1*, *Aqp-2*, and *Aqp-3*, which may be the main reason for the relieved edema in colon tissues of CRF mice (**Figure 4A**).

As "healthy" gut microbiota products, SCFAs preferentially supply energy to intestinal epithelial cells (Yang et al., 2018). In this study, we observed the alterations of fecal SCFAs in CRF mice indicated by the increase of acetic acid and decrease of the other two SCFAs (Propionic acid and valeric acid), which were significantly repressed by SR decoction (**Figure 5A**). A similar result was obtained in a previous study that reported the markedly higher levels of acetic acid in feces of nephropathy mice (Yang et al., 2018). Acetic acid is involved in the citric acid cycle through the synthesis of acetyl coenzyme A and renal fibrosis will inhibit such a biological process (Hewitson and Smith, 2021), which may attribute to the sharp increase of acetic acid in CRF mice. In addition to providing the energy source for enterocytes, SCFAs have diverse regulatory functions on host physiology and immunity. For instance, SCFAs are pivotal for gut barrier integrity by promoting mucus production and suppressing inflammatory responses (Basson et al., 2016). This perhaps explains why SR decoction prevented the intestinal structure of CRF mice from damage (**Figure 4**). Noticeably, propionic acid can reduce urea and creatinine concentrations in the plasma of CRF patients (Huang et al., 2020), so an elevated level of propionic acid should be beneficial to the amelioration of CRF. Based on the above, the protective effect of SR decoction on CRF should be associated with its regulation of SCFA metabolic balance. Indeed, it was reported that gallic acid (a main component of SR decoction) could increase acetic acid consumption by promoting the citric acid cycle (Li et al., 2019; Wang et al., 2019).

Indole and its related bacterial metabolites were known to reduce intestinal inflammation, prevent gut barrier dysfunction, and significantly affect host metabolism (Beaumont et al., 2018). Our result shows that SR decoction statistically promoted the production of fecal indole in CRF mice (**Figure 5C**), suggesting its favorite effect on intestinal functions in the development of nephropathy. Aside from SCFAs and indoles, we also measured the content of fecal BAs. Of the BA pool, most BAs are taken up in the distal ileum and return to the liver. However, about 5% of the remaining BAs will escape intestinal uptake and can be metabolized by the gut microbiota to secondary BAs (Porez et al., 2012). In the intestine, BAs facilitate the digestion and absorption of dietary fat, steroids, or exogenous drug. Besides, BAs act as signaling molecules to modulate glucose and energy homeostasis (Degirolamo et al., 2014). Of note, a high concentration of BAs can cause inflammation, cellular apoptosis,

or even accumulation of BAs in the liver (Kuipers et al., 2014). And patients with fatty acid diseases also have increased serum bile acids (Akchurin and Kaskel, 2015). Thus, the increase of total and individual BAs in feces may implicate the deteriorated liver function of CRF mice (**Figures 5D–F**). Nevertheless, SR decoction had a little or even worse effect on the alteration of fecal BAs except for CDCA and TUDCA (**Figure 5F**). It was suggested that BAs are not the main target of SR decoction in CRF treatment.

Considering the significance of gut microbiota in the production of intestinal metabolites, we explored the effect of SR decoction on intestinal floral structure in CRF mice. Our studies suggest that SR decoction reduced gut microbiota diversity in CRF mice (**Figure 6A**). This might be due to the antimicrobial effects of SR components like Rhein and Gallic acid, which were reported to inhibit the growth of some harmful bacteria, such as *Helicobacter pylori*, *Escherichia coli*, and *Streptococcus mutans* (Shao et al., 2015; Zhou et al., 2015). Though SR decoction did not affect the gut microbiota at phylum levels, it significantly regulated the abundances of several bacterial families, that is, increased the population of Bacteroidales but decreased the contents of Rikenellaceae and Erysipelotrichaceae in CRF mice (**Figure 6E**). Bacteroidales can alleviate renal inflammation and damage by promoting propionic and butyric acid levels (Marzocco et al., 2018). By contrast, Erysipelotrichaceae is closely related to the synthesis of phenyl sulfate, which contributes to the formation of albuminuria and the subsequent progression of CRF (Kikuchi et al., 2019). At genus levels, the abundances of a wide range of bacteria were also altered in CRF mice (**Figure 6F**). Among them, *Desulfovibrio* produces genotoxic hydrogen sulfide (H_2S) gas, causing hypoplasia and hyperpermeability of intestinal epithelial cells (Rohr et al., 2020). The *Blautia*, *Acetatifactor*, and *Ruminococcus* genera are the main acetate genera, and their significant upregulation may be the reason for large increased acetic acid in CRF mouse feces (Cai et al., 2020). Genus *Parvibacter* is responsible for the metabolism of exogenous harmful substances (Choi et al., 2020). Conversely, SR decoction significantly reversed abnormal changes of these genera in CRF mice (**Figure 6F**). These results fully demonstrated the remodeling effect of SR decoction on the destructed structure of gut microbiota in mice with nephropathy. In a previous report, the dysbiosis of gut microbiota in CRF mice was characterized by increased pathogenic flora (Sun et al., 2021). Clinical trials also show that the abundances of Actinobacteria, Firmicutes, and Proteobacteria had the most significant increases at family levels in CRF patients compared with healthy controls (Vaziri et al., 2013). Most of the increased bacteria at genus levels also belonged to the three bacterial families in our study. Additionally, CRF can induce an increased production of urea. When the high-level urea enters the intestinal tract, it will stimulate the proliferation of bacteria with urease activity (Hobby et al., 2019). In this study, several bacteria elevated at genus levels also have urease activities, such as *Blautia*, *Ruminococcus*, *Clostridium*, *Enterorhabdus*, and *Alistipes*. The above reasons may explain why most representative bacteria genera displayed the highest levels in the CRF group (**Figure 6F**).

By PICRUSt analysis, SR decoction was found to affect the metabolism of gut bacteria in CRF mice, alluding to its regulatory effect on intestinal bacteria activities (**Figure 7C**). By correlation analysis, these altered intestinal florae were demonstrated to be associated with the production of intestinal metabolites and CRF-related physiochemical parameters (**Figure 7D**). Similar results were reported in clinical studies. For instance, *Eggerthella lenta* was one of the most enriched species in CRF patients and correlated with the production of several toxins (Moco et al., 2012). Further, severely aberrant gut microbiota and damaged mucosa in CRF patients displayed the potential for accelerated biosynthesis of toxic compounds, leading to a worsened kidney disease (Wang et al., 2020). It seemed that the colon mucosal barrier damage was a crucial inducer in CRF occurrence. In this study, we revealed that SR decoction had protective effects on both microbial structures and gut barrier integrity. Finally, we used germ-free mice to explore whether the original ingredients of SR decoction failed to directly protect mice against CRF before they were metabolized by intestinal flora. Indeed, the results indicate that SR decoction can't initiate a therapeutic effect on CRF without the intestinal bacteria transformation (**Figure 8**). On the other hand, though antibiotic treatment partly improved CRF symptoms, plasma creatinine and urea levels were elevated in CRF mice with gut microbiota depletion compared to the Ctrl group. So did the pathological changes, such as interstitial fibrosis, collagen fiber proliferation, and renal glomerular sclerosis. These results illustrated that gut microbiota is an important but not the only factor affecting CRF formation.

Previous studies have reported the regulatory effects of *rhubarb* or its chemical components on the intestinal flora. For example, Emodin alleviated gut barrier damage in mice by improving the distribution patterns of intestinal bacteria (Zeng et al., 2016). Rhein treatment increased Lactobacillus abundance, leading to a decreased uric acid level (Wu et al., 2020). As an active ingredient in dietary polyphenols, Gallic acid could elevate the diversity of intestinal flora (Geldert et al., 2021). Besides, Rhein-8-O-β-D-glucoside will be firstly metabolized to Rhein by intestinal flora in the gut, and Rhein raised the stability of gut microbiota (Li et al., 2020). Based on the above, we speculate that several chemical compounds of SR (like Rhein, Gallic acid, and Emodin) may directly display regulatory effects on gut microbiota structure and subsequent treatment of CRF. Besides, some other components (like Rhein-8-O-β-D-glucoside and polysaccharides) will act as prodrugs, and their metabolites transformed by intestinal bacteria further eased CRF symptoms. These presumptions need to be confirmed in future work.

CONCLUSION

In summary, this study proved that SR decoction mitigated CRF progression in mice, as indicated by the acceleration of renal fibrosis, reversal of inflammation and abnormal water transport in the kidney, and alleviation of the deteriorated gut barrier. The potential molecular mechanisms underlying the therapeutic effects of SR decoction were related to the reshaping of imbalanced gut microbiota and suppression of abnormal intestinal metabolite production (**Figure 9**). These findings shed light on the potential clinical application of SR decoction in nephropathy treatment.

DATA AVAILABILITY STATEMENT

The datasets presented in this study can be found in online repositories. The names of the repository/repositories and accession number(s) can be found below: https://www.ncbi.nlm.nih.gov/, PRJNA791187.

ETHICS STATEMENT

The animal study was reviewed and approved by The animal study was reviewed and approved by the Ethics Committee of Hubei University of Chinese Medicine (Hubei, China).

AUTHOR CONTRIBUTIONS

HL and YB designed the study. RW, BH, CY, ZZ, MY, and QC were responsible for the acquisition of data. BH interpreted the experimental data. RW and HL were the major contributors in drafting and revising the manuscript. All authors read and approved the final manuscript.

FUNDING

This work was supported by Health Commission of Hubei Province of China (NO. ZY 2021Z005), National Natural Science Foundation of China (NO. 31902356 and NO. 81873098), Major Science and Technology Project in Hubei Province (NO.2021ACA004-03), and Major Science and Technology Project in Yunnan Province (NO. 202102AE090042).

SUPPLEMENTARY MATERIAL

The Supplementary Material for this article can be found online at: https://www.frontiersin.org/articles/10.3389/fphar.2022.842720/full#supplementary-material

REFERENCES

Akchurin, O. M., and Kaskel, F. (2015). Update on Inflammation in Chronic Kidney Disease. *Blood Purif.* 39 (1-3), 84–92. doi:10.1159/000368940

Ammirati, A. L. (2020). Chronic Kidney Disease. *Rev. Assoc. Med. Bras (1992)* 66Suppl 1 (Suppl. 1), s03–s09. doi:10.1590/1806-9282.66.S1.3

Basson, A., Trotter, A., Rodriguez-Palacios, A., and Cominelli, F. (2016). Mucosal Interactions between Genetics, Diet, and Microbiome in Inflammatory Bowel Disease. *Front. Immunol.* 7, 290. doi:10.3389/fimmu.2016.00290

Baum, N., Dichoso, C. C., and Carlton, C. E. (1975). Blood Urea Nitrogen and Serum Creatinine. Physiology and Interpretations. *Urology* 5 (5), 583–588. doi:10.1016/0090-4295(75)90105-3

Beaumont, M., Neyrinck, A. M., Olivares, M., Rodriguez, J., Rocca Serra, A., Roumain, M., et al. (2018). The Gut Microbiota Metabolite Indole Alleviates Liver Inflammation in Mice. *FASEB j.* 32, 6681–6693. doi:10.1096/fj.201800544

Black, L. M., Lever, J. M., and Agarwal, A. (2019). Renal Inflammation and Fibrosis: A Double-Edged Sword. *J. Histochem. Cytochem.* 67 (9), 663–681. doi:10.1369/0022155419852932

Cai, T. T., Ye, X. L., Li, R. R., Chen, H., Wang, Y. Y., Yong, H. J., et al. (2020). Resveratrol Modulates the Gut Microbiota and Inflammation to Protect against Diabetic Nephropathy in Mice. *Front. Pharmacol.* 11, 1249. doi:10.3389/fphar.2020.01249

Cao, Y. J., Pu, Z. J., Tang, Y. P., Shen, J., Chen, Y. Y., Kang, A., et al. (2017). Advances in Bio-Active Constituents, Pharmacology and Clinical Applications of Rhubarb. *Chin. Med.* 12, 36. doi:10.1186/s13020-017-0158-5

Chen, L., Chen, D. Q., Liu, J. R., Zhang, J., Vaziri, N. D., Zhuang, S., et al. (2019). Unilateral Ureteral Obstruction Causes Gut Microbial Dysbiosis and Metabolome Disorders Contributing to Tubulointerstitial Fibrosis. *Exp. Mol. Med.* 51 (3), 1–18. doi:10.1038/s12276-019-0234-2

Choi, B. S., Varin, T. V., St-Pierre, P., Pilon, G., Tremblay, A., and Marette, A. (2020). A Polyphenol-Rich cranberry Extract Protects against Endogenous Exposure to Persistent Organic Pollutants during Weight Loss in Mice. *Food Chem. Toxicol.* 146, 111832. doi:10.1016/j.fct.2020.111832

Claramunt, D., Gil-Peña, H., Fuente, R., García-López, E., Loredo, V., Hernández-Frías, O., et al. (2015). Chronic Kidney Disease Induced by Adenine: a Suitable Model of Growth Retardation in Uremia. *Am. J. Physiol. Ren. Physiol* 309 (1), F57–F62. doi:10.1152/ajprenal.00051.2015

Degirolamo, C., Rainaldi, S., Bovenga, F., Murzilli, S., and Moschetta, A. (2014). Microbiota Modification with Probiotics Induces Hepatic Bile Acid Synthesis via Downregulation of the Fxr-Fgf15 axis in Mice. *Cell Rep* 7 (1), 12–18. doi:10.1016/j.celrep.2014.02.032

Dos Santos, I. F., Sheriff, S., Amlal, S., Ahmed, R. P. H., Thakar, C. V., and Amlal, H. (2019). Adenine Acts in the Kidney as a Signaling Factor and Causes Salt- and Water-Losing Nephropathy: Early Mechanism of Adenine-Induced Renal Injury. *Am. J. Physiol. Ren. Physiol* 316 (4), F743–f757. doi:10.1152/ajprenal.00142.2018

Ebert, T., Pawelzik, S. C., Witasp, A., Arefin, S., Hobson, S., Kublickiene, K., et al. (2020). Inflammation and Premature Ageing in Chronic Kidney Disease. *Toxins (Basel)* 12 (4), 227. doi:10.3390/toxins12040227

Esteva-Font, C., Ballarin, J., and Fernández-Llama, P. (2012). Molecular Biology of Water and Salt Regulation in the Kidney. *Cell Mol Life Sci* 69 (5), 683–695. doi:10.1007/s00018-011-0858-4

GBD Chronic Kidney Disease Collaboration (2020). Global, Regional, and National burden of Chronic Kidney Disease, 1990-2017: a Systematic Analysis for the Global Burden of Disease Study 2017. *Lancet* 395 (10225), 709–733. doi:10.1016/s0140-6736(20)30045-3

Geldert, C., Abdo, Z., Stewart, J. E., and H S, A. (2021). Dietary Supplementation with Phytochemicals Improves Diversity and Abundance of Honey Bee Gut Microbiota. *J. Appl. Microbiol.* 130 (5), 1705–1720. doi:10.1111/jam.14897

Giordano, L., Mihaila, S. M., Eslami Amirabadi, H., and Masereeuw, R. (2021). Microphysiological Systems to Recapitulate the Gut-Kidney Axis. *Trends Biotechnol.* 39 (8), 811–823. doi:10.1016/j.tibtech.2020.12.001

Heinrich, M., Appendino, G., Efferth, T., Fürst, R., Izzo, A. A., Kayser, O., et al. (2020). Best Practice in Research - Overcoming Common Challenges in Phytopharmacological Research. *J. Ethnopharmacol.* 246, 112230. doi:10.1016/j.jep.2019.112230

Hewitson, T. D., and Smith, E. R. (2021). A Metabolic Reprogramming of Glycolysis and Glutamine Metabolism Is a Requisite for Renal Fibrogenesis-Why and How? *Front. Physiol.* 12, 645857. doi:10.3389/fphys.2021.645857

Hobby, G. P., Karaduta, O., Dusio, G. F., Singh, M., Zybailov, B. L., and Arthur, J. M. (2019). Chronic Kidney Disease and the Gut Microbiome. *Am. J. Physiol. Ren. Physiol.* 316 (6), F1211–f1217. doi:10.1152/ajprenal.00298.2018

Hua, Y., Ying, X., Qian, Y., Liu, H., Lan, Y., Xie, A., et al. (2019). Physiological and Pathological Impact of AQP1 Knockout in Mice. *Biosci. Rep.* 39 (5), BSR20182303. doi:10.1042/bsr20182303

Huang, Y., Zhou, J., Wang, S., Xiong, J., Chen, Y., Liu, Y., et al. (2020). Indoxyl Sulfate Induces Intestinal Barrier Injury through IRF1-DRP1 axis-mediated Mitophagy Impairment. *Theranostics* 10 (16), 7384–7400. doi:10.7150/thno.45455

Ji, C., Deng, Y., Yang, A., Lu, Z., Chen, Y., Liu, X., et al. (2020). Rhubarb Enema Improved Colon Mucosal Barrier Injury in 5/6 Nephrectomy Rats May Associate with Gut Microbiota Modification. *Front. Pharmacol.* 11, 1092. doi:10.3389/fphar.2020.01092

Jiang, S., Xie, S., Lv, D., Zhang, Y., Deng, J., Zeng, L., et al. (2016). A Reduction in the Butyrate Producing Species Roseburia Spp. And Faecalibacterium Prausnitzii Is Associated with Chronic Kidney Disease Progression. *Antonie Van Leeuwenhoek* 109 (10), 1389–1396. doi:10.1007/s10482-016-0737-y

Jones, J. D., and Brunett, P. C. (1975). Creatinine Metabolism and Toxicity. *Kidney Int. Suppl.* (3), 294–298.

Kikuchi, K., Saigusa, D., Kanemitsu, Y., Matsumoto, Y., Thanai, P., Suzuki, N., et al. (2019). Gut Microbiome-Derived Phenyl Sulfate Contributes to Albuminuria in Diabetic Kidney Disease. *Nat. Commun.* 10 (1), 1835. doi:10.1038/s41467-019-09735-4

Koizumi, M., Tatebe, J., Watanabe, I., Yamazaki, J., Ikeda, T., and Morita, T. (2014). Aryl Hydrocarbon Receptor Mediates Indoxyl Sulfate-Induced Cellular Senescence in Human Umbilical Vein Endothelial Cells. *J. Atheroscler. Thromb.* 21 (9), 904–916. doi:10.5551/jat.23663

Komada, T., and Muruve, D. A. (2019). The Role of Inflammasomes in Kidney Disease. *Nat. Rev. Nephrol.* 15 (8), 501–520. doi:10.1038/s41581-019-0158-z

Kong, Y., Feng, W., Zhao, X., Zhang, P., Li, S., Li, Z., et al. (2020). Statins Ameliorate Cholesterol-Induced Inflammation and Improve AQP2 Expression by Inhibiting NLRP3 Activation in the Kidney. *Theranostics* 10 (23), 10415–10433. doi:10.7150/thno.49603

Kuipers, F., Bloks, V. W., and Groen, A. K. (2014). Beyond Intestinal Soap-Bbile Acids in Metabolic Control. *Nat. Rev. Endocrinol.* 10 (8), 488–498. doi:10.1038/nrendo.2014.60

Li, L. Z., Tao, S. B., Ma, L., and Fu, P. (2019). Roles of Short-Chain Fatty Acids in Kidney Diseases. *Chin. Med. J. (Engl)* 132 (10), 1228–1232. doi:10.1097/cm9.0000000000000228

Li, Q., Guo, Y., Yu, X., Liu, W., and Zhou, L. (2020). Protective Mechanism of Rhubarb Anthraquinone Glycosides in Rats with Cerebral Ischaemia-Reperfusion Injury: Interactions between Medicine and Intestinal Flora. *Chin. Med.* 15, 60. doi:10.1186/s13020-020-00341-x

Li, H., Feng, Y., Sun, W., Kong, Y., and Jia, L. (2021). Antioxidation, Anti-inflammation and Anti-fibrosis Effect of Phosphorylated Polysaccharides from Pleurotus Djamor Mycelia on Adenine-Induced Chronic Renal Failure Mice. *Int. J. Biol. Macromol* 170, 652–663. doi:10.1016/j.ijbiomac.2020.12.159

Litman, T., Søgaard, R., and Zeuthen, T. (2009). Ammonia and Urea Permeability of Mammalian Aquaporins. *Handb Exp. Pharmacol.* 190, 327–358. doi:10.1007/978-3-540-79885-9_17

Liu, H., Zheng, J., Lai, H. C., Hu, B., Zhu, L., Leung, E. L., et al. (2020). Microbiome Technology Empowers the Development of Traditional Chinese Medicine. *Sci. China Life Sci.* 63 (11), 1759–1761. doi:10.1007/s11427-020-1778-7

Ma, T. T., and Meng, X. M. (2019). TGF-β/Smad and Renal Fibrosis. *Adv. Exp. Med. Biol.* 1165, 347–364. doi:10.1007/978-981-13-8871-2_16

Mack, M., and Yanagita, M. (2015). Origin of Myofibroblasts and Cellular Events Triggering Fibrosis. *Kidney Int.* 87 (2), 297–307. doi:10.1038/ki.2014.287

Marzocco, S., Fazeli, G., Di Micco, L., Autore, G., Adesso, S., Dal Piaz, F., et al. (2018). Supplementation of Short-Chain Fatty Acid, Sodium Propionate, in Patients on Maintenance Hemodialysis: Beneficial Effects on Inflammatory Parameters and Gut-Derived Uremic Toxins, A Pilot Study (PLAN Study). *J. Clin. Med.* 7 (10), 315. doi:10.3390/jcm7100315

Meijers, B., Evenepoel, P., and Anders, H. J. (2019). Intestinal Microbiome and Fitness in Kidney Disease. *Nat. Rev. Nephrol.* 15 (9), 531–545. doi:10.1038/s41581-019-0172-1

Mishima, E., Fukuda, S., Shima, H., Hirayama, A., Akiyama, Y., Takeuchi, Y., et al. (2015). Alteration of the Intestinal Environment by Lubiprostone Is Associated with Amelioration of Adenine-Induced CKD. *J. Am. Soc. Nephrol.* 26 (8), 1787–1794. doi:10.1681/asn.2014060530

Miyazaki-Anzai, S., Masuda, M., Shiozaki, Y., Keenan, A. L., Chonchol, M., Kremoser, C., et al. (2021). Free Deoxycholic Acid Exacerbates Vascular Calcification in CKD through ER Stress-Mediated ATF4 Activation. *Kidney360* 2 (5), 857–868. doi:10.34067/kid.0007502020

Moco, S., Martin, F. P., and Rezzi, S. (2012). Metabolomics View on Gut Microbiome Modulation by Polyphenol-Rich Foods. *J. Proteome Res.* 11 (10), 4781–4790. doi:10.1021/pr300581s

Pelagalli, A., Squillacioti, C., Mirabella, N., and Meli, R. (2016). Aquaporins in Health and Disease: An Overview Focusing on the Gut of Different Species. *Int. J. Mol. Sci.* 17 (8), 1213. doi:10.3390/ijms17081213

Porez, G., Prawitt, J., Gross, B., and Staels, B. (2012). Bile Acid Receptors as Targets for the Treatment of Dyslipidemia and Cardiovascular Disease. *J. Lipid Res.* 53 (9), 1723–1737. doi:10.1194/jlr.R024794

Rohr, M. W., Narasimhulu, C. A., Rudeski-Rohr, T. A., and Parthasarathy, S. (2020). Negative Effects of a High-Fat Diet on Intestinal Permeability: A Review. *Adv. Nutr.* 11 (1), 77–91. doi:10.1093/advances/nmz061

Schunk, S. J., Floege, J., Fliser, D., and Speer, T. (2021). WNT-β-catenin Signalling - a Versatile Player in Kidney Injury and Repair. *Nat. Rev. Nephrol.* 17 (3), 172–184. doi:10.1038/s41581-020-00343-w

Shao, D., Li, J., Li, J., Tang, R., Liu, L., Shi, J., et al. (2015). Inhibition of Gallic Acid on the Growth and Biofilm Formation of *Escherichia coli* and Streptococcus Mutans. *J. Food Sci.* 80 (6), M1299–M1305. doi:10.1111/1750-3841.12902

Sun, Y. B., Qu, X., Caruana, G., and Li, J. (2016). The Origin of Renal Fibroblasts/myofibroblasts and the Signals that Trigger Fibrosis. *Differentiation* 92 (3), 102–107. doi:10.1016/j.diff.2016.05.008

Sun, C. Y., Li, J. R., Wang, Y. Y., Lin, S. Y., Ou, Y. C., Lin, C. J., et al. (2021). Indoxyl Sulfate Caused Behavioral Abnormality and Neurodegeneration in Mice with Unilateral Nephrectomy. *Aging (Albany NY)* 13 (5), 6681–6701. doi:10.18632/aging.202523

Tian, N., Gao, Y., Wang, X., Wu, X., Zou, D., Zhu, Z., et al. (2018). Emodin Mitigates Podocytes Apoptosis Induced by Endoplasmic Reticulum Stress through the Inhibition of the PERK Pathway in Diabetic Nephropathy. *Drug Des. Devel Ther.* 12, 2195–2211. doi:10.2147/dddt.S167405

Vaziri, N. D., Wong, J., Pahl, M., Piceno, Y. M., Yuan, J., DeSantis, T. Z., et al. (2013). Chronic Kidney Disease Alters Intestinal Microbial flora. *Kidney Int.* 83 (2), 308–315. doi:10.1038/ki.2012.345

Wang, V., Vilme, H., Maciejewski, M. L., and Boulware, L. E. (2016). The Economic Burden of Chronic Kidney Disease and End-Stage Renal Disease. *Semin. Nephrol.* 36 (4), 319–330. doi:10.1016/j.semnephrol.2016.05.008

Wang, S., Lv, D., Jiang, S., Jiang, J., Liang, M., Hou, F., et al. (2019). Quantitative Reduction in Short-Chain Fatty Acids, Especially Butyrate, Contributes to the Progression of Chronic Kidney Disease. *Clin. Sci. (Lond)* 133 (17), 1857–1870. doi:10.1042/cs20190171

Wang, X., Yang, S., Li, S., Zhao, L., Hao, Y., Qin, J., et al. (2020). Aberrant Gut Microbiota Alters Host Metabolome and Impacts Renal Failure in Humans and Rodents. *Gut* 69 (12), 2131–2142. doi:10.1136/gutjnl-2019-319766

Wu, J., Wei, Z., Cheng, P., Qian, C., Xu, F., Yang, Y., et al. (2020). Rhein Modulates Host Purine Metabolism in Intestine through Gut Microbiota and Ameliorates Experimental Colitis. *Theranostics* 10 (23), 10665–10679. doi:10.7150/thno.43528

Wyngaarden, J. B., and Dunn, J. T. (1957). 8-Hydroxyadenine as the Intermediate in the Oxidation of Adenine to 2, 8-dihydroxyadenine by Xanthine Oxidase. *Arch. Biochem. Biophys.* 70 (1), 150–156. doi:10.1016/0003-9861(57)90088-7

Xiang, H., Zuo, J., Guo, F., and Dong, D. (2020). What We Already Know about Rhubarb: a Comprehensive Review. *Chin. Med.* 15, 88. doi:10.1186/s13020-020-00370-6

Yang, J., Li, Q., Henning, S. M., Zhong, J., Hsu, M., Lee, R., et al. (2018). Effects of Prebiotic Fiber Xylooligosaccharide in Adenine-Induced Nephropathy in Mice. *Mol. Nutr. Food Res.* 62, 1800014. doi:10.1002/mnfr.201800014

Yao, M., Gao, J., Li, G. Q., and Xie, Z. (2012). Quantifying Four-Probe Metabolites in a Single UPLC-MS/MS Run to Explore the Effects of Cooked Rhubarb on Cytochrome P450 Isozymes. *Bioanalysis* 4 (22), 2693–2703. doi:10.4155/bio.12.236

Ye, B., Chen, X., Dai, S., Han, J., Liang, X., Lin, S., et al. (2019). Emodin Alleviates Myocardial Ischemia/reperfusion Injury by Inhibiting Gasdermin D-Mediated Pyroptosis in Cardiomyocytes. *Drug Des. Devel Ther.* 13, 975–990. doi:10.2147/dddt.S195412

Zeng, Y. Q., Dai, Z., Lu, F., Lu, Z., Liu, X., Chen, C., et al. (2016). Emodin via Colonic Irrigation Modulates Gut Microbiota and Reduces Uremic Toxins in Rats with Chronic Kidney Disease. *Oncotarget* 7 (14), 17468–17478. doi:10.18632/oncotarget.8160

Zhang, Q., Liu, L., Lin, W., Yin, S., Duan, A., Liu, Z., et al. (2017). Rhein Reverses Klotho Repression via Promoter Demethylation and Protects against Kidney and Bone Injuries in Mice with Chronic Kidney Disease. *Kidney Int.* 91 (1), 144–156. doi:10.1016/j.kint.2016.07.040

Zhang, Z. H., Li, M. H., Liu, D., Chen, H., Chen, D. Q., Tan, N. H., et al. (2018). Rhubarb Protect against Tubulointerstitial Fibrosis by Inhibiting TGF-β/Smad

Pathway and Improving Abnormal Metabolome in Chronic Kidney Disease. *Front. Pharmacol.* 9, 1029. doi:10.3389/fphar.2018.01029

Zhou, Y. X., Xia, W., Yue, W., Peng, C., Rahman, K., and Zhang, H. (2015). Rhein: A Review of Pharmacological Activities. *Evid. Based Complement. Alternat Med.* 2015, 578107. doi:10.1155/2015/578107

Zhou, S., He, Y., Zhang, W., Xiong, Y., Jiang, L., Wang, J., et al. (2021). Ophiocordyceps Lanpingensis Polysaccharides Alleviate Chronic Kidney Disease through MAPK/NF-κB Pathway. *J. Ethnopharmacol.* 276, 114189. doi:10.1016/j.jep.2021.114189

Zhu, T., Liu, X., Wang, X., Cao, G., Qin, K., Pei, K., et al. (2016). Profiling and Analysis of Multiple Compounds in Rhubarb Decoction after Processing by Wine Steaming Using UHPLC-Q-TOF-MS Coupled with Multiple Statistical Strategies. *J. Sep. Sci.* 39 (15), 3081–3090. doi:10.1002/jssc.201600256

Zhuang, T., Gu, X., Zhou, N., Ding, L., Yang, L., and Zhou, M. (2020). Hepatoprotection and Hepatotoxicity of Chinese Herb Rhubarb (Dahuang): How to Properly Control the "General (Jiang Jun)" in Chinese Medical Herb. *Biomed. Pharmacother.* 127, 110224. doi:10.1016/j.biopha.2020.110224

Conflict of Interest: The authors declare that the research was conducted in the absence of any commercial or financial relationships that could be construed as a potential conflict of interest.

Publisher's Note: All claims expressed in this article are solely those of the authors and do not necessarily represent those of their affiliated organizations, or those of the publisher, the editors and the reviewers. Any product that may be evaluated in this article, or claim that may be made by its manufacturer, is not guaranteed or endorsed by the publisher.

frontiers | Frontiers in Pharmacology

REVIEW
published: 05 April 2022
doi: 10.3389/fphar.2022.862831

New Therapeutic Horizon of Graves' Hyperthyroidism: Treatment Regimens Based on Immunology and Ingredients From Traditional Chinese Medicine

Qiongyao He[1,2], *Hui Dong*[1], *Minmin Gong*[1], *Yujin Guo*[1], *Qingsong Xia*[1], *Jing Gong*[3]* and *Fuer Lu*[3]*

[1]Institute of Integrated Traditional Chinese and Western Medicine, Tongji Hospital, Tongji Medical College, Huazhong University of Science and Technology, Wuhan, China, [2]Grade 2017 of Integrated Traditional Chinese and Western Clinical Medicine, Second Clinical School, Tongji Hospital, Tongji Medical College, Huazhong University of Science and Technology, Wuhan, China, [3]Department of Integrated Traditional Chinese and Western Medicine, Tongji Medical College, Tongji Hospital, Huazhong University of Science and Technology, Wuhan, China

OPEN ACCESS

Edited by:
Shuai Ji,
Xuzhou Medical University, China

Reviewed by:
Silvia Martina Ferrari,
University of Pisa, Italy
Daniela Gallo,
University of Insubria, Italy

***Correspondence:**
Fuer Lu
felutjh88@163.com
Jing Gong
jgongtcm@126.com

Specialty section:
This article was submitted to Ethnopharmacology, a section of the journal Frontiers in Pharmacology

Received: 26 January 2022
Accepted: 09 March 2022
Published: 05 April 2022

Citation:
He Q, Dong H, Gong M, Guo Y, Xia Q, Gong J and Lu F (2022) New Therapeutic Horizon of Graves' Hyperthyroidism: Treatment Regimens Based on Immunology and Ingredients From Traditional Chinese Medicine. Front. Pharmacol. 13:862831. doi: 10.3389/fphar.2022.862831

Graves' disease is an autoimmune disease characterized by goiter and hyperthyroidism, and 25% patients develop GO. Traditional treatment options, such as antithyroid drugs, radioiodine or thyroidectomy, have remained largely unchanged over the past 70 years. For many patients, there is a high rate of recurrence after antithyroid drugs and lifelong hypothyroidism after ablation and thyroidectomy. The symptoms and quality of life of some patients have not been effectively improved. The clinical demand for new therapeutic regimens, coupled with a deeper understanding of the pathophysiology and immunobiology of Graves' disease, has led to the emergence of several new therapeutic ideas, including biologics, small molecule peptides, immunomodulators and teprotumumab, a specific antibody targeting IGF-1R. Besides, the elements of TCM have attracted more and more interests in modern medicine, because some effective components have been successfully used in the treatment of autoimmune diseases. Based on the pathophysiology and efficacy of clinical management and treatment in Graves' hyperthyroidism, here we review the new strategies under investigation and summarize the effective components of traditional Chinese medicine used for Graves' hyperthyroidism, and explore their mechanisms. These therapies have opened a new window for the treatment of Graves' disease, but the exact mechanism and the research direction still need to be further explored.

Keywords: graves' ophthalmopathy, graves' disease (GD), traditional chinese medicine, immunology, treatment regimens

HIGHLIGHTS

1) The pathogenesis of Graves' disease is that thyroid stimulating hormone receptor (TSHR) antigen secreted by thyroid gland is specifically recognized by immune cells and reactive thyroid stimulating hormone receptor antibody (TRAB) is secreted to act on thyroid follicular cells and orbital fibroblasts.

2) Antithyroid drugs, radioactive iodine and thyroidectomy are three traditional treatment methods. Now, biological agents, small molecule peptides, immunomodulators and antibodies targeting growth factor-I receptor (IGF-1R) have also been proposed.
3) There are risks of disease recurrence, lifelong replacement therapy of thyroid hormone and complications associated with traditional treatment regimens, while other new treatment regimens have limitations.
4) The effective components of traditional Chinese medicine can effectively relieve large goiter and reduce side effects of antithyroid drugs (ATD), relieve symptoms of Graves' ophthalmopathy (GO), alleviate the hypermetabolic symptoms of Graves' disease (GD), reduce allergic symptoms and increase the dosage of ATD used in allergic patients.
5) The mechanism of effective components of traditional Chinese medicine (TCM) is different from the existing treatment projects, and it still needs a lot of high-quality randomized controlled trial (RCT) studiesand in-depth explorations to confirm the efficacy and elucidate the exact mechanism.

INTRODUCTION

GD is an organ-specific autoimmune disease that causes excessive thyroid hormone secretion (hyperthyroidism). GD is the most common cause of persistent hyperthyroidism in adults. Approximately 3% of women and 0.5% of men will develop Graves' disease during their lifetime (Burch and Cooper, 2015). It is clinically characterized by thyrotoxicosis, serum anti-thyroid antibodies (ATA) and the presence of autoreactive lymphocytes in the glands. Thyroid stimulating hormone (TSH) receptor (TSHR), thyroid peroxidase (TPO) and thyroglobulin (TG) have unusual properties (" immunogenicity") and can disrupt immune tolerance. (Burch and Cooper, 2015). Abnormal release of thyroid hormone affects many body systems, so signs and symptoms associated with GD can vary widely and can significantly affect overall health. Common symptoms include shaking, heat sensitivity and warmth, loss of weight even with normal eating habits, anxiety and irritability, goiter, changes of menstrual cycle, erectile dysfunction and loss of libido, fatigue, frequent bowel movements, palpitations, etc. At present, ATD are the first-line treatment for GD. Ablative therapy with radioactive iodine (RAI) or surgical thyroidectomy can lead to hypothyroidism and lifelong replacement therapy of thyroid hormone. High-dose intravenous immunoglobulin or corticosteroid (CS) can reduce inflammation and orbital congestion in patients with active GO. Orbital decompression surgery and post-globular radiotherapy are also selectable treatment methods for Graves' oculopathy, but side effects limit their widespread application.

The clinical demand for new therapeutic regimens of Graves' disease has led to the emergence of several new therapeutic ideas, including biologics, small molecule peptides, immunomodulators and teprotumumab. Elements of TCM have also attracted more and more interests in modern medicine because they have unique curative effects and mechanisms of action. Nutraceuticals are included in TCM, which are defined as a food, or parts of a food, that provide medical or health benefits, including the prevention of different pathological conditions, and thyroid diseases, or the treatment of them. Nutraceuticals have a place in complementary medicines, being positioned in an area among food, food supplements, and pharmaceuticals. The market of certain nutraceuticals such as thyroid supplements has been growing in the last years (Benvenga et al., 2020). Based on the pathology and efficacy of clinical management and treatment in Graves' hyperthyroidism, this article summarizes the new strategies under investigation and the effective components of traditional Chinese medicine used for Graves' hyperthyroidism, and explores corresponding mechanisms.

PATHOPHYSIOLOGY

GD is an autoimmune disease caused by the abnormally activated immune system and the loss of immune tolerance to TSHR (Smith and Hegedüs, 2016). TSHR peptide secreted by thyroid tissue is taken up by dendritic cells, and the major histocompatibility complex (MHC) class II molecules on the surface of dendritic cells bind to T cell antigen receptor (TCR) on the surface of T lymphocytes to present TSHR peptide to T lymphocytes. Once CD154 molecules on the surface of activated T lymphocytes recognize CD40 molecules on the surface of B cells, the CD40-CD154 interaction initiates the costimulatory pathway, providing the first signal needed to initiate the adaptive humoral immune response (Smith and Hegedüs, 2016). This interaction between B and T lymphocytes is thought to play a central role in the pathogenesis of GD, as it is required for the formation and maturation of B cells in the germinal centers of the thyroid, permitting the production of pathogenic thyroid-stimulating antibodies (Armengol et al., 2001; Huber et al., 2012; Smith and Hegedüs, 2016). B cell activating factor (BAFF) is a member of the tumor necrosis factor (TNF) family of cytokines that plays an important role in the activation, differentiation and survival of B lymphocytes. Elevated circulating BAFF levels have been found in patients with various autoimmune diseases, including GD, in which elevated levels of thyroid hormone and TRAB have been shown to correlate with serum BAFF levels (Lin et al., 2016). The interaction of BAFF and BAFF receptor on the surface of B lymphocytes is the second signal to initiate adaptive humoral immune response.

After the humoral immune response is activated, B lymphocytes secrete large amounts of TRAB, which can be divided into two forms: stimulating type and blocking type (Diana et al., 2016). Circulatory stimulating TRAB is similar to TSH agonist and specifically binds to TSHR to stimulate the proliferation and hypertrophy of thyroid cell, promoting the expression of sodium-iodine cotransporter, thyroglobulin and thyroid peroxidase genes, and ultimately promote the production of thyroid hormone and hyperthyroidism (Smith and Hegedüs, 2016). Blocking TRAB has no functional activity in combination with TSHR and is considered as a neutralizing

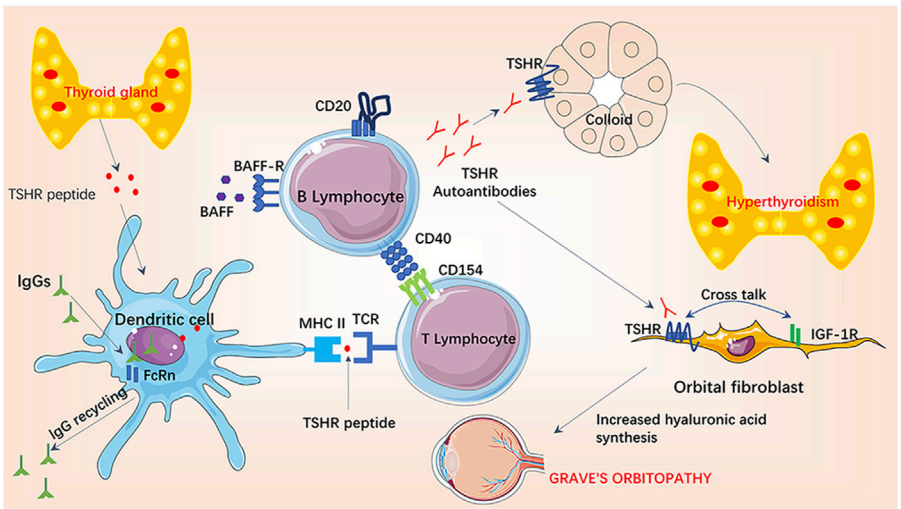

FIGURE 1 | Pathogenesis of Graves' hyperthyroidism and Graves' orbitopathy.

antibody. TRAB also acts on TSHR on the surface of orbital fibroblasts, leading to the release of hydrophilic mucopolysaccharide and pro-inflammatory cytokines, which intensifies the orbital inflammatory process, leading to local edema, congestion and eyeball herniation (Armengol et al., 2001; Graves' disease, 2000). Moreover, recent *in vitro* experiments have shown that insulin-like growth factor-1 receptor (IGF-1R) is another key player and associated autoantigen in the pathogenesis of GO (Wang and Smith, 2014). TSHR and IGF-1R co-locate to thyroid cells and orbital fibroblasts (Smith and Janssen, 2019). When TRAB binds to cells expressing TSHR ligands, "crosstalk" between TSHR and IGF-1R leads to activation of IGF-1R -dependent downstream intracellular pathways (Krieger et al., 2016; Krieger et al., 2017; Marcus-Samuels et al., 2018; Krieger et al., 2019). T helper 1 (Th1) immune response prevails in the immunopathogenesis of GD and GO, during which Th1 chemokines, and the chemokine receptor (C-X-C) R3, play a key role. In GD, recruited Th1 lymphocytes lead to an increased IFN-γ and TNF-α production, that stimulates Th1 chemokines secretion from thyroid cells, reiterating the autoimmune process. Elevated serum Th1 chemokines levels are associated with the active phases of GD (Antonelli et al., 2020). (**Figure 1**)

TSHR peptide secreted by thyroid tissue is taken up by dendritic cells, then MHC class II molecules on the surface of dendritic cells bind to TCR on the surface of T lymphocytes to present TSHR peptide to T lymphocytes. Once CD154 molecules on the surface of activated T lymphocytes recognizes CD40 molecules on the surface of B cells, the CD40-CD154 interaction initiates the costimulatory pathway, providing the first signal needed to initiate the adaptive humoral immune response, then the interaction of BAFF and BAFF receptor on the surface of B lymphocytes provides the second signal. After the humoral immune response is activated, B lymphocytes secrete large amounts of TRAB, of which stimulating type binds to TSHR. TSHR can co-locate with IGF-1R on thyroid cells and orbital fibroblasts to activate subsequent hyperthyroidism and GO.

TSHR, thyroid stimulating hormone (TSH) receptor; BAFF, B cell activating factor; IGF-1R, insulin-like growth factor-I receptor; FcRn, neonatal immunoglobulin receptor.

MANAGEMENT OF GRAVES' HYPERTHYROIDISM AND NEGATIVE EFFECTS

Currently, there are three traditional methods for the treatment of Graves' hyperthyroidism: drugs to inhibit thyroid hormone production, thyroidectomy and thyroid tissue contraction induced by RAI. To date, ATD have been the preferred method for patients worldwide (Bartalena, 2013; Kahaly et al., 2018). ATD inhibits iodination, a process catalyzed by thyroid peroxidase, of which methimazole (MMI) is a classical and widely distributed ATD (Taurog et al., 1976; Davidson et al., 1978). By contrast, Carbimazole (CBM), an inactive drug, is in much smaller supply worldwide. CBM is rapidly metabolized in the blood to MMI and is on average 2 times less potent than MMI at the same dose (Jansson et al., 1983). Propyl thiouracil (PTU) is the least potent compound at the same dose (10 times less potent than MMI). MMI is considered as the standard ATD with the highest efficacy due to its acceptable and low side effects as well as longest half-life (Cooper, 2003; 2005). However, the efficacy of ATD treatment is limited. Patients with persistent TRAB elevation or hyperthyroidism at 18th month of maintenance therapy, or patients with recurrence after completing the MMI course, can also choose radical treatment with RAI or total

thyroidectomy (TX). TX should be performed by an expert who performs considerable thyroid surgeons, while RAI should be avoided in GD patients with active GO or with a history of smoking (Kahaly, 2020).

However, there are many negative effects of currently available GD treatments. In a study, 2,430 newly diagnosed GD patients were recruited from 13 Endocrine clinics in Sweden, and it found remission rates were 45.3% (351/774) for first-line treatment with ATD, 81.5% (324/264) for I131, and 96.3% (52/54) for surgery (Starling, 2019). The remission rate was even lower (29.4%) if a second round of ATD was given to patients who had relapsed after receiving ATD. Frequent relapses are the main problems and large goiter size was significantly associated with an increased recurrence hazard ratio. Patients who choose ATD as first-line treatment should be informed that they have only a 50.3% chance of avoiding ablation and only a 40% chance of long-term normal thyroid function (Starling, 2019). To help the clinician to tailor a treatment for newly diagnosed Graves' hyperthyroidism in real life, the GREAT (Graves' Recurrent Events After Therapy) score and the Clinical Severity Score (CSS) have been developed, which are useful tools to predict at baseline relapse of hyperthyroidism after treatment (Masiello et al., 2018).

The risk of hypothyroidism with levothyroxine (LT) 4 therapy after radioiodine (RAI) treatment is significantly higher than that during long-term ATD therapy. What's more, RAI therapy has been significantly associated with GO exacerbation, partly due to increased TRAB titers after RAI. In the most robust study, 443 GD patients were randomized to receive RAI or methimazole. The frequency of GO occurrence or progression was significantly higher in the RAI group (15%) than those in the MMI group (2%) (OR 6.5 [95% CI: 2.2 -- 19.4]) (El Kawkgi et al., 2021). However, oral steroid prophylaxis for Graves' orbitopathy after radioactive iodine treatment for Graves' disease is not only effective, but also safe (Rosetti et al., 2020).

As for thyroid surgery, patients need life-long thyroxine replacement therapy and possibly have abnormal low circulating parathyroid hormone (PTH) levels after surgery, which can lead to disorders of the calcium-phosphate balance (Jørgensen et al., 2021). A study including 7,366 thyroidectomy patients showed that patients with severe hypocalcemia had a higher rate of recurrent laryngeal nerve injury (13.4% vs. 6.6%), unplanned reoperation (4.4% vs. 1.3%), and longer hospitalization (30.4% vs. 6.2%) ($p < 0.01$) (Kazaure et al., 2021).

NEW TREATMENT STRATEGIES FOR GRAVES' HYPERTHYROIDISM

The need for new treatment regimens, combined with a better understanding of basic immunobiology, has led to the emergence of new approaches to treat graves' hyperthyroidism. Therapies currently under investigation include biologics, small molecule peptides, immunomodulators and teprotumumab (Kahaly, 2020). Additionally, Th1 immune response prevails in the immune-pathogenesis of GD and GO, during the active phase, when Th1 chemokines, and their (C-X-C) R3 receptor, play a key role. In thyrocytes, the inhibition of Th1 chemokines secretion was stronger with peroxisome proliferators-activated receptors (PPAR)-α than PPAR-γ ligands (90% with fenofibrate and 85% with ciprofibrate), suggesting that PPAR-α can modulate the immune response (Antonelli et al., 2020).

Depletion of B Lymphocytes (CD20 Depletion)

As a B-cell depletion therapy, Rituximab (RTX) has been used to treat lymphoproliferative malignancies such as lymphoma for more than 20 years and has been increasingly used in autoimmune diseases over the past decades. Although anti-CD20 monoclonal antibody RTX is widely studied of B cell therapies, the exact mechanism by which RTX has beneficial effects remains uncertain. (Pavanello et al., 2017).

Disruption of B Cell Activation or Activity (Blocking CD40 Interactions)

Anti-CD40 monoclonal antibody Iscalimab (CFZ533) targets the CD40-CD154 costimulatory pathway, resulting in reduced B cell activation signaling (Ristov et al., 2018). Iscalimab is a non-consumable immunoglobulin silencing antibody designed to block CD40 receptor interactions without removing CD40-expressing cells. Like RTX, Iscalimab is another immunosuppressive therapy (Pavanello et al., 2017).

Blocking Immunoglobulin Recirculation (FcRn Therapy)

Neonatal immunoglobulin receptor (FcRn) is associated with the long half-life of IgG antibodies such as TRAB. FcRn participates in the recycling process by binding to IgG antibodies through endocytosis under acidic conditions in the lysosome, after which a number of IgG copies are released back into the tissue to participate in the immune response (Smith et al., 2018). Inhibition of FcRn is an attractive new therapeutic concept, in which accelerated antibody catabolism and reduced circulating pathogenic TRAB levels are beneficial for GD treatment. The two most widely studied compounds targeting FcRn are efgartigimod and Rozanolixizumb (Zuercher et al., 2019), both of which are currently in phase 3 trial to treat autoimmune diseases. Efgartigimod is a humanized IgG-1 derived Fc fragment, while Rozanolixizumab is a humanized anti-FcRn monoclonal antibody, both of which can block FcRn-IgG interaction. (Kiessling et al., 2017; Smith et al., 2018).

Inhibiting B Cell Proliferation and Differentiation (Blocking BAFF)

BAFF is a member of the TNF family of cytokines that play an important role in B lymphocyte activation, differentiation, and survival. The increased expression of BAFF and its major receptor (BAFF-R) in infiltrating immune cells and thyroid cells of GD patients suggests that BAFF-BAFF-R interaction plays a key role in the pathogenesis of GD. (Lin et al., 2016). BAFF monoclonal antibody belimumab binds to and antagonizes the bioactivity of

soluble BAFF. Blocking the interaction between BAFF and its receptor has a negative effect on B cell proliferation, indirectly reducing B cell survival rate and reducing the production of autoantibodies (Stohl et al., 2012; Campi et al., 2015).

Specifically Targeting TSHR

Including small molecule TSHR antagonist Antag-3, VA-K-14, S37a, K1-70, etc (Neumann et al., 2010; Neumann et al., 2014). Antag-3 inhibits TSH-stimulated cyclic adenosine phosphate (cAMP) production *in vitro* and reduces thyroid hormone levels in mice treated with thyroid-stimulated monoclonal antibody M22. Two other TSHR antagonist compounds, VA-K-14 and S37a, have been identified by high-throughput library screening. They can both inhibit TSH expression and TRAB-induced signaling *in vitro* (Latif et al., 2016; Marcinkowski et al., 2019). TSHR-blocking antibody K1-70, which could completely inhibit the elevation of serum thyroxine, suggesting a potential therapeutic effect for GD with high serum TRAB level (Furmaniak et al., 2012). Specific immunotherapy against TSHR involves the use of drugs with a broad immunosuppressive effect and therefore has the potential for infectious side effects.

IGF-1R Inhibitor

There is considerable evidence show that IGF-1R is meaningfully involved in the development of GO (Smith and Janssen, 2019). Orbital fibroblasts, T cells and B cells overexpress IGF-1R (Pritchard et al., 2003; Douglas et al., 2007; Douglas et al., 2008), there is a functional collaboration between IGF-1R and TSHR (Tsui et al., 2008), while TSHR in GD patients targeted by TRAB causes pathological symptoms (Pritchard et al., 2002; Pritchard et al., 2003). Teprotumumab, an IGF-1R inhibitor, is the only Food and Drug Administration (FDA)-approved treatment for GO based on the understanding that IGF-1R plays an important role in the pathogenesis of GO (Markham, 2020).

Newly developed biological agents, small molecules, and peptide treatment such as immune regulator also have potential limitations due to the unclear beneficial effects and exact mechanism. Besides, it is unknown whether these agents will improve the long-term risk of hypothyroidism, decrease overactive goiter and prevent the late recurrence. Combined with the high cost and potential risk of immune damage from nonspecific treatments, such as infusion reactions, gastrointestinal symptoms, and severe infections, common use of these drugs in adults with GD is not currently recommended (Lane et al., 2020).

EFFECTIVE INGREDIENTS FROM TRADITIONAL CHINESE MEDICINE AND ACTION MECHANISMS FOR GD

Ingredients of traditional Chinese medicine are attracting increasing interests in modern medicine, as some ingredients have been successfully used to treat autoimmune diseases (Ma et al., 2013; Ma and Jiang, 2016; Shen and Wang, 2018).

Diosgenin From *Trigonella foenum-graecum* L [Fabaceae; Common Fenugreek Seed] or *Dioscorea Bulbifera* L [Dioscoreaceae; Sevenlobed Yam Rhizome]

Diosgenin (Dio) is a natural steroid saponin, which is produced in large quantities in *Trigonella foenum-graecum* L [Fabaceae; Common fenugreek seed] and *Dioscorea bulbifera* L [Dioscoreaceae; Sevenlobed yam rhizome] (He et al., 2012). Dio had control effects on goiter and hyperthyroidism in GD mice. Interestingly, thyroid hormone tatalthyroxine (TT4) expression and thyroid size in normal mice were only slightly affected, and the difference was not statistically significant even after high-dose Dio treatment. Thus, Dio selectively affects the proliferating thyroid rather than the normal thyroid, suggesting that Dio may be a safe anti-goiter agent to avoid hypothyroidism. The target of Dio may not be expression of TRAB, but thyroid cell proliferation (Cai et al., 2014). In addition to TRAB, several other growth factors are involved in the proliferation of GD cells, among which IGF-1 is considered as the most important factor (Völzke et al., 2007). Dio inhibits IGF-1-induced thyroid cell proliferation *in vitro* by decreasing the expression of IGF-1, nuclear factor-k-gene binding (NF-κB), cyclin D1 and proliferating cell nuclear antigen (PCNA). In mouse thyroid culture cells (FRTL), IGF-1 promotes cell cycle progression by up-regulating G1/S-specific cyclin D1 through activation of NF-κBpathway (Ren et al., 2009). NF-κB is a protein complex that plays a key role in regulating cell proliferation and cell survival. In the inactive state, NF-κB is located in the cytoplasm and binds to inhibitory protein recombinant inhibitory subunit of NF kappa B alpha (IκBα). As a stimulus, IGF-1 induces phosphorylation and degradation of IκBα, leading to NF-κB activation. Activated NF-κB enters the nucleus and activates transcription of target genes (Salminen and Kaarniranta, 2010). Cyclin D1 co-phosphorylates retinoblastoma (RB) protein with cyclin-dependent kinase (CDK) and promotes the release of binding E2F transcription factor. These events promote transcription of E2F target genes and participate in the entry and completion of S phase (Stacey, 2003). One E2F target gene is PCNA, a cofactor of the DNA polymerase delta, which is required for DNA synthesis in the S phase (Travali et al., 1989). This study demonstrated that Dio could simultaneously inhibit the overexpression of these proliferation-related proteins in the thyroid of GD mice, suggesting that Dio is a potential new drug candidate for the treatment of GD. Because Dio has multiple biological activities, this compound may affect multiple molecules of the proliferation pathway or pathological aspects of GD (Cai et al., 2014). (**Figure 2**)

IGF-1 induces phosphorylation and degradation of IκBα, leading to NF-κB activation. Activated NF-κB enters the nucleus and activates transcription of Cyclin D1. Cyclin D1 co-phosphorylates RB protein with CDK and promotes the release of binding E2F transcription factor from RB. Then E2F targets at the expression of gene PCNA, a cofactor of the DNA polymerase delta, and promotes the transcription and translation of downstream proliferation-related proteins. Dio can decrease

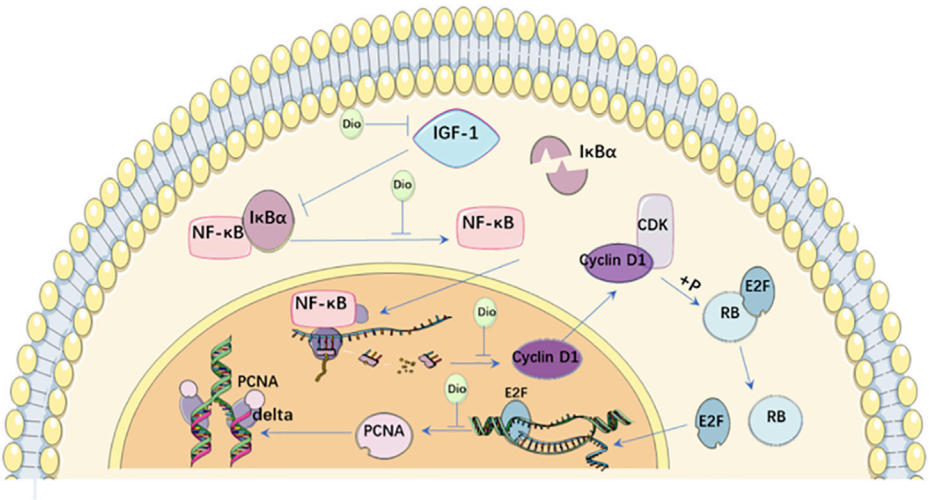

FIGURE 2 | Action mechanisms of Dio on Graves' disease.

the expression of IGF-1, NF-κB, Cyclin D1 and PCNA to inhibit thyroid cell proliferation.

Dio, Diosgenin; IGF-1, Insulin-like growth factor-I receptor; NF-κB, nuclear factor-k-gene binding IκBα, recombinant inhibitory subunit of NF kappa B alpha; PCNA, proliferating cell nuclear antigen; CDK, cyclin-dependent kinase; E2F, E2F transcription factor; RB, retinoblastoma.

Resveratrol From *Reynoutria japonica* Houtt [Polygonaceae; Polygoni Cuspidati Rhizoma et Radix]

Resveratrol is the active ingredient in *Reynoutria japonica* Houtt [Polygonaceae; Polygoni cuspidati rhizoma et radix] (Ravagnan et al., 2013). Resveratrol is a stilbenoid produced by plants in response to injury and is associated with increased levels of Cu/Zn superoxide dismutase and glyoxal oxidase (Lucini et al., 2018). Resveratrol was found to reduce oxidative stress in GO patients, and increased the nuclear and transcriptional activity of Nuclear Factor 2 (NRF2), thereby increasing its ability to bind to antioxidant genes (ARE) (Gong et al., 2017). NRF2 is an zipper protein with alkaline leucine. Under normal conditions, it is retained in the cytoplasm by Kelch-like ECh-associated protein 1 (Keap1) and degraded by specific cyclin 3 (CUL3) (Itoh et al., 1999). Oxidative stress disrupts the KEAP1-CUL3 ubiquitination system by interacting with the cysteine residues of Keap1, thereby allowing NRF2 to be transported into the nucleus, binding to ARE and promoting downstream product expressions (Dinkova-Kostova et al., 2002; Yamamoto et al., 2008). Some studies have shown that oxidative stress is related to the pathogenesis of GO. In addition, some studies have shown that GO orbital fibroblasts are hypersensitive to oxidative stress. Resveratrol can reduce the production of reactive oxygen species (ROS) and human heme oxygenase 1 (HO-1) induced by oxidative stress, and inhibit lipogenesis and lipid droplet accumulation (Kim et al., 2015). Resveratrol enhances the nuclear translocation of NRF2 in cultured orbital fibroblasts, promotes the activation of NRF2-ARE pathway, and induces the expression of antioxidant gene ARE. However, NRF2 silence decreases the protective effect induced by Resveratrol in orbital fibroblasts. In conclusion, Resveratrol can relieve oxidative stress-related symptoms by stimulating the NRF2-ARE pathway and inhibit adipogenesis of orbital fibroblasts *in vivo* by reducing ROS production (Li et al., 2020).

Icariin From *Epimedium Brevicornu* Maxim [Berberidaceae; Epimedium Alpinum Aboveground Part or Leaf]

Icariin inhibits the differentiation of preadipocytes into mature adipocytes by inhibiting autophagy, and these effects are mediated by inhibiting the activation of the 5 ′-adenosine phosphate activated protein kinase/mechanistic target of rapamycin (AMPK/mTOR) pathway (Li et al., 2017). In a thyrotropin receptor-induced GO mouse model, Icariin reduces adipose tissue dilation in orbital muscle and lipid drop accumulation by inhibiting AMPK/mTOR mediated autophagy (Li et al., 2017). In addition, a decoction including *Epimedium brevicornu* Maxim [Berberidaceae; Epimedium alpinum aboveground part or leaf], Pingmu decoction, can reduce the accumulation of orbital adipose cells in GO inactive phase to play a therapeutic role, which may be explained by increased expressions of death receptor (Fas)/death receptor ligand (Fas L) and apoptosis. Pingmu decoction can reduce the cell viability of preorbital adipocytes, inhibit their adipocyte differentiation, and promote the apoptosis of mature adipocytes by activating death signaling pathways through Fas and Fas L. These results suggested the therapeutic mechanism of Pingmu decoction in reducing the accumulation of orbital adipose cells in GO development (Zhang et al., 2017).

Celastrol From *Celastrus orbiculatus* Thunb [Celastraceae; Celastrus Orbiculatus Stem]

Celastrol, a triterpenoid compound isolated from Traditional Chinese medicine like *Celastrus orbiculatus* Thunb [Celastraceae; Celastrus orbiculatus stem], is a promising drug for the treatment of various inflammatory and autoimmune diseases. Cytokines play a key role in the development of GO and are essential for the development and maintenance of inflammation. It has been reported that Interleukin (IL)-1β mRNA expression level is higher in orbital tissues of GO patients, and IL-1β mediates inflammatory response (Wakelkamp et al., 2003). Celastrol significantly inhibited IL-1β, and thus inhibited IL-1β-induced production of orbital fibroblast cytokines IL-6, IL-8, intercellular adhesion molecule (ICAM-1), and cyclooxygenase-2(COX-2) (Chen and Greene, 2004; Konuk et al., 2006). ICAM-1 expression is involved in the migration of lymphocytes to orbital inflammatory sites (Sikorski et al., 1993). COX-2 is also considered to be the key to the inflammatory response of GO patients, and the expression of COX-2 is positively correlated with the increasing severity of orbital diseases (Konuk et al., 2006). IL-1β promotes orbital fibroblasts in patients with GO producing high levels of COX-2 through activation of the NF-κB pathway. Celastrol inhibits IL-6, IL-8, ICAM-1, and COX-2 cytokines production in IL-1β-induced orbital fibroblasts, which suppresses inflammation and inhibits the progression of GO (Li et al., 2016).

Gypenosides From *Gynostemma pentaphyllum* (Thunb.) Makino [Cucurbitaceae; Gynostemma PentaphyllumAerial Part]

Gypenosides are saponins extracted from *Gynostemma pentaphyllum* (Thunb.) Makino [Cucurbitaceae; Gynostemma pentaphyllumaerial part]. They are the pharmacological active components in gynost' pentaphyllum and have a variety of biological activities. Gypenosides can regulate the activation of immune cells and the expression of cytokines, and inhibit the inflammatory response of different diseases (Wang et al., 2017; Wang et al., 2018). Gypenosides have anti-inflammatory and antioxidant biological effects. Through GO analysis, PPI network construction and molecular docking, it is found that Gypenosides may play anti-inflammatory and antioxidant roles in GO through signal transducer and activator of transcription (STAT1) and STAT3 signaling pathways. Inhibiting the expression of STAT1 signaling pathway, Interferon (IFN)-γ-induced productions of chemokine 10 (IP-10)/CXC-chemokine ligand 10 (CXCL10) in orbital fibroblasts of GO patients can be inhibited, thus alleviating orbital inflammation (Pu et al., 2019). The STAT3 signaling pathway plays an anti-inflammatory, antioxidant and immunomodulatory role in chronic respiratory diseases, breast cancer and liver inflammation (Alhusaini et al., 2018; Natarajan et al., 2019; Xiang et al., 2019). Inflammation and oxidative stress damage of orbital tissues are the main pathogenesis of GO (Li et al., 2016; Rotondo Dottore et al., 2017). Therefore, STAT1 and STAT3 signaling pathways may be the key target signaling pathways for Gynostevenosides in the treatment of GO, reducing tissue damage and remodeling caused by orbital inflammation and oxidation (Li et al., 2019).

Astragaloside IV From *Astragalus mongholicus* Bunge [Fabaceae; Astrgali Mongholici Radix]

Astragaloside IV (AS-VI) is the main active ingredient of *Astragalus mongholicus* Bunge [Fabaceae; Astrgali mongholici radix]. AS-VI has antioxidant and anti-inflammatory properties and has shown therapeutic potential in numerous ischemic and inflammatory diseases (Li et al., 2018). IL-1β increases the mRNA expression of inflammatory cytokines IL-6, IL-8, TNF-α and monocyte chemotactic protein-1 (MCP-1) in cultured orbital fibroblasts. This IL-1β -induced inflammation is accompanied by increased autophagy activity, reflected in increased expression of the autophagy effector proteins Beclin-1 and angiotensinogen (AGT)-5 and the conversion of autophagy markers microtubule-associated protein light chain 3 (LC3)-I to LC3-II. Preconditioning with the autophagy inhibitors 3-methyladenine (3-MA) and Bafilomycin A1, or silencing the autophagy related proteins Beclin-1 and ATG-5, could prevent IL-1β-induced orbital fibroblast inflammation, while preconditioning with the autophagy activator rapamycin had the opposite effect. These data suggests that autophagy is involved in GO orbital inflammation. AS-VI treatment significantly reduced IL-1β-induced inflammatory cytokine production *in vitro* and reduced GO orbital inflammation, fat accumulation, collagen deposition, and macrophage infiltration *in vivo*. The protective effect of AS-IV on GO was also associated with decreased autophagy activity of orbital fibroblasts and orbital tissues respectively (Li et al., 2018).

Ingredients From *Prunella vulgaris* L [Lamiaceae; Prunellae Spica Fruit]

Spica Prunellae (SP), the fruit of *Prunella vulgaris* L [Lamiaceae; Prunellae spica fruit], is a traditional antipyretic botanical drug widely distributed in Northeast Asia (Zhang et al., 2020). SP has been widely used in thyroid diseases, such as goiter and subacute thyroiditis (Li et al., 2019). And in many herbal formulations, SP is treated as an important ingredient for the treatment of GO (Yang et al., 2007). According to the compound-hub gene-pathway network, Quercetin, Ursolic acid and Rutin interacted with the large number of targets, indicating the main active ingredients in SP and the important roles in the anti-GO system (Zhang et al., 2020). Quercetin is a flavonoid phytoestrogen exhibiting antioxidant and anti-inflammatory properties and reducing proliferation in orbital fibroblasts. Ursolic acid and Rutin are reported to promote apoptosis and regulate immune systems in cell and animal models (Zhang et al., 2020). The PI3K-Akt signaling pathway plays a key role in both immune inflammation and proliferation and apoptosis in GO, and this process may be an effective therapeutic target for SP (Bahn, 2010). In terms of immune inflammation, pro-inflammatory cytokines COX-2, IL6 and TNFα are confirmed

to be involved in the pathogenesis of GO. Previous studies have shown that COX-2 decreased with declined GO clinical activity scores and is now considered to be critical to the inflammatory process in patients with GO (Dubois et al., 1998; Konuk et al., 2006; Vondrichova et al., 2007). COX-2 is involved in the biosynthesis of prostaglandins, which plays a key role in inflammation. IL6 is related to the pathogenesis of autoimmune diseases and the AKT/NF-κB signaling pathway has been reported to contribute to IL6 production in the retrobulbar space during GO activity (Gillespie et al., 2012). Similarly, elevated serum TNF levels in GO inflammation have been shown to be mediated by the AKT/NF-κB signaling pathway. Currently, some TNF inhibitors, like SP, have been reported to achieve promising results in patients with GO, regardless of rare adverse reactions (Kapadia and Rubin, 2006). For proliferation and apoptosis (Kumar et al., 2011; Li and Smith, 2014; Woeller et al., 2019), the PI3K-Akt signaling pathway seems to play an important role in mediating cell growth and death in GO. Recent studies have shown that orbital fibroblasts overexpress TSHR and increase the expression and proliferation of inflammatory genes by activating the PI3K-Akt pathway. In addition, the PI3K-Akt signaling pathway is also involved in cell proliferation of preorbital adipose cells (Wang et al., 2019), thus promoting GO progression. Caspase 3 (CASP3) activation is one of the last steps of apoptosis, and SP shows a pro-apoptotic effect in GO by activating CASP3 (Zhu et al., 2018).

Triptolide From *Tripterygium wilfordii* Hook.f [Celastraceae; Tripterygium Wilfordii Radix]

Triptolide, a diterpenoid tricyclic oxide compound purified from the roots of *Tripterygium wilfordii* Hook. f [Celastraceae; Tripterygium wilfordii radix], has been identified as one of the main components responsible for the immunosuppressive properties of this botanical drug (Gu et al., 1995). The immunosuppressive activity of Triptolide has been studied *in vitro* and *in vivo*, and it has been found to inhibit T cell proliferation, induce T cell apoptosis, reduce IL-2 synthesis, and inhibit the expression of NF -κB in T cells (Yang et al., 1994; Yang et al., 1998; Li et al., 2002; Qiu and Kao, 2003). Triptplide could relieve the clinical manifestations of exophthalmos, diplopia and periorbital swelling caused by inflammatory cell infiltration and accumulation of adipose tissue in the extraocular muscle and orbital connective tissue. Abnormal expression of human leukocyte antigen -DR (HLA-DR) on fibroblasts is associated with the development of GO (Heufelder et al., 1991; Hiromatsu et al., 1995), and it has been reported that the expression of various adhesion molecules (e.g., ICAM-1) on orbital fibroblasts (RFs) is involved in the migration of lymphocytes to the site of orbital inflammation. The cell surface molecule CD40 is a key signal molecule for B lymphocyte expression, and it has been established that CD40 is expressed in RFs and plays an important role in the interaction between RFs and T lymphocytes. The expression of HLA-DR, ICAM-1, and CD40 are all induced by IFN-γ. Triptolide inhibited IFN-γ-induced RFs activation in GO patients, decreased the expression of HLA-DR, ICAM-1 and CD40, and inhibited cell proliferation and hyaluronic acid (HA) synthesis in GO patients (Yan and Wang, 2006).

Bupleurum Saponins From *Bupleurum falcatum* L [Apiaceae; Bupleuri Radix]

Bupleurum saponins, the active component of *Bupleurum falcatum* L [Apiaceae; Bupleuri radix], which have strong antioxidant effects, can improve hyperthyroidism and related organ damages induced by Levothyroxine (LT4). They have good bidirectional regulation effects on hyperthyroidism and secondary hypothyroidism (Kim et al., 2012). In addition, some traditional Chinese medicines with good efficacy are widely used in clinical practice, such as *Prunella vulgaris* L [Lamiaceae; Prunellae spica fruit], *Bupleurum falcatum* L [Apiaceae; Bupleuri radix], *Fritillaria thunbergii* Miq [Liliaceae; Fritillaria thunbergii bulb] and *Paeonia lactiflora* Pall [Paeoniaceae; Paeonia species flower et root], etc. The active components and mechanisms are to be thoroughly studied.

PROSPECTS OF TRADITIONAL CHINESE MEDICINE ON TREATING GD

Traditional Chinese Medicine Relieves Large Goiter and Reduce Side Effects of ATD

Many botanical drugs or ingredients could reduce large goiter. For example, Dio reduced goiter formation in GD patients, and the effect was independent of TRAB levels, and the underlying mechanism involved inhibiting thyroid cell proliferation by inhibiting gene transcription and protein expression of certain proliferation-related proteins. Some Chinese botanical drugs can induce apoptosis in combination with ATD in GD. A study including 13 patients of Graves'disease showed that compared with ATD alone, thyroid volume decreased significantly after combined treatment ($p < 0.01$) (Zhao et al., 1999). Typical apoptotic appearances, such as vacuolar cells, marginal nuclei, chromatin aggregation, and nuclear fragmentation, could be seen under light microscopy, and the apoptosis rates are 2.11 % and 18.66% before and after administration ($p < 0.01$) (Zhao et al., 1999). Moreover, Dio selectively affects the proliferating thyroid rather than the normal thyroid, suggesting that Dio may be a safe anti-goiter agent to avoid hypothyroidism (Cai et al., 2014). This suggests that traditional Chinese medicine can make up for the deficiency in ATD therapy and effectively relieve the enlargement of abnormal thyroid volume without causing secondary hypothyroidism or other adverse reactions.

Traditional Chinese Medicine Relieves Symptoms of GO

In addition to the inhibition of orbital fibroblasts to release hydrophilic polysaccharide and proinflammatory cytokines (Armengol et al., 2001; 2020) to alleviate the orbital inflammatory process and local symptoms such as edema, hyperemia and exophthalmos, some effective components of

traditional Chinese are effective in reducing the accumulation of orbital fat cells, reducing orbital pressure and improving malignant exophthalmus. For example, resveratrol can enhance oxidative stress and inhibit the adipogenesis and accumulation of lipid droplets, Icariin inhibits the differentiation of preadipocytes into mature adipocytes by inhibiting autophagy; Epimedium glycoside can reduce the vitality of preorbital fat cells, restrain adipocyte's differentiation, and activate death signaling pathways through Fas and Fas L to promote the apoptosis of mature fat cells; and SP promotes adipocyte apoptosis by activating CASP3 in GO.

Traditional Chinese Medicine Alleviates the Hypermetabolic Symptoms of GD

As for the relief of symptoms in patients with hyperthyroidism, Astragalus can regulate the immune function of GD patients and significantly reduce the levels of serum IL-β, TNFα, IL-6, IL-8 and MCP-1, thus relieving hyperhidrosis, palpitation and other clinical symptoms, which plays an important role in the adjuvant treatment of GD (Wu et al., 2011). *Dendrobium officinale* Kimura and Migo [Orchidaceae; Dendrobium stem] (DOF) can reduce the liver function injury caused by overactive thyroid axis by affecting thyroxine metabolism, reduce blood flow in microcirculation of face and ears, lower the facial temperature and heart rate, and alleviate symptoms such as zygotic redness, irritability and liver function damage in patients (Lei et al., 2015).

Traditional Chinese Medicine Reduces Allergic Symptoms and Increases the Dosage of ATD Used in Allergic Patients

When patients with hyperthyroidism take antithyroid drugs, drug allergy is easy to occur. The main manifestations are skin fever, itching, maculopapule or urticaria on the face and trunk. In addition to alleviating the symptoms of hyperthyroidism, some Chinese medicines can also alleviate ATD allergic reaction. The compound hyperthyroidism tablet, which contains nine kinds of botanical drugs directed at GD and small dose MMI, has a good effect on the hyperthyroidism with deficiency of qi and Yin, and can be effective in desensitization and treatment of drug rash (Wang, 2000). For patients who refuse surgery or RAI treatment, gradually increasing the treatment dose of ATD assisted by Traditional Chinese medicine may be a treatment choice for them. However, the number of relevant researches is small, and more efforts are still needed to conduct drug screening and mechanism research.

Limitations and Research Direction of Traditional Chinese Medicine in the Treatment of GD

Although some botanical drugs and effective components can compensate for the deficiency of existing treatments, the researches of Chinese medicine are still limited in quantity and quality. The existing studies were inclined to improve the exophthalmos of GD and the goiter, relevant symptoms of nervous, cardiovascular, digestive, reproductive, skin and skeletal systems caused by hyperthyroidism were ignored. What's more, thyroid function - with the exception of restored thyroid stimulating hormone (TSH) - was not significantly altered by TCM (Zen et al., 2007). A systematic review included in 17 randomized controlled clinical trials with 1,536 participants showed that the serum glutamic pyruvate transaminase (SGPT) of participants slightly increased and menstrual quantity decreased during TCM treatment, but all of the aforementioned studies indicate that the occurrence rates of reported adverse effects in TCM intervention groups were fewer than controls (Xu et al., 2014). Three studies reported drug-induced symptoms (such as nausea, vomiting, and gain weight), and the respondents had fewer adverse symptoms in the TCM intervention groups compared with the controls (RR: 0.32; 95% CI: 0.20–0.53; $p < 0.00001$; fixed model; I2 = 0%; three trials; n = 197) (Liu et al., 2019). What's more, majority of them were mild and tolerable and disappeared spontaneously after reducing the dosage of TCM or drug withdrawal. Four studies did not provided clearly proportions, and other studies still at the stage of compound preparation or clinical efficacy evaluation and did not report the safety events. Some traditional Chinese medicines are widely used in clinical practice and have good efficacy, such as *Prunella vulgaris* L [Lamiaceae; Prunellae spica fruit], *Bupleurum falcatum* L [Apiaceae; Bupleuri radix], *Fritillaria thunbergii* Miq [Liliaceae; Fritillaria thunbergii bulb] and *Paeonia lactiflora* Pall [Paeoniaceae; Paeonia species flower et root]; however, relevant studies to explore the effective molecules of traditional Chinese medicine and their exact mechanisms were seriously deficient, which also points out the direction we need to work on in the future.

The current researches about GD with single drug are numerous, such as TCM containing high-level iodine (*Laminaria japonica* Aresch [Laminariaceae; Ecklonia kurome leaf], *Dioscorea bulbifera* L [Dioscoreaceae; Aerial yam aerial parts et rhizome], FossiliaOssisMastrodi, Ostrea gigas tnunb, *Prunella vulgaris* L [Lamiaceae; Prunellae spica fruit], etc.), botanical drugs with immunosuppressive effects (*Tripterygium wilfordii* Hook. f [Celastraceae; Tripterygium wilfordii radix], *Dioscorea bulbifera* L [Dioscoreaceae; Sevenlobed yam rhizome], *Malus toringo* (Siebold) de Vriese [Rosaceae; Malus spectabilis flower], *Ranunculus ternatus* Thunb [Ranunculaceae; Ranunculi ternati radix], etc.), botanical drugs with immunomodulatory effects (*Astragalus mongholicus* Bunge [Fabaceae; Astrgali mongholici radix], *Scrophularia ningpoensis* Hemsl [Scrophulariaceae; Scrophulariae radix], *Paeonia lactiflora* Pall [Paeoniaceae; Paeonia species flower et root], *Anemarrhena asphodeloides* Bunge [Asparagaceae; Anemarrhenae rhizoma], *Rehmannia glutinosa* (Gaertn.) DC [Orobanchaceae; Rehmanniae radix], Carapax Trionycis, *Dendrobium officinale* Kimura and Migo [Orchidaceae; Dendrobium stem], etc.) and other traditional Chinese medicines with good clinical effect (*Bupleurum falcatum* L [Apiaceae; Bupleuri radix], *Gentiana scabra* Bunge [Gentianaceae; Gentianae radix et rhizoma], *Prunella vulgaris* L [Lamiaceae; Prunellae spica fruit], *Calamus draco* Willd [Arecaceae; Dragon's blood palm], etc.).

The composition of Chinese traditional medicine is complex and the molecular targets are multiple, which are the main causes of its unsure clinical efficacy. But with the development of biochemistry, molecular biology, immunology, pharmacology, chemistry and pharmacology of plants, and the emergence of new methods and technologies such as surface plasmon resonance (SPR) analysis, drug affinity reaction target stability (DARTS) analysis, Chinese medicine component chip, drug molecular target hook, screening analysis platform and pathway enrichment analysis, the relevant scientific research work has been continuously improved, and the mechanism exploration of effective molecules and exact targets of single Chinese medicine have gradually become clear. In general, we should still focus on efficacy and screening out the ingredients of TCM with better efficacy and clear mechanism. There is still a long way to go to analyze and extract effective molecules of botanical drugs, prepare finished drug product and promote the modernization, quality and standardization, and finally promote the high-level clinical service with new methods and technologies.

CONCLUSION

The inadequacy of traditional treatment promotes the emergence of new therapeutic ideas, including biologics, small molecule peptides, immunomodulators and specific antibody IGF-1R. However, due to the precise mechanism of the treatment effect is unknown and the risk of complications during treatment process, they have not been actively put into clinical use. What's more, these new treatments are mostly targeting the upstream and downstream of the abnormal activation of TSHR to reduce the abnormal thyroid hormone secretion, and lacking relevant research and treatment strategies for abnormal hyperplasia and hypertrophy of thyroid follicular epithelial cells, accumulation of orbital adipose cells and formation of lipid drops in patients with GO, hyper sweating, palpitations, zygomatic redness, irritability, impaired liver function and anaphylactic reaction towards ATD. Some active ingredients can inhibit the excessive proliferation of thyroid follicular epithelial cells and relieve eye symptom and systemic manifestation of GD, as well as playing roles in desensitization and treatment of ATD related allergic reaction. But due to the exility of number and the lack of depth, many studies only stay in the clinical efficacy evaluation stage of compound preparations, and lacking specific verification of effective molecules and molecular mechanisms of actions in single element. Though some adverse effects of TCM had been reported, such as menstrual disorders, gastrointestinal events, impaired liver function and rash, they were mild and recovered after the decrease of TCM dose. The effective components of Traditional Chinese medicine might open a new window for the treatment of GD, but high-quality RCT studies and the exact mechanisms still need to be further explored.

AUTHOR CONTRIBUTIONS

QH and JG conceived the paper. QH, JG, and FL wrote the article. JG, HD, MG, YG, and QX revised the figures and reviewed the article. All authors reviewed and approved the final version of the manuscript.

FUNDING

This study was supported by the National Natural Science Foundation of China, (Grant NO.82174327).

REFERENCES

Alhusaini, A., Faddaa, L., Ali, H. M., Hassan, I., El Orabi, N. F., and Bassiouni, Y. (2018). Amelioration of the Protein Expression of Cox2, NFκB, and STAT-3 by Some Antioxidants in the Liver of Sodium Fluoride-Intoxicated Rats. *Dose Response* 16 (3), 1559325818800153. doi:10.1177/1559325818800153

Antonelli, A., Fallahi, P., Elia, G., Ragusa, F., Paparo, S. R., Ruffilli, I., et al. (2020). Graves' Disease: Clinical Manifestations, Immune Pathogenesis (Cytokines and Chemokines) and Therapy. *Best Pract. Res. Clin. Endocrinol. Metab.* 34 (1), 101388. doi:10.1016/j.beem.2020.101388

Armengol, M. P., Juan, M., Lucas-Martín, A., Fernández-Figueras, M. T., Jaraquemada, D., Gallart, T., et al. (2001). Thyroid Autoimmune Disease: Demonstration of Thyroid Antigen-specific B Cells and Recombination-Activating Gene Expression in Chemokine-Containing Active Intrathyroidal Germinal Centers. *Am. J. Pathol.* 159 (3), 861–873. doi:10.1016/s0002-9440(10)61762-2

Bahn, R. S. (2010). Graves' Ophthalmopathy. *N. Engl. J. Med.* 362 (8), 726–738. doi:10.1056/NEJMra0905750

Bartalena, L. (2013). Diagnosis and Management of Graves Disease: a Global Overview. *Nat. Rev. Endocrinol.* 9 (12), 724–734. doi:10.1038/nrendo.2013.193

Benvenga, S., Ferrari, S. M., Elia, G., Ragusa, F., Patrizio, A., Paparo, S. R., et al. (2020). Nutraceuticals in Thyroidology: A Review of *In Vitro*, and *In Vivo* Animal Studies. *Nutrients* 12 (5), 544–7. doi:10.3390/nu12051337

Burch, H. B., and Cooper, D. S. (2015). Management of Graves Disease: A Review. *Jama* 314 (23), 2544–2554. doi:10.1001/jama.2015.16535

Cai, H., Wang, Z., Zhang, H. Q., Wang, F. R., Yu, C. X., Zhang, F. X., et al. (2014). Diosgenin Relieves Goiter via the Inhibition of Thyrocyte Proliferation in a Mouse Model of Graves' Disease. *Acta Pharmacol. Sin* 35 (1), 65–73. doi:10.1038/aps.2013.133

Campi, I., Tosi, D., Rossi, S., Vannucchi, G., Covelli, D., Colombo, F., et al. (2015). B Cell Activating Factor (BAFF) and BAFF Receptor Expression in Autoimmune and Nonautoimmune Thyroid Diseases. *Thyroid* 25 (9), 1043–1049. doi:10.1089/thy.2015.0029

Chen, L. F., and Greene, W. C. (2004). Shaping the Nuclear Action of NF-kappaB. *Nat. Rev. Mol. Cel Biol* 5 (5), 392–401. doi:10.1038/nrm1368

Cooper, D. S. (2005). Antithyroid Drugs. *N. Engl. J. Med.* 352 (9), 905–917. doi:10.1056/NEJMra042972

Cooper, D. S. (2003). Antithyroid Drugs in the Management of Patients with Graves' Disease: an Evidence-Based Approach to Therapeutic Controversies. *J. Clin. Endocrinol. Metab.* 88 (8), 3474–3481. doi:10.1210/jc.2003-030185

Davidson, B., Soodak, M., Neary, J. T., Strout, H. V., Kieffer, J. D., Mover, H., et al. (1978). The Irreversible Inactivation of Thyroid Peroxidase by Methylmercaptoimidazole, Thiouracil, and Propylthiouracil *In Vitro* and its Relationship to *In Vivo* Findings. *Endocrinology* 103 (3), 871–882. doi:10.1210/endo-103-3-871

Diana, T., Wüster, C., Kanitz, M., and Kahaly, G. J. (2016). Highly Variable Sensitivity of Five Binding and Two Bio-Assays for TSH-Receptor Antibodies. *J. Endocrinol. Invest.* 39 (10), 1159–1165. doi:10.1007/s40618-016-0478-9

Dinkova-Kostova, A. T., Holtzclaw, W. D., Cole, R. N., Itoh, K., Wakabayashi, N., Katoh, Y., et al. (2002). Direct Evidence that Sulfhydryl Groups of Keap1 Are

the Sensors Regulating Induction of Phase 2 Enzymes that Protect against Carcinogens and Oxidants. *Proc. Natl. Acad. Sci. U S A.* 99 (18), 11908–11913. doi:10.1073/pnas.172398899

Douglas, R. S., Gianoukakis, A. G., Kamat, S., and Smith, T. J. (2007). Aberrant Expression of the Insulin-like Growth Factor-1 Receptor by T Cells from Patients with Graves' Disease May Carry Functional Consequences for Disease Pathogenesis. *J. Immunol.* 178 (5), 3281–3287. doi:10.4049/jimmunol.178.5.3281

Douglas, R. S., Naik, V., Hwang, C. J., Afifiyan, N. F., Gianoukakis, A. G., Sand, D., et al. (2008). B Cells from Patients with Graves' Disease Aberrantly Express the IGF-1 Receptor: Implications for Disease Pathogenesis. *J. Immunol.* 181 (8), 5768–5774. doi:10.4049/jimmunol.181.8.5768

Dubois, R. N., Abramson, S. B., Crofford, L., Gupta, R. A., Simon, L. S., Van De Putte, L. B., et al. (1998). Cyclooxygenase in Biology and Disease. *Faseb j* 12 (12), 1063–1073. doi:10.1096/fasebj.12.12.1063

El Kawkgi, O. M., Ross, D. S., and Stan, M. N. (2021). Comparison of Long-term Antithyroid Drugs versus Radioactive Iodine or Surgery for Graves' Disease: A Review of the Literature. *Clin. Endocrinol.* 95 (1), 3–12. doi:10.1111/cen.14374

Furmaniak, J., Sanders, J., Young, S., Kabelis, K., Sanders, P., Evans, M., et al. (2012). *In Vivo* effects of a Human Thyroid-Stimulating Monoclonal Autoantibody (M22) and a Human Thyroid-Blocking Autoantibody (K1-70). *Auto Immun. Highlights* 3 (1), 19–25. doi:10.1007/s13317-011-0025-9

Gillespie, E. F., Raychaudhuri, N., Papageorgiou, K. I., Atkins, S. J., Lu, Y., Charara, L. K., et al. (2012). Interleukin-6 Production in CD40-Engaged Fibrocytes in Thyroid-Associated Ophthalmopathy: Involvement of Akt and NF-κB. *Invest. Ophthalmol. Vis. Sci.* 53 (12), 7746–7753. doi:10.1167/iovs.12-9861

Gong, W., Li, J., Chen, Z., Huang, J., Chen, Q., Cai, W., et al. (2017). Polydatin Promotes Nrf2-ARE Anti-oxidative Pathway through Activating CKIP-1 to Resist HG-Induced Up-Regulation of FN and ICAM-1 in GMCs and Diabetic Mice Kidneys. *Free Radic. Biol. Med.* 106, 393–405. doi:10.1016/j.freeradbiomed.2017.03.003

Graves' disease (2020). Graves' Disease. *Nat. Rev. Dis. Primers* 6 (1), 53. doi:10.1038/s41572-020-0195-8

Gu, W. Z., Chen, R., Brandwein, S., McAlpine, J., and Burres, N. (1995). Isolation, Purification, and Characterization of Immunosuppressive Compounds from Tripterygium: Triptolide and Tripdiolide. *Int. J. Immunopharmacol.* 17 (5), 351–356. doi:10.1016/0192-0561(95)00022-t

He, Z., Tian, Y., Zhang, X., Bing, B., Zhang, L., Wang, H., et al. (2012). Anti-tumour and Immunomodulating Activities of Diosgenin, a Naturally Occurring Steroidal Saponin. *Nat. Prod. Res.* 26 (23), 2243–2246. doi:10.1080/14786419.2011.648192

Heufelder, A. E., Smith, T. J., Gorman, C. A., and Bahn, R. S. (1991). Increased Induction of HLA-DR by Interferon-Gamma in Cultured Fibroblasts Derived from Patients with Graves' Ophthalmopathy and Pretibial Dermopathy. *J. Clin. Endocrinol. Metab.* 73 (2), 307–313. doi:10.1210/jcem-73-2-307

Hiromatsu, Y., Tanaka, K., Ishisaka, N., Kamachi, J., Kuroki, T., Hoshino, T., et al. (1995). Human Histocompatibility Leukocyte Antigen-DR and Heat Shock Protein-70 Expression in Eye Muscle Tissue in Thyroid-Associated Ophthalmopathy. *J. Clin. Endocrinol. Metab.* 80 (2), 685–691. doi:10.1210/jcem.80.2.7531718

Huber, A. K., Finkelman, F. D., Li, C. W., Concepcion, E., Smith, E., Jacobson, E., et al. (2012). Genetically Driven Target Tissue Overexpression of CD40: a Novel Mechanism in Autoimmune Disease. *J. Immunol.* 189 (6), 3043–3053. doi:10.4049/jimmunol.1200311

Itoh, K., Wakabayashi, N., Katoh, Y., Ishii, T., Igarashi, K., Engel, J. D., et al. (1999). Keap1 Represses Nuclear Activation of Antioxidant Responsive Elements by Nrf2 through Binding to the Amino-Terminal Neh2 Domain. *Genes Dev.* 13 (1), 76–86. doi:10.1101/gad.13.1.76

Jansson, R., Dahlberg, P. A., Johansson, H., and Lindström, B. (1983). Intrathyroidal Concentrations of Methimazole in Patients with Graves' Disease. *J. Clin. Endocrinol. Metab.* 57 (1), 129–132. doi:10.1210/jcem-57-1-129

Jørgensen, C. U., Homøe, P., Dahl, M., and Hitz, M. F. (2021). Postoperative Chronic Hypoparathyroidism and Quality of Life after Total Thyroidectomy. *JBMR Plus* 5 (4), e10479. doi:10.1002/jbm4.10479

Kahaly, G. J., Bartalena, L., Hegedüs, L., Leenhardt, L., Poppe, K., and Pearce, S. H. (2018). 2018 European Thyroid Association Guideline for the Management of Graves' Hyperthyroidism. *Eur. Thyroid J.* 7 (4), 167–186. doi:10.1159/000490384

Kahaly, G. J. (2020). Management of Graves Thyroidal and Extrathyroidal Disease: An Update. *J. Clin. Endocrinol. Metab.* 105 (12), 3704–3720. doi:10.1210/clinem/dgaa646

Kapadia, M. K., and Rubin, P. A. (2006). The Emerging Use of TNF-Alpha Inhibitors in Orbital Inflammatory Disease. *Int. Ophthalmol. Clin.* 46 (2), 165–181. doi:10.1097/00004397-200604620-00014

Kazaure, H. S., Zambeli-Ljepovic, A., Oyekunle, T., Roman, S. A., Sosa, J. A., Stang, M. T., et al. (2021). Severe Hypocalcemia after Thyroidectomy: An Analysis of 7366 Patients. *Ann. Surg.* 274 (6), e1014–e1021. doi:10.1097/sla.0000000000003725

Kiessling, P., Lledo-Garcia, R., Watanabe, S., Langdon, G., Tran, D., Bari, M., et al. (2017). Erratum for the Research Article: "The FcRn Inhibitor Rozanolixizumab Reduces Human Serum IgG Concentration: A Randomized Phase 1 Study" by P. Kiessling, R. Lledo-Garcia, S. Watanabe, G. Langdon, D. Tran, M. Bari, L. Christodoulou, E. Jones, G. Price, B. Smith, F. Brennan, I. White, S. Jolles. *Sci. Transl Med.* 9 (414), eaar6448. doi:10.1126/scitranslmed.aar6448

Kim, C. Y., Lee, H. J., Chae, M. K., Byun, J. W., Lee, E. J., and Yoon, J. S. (2015). Therapeutic Effect of Resveratrol on Oxidative Stress in Graves' Orbitopathy Orbital Fibroblasts. *Invest. Ophthalmol. Vis. Sci.* 56 (11), 6352–6361. doi:10.1167/iovs.15-16870

Kim, S. M., Kim, S. C., Chung, I. K., Cheon, W. H., and Ku, S. K. (2012). Antioxidant and Protective Effects of Bupleurum Falcatum on the L-Thyroxine-Induced Hyperthyroidism in Rats. *Evid. Based Complement. Alternat Med.* 2012, 578497. doi:10.1155/2012/578497

Konuk, E. B., Konuk, O., Misirlioglu, M., Menevse, A., and Unal, M. (2006). Expression of Cyclooxygenase-2 in Orbital Fibroadipose Connective Tissues of Graves' Ophthalmopathy Patients. *Eur. J. Endocrinol.* 155 (5), 681–685. doi:10.1530/eje.1.02280

Krieger, C. C., Boutin, A., Jang, D., Morgan, S. J., Banga, J. P., Kahaly, G. J., et al. (2019). Arrestin-β-1 Physically Scaffolds TSH and IGF1 Receptors to Enable Crosstalk. *Endocrinology* 160 (6), 1468–1479. doi:10.1210/en.2019-00055

Krieger, C. C., Perry, J. D., Morgan, S. J., Kahaly, G. J., and Gershengorn, M. C. (2017). TSH/IGF-1 Receptor Cross-Talk Rapidly Activates Extracellular Signal-Regulated Kinases in Multiple Cell Types. *Endocrinology* 158 (10), 3676–3683. doi:10.1210/en.2017-00528

Krieger, C. C., Place, R. F., Bevilacqua, C., Marcus-Samuels, B., Abel, B. S., Skarulis, M. C., et al. (2016). TSH/IGF-1 Receptor Cross Talk in Graves' Ophthalmopathy Pathogenesis. *J. Clin. Endocrinol. Metab.* 101 (6), 2340–2347. doi:10.1210/jc.2016-1315

Kumar, S., Nadeem, S., Stan, M. N., Coenen, M., and Bahn, R. S. (2011). A Stimulatory TSH Receptor Antibody Enhances Adipogenesis via Phosphoinositide 3-kinase Activation in Orbital Preadipocytes from Patients with Graves' Ophthalmopathy. *J. Mol. Endocrinol.* 46 (3), 155–163. doi:10.1530/jme-11-0006

Lane, L. C., Cheetham, T. D., Perros, P., and Pearce, S. H. S. (2020). New Therapeutic Horizons for Graves' Hyperthyroidism. *Endocr. Rev.* 41 (6), 873–884. doi:10.1210/endrev/bnaa022

Latif, R., Realubit, R. B., Karan, C., Mezei, M., and Davies, T. F. (2016). TSH Receptor Signaling Abrogation by a Novel Small Molecule. *Front. Endocrinol. (Lausanne)* 7, 130. doi:10.3389/fendo.2016.00130

Lei, S. S., Lv, G. Y., Jin, Z. W., Li, B., Yang, Z. B., and Chen, S. H. (2015). Effect of Extracts from Dendrobii Ifficinalis Flos on Hyperthyroidism Yin Deficiency Mice. *Zhongguo Zhong Yao Za Zhi* 40 (9), 1793–1797. doi:10.4268/cjcmm20150931

Li, B., and Smith, T. J. (2014). PI3K/AKT Pathway Mediates Induction of IL-1RA by TSH in Fibrocytes: Modulation by PTEN. *J. Clin. Endocrinol. Metab.* 99 (9), 3363–3372. doi:10.1210/jc.2014-1257

Li, F., Wu, Y., Chen, L., Hu, L., and Liu, X. (2019). Initial Treatment Combined with Prunella Vulgaris Reduced Prednisolone Consumption for Patients with Subacute Thyroiditis. *Ann. Transl Med.* 7 (3), 45. doi:10.21037/atm.2019.01.07

Li, H., Liu, Z. H., Dai, C. S., Liu, D., and Li, L. S. (2002). Triptolide Inhibits Proinflammatory Factor-Induced Over-expression of Class II MHC and B7 Molecules in Renal Tubular Epithelial Cells. *Acta Pharmacol. Sin* 23 (9), 775–781. doi:10.1016/S0300-483X(02)00320-7

Li, H., Min, J., Chen, Y., Li, H., and Zhang, Y. (2020). Polydatin Attenuates Orbital Oxidative Stress in Graves' Orbitopathy through the NRF2 Pathway. *Chem. Biol. Interact* 315, 108894. doi:10.1016/j.cbi.2019.108894

Li, H., Yuan, Y., Zhang, Y., He, Q., Xu, R., Ge, F., et al. (2016). Celastrol Inhibits IL-1β-induced Inflammation in Orbital Fibroblasts through the Suppression of NF-κB Activity. *Mol. Med. Rep.* 14 (3), 2799–2806. doi:10.3892/mmr.2016.5570

Li, H., Yuan, Y., Zhang, Y., Zhang, X., Gao, L., and Xu, R. (2017). Icariin Inhibits AMPK-dependent Autophagy and Adipogenesis in Adipocytes *In Vitro* and in a Model of Graves' Orbitopathy *In Vivo*. *Front. Physiol.* 8, 45. doi:10.3389/fphys.2017.00045

Li, H., Zhang, Y., Min, J., Gao, L., Zhang, R., and Yang, Y. (2018). Astragaloside IV Attenuates Orbital Inflammation in Graves' Orbitopathy through Suppression of Autophagy. *Inflamm. Res.* 67 (2), 117–127. doi:10.1007/s00011-017-1100-0

Li, K., Li, H., Xu, W., Liu, W., Du, Y., He, J. F., et al. (2019). Research on the Potential Mechanism of Gypenosides on Treating Thyroid-Associated Ophthalmopathy Based on Network Pharmacology. *Med. Sci. Monit.* 25, 4923–4932. doi:10.12659/msm.917299

Lin, J. D., Wang, Y. H., Fang, W. F., Hsiao, C. J., Chagnaadorj, A., Lin, Y. F., et al. (2016). Serum BAFF and Thyroid Autoantibodies in Autoimmune Thyroid Disease. *Clin. Chim. Acta* 462, 96–102. doi:10.1016/j.cca.2016.09.004

Liu, X., Gao, C., Liu, X., and Gao, T. (2019). Efficacy and Safety of Tripterygium Glycosides for Graves Ophthalmopathy: A Systematic Review and Meta-Analysis. *Medicine (Baltimore)* 98 (50), e18242. doi:10.1097/md.0000000000018242

Lucini, L., Baccolo, G., Rouphael, Y., Colla, G., Bavaresco, L., and Trevisan, M. (2018). Chitosan Treatment Elicited Defence Mechanisms, Pentacyclic Triterpenoids and Stilbene Accumulation in Grape (Vitis vinifera L.) Bunches. *Phytochemistry* 156, 1–8. doi:10.1016/j.phytochem.2018.08.011

Ma, H. D., Deng, Y. R., Tian, Z., and Lian, Z. X. (2013). Traditional Chinese Medicine and Immune Regulation. *Clin. Rev. Allergy Immunol.* 44 (3), 229–241. doi:10.1007/s12016-012-8332-0

Ma, Q., and Jiang, J. G. (2016). Functional Components from Nature-Derived Drugs for the Treatment of Rheumatoid Arthritis. *Curr. Drug Targets* 17 (14), 1673–1686. doi:10.2174/1389450117666160527122233

Marcinkowski, P., Hoyer, I., Specker, E., Furkert, J., Rutz, C., Neuenschwander, M., et al. (2019). A New Highly Thyrotropin Receptor-Selective Small-Molecule Antagonist with Potential for the Treatment of Graves' Orbitopathy. *Thyroid* 29 (1), 111–123. doi:10.1089/thy.2018.0349

Marcus-Samuels, B., Krieger, C. C., Boutin, A., Kahaly, G. J., Neumann, S., and Gershengorn, M. C. (2018). Evidence that Graves' Ophthalmopathy Immunoglobulins Do Not Directly Activate IGF-1 Receptors. *Thyroid* 28 (5), 650–655. doi:10.1089/thy.2018.0089

Markham, A. (2020). Teprotumumab: First Approval. *Drugs* 80 (5), 509–512. doi:10.1007/s40265-020-01287-y

Masiello, E., Veronesi, G., Gallo, D., Premoli, P., Bianconi, E., Rosetti, S., et al. (2018). Antithyroid Drug Treatment for Graves' Disease: Baseline Predictive Models of Relapse after Treatment for a Patient-Tailored Management. *J. Endocrinol. Invest.* 41 (12), 1425–1432. doi:10.1007/s40618-018-0918-9

Natarajan, K., Meganathan, V., Mitchell, C., and Boggaram, V. (2019). Organic Dust Induces Inflammatory Gene Expression in Lung Epithelial Cells via ROS-dependent STAT-3 Activation. *Am. J. Physiol. Lung Cel Mol Physiol.* 317 (1), L127–l140. doi:10.1152/ajplung.00448.2018

Neumann, S., Huang, W., Eliseeva, E., Titus, S., Thomas, C. J., and Gershengorn, M. C. (2010). A Small Molecule Inverse Agonist for the Human Thyroid-Stimulating Hormone Receptor. *Endocrinology* 151 (7), 3454–3459. doi:10.1210/en.2010-0199

Neumann, S., Nir, E. A., Eliseeva, E., Huang, W., Marugan, J., Xiao, J., et al. (2014). A Selective TSH Receptor Antagonist Inhibits Stimulation of Thyroid Function in Female Mice. *Endocrinology* 155 (1), 310–314. doi:10.1210/en.2013-1835

Pavanello, F., Zucca, E., and Ghielmini, M. (2017). Rituximab: 13 Open Questions after 20years of Clinical Use. *Cancer Treat. Rev.* 53, 38–46. doi:10.1016/j.ctrv.2016.11.015

Pritchard, J., Han, R., Horst, N., Cruikshank, W. W., and Smith, T. J. (2003). Immunoglobulin Activation of T Cell Chemoattractant Expression in Fibroblasts from Patients with Graves' Disease Is Mediated through the Insulin-like Growth Factor I Receptor Pathway. *J. Immunol.* 170 (12), 6348–6354. doi:10.4049/jimmunol.170.12.6348

Pritchard, J., Horst, N., Cruikshank, W., and Smith, T. J. (2002). Igs from Patients with Graves' Disease Induce the Expression of T Cell Chemoattractants in Their Fibroblasts. *J. Immunol.* 168 (2), 942–950. doi:10.4049/jimmunol.168.2.942

Pu, W. L., Bai, R. Y., Zhou, K., Peng, Y. F., Zhang, M. Y., Hottiger, M. O., et al. (2019). Baicalein Attenuates Pancreatic Inflammatory Injury through Regulating MAPK, STAT 3 and NF-κB Activation. *Int. Immunopharmacol.* 72, 204–210. doi:10.1016/j.intimp.2019.04.018

Qiu, D., and Kao, P. N. (2003). Immunosuppressive and Anti-inflammatory Mechanisms of Triptolide, the Principal Active Diterpenoid from the Chinese Medicinal Herb Tripterygium Wilfordii Hook. F. *Drugs R. D* 4 (1), 1–18. doi:10.2165/00126839-200304010-00001

Ravagnan, G., De Filippis, A., Cartenì, M., De Maria, S., Cozza, V., Petrazzuolo, M., et al. (2013). Polydatin, a Natural Precursor of Resveratrol, Induces β-defensin Production and Reduces Inflammatory Response. *Inflammation* 36 (1), 26–34. doi:10.1007/s10753-012-9516-8

Ren, M., Zhong, X., Ma, C. Y., Sun, Y., Guan, Q. B., Cui, B., et al. (2009). Insulin-like Growth Factor-1 Promotes Cell Cycle Progression via Upregulation of Cyclin D1 Expression through the Phosphatidylinositol 3-kinase/nuclear Factor-kappaB Signaling Pathway in FRTL Thyroid Cells. *Acta Pharmacol. Sin.* 30 (1), 113–119. doi:10.1038/aps.2008.8

Ristov, J., Espie, P., Ulrich, P., Sickert, D., Flandre, T., Dimitrova, M., et al. (2018). Characterization of the *In Vitro* and *In Vivo* Properties of CFZ533, a Blocking and Non-depleting Anti-CD40 Monoclonal Antibody. *Am. J. Transpl.* 18 (12), 2895–2904. doi:10.1111/ajt.14872

Rosetti, S., Tanda, M. L., Veronesi, G., Masiello, E., Premoli, P., Gallo, D., et al. (2020). Oral Steroid Prophylaxis for Graves' Orbitopathy after Radioactive Iodine Treatment for Graves' Disease Is Not Only Effective, but Also Safe. *J. Endocrinol. Invest.* 43 (3), 381–383. doi:10.1007/s40618-019-01126-2

Rotondo Dottore, G., Leo, M., Casini, G., Latrofa, F., Cestari, L., Sellari-Franceschini, S., et al. (2017). Antioxidant Actions of Selenium in Orbital Fibroblasts: A Basis for the Effects of Selenium in Graves' Orbitopathy. *Thyroid* 27 (2), 271–278. doi:10.1089/thy.2016.0397

Salminen, A., and Kaarniranta, K. (2010). Insulin/IGF-1 Paradox of Aging: Regulation via AKT/IKK/NF-kappaB Signaling. *Cell Signal* 22 (4), 573–577. doi:10.1016/j.cellsig.2009.10.006

Shen, R., and Wang, J. H. (2018). The Effect of Icariin on Immunity and its Potential Application. *Am. J. Clin. Exp. Immunol.* 7 (3), 50–56.

Sikorski, E. E., Hallmann, R., Berg, E. L., and Butcher, E. C. (1993). The Peyer's Patch High Endothelial Receptor for Lymphocytes, the Mucosal Vascular Addressin, Is Induced on a Murine Endothelial Cell Line by Tumor Necrosis Factor-Alpha and IL-1. *J. Immunol.* 151 (10), 5239–5250.

Smith, B., Kiessling, A., Lledo-Garcia, R., Dixon, K. L., Christodoulou, L., Catley, M. C., et al. (2018). Generation and Characterization of a High Affinity Anti-human FcRn Antibody, Rozanolixizumab, and the Effects of Different Molecular Formats on the Reduction of Plasma IgG Concentration. *MAbs* 10 (7), 1111–1130. doi:10.1080/19420862.2018.1505464

Smith, T. J., and Hegedüs, L. (2016). Graves' Disease. *N. Engl. J. Med.* 375 (16), 1552–1565. doi:10.1056/NEJMra1510030

Smith, T. J., and Janssen, J. A. M. J. L. (2019). Insulin-like Growth Factor-I Receptor and Thyroid-Associated Ophthalmopathy. *Endocr. Rev.* 40 (1), 236–267. doi:10.1210/er.2018-00066

Stacey, D. W. (2003). Cyclin D1 Serves as a Cell Cycle Regulatory Switch in Actively Proliferating Cells. *Curr. Opin. Cel Biol* 15 (2), 158–163. doi:10.1016/s0955-0674(03)00008-5

Starling, S. (2019). Long-term Treatment Outcomes for Graves Disease. *Nat. Rev. Endocrinol.* 15 (11), 628. doi:10.1038/s41574-019-0268-5

Stohl, W., Hiepe, F., Latinis, K. M., Thomas, M., Scheinberg, M. A., Clarke, A., et al. (2012). Belimumab Reduces Autoantibodies, Normalizes Low Complement Levels, and Reduces Select B Cell Populations in Patients with Systemic Lupus Erythematosus. *Arthritis Rheum.* 64 (7), 2328–2337. doi:10.1002/art.34400

Taurog, A., Riesco, G., and Larsen, P. R. (1976). Formation of 3,3'-diiodothyronine and 3',5',3-triiodothyronine (Reverse T3) in Thyroid Glands of Rats and in Enzymatically Iodinated Thyroglobulin. *Endocrinology* 99 (1), 281–290. doi:10.1210/endo-99-1-281

Travali, S., Ku, D. H., Rizzo, M. G., Ottavio, L., Baserga, R., and Calabretta, B. (1989). Structure of the Human Gene for the Proliferating Cell Nuclear Antigen. *J. Biol. Chem.* 264 (13), 7466–7472. doi:10.1016/s0021-9258(18)83257-4

Tsui, S., Naik, V., Hoa, N., Hwang, C. J., Afifiyan, N. F., Sinha Hikim, A., et al. (2008). Evidence for an Association between Thyroid-Stimulating Hormone and Insulin-like Growth Factor 1 Receptors: a Tale of Two Antigens Implicated in Graves' Disease. *J. Immunol.* 181 (6), 4397–4405. doi:10.4049/jimmunol.181.6.4397

Völzke, H., Friedrich, N., Schipf, S., Haring, R., Lüdemann, J., Nauck, M., et al. (2007). Association between Serum Insulin-like Growth Factor-I Levels and Thyroid Disorders in a Population-Based Study. *J. Clin. Endocrinol. Metab.* 92 (10), 4039–4045. doi:10.1210/jc.2007-0816

Vondrichova, T., de Capretz, A., Parikh, H., Frenander, C., Asman, P., Aberg, M., et al. (2007). COX-2 and SCD, Markers of Inflammation and Adipogenesis, Are Related to Disease Activity in Graves' Ophthalmopathy. *Thyroid* 17 (6), 511–517. doi:10.1089/thy.2007.0028

Wakelkamp, I. M., Bakker, O., Baldeschi, L., Wiersinga, W. M., and Prummel, M. F. (2003). TSH-R Expression and Cytokine Profile in Orbital Tissue of Active vs. Inactive Graves' Ophthalmopathy Patients. *Clin. Endocrinol. (Oxf)* 58 (3), 280–287. doi:10.1046/j.1365-2265.2003.01708.x

Wang, F., Dang, Y., Wang, J., Zhou, T., and Zhu, Y. (2018). Gypenosides Attenuate Lipopolysaccharide-Induced Optic Neuritis in Rats. *Acta Histochem.* 120 (4), 340–346. doi:10.1016/j.acthis.2018.03.003

Wang, P. (2000). Clinical Observation of Compound Thyrokang Tablets in the Treatment of Subclinical Hyperthyroidism with Deficiency of Qi and Yin. *Med. Health Technol.*, R259.

Wang, X., Yang, L., Yang, L., Xing, F., Yang, H., Qin, L., et al. (2017). Gypenoside IX Suppresses P38 MAPK/Akt/NFκB Signaling Pathway Activation and Inflammatory Responses in Astrocytes Stimulated by Proinflammatory Mediators. *Inflammation* 40 (6), 2137–2150. doi:10.1007/s10753-017-0654-x

Wang, X. X., Wang, X. X., Jia, X. F., Guo, T., Xian, T. Z., Liu, L., et al. (2019). Novel Role of SF1 in Alleviating Thyroid-Associated Ophthalmopathy through the AMPK/mTOR Signaling Pathway. *Gene* 691, 132–140. doi:10.1016/j.gene.2018.11.097

Wang, Y., and Smith, T. J. (2014). Current Concepts in the Molecular Pathogenesis of Thyroid-Associated Ophthalmopathy. *Invest. Ophthalmol. Vis. Sci.* 55 (3), 1735–1748. doi:10.1167/iovs.14-14002

Woeller, C. F., Roztocil, E., Hammond, C., and Feldon, S. E. (2019). TSHR Signaling Stimulates Proliferation through PI3K/Akt and Induction of miR-146a and miR-155 in Thyroid Eye Disease Orbital Fibroblasts. *Invest. Ophthalmol. Vis. Sci.* 60 (13), 4336–4345. doi:10.1167/iovs.19-27865

Wu, J., Liu, D. F., and Chen, Y. (2011). Effects of Radix Astragali on IL-1beta, TNF-Alpha and Antigen Expression of Peripheral Blood Mononuclear Cells in Patients with Graves Disease. *Zhongguo Zhong Xi Yi Jie He Za Zhi* 31 (11), 1487–1490. doi:10.1097/MOP.0b013e328341d1da

Xiang, S., Dauchy, R. T., Hoffman, A. E., Pointer, D., Frasch, T., Blask, D. E., et al. (2019). Epigenetic Inhibition of the Tumor Suppressor ARHI by Light at Night-Induced Circadian Melatonin Disruption Mediates STAT3-Driven Paclitaxel Resistance in Breast Cancer. *J. Pineal Res.* 67 (2), e12586. doi:10.1111/jpi.12586

Xu, J. P., Xu, J. P., Xu, C., Chen, J., Jin, Z. H., Zheng, H. F., et al. (2014). Peripheral Blood Cell Factors of Graves Ophthalmopathy and Effect of Intervention with Tripterygium Glycosides. *Zhongguo Zhong Yao Za Zhi* 39 (3), 544–547. doi:10.4268/cjcmm20140336

Yamamoto, T., Suzuki, T., Kobayashi, A., Wakabayashi, J., Maher, J., Motohashi, H., et al. (2008). Physiological Significance of Reactive Cysteine Residues of Keap1 in Determining Nrf2 Activity. *Mol. Cel. Biol.* 28 (8), 2758–2770. doi:10.1128/mcb.01704-07

Yan, S. X., and Wang, Y. (2006). Inhibitory Effects of Triptolide on Interferon-Gamma-Induced Human Leucocyte Antigen-DR, Intercellular Adhesion Molecule-1, CD40 Expression on Retro-Ocular Fibroblasts Derived from Patients with Graves' Ophthalmopathy. *Clin. Exp. Ophthalmol.* 34 (3), 265–271. doi:10.1111/j.1442-9071.2006.01190.x

Yang, K., Guo, K. Q., and Wu, H. Y. (2007). Clinical Effect of Prunellae Oral Liquid on Goiter with Different Thyroid Function. *Zhongguo Zhong Xi Yi Jie He Za Zhi* 27 (1), 37–39.

Yang, S. X., Xie, S. S., Gao, H. L., Ma, D. L., and Long, Z. Z. (1994). Triptolide Suppresses T-Lymphocyte Proliferation by Inhibiting Interleukin-2 Receptor Expression, but Spares Interleukin-2 Production and mRNA Expression. *Int. J. Immunopharmacol.* 16 (11), 895–904. doi:10.1016/0192-0561(94)90044-2

Yang, Y., Liu, Z., Tolosa, E., Yang, J., and Li, L. (1998). Triptolide Induces Apoptotic Death of T Lymphocyte. *Immunopharmacology* 40 (2), 139–149. doi:10.1016/s0162-3109(98)00036-8

Zen, X. X., Yuan, Y., Liu, Y., Wu, T. X., and Han, S. (2007). Chinese Herbal Medicines for Hyperthyroidism. *Cochrane Database Syst. Rev.* 2007 (2), Cd005450. doi:10.1002/14651858.CD005450.pub2

Zhang, R., Tan, J., Wang, R., Zhang, G., Jia, Q., Meng, Z., et al. (2017). Analysis of Risk Factors of Rapid Thyroidal Radioiodine-131 Turnover in Graves' Disease Patients. *Sci. Rep.* 7 (1), 8301. doi:10.1038/s41598-017-08475-z

Zhang, X., Du, W., and Fang, Q. (2017). Risk Factors for Postoperative Haemorrhage after Total Thyroidectomy: Clinical Results Based on 2,678 Patients. *Sci. Rep.* 7 (1), 7075. doi:10.1038/s41598-017-07334-1

Zhang, Y., Li, H., Gao, L., Zhang, X., and Xie, R. (2017). Pingmu Decoction Induces Orbital Preadipocytes Apoptosis *In Vitro*. *Evid. Based Complement. Alternat Med.* 2017, 2109249. doi:10.1155/2017/2109249

Zhang, Y., Li, X., Guo, C., Dong, J., and Liao, L. (2020). Mechanisms of Spica Prunellae against Thyroid-Associated Ophthalmopathy Based on Network Pharmacology and Molecular Docking. *BMC Complement. Med. Ther.* 20 (1), 229. doi:10.1186/s12906-020-03022-2

Zhao, J., Gao, L., and Liu, X. (1999). Preliminary Study on Chinese Herb Induced Apoptosis of Thyrocytes in Graves' Disease. *Zhongguo Zhong Xi Yi Jie He Za Zhi* 19 (6), 335–336.

Zhu, J., Zhang, W., Zhang, Y., Wang, Y., Liu, M., and Liu, Y. (2018). Effects of Spica Prunellae on Caspase-3-Associated Proliferation and Apoptosis in Human Lung Cancer Cells *In Vitro*. *J. Cancer Res. Ther.* 14 (4), 760–763. doi:10.4103/jcrt.JCRT_1289_16

Zuercher, A. W., Spirig, R., Baz Morelli, A., Rowe, T., and Käsermann, F. (2019). Next-generation Fc Receptor-Targeting Biologics for Autoimmune Diseases. *Autoimmun. Rev.* 18 (10), 102366. doi:10.1016/j.autrev.2019.102366

Conflict of Interest: The authors declare that the research was conducted in the absence of any commercial or financial relationships that could be construed as a potential conflict of interest.

Publisher's Note: All claims expressed in this article are solely those of the authors and do not necessarily represent those of their affiliated organizations, or those of the publisher, the editors and the reviewers. Any product that may be evaluated in this article, or claim that may be made by its manufacturer, is not guaranteed or endorsed by the publisher.

frontiers | Frontiers in Pharmacology

ORIGINAL RESEARCH
published: 25 April 2022
doi: 10.3389/fphar.2022.867525

Bletilla striata Oligosaccharides Improve Ulcerative Colitis by Regulating Gut Microbiota and Intestinal Metabolites in Dextran Sulfate Sodium-Induced Mice

Tianxiang Zhu[1†], Baifei Hu[1†], Cheng Ye[2], Haiming Hu[1], Mingzhu Yin[1], Zhigang Zhang[1], Shuiqing Li[1], Yanju Liu[1] and Hongtao Liu[1]**

[1]College of Basic Medicine, Hubei University of Chinese Medicine, Wuhan, China, [2]Wuhan Customs Technology Center, Wuhan, China

OPEN ACCESS

Edited by:
Qi Wang,
Harbin Medical University, China

Reviewed by:
Yue Wang,
Second Hospital of Anhui Medical University, China
Daqiang Wu,
Anhui University of Chinese Medicine, China

***Correspondence:**
Yanju Liu
lyj1965954@hbtcm.edu.cn
Hongtao Liu
hongtaoliu@hbtcm.edu.cn

[†]These authors have contributed equally to this work

Specialty section:
This article was submitted to Ethnopharmacology, a section of the journal Frontiers in Pharmacology

Received: 01 February 2022
Accepted: 28 March 2022
Published: 25 April 2022

Citation:
Zhu T, Hu B, Ye C, Hu H, Yin M, Zhang Z, Li S, Liu Y and Liu H (2022) Bletilla striata Oligosaccharides Improve Ulcerative Colitis by Regulating Gut Microbiota and Intestinal Metabolites in Dextran Sulfate Sodium-Induced Mice. Front. Pharmacol. 13:867525. doi: 10.3389/fphar.2022.867525

This study aimed to elucidate the mechanism of *Bletilla striata* oligosaccharides (BO) in the treatment of ulcerative colitis (UC). A UC mouse model was induced by 3% Dextran sodium sulfate (DSS), and BO (200 mg/kg/d) were administered for intervention. The results show that BO effectively inhibited the release of intestinal inflammatory cytokines such as IL-6, TNF-α, and IL-1β. Also, BO profoundly elevated the secretion of mucins and the expression of tight junction (TJ) proteins to attenuate dysfunction of the intestinal barrier. The 16S rDNA sequencing and liquid chromatography/gas chromatography-mass spectrometer (LC/GC-MS) analysis of mouse feces revealed that BO regulated the disturbance of gut microbiota and intestinal metabolites. By using the *in vitro* fermentation broth of BO and gut microbiota-depleted mice treated with antibiotics, we confirmed the protection of BO against UC. In conclusion, BO played a role in improving UC by modulating gut microbial composition and intestinal metabolites, which provided new therapeutic strategies for UC treatment.

Keywords: ***Bletilla striata*** **oligosaccharides, ulcerative colitis, gut microbiota, intestinal metabolites, intestinal barrier**

INTRODUCTION

Ulcerative colitis (UC) is an idiopathic and chronic inflammatory bowel disease (IBD), and the main symptoms are episodes of abdominal pain and bloody diarrhea (Feuerstein et al., 2019). Patients with UC may experience intestinal perforation in severe cases. UC is characterized by a long course of the disease, difficulty in curing, and various complications, which seriously affect the life quality of patients. According to statistics, the incidence of UC increased year by year. In China, patients with IBD will reach 1.5 million by 2025 (Kaplan, 2015). In recent years, the primary clinical drugs for UC treatment included 5-aminosalicylic acid, corticosteroids, immunosuppressants, and monoclonal antibodies, but these drugs may have clinical limitations or even severe side effects (Eisenstein, 2018). This makes it more urgent to explore new therapeutic candidates and methods.

The pathogenesis of UC is related to impaired intestinal barrier, abnormal immune response, dysbiosis of gut microbiota, genetic mutation, and environmental changes (Porter et al., 2020). Among them, intestinal flora disturbance is a crucial contributor to the occurrence of UC (Sheehan

et al., 2015). Gut microbiota exerts an essential regulatory role in maintaining the physiological activities of hosts under normal circumstances. At the same time, the imbalance between beneficial and harmful bacteria will destroy the intestinal barrier and thus induce or aggravate the development of UC (Pei et al., 2019). For example, the abundance of adherent-invasive *Escherichia coli*, *Clostridium,* and *Fusobacterium* increased. In contrast, the contents of *Faecalibacterium prausnitzii*, *Bifidobacterium*, and *Roseburia* decreased significantly in UC patients' intestines (Zhang et al., 2017). Metabolites of gut microbiota, like bile acids (BAs), short-chain fatty acids (SCFAs), and tryptophan catabolites, are also involved in the pathogenesis of UC (Louis et al., 2014). During UC progression, BA synthesis, transport, and excretion in the liver are aberrant, leading to the accumulation of BAs in the intestine and causing intestinal inflammation (Negroni et al., 2020). Evidence demonstrated that deficiency of secondary BAs, which are generated by hydrolysis of intestinal flora, may disrupt the intestinal mucosal integrity and exacerbate the severity of colitis (Sinha et al., 2020). SCFAs, including acetic acid, propionic acid, and butyric acid, are produced by gut microbial metabolism of indigestible fiber-rich diets (Sun et al., 2017). It was reported that butyric acid improved the intestinal barrier dysfunction and offered adequate treatment of DSS-induced colitis by regulating autophagy through Hypoxia-inducible factor-1α (HIF-1α) (Zhou et al., 2020). Tryptophan, an essential amino acid in humans, is metabolized by gut microbiota to produce indole-3-ethanol, indole-3-pyruvate, and indole-3-aldehyde. All of these catabolites initiate protective functions on the intestinal barrier. Thus, it might be a new strategy to improve UC by modulating gut microbiota homeostasis.

Natural products such as polyphenols, alkaloids, and polysaccharides have been certificated to have favorable anti-UC activity (Liu et al., 2018; Ji et al., 2020). For thousands of years, the traditional Chinese medicine *Bletilla striata* (Thunb.) Rchb. f. [Orchidaceae] has been used in China mainly to treat traumatic bleeding and digestive system disorders (Xu et al., 2019). *B. striata* contains a variety of natural chemical constituents such as polysaccharides, glycosides, phenanthrenes, quinones, and bibenzyls (Xu et al., 2019). Among them, the polysaccharides have the highest content in *B. striata* tuber (Zhang et al., 2019). Luo et al. (2018) discovered that *B. striata* polysaccharide (BP) might be a novel protective agent of the intestinal epithelial barrier. However, due to the complex structure and high viscosity of BP, the in-depth research of BP activity has been limited.

Oligosaccharides are a new type of available glycogen with high solubilities and biological activities. Compared to npolysaccharides, oligosaccharides can be easily decomposed and utilized by multiple intestinal florae, thus influencing the enteric homeostasis to benefit human health (Goh & Klaenhammer, 2015). In this study, we proposed to degrade BP into oligosaccharides effectively and investigated its molecular mechanism for improving UC through the metabolic regulation of gut microbiota.

MATERIALS AND METHODS

Reagents and Antibodies

B. striata oligosaccharides (BO) were extracted from *B. striata* (**Supplementary Methods**; **Supplementary Figures S1, S2**). The preparation methods were carried out according to the previous report, and the molecular weight of BO was 720–1080 Da (Chen et al., 2019; Hu et al., 2020). *Bletilla striata* (Thunb.) Rchb.f. [Orchidaceae] was purchased from Hubei Zexi Chinese Medicine Technology Co., Ltd. (Qichun, Hubei, China) and authenticated by Xiongjie Sun in Hubei University of Chinese Medicine. Dextran sulfate sodium (DSS, MW 36000–50000) was purchased from MP Biomedicals (Santa Ana, CA, United States). Mouse NGAL (Neutrophil Gelatinase Associated Lipocalin) ELISA kit was bought from Elabscience Biotechnology Co., Ltd. (Wuhan, China). TRIzol Reagent and Biotin-avidin IHC kits were obtained from summer Biotechnology Co., Ltd. (Beijing, China). FastHS SYBR QPCR mixture and AMeasy 1st Strand cDNA synthesis kit were bought from AllMEEK (Beijing, China). Tryptone and yeast extract (YE) were purchased from Amresco (Washington, DC, United States). L-Cysteine, ascorbic acid, ampicillin, vancomycin, neomycin sulfate, metronidazole, and SCFAs (Acetic acid, propanoic acid, butyric acid, and valeric acid) were obtained from Aladdin (Shanghai, China). Tryptamine, 5-hydroxytryptamine (5-HT), indole, Cholic acid (CA), Chenodeoxycholic acid (CDCA) deoxycholic acid (DCA), taurocholic acid (TCA), ursodeoxycholic acid (UDCA), taurochenodeoxycholic acid (TCDCA), cholic acid-2,2,3,4,4-d5 (d_5-CA) and sodium taurocholate-2,2,4,4-d4 (d_4-TCA) were purchased from Sigma Aldrich (St. Louis, MO, United States). Tauro-β-murocholicacid (T-β-MCA) was bought from TRC (Toronto, ON, Canada).

Antibodies for extracellular regulated kinase 1 and 2 (ERK1/2), p-ERK, zonula occludens-1 (ZO-1), and Claudin-1 were bought from Santa Cruz Biotechnology (Santa Cruz, CA, United States). Antibodies for NOD-like receptor pyrin domain containing 3 (NLRP3), c-Jun N-terminal kinase (JNK), and p-JNK were purchased from Cell Signaling Technology (Danvers, MA, United States).

Animal Experiment

Six-week-old Specific pathogen free (SPF) male BALB/c mice (22 ± 2 g) were purchased from Hubei Provincial Center for Disease Control and Prevention (Wuhan, China). All mice were housed under temperature-controlled conditions (12 h light/dark cycle, 22 ± 1°C) with free access to sterile water and standard food. After the acclimation, mice were randomly divided into four groups: 1) Ctrl group, treated with distilled water; 2) DSS group, received 3% DSS (in drinking water) from day 15 to 21; 3) BO group, in which mice were given BO (200 mg/kg/d) by gavage for 21 days; 4) DSS + BO group, in which mice were given BO by gavage from day 1 to 21 and received 3% DSS from day 15 to 21. The dose of BO was based on a study of flaxseed oligosaccharides in colitis (Xu et al., 2020). During the experiment, the weight loss, stool consistency, and gross bleeding were recorded daily for the

assessment of disease activity index (DAI) score (**Supplementary Table S1**). After the treatment, all mice were euthanized, and the major tissues were collected. All samples were stored at −80°C for further analysis. In addition, colons were removed to measure the length, and part of the distal colon was fixed with 4% paraformaldehyde. The animal experiment was performed according to the requirement of the Animal Ethical Experimentation Committee of the Hubei University of Chinese Medicine and the National Act on Use of Experimental Animals (China).

Fermentation Experiment

The culture medium was prepared based on a simulated intestinal environment medium, the components of which were provided in **Supplementary Table S2**. After the pH was adjusted to 7.5–7.6, the intestinal flora culture medium was autoclaved at 121°C for 20 min. Filter-sterilized 25% ascorbic acid was added to the medium after high temperature and pressure sterilization. Fresh fecal samples from normal BALB/c mice were evenly dispersed in 1% sterile PBS to obtain 20% (w/v) fecal suspension, followed by centrifugation at 3000 rpm for 5 min. Next, 6 ml of the collected supernatant was added to 54 ml of intestinal flora culture medium (containing 1.8 g BO) with a final ratio of 1:9 (v/v). Then, the fermentation broth was placed in an anaerobic culture tank (including 10% H_2, 10% CO_2, and 80% N_2) and incubated at 37°C for 24 h. After the anaerobic fermentation, the broth was centrifuged at 12,000 rpm for 10 min, and the supernatant was collected and filtered with a 0.22 μm microporous membrane for the animal experiment.

Antibiotic Treatment

Six-week-old male BALB/c mice were randomly divided into five groups: Ctrl group, DSS group, DSS + Antibiotic mixtures (Abx) group, DSS + Abx + BO group and DSS + Abx + BO fermentation broth (BO FB) group. Abx included ampicillin (1 mg/ml), vancomycin (0.5 mg/ml), neomycin sulfate (1 mg/ml), and metronidazole (0.5 mg/ml). The administration protocol was detailed in **Figure 5A**, and the administration route and dose were the same as above. The body weight, stool consistency, and rectal bleeding were recorded daily for assessment of DAI score.

Before the BO treatment, fecal samples were collected to extract and quantify bacterial genomic DNA to confirm that the gut microbiota was depleted in mice. The experimental details were provided in **Supplementary Methods** and **Supplementary Table S3**. At the end of the animal experiment, the mice were sacrificed, and major tissues were collected as above.

RNA Extraction and Quantitative Real-Time PCR

Total RNA was isolated from colon tissues using Trizol reagents (summer Bio, Beijing, China). cDNA was generated using an AMeasy 1st Strand cDNA synthesis kit (AllMEEK, Beijing, China). Next, RT-qPCR was performed using a 2 × FastHS SYBR QPCR mixture (AllMEEK, Beijing, China) on a CFX Connect Real-time system (Bio-Rad, Hercules, CA, United States). The amplification protocol was as follows: initial denaturation step at 95°C (15 min), 40 cycles at 95°C (8 s), 60°C (30 s) for amplification. All primer sequences are shown in **Supplementary Table S4**. Glyceraldehyde-3-phosphate dehydrogenase (GAPDH) was used as an internal reference to normalize the expressions of target genes. The $2^{-\Delta\Delta CT}$ method was used to calculate the relative mRNA expression.

Western Blotting

Colon tissues were homogenized using RIPA buffer (Cell Signaling Technology Inc., MA, United States) supplemented with a protease inhibitor cocktail (Merck, Darmstadt, Germany). Protein concentration was measured with a BCA protein assay kit (Thermo Fisher Scientific, Waltham, MA, United States). Protein samples were separated by SDS-PAGE and transferred onto PVDF membranes. The membranes were blocked with 5% skim milk for 1 h and incubated with primary antibodies at 4°C overnight, including NLRP3 (1:1,000, Cat #15101), p-ERK (1:200, Cat #sc-9383), ERK (1:200, Cat #sc-514302), p-JNK (1:1,000, Cat #9251), JNK (1:1,000, Cat #9252), and β-Actin (1:500, Cat #sc-81178). Then, the membranes were washed and interacted with horseradish peroxidase-conjugated secondary antibody (1:5,000) at room temperature for 1.5 h. Finally, the target protein bands were detected by enhanced chemiluminescence (ECL) (Sigma Aldrich, MO, United States). The densitometry analysis was performed using Image J2x software (National Institute of Health, United States).

Histological Analysis

Colon tissues were fixed with 4% paraformaldehyde, dehydrated, embedded in paraffin, and cut into sections of 5 μm. Hematoxylin and eosin (H&E) staining kit (Beyotime Institute of Biotechnology, Shanghai, China) was used for slide staining. The production of intestinal mucins was assayed by staining with an Alcian Blue staining kit (Vectorlabs, Beijing, China) and fluorescein isothiocyanate conjugated-wheat germ agglutinin (WGA-FITC) immunofluorescence (Sigma Aldrich, MO, United States). The immunohistochemistry of colon tissues was analyzed using anti-ZO-1 (1:50, Cat #sc-33725) and anti-Claudin-1 (1:50, Cat #sc166338) antibodies. Images of colon structures were obtained by a Leica DMIL 4000B light microscope with a Leica DFC450C digital camera (Wetzlar, Germany).

Analysis of Intestinal Metabolites in Feces

For the quantification of fecal BAs, 50 mg of stool samples were dissolved in 1 ml water-methanol-formic acid solution (25:74:1, V/V/V) containing d5-CA and d4-TCA as internal standards. The mixture was homogenized and centrifuged at 12,000 ×g for 15 min at 4°C. After filtration with 0.22 μm microporous membranes, all samples were analyzed by a liquid

chromatography-mass spectrometer (LC-MS). The LC-MS parameters referred to previous studies (Zheng et al., 2021). For the analysis of SCFAs and tryptophan metabolites, 50 mg of stool sample was dissolved in 1 ml 50% (V/V) methanol aqueous solution (containing 0.2% HCl). After the treatment as above, all samples were analyzed by LC-MS or gas chromatography-mass spectrometer (GC-MS). The detailed LC/GC-MS parameters were provided in **Supplementary Methods**.

16S rDNA Sequencing of Gut Microbiota

Fast DNA™ SPIN Kit (MP Biomedicals, CA, United States) was used to extract fecal bacterial genomic DNA. Barcoded conventional primers (forward 338 F, 5′-ACTCCTACGGGA GGCAGCAG-3′; reverse 806 R, 5′-GACTACHVGGGTWTCTAAT-3′) were applied to amplify V3–V4 hypervariable regions of bacterial 16S rDNA gene by RT-qPCR. The reaction process was as follows: an initiation at 95°C for 5 min, 20 cycles at 95°C for 30 s, 55°C for 30 s and 72°C for 30 s. Finally, the reaction was extended 10 min at 72°C. The purified amplicons were pooled in paired-end sequencing (2 × 300) on an Illumina MiSeq platform (Illumina, San Diego, CA, United States) by Beijing Allwegene Tech (Beijing, China). The data of high-quality sequence was analyzed using QIIME package (Quantitative Insights into Microbial Ecology, United States) (Version 1.8, http://qiime.org). The main criteria for selecting sequences were nucleotide ≥110, sequence overlaps ≥10 bp, an average quality score higher than 20 in a sliding window of 50 bp, an exact match to primers, and clear features. UCLUST (Version 1.2.22, http://www.Drive5.com/uclust/downloads1-2-22q.html) divided the unique sequence into an operational taxonomic unit (OTU) when the similarity is more significant than 97%. Chimeric sequences were screened and removed using Usearch (Version 8 January 1861, http://www.drive5.com/usearch). The taxonomy of each 16S rDNA gene sequence was identified by UCLUST against the Silva (Release 128 http://www.arb-silva.de) and Greengene 16S rRNA database (Release 13.5, http://greengenes.secondgenome.com/), with a minimum threshold of 90% confidence for identification. At last, an OTU table was generated for gut microbiota composition and abundance analysis. Functional prediction of bacterial communities was finished by a bioinformatic tool (PICRUSt, Phylogenetic Investigation of Communities by Reconstruction of Unobserved States). Spearman's rank correlation coefficient analyzed the Correlation between intestinal flora and different indicators.

Statistical Analysis

Results were presented as mean ± SD. Statistical differences were evaluated by one-way analysis of variance (ANOVA) followed by Tukey-Kramer test among groups. It was significant for all statistical analyses that the probability value was less than 0.05. Data were calculated using Prism version 8.0 GraphPad Software.

RESULTS

Improvement of *Bletilla striata* Oligosaccharides on Physiological Indices in UC Mice

In the present study, DSS was used to induce UC in mice. From the fourth day of DSS administration, the mice exhibited evident body weight loss, and the weight loss was slowed down by BO treatment (**Figure 1A**). DAI scores were performed to determine the severity of UC based on body weight loss, stool consistency, and gross bleeding (Murthy et al., 1993). As shown in **Figure 1B**, the DAI scores in UC mice dropped after BO administration. Also, BO were found to inhibit the increase of spleen index in UC mice ($p < 0.05$, vs. DSS group) (**Figure 1C**). Meanwhile, a pronounced decrease in the length of the colon was observed in UC mice, and this was expectedly rescued by BO ($p < 0.05$, vs. DSS group) (**Figures 1D,E**). Furthermore, H&E staining of colon tissues demonstrated that the muscular layer and crypt of colon tissues were severely disrupted, accompanied by an absence of goblet cells and massive infiltration of inflammatory cells in UC mice, while these damages were significantly restored by BO treatment (**Figure 1F**). The glycoprotein change in mucins was detected by Alcian blue and WGA-FITC staining (**Figures 1G,H**). It was shown that BO reversed the reduction of glycoprotein mucins in the colon of UC mice. Lipocalin-2 (Lcn2) is an emerging clinically significant biomarker for IBD. Therefore, the serum Lcn2 in UC mice were determined using an ELISA kit. The results demonstrated that BO reduced the content of serum Lcn2 in UC mice (**Supplementary Figure S3**).

Inhibitory Effect of *Bletilla striata* Oligosaccharides on Intestinal Inflammation and Intestinal Barrier Damage in UC Mice

Next, RT-qPCR, WB, and immunohistochemistry were adopted to assess the protective effect of BO on colon tissues. Compared to the DSS group, BO inhibited the overexpression of interleukin-6 (IL-6), interleukin-1β (IL-1β), inducible nitric oxide synthase (iNOS), tumor necrosis factor-α (TNF-α), NOD-like receptor pyrin domain containing 3 (NLRP3), and cyclooxygenase-2 (COX-2) in UC mice ($p < 0.05$ or 0.01, vs. DSS group) (**Figure 2A**). At the protein level, BO not only reduced the expression of NLRP3 but also blocked the activation of ERK and JNK in the colon of UC mice ($p < 0.05$ or 0.01, vs. DSS group) (**Figures 2B,C**).

We also assessed the effect of BO treatment on abnormal intestinal fluid metabolism (an indicator of severe diarrhea) in UC mice. As indicated in **Figure 2D**, the expression of epithelial sodium channel-β (ENaC-β), aquaporin 2 (AQP2), and aquaporin 3 (AQP3) was curbed in the DSS group ($p < 0.01$, vs. Ctrl group). In contrast, BO treatment significantly promoted the expressions of these genes ($p < 0.05$ or 0.01, vs. DSS group). Then, the damage to the intestinal barrier was

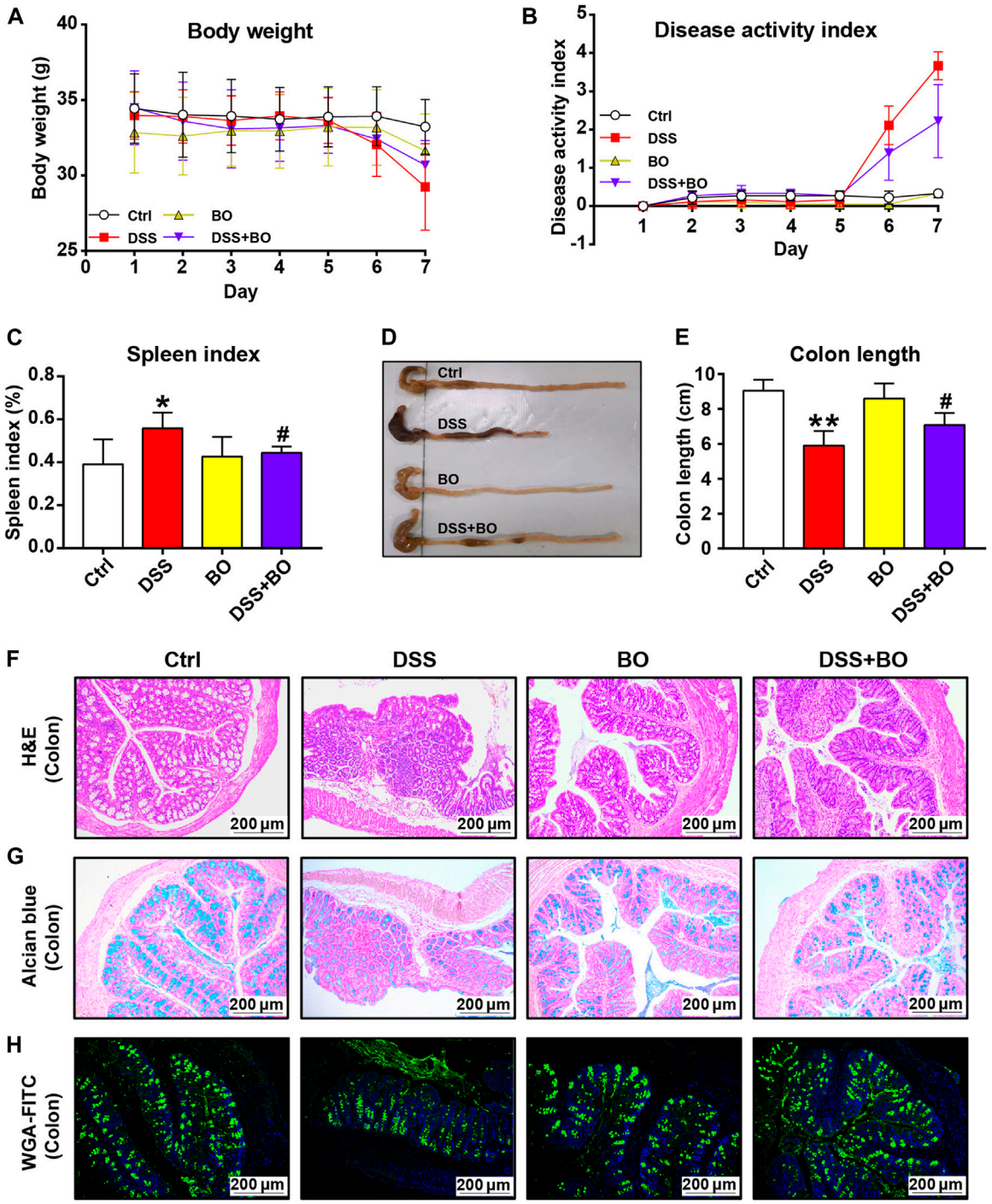

FIGURE 1 | BO ameliorated pathological indices of UC mice. **(A)** Changes in body weight during disease progression. **(B)** DAI scores. **(C)** Spleen index. **(D)** Photographs of the colon. **(E)** Colon length. **(F)** Hematoxylin & eosin (H&E) staining for morphological structure of colon tissues. Scale bar = 200 μm. **(G,H)** Glycoprotein change of mucins in the colon stained with Alcian blue **(G)** and wheat germ agglutinin labeled with FITC. **(H)** Scale bar = 200 μm. Data were shown as mean ± SD ($n = 6$). $^{*}p < 0.05$, $^{**}p < 0.01$ vs. Ctrl group; $^{\#}p < 0.05$, $^{\#\#}p < 0.01$ vs. DSS group.

measured. As expected, BO acquired a notable increase in the mRNA expressions of Mucin 2 (MUC2) and Mucin 3 (MUC3) but suppressed the mRNA level of matrix metalloproteinase-9 (MMP-9) in the colon of UC mice ($p < 0.05$ or 0.01, vs. DSS group) (**Figure 2D**). Further, the immunohistochemical analysis of ZO-1 and Claudin-1 demonstrated that BO could restore the integrity of the intestinal barrier in UC mice (**Figure 2E**). Similarly, WB assays for ZO-1 and Claudin-1

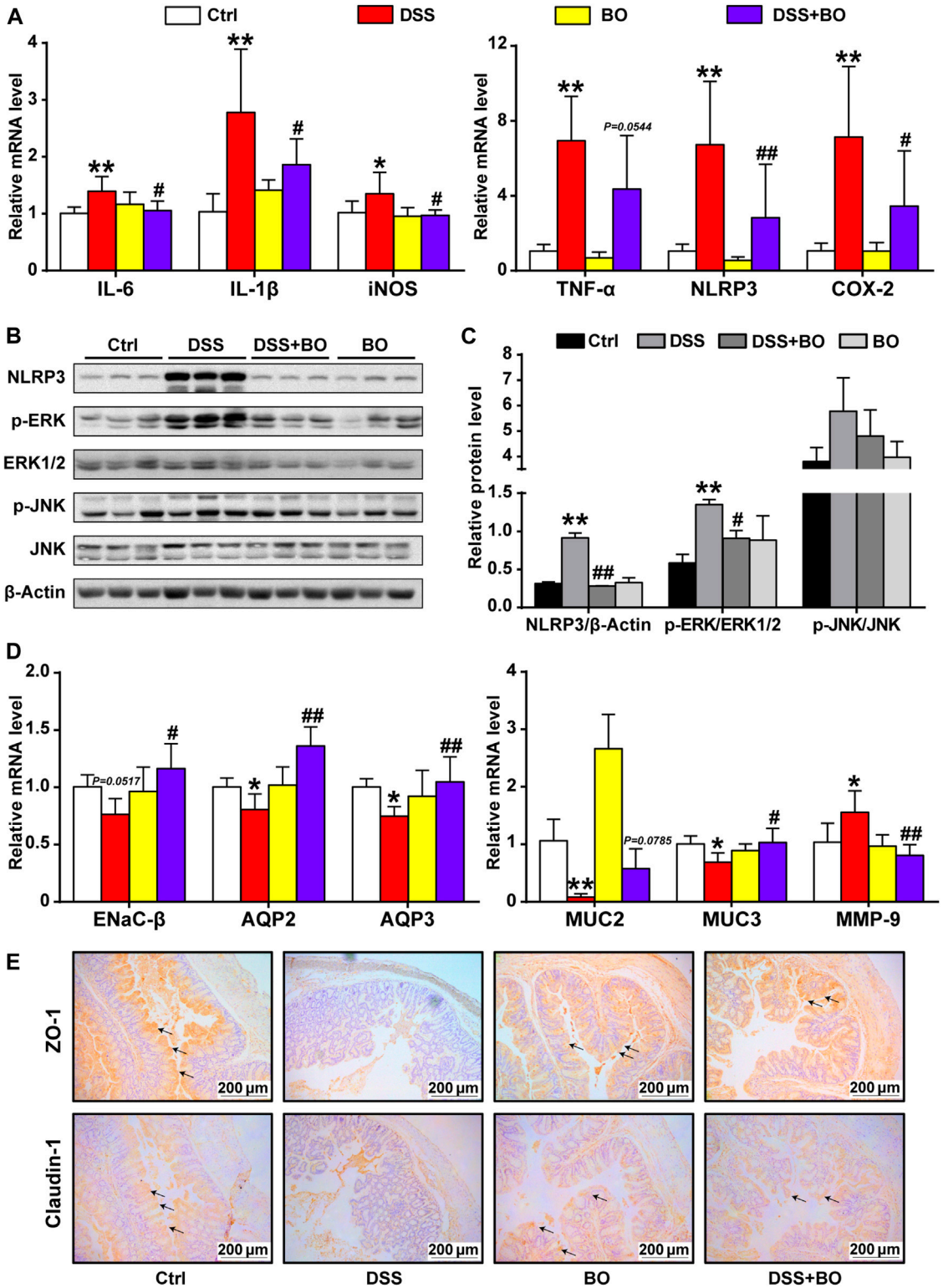

FIGURE 2 | BO inhibited inflammatory responses and gut barrier damage in the colon of UC mice. **(A)** mRNA levels of inflammatory factors by RT-qPCR, including IL-6, IL-1β, iNOS, TNF-α, NLRP3, and COX-2. **(B)** Protein expressions of NLRP3, p-ERK, ERK1/2, p-JNK, and JNK in colon tissues by WB. **(C)** Relative intensities of NLRP3, p-ERK, and p-JNK at protein levels. **(D)** Expressions of regulators related to aqueous metabolism, intestinal integrity, and gut barrier at mRNA levels, including ENaC-β, AQP2, AQP3, MUC2, MUC3, and MMP-9. **(E)** Immunohistochemical analysis of ZO-1 and Claudin-1 in colon tissues. Scale bar = 200 μm. Data were shown as mean ± SD (n = 6). $^{*}p < 0.05$, $^{**}p < 0.01$ *vs.* Ctrl group; $^{\#}p < 0.05$, $^{\#\#}p < 0.01$ vs. DSS group.

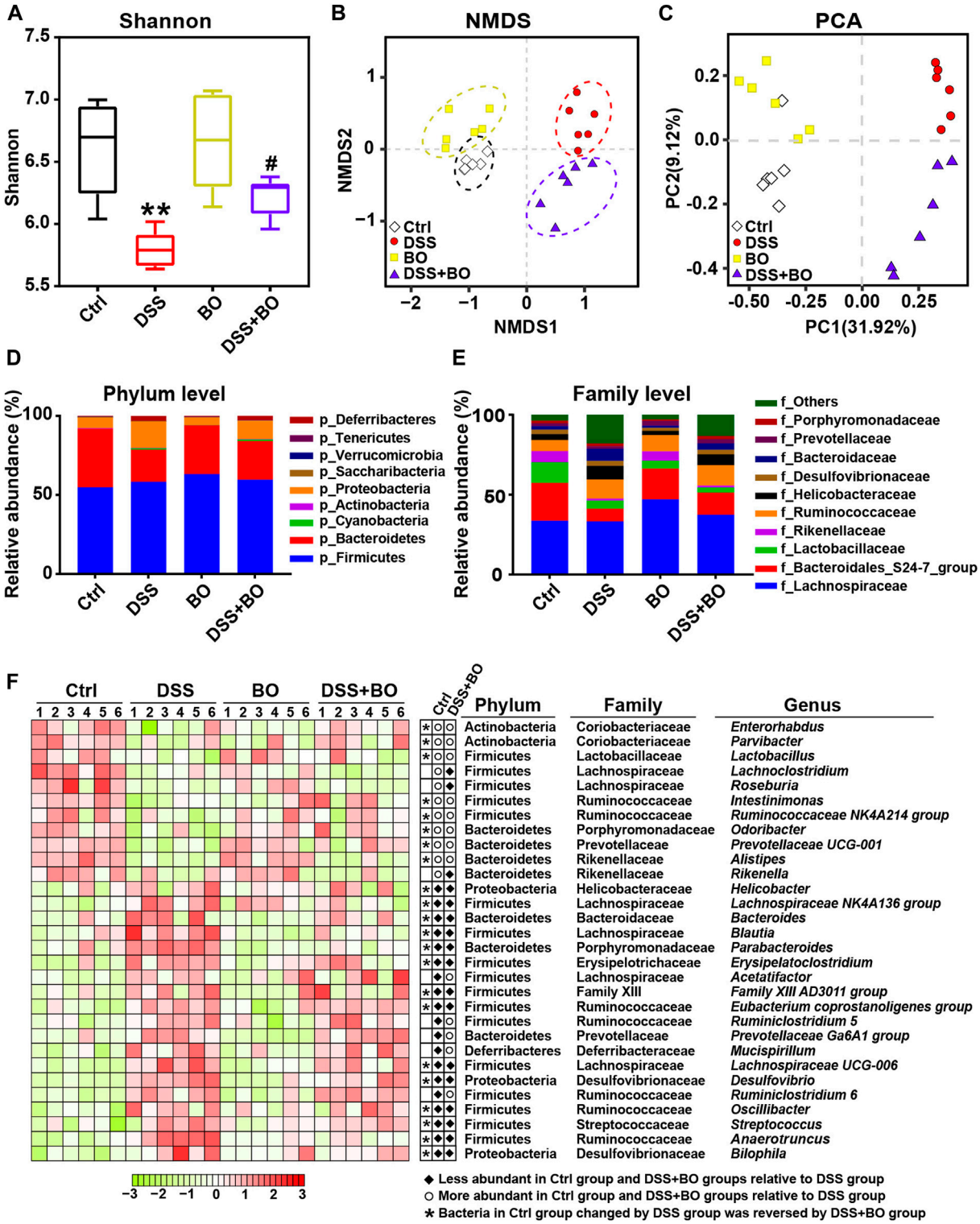

FIGURE 3 | BO alleviated gut dysbiosis in UC mice. **(A)** α-diversity assay calculated with Shannon index. **(B)** Principal component analysis (PCA). **(C)** Non-metric multidimensional scaling (NMDS). **(D)** Taxonomic profiling of gut microbiota at the phylum level. **(E)** Taxonomic profiling of gut microbiota at the family level. **(F)** Variation of 30 OTUs with the greatest changes among four experimental groups at the genus level indicated by a heatmap. Data were shown as means ± SD ($n = 6$). $^{**}p < 0.01$ vs. Ctrl group; $^{\#}p < 0.05$ vs. DSS group.

were consistent with immunohistochemical results (**Supplementary Figure S4**).

Modulation of Imbalanced Gut Microbiota in UC Mice by *Bletilla striata* Oligosaccharides

Since the occurrence of IBD is closely related to the imbalance of gut microbiota, 16S rDNA sequencing was used to investigate the role of BO in regulating gut microbiota of UC mice. The α-diversity was evaluated by the Shannon index, which was reduced in the DSS group (p <0.01, vs. Ctrl group) (**Figure 3A**), indicating severely damaged richness and diversity of gut microbiota in UC mice. After BO treatment, the reduction of α-diversity was partly restored (p <0.01, vs. Ctrl group). Principal component analysis (PCA) and nonmetric multidimensional scaling (NMDS) reflected the β-diversity of gut microbiota among groups. The result shows that four experimental groups were separated entirely into different clusters, suggesting that each group of mice had its unique intestinal bacteria communities (**Figures 3B,C**).

In our study, Firmicutes, Bacteroidetes, and Proteobacteria are the highest in the contents of gut microbiota in BALB/c mice at the phylum level. In comparison with the Ctrl group, the relative abundance of Bacteroidetes was decreased while Proteobacteria was increased in the DSS group (p < 0.05). In contrast, BO intervention effectively reversed the changes of both phyla (p < 0.05, vs. DSS group) (**Figure 3D**). At the family level, BO prevented the decrease in the populations of Rikenellaceae and Bacteroidales S24-7 group, and lowered the abundances of Helicobacteraceae and Bacteroidaceae in UC mice (p < 0.05) (**Figure 3E**). At the genus level, the abundances of 30 OTUs with the most significant changes were shown in a heatmap. Among them, most of the bacteria performed an apparent increase in UC mice like *Parabacteroides*, *Bacteroides*, *Oscillibacter*, and *Helicobacter* (p < 0.05 or 0.01, vs. Ctrl group) (**Figure 3F**; **Supplementary Figure S5**). Conversely, the contents of other bacteria in the DSS group were lower than those in the Ctrl group, such as Ruminococcaceae *NK4A214 group*, *Odoribacter*, and Prevotellaceae *UCG-001* (p < 0.05 or 0.01) (**Figure 3F**; **Supplementary Figure S5**). Notably, BO treatment remarkably suppressed the alteration of these imbalanced genera in UC mice (p < 0.05 or 0.01, vs. DSS group) (**Figure 3F**; **Supplementary Figure S5**).

Next, the Phylogenetic Investigation of Communities by Reconstruction of Unobserved States (PICRUSt) analysis was performed to assess the modulatory effect of BO on metabolic pathways of gut microbiota in UC mice. Based on 147 Keyoto Encyclopedia of Genes and Genomes (KEGG) pathways, 12 evidently changed pathways were chosen for comparisons among four experimental groups. It was suggested that five pathways were downregulated in the DSS group in comparison with those in the Ctrl group, while three pathways were upregulated (**Supplementary Figure S6A**). On the contrary, three of these altered pathways were recovered to different contents by BO treatment, including Sulfur metabolism, Selenocompound metabolism, Alanine, aspartate, and glutamate metabolism (**Supplementary Figure S6B**).

Regulatory Effect of *Bletilla striata* Oligosaccharides on Production of Intestinal Metabolites in UC Mice

The altered production of intestinal metabolites usually accompanies the changes in gut microbiota. As indicated in **Figure 4A**, the levels of CDCA and T-β-MCA were increased in UC mice (p < 0.05, vs. Ctrl group), while the productions of TCA, TCDCA, UDCA, and DCA were significantly reduced (p < 0.05, vs. Ctrl group). After BO treatment, these altered individual BAs were reversed to certain extents, but no significant difference was captured compared with the DSS group. Compared to the Ctrl group, the contents of four SCFAs in feces of UC mice were considerably reduced (p < 0.01), including acetic acid, propanoic acid, butanoic acid, and pentanoic acid. Among them, the amount of acetic acid was profoundly increased after BO administration (p < 0.05, vs. DSS group) (**Figure 4B**). Additionally, we examined tryptophan catabolites (indole and 5-HT). No significant difference of indole was detected among the four experimental groups. However, the level of 5-HT was abnormally increased in UC mice and downregulated after BO treatment (p < 0.05, vs. DSS group) (**Figure 4C**).

Correlation Between Intestinal Bacterial Abundances and UC-Related Pathological Indices

To explore the relationship between alteration of gut microbiota and UC-related pathological parameters, we calculated the Spearman's correlation coefficient between four experimental groups as indicated in **Supplementary Figure S8**. It was found that most of the changed intestinal bacteria at genus levels were positively or negatively correlated with physiochemical parameters, inflammatory responses, intestinal barrier integrity, and bacterial metabolism, suggesting the pivotal role of gut microbiota in the occurrence of UC.

Effects of *Bletilla striata* Oligosaccharides and *Bletilla striata* Oligosaccharides Fermentation Broth on DSS-Induced UC in Mice With Gut Microbiota Depletion

To confirm the significance of BO in the protection against UC, we treated mice with Abx for 4 weeks to deplete the gut microbiota (**Figure 5A**). As shown in **Supplementary Figure S7**, the quantification of intestinal bacteria by RT-qPCR proved that Abx entirely destroyed the gut microbiota of mice. In addition, compared to the DSS group, the physiological indices, inflammatory responses, and gut barrier damage were not improved or even worsened in mice from the DSS + Abx group or DSS + Abx + BO group (**Figures 5**, **6**). On the contrary, BO fermentation broth (BO FB) significantly suppressed the alteration of physiological indices in UC mice with gut microbiota depletion, such as the weight loss (**Figure 5B**), DAI scores (**Figure 5C**), spleen index (**Figure 5D**), and colon length (**Figures 5E,F**) (p < 0.01 or 0.05, vs. DSS + Abx group). Moreover, BO FB considerably reversed the upregulation of inflammatory cytokines (TNF-α and COX-2) and reduction of MUC3 in the colon

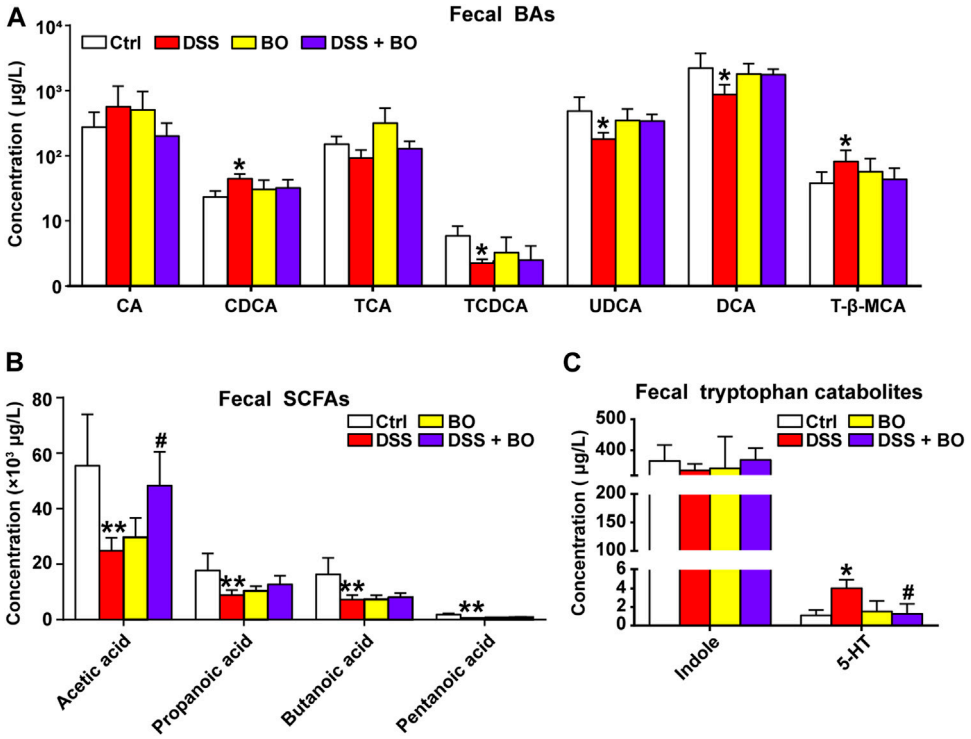

FIGURE 4 | Intervention of BO on intestinal metabolites in feces of UC mice. **(A)** Contents of individual BAs in feces. **(B,C)** Changes of SCFAs. **(B)** and tryptophan catabolites. **(C)** in feces among four experimental groups. Data were shown as mean ± SD ($n \geq 3$). $^{*}p < 0.05$, $^{**}p < 0.01$ vs. Ctrl group; $^{\#}p < 0.05$, $^{\#\#}p < 0.01$ vs. DSS group.

(**Figure 6A**), and damage to the gut barrier (**Figures 6B–D**) in gut microbiota-depleted UC mice. At the protein level, BO FB not only promoted the expression of ZO-1 and Claudin-1 but also inhibited the expression of NLRP3 and p-ERK (**Supplementary Figure S9**).

DISCUSSION

Accumulating evidence shows that the symptoms of DSS-induced UC mice were similar to those of UC patients. In the present study, UC mice were characterized by diarrhea, abdominal pain, and bloody stools, consistent with a previous report (Kim et al., 2012). However, after BO treatment, the severity of bloody stools was lessened with the reinstated colon injury and reduced spleen weight in UC mice, indicating the preventive effect of BO on the occurrence of UC (**Figures 1A–E**). Moreover, BO effectively suppressed DSS-induced damage to the intestinal tract in UC mice (**Figures 1F–H**), parallel to our previous studies, in which BO were found to avoid the destruction of gut barrier in obese mice by the regulation of gut microbiota (Hu et al., 2020).

NLRP3 inflammasome is widely distributed in epithelial and immune cells, where NLRP3 can activate the MAPK signaling pathways and further lead to the secretion of proinflammatory cytokines in UC (Zhen & Zhang, 2019). MAPKs are a group of cytoplasmic enzymes that mediate the transmission of inflammatory signals from the cell membrane to the nucleus. Upon activation, MAPKs can phosphorylate the serine/threonine amino acids of downstream intracellular proteins, which further initiate the subsequent cascade reactions (Hommes et al., 2003). In this study, BO repressed the phosphorylation of ERK and JNK (members of MAPK family) by inactivating the NLRP3 inflammasome (**Figures 2A–C**). In addition, TNF-α not only mediates the expression of IL-6 and IL-1β but also acts as a key binding site for the NF-κB pathway that is vital to the pathogenesis of UC (Sands & Kaplan, 2007). Here, the over-expressions of three cytokines were significantly inhibited by BO treatment (**Figure 2A**), suggesting that BO may improve UC by downregulating the *in vivo* inflammation. Besides, BO reduced the expressions of COX-2 and iNOS in the colon of UC mice (**Figure 2A**). COX-2 was reported to affect intestinal epithelial regeneration and induce the pro-inflammatory response initiated by TNF-α (Li et al., 2018), and iNOS directly caused intestinal damage by promoting the production of NO (Gochman et al., 2012). Both kinases are also inducers of cellular stress, indicative of a potential of BO for ameliorating oxidative injury in the development of UC.

Diarrhea is one of the most apparent symptoms of UC, and its pathogenesis may attribute to the sustained and diffuse inflammation that increases the risk of intestinal mucosal damage and finally cause the dysfunction of ion transporters and channels in intestinal epithelia (Anbazhagan et al., 2018). In this study, the mRNA levels of AQP2, AQP3, and ENaC-β were statistically increased in UC mice after BO treatment (**Figure 2D**). We presume that BO might alleviate diarrhea by strengthening the absorption of Na^{+} and water in the intestinal lumen of UC mice. On

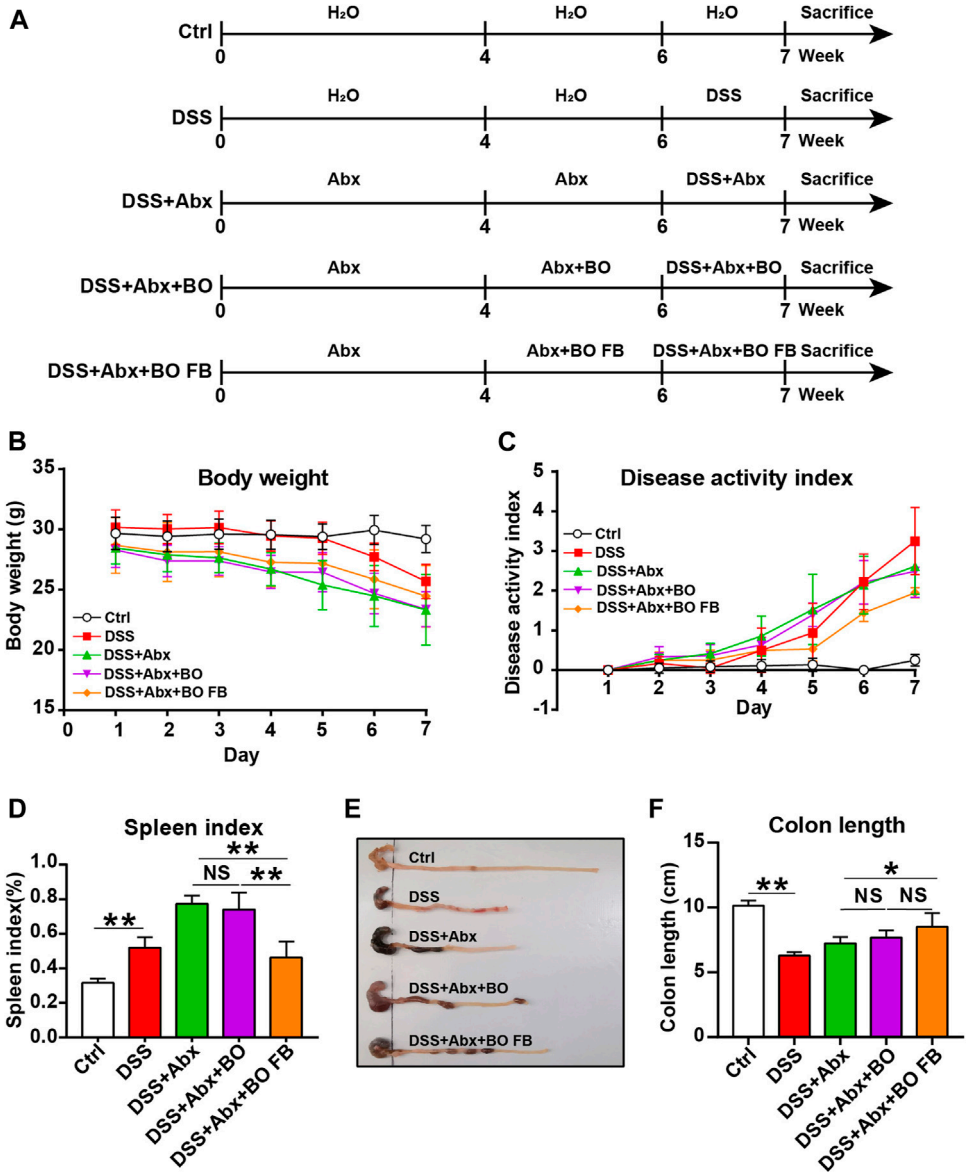

FIGURE 5 | Effect of BO and BO fermentation broth on physiological indices of UC mice with depleted gut microbiota. **(A)** BALB/c mice were treated with Abx (ampicillin, 1 mg/ml; vancomycin, 0.5 mg/ml; neomycin sulfate, 1 mg/ml; metronidazole, 0.5 mg/ml) for 4 weeks, followed by the treatment with DSS, BO, or BO fermentation broth. **(B)** Body weight. **(C)** DAI scores. **(D)** Spleen index. **(E)** Photographs of the colon. **(F)** Colon length. Data were shown as means ± SD ($n = 6$). $^{*}p < 0.05$, $^{**}p < 0.01$.

the other hand, the mucus protein secreted by goblet cells forms a mucus layer, which covers the intestinal mucosa surface and constitutes the first defense line of the gut barrier (Schoultz & Keita, 2019). In addition, the interaction of TJ proteins like Occludin, Claudin-1, and ZO-1 controls intestinal epithelial permeability under physiological state (Konig et al., 2016), while DSS administration may directly cause the loss of goblet cells and destruction of TJ proteins, ultimately resulting in the infiltration of intestinal pathogens (Landy et al., 2016). Interestingly, BO significantly increased the expression of glycoprotein mucins and TJ proteins (**Figures 2D,E**). Based on these findings, we proposed the effectiveness of BO on repairing intestinal barrier damage.

Once the intestinal mucus layer is disrupted, harmful bacteria can easily penetrate intestinal epithelia and lead to changes in gut microbial composition (Pei et al., 2019). In our study, a significant decrease in α-diversity was observed in UC mice, which meant the reduction of species diversity of intestinal flora in the occurrence of UC (**Figure 3A**). The abundance analysis of gut microbiota at phylum, family, and genus levels further revealed the variability of intestinal florae between the DSS group and the DSS + BO group (**Figures 3D–F**). *Helicobacter*, *Desulfovibrio*, and *Oscillibacter* are among these most changed genera. *Helicobacter* can induce the activation of pathogenic T cells, disrupt intestinal immune function, and finally promotes UC development (Chow et al.,

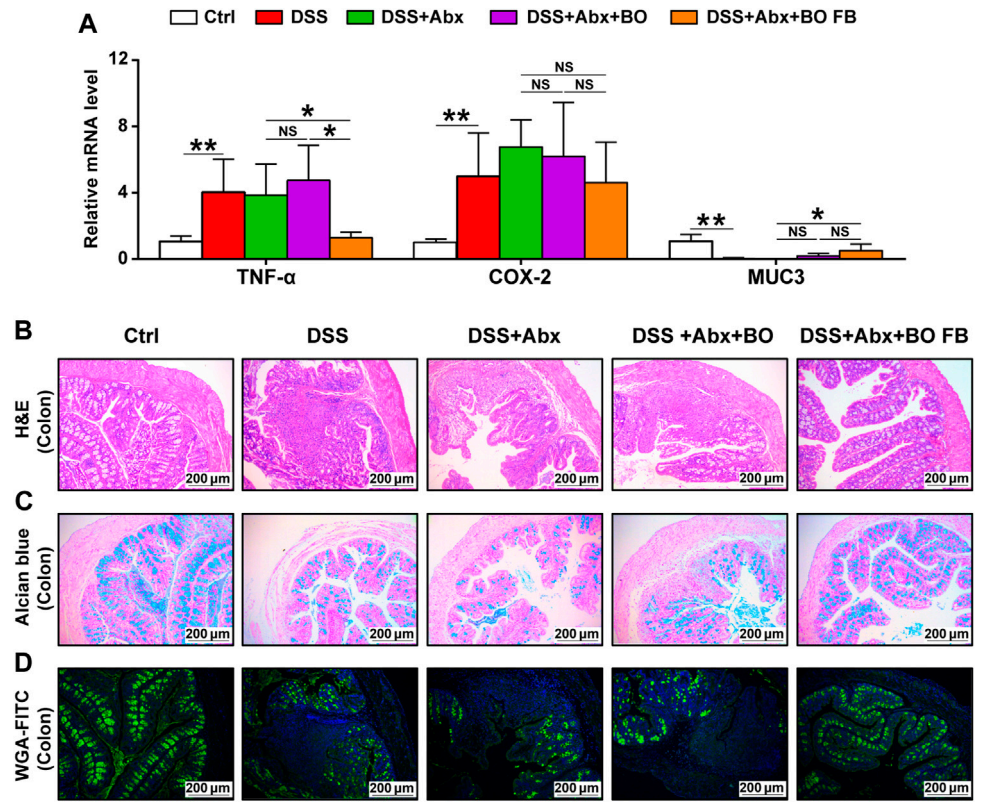

FIGURE 6 | Effect of BO and BO fermentation broth on intestinal inflammation and gut barrier damage in UC mice with depleted gut microbiota. **(A)** Expressions of TNF-α, COX-2, and MUC3 at mRNA levels. **(B)** Morphological analysis of the colon stained by Hematoxylin & eosin (H&E). Scale bar = 200 μm. **(C)** Morphological analysis of the colon stained by Alcian blue. Scale bar = 200 μm. **(D)** Morphological analysis of the colon stained by wheat germ agglutinin labeled with FITC. Scale bar = 200 μm. Data were shown as mean ± SD (n = 6). *p < 0.05, **p < 0.01.

2011; Xu et al., 2018). *Desulfovibrio* is one of the major sulfate-reducing bacteria in the intestine of humans and contributes to the generation of H_2S that is toxic to intestinal epithelia and may induce cellular apoptosis (Rowan et al., 2010). *Oscillibacter* can worsen intestinal permeability and will be obviously elevated after DSS administration (Wu et al., 2019). The abundance of this bacterial is also positively correlated with the levels of pro-inflammatory cytokines such as IL-6 and IL-1β (Wu et al., 2019). Furthermore, *Oscillibacter* was found to be relevant to the expressions of NLRP3 and TNF-α in our study (**Supplementary Figure S8**). The aberrant proliferation of these bacteria is detrimental to the intestinal structure and will exacerbate the development of UC. Expectedly, their abundances were decreased in UC mice after BO treatment (**Figure 3F**; **Supplementary Figure S5**). Further, by PICRUSt analysis, BO were found to revert the altered metabolic pathways of gut microbiota in UC mice, implicating its ability to regulate the metabolism of flora (**Supplementary Figure S6**).

Interestingly, several intestinal bacteria that metabolize BAs were also changed in UC mice, such as *Bacteroides*, *Ruminococcaceae*, and *Lactobacillus* (**Figure 3F**; **Supplementary Figure S5**). It was reported that conjugated BAs (TCA and TCDCA) could be hydrolyzed into primary BAs (CA and CDCA) by *Bacteroides* through bile salt hydrolase (BSH) in the intestine (Jia et al., 2018). Then, CA and CDCA were converted into secondary BAs (DCA and LCA) *via* the 7α dehydroxylation of *Ruminococcaceae* (Camilleri, 2015). In this study, the sequencing of gut microbiota revealed an increased *Bacteroides* and a decreased *Ruminococcaceae* in UC mice, which led to a decrement of secondary BAs (**Figure 4A**). A similar result was illustrated in recent studies (Dong et al., 2021; Gao et al., 2021; Sinha et al., 2020). For example, the lack of secondary BAs like DCA and UDCA may aggravate intestinal inflammation due to the inhibition of immune regulators. On the other hand, the decrease of beneficial bacteria *Lactobacillus* will cause the accumulation of T-β-MCA in the intestine, an antagonist of FXR, and thus interrupts the activation of intestinal FXR signaling (Li et al., 2013). In the present study, BO restored the abundance changes of *Bacteroides* and Ruminococcaceae, and partly ameliorated the disturbance of BA metabolism (**Figure 4A**), suggesting a potential modulatory effect on the production of secondary BAs in UC mice. Besides, SCFAs can provide energy to colon cells, block the NLRP3 inflammasome activation, protect the intestinal barrier integrity, and prevent the deterioration of UC (Feng et al., 2018). Here, we found that the levels of four SCFAs were statistically reduced in feces of the DSS group, accompanied by the decrease of SCFA-producing bacteria like *Odoribacter* and *Intestinimonas* (**Figure 3F**; **Supplementary Figure S5**). Conversely, BO increased the abundances of both bacteria with the high acetic acid content, which could enhance epithelia-mediated intestinal defense function (Fukuda et al., 2011). In addition, BO

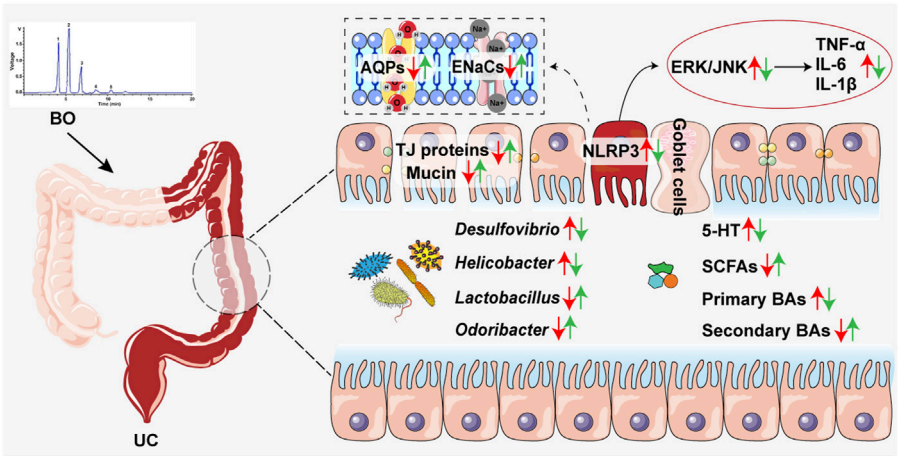

FIGURE 7 | Schematic diagram showing how BO improved UC. Red arrows, increased or decreased changes between the Ctrl group and the DSS group. Green arrows, increased or decreased changes between the DSS and the DSS + BO groups.

suppressed the production of tryptophan metabolite (5-HT) in the DSS group (**Figure 4C**). The harmful effect of 5-HT on UC was attributed to the stimulation of colonic leukocyte recruitment and overexpression of NADPH oxidase (Dong et al., 2019). By correlation analysis, these changed intestinal bacteria were further proved to be associated with the abnormality of their metabolites (**Supplementary Figure S8**). Thus, BO may prevent the development of UC by modulating the imbalance of gut microbiota and the alteration of intestinal metabolites.

It is difficult for complex carbohydrates to be absorbed in the intestinal tract, but they can be metabolized by gut microbiota as the substrates and then exert indirect biological activities. Indeed, this was confirmed in our antibiotic experiments, in which it was BO fermentation broth rather than BO that improved the physiochemical indices in UC mice with depleted gut microbiota (**Figures 5**, **6**). It points toward the necessity of gut microbiota in mediating the metabolism of BO and subsequent prevention of UC.

CONCLUSION

Taken together, this study demonstrated that BO displayed a preventive effect on UC, accompanied by the suppression of intestinal inflammation and gut barrier damage. The underlying therapeutic mechanisms were associated with inhibiting gut microbiota dysbiosis and reversing abnormal production of intestinal metabolites (**Figure 7**). Overall, our findings revealed a potential application of BO in the treatment of UC in the future.

DATA AVAILABILITY STATEMENT

The datasets presented in this study can be found in online repositories. The names of the repository/repositories and accession number(s) can be found below: National Center for Biotechnology Information (NCBI) BioProject database under accession number PRJNA787415.

ETHICS STATEMENT

The animal study was reviewed and approved by the Animal Ethical Experimentation Committee of Hubei University of Chinese Medicine and the National Act on Use of Experimental Animals (China).

AUTHOR CONTRIBUTIONS

HL and YL designed the study. TZ, BH, CY, HH, MY, ZZ, and SL were responsible for the acquisition of data. BH and YL interpreted the experimental data. TZ and HL were the major contributors in drafting and revising the manuscript. All authors read and approved the final manuscript.

FUNDING

This work was supported by Department of Science and Technology of Hubei Province (No. 2021CFA014), Major Science and Technology Project in Yunnan Province (No. 202102AE090042), Key Research and Development Plan of Ningxia Autonomous Region (No. 2021BEG02019), Health Commission of Hubei Province of China (No. ZY2021Z005), and Project of Excellent Young and Middle-aged Scientific and Technological Innovation Team in Colleges and Universities of Hubei Province (No. T2020013). The funding bodies were not involved in study design and collection, analysis and interpretation of data and writing of the manuscript.

ACKNOWLEDGMENTS

We would like to thank Allwegene Technologies Co., Ltd. for providing sequencing services and helpful discussions about sequencing and data analysis.

SUPPLEMENTARY MATERIAL

The Supplementary Material for this article can be found online at: https://www.frontiersin.org/articles/10.3389/fphar.2022.867525/full#supplementary-material

REFERENCES

Anbazhagan, A. N., Priyamvada, S., Alrefai, W. A., and Dudeja, P. K. (2018). Pathophysiology of IBD Associated Diarrhea. *Tissue Barriers* 6 (2), e1463897. doi:10.1080/21688370.2018.1463897

Camilleri, M. (2015). Bile Acid Diarrhea: Prevalence, Pathogenesis, and Therapy. *Gut Liver* 9 (3), 332–339. doi:10.5009/gnl14397

Chen, J., Lv, L., Li, Y., Ren, X., Luo, H., Gao, Y., et al. (2019). Preparation and Evaluation of Bletilla Striata Polysaccharide/graphene Oxide Composite Hemostatic Sponge. *Int. J. Biol. Macromol* 130, 827–835. doi:10.1016/j.ijbiomac.2019.02.137

Chow, J., Tang, H., and Mazmanian, S. K. (2011). Pathobionts of the Gastrointestinal Microbiota and Inflammatory Disease. *Curr. Opin. Immunol.* 23 (4), 473–480. doi:10.1016/j.coi.2011.07.010

Dong, S., Chen, M., Dai, F., Xuan, Q., Chen, P., Feng, D., et al. (2019). 5-Hydroxytryptamine (5-Ht)-Exacerbated DSS-Induced Colitis Is Associated with Elevated NADPH Oxidase Expression in the colon. *J. Cel Biochem* 120 (6), 9230–9242. doi:10.1002/jcb.28198

Dong, S., Zhu, M., Wang, K., Zhao, X., Hu, L., Jing, W., et al. (2021). Dihydromyricetin Improves DSS-Induced Colitis in Mice via Modulation of Fecal-Bacteria-Related Bile Acid Metabolism. *Pharmacol. Res.* 171, 105767. doi:10.1016/j.phrs.2021.105767

Eisenstein, M. (2018). Gut Reaction. *Nature* 563 (7730), S34–S35. doi:10.1038/d41586-018-07277-1

Feng, Y., Wang, Y., Wang, P., Huang, Y., and Wang, F. (2018). Short-Chain Fatty Acids Manifest Stimulative and Protective Effects on Intestinal Barrier Function through the Inhibition of NLRP3 Inflammasome and Autophagy. *Cell Physiol Biochem* 49 (1), 190–205. doi:10.1159/000492853

Feuerstein, J. D., Moss, A. C., and Farraye, F. A. (2019). Ulcerative Colitis. *Mayo Clin. Proc.* 94 (7), 1357–1373. doi:10.1016/j.mayocp.2019.01.018

Fukuda, S., Toh, H., Hase, K., Oshima, K., Nakanishi, Y., Yoshimura, K., et al. (2011). Bifidobacteria Can Protect from Enteropathogenic Infection through Production of Acetate. *Nature* 469 (7331), 543–547. doi:10.1038/nature09646

Gao, R. Y., Shearn, C. T., Orlicky, D. J., Battista, K. D., Alexeev, E. E., Cartwright, I. M., et al. (2021). Bile Acids Modulate Colonic MAdCAM-1 Expression in a Murine Model of Combined Cholestasis and Colitis. *Mucosal Immunol.* 14 (2), 479–490. doi:10.1038/s41385-020-00347-6

Gochman, E., Mahajna, J., Shenzer, P., Dahan, A., Blatt, A., Elyakim, R., et al. (2012). The Expression of iNOS and Nitrotyrosine in Colitis and colon Cancer in Humans. *Acta Histochem.* 114 (8), 827–835. doi:10.1016/j.acthis.2012.02.004

Goh, Y. J., and Klaenhammer, T. R. (2015). Genetic Mechanisms of Prebiotic Oligosaccharide Metabolism in Probiotic Microbes. *Annu. Rev. Food Sci. Technol.* 6, 137–156. doi:10.1146/annurev-food-022814-015706

Hommes, D. W., Peppelenbosch, M. P., and van Deventer, S. J. (2003). Mitogen Activated Protein (MAP) Kinase Signal Transduction Pathways and Novel Anti-inflammatory Targets. *Gut* 52 (1), 144–151. doi:10.1136/gut.52.1.144

Hu, B., Ye, C., Leung, E. L., Zhu, L., Hu, H., Zhang, Z., et al. (2020). Bletilla Striata Oligosaccharides Improve Metabolic Syndrome through Modulation of Gut Microbiota and Intestinal Metabolites in High Fat Diet-Fed Mice. *Pharmacol. Res.* 159, 104942. doi:10.1016/j.phrs.2020.104942

Ji, X., Yin, M., Nie, H., and Liu, Y. (2020). A Review of Isolation, Chemical Properties, and Bioactivities of Polysaccharides from Bletilla Striata. *Biomed. Res. Int.* 2020, 5391379. doi:10.1155/2020/5391379

Jia, W., Xie, G., and Jia, W. (2018). Bile Acid-Microbiota Crosstalk in Gastrointestinal Inflammation and Carcinogenesis. *Nat. Rev. Gastroenterol. Hepatol.* 15 (2), 111–128. doi:10.1038/nrgastro.2017.119

Kaplan, G. G. (2015). The Global burden of IBD: from 2015 to 2025. *Nat. Rev. Gastroenterol. Hepatol.* 12 (12), 720–727. doi:10.1038/nrgastro.2015.150

Kim, J. J., Shajib, M. S., Manocha, M. M., and Khan, W. I. (2012). Investigating Intestinal Inflammation in DSS-Induced Model of IBD. *J. Vis. Exp.* 60, 3678. doi:10.3791/3678

König, J., Wells, J., Cani, P. D., García-Ródenas, C. L., MacDonald, T., Mercenier, A., et al. (2016). Human Intestinal Barrier Function in Health and Disease. *Clin. Transl Gastroenterol.* 7 (10), e196. doi:10.1038/ctg.2016.54

Landy, J., Ronde, E., English, N., Clark, S. K., Hart, A. L., Knight, S. C., et al. (2016). Tight Junctions in Inflammatory Bowel Diseases and Inflammatory Bowel Disease Associated Colorectal Cancer. *World J. Gastroenterol.* 22 (11), 3117–3126. doi:10.3748/wjg.v22.i11.3117

Li, F., Jiang, C., Krausz, K. W., Li, Y., Albert, I., Hao, H., et al. (2013). Microbiome Remodelling Leads to Inhibition of Intestinal Farnesoid X Receptor Signalling and Decreased Obesity. *Nat. Commun.* 4, 2384. doi:10.1038/ncomms3384

Li, Y., Soendergaard, C., Bergenheim, F. H., Aronoff, D. M., Milne, G., Riis, L. B., et al. (2018). COX-2-PGE2 Signaling Impairs Intestinal Epithelial Regeneration and Associates with TNF Inhibitor Responsiveness in Ulcerative Colitis. *EBioMedicine* 36, 497–507. doi:10.1016/j.ebiom.2018.08.040

Liu, B., Li, S., Sui, X., Guo, L., Liu, X., Li, H., et al. (2018). Root Extract of Polygonum Cuspidatum Siebold & Zucc. Ameliorates DSS-Induced Ulcerative Colitis by Affecting NF-kappaB Signaling Pathway in a Mouse Model via Synergistic Effects of Polydatin, Resveratrol, and Emodin. *Front. Pharmacol.* 9, 347. doi:10.3389/fphar.2018.00347

Louis, P., Hold, G. L., and Flint, H. J. (2014). The Gut Microbiota, Bacterial Metabolites and Colorectal Cancer. *Nat. Rev. Microbiol.* 12 (10), 661–672. doi:10.1038/nrmicro3344

Luo, L., Zhou, Z., Xue, J., Wang, Y., Zhang, J., Cai, X., et al. (2018). Bletilla Striata Polysaccharide Has a Protective Effect on Intestinal Epithelial Barrier Disruption in TAA-Induced Cirrhotic Rats. *Exp. Ther. Med.* 16 (3), 1715–1722. doi:10.3892/etm.2018.6430

Murthy, S. N., Cooper, H. S., Shim, H., Shah, R. S., Ibrahim, S. A., and Sedergran, D. J. (1993). Treatment of Dextran Sulfate Sodium-Induced Murine Colitis by Intracolonic Cyclosporin. *Dig. Dis. Sci.* 38 (9), 1722–1734. doi:10.1007/BF01303184

Negroni, A., Fiaschini, N., Palone, F., Vitali, R., Colantoni, E., Laudadio, I., et al. (2020). Intestinal Inflammation Alters the Expression of Hepatic Bile Acid Receptors Causing Liver Impairment. *J. Pediatr. Gastroenterol. Nutr.* 71 (2), 189–196. doi:10.1097/MPG.0000000000002759

Pei, L. Y., Ke, Y. S., Zhao, H. H., Wang, L., Jia, C., Liu, W. Z., et al. (2019). Role of Colonic Microbiota in the Pathogenesis of Ulcerative Colitis. *BMC Gastroenterol.* 19 (1), 10. doi:10.1186/s12876-019-0930-3

Porter, R. J., Kalla, R., and Ho, G. T. (2020). Ulcerative Colitis: Recent Advances in the Understanding of Disease Pathogenesis. *F1000Res* 9, F1000. Faculty Rev-1294. doi:10.12688/f1000research.20805.1

Rowan, F., Docherty, N. G., Murphy, M., Murphy, B., Calvin Coffey, J., and O'Connell, P. R. (2010). Desulfovibrio Bacterial Species Are Increased in Ulcerative Colitis. *Dis. Colon Rectum* 53 (11), 1530–1536. doi:10.1007/DCR.0b013e3181f1e620

Sands, B. E., and Kaplan, G. G. (2007). The Role of TNFalpha in Ulcerative Colitis. *J. Clin. Pharmacol.* 47 (8), 930–941. doi:10.1177/0091270007301623

Schoultz, I., and Keita, Å. V. (2019). Cellular and Molecular Therapeutic Targets in Inflammatory Bowel Disease-Focusing on Intestinal Barrier Function. *Cells* 8 (2), 193. doi:10.3390/cells8020193

Sheehan, D., Moran, C., and Shanahan, F. (2015). The Microbiota in Inflammatory Bowel Disease. *J. Gastroenterol.* 50 (5), 495–507. doi:10.1007/s00535-015-1064-1

Sinha, S. R., Haileselassie, Y., Nguyen, L. P., Tropini, C., Wang, M., Becker, L. S., et al. (2020). Dysbiosis-Induced Secondary Bile Acid Deficiency Promotes Intestinal Inflammation. *Cell Host Microbe* 27 (4), 659–e5. e655. doi:10.1016/j.chom.2020.01.021

Sun, M., Wu, W., Liu, Z., and Cong, Y. (2017). Microbiota Metabolite Short Chain Fatty Acids, GPCR, and Inflammatory Bowel Diseases. *J. Gastroenterol.* 52 (1), 1–8. doi:10.1007/s00535-016-1242-9

Wu, M., Li, P., An, Y., Ren, J., Yan, D., Cui, J., et al. (2019). Phloretin Ameliorates Dextran Sulfate Sodium-Induced Ulcerative Colitis in Mice by Regulating the Gut Microbiota. *Pharmacol. Res.* 150, 104489. doi:10.1016/j.phrs.2019.104489

Xu, D., Pan, Y., and Chen, J. (2019). Chemical Constituents, Pharmacologic Properties, and Clinical Applications of Bletilla Striata. *Front. Pharmacol.* 10, 1168. doi:10.3389/fphar.2019.01168

Xu, M., Pokrovskii, M., Ding, Y., Yi, R., Au, C., Harrison, O. J., et al. (2018). c-MAF-dependent Regulatory T Cells Mediate Immunological Tolerance to a Gut Pathobiont. *Nature* 554 (7692), 373–377. doi:10.1038/nature25500

Xu, Z., Chen, W., Deng, Q., Huang, Q., Wang, X., Yang, C., et al. (2020). Flaxseed Oligosaccharides Alleviate DSS-Induced Colitis through Modulation of Gut Microbiota and Repair of the Intestinal Barrier in Mice. *Food Funct.* 11 (9), 8077–8088. doi:10.1039/d0fo01105c

Zhang, C., He, Y., Chen, Z., Shi, J., Qu, Y., and Zhang, J. (2019). Effect of Polysaccharides from Bletilla Striata on the Healing of Dermal Wounds in Mice. *Evid. Based Complement. Alternat Med.* 2019, 9212314. doi:10.1155/2019/9212314

Zhang, S. L., Wang, S. N., and Miao, C. Y. (2017). Influence of Microbiota on Intestinal Immune System in Ulcerative Colitis and its Intervention. *Front. Immunol.* 8, 1674. doi:10.3389/fimmu.2017.01674

Zhen, Y., and Zhang, H. (2019). NLRP3 Inflammasome and Inflammatory Bowel Disease. *Front. Immunol.* 10, 276. doi:10.3389/fimmu.2019.00276

Zheng, J., Ye, C., Hu, B., Yang, H., Yao, Q., Ma, J., et al. (2021). Bile Acid Profiles in Bile and Feces of Obese Mice by a High-Performance Liquid Chromatography-Tandem Mass Spectrometry. *Biotechnol. Appl. Biochem.* 68 (6), 1332–1341. doi:10.1002/bab.2055

Zhou, C., Li, L., Li, T., Sun, L., Yin, J., Guan, H., et al. (2020). SCFAs Induce Autophagy in Intestinal Epithelial Cells and Relieve Colitis by Stabilizing HIF-1α. *J. Mol. Med. (Berl)* 98 (8), 1189–1202. doi:10.1007/s00109-020-01947-2

Conflict of Interest: The authors declare that the research was conducted in the absence of any commercial or financial relationships that could be construed as a potential conflict of interest.

Publisher's Note: All claims expressed in this article are solely those of the authors and do not necessarily represent those of their affiliated organizations, or those of the publisher, the editors and the reviewers. Any product that may be evaluated in this article, or claim that may be made by its manufacturer, is not guaranteed or endorsed by the publisher.

GLOSSARY

5-HT 5-hydroxytryptamine

Abx antibiotic mixtures

AQP aquaporin

BAs bile acids

BO *Bletilla striata* oligosaccharide

BP *Bletilla striata* polysaccharide

CA cholic acid

CDCA chenodeoxycholic acid

COX-2 cyclooxygenase-2

DAI disease activity index

DCA deoxycholic acid

DSS dextran sulfate sodium

ENaC epithelial sodium channel

ERK1/2 extracellular regulated kinase 1/2

IBD inflammatory bowel disease

IL interleukin

iNOS inducible nitric oxide synthase

JNK c-Jun N-terminal kinase

LC/GC-MS liquid chromatography/gas chromatography-mass spectrometer

Lcn2 Lipocalin-2

MMP-9 matrix metalloproteinase-9

MUC mucin

NLRP3 NOD-like receptor pyrin domain containing 3

SCFAs Short-chain fatty acids

TCA taurocholic acid

TCDCA taurochenodeoxycholic acid

TNF-α tumor necrosis factor-α

T-β-MCA tauro-β-murocholic acid

UC ulcerative colitis

UDCA ursodeoxycholic acid

ZO-1 zonula occludens-1

frontiers | Frontiers in Pharmacology

ORIGINAL RESEARCH
published: 23 June 2022
doi: 10.3389/fphar.2022.908227

The Effect of Triptolide Combined With Crocin on Arthritis in Mice: From Side Effect Attenuation to Therapy

Min Yan[1†], Yinyin Yan[1,2†], Zhenqiang Zhang[1], Guoqiang Wang[1], Wenbo Shi[1,2], Mengyuan Jiang[1], Junwei Zhao[3], Xiangxiang Wu[1]* and Huahui Zeng[1,2]**

[1]Academy of Chinese Medicine Sciences, Henan University of Chinese Medicine, Zhengzhou, China, [2]School of Medicine, Henan University of Chinese Medicine, Zhengzhou, China, [3]Department of Clinical Laboratory, Core Unit of National Clinical Research Center for Laboratory Medicine, The First Affiliated Hospital of Zhengzhou University, Zhengzhou, China

Clinical use of triptolide (TP) is restricted due to severe toxicity. This study assessed the protective effect of crocin (CR) as a natural antioxidant against TP-induced toxicity in bovine collagen type II-induced arthritis (CIA) in mice. The mice in the CIA model group showed macroscopic signs of severe arthritis. The anti-arthritis effects in the control, TP + CR, and TP groups were evaluated through assessment of foot volume, arthritis score, and proinflammatory cytokines, and collagen antibody assay. Crocin reduced TP-induced toxicity, as evidenced by evaluation of survival rate, body weight, visceral index, hepatic and renal functions, histopathologic analyses, and antioxidant enzyme activities. Transcriptome sequencing resulted in identification of 76 differentially expressed genes (DEGs) associated with hepatotoxicity between the TP and TP + CR groups. Of these, Three DEGs (Cyp1a2,Gsta4, and Gstp1) were validated using quantitative real-time PCR analysis. In conclusion, CR protected CIA mice from TP-induced toxicity through modulation of the cytochrome P450 and glutathione metabolism pathways.

Keywords: triptolide, crocin, compatibility, toxicity, arthritis

OPEN ACCESS

Edited by:
Qi Wang,
Harbin Medical University, China

Reviewed by:
Amany Mohammed Gad,
Sinai University, Egypt
Quan Xia,
First Affiliated Hospital of Anhui Medical University, China

****Correspondence:***
Junwei Zhao
junweizhao@alumni.sjtu.edu.cn
Xiangxiang Wu
wuxx-415@126.com
Huahui Zeng
hhzeng@hactcm.edu.cn

[†]These authors have contributed equally to this work

Specialty section:
This article was submitted to Ethnopharmacology, a section of the journal Frontiers in Pharmacology

Received: *30 March 2022*
Accepted: *01 June 2022*
Published: *23 June 2022*

Citation:
Yan M, Yan Y, Zhang Z, Wang G, Shi W, Jiang M, Zhao J, Wu X and Zeng H (2022) The Effect of Triptolide Combined With Crocin on Arthritis in Mice: From Side Effect Attenuation to Therapy. Front. Pharmacol. 13:908227. doi: 10.3389/fphar.2022.908227

1 INTRODUCTION

Triptolide (TP), the most studied bioactive chemical monomer of the Chinese herb Tripterygium wilfordii Hook. F., is a highly potent and effective anti-inflammatory, immunosuppressive, anti-rheumatoid, and anticancer agent (Tian et al., 2021; Tong et al., 2021; Zhang et al., 2021; Zhao et al., 2021).

Rheumatoid arthritis (RA) is a typical autoimmune disease often with symmetric facet joint disease, characterized by synovial hyperplasia, cartilage damages, and bone erosion. The collagen type II-induced arthritis (CIA) animal model (Trentham et al., 1977), is the most commonly studied model of RA (Zhao et al., 2022). In this model, antibodies against type II collagen play a crucial role for arthritis pathology (Yabe et al., 2021). The CIA model shares many pathological and histological similarities with RA, such as synovial hyperplasia, cartilage degradation and overproduction of inflammatory cytokines (Brand et al., 2007; Liang et al., 2018).

The Chinese herb Tripterygium wilfordii Hook. F. and its extracts have been used as an anti-rheumatic in China for many years (Qin, 2019). However, TP is highly toxic, suffers from poor aqueous solubility, and induces significant adverse effects, which limits its clinical use. Therefore, there is an urgent need to reduce TP-related toxicity without affecting therapeutic potency. Many strategies have been explored, including new dosage forms, structural modifications, and

combination with other Chinese herbs (e.g., TP combined with chlorogenic acid or glycyrrhizic acid (GA)) (Tan et al., 2018; Wang et al., 2018; Zeng et al., 2020; Zhang et al., 2020; Yalikong et al., 2021).

Modern pharmacological studies of saffron and its main constituents have revealed a wide spectrum of biological activities (i.e., anti-inflammatory, antinociceptive, antioxidant, immunoregulatory effects, neurodegenerative diseases, cardiovascular diseases, anticancer, anti-arthritic effects and protection against natural and chemical toxins) (Attia et al., 2021; Xing et al., 2021). Crocin, mono, and diglycosyl esters of a polyene dicarboxylic acid are some of the main active components that are responsible for the pharmacological effects of saffron (Abdi et al., 2022; Salem et al., 2022; Xu et al., 2022).

Crocin (CR) is thought to protect against toxicity of viscera induced by some materials (El-Beshbishy et al., 2012; Razavi and Hosseinzadeh, 2015). In addition, pharmacokinetic studies have shown that crocin is not bioavailable after oral administration in blood circulation. Instead, it is rapidly transformed into crocetin in the gastrointestinal tract with high relative bioavailability (Zhang et al., 2017; Hosseini et al., 2018). However, there have been no studies to evaluate combination treatment with CR and TP as this treatment strategy may potentially reduce TP-related toxicity without impacting therapeutic efficacy. Therefore, this study focused on the mechanisms by which crocin mitigates TP-induced toxicity in a mouse bovine collagen type II-induced arthritis model.

2 MATERIALS AND METHODS

2.1 Drugs, Reagents, and Animals

Triptolide (purity >98%) was purchased from Xi'an Haoxuan Biotechnology Co. Ltd. (Shanxi, China). Crocin (purity >98%) was obtained from TCI Chemical Industry (Shanghai, China). Glycyrrhizic acid (GA, purity 95%) was purchased from Cool Chemistry (Beijing, China).

Bovine type II collagen (2 mg/ml), Mouse Anti-Type II Collagen IgG Antibody ELISA Kits, complete Freund's adjuvant (CFA, 4 mg/ml), and incomplete Freund's adjuvant (IFA, 5 ml) were purchased from Condrex ((Norcross, GA, United States). BeyoRT™ III First Strand cDNA Synthesis Kit (Cat No. D7178M, Shanghai Biyuntian Biotechnology Co., Ltd., Shanghai, China), PowerUp™ SYBR™ Green Master Mix (Cat No. A25742, Thermo Fisher Scientific, United States), and kits for analysis of creatinine (CRE, Cat No. C011-2-1), blood urea nitrogen (BUN, Cat No. C013-1-1), alanine/aspartate transaminase (ALT/AST, Cat No. C009-2-1/C010-2-1), superoxide dismutase (SOD, Cat No. A001-1), malondialdehyde (MDA, Cat No. A003-1), catalase (CAT, Cat No. A007-2-1) and glutathione (GSH, Cat No. A006-2-1) were purchased from Nanjing Jiancheng Bioengineering Institute (Nanjing, China). Other chemicals and reagents used were of analytical grade.

Kunming (KM) mice (male, 7–8 weeks old, 20 ± 2 g) were purchased from Huaxing Laboratory Animal Farm (Zhengzhou, China) [License No: SCXK (Yu) 20190002]. Prior to experiments, all animals were acclimated to the experimental environment for 7 days and housed in a controlled environment (25 ± 1°C, humidity of 55 ± 5%) with a 12-h light/dark cycle. The mice were allowed free access to standard diet and water during the acclimation period. The experiments performed in this study were approved by the Animal Ethics Committee In Henan University of Chinese Medicine.

2.2 Collagen-Induced Arthritis Model and Grouping

The collagen-induced arthritis (CIA) model was established using bovine type II collagen, and the clinical severity of arthritis was scored as previously described [6]. Foot volume was measured using a volume-plethysmograph (PV-200, TECHMAN,Co. Ltd., Chengdu, China). The arthritis score (or deformation index) was used to describe the shape and joint swelling of the paws of CIA mice. Total scores for each mouse greater than eight were considered successful CIA models, and all mice in the control group had arthritis index scores of 0. A schematic for the animal modeling, mode of drug administration, and subsequent procedures is shown in **Figure 1**. After successful modeling, the mice were randomly divided into seven groups (n = 8) as follows:

A. normal saline (Control);
B. Collagen-induced arthritis model group (CIA);
C. 300 μg/kg TP treatment group (TP);
D. 300 μg/kg TP+50 mg/kg CR group (TP + LCR);
E. 300 μg/kg TP+100 mg/kg CR group (TP + MCR);
F. 300 μg/kg TP+200 mg/kg CR group (TP + HCR);
G. 300 μg/kg TP+50 mg/kg GA (TP + GA) as the positive drug control group (Yang et al., 2017).

A stock solution of TP was prepared in DMSO at 5 mg/ml, then diluted in saline to prepare the working solution. Doses and frequency of administration were determined during prior experiments. The animals were administered the indicated experimental treatments once every 2 days by oral gavage for 20 days (0.2 ml/10 g).

2.3 Drug Treatment Toxicity and Efficacy

Body weight, paw volume, and arthritis score were recorded during drug administration. Twenty-4 hours after the last drug treatment, the whole blood of each mouse was obtained via orbital collection. Serum was obtained by centrifugation (4°C, 3,000 rpm, 10 min). The serum levels of AST/ALT and BUN/CRE were quantified using specific commercial diagnostic kits. The levels of serum inflammatory cytokines (IL-1β, IL-6, and TNF-α) and mouse anti-type II collagen IgG were detected using ELISA kits according to the manufacturer's instructions. The mice were sacrificed and the ankle joints were fixed in 10% formalin, decalcified, paraffin-embedded, and stained with hematoxylin and eosin (H&E).

2.4 *In Vivo* Drug Toxicity Study

To determine the mechanism by which CR protected against TP-induced toxicity, healthy mice were treated with TP + CR. The

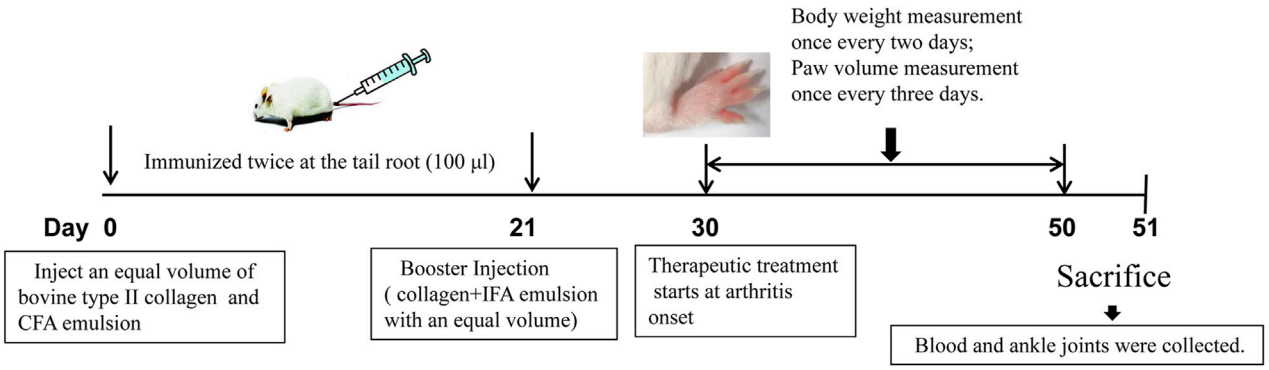

FIGURE 1 | Schematic representation of CIA mouse model generation and treatment with TP or TP + CR. TP: triptolide; CR: crocin; CIA: collagen-induced arthritis.

mice were randomly placed in the following seven groups (n = 10): A. Control (normal saline, NS); B. Low-dose TP (LTP, 100 μg/kg); C. Moderate-dose TP (MTP, 300 μg/kg); D. High-dose TP (HTP, 500 μg/kg); E. 100 μg/kg TP+100 mg/kg CR (LTP + CR); F. 300 μg/kg TP+100 mg/kg CR (MTP + CR); G. 500 μg/kg TP+100 mg/kg CR (HTP + CR). The mice were administrated the treatments daily via oral gavage for 7 days at a volume of 0.2 ml/10 g per dose. The mice were observed daily for 7 days to monitor body weight and mortality.

The mice were sacrificed and the organs (hearts, livers, spleens, lungs, kidneys, testes, stomach, and intestine) from each group were quickly harvested and washed with pre-cooled 0.9% saline solution to remove the blood. The visceral index was calculated as the ratio of visceral weight to body weight Using the following formula: Visceral index (%) = (viscera weight/body weight) × 100%. Hepatic and renal functional markers (AST/ALT and BUN/CRE) were measured as described in **Section 2.3**.

A portion of each sample was snap-frozen in liquid nitrogen and stored at −80°C for biochemical analysis. Portions of tissues were fixed in 10% formalin for hematoxylin and eosin (H&E) staining and visualized using a light microscope. Body weight, visceral index, histopathology, hematology, and biochemistry factors were investigated as part of the systemic toxicity evaluation.

2.5 Determination of Antioxidant Enzyme Activities

The livers were homogenized in cold saline and centrifuged at 12,000 rpm for 20 min at 4°C. The suspensions were used to assay SOD and CAT activities, and MDA and GSH levels using commercial detection kits according to the manufacturer's instructions.

2.6 Transcriptome Sequencing (mRNA-Seq)

Liver tissues were selected from the Control, MTP, and MTP + CR groups for transcriptome studies. Library construction, mRNA-seq, and bioinformatic analysis were performed by Sinotech Genomics Co., Ltd. (Shanghai, China). The general workflow was as follows: RNA extraction and detection; mRNA enrichment and reverse transcription; cDNA purification, end repair, A-tailing, and sequencing adapters; and PCR enrichment and library construction. An Illumina NovaSeq 6000 (Illumina, United States) was used for RNA sequencing according to a previous study (Fu, Y. et al., 2020). The original data (raw reads) was trimmed to filter out unqualified sequences, then clean reads were mapped to the reference genome using Hisat2 (Hierarchical Indexing for Spliced Alignment of Transcripts, version 2.0.5). Gene abundance was expressed as fragments per kilobase of exon per million reads mapped (FPKM). Stringtie software was used to count the fragments within each gene, and the TMM algorithm was used for normalization. Differential expression analysis for mRNA was performed using R package edgeR. Differentially expressed RNAs with fold change values >1.5 and q values <0.05 were retained for further analysis, as these were considered as significantly modulated. The raw data are available under GEO: GSE202175.

2.7 Identification of Hepatotoxicity Targets

DisGeNet (http://www.disgenet.org/) and GeneCards (https://www.genecards.org/) were used to combine the relevant literature to generate a pool of hepatotoxicity targets with the keywords "hepatotoxicity or liver injury." In the DisGeNet database, genes with EI ≥ 1 were selected. In the GeneCards database, genes with relevance scores ≥10 were selected. Finally, the combined targets were transferred from "*Homo sapiens*" to "*Mus musculus*" (https://string-db.org/).

2.8 Gene Ontology and Pathway Enrichment Analysis

Hepatotoxicity targets, differentially expressed mRNAs between the MTP group and the Control group, and differentially expressed mRNAs between the MTP + CR group and the MTP group were analyzed using a Venn diagram (http://bioinformatics.psb.ugent.be/webtools/Venn/). The intersecting genes in the Venn diagram were further investigated at the functional level. Gene Ontology (GO) analysis for biological processes, cellular components, and molecular function and KEGG (Kyoto Encyclopedia of

TABLE 1 | Primer sequences for qRT-PCR.

Gene Name	Sequence (5'→3')	Size (Bp)	NCBI GeneID
GSTP1	Forward ATGCCACCATACACCATTGTC Reverse GGGAGCTGCCCATACAGAC	161	14870
GSTA4	Forward TGATTGCCGTGGCTCCATTTA Reverse CAACGAGAAAAGCCTCTCCGT	135	14860
CYP1A2	Forward AGTACATCTCCTTAGCCCCAG Reverse GGTCCGGGTGGATTCTTCAG	118	13077
GAPDH	Forward AGGTCGGTGTGAACGGATTTG Reverse TGTAGACCATGTAGTTGAGGTCA	123	14433

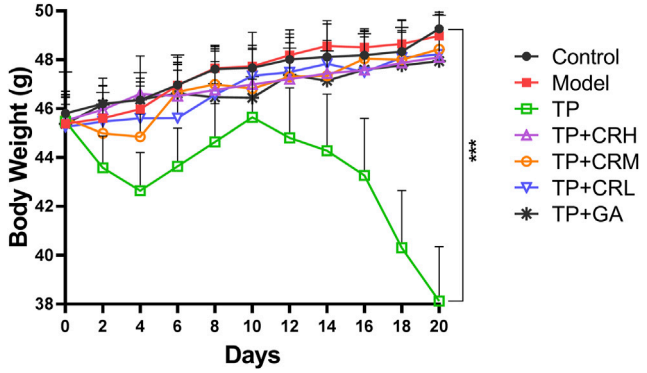

FIGURE 2 | Body weight changes during 20 days of treatment. (n = 8) ***$p < 0.001$ vs Control.

Genes and Genomes) pathway analysis were performed using STRING database. The background species was defined as "*Mus musculus*."

2.9 Quantitative Real-Time PCR Analysis (qRT-PCR)

The relative levels of important differentially expressed genes (DEGs) identified in mRNA seq and KEGG analyses were selected for validation using qRT-PCR. Total RNA extracted from liver tissue using Trizol reagent (Invitrogen) for mRNA-seq was used for qRT-PCR. Total RNA was converted to cDNA according to the reverse transcription kit protocol. Then, PCR amplification was performed using SYBR green PCR master mix on an ABI 7500 FAST instrument. The primers for qRT-PCR are listed in **Table 1**. Glyceraldehyde-3-phosphate dehydrogenase (GAPDH) was used as the internal reference gene. The $2^{-\triangle\triangle CT}$ method was used to calculate the relative expression levels of the verified genes.

2.10 Statistical Analysis

All data were processed using GraphPad Prism7 software and presented as the mean ± standard deviation ($\bar{x}$ ±S). Statistical significance ($p < 0.05$, $p < 0.01$, or $p < 0.001$) was using Student's *t*-test or one way ANOVA.

3 RESULTS

3.1 Assessment of Drug Side Effects in Mice With Collagen-Induced Arthritis

The side effects of the administered drugs on CIA mice were evaluated for 20 days after drug administrations. The parameters measured were changes in body weight, and hepatic and renal functions. The TP group showed obvious weight reduction compared to the other groups ($p < 0.001$), while other groups did not significantly differ from the control group (**Figure 2**). TP induced weight loss was significantly reversed by CR or GA combined treatment with TP. Compared with the control group, blood serum analysis demonstrated that the levels of AST, ALT, and BUN were significantly elevated in the TP group ($p < 0.01$). In contrast, co-administration of TP with CR or GA mitigated the changes observed in the TP group (**Figure 3**).

3.2 Evaluation of Therapeutic Effects in the CIA Model

Collagen-induced arthritis model mice were used to evaluate the therapeutic efficacy of TP + CR. Changes in foot volume and arthritis scores were evaluated every 3 days during drug treatment (**Figure 4A,B**). The foot volume and arthritis scores in the treatment groups were significantly lower than those in the model group at day 18 post-treatment (**Figure 4 a,b**).

Levels of TNF-α, IL-1β, IL-6, and anti-type II collagen antibody in serum were quantitated using ELISA (**Figure 5**). The level of TNF-α in the serum of the model group was significantly higher than that in the control group ($p < 0.05$), and levels of IL-1β and IL-6 were increased, but the increases were not statistically significant. The three proinflammatory cytokines measured were reduced to different degrees in each treatment group compared with those in the model group. Anti-type II bovine collagen antibody was not detected in the control group, and was significantly increased in the model group ($p < 0.001$). The levels of collagen antibody were lower in each administration group compared with those in the model group ($p < 0.001$).

Mice in the CIA group showed macroscopic signs of severe arthritis such as deformity, swelling, and redness in the hind paw and ankle joints (**Figure 6B**). Foot swelling was significantly reduced in each treatment group compared with that in the Model group (**Figure 6C–G**). As shown in **Figures 6a,b**, the histological tissue sections showed that the surfaces of the ankle joints in the control

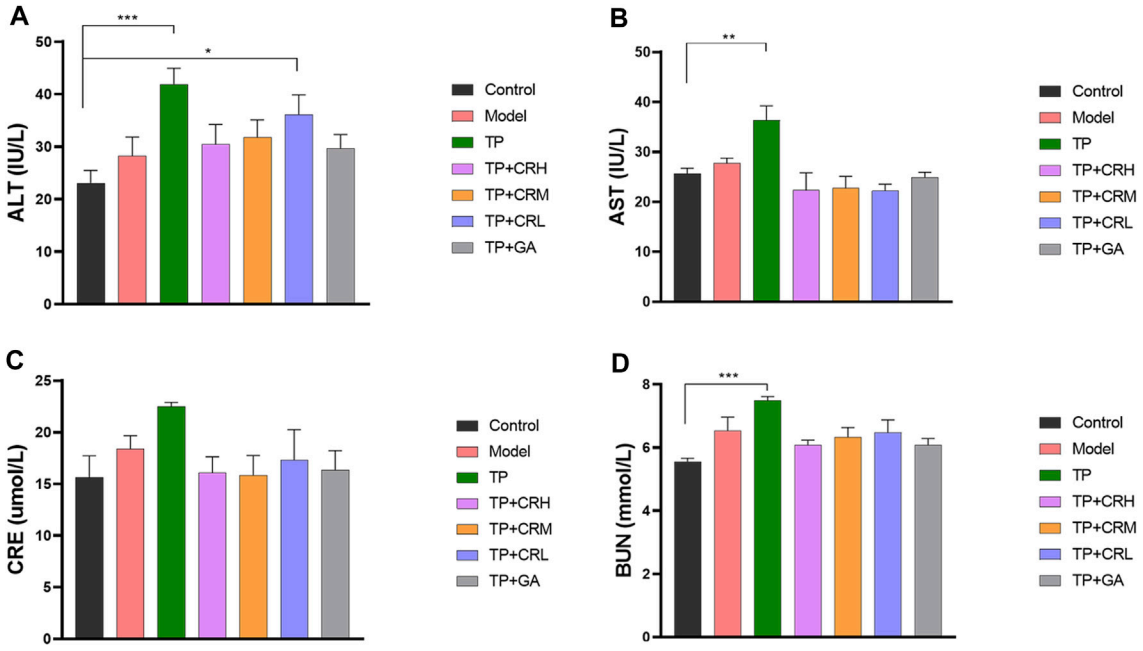

FIGURE 3 | The levels of ALT **(A)**, AST **(B)**, CRE **(C)**, BUN **(D)** in the CIA mice liver were determined using respective kits, after 20 days of different treatment. (n = 8) $^{**}p < 0.01$,$^{***}p < 0.001$ vs. Control. ALT, alanine transaminase; AST, aspartate transaminase; CRE, creatinine; BUN, blood urea nitrogen; CIA, collagen-induced arthritis.

group had normal morphology and smooth articular cartilage. In contrast, structural damage and edema of the ankle joint, synovial hyperplasia, and joint cavitation were observed in the CIA model group. The treatment groups showed differing degrees of improvement compared with the Model group (**Figure 6C–G**). In particular, the TP + CRH and TP + GA groups showed normal morphology similar to that in the Control group.

3.3 Evaluation of Toxicity of TP + CR in Normal Kunming Mice

Survival rates and body weights were evaluated 7 days after treatment administration (**Figure 7**). The HTP and HTP + CR groups were the only groups in which mice died. The survival rate in the HTP + CR group was significantly higher than that in the HTP group. Body weight was lower on the seventh day in all but the LTP + CR and MTP + CR groups compared with that in the control group. Treatment with MTP or HTP induced significant weight loss. Furthermore, the MTP and HTP groups showed significantly lower organ coefficients ($p < 0.05$), while the other groups did not significantly differ from the control group (**Table 2**). The weight indices of multiple organs appeared normal following co-administration of TP and CR. In addition, biochemical analysis was performed to evaluate drug-induced hepatic and renal damage. As shown in **Table 3**, the serum ALT/AST and BUN/CRE levels were significantly elevated following TP administration compared with those in the control and the co-administration groups. Co-administration of TP and CR group did not induce changes in serum ALT/AST or BUN/CRE compared to the control group. These results showed that administration of CR significantly mitigated TP-induced changes in hepatic and renal functions.

3.4 Crocin Alleviates Damage of Histological Structure Induced by TP Toxicity

We performed histopathological analyses of H&E-stained tissue sections from hearts, livers, spleens, lungs, kidneys, testes, stomach, and intestines. As shown in **Figure 8** and **Table 4**, tissue injury was significantly reduced in the TP + CR group.

3.5 Determination of Antioxidant Enzyme Activities

As shown in **Figure 9**, the activities of hepatic CAT and SOD, and the levels of GSH and MDA, were measured in each group. Hepatic SOD and CAT activities, and GSH content, decreased in a TP dose-dependent manner ($p < 0.01$). There were no significant differences between the TP + CR group and the control groups. Moreover, MDA content was higher in the MTP and HTP groups than in the control group ($p < 0.05$). However, there was no significant difference in MDA content in the liver between the TP + CR group and the control group.

3.6 Differentially Expressed mRNAs and KEGG Analysis

Expression profiling studies were performed on the RNAs from four independent liver tissue samples in each group. The volcano

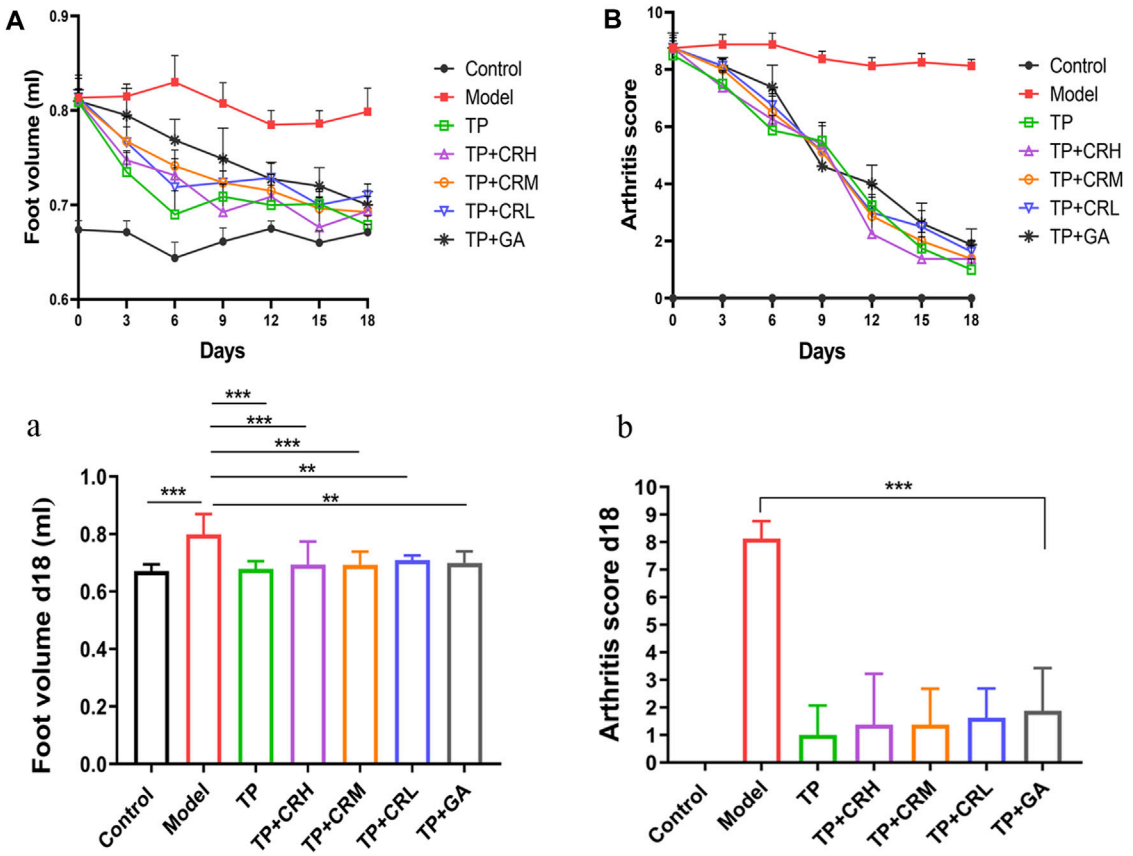

FIGURE 4 | Changes in arthritic foot volume (**(A)**/a) and arthritis scores (**(B)**/b) in the CIA mice through the administration course (n = 8). $^{**}p < 0.01$, $^{***}p < 0.001$ vs Control. CIA: collagen-induced arthritis.

plot of differentially expressed mRNAs among three groups is shown in **Figure 10**.

Compared with the Control group, 1,148 mRNAs were identified to be differently expressed in the MTP groups. Furthermore, 1,526 mRNAs were differentially expressed in the MTP + CR group compared with the MTP group (**Figure 11A**). There were 76 differentially expressed mRNAs identified in the MTP group compared with Control group as well as in the MTP + CR group compared with MTP group, which were also associated with hepatotoxicity. Kyoto Encyclopedia of Genes and Genomes analysis showed that the differentially expressed mRNAs related to hepatotoxicity were mainly enriched in the complement and coagulation cascades, p53 signaling pathway, glutathione metabolism, IL-17 signaling pathway, and drug metabolism-cytochrome P450 (**Figure 11B**).

3.7 Validation of RNA-Seq Results Using qRT-PCR

Expression of mRNA was restricted to FPKM > 20, which resulted in selection of 23 DEGs. Analysis of the expression trends of the top 23 DEGs (**Figure 12**) resulted in selection of Cyp1a2, Gstp1, and Gsta4, which were related to drug metabolism-cytochrome P450 and glutathione metabolism, for further qRT-PCR verification. As shown in **Figure 13**, Cyp1a2, Gsta4, and Gstp1 expression levels were decreased in the MTP group, and these decreases were mitigated in the MTP + CR group.

4 DISCUSSION

The therapeutic window for TP is very narrow, resulting in sometimes overlapping therapeutic and toxic ranges. Therefore, identification of methods to attenuate toxicity without impacting efficacy is of great importance.

Previous studies showed that crocin has a considerable anti-inflammatory and antioxidant potency (Li et al., 2018; Korani et al., 2019; Yaribeygi et al., 2021). In addition, combined treatment with GA and TP increase efficacy while decreasing toxicity in RA treatment (Tai et al., 2014). Therefore, in this study, we explored the ability of the novel treatment combination of TP + CR to treat arthritis with reduced TP-induced toxicity using GA combined with TP as the positive control. As a result, the anti-arthritis effects in the TP + CR group were equivalent to those in the TP and TP + GA groups, as determined by evaluation of foot volume and arthritis score, proinflammatory cytokine levels, and collagen antibody assay.

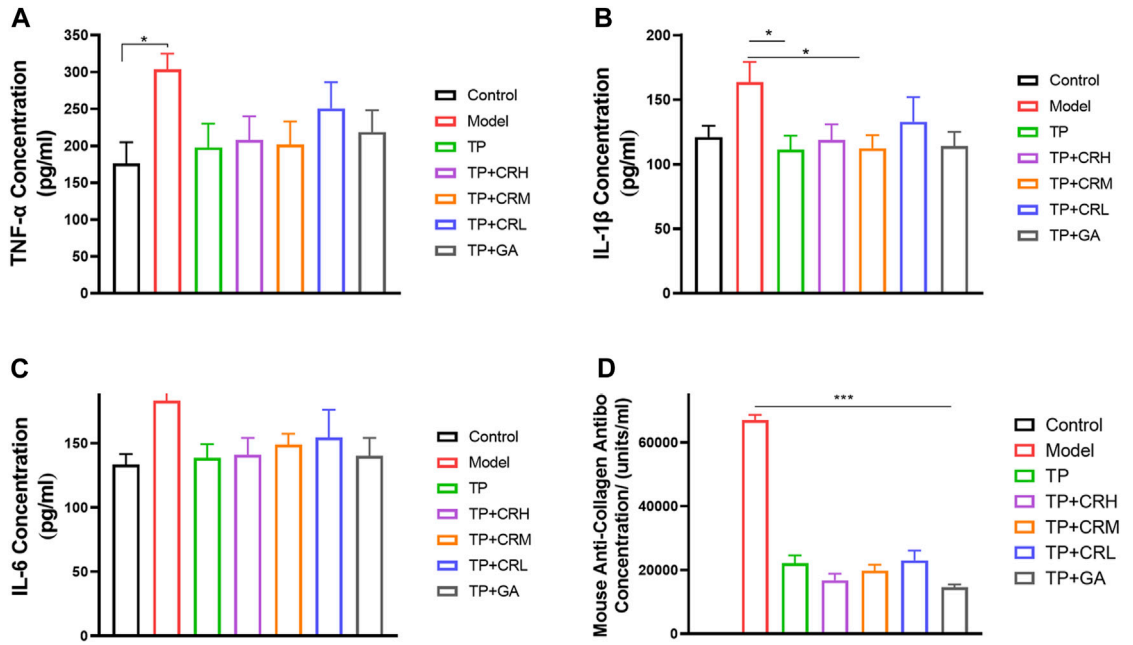

FIGURE 5 | Quantitation of proinflammatory cytokines **(A)** TNF-α; **(B)** IL-1β; **(C)** IL-6 and anti-type II collagen antibody **(D)** in serum of each group using ELISA. (n = 6).

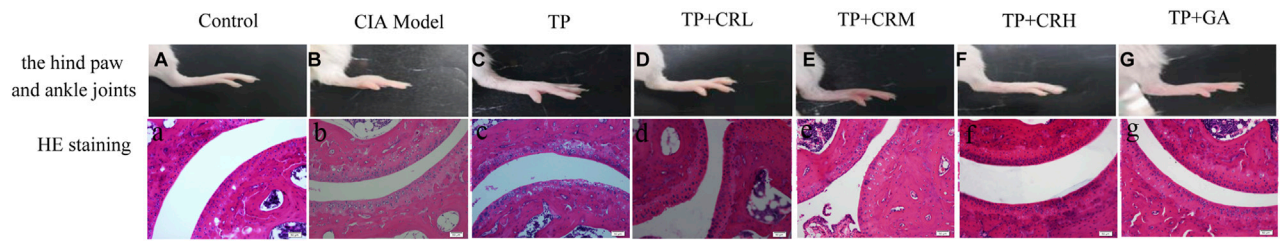

FIGURE 6 | Photos of right hind paws **(A–G)** and histopathological analysis of ankle joints stained with H&E **(a–g)**.

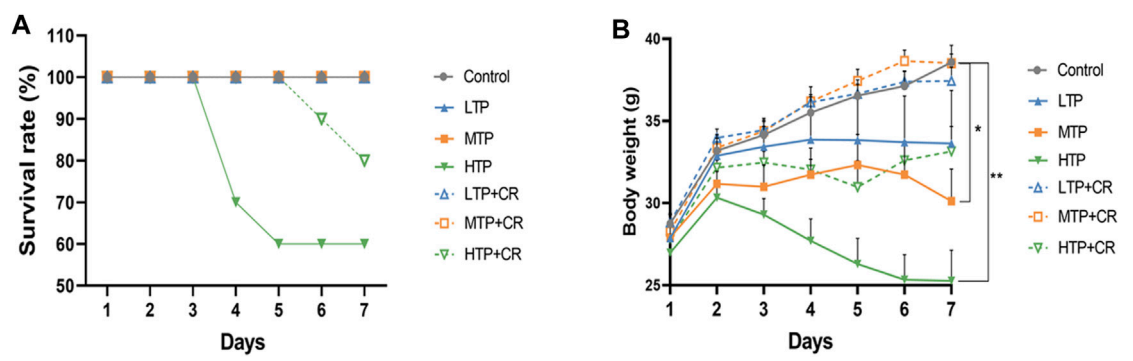

FIGURE 7 | The survival rates **(A)** (n = 10) and body weight changes **(B)** (n = 6) of different groups over 7 days *$p < 0.05$, **$p < 0.01$ vs Control.

Animal toxicity experiments showed that CR reduced TP-induced multi-organ damage (**Figure 8** and **Table 4**), and reduced mortality.

Hepatotoxicity is the most significant TP-induced side effect and the mechanism is complex, which is believed to occur via oxidative stress, abnormal liver drug enzyme activity, and immune-mediated

TABLE 2 | Comparison of organ coefficients in each group ($\bar{x}$ ± S, n = 6).

Groups	Heart	Liver	Spleen	Lung	Kidney	Testis
Control	0.569 ± 0.019	5.665 ± 0.410	0.514 ± 0.090	0.729 ± 0.074	1.437 ± 0.117	0.635 ± 0.049
LTP	0.544 ± 0.022	5.301 ± 0.342	0.507 ± 0.041	0.682 ± 0.052	1.405 ± 0.087	0.604 ± 0.123
MTP	0.530 ± 0.023**	5.086 ± 0.345*	0.405 ± 0.064*	0.641 ± 0.055*	1.239 ± 0.158*	0.561 ± 0.038*
HTP	0.476 ± 0.036**	4.936 ± 0.413*	0.388 ± 0.092*	0.591 ± 0.052**	1.165 ± 0.202*	0.482 ± 0.112*
LTP + CR	0.564 ± 0.030	5.530 ± 0.455	0.509 ± 0.114	0.714 ± 0.063	1.424 ± 0.075	0.629 ± 0.037
MTP + CR	0.563 ± 0.029$^{\#}$	5.527 ± 0.233$^{\#}$	0.491 ± 0.026$^{\#}$	0.725 ± 0.066$^{\#}$	1.428 ± 0.093$^{\#}$	0.624 ± 0.050$^{\#}$
HTP + CR	0.548 ± 0.051$^{\#}$	5.499 ± 0.306$^{\#}$	0.499 ± 0.024$^{\#}$	0.704 ± 0.092$^{\#}$	1.400 ± 0.048$^{\#}$	0.621 ± 0.101$^{\#}$

Notes: *p < *0.05*, **p < *0.01 any group vs Control;* $^{\#}$p < *0.05, XTP + CR, vs XTP (X represent L, M, or H).*

TABLE 3 | Comparison of hepatic and renal functions among the groups of mice ($\bar{x}$ ± S, n = 6).

Groups	AST (IU/L)	ALT (IU/L)	BUN(mmol/L)	CRE(μmol/L)
Control	23.373 ± 2.829	30.512 ± 9.592	4.634 ± 0.291	14.037 ± 1.952
LTP	34.526 ± 6.497**	43.86 ± 7.142*	4.953 ± 0.221	16.931 ± 2.284
MTP	41.998 ± 4.595**	45.382 ± 10.674*	5.609 ± 0.188**	21.782 ± 1.902*
HTP	50.125 ± 7.816**	49.224 ± 15.304*	7.948 ± 1.171**	22.802 ± 2.866*
LTP + CR	24.32 ± 8.476$^{\#}$	26.774 ± 12.049$^{\#}$	4.781 ± 0.195	15.259 ± 1.229
MTP + CR	25.064 ± 6.311$^{\#\#}$	30.371 ± 4.409$^{\#}$	4.916 ± 0.480$^{\#\#}$	15.625 ± 0.914$^{\#\#}$
HTP + CR	25.428 ± 5.766$^{\#\#}$	34.528 ± 3.703$^{\#}$	5.017 ± 0.485$^{\#\#}$	17.533 ± 3.445$^{\#}$

Notes: *p < *0.05*, **p < *0.01 any group vs Control;* $^{\#}$p < *0.05,* $^{\#\#}$p < *0.01, XTP + CR, vs XTP (X represent L, M, or H).*

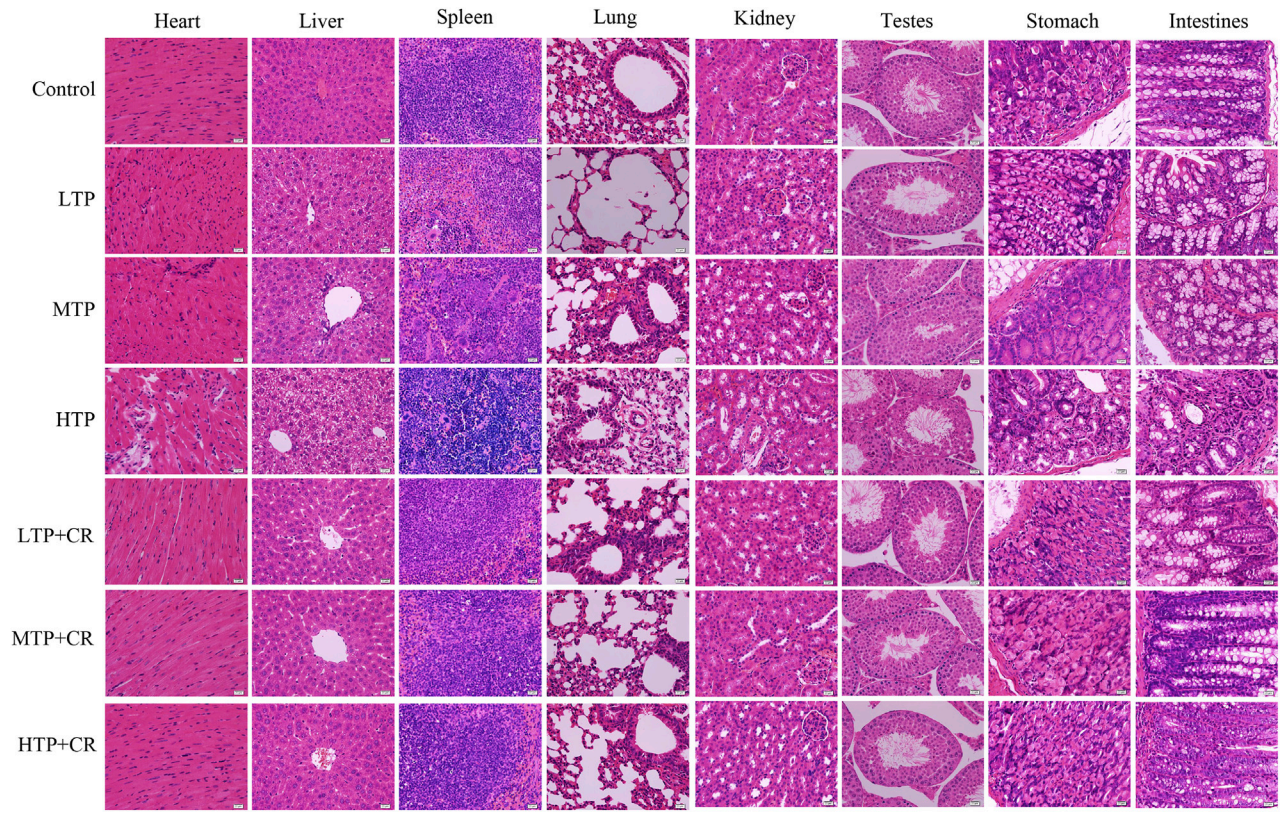

FIGURE 8 | Histopathological observations of H&E staining on the main visceral organs of the mice. Images were obtained at 400X magnification (scale bar = 20 μm).

TABLE 4 | Morphological and pathological manifestations of mice in each group.

	Control	TP Groups	TP + CR Groups
Heart	The myocardial fibers were orderly and tightly arranged	LTP and MTP groups: the transverse striations were ambiguous and there was interstitial congestion HTP group: cardiomyocytes had been dissolved, interstitial fibers showed hyperplasia, and inflammatory cell infiltration occurred	Myocardial damage was significantly ameliorated and histological morphology tended to be normal
Liver	Normal cell morphology, clear hepatic lobule structure, and neatly arranged hepatocytes with no inflammatory cell infiltration	LTP group: few inflammatory cells were observed MTP group: hepatocyte edema and punctate necrosis Disordered hepatic cell cord arrangement, and compressed sinusoids HTP group: hepatocytes exhibited diffuse hydropic or fatty degeneration	Clear structure with no edema, and small fat vacuoles were observed in part of the hepatocyte cytoplasm. Hepatocellular injury was significantly improved
Spleen	Splenic corpuscle was circular and the structure was clear MTP group: Significant increase in the number of multinucleated macrophages and erythrocytes HTP group: white pulp structures were disordered and numerous apoptotic bodies were present	LTP group: Decreased lymphocyte density, increased red pulp macrophages	White pulp injury was significantly reduced and no abnormal changes were observed
Lung	The alveolar structure in H&E staining was normal, the lung tissue was well structured, and there was no inflammatory cell infiltration	MTP and HTP group: alveolar and alveolar interstitial inflammatory cell infiltration and edema	Normal alveoli and few inflammatory cells
Kidney	Tubular epithelial cells and glomerular structures were clear and intact	With increased TP drug dosage, the proximal convoluted tubules were edematous and glomerular capillaries were markedly dilated. Infiltration of inflammatory cells was observed	Normal histological morphology. Slight hyperplasia of fibrous tissue was observed in the interstitium
Testes	Clear structure of seminiferous tubules and orderly arrangement of spermatogenic cells. Mature sperm were observed	Compared to that in the healthy testes, the number of spermatogenic cells in the seminiferous tubules was reduced, and they were disorganized	Compared with the model group, the number of spermatogenic cells was increased and the cells were arranged in an orderly fashion
Stomach	The control group showed a normal structure and no histopathological changes	HTP group: tissue structure was disordered, mucosal epithelial cells had shed, and inflammatory cell infiltration was observed	CR treatment significantly ameliorated gastric mucosa damage; regular glandular structure was observed, and reduced inflammatory cell infiltration
Intestine	The mucosal epithelial cells were arranged neatly	HTP group: The epithelial cells had shed and inflammatory cells had infiltrated the lamina propria	The tissues were clear and intact

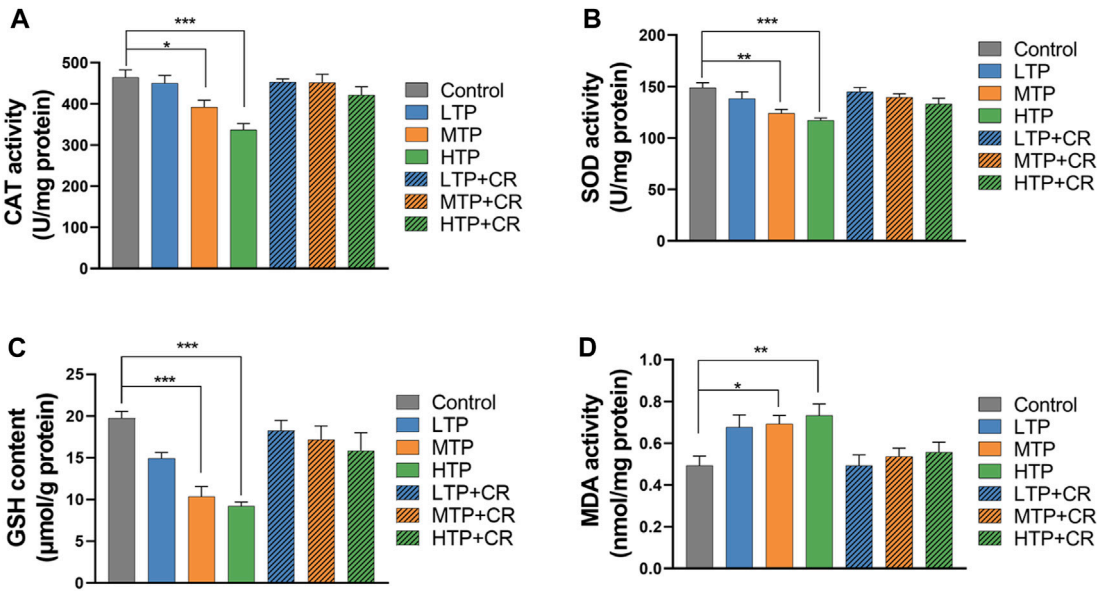

FIGURE 9 | Levels of CAT **(A)**, SOD **(B)**, GSH **(C)**, and MDA **(D)** in liver homogenates of mice (n = 6). *$p < 0.05$, **$p < 0.01$, ***$p < 0.001$ vs Control.

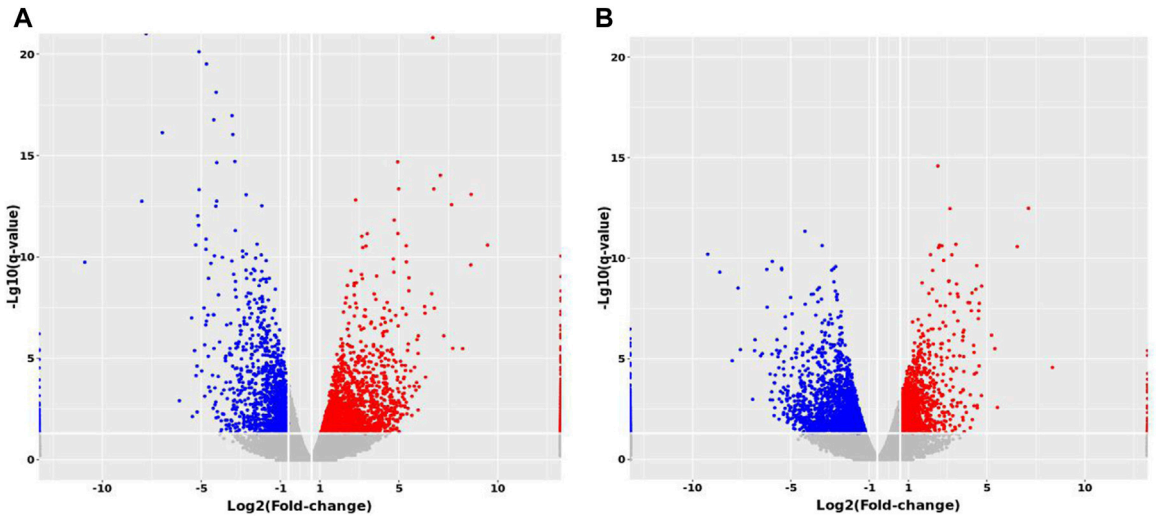

FIGURE 10 | Volcano maps of differentially expressed mRNAs between groups. **(A)** MTP vs. Control **(B)** MTP + CR vs. MTP.

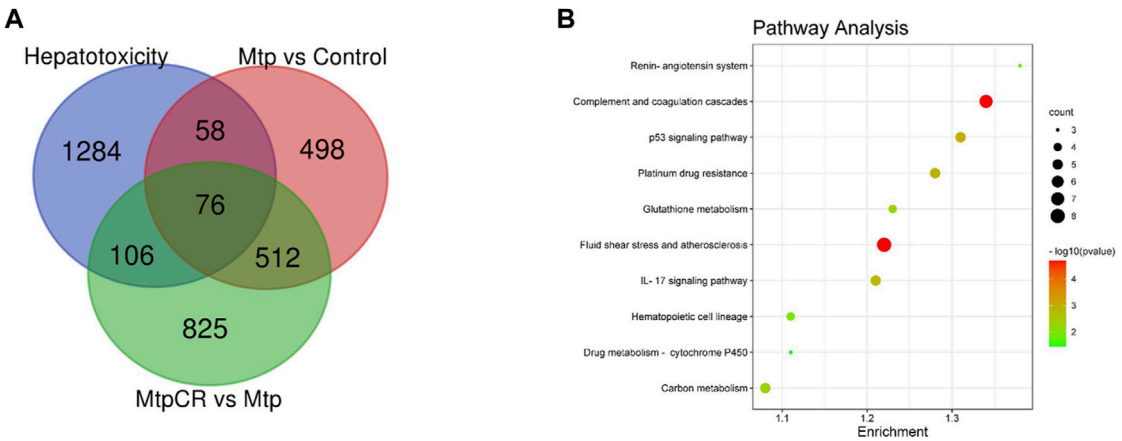

FIGURE 11 | Venn diagram showing the number of differently expressed mRNAs related to hepatotoxicity **(A)** and pathway enrichment analysis **(B)**.

injury (Tian et al., 2019). Crocin has been shown to act on multiple pharmacological targets, such as antioxidant, anti-inflammatory, and immunoregulatory systems that may be involved in TP-induced toxicity (Attia et al., 2021).

Previous animal studies have shown that crocin is a protective against doxorubicin-induced nephrotoxicity and cyclophosphamide-induced hepatotoxicity through modulation of antioxidant enzymes and inflammatory mediators (Jnaneshwari et al., 2013; Hussain et al., 2021). Combined treatment with vitamin C and TP could combat oxidative stress by regulating the levels of SOD, GSH, CAT and MD (Xu et al., 2019), which agrees with the known mechanisms for TP-induced hepatotoxicity (Cao et al., 2022). TP may lead to emergency oxidative damage of liver cells by reducing thioredoxin activity (Shen et al., 2019). In this study, we evaluated changes in oxidative stress markers in the liver, the primary organ responsible for drug metabolism. The results showed that co-administration of TP + CR reversed TP-induced changes in SOD and CAT activities, and GSH and MDA levels, in a dose-dependent manner.

The metabolism of TP and other drugs depends on enzymes in liver microsomes, which involve phase I and phase II metabolism. Cytochrome P450s, representative enzymes of Phase I, are responsible for the hydroxylation of triptolide *in vitro* and CYP3A4 enzyme mediated metabolic elimination is an important detoxification pathway for TP (Xiao et al., 2020). Glutathione-S-transferases are a superfamily of phase-II metabolic enzymes that protect against oxidative stress (Singh and Reindl, 2021). Transcriptome sequencing and KEGG analysis in this study showed that differentially expressed mRNAs related to hepatotoxicity (76 mRNAs) were mainly enriched in glutathione metabolism, IL-17 signaling pathway, and drug metabolism-

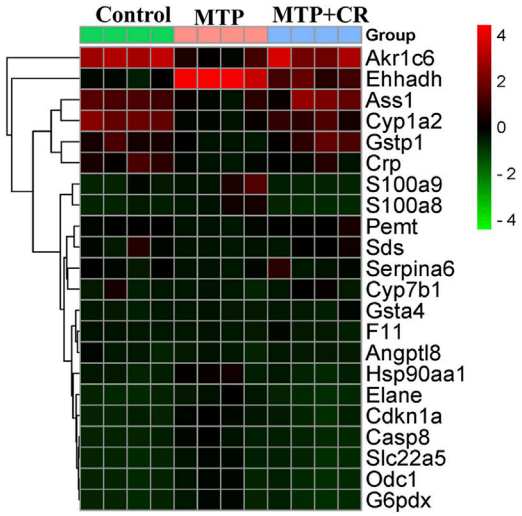

FIGURE 12 | The heat maps of the Top 23 differentially-expressed mRNAs among three groups.

cytochrome P450. We selected the most significantly differentially expressed genes, Cyp1a2, Gstp1, and Gsta4, for confirmation by qRT-PCR. Our results showed that co-administration of TP + CR reversed TP-induced decreased in Cyp1a2, Gsta4, and Gstp1 expression. Cyp1a2 is an important phase-I metabolic enzyme in the cytochrome P450 family of enzymes. Gsta4 and Gstp1 can catalyze the binding of glutathione to TP metabolites *in vivo*, thus reducing the toxicity of TP. Therefore, our results indicated that phase I and phase II metabolic enzymes both participate in critical detoxification processes in TP-induced liver injury, and crocin could reduce TP-induced liver injury by down-regulating gene expression of these enzymes. In addition, IL-17 mediated the immune response of TP and played an essential role in the liver injury pathology (Wei et al., 2017). Our results also revealed that crocin might be involved in IL-17 mediated immune regulation. However, further research is still required.

In conclusion, our results demonstrated that co-administration of TP and CR could protect CIA mice from TP-induced multi-organ damage without reducing the therapeutic efficacy of TP. The mechanisms by which CR protected against TP-induced toxicity may have been related to the drug metabolism-cytochrome P450 and glutathione metabolism pathways. Our study demonstrated that CR could be used to attenuate TP toxicity without impacting therapeutic efficacy. Future studies should clarify the specific mechanisms by which CR protects against TP-induced toxicity, and ongoing studies are exploring new dosage forms and administration strategies for CR and TP.

DATA AVAILABILITY STATEMENT

The datasets presented in this study can be found in online repositories. The names of the repository/repositories and accession number(s) can be found below: https://www.ncbi.nlm.nih.gov/geo/, GSE202175

ETHICS STATEMENT

The animal study was reviewed and approved by the Animal Ethics Committee In Henan University of Chinese Medicine.

AUTHOR CONTRIBUTIONS

MY and YY performed the experiments, analyzed the data, prepared figures and/or tables, and authored or reviewed drafts of the paper. ZZ conceived the experiments and approved the final draft. GW, WS and MJ performed the experiments, samples collection, and approved the final draft. JZ, XW and HZ conceived and designed the experiments, analyzed the data, authored or reviewed drafts of the paper, and approved the final draft.

FUNDING

This study was sponsored by National Natural Science Foundation of China (21601053, U1604185), Henan Scientific and technological Innovation Talents Project (20HASTIT050), Henan Science Fund for Excellent Young Scholars (212300410057), the Scientific and Technological Brainstorm Project of Henan Province (202102310515), Innovative Research Team in Science and Technology of Henan Province (211RTSTHN026), Henan provincial Key Scientific Research Projects (22102310638), Henan Scientific Research Funding Project for Overseas Staffs 2020 (No: 29).

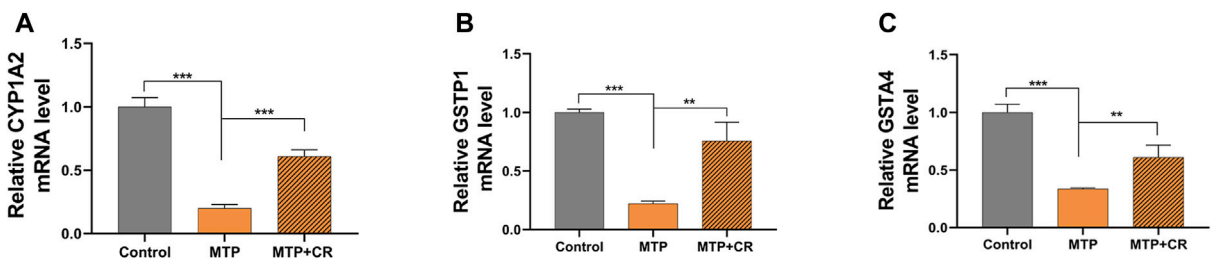

FIGURE 13 | Confirmation of mRNA expression by qRT-PCR **(A)** the CYP1A2 mRNA level; **(B)** the GSTP1 mRNA level; **(C)** the GSTA4 mRNA level. $^{**}p < 0.01$,$^{***}p < 0.001$ vs MTP.

REFERENCES

Abdi, H., Aganj, Z., Hosseinzadeh, H., and Mosaffa, F. (2022). Crocin Restores the Balance of Th1/Th2 Immune Cell Response in ConA-Treated Human Lymphocytes. *Pharmacol. Rep.* 74, 513–522. *[Preprint]*. doi:10.1007/s43440-022-00362-3

Attia, A. A., Ramdan, H. S., Al-Eisa, R. A., Adle Fadle, B. O. A., and El-Shenawy, N. S. (2021). Effect of Saffron Extract on the Hepatotoxicity Induced by Copper Nanoparticles in Male Mice. *Molecules* 26 (10), 3045. doi:10.3390/molecules26103045

Brand, D. D., Latham, K. A., and Rosloniec, E. F. (2007). Collagen-induced Arthritis. *Nat. Protoc.* 2 (5), 1269–1275. doi:10.1038/nprot.2007.173

Cao, Z., Liu, B., Li, L., Lu, P., Yan, L., and Lu, C. (2022). Detoxification Strategies of Triptolide Based on Drug Combinations and Targeted Delivery Methods. *Toxicology* 469, 153134. doi:10.1016/j.tox.2022.153134

El-Beshbishy, H. A., Hassan, M. H., Aly, H. A., Doghish, A. S., and Alghaithy, A. A. (2012). Crocin "saffron" Protects against Beryllium Chloride Toxicity in Rats through Diminution of Oxidative Stress and Enhancing Gene Expression of Antioxidant Enzymes. *Ecotoxicol. Environ. Saf.* 83, 47–54. doi:10.1016/j.ecoenv.2012.06.003

Hosseini, A., Razavi, B. M., and Hosseinzadeh, H. (2018). Pharmacokinetic Properties of Saffron and its Active Components. *Eur. J. Drug. Metab. Pharmacokinet.* 43 (4), 383–390. doi:10.1007/s13318-017-0449-3

Hussain, M. A., Abogresha, N. M., AbdelKader, G., Hassan, R., Abdelaziz, E. Z., and Greish, S. M. (2021). Antioxidant and Anti-inflammatory Effects of Crocin Ameliorate Doxorubicin-Induced Nephrotoxicity in Rats. *Oxid. Med. Cell. Longev.* 2021, 8841726. doi:10.1155/2021/8841726

Jnaneshwari, S., Hemshekhar, M., Santhosh, M. S., Sunitha, K., Thushara, R., Thirunavukkarasu, C., et al. (2013). Crocin, a Dietary Colorant, Mitigates Cyclophosphamide-Induced Organ Toxicity by Modulating Antioxidant Status and Inflammatory Cytokines. *J. Pharm. Pharmacol.* 65 (4), 604–614. doi:10.1111/jphp.12016

Korani, S., Korani, M., Sathyapalan, T., and Sahebkar, A. (2019). Therapeutic Effects of Crocin in Autoimmune Diseases: A Review. *BioFactors* 45 (6), 835–843. doi:10.1002/biof.1557

Li, L., Zhang, H., Jin, S., and Liu, C. (2018). Effects of Crocin on Inflammatory Activities in Human Fibroblast-like Synoviocytes and Collagen-Induced Arthritis in Mice. *Immunol. Res.* 66 (3), 406–413. doi:10.1007/s12026-018-8999-2

Liang, H., Peng, B., Dong, C., Liu, L., Mao, J., Wei, S., et al. (2018). Cationic Nanoparticle as an Inhibitor of Cell-free DNA-Induced Inflammation. *Nat. Commun.* 9 (1), 4291. doi:10.1038/s41467-018-06603-5

Qin, W. Z. (2019). "Chapter 2 Rheumatoid Arthritis," in *The Study on Tripterygium Wilfordii*. Editor S Tu (BeiJing, China: science press), 378–387.

Razavi, B. M., and Hosseinzadeh, H. (2015). Saffron as an Antidote or a Protective Agent against Natural or Chemical Toxicities. *Daru* 23 (1), 31. doi:10.1186/s40199-015-0112-y

Salem, M., Shaheen, M., Tabbara, A., and Borjac, J. (2022). Saffron Extract and Crocin Exert Anti-inflammatory and Anti-oxidative Effects in a Repetitive Mild Traumatic Brain Injury Mouse Model. *Sci. Rep.* 12 (1), 5004. doi:10.1038/s41598-022-09109-9

Shen, F., Xiong, Z., Kong, J., Wang, L., Cheng, Y., Jin, J., et al. (2019). Triptolide Impairs Thioredoxin System by Suppressing Notch1-Mediated PTEN/Akt/Txnip Signaling in Hepatocytes. *Toxicol. Lett.* 300, 105–115. doi:10.1016/j.toxlet.2018.10.024

Singh, R. R., and Reindl, K. M. (2021). Glutathione S-Transferases in Cancer. *Antioxidants (Basel)* 10 (5), 701. doi:10.3390/antiox10050701

Tai, T., Huang, X., Su, Y., Ji, J., Su, Y., Jiang, Z., et al. (2014). Glycyrrhizin Accelerates the Metabolism of Triptolide through Induction of CYP3A in Rats. *J. Ethnopharmacol.* 152 (2), 358–363. doi:10.1016/j.jep.2014.01.026

Tan, Q. Y., Hu, Q., Zhu, S. N., Jia, L. L., Xiao, J., Su, H. Z., et al. (2018). Licorice Root Extract and Magnesium Isoglycyrrhizinate Protect against Triptolide-Induced Hepatotoxicity via Up-Regulation of the Nrf2 Pathway. *Drug. Deliv.* 25 (1), 1213–1223. doi:10.1080/10717544.2018.1472676

Tian, Y., Li, P., Xiao, Z., Zhou, J., Xue, X., Jiang, N., et al. (2021). Triptolide Inhibits Epithelial-Mesenchymal Transition Phenotype through the p70S6k/GSK3/β-Catenin Signaling Pathway in Taxol-Resistant Human Lung Adenocarcinoma. *Transl. Lung. Cancer. Res.* 10 (2), 1007–1019. doi:10.21037/tlcr-21-145

Tian, Y. G., Su, X. H., Liu, L. L., Kong, X. Y., and Lin, N. (2019). Overview of Hepatotoxicity Studies on Tripterygium Wilfordii in Recent 20 Years. *Zhongguo. Zhong. Yao. Za. Zhi.* 44 (16), 3399–3405. doi:10.19540/j.cnki.cjcmm.20190527.408

Tong, L., Zhao, Q., Datan, E., Lin, G. Q., Minn, I., Pomper, M. G., et al. (2021). Triptolide: Reflections on Two Decades of Research and Prospects for the Future. *Nat. Prod. Rep.* 38 (4), 843–860. doi:10.1039/d0np00054j

Trentham, D. E., Townes, A. S., and Kang, A. H. (1977). Autoimmunity to Type II Collagen an Experimental Model of Arthritis. *J. Exp. Med.* 146 (3), 857–868. doi:10.1084/jem.146.3.857

Wang, J. M., Chen, R. X., Zhang, L. L., Ding, N. N., Liu, C., Cui, Y., et al. (2018). *In Vivo* protective Effects of Chlorogenic Acid against Triptolide-Induced Hepatotoxicity and its Mechanism. *Pharm. Biol.* 56, 626–631. doi:10.1080/13880209.2018.1527370

Wei, C. B., Tao, K., Jiang, R., Zhou, L. D., Zhang, Q. H., and Yuan, C. S. (2017). Quercetin Protects Mouse Liver against Triptolide-Induced Hepatic Injury by Restoring Th17/Treg Balance through Tim-3 and TLR4-MyD88-NF-Kb Pathway. *Int. Immunopharmacol.* 53, 73–82. doi:10.1016/j.intimp.2017.09.026

Xiao, X., Zhang, T., Huang, J., Zhao, Q., and Li, F. (2020). Effect of CYP3A4 on Liver Injury Induced by Triptolide. *Biomed. Chromatogr.* 34, e4864. doi:10.1002/bmc.4864

Xing, B., Li, S., Yang, J., Lin, D., Feng, Y., Lu, J., et al. (2021). Phytochemistry, Pharmacology, and Potential Clinical Applications of Saffron: A Review. *J. Ethnopharmacol.* 281, 114555. doi:10.1016/j.jep.2021.114555

Xu, P., Li, Y., Yu, Z., Yang, L., Shang, R., and Yan, Z. (2019). Protective Effect of Vitamin C on Triptolide-Induced Acute Hepatotoxicity in Mice through Mitigation of Oxidative Stress. *An. Acad. Bras. Cienc.* 91, e20181257. doi:10.1590/0001-3765201920181257

Xu, Z., Lin, S., Tong, Z., Chen, S., Cao, Y., Li, Q., et al. (2022). Crocetin Ameliorates Non-alcoholic Fatty Liver Disease by Modulating Mitochondrial Dysfunction in L02 Cells and Zebrafish Model. *J. Ethnopharmacol.* 285, 114873. doi:10.1016/j.jep.2021.114873

Yabe, R., Chung, S. H., Murayama, M. A., Kubo, S., Shimizu, K., Akahori, Y., et al. (2021). TARM1 Contributes to Development of Arthritis by Activating Dendritic Cells through Recognition of Collagens. *Nat. Commun.* 12, 94. doi:10.1038/s41467-020-20307-9

Yalikong, A., Li, X. Q., Zhou, P. H., Qi, Z. P., Li, B., Cai, S. L., et al. (2021). A Triptolide Loaded HER2-Targeted Nano-Drug Delivery System Significantly Suppressed the Proliferation of HER2-Positive and BRAF Mutant Colon Cancer. *Int. J. Nanomedicine.* 16, 2323–2335. doi:10.2147/IJN.S287732

Yang, G., Wang, L., Yu, X., Huang, Y., Qu, C., Zhang, Z., et al. (2017). Protective Effect of 18β-Glycyrrhetinic Acid against Triptolide-Induced Hepatotoxicity in Rats. *Evidence-Based Complementary Altern. Med.* 2017, 3470320. doi:10.1155/2017/3470320

Yaribeygi, H., Maleki, M., Mohammadi, M. T., Sathyapalan, T., Jamialahmadi, T., and Sahebkar, A. (2021). Crocin Improves Diabetes-Induced Oxidative Stress via Downregulating the Nox-4 in Myocardium of Diabetic Rats. *Adv. Exp. Med. Biol.* 1328, 275–285. doi:10.1007/978-3-030-73234-9_18

Zeng, H., Zhu, X., Tian, Q., Yan, Y., Zhang, L., Yan, M., et al. (2020). *In Vivo* antitumor Effects of Carboxymethyl Chitosan-Conjugated Triptolide after Oral Administration. *Drug. Deliv.* 27, 848–854. doi:10.1080/10717544.2020.1770370

Zhang, L., Yan, M., Chen, K., Tian, Q., Song, J., Zhang, Z., et al. (2020). Novel Carboxylated Chitosan-Based Triptolide Conjugate for the Treatment of Rheumatoid Arthritis. *Pharmaceutics* 12 (3), 202. doi:10.3390/pharmaceutics12030202

Zhang, Y., Fei, F., Zhen, L., Zhu, X., Wang, J., Li, S., et al. (2017). Sensitive Analysis and Simultaneous Assessment of Pharmacokinetic Properties of Crocin and Crocetin after Oral Administration in Rats. *J. Chromatogr. B. Anal. Technol. Biomed. Life. Sci.* 1044-1045, 1–7. doi:10.1016/j.jchromb.2016.12.003

Zhang, Y., Mao, X., Li, W., Chen, W., Wang, X., Ma, Z., et al. (2021). Tripterygium Wilfordii: An Inspiring Resource for Rheumatoid Arthritis Treatment. *Med. Res. Rev.* 41, 1337–1374. doi:10.1002/med.21762

Zhao, J., Zhang, F., Xiao, X., Wu, Z., Hu, Q., Jiang, Y., et al. (2021). Tripterygium Hypoglaucum (Levl.) Hutch and its Main Bioactive Components: Recent Advances in Pharmacological Activity, Pharmacokinetics and Potential Toxicity. *Front. Pharmacol.* 12, 715359. doi:10.3389/fphar.2021.715359

Zhao, Z., Zhang, Y., Gao, D., Zhang, Y., Han, W., Xu, X., et al. (2022). Inhibition of Histone H3 Lysine-27 Demethylase Activity Relieves Rheumatoid Arthritis Symptoms via Repression of IL6 Transcription in Macrophages. *Front. Immunol.* 13, 818070. doi:10.3389/fimmu.2022.818070

Conflict of Interest: The authors declare that the research was conducted in the absence of any commercial or financial relationships that could be construed as a potential conflict of interest.

Publisher's Note: All claims expressed in this article are solely those of the authors and do not necessarily represent those of their affiliated organizations, or those of the publisher, the editors and the reviewers. Any product that may be evaluated in this article, or claim that may be made by its manufacturer, is not guaranteed or endorsed by the publisher.

frontiers | Frontiers in Pharmacology

ORIGINAL RESEARCH
published: 13 July 2022
doi: 10.3389/fphar.2022.934057

Epimedium koreanum Nakai–Induced Liver Injury—A Mechanistic Study Using Untargeted Metabolomics

Pin Li, Lin Zhang, Zhaojuan Guo, Qianjun Kang, Cong Chen, Xiaoyao Liu, Quantao Ma, Jingxuan Zhang, Yujie Hu and Ting Wang**

Beijing Institute of Traditional Chinese Medicine, Beijing University of Chinese Medicine, Beijing, China

Epimedii Folium is widely used worldwide as an herbal supplement, and the risk of its induced liver damage has emerged in recent years. Our preliminary study has found that, among several Epimedii Folium species specified in the Chinese Pharmacopoeia, *Epimedium koreanum* Nakai has a more severe propensity for hepatotoxicity. However, the mechanism of hepatotoxicity of *Epimedium koreanum* Nakai is still unclear. In this study, untargeted metabolomics was performed to analyze the serum and liver tissue to explore the mechanism of hepatotoxicity of *Epimedium koreanum* Nakai. The results of experiments *in vivo* showed that, after 28 days of exposure to *Epimedium koreanum* Nakai ethanol extract (EEE), the liver weight, levels of AST, ALP, TBIL, etc. in serum of rats in the EEE group were significantly increased, as well as severe cytoplasmic vacuolation appeared in the liver tissue, which suggested that EEE has significant hepatotoxicity. Subsequently, the results of metabolomics revealed significant changes in the metabolic profile in the liver and serum of rats after EEE exposure, in which metabolites in serum such as flavin mononucleotide, phenylacetylglycine, glutathione, L-tryptophan, and sphingomyelin were able to accurately identify liver injury caused by EEE and could be used as serum markers to reflect EEE-induced liver injury. The KEGG pathway enrichment analysis revealed that EEE caused extensive effects on rats' metabolic pathways. Some of the most affected pathways included glutathione metabolism, glutamate metabolism pathway, primary bile acid biosynthesis pathway, and sphingolipid metabolism pathway, which were all directed to the biological process of ferroptosis. Then, the main markers related to ferroptosis in the liver were examined, and the results demonstrated that the content of malondialdehyde was significantly increased, the activity of superoxide dismutase was significantly reduced, the ferroptosis inhibitory proteins GPX4 and System x_c^- were significantly downregulated, and the ferroptosis-promoting protein ACSL4 was significantly up-regulated. Judging from these results, we concluded that the mechanism of hepatotoxicity of *Epimedium koreanum* Nakai was probably related to the induction of ferroptosis in hepatocytes.

Keywords: herb-induced liver injury, Epimedium koreanum Nakai, metabolomics, glutathione, ferroptosis

OPEN ACCESS

Edited by:
Shuai Ji,
Xuzhou Medical University, China

Reviewed by:
Zhilei Wang,
Chengdu University of Traditional Chinese Medicine, China
Li Chao,
Shandong First Medical University, China

****Correspondence:***
Lin Zhang
zlbucm@163.com
Ting Wang
wangting1973@sina.com

Specialty section:
This article was submitted to Ethnopharmacology, a section of the journal Frontiers in Pharmacology

Received: *02 May 2022*
Accepted: *30 May 2022*
Published: *13 July 2022*

Citation:
Li P, Zhang L, Guo Z, Kang Q, Chen C, Liu X, Ma Q, Zhang J, Hu Y and Wang T (2022) Epimedium koreanum Nakai–Induced Liver Injury—A Mechanistic Study Using Untargeted Metabolomics. Front. Pharmacol. 13:934057. doi: 10.3389/fphar.2022.934057

INTRODUCTION

Epimedii Folium (Yinyanghuo in Chinese) is the dried leaf of *Epimedium brevicornu* Maxim., *Epimedium sagittatum* (Siebold&Zucc.) Maxim., or *Epimedium pubescens* Maxim. or *Epimedium koreanum* Nakai, in the family berberidaceae (Chinese Pharmacopoeia Commission, 2020). In the theory of Traditional Chinese Medicine, Epimedii Folium has the ability to dispel wind and cold, tonify the kidneys, and strengthen the tendons (Ma et al., 2011). It is widely used to treat various diseases, such as osteoporosis, impotence, infertility, cardiovascular disease, and amnesia (Ma et al., 2011). However, in recent years, two registered drugs with Epimedii Folium as the main ingredient, Zhuangguguanjie Pill and Xianlinggubao Capsules, were reported to be associated with liver injury in humans in clinical applications (Cheng et al., 2013; Tang et al., 2017; Tang et al., 2018; Wu et al., 2019), which has attracted widespread attention. Drug-induced liver injury is one of the most serious and common adverse drug reactions in clinical practice (Navarro et al., 2017), and severe liver injury may induce acute liver failure in patients and even lead to the death of patients (Tujios and Fontana, 2011; Iorga et al., 2017). Therefore, it is important to investigate the potential risk of liver injury of Epimedii Folium. At present, the research on the hepatotoxicity of Epimedii Folium has been gradually carried out. Some researchers have found that Icariside I and Icariside II (the main components of Epimedii Folium) could induce specific hepatotoxicity by enhancing the activation of nlrp3 inflammasome (Wang Z et al., 2020; Gao et al., 2021). Other researchers alsohave found that both 2″-O-rhamnosylicariside II and Sagittatoside B caused severe hepatocyte vacuolation and hepatocyte degeneration in adult zebrafish after 15 consecutive days of treatment (Zhong et al., 2019). However, there are few studies on the mechanism of Epimedii Folium inducing hepatotoxicity *in vivo*.

Most of the liver injury caused by Chinese herbal medicine *in vivo* is extremely complex and shows significant individual differences (García-Cortés et al., 2016; Brown, 2017). Metabolomics reveals the intrinsic mechanisms of growth and development, disease, and environmental influences on the body through a comprehensive and systematic analysis of metabolites in body fluids, tissues, or cells (Gong et al., 2017; Gika et al., 2019), which has been increasingly applied in exploring the mechanism of hepatotoxicity of herbal medicines (Duan et al., 2018). Zhaoyan Zhang et al. found that Polygoni Multiflori Radix extracts could cause liver damage by interfering with α-linolenic acid metabolism, taurine and taurine metabolism, glycerophospholipid metabolism, and primary bile acid biosynthetic pathways based on a metabolomic approach (Zhang et al., 2019). Yusha Luo et al. found that gardenia might cause liver injury by disrupting pyrimidine, purine, and amino acid metabolism and pantothenic acid and Coenzyme A biosynthesis through metabolomic methods (Luo et al., 2021). Applying metabolomics to study the hepatotoxicity of Epimedii Folium can help not only to clarify the toxicological characteristics of Epimedii Folium but also to reveal its potential mechanism.

In a previous study, we have found that *Epimedium koreanum* Nakai had more severe hepatotoxicity among several Epimedii Folium prescribed in the Chinese Pharmacopoeia, and its mechanism of hepatotoxicity was considered to be related to oxidative stress by experiments *in vitro* (Zhang L et al., 2020). However, the detailed mechanism of liver injury caused by *Epimedium koreanum* Nakai *in vivo* has not been elucidated. Based on the status of the prophase management research, we planned to study the mechanism of hepatotoxicity of *Epimedium koreanum* Nakai in this study by hepatotoxicity evaluation *in vivo* and non-targeted metabolomics method. The hepatotoxicity of *Epimedium koreanum* Nakai ethanol extract (EEE) was first investigated and validated by histopathological and biochemical methods, and the serum and liver samples were analyzed by untargeted metabolomics. Then, the differential metabolites of these samples were identified and screened using the UPLC-Q-TOF/MS technology platform and were analyzed to predict the pathways of EEE-induced liver injury *in vivo*. Subsequently, the mechanisms were investigated and analyzed by detecting key indicators in the pathway. This study could provide a reference for the safe utilization of Epimedii Folium in clinical practice.

MATERIALS AND METHODS

Chemicals and Reagents

Methanol and acetonitrile (UHPLC grade) were purchased from Fisher Chemical (Darmstadt, Germany). Ammonium acetate (70221) and sodium pentobarbital (P3761) were purchased from Sigma-Aldrich (St. Louis, Missouri, United States). Icaritin (110737-201516, purity >98%) and epimedin C (111780-201503, purity >98%) were purchased from the National Medical Products Administration (Beijing, China). Epimedin A (C15J3G1, purity >98%), epimedin B (C28S3G1, purity >98%), epimedin C (H16D5X1, purity >98%), and baohuoside I (H16D5X1, purity >98%) were purchased from Shanghai yuanye Bio-Technology Co., Ltd. (Shanghai, China). Alkaline phosphatase (ALP, AUZ8511), alanine transaminase (ALT, AUZ9151), aspartate aminotransferase (AST, AUZ9022), direct bilirubin (DBIL, AUZ9056), and total bilirubin (TBIL, AUZ8613) assay kits were purchased from Beckman Coulter (Suzhou, China). The malondialdehyde (MDA, M496) assay kit was purchased from Dongren Chemical Technology Co., Ltd. (Shanghai, China). The superoxide dismutase (SOD, S0101S) activity assay kit was purchased from Beyotime Biotechnology (Shanghai, China). *Epimedium koreanum* Nakai was obtained from the backup samples of previous experiments in our laboratory's herbal sample collection room (Zhang L et al., 2020).

EEE was produced by extracting dried *Epimedium koreanum* Nakai twice with 10 volumes of 70% ethanol-water (V/V), and the extract solution from both times was filtered and concentrated at 50 °C under negative pressure. The concentrates were freeze-dried to obtain a brown extract, and the ratio of the obtained extract from the original herb was 35.2%.

Quality Assessment of *Epimedium koreanum* Nakai Ethanol Extract

To evaluate the quality of EEE, we determined the concentrations of the five main components in EEE using high-performance liquid chromatography (HPLC). Standard solutions preparation: a mixed standard solution of icaritin, epimedin C, epimedin A, epimedin B, epimedin C, and baohuoside I was prepared using 50% DMSO: H_2O solution with the concentrations of 11.1 μg/ml, 12.5 μg/ml, 22.9 μg/ml, 12.1 μg/ml, and 9.4 μg/ml for each compound.

Sample solution preparation: 0.5 g EEE was added into 100 ml 50% DMSO: H_2O solution (V/V) and sonicated for 30 min to dissolve fully. After cooling to room temperature, the solution was filtered using a 0.45 μm membrane to obtain the sample solution.

The HPLC method used for the detection was described in the following way: C_{18} column (Platisil, 4.6 mm × 250 mm, 5 μm, Decima Technology Co., Ltd., Beijing, China). The mobile phase was acetonitrile (A): water (B), and the procedure of gradient elution was (time/A%): 0–25 min, 25%–27%; 25–45 min, 27%–49%; 45–65 min, 49%–81%. The chromatographic analysis was performed with the column temperature maintained at 25°C, mobile phase flow rate at 1 ml/min, detection wavelength at 277 nm, and sample injection volume of 10 μl.

Animals Handling and Experimental Design

Male Sprague Dawley rats (180–200 g) were purchased from Beijing Vital River Laboratory Animal Technology Co., Ltd (license number SCXK-[jing] 2016–0011). The rats used for the experiments were housed at the Animal Experiment Center of Beijing University of Chinese Medicine, where room temperature was maintained at 20 ± 2°C and humidity at 60–70%, and a 12-h light/dark cycle was maintained. Rats had free access to a standard diet and water throughout the experimental period. All rats were acclimatized to this environment for 4 days before the experiment.

After acclimatization, the experimental rats were randomly divided into control and EEE groups ($n = 6$, each group). EEE was processed as solutions with deionized water before being used. The EEE group was administered EEE solution at 2 g original herb/kg (0.704 g EEE/kg) for 28 days, in a volume of 1 ml/100 g, once a day. The dosage of EEE was based on our previous studies (Zhang et al., 2018). The control group was also given an equal amount of purified water. Throughout the experiment, all rats were unfettered access to water and food and were weighed every 7 days. On the 28th day, 2 h after the administration, the rats were anesthetized intraperitoneally with sodium pentobarbital, blood were collected from the abdominal aorta to prepare serum samples, and liver tissues were dissected and collected. The study protocol was carried out under the approval and supervision of the Center for Experimental Animal Welfare and Ethics of Beijing University of Traditional Chinese Medicine.

Serum Biochemical Analysis

Blood from rats was collected in 5 ml Vacutainer tubes and then centrifuged for 15 min (1,500 g, 4°C) to collect the upper serum layer as serum samples. Liver injury was assessed by measuring AST, ALT, ALP, DBIL, and TBIL in each rat serum sample using CX4 Pro automated biochemical analyzer (Beckman, Brea, CA, United States) according to the manufacturer's instructions.

Organ Weight and Histopathological Assessment

After dissection, the livers and brains of the rats were immediately harvested and weighed after washing with normal saline and wiping dry. Part of rat liver tissue was fixed with 10% neutral formalin for 48–72 h, dehydrated, embedded in paraffin, sectioned, stained with hematoxylin and eosin (H&E), and the pathological changes of liver tissues were observed under the microscope. The remaining livers were kept at −80°C for metabolomics, western blot, MDA, and SOD analysis.

Preparation of Liver and Serum Metabolisms Samples

In addition to using for histopathological assessment, the rest of the liver tissues were immediately frozen in liquid nitrogen and stored at −80 °C. For UPLC-Q-TOF/MS analysis, liver tissues were cut on dry ice, and 100 mg were weighed precisely into Eppendorf tubes (2 ml) with 1 ml of pre-chilled methanol: acetonitrile: water (2:2:1, v/v), which were homogenized and broken by a homogenizer. The homogenate was centrifuged for 15 min (14,000 g, 4°C), and 900 μl of supernatant from each tube was placed in a new Eppendorf tube and dried in a vacuum centrifuge as the test sample. The samples were redissolved in 100 μl of acetonitrile/water (1:1, v/v) solvent for UPLC-Q-TOF/MS analysis.

The rest of the serum samples were aspirated and placed in Eppendorf tubes (2 ml) frozen in liquid nitrogen and stored at −80°C. For UPLC-Q-TOF/MS analysis, serum samples were slowly thawed at 4°C, and 100 μl aliquots were vortexed with 400 μl cold methanol/acetonitrile (1:1, v/v) incubating at −20°C for 30 min to remove proteins. The mixture was centrifuged for 15 min (14,000 g, 4°C), and 400 μl of supernatant from each tube was placed in a new tube and dried under a vacuum. The samples were redissolved in 100 μl of acetonitrile/water (1:1, v/v) solvent for UPLC-Q-TOF/MS analysis.

UPLC-Q-TOF/MS Analysis

Samples were analyzed using UPLC (1,290 Infinity LC, Agilent Technologies) coupled with quadrupole time-of-flight (AB Sciex Triple TOF 6600). For HILIC separation, a 2.1 mm × 100 mm ACQUIY UPLC BEH 1.7 μm column (Waters, Ireland) was used. In the positive and negative ESI modes, the mobile phases contained 25 mM ammonium acetate and 25 mM ammonium hydroxide aqueous solution (A) and acetonitrile (B). The gradient elution procedure was as follows (time/B): 0–0.5 min, 95%; 0.5–7 min, 95%–65%; 7–8 min, 65%–40%; 8–9 min, 40%; 9–9.1 min, 40%–95%; 9.1–12 min, 95%. The samples were placed in a 4°C autosampler throughout the analysis. To avoid the effects of fluctuations in the instrument detection signal, samples were analyzed continuously in random order. QC samples were inserted in the sample queue to monitor and

evaluate the stability of the system and the reliability of the experimental data. The gradient flow rate was 0.3 ml/min, and the column temperature was kept constant at 25°C. A 2 μl aliquot of each sample was injected.

For mass spectrum (MS) analysis, the AB Triple TOF 6600 mass spectrometer was used for the acquisition of primary and secondary spectra of the samples. The ESI source conditions after BEH Amide chromatographic separation were as follows: Ion Source Gas1 (Gas1): 60, Ion Source Gas2 (Gas2). 60, Curtain gas (CUR): 30, source temperature: 600°C, IonSapary Voltage Floating (ISVF) ± 5500 V (positive and negative modes); TOF MS scan m/z range: 60–1,000 Da, product ion scan m/z range: 60–1,000 Da, product ion scan m/z range: 25–1,000 Da, TOF MS scan accumulation time 0.20 s/spectra, product ion scan accumulation time 0.05 s/spectra; secondary mass spectra were obtained using information. The secondary mass spectra were acquired using information-dependent acquisition (IDA) and high sensitivity mode, Declustering potential (DP): ±60 V (positive and negative modes), Collision Energy: 35 ± 15 eV, IDA settings as follows Exclude isotopes within 4 Da, Candidate ions to monitor per cycle: 10.

Data Extraction and Multivariate Analysis

Raw data of UPLC-Q-TOF/MS in Wiff format were converted to mzXML format using ProteoWizard, and then XCMS software was used for peak alignment, retention time correction, and extraction of peak areas. In the extracted ion features, only those with more than 50% of non-zero measurements were retained. Compound identification of metabolites was performed by comparing accurate m/z values (<10 ppm) and MS/MS spectra with an in-house database built from available authentic standards.

After normalizing the processed data to the total peak intensity, preto-scale principal component analysis (PCA) and orthogonal partial least squares discriminant analysis (OPLS-DA) multivariate data analysis were performed using the R package (ropls) (Thévenot et al., 2015).

Metabolic Pathways Analysis and Metabolic Fingerprints Identification

Metabolites obtained from metabolome analysis, with VIP >1 in the OPLS-DA analysis, were further applied to Student's t-test. Metabolites, that p-value < 0.05 and VIP >1, were selected as candidate biomarkers. Pathway analysis of candidate biomarkers was performed using MetaboAnalyst 5.0. The predictive performance of potential biomarkers for liver toxicity was analyzed using receiver operating characteristic curves (ROC) to establish metabolic fingerprints.

Western Blotting, MDA, and SOD Analysis

Liver tissue, which was kept at −80°C for western blotting, was cut on dry ice, an appropriate amount of liver tissue was weighed, RIPA protein extract was added, and then fully disrupted with a tissue homogenizer, and then placed on ice for 10 min. Then the supernatant was collected by centrifugation (14,000 g, 4°C) for 30 min. The protein concentration was assessed by using the BCA protein assay kit. Electrophoresis was performed by using 10% sodium dodecyl sulphate polyacrylamide gel electrophoresis (SDS-PAGE) to separate the proteins. After electrophoresis, proteins were transferred onto polyvinylidene fluoride (PVDF) membranes using a semi-dry method. The PVDF membranes were immersed in 5% TBST skim milk powder solution for 60 min at room temperature for non-specific closure. Then the PVDF membranes were then incubated for 12 h at 4 °C with the following primary antibodies: anti-GPX4 antibody (ab125066, Abcam, Cambridge, UK; 1:20,000), anti-ACSL4 antibody (ab155282, Abcam; 1:10,000), anti-System x_c^- antibody (ab175186, Abcam; 1:20,000), anti GAPDH antibody (ab9485, Abcam; 1:5,000). After the primary antibody incubation was completed, the PVDF membrane was washed 3 times with TBST, then incubated with hrp-labeled secondary antibody for 1 h at room temperature, and then the PVDF membrane was washed three times with TBST, 5 min each time. Add ECL-plus chemistry and incubate. The film was exposed using an Amersham Imager 680 blot and gel imager, and the grayscale values of the protein bands were analyzed. MDA content in rat liver tissue was assayed according to the manufacturer's instructions, as well as SOD activity.

Statistical Analysis

Experimental data were expressed as mean ± standard deviation (SD), and statistical analysis of data was performed using GraphPad Prism software (version 8.0). p-values of <0.05 (*), ≤0.01 (**) were adopted for statistical significance. Bodyweight, liver weight, liver/brain weight ratio, liver/body weight ratio, AST, ALP, TBIL, SOD, MDA, and Western blot data were analyzed using Student's t-test. All mass spectrometry data were processed by XCMS for peak alignment, retention time correction, and extraction of peak areas. The intensity of each ion was normalized according to the total ion count. PCA and OPLS-DA were performed using the R package (ropls). Pathway analysis was performed based on MetaboAnalyst 5.0.

RESULTS

Major Compounds Concentrations Analysis

To ensure the reproducibility and accuracy of the experimental procedure, it is important to evaluate the quality of EEE. Five major components (epimedin A, epimedin B, epimedin C, icaritin, and baohuoside I) in EEE were selected as quality control indicators, and the concentrations of these key compounds in EEE were determined by HPLC. The concentrations of epimedin A, epimedin B, epimedin C, icaritin, and baohuoside I in EEE were 4.5, 7.3, 4.3, 31.8, 6.8 mg/g, respectively. The results are presented in **Figure 1**.

Toxic Performances of EEE-Induced Liver Injury in Rats

In this study, the body weight, organ weights, serum biochemical parameters, and liver pathology of rats after 28 days of exposure were analyzed to clarify the hepatotoxicity of EEE. Our results showed a gradual increase in body weight of rats in the control and EEE groups during the dosing period; after 28 days of exposure, the body weight

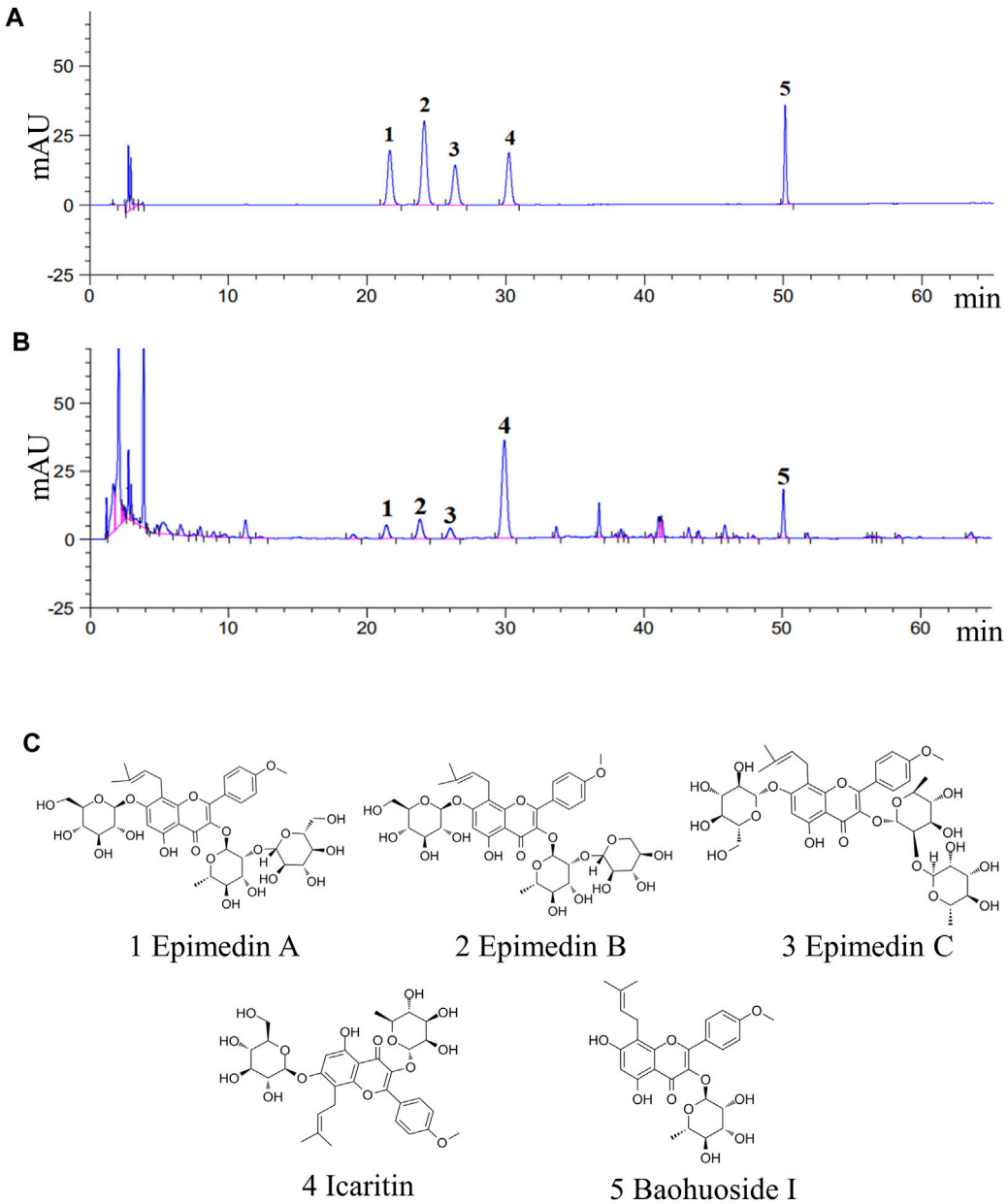

FIGURE 1 | The five main compounds in EEE were quantified by HPLC analysis. **(A,B)** HPLC analysis chromatograms of the 5 main components and EEE samples. 1, epimedin A ($C_{40}H_{52}O_{19}$); 2, epimedin B($C_{38}H_{48}O_{19}$); 3, epimedin C($C_{39}H_{50}O_{19}$); 4, icaritin ($C_{21}H_{20}O_6$); 5, baohuoside I($C_{27}H_{30}O_{10}$). **(C)** Molecular structures of the 5 main components in EEE.

of rats in the EEE group was significantly higher than that in the control group ($p = 0.0157$) (**Figure 2A**). The liver weight, liver/brain weight ratio, and liver/body weight ratio of rats were significantly higher after EEE exposure compared with the control group ($p = 0.006$, 0.008, and 0.0322) (**Figure 2B**). The results of serum biochemical indexes showed that AST, ALP, and TBIL were significantly higher in rats after treatment with EEE ($p = 0.01$, 0.0345, and 0.018) (**Figure 2C**). H&E staining analysis of liver sections showed no significant histopathological damage in the control group (**Figure 2D**). In the EEE group, liver sections showed significant histopathological changes, including visible swelling, hepatocyte steatosis, and severe cytoplasmic vacuolation (**Figure 2D**).

Liver and Serum Metabolomic Profile Analysis of EEE-Induced Liver Injury

The overall metabolic profiles of liver tissues and serum samples in the control and EEE groups were obtained by UPLC-Q-TOF/MS in positive and negative ionization modes, respectively. The

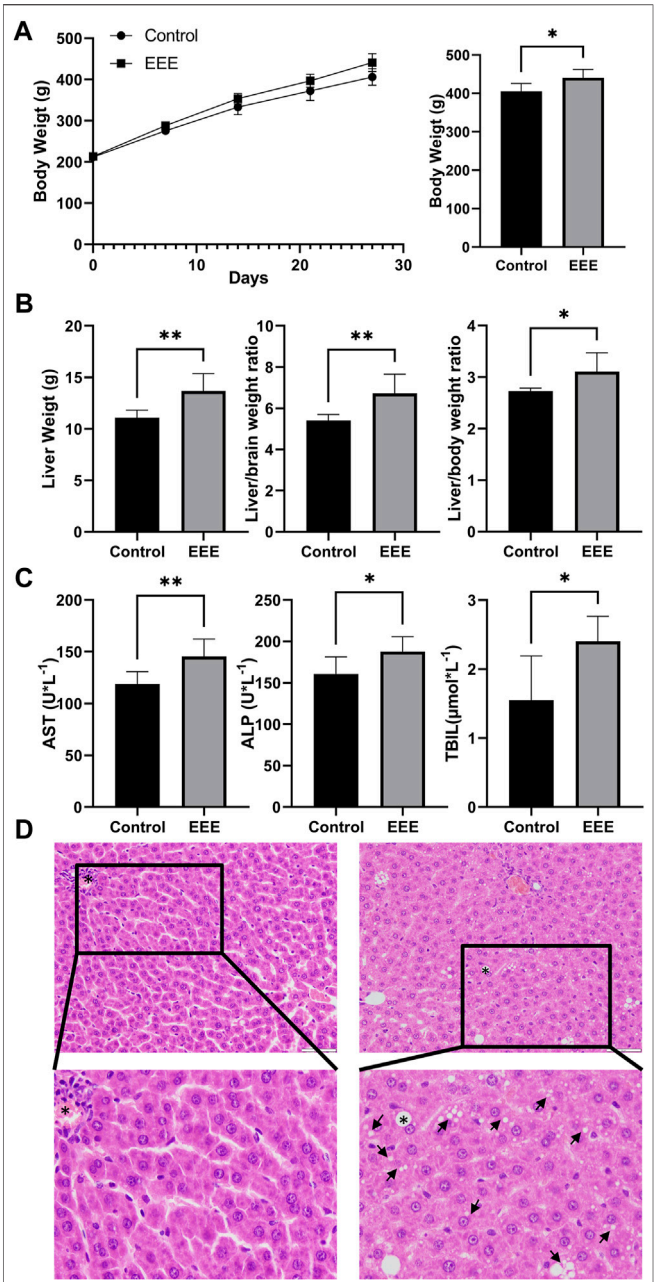

FIGURE 2 | The phenotype of EEE-induced liver injury in rats. **(A)** The EEE-induced phenotype of rat liver injury. The rats were randomly divided into the following two groups: a normal control group of rats (Control); a group of rats exposed to EEE (EEE). Results are presented as mean ± SD in rats, and significant differences are indicated (*P< 0.05, **P≤ 0.01 vs. Control group, n = 6). **(A)** Bodyweight of rats during EEE exposure. **(B)** liver weight, liver/brain weight ratio, and liver/body weight ratio after 28 days of exposure. **(C)** Serum levels of AST, ALP, and TBIL were determined after 28 days of exposure. **(D)** Histopathological damage of rat liver was assessed by HE staining (H&E staining, ×200 magnification).

score plots of PCA analysis based on the data in positive and negative ion mode were shown in **Figures 3A–F**. The QC samples were tightly aggregated in the scoring plots for liver, serum positive ion, and negative ion modes, which indicated the stability of the UPLC-Q-TOF/MS system throughout the analysis process and ensured the reliability and accuracy of the results. In the PCA model of liver and serum positive and negative ion assay results, a clear trend of separation was shown between the control and EEE groups (**Figures 3A,D**). This indicated that the liver and serum metabolic profiles of rats in the EEE administration group were quite different from the control group.

For further screening of differential metabolites in the liver and serum of rats after EEE exposure, the data were first analyzed by applying supervised statistical methods of OPLS-DA and S-plot. The OPLS-DA results (**Figures 3B,C,E,F**) showed significant separation between liver tissue and serum in the control and EEE groups. In the S-plots (**Figures 3B,C,E,F**), metabolites were considered to make a significant contribution to the clustering and identification between two groups when the variable VIP value ≥1 and $|P$ (corr)$|$ value ≥0.5. Then the metabolomics data were further analyzed by using the student's t-test. Liver and serum differential metabolites that changed significantly between the control and EEE groups were screened according to VIP >1 and P< 0.05. The previously screened differential metabolites were identified by accurate mass-to-charge ratios, and the true mass error was limited to 10 ppm. The structures of the identified metabolites were analyzed and validated, and exogenous metabolites such as pharmaceuticals were removed. Finally, 78 endogenous differential metabolites were obtained in the liver, of which 40 were up-regulated and 38 down-regulated. 50 endogenous differential metabolites were obtained in serum, of which 28 were up-regulated, and 22 were down-regulated (**Figure 3G**). The m/z, retention time, and structural formulae of liver and serum differential metabolites were listed in **Supplementary Tables S1 and S2**. Cluster analysis and heatmap were performed for 78 liver differential metabolites, 50 serum differential metabolites, respectively. The results showed that the 78 liver differential metabolites and 50 serum differential metabolites could effectively distinguish the control group from the EEE group (**Figures 3I, J**).

The Metabolite Fingerprint of EEE-Induced Liver Injury

Herb-induced liver injury is insidious, so screening for appropriate serum metabolic fingerprints can help establish an early warning method to avoid liver injury. It was found that 14 differential metabolites were significantly different in both liver and serum after EEE exposure (**Figure 3H**). Among the 14 shared differential metabolites, 12 showed consistent changes in liver and serum (**Figures 4A,B**). Among them, glutathione (GSH), sphingomyelin, cholic acid, deoxycholic acid, N-acetylhistamine, and phenylacetylglycine were significantly decreased in liver and serum after EEE exposure. Flavin mononucleotide (FMN), L-tryptophan, fumaric acid, N-acetylornithine, hippuric acid, and lumichrome were significantly increased in liver and serum after EEE exposure. ROC curves were used to analyze the predictive performance of 14 differential metabolites for liver injury, and the top 4 differential metabolites with AUC values in liver and serum were selected to plot ROC curves (**Figures 4C–F**).

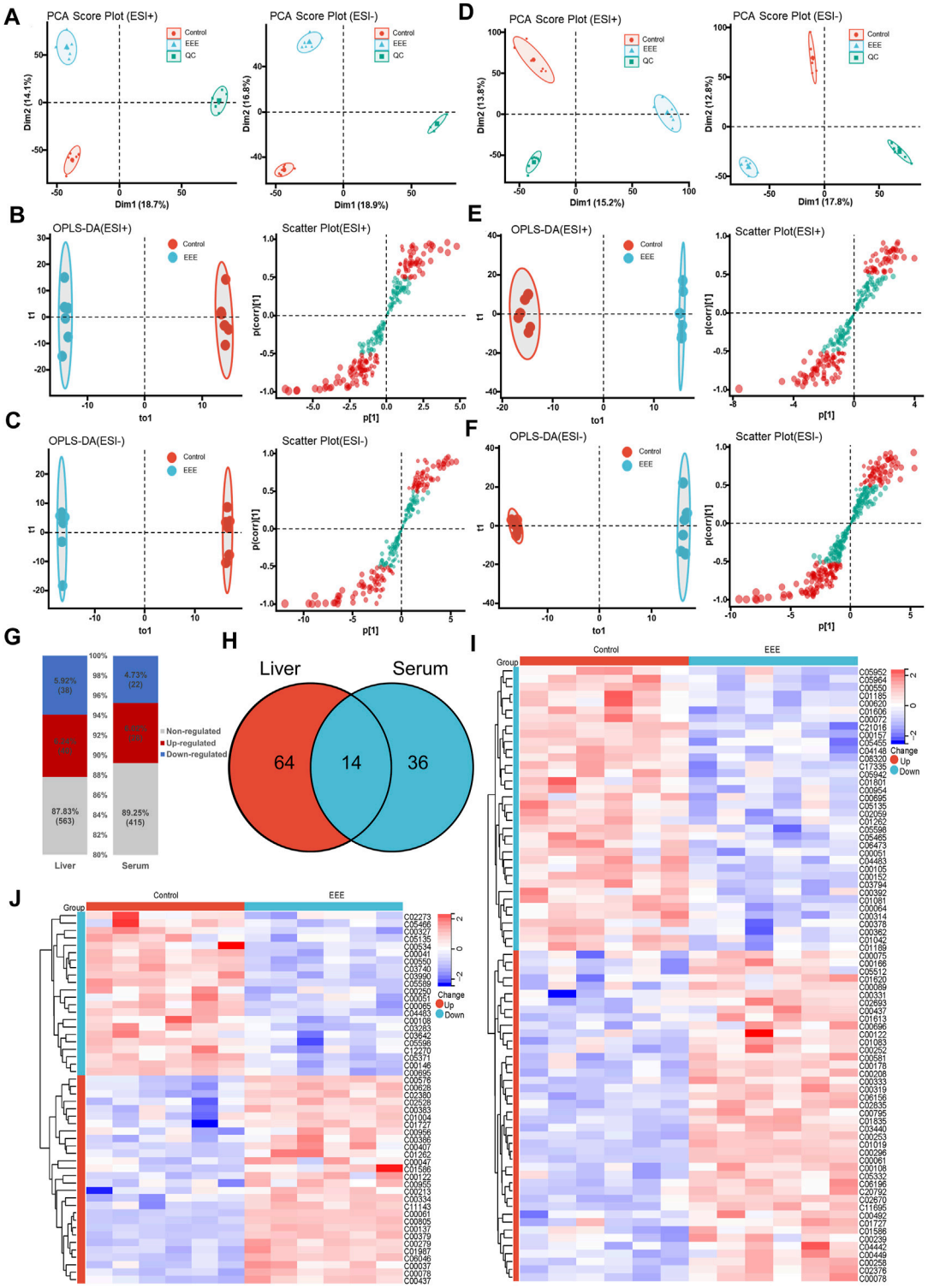

FIGURE 3 | Metabolomic analysis of rats after EEE exposure. **(A–C)** Metabolomic analysis of rat liver tissues. PCA scores **(A)**, OPLS-DA scores **(B)**, and S-plot **(C)** of different groups in liver tissues under positive and negative ESI mode. **(D–F)** Metabolomic analysis of rat serum. PCA scores **(D)**, OPLS-DA scores **(E)**, and S-plot **(F)** of different groups in serum with positive and negative ESI patterns. **(G)** Liver and serum metabolite profiles between normal and EEE rats. **(H)** Shared and unique amounts of liver and serum metabolites were also visualized in the Venn diagram between normal and EEE group rats. **(I)** Heat map of 78 metabolites significantly altered in the liver, clustered in the normal EEE group. The colors from blue to red indicate the relative amounts of metabolites. **(J)** Heat map of 50 metabolites significantly altered in serum, clustered in the normal, EEE group. The colors from blue to red indicate the relative content of metabolites.

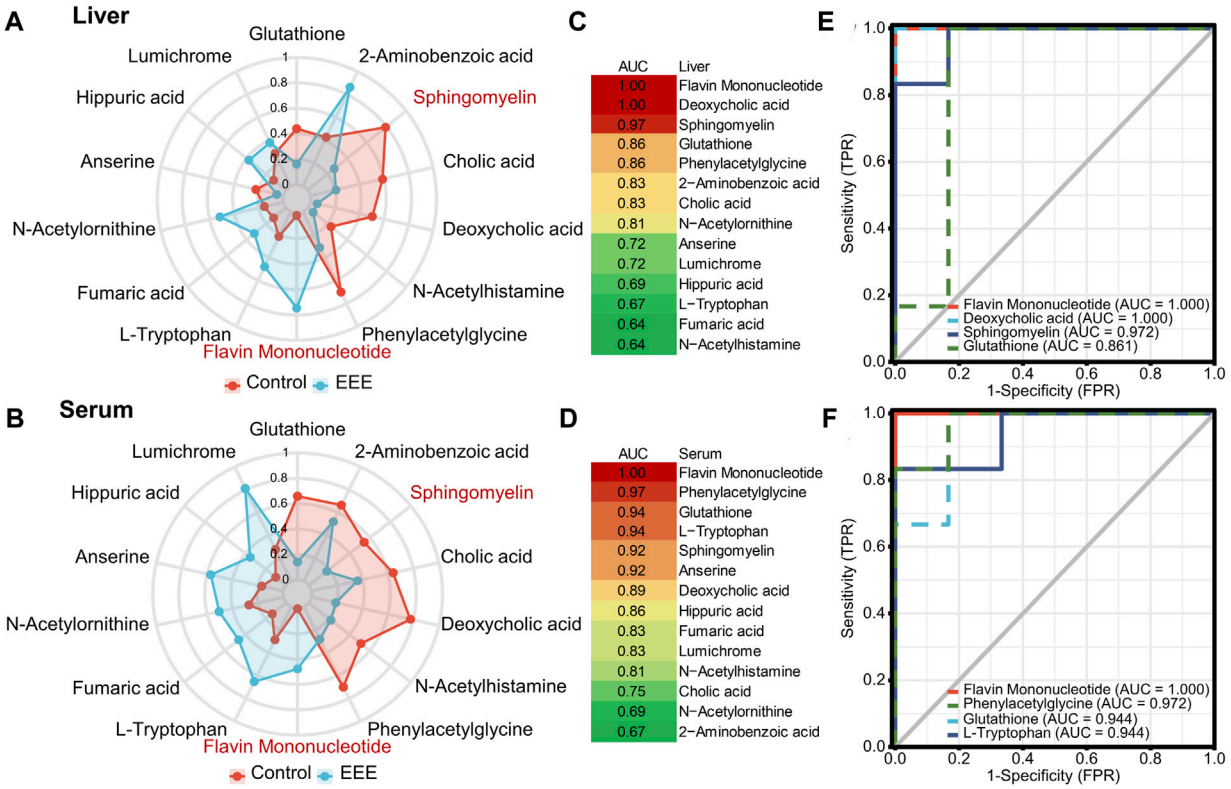

FIGURE 4 | Screening for biomarkers associated with EEE-induced liver injury. **(A,B)** Spider plots of 14 liver and serum shared differentially expressed metabolites between the Control and EEE groups. The red line represents the control group, and the blue line represents the EEE group. **(C,D)** Heat map of AUC values of 14 liver and serum shared differentially expressed metabolites. **(E,F)** ROC curves of differentially expressed metabolites with top 4 AUC values in liver and serum.

In the liver, three metabolites' AUC values > 0.9, including FMN, deoxycholic acid, and sphingomyelin. In serum, six metabolites' AUC values > 0.9, including FMN, phenylacetylglycine, GSH, L-tryptophan, sphingomyelin, and anserine. Among them, the AUC values of FMN and sphingomyelin were greater than 0.9 in both liver and serum, which could be used as potential biomarkers of EEE hepatotoxicity.

Pathway Enrichment and Mechanisms Analysis

To further analyze the effect of EEE exposure on metabolic pathways, the obtained differential metabolites in liver and serum were submitted into MetaboAnalyst 5.0 for KEGG pathway analysis, and the results revealed that the differential metabolites in liver and serum were respectively enriched to 71 and 64 pathways, of which 49 pathways were shared (**Figure 5A**). According to the KEGG pathway classification, 49 shared pathways are mainly involved in amino acid metabolism, lipid metabolism, digestive system, carbohydrate metabolism, metabolism of cofactors and vitamins, cell growth and death, etc. (**Figure 5B**). The disturbances of alanine, aspartate and glutamate metabolism, phenylalanine metabolism, arginine biosynthesis, tryptophan metabolism, and glutathione metabolism were observed in amino acid metabolism, disturbances in primary bile acid biosynthesis and sphingolipid metabolism were observed in lipid metabolism, and the disturbances in tricarboxylic citrate cycle, pentose phosphate pathway, and pyruvate metabolism were observed in carbohydrate metabolism. For the digestive system, disturbances in bile secretion, cholesterol metabolism, and other pathways were observed. In addition to the disruptions of thiamine metabolism, riboflavin metabolism, vitamin B6 metabolism, and ferroptosis and necroptosis pathways were observed (**Figure 5C**).

The KEGG enrichment results were imported into Cytoscape software to construct the KEGG pathways-metabolites network (**Figure 5D**), it was found that EEE could broadly affect amino acid and lipid metabolism in rats, mainly including primary bile acid biosynthesis, sphingolipid metabolism, bile secretion, cholesterol metabolism, and glutathione metabolism. These pathways are mainly involved in the metabolism of glutathione and the biosynthesis of unsaturated fatty acids. Among these pathways, studies have shown that glutathione metabolism, cholesterol metabolism, and sphingolipid metabolism are closely related to ferroptosis (Agmon and Stockwell, 2017; Stockwell et al., 2020; Liu et al., 2021). Also, the key differential metabolites of GSH, FMN, fumaric acid, etc. in these pathways have important roles in ferroptosis (Ursini and Maiorino, 2020; Wang H et al., 2020; Vabulas, 2021).

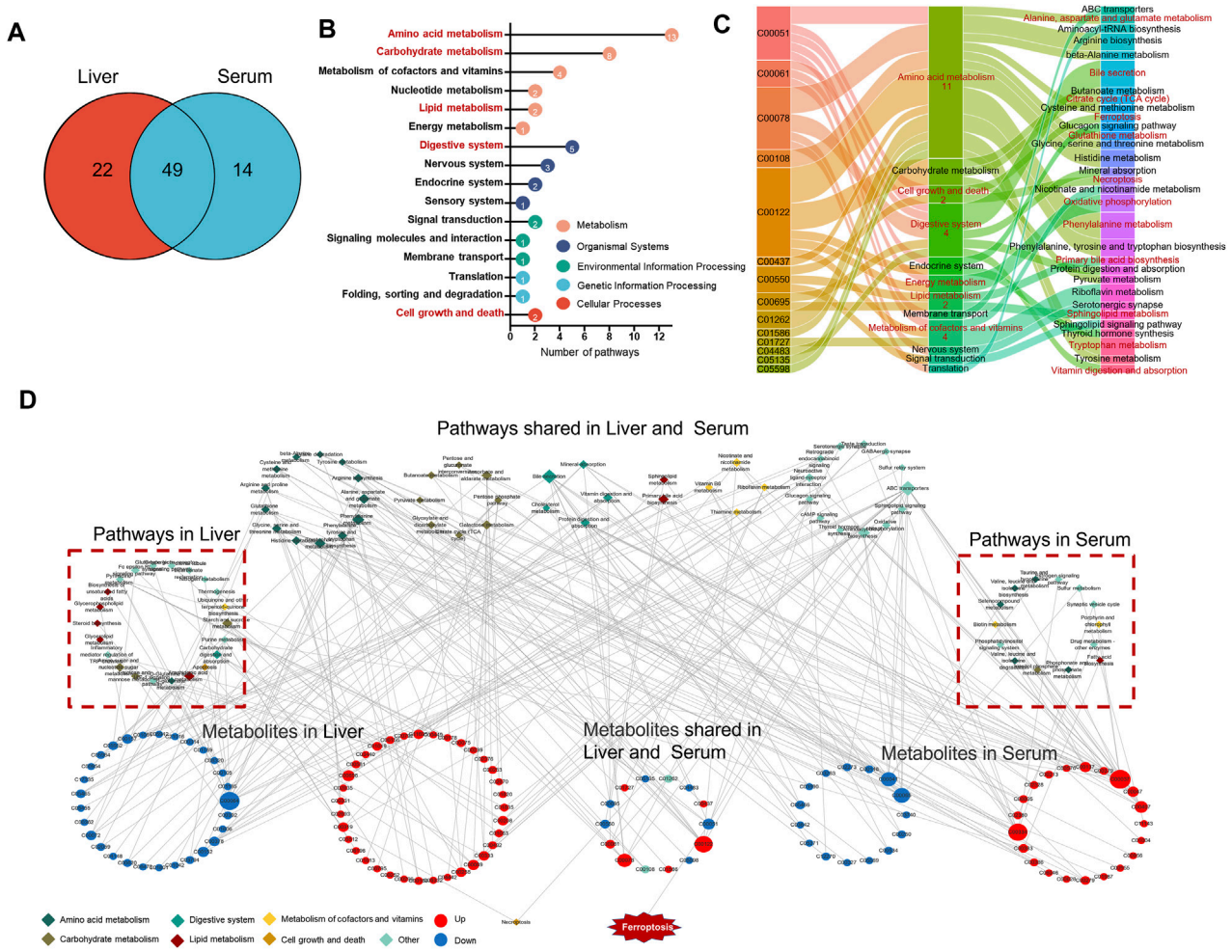

FIGURE 5 | The metabolic pathways and metabolism-related networks of the differential metabolites. **(A)** Venn diagram showing the number of shared and unique pathways for liver and serum differential metabolites. **(B)** Cleveland dot plots show the categories of 49 metabolic pathways shared by liver and serum. **(C)** Sankey diagrams show the relationship of 14 metabolites shared by the liver and serum with key metabolic pathways. **(D)** Network of liver and serum differential metabolites in relation to the KEGG pathway.

Combining the above metabolic pathway analysis, the hypothesis was proposed that EEE caused liver injury by inducing ferroptosis.

EEE-Induced Liver Injury Associated With Ferroptosis

To verify whether EEE causes liver injury by inducing ferroptosis in the liver of rats, the typical indicators related to ferroptosis were examined, including the lipid peroxidation marker (MDA), intracellular major antioxidant activity enzyme (SOD), ferroptosis inhibitory protein (GPX4), System x_c^-, ferroptosis-promoting protein (ACSL4). The results showed that EEE exposure could significantly increase MDA content and significantly lower SOD activity in rat liver (P = 0.0147, 0.0084) (**Figures 6A,B**). In addition, the results of the Western blot assay showed that EEE exposure significantly decreased the protein expression of glutathione peroxidase 4 (GPX4), System x_c^-, while the expression of ACSL4 protein significantly increased (P = 0.0066, 0.0155, 0.0071) (**Figures 6C–F**). Taken together, these results supported that liver injury in rats after EEE exposure could be strongly associated with ferroptosis.

DISCUSSION

The factors contributing to liver toxicity with herbal medicines are complex, and studying their mechanisms is a great challenge. Liver plays a crucial role in the metabolism, detoxification, and excretion of exogenous chemicals (Sun et al., 2021). When herbal medicines enter the body, they undergo metabolic reactions, and endogenous small molecules change over time as they are metabolized, and these changes in endogenous small molecules may induce liver injury (Liu et al., 2016). Metabolomics is used to characterize changes in the organism in response to external factors by detecting small molecules at the most downstream level

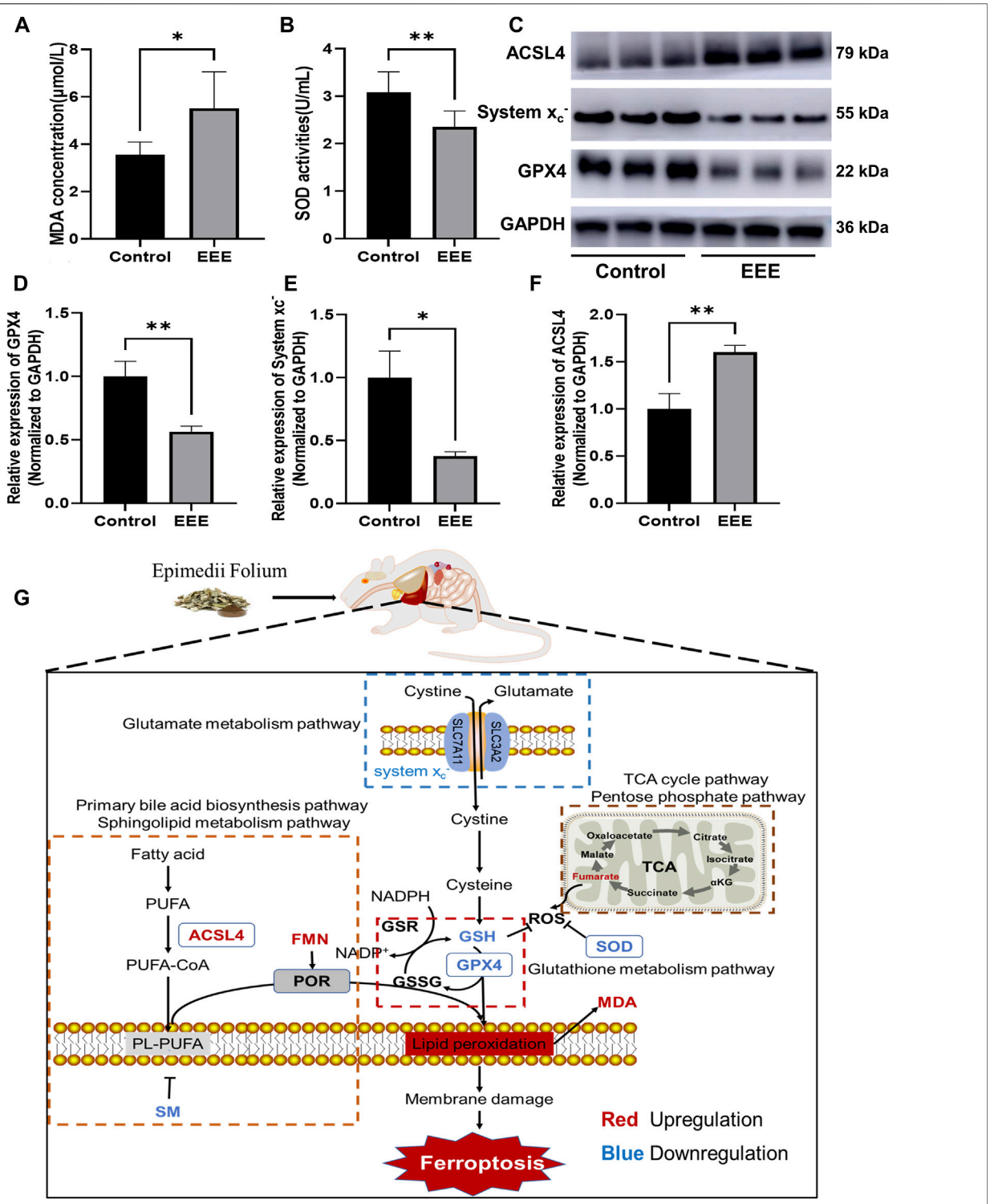

FIGURE 6 | Changes of ferroptosis markers in rat liver after EEE exposure. **(A)** The MDA contents were significantly higher than in the control group. **(B)** The SOD activity was significantly lower than the control group. **(C)** The protein content of GPX4, System x_c^-, and ACSL4 in the liver was detected by immunoblotting. Results are presented as mean ± SD in rats, and significant differences are indicated (*p< 0.05, **p< 0.01 vs. Control group, n = 6). **(D)** After EEE exposure, the expression of GPX4 protein was significantly lower than in the control group. **(E)** After EEE exposure, the expression of System x_c^- protein was significantly lower than in the control group. **(F)** After EEE exposure, the expression of ACSL4 protein was significantly higher than in the control group. **(G)** Mechanism of EEE-induced liver injury by triggering ferroptosis based on metabolomic analysis.

of the system biology (Cuykx et al., 2018). This makes metabolomics fingerprinting very sensitive, and even small external factors may induce changes. Metabolomics allows systematic filtering of the metabolic change patterns of the body through the analysis of endogenous metabolites (Wang et al., 2011). And metabolomics helps to identify potential biomarkers and disordered metabolic pathways by comparing metabolic profiles in normal and toxic states, thus elucidating possible mechanisms (Chen et al., 2020). In this study, the hepatotoxicity of EEE in rats was evaluated, and the relevant mechanisms were explored.

Our results showed that the liver weight, liver/body weight ratio, and liver/brain weight ratio of EEE-exposed rats were significantly higher than those of the control group (**Figures 2A,B**). This demonstrated the toxic effects of EEE on the liver. Serum biochemical parameters are the most commonly used markers of liver function (Green and Flamm, 2002). In our experiments, AST, ALP, and TBIL in the serum of rats exposed to EEE were significantly altered compared with control rats (**Figure 2C**). Pathology of the liver by microscopy revealed severe cytoplasmic vacuolation in liver cells of rats in the EEE group. Organ weight is one of the most sensitive toxicity indicators, and changes are often earlier or more severe than changes in histopathology or serum indicators (Piao et al., 2013); our results showed that the differences in the indicators such as liver weight, liver/body weight ratio, and liver/brain weight ratio of rats were more obvious than serum biochemical indicators such as AST, ALP, this suggested that the effects of EEE on the liver itself predate the changes in blood biochemistry. These results suggested that EEE might have caused significant damage to the rat liver; how EEE induces these pathological changes requires further investigation.

A metabolomic approach was applied to explore the mechanism of EEE-induced liver injury. The results revealed that EEE exposure led to extensive differences in the metabolism of serum and liver in rats. In-depth analysis revealed that 14 identical endogenous metabolites in serum and liver were significantly different from the normal group after EEE exposure and could serve as metabolic fingerprints for EEE-induced liver injury. Among them, FMN and sphingomyelin had AUC values greater than 0.9 in both liver and serum by ROC analysis and could be used to predict hepatotoxicity of EEE. And the subsequent analysis showed that FMN and sphingomyelin had an important role in the mechanism of EEE-induced liver injury.

The KEGG pathway enrichment analysis was performed on differential metabolites to deeply analyze the mechanism of liver injury caused by EEE. The enrichment results showed that EEE exposure had a great effect on amino acid metabolism, lipid metabolism pathways, especially on primary bile acid biosynthesis, sphingolipid metabolism, bile secretion, cholesterol metabolism, glutathione metabolism, and other pathways related to glutathione metabolism and unsaturated fatty acid biosynthesis metabolism have greater interference (**Figures 5A–C**). Extensive studies have shown that unsaturated fatty acid peroxidation due to abnormal glutathione metabolism is one of the typical features of ferroptosis (Xie et al., 2016; Doll et al., 2019; Li et al., 2020) (**Figure 5D**). Ferroptosis is a new type of cell death discovered in recent years, and the process of cell death is usually accompanied by massive iron accumulation and lipid peroxidation (Chen et al., 2021). Increased lipid peroxide content is an important marker for the development of ferroptosis. MDA is one of the degradation products of polyunsaturated fatty acid peroxides, and MDA increases significantly when ferroptosis occurs (Tang et al., 2021). Superoxide dismutase (SOD) is widely found in human tissues and is an important antioxidant that plays an important role in maintaining the redox balance of cells (Rosa et al., 2021). Our previous study found that EEE significantly enhanced reactive oxygen species (ROS) levels, decreased GSH levels, and promoted MDA production in HL7702 and HepG2 cells *in vitro* (Zhang L et al., 2020). Based on these results, we hypothesize that ferroptosis may be the key to EEE-induced liver injury.

The related markers were analyzed to confirm the conjecture that EEE causes ferroptosis; the results of metabolomic showed that GSH in the liver and serum of rats was significantly reduced after EEE exposure (**Figures 4A,B**). Meanwhile, the SOD activity in liver tissues was significantly decreased, and the level of MDA was significantly increased (**Figures 6A,B**). Among them, the changes in GSH and MDA were consistent with the results of our previously published *in vitro* experiments. In addition, the metabolomic analysis revealed significantly higher levels of fumaric acid in liver tissue and serum of rats in the EEE group (**Figures 4A,B**). It has been found that glutathione succinate (GSF), the covalently bound product of fumaric acid and glutathione, is a substrate for glutathione reductase and can enhance ROS production by consuming NADPH(Sullivan et al., 2013). This finding is consistent with the *in vitro* results that ROS levels were significantly increased in HL7702 and HepG2 cells after EEE incubation. In conclusion, the above results demonstrated that EEE induced ferroptosis in rat liver by disrupting redox balance.

Ferroptosis initiation and execution are tightly controlled by iron, lipid, amino acid, and glutathione metabolism; the results of metabolomic showed that amino acid and glutathione metabolic pathways were extensively affected in rat liver after EEE exposure (**Figure 5B**), the cystine/glutamate transporter (System x_c^-) is involved in this procedure and plays an important part in the process (Koppula et al., 2018). The System x_c^- is an amino acid antiporter, a transmembrane structure formed by light solute carrier family 7 member 11 and Solute Carrier Family 3 Member 2 (Liu et al., 2020). The System x_c^- is primarily responsible for pumping intracellular glutamate out of the cell in exchange for extracellular cysteine (Koppula et al., 2021). Cystine entering the cell is converted to cysteine, which is then combined with glutamate and glycine to synthesize the endogenous antioxidant GSH (Lu, 2009), GSH is a tripeptide antioxidant and a cofactor of selenium-dependent GPX4 in reducing lipid peroxidation, reduced GSH synthesis can indirectly inactivate GPX4, lead to the bioaccumulation of intracellular ROS and cause lipid peroxidation (Dixon et al., 2012). GPX4, a member of the GPX family, is the only enzyme, which reduces phospholipid hydrogen peroxide and plays an essential role in maintaining

redox homeostasis in cells, GPX4 limits the propagation of lipid peroxidation in membranes by reducing toxic lipid peroxides (L-OOH) to non-toxic lipid alcohols (L-OH), which in turn prevents ferroptosis (Forcina and Dixon, 2019). Thus, ferroptosis is irreversible when oxidative damage leads to a large production of lipid peroxides or when excessive depletion of GSH leads to a decrease in GPX4 activity (Yang and Stockwell, 2016). Recent studies have shown that inhibition of the System x_c^-, which reduces the uptake of cystine, impairs the antioxidant defense system of cells and eventually leads to ferroptosis (Dixon et al., 2014). It was also found that overexpression of GPX4 in cells caused resistance to ferroptosis, while knockdown of GPX4 promoted ferroptosis (Bersuker et al., 2019). Therefore, with reduced GPX4, System x_c^- expression is a key marker of ferroptosis. In our experiments, the expression of System x_c^- and GPX4 in rat liver was significantly reduced after EEE exposure (**Figures 6D,E**), which is one of the pieces of evidence confirming that EEE might induce ferroptosis. Iron-catalyzed excessive peroxidation of phospholipids (PLs) containing polyunsaturated fatty acids (PUFAs) is a major feature of ferroptosis, and these phospholipids are abundant in mammalian cell membranes (Tang et al., 2021).

The results of metabolomic showed that fatty acid metabolism pathways such as the Primary bile acid biosynthesis pathway and sphingolipid metabolism pathway in rat livers were extensively affected after EEE exposure (**Figure 5B**, **Figure 6G**). The study revealed through lipidomic analysis that Acyl-CoA Synthetase Long Chain Family Member 4 (ACSL4) could have an essential role in ferroptosis by regulating the metabolism of lipid components (Doll et al., 2017). Several studies have identified ACSL4 as a key factor in determining ferroptosis sensitivity (Yuan et al., 2016; Doll et al., 2017; Kagan et al., 2017). A significant increase in ACSL4 expression in rat liver tissue after exposure to EEE was observed (**Figures 6C,F**). Therefore, based on the above results, we infer that EEE may induce hepatic lipid metabolism disturbance and promote ferroptosis by upregulating ACSL4.

In addition, interestingly, FMN, sphingomyelin, which had AUC values greater than 0.9 in both liver and serum, also had an important role in ferroptosis. Among them, FMN is a biomolecule produced by riboflavin (vitamin B2) through riboflavin kinase, which is an auxiliary group of various oxidoreductases (such as NADH dehydrogenase) (Akasov et al., 2019). FMN is a more potent oxidant than Nicotinamide adenine dinucleotide (NAD) and enhances the ability of cytochrome P450 oxidoreductase (POR) to auto-oxidize and produce ROS, and promotes PUFAs peroxidation to induce ferroptosis (Esteves et al., 2020; Yan et al., 2021). Sphingolipids are significant components of animal plasma membranes; some studies have found that it may act as a "biophysical antioxidant" by changing the oxidation rate of PUFA, limiting the propagation of the lipid peroxidation process, and thereby reducing ferroptosis (Coliva et al., 2020; Aldrovandi et al., 2021). Our experiments revealed that the content of FMN in the liver and serum was significantly increased, and the content of sphingomyelin was significantly decreased after EEE exposure (**Figures 4A,B**). These also indicated that EEE exposure resulted in severe redox derangements in rat liver, leading to the development of lipid peroxidation, which in turn caused ferroptosis in hepatocytes.

Some researchers have found that GPX4 and GSH, which have important regulatory roles in ferroptosis, may have inhibitory effects on NLRP3 inflammasome activation (Wang et al., 2019; Zhang et al., 2021). In our study, it was also found that GPX4 and GSH decreased after EEE administration, which could not only induce ferroptosis in liver cells to produce direct toxicity, but also lead to non-specific liver injury by activating the NLRP3 inflammasome. According to literature reports, not only EEE can cause direct liver injury, but its main components such as icariside I and icariside II can also induce idiosyncratic liver injury (IDILI) by activating the NLRP3 inflammasome (Wang Z et al., 2020; Gao et al., 2021). In addition, in the KEGG pathway analysis, we found that metabolic disturbance caused by EEE might also cause necroptosis in hepatocytes. Necroptosis is a way of programmed cell death mediated by inflammation (Dhuriya and Sharma, 2018). NLRP3 inflammasome activation often leads to necroptosis in cells (Huang et al., 2021). In addition, studies have found that GPX4 is not only an inhibitor of ferroptosis, but also plays an important role in inhibiting necroptosis (Canli et al., 2016). At the same time, some studies have found that the redox homeostasis of cells also plays an important role in necroptosis (Florean et al., 2019; Zhang Y et al., 2020; Li et al., 2021). Decreased GSH and SOD levels lead to increased oxidative stress in cells, which can induce necroptosis in cells (Xie et al., 2015). Taken together, EEE exposure caused a severe imbalance in redox homeostasis in the rat organism, induced ferroptosis in hepatocytes, and activated inflammatory pathways promoting necroptosis. As for the relationship between EEE and IDILI, we expected to have some new findings in further research. In combination, we found that the liver injury caused by EEE exposure might be related to the extensive disruption of amino acid metabolism, glutathione metabolism, and lipid metabolism in rat liver, and the regulation of the expression of key ferroptosis proteins such as GPX4, System x_c^-, and ACSL4, resulting in the decrease of antioxidant active substances such as GSH, sphingomyelin and SOD, and the increase of pro-oxidant active substances such as FMN and ROS, which disrupt the redox balance in the liver and promote lipid peroxidation (increased MDA content), causing ferroptosis (**Figure 6G**).

CONCLUSION

In conclusion, our study confirmed that EEE could induce liver injury in rats, and its hepatotoxicity mechanism was related to the induction of ferroptosis in hepatocytes. During the performance of metabolic profiling of rat liver and serum, we found the metabolic difference and screened two differential metabolites (FMN, SM) shared by liver and serum as potential biomarkers for EEE-induced liver injury (ROC AUC >0.9). By analyzing the differential metabolites and enrichment pathways, the results suggested that EEE might induce liver injury by

disrupting the redox homeostasis of rat liver tissue inducing ferroptosis. This finding was confirmed by the expression of ferroptosis marker proteins GPX4, System x_c^-, ACSL4, as well as SOD activity and MDA content in the liver. These results provided a theoretical basis for further research on the mechanism of EEE-induced liver injury. However, there were some limitations in this study. The current experimental results did not fully uncover the mechanism of *Epimedium koreanum* Nakai hepatotoxicity, and the main components responsible for hepatotoxicity had not been clarified, which needed further exploration and research.

DATA AVAILABILITY STATEMENT

The original contributions presented in the study are included in the article/**Supplementary Material**; further inquiries can be directed to the corresponding authors.

ETHICS STATEMENT

The animal study was reviewed and approved by the Center for Experimental Animal Welfare and Ethics of Beijing University of Traditional Chinese Medicine.

AUTHOR CONTRIBUTIONS

LZ, TW designed and supervised the research. PL, CC participated in the animal experiments. CC, ZG, QK, XL, QM, and YH took part in collecting tissue samples at the end of the experiment. JZ performed the pathological data analysis. LZ, PL performed the data analysis for metabolomics. LZ, PL prepared the manuscript draft. LZ and TW revised the manuscript and provided extensive discussions. All authors participated in the discussions and editing of the manuscript.

FUNDING

This study was supported by the National Natural Science Funds of China (Grant No. 82004053) and the New Teacher Initial Fund Project of the Beijing University of Chinese Medicine (Grant No. 2020-JYB-XJSJJ-020).

SUPPLEMENTARY MATERIAL

The Supplementary Material for this article can be found online at: https://www.frontiersin.org/articles/10.3389/fphar.2022.934057/full#supplementary-material

REFERENCES

Agmon, E., and Stockwell, B. R. (2017). Lipid Homeostasis and Regulated Cell Death. *Curr. Opin. Chem. Biol.* 39, 83–89. doi:10.1016/j.cbpa.2017.06.002

Akasov, R. A., Sholina, N. V., Khochenkov, D. A., Alova, A. V., Gorelkin, P. V., Erofeev, A. S., et al. (2019). Photodynamic Therapy of Melanoma by Blue-Light Photoactivation of Flavin Mononucleotide. *Sci. Rep.* 9, 9679. doi:10.1038/s41598-019-46115-w

Aldrovandi, M., Fedorova, M., and Conrad, M. (2021). Juggling with Lipids, a Game of Russian Roulette. *Trends Endocrinol. Metab.* 32, 463–473. doi:10.1016/j.tem.2021.04.012

Bersuker, K., Hendricks, J. M., Li, Z., Magtanong, L., Ford, B., Tang, P. H., et al. (2019). The CoQ Oxidoreductase FSP1 Acts Parallel to GPX4 to Inhibit Ferroptosis. *Nature* 575, 688–692. doi:10.1038/s41586-019-1705-2

Brown, A. C. (2017). Liver Toxicity Related to Herbs and Dietary Supplements: Online Table of Case Reports. Part 2 of 5 Series. *Food Chem. Toxicol.* 107, 472–501. doi:10.1016/j.fct.2016.07.001

Canli, Ö., Alankuş, Y. B., Grootjans, S., Vegi, N., Hültner, L., Hoppe, P. S., et al. (2016). Glutathione Peroxidase 4 Prevents Necroptosis in Mouse Erythroid Precursors. *Blood* 127, 139–148. doi:10.1182/blood-2015-06-654194

Chen, J. Q., Chen, Y. Y., Tao, H. J., Pu, Z. J., Shi, X. Q., Zhang, J., et al. (2020). An Integrated Metabolomics Strategy to Reveal Dose-Effect Relationship and Therapeutic Mechanisms of Different Efficacy of Rhubarb in Constipation Rats. *J. Pharm. Biomed. Anal.* 177, 112837. doi:10.1016/j.jpba.2019.112837

Chen, X., Yu, C., Kang, R., Kroemer, G., and Tang, D. (2021). Cellular Degradation Systems in Ferroptosis. *Cell Death Differ.* 28, 1135–1148. doi:10.1038/s41418-020-00728-1

Cheng, Y., Liu, Y., Wang, H., Li, J., Ren, J., Zhu, L., et al. (2013). A 26-week Repeated Dose Toxicity Study of Xian-Ling-Gu-Bao in Sprague-Dawley Rats. *J. Ethnopharmacol.* 145, 85–93. doi:10.1016/j.jep.2012.09.055

Chinese Pharmacopoeia Commission (2020). *Pharmacopeia of the People's Republic of China*. 2020 edition. Beijing, China: China Medical Science and Technology Press.

Coliva, G., Lange, M., Colombo, S., Chervet, J. P., Domingues, M. R., and Fedorova, M. (2020). Sphingomyelins Prevent Propagation of Lipid Peroxidation-LC-MS/MS Evaluation of Inhibition Mechanisms. *Molecules* 25, 1925. doi:10.3390/molecules25081925

Cuykx, M., Rodrigues, R. M., Laukens, K., Vanhaecke, T., and Covaci, A. (2018). *In Vitro* Assessment of Hepatotoxicity by Metabolomics: a Review. *Arch. Toxicol.* 92, 3007–3029. doi:10.1007/s00204-018-2286-9

Dhuriya, Y. K., and Sharma, D. (2018). Necroptosis: a Regulated Inflammatory Mode of Cell Death. *J. Neuroinflammation* 15, 199. doi:10.1186/s12974-018-1235-0

Dixon, S. J., Lemberg, K. M., Lamprecht, M. R., Skouta, R., Zaitsev, E. M., Gleason, C. E., et al. (2012). Ferroptosis: an Iron-dependent Form of Nonapoptotic Cell Death. *Cell* 149, 1060–1072. doi:10.1016/j.cell.2012.03.042

Dixon, S. J., Patel, D. N., Welsch, M., Skouta, R., Lee, E. D., Hayano, M., et al. (2014). Pharmacological Inhibition of Cystine-Glutamate Exchange Induces Endoplasmic Reticulum Stress and Ferroptosis. *Elife* 3, e02523. doi:10.7554/eLife.02523

Doll, S., Proneth, B., Tyurina, Y. Y., Panzilius, E., Kobayashi, S., Ingold, I., et al. (2017). ACSL4 Dictates Ferroptosis Sensitivity by Shaping Cellular Lipid Composition. *Nat. Chem. Biol.* 13, 91–98. doi:10.1038/nchembio.2239

Doll, S., Freitas, F. P., Shah, R., Aldrovandi, M., da Silva, M. C., Ingold, I., et al. (2019). FSP1 Is a Glutathione-independent Ferroptosis Suppressor. *Nature* 575, 693–698. doi:10.1038/s41586-019-1707-0

Duan, L., Guo, L., Wang, L., Yin, Q., Zhang, C. M., Zheng, Y. G., et al. (2018). Application of Metabolomics in Toxicity Evaluation of Traditional Chinese Medicines. *Chin. Med.* 13, 60. doi:10.1186/s13020-018-0218-5

Esteves, F., Campelo, D., Gomes, B. C., Urban, P., Bozonnet, S., Lautier, T., et al. (2020). The Role of the FMN-Domain of Human Cytochrome P450 Oxidoreductase in its Promiscuous Interactions with Structurally Diverse Redox Partners. *Front. Pharmacol.* 11, 299. doi:10.3389/fphar.2020.00299

Florean, C., Song, S., Dicato, M., and Diederich, M. (2019). Redox Biology of Regulated Cell Death in Cancer: A Focus on Necroptosis and Ferroptosis. *Free Radic. Biol. Med.* 134, 177–189. doi:10.1016/j.freeradbiomed.2019.01.008

Forcina, G. C., and Dixon, S. J. (2019). GPX4 at the Crossroads of Lipid Homeostasis and Ferroptosis. *Proteomics* 19, e1800311. doi:10.1002/pmic.201800311

Gao, Y., Xu, G., Ma, L., Shi, W., Wang, Z., Zhan, X., et al. (2021). Icariside I Specifically Facilitates ATP or Nigericin-Induced NLRP3 Inflammasome

Activation and Causes Idiosyncratic Hepatotoxicity. *Cell Commun. Signal* 19, 13. doi:10.1186/s12964-020-00647-1

García-Cortés, M., Robles-Díaz, M., Ortega-Alonso, A., Medina-Caliz, I., and Andrade, R. (2016). Hepatotoxicity by Dietary Supplements: A Tabular Listing and Clinical Characteristics. *Int. J. Mol. Sci.* 17, 537. doi:10.3390/ijms17040537

Gika, H., Virgiliou, C., Theodoridis, G., Plumb, R. S., and Wilson, I. D. (2019). Untargeted LC/MS-based Metabolic Phenotyping (Metabonomics/metabolomics): The State of the Art. *J. Chromatogr. B Anal. Technol. Biomed. Life Sci.* 1117, 136–147. doi:10.1016/j.jchromb.2019.04.009

Gong, Z. G., Hu, J., Wu, X., and Xu, Y. J. (2017). The Recent Developments in Sample Preparation for Mass Spectrometry-Based Metabolomics. *Crit. Rev. Anal. Chem.* 47, 325–331. doi:10.1080/10408347.2017.1289836

Green, R. M., and Flamm, S. (2002). AGA Technical Review on the Evaluation of Liver Chemistry Tests. *Gastroenterology* 123, 1367–1384. doi:10.1053/gast.2002.36061

Huang, Y., Xu, W., and Zhou, R. (2021). NLRP3 Inflammasome Activation and Cell Death. *Cell Mol. Immunol.* 18, 2114–2127. doi:10.1038/s41423-021-00740-6

Iorga, A., Dara, L., and Kaplowitz, N. (2017). Drug-Induced Liver Injury: Cascade of Events Leading to Cell Death, Apoptosis or Necrosis. *Int. J. Mol. Sci.* 18, 1018. doi:10.3390/ijms18051018

Kagan, V. E., Mao, G., Qu, F., Angeli, J. P., Doll, S., Croix, C. S., et al. (2017). Oxidized Arachidonic and Adrenic PEs Navigate Cells to Ferroptosis. *Nat. Chem. Biol.* 13, 81–90. doi:10.1038/nchembio.2238

Koppula, P., Zhang, Y., Zhuang, L., and Gan, B. (2018). Amino Acid Transporter SLC7A11/xCT at the Crossroads of Regulating Redox Homeostasis and Nutrient Dependency of Cancer. *Cancer Commun. (Lond)* 38, 12. doi:10.1186/s40880-018-0288-x

Koppula, P., Zhuang, L., and Gan, B. (2021). Cystine Transporter SLC7A11/xCT in Cancer: Ferroptosis, Nutrient Dependency, and Cancer Therapy. *Protein Cell* 12, 599–620. doi:10.1007/s13238-020-00789-5

Li, J., Cao, F., Yin, H. L., Huang, Z. J., Lin, Z. T., Mao, N., et al. (2020). Ferroptosis: Past, Present, and Future. *Cell Death Dis.* 11, 88. doi:10.1038/s41419-020-2298-2

Li, T., Zhang, J., Wang, P.-J., Zhang, Z.-W., and Huang, J.-Q. (2021). Selenoproteins Protect against Avian Liver Necrosis by Metabolizing Peroxides and Regulating Receptor Interacting Serine Threonine Kinase 1/Receptor Interacting Serine Threonine Kinase 3/Mixed Lineage Kinase Domain-like and Mitogen-Activated Protein Kinase Signaling. *Front. Physiol.* 12, 696256. doi:10.3389/fphys.2021.696256

Liu, C., Fan, H., Li, Y., and Xiao, X. (2016). Research Advances on Hepatotoxicity of Herbal Medicines in China. *Biomed. Res. Int.* 2016, 7150391. doi:10.1155/2016/7150391

Liu, J., Xia, X., and Huang, P. (2020). xCT: A Critical Molecule that Links Cancer Metabolism to Redox Signaling. *Mol. Ther.* 28, 2358–2366. doi:10.1016/j.ymthe.2020.08.021

Liu, W., Chakraborty, B., Safi, R., Kazmin, D., Chang, C. Y., and McDonnell, D. P. (2021). Dysregulated Cholesterol Homeostasis Results in Resistance to Ferroptosis Increasing Tumorigenicity and Metastasis in Cancer. *Nat. Commun.* 12, 5103. doi:10.1038/s41467-021-25354-4

Lu, S. C. (2009). Regulation of Glutathione Synthesis. *Mol. Asp. Med.* 30, 42–59. doi:10.1016/j.mam.2008.05.005

Luo, Y., Gao, F., Chang, R., Zhang, X., Zhong, J., Wen, J., et al. (2021). Metabolomics Based Comprehensive Investigation of Gardeniae Fructus Induced Hepatotoxicity. *Food Chem. Toxicol.* 153, 112250. doi:10.1016/j.fct.2021.112250

Ma, H., He, X., Yang, Y., Li, M., Hao, D., and Jia, Z. (2011). The Genus Epimedium: an Ethnopharmacological and Phytochemical Review. *J. Ethnopharmacol.* 134, 519–541. doi:10.1016/j.jep.2011.01.001

Navarro, V. J., Khan, I., Björnsson, E., Seeff, L. B., Serrano, J., and Hoofnagle, J. H. (2017). Liver Injury from Herbal and Dietary Supplements. *Hepatology* 65, 363–373. doi:10.1002/hep.28813

Phapale, P. (2021). Pharmaco-metabolomics Opportunities in Drug Development and Clinical Research. *Anal. Sci. Adv.* 2, 611–616. doi:10.1002/ansa.202000178

Piao, Y., Liu, Y., and Xie, X. (2013). Change Trends of Organ Weight Background Data in Sprague Dawley Rats at Different Ages. *J. Toxicol. Pathol.* 26, 29–34. doi:10.1293/tox.26.29

Rosa, A. C., Bruni, N., Meineri, G., Corsi, D., Cavi, N., Gastaldi, D., et al. (2021). Strategies to Expand the Therapeutic Potential of Superoxide Dismutase by Exploiting Delivery Approaches. *Int. J. Biol. Macromol.* 168, 846–865. doi:10.1016/j.ijbiomac.2020.11.149

Stockwell, B. R., Jiang, X., and Gu, W. (2020). Emerging Mechanisms and Disease Relevance of Ferroptosis. *Trends Cell Biol.* 30, 478–490. doi:10.1016/j.tcb.2020.02.009

Sullivan, L. B., Martinez-Garcia, E., Nguyen, H., Mullen, A. R., Dufour, E., Sudarshan, S., et al. (2013). The Proto-Oncometabolite Fumarate Binds Glutathione to Amplify ROS-dependent Signaling. *Mol. Cell* 51, 236–248. doi:10.1016/j.molcel.2013.05.003

Sun, M., Zhang, J., Liang, S., Du, Z., Liu, J., Sun, Z., et al. (2021). Metabolomic Characteristics of Hepatotoxicity in Rats Induced by Silica Nanoparticles. *Ecotoxicol. Environ. Saf.* 208, 111496. doi:10.1016/j.ecoenv.2020.111496

Tang, J.-F., Wang, X.-Y., Wen, Q., Tang, S., Sang, F., Li, W.-X., et al. (2017). Idiosyncratic Hepatotoxicity Evaluation of Zhuangguguanjie Wan Mediated by Immune Stress. *Acta Pharm. Sin.* 52, 1033–1040. doi:10.16438/j.0513-4870.2017-0303

Tang, J., Wang, X., Yang, W., Li, W., Li, Y., Bai, Z., et al. (2018). Cytokine Analysis of Zhuangguguanjie Wan-Induced Idiosyncratic Liver Injury Based on Mathematical Modeling. *Acta Pharm. Sin.* 53, 574–584. doi:10.16438/j.0513-4870.2018-0008

Tang, D., Chen, X., Kang, R., and Kroemer, G. (2021). Ferroptosis: Molecular Mechanisms and Health Implications. *Cell Res.* 31, 107–125. doi:10.1038/s41422-020-00441-1

Thévenot, E. A., Roux, A., Xu, Y., Ezan, E., and Junot, C. (2015). Analysis of the Human Adult Urinary Metabolome Variations with Age, Body Mass Index, and Gender by Implementing a Comprehensive Workflow for Univariate and OPLS Statistical Analyses. *J. Proteome Res.* 14, 3322–3335. doi:10.1021/acs.jproteome.5b00354

Tujios, S., and Fontana, R. J. (2011). Mechanisms of Drug-Induced Liver Injury: from Bedside to Bench. *Nat. Rev. Gastroenterol. Hepatol.* 8, 202–211. doi:10.1038/nrgastro.2011.22

Ursini, F., and Maiorino, M. (2020). Lipid Peroxidation and Ferroptosis: The Role of GSH and GPx4. *Free Radic. Biol. Med.* 152, 175–185. doi:10.1016/j.freeradbiomed.2020.02.027

Vabulas, R. M. (2021). Ferroptosis-Related Flavoproteins: Their Function and Stability. *Int. J. Mol. Sci.* 22, 430. doi:10.3390/ijms22010430

Wang, J. B., Kong, W. J., Wang, H. J., Zhao, H. P., Xiao, H. Y., Dai, C. M., et al. (2011). Toxic Effects Caused by Rhubarb (Rheum Palmatum L.) Are Reversed on Immature and Aged Rats. *J. Ethnopharmacol.* 134, 216–220. doi:10.1016/j.jep.2010.12.008

Wang, F., Liu, Y., Yuan, J., Yang, W., and Mo, Z. (2019). Compound C Protects Mice from HFD-Induced Obesity and Nonalcoholic Fatty Liver Disease. *Int. J. Endocrinol.* 2019, 3206587. doi:10.1155/2019/3206587

Wang, H., Liu, C., Zhao, Y., and Gao, G. (2020). Mitochondria Regulation in Ferroptosis. *Eur. J. Cell Biol.* 99, 151058. doi:10.1016/j.ejcb.2019.151058

Wang, Z., Xu, G., Wang, H., Zhan, X., Gao, Y., Chen, N., et al. (2020). Icariside II, a Main Compound in Epimedii Folium, Induces Idiosyncratic Hepatotoxicity by Enhancing NLRP3 Inflammasome Activation. *Acta Pharm. Sin. B* 10, 1619–1633. doi:10.1016/j.apsb.2020.03.006

Wu, W., Wang, T., Sun, B., Liu, D., Lin, Z., Miao, Y., et al. (2019). Xian-Ling-Gu-Bao Induced Inflammatory Stress Rat Liver Injury: Inflammatory and Oxidative Stress Playing Important Roles. *J. Ethnopharmacol.* 239, 111910. doi:10.1016/j.jep.2019.111910

Xie, X., Zhao, Y., Ma, C. Y., Xu, X. M., Zhang, Y. Q., Wang, C. G., et al. (2015). Dimethyl Fumarate Induces Necroptosis in Colon Cancer Cells through GSH Depletion/ROS increase/MAPKs Activation Pathway. *Br. J. Pharmacol.* 172, 3929–3943. doi:10.1111/bph.13184

Xie, Y., Hou, W., Song, X., Yu, Y., Huang, J., Sun, X., et al. (2016). Ferroptosis: Process and Function. *Cell Death Differ.* 23, 369–379. doi:10.1038/cdd.2015.158

Yan, B., Ai, Y., Sun, Q., Ma, Y., Cao, Y., Wang, J., et al. (2021). Membrane Damage during Ferroptosis Is Caused by Oxidation of Phospholipids Catalyzed by the Oxidoreductases POR and CYB5R1. *Mol. Cell* 81, 355. doi:10.1016/j.molcel.2020.11.024

Yang, W. S., and Stockwell, B. R. (2016). Ferroptosis: Death by Lipid Peroxidation. *Trends Cell Biol.* 26, 165–176. doi:10.1016/j.tcb.2015.10.014

Yuan, H., Li, X., Zhang, X., Kang, R., and Tang, D. (2016). Identification of ACSL4 as a Biomarker and Contributor of Ferroptosis. *Biochem. Biophys. Res. Commun.* 478, 1338–1343. doi:10.1016/j.bbrc.2016.08.124

Zhang, A., Sun, H., Yan, G., Wang, P., and Wang, X. (2016). Mass Spectrometry-Based Metabolomics: Applications to Biomarker and Metabolic Pathway Research. *Biomed. Chromatogr.* 30, 7–12. doi:10.1002/bmc.3453

Zhang, L., Zhang, J., Fan, Q., Su, Z., Chen, C., Peng, L., et al. (2018). Hepatoxicity of Epimedii Folium in Rat Model Based on Uniform Design and Regression Analysis. *Chin. J. Exp. Traditional Med. Formulae* 24, 189–197. doi:10.13422/j.cnki.syfjx.20180617

Zhang, Z., Yang, L., Huang, X., and Gao, Y. (2019). Metabolomics Profiling of Polygoni Multiflori Radix and Polygoni Multiflori Radix Preparata Extracts Using UPLC-Q/TOF-MS. *Chin. Med.* 14, 46. doi:10.1186/s13020-019-0268-3

Zhang, T., Tsutsuki, H., Islam, W., Ono, K., Takeda, K., Akaike, T., et al. (2021). ATP Exposure Stimulates Glutathione Efflux as a Necessary Switch for NLRP3 Inflammasome Activation. *Redox Biol.* 41, 101930. doi:10.1016/j.redox.2021.101930

Zhang, L., Xu, A. L., Yang, S., Zhao, B. S., and Wang, T. (2020). *In Vitro* Screening and Toxic Mechanism Exploring of Leading Components with Potential Hepatotoxicity of Herba Epimedii Extracts. *Toxicol Vitro* 62, 104660. doi:10.1016/j.tiv.2019.104660

Zhang, Y., Yu, D., Zhang, J., Bao, J., Tang, C., and Zhang, Z. (2020). The Role of Necroptosis and Apoptosis through the Oxidative Stress Pathway in the Liver of Selenium-Deficient Swine. *Metallomics* 12, 607–616. doi:10.1039/c9mt00295b

Zhong, R., Chen, Y., Ling, J., Xia, Z., Zhan, Y., Sun, E., et al. (2019). The Toxicity and Metabolism Properties of Herba Epimedii Flavonoids on Laval and Adult Zebrafish. *Evid. Based Complement. Altern. Med.* 2019, 3745051. doi:10.1155/2019/3745051

Conflict of Interest: The authors declare that the research was conducted in the absence of any commercial or financial relationships that could be construed as a potential conflict of interest.

Publisher's Note: All claims expressed in this article are solely those of the authors and do not necessarily represent those of their affiliated organizations or those of the publisher, the editors, and the reviewers. Any product that may be evaluated in this article, or claim that may be made by its manufacturer, is not guaranteed or endorsed by the publisher.

frontiers | Frontiers in Pharmacology

REVIEW
published: 19 July 2022
doi: 10.3389/fphar.2022.909363

Biotransformation, Pharmacokinetics, and Pharmacological Activities of Ginsenoside Rd Against Multiple Diseases

Jing Li[1†], Qingxia Huang[1,2†], Yao Yao[1], Peng Ji[1], E. Mingyao[1], Jinjin Chen[1], Zepeng Zhang[1,3], Hongyu Qi[1], Jiaqi Liu[1], Zhaoqiang Chen[1], Daqing Zhao[1], Lei Zhou[4] and Xiangyan Li[1]**

[1]Jilin Ginseng Academy, Key Laboratory of Active Substances and Biological Mechanisms of Ginseng Efficacy, Ministry of Education, Jilin Provincial Key Laboratory of Bio-Macromolecules of Chinese Medicine, Changchun University of Chinese Medicine, Changchun, China, [2]Research Center of Traditional Chinese Medicine, College of Traditional Chinese Medicine, Changchun University of Chinese Medicine, Changchun, China, [3]College of Acupuncture and Tuina, Changchun University of Chinese Medicine, Changchun, China, [4]Department of Pathology, Affiliated Hospital of Changchun University of Chinese Medicine, Changchun, China

OPEN ACCESS

Edited by:
Qi Wang,
Harbin Medical University, China

Reviewed by:
Hyeong-Geug Kim,
Indiana University–Purdue University Indianapolis, United States
Yang Huang,
Guangzhou Medical University, China

***Correspondence:**
Lei Zhou
zhoulei2022@126.com
Xiangyan Li
xiangyan_li1981@163.com

†These authors have contributed equally to this work

Specialty section:
This article was submitted to Ethnopharmacology, a section of the journal Frontiers in Pharmacology

Received: 31 March 2022
Accepted: 01 June 2022
Published: 19 July 2022

Citation:
Li J, Huang Q, Yao Y, Ji P, Mingyao E, Chen J, Zhang Z, Qi H, Liu J, Chen Z, Zhao D, Zhou L and Li X (2022) Biotransformation, Pharmacokinetics, and Pharmacological Activities of Ginsenoside Rd Against Multiple Diseases. Front. Pharmacol. 13:909363. doi: 10.3389/fphar.2022.909363

Panax ginseng C.A. Mey. has a history of more than 4000 years and is widely used in Asian countries. Modern pharmacological studies have proved that ginsenosides and their compounds have a variety of significant biological activities on specific diseases, including neurodegenerative diseases, certain types of cancer, gastrointestinal disease, and metabolic diseases, in which most of the interest has focused on ginsenoside Rd. The evidentiary basis showed that ginsenoside Rd ameliorates ischemic stroke, nerve injury, cancer, and other diseases involved in apoptosis, inflammation, oxidative stress, mitochondrial damage, and autophagy. In this review, we summarized available reports on the molecular biological mechanisms of ginsenoside Rd in neurological diseases, cancer, metabolic diseases, and other diseases. We also discussed the main biotransformation pathways of ginsenoside Rd obtained by fermentation.

Keywords: ***Panax ginseng*** **C.A. Mey., ginsenoside Rd, biotransformation, pharmacokinetics, molecular mechanisms**

HIGHLIGHTS

1) Approximately 120 studies on the use of ginsenoside Rd for the treatment of multiple diseases have been published.
2) This is the first review to report about the biotransformation, pharmacokinetics, and pharmacological effects of ginsenoside Rd.
3) The potential pharmacological mechanisms of ginsenoside Rd have been documented.
4) No specific reviews have been conducted by now.

INTRODUCTION

Panax ginseng C.A. Mey. is a well-known herbal medicine widely used in China, Korea, Japan, and other East Asian countries. At present, the ginseng root and its extract are the most widely used herbal medicine. Modern pharmacological studies have proved that ginsenosides are the main active ingredient of ginseng and have a wide range of pharmacological effects, such as anti-inflammatory

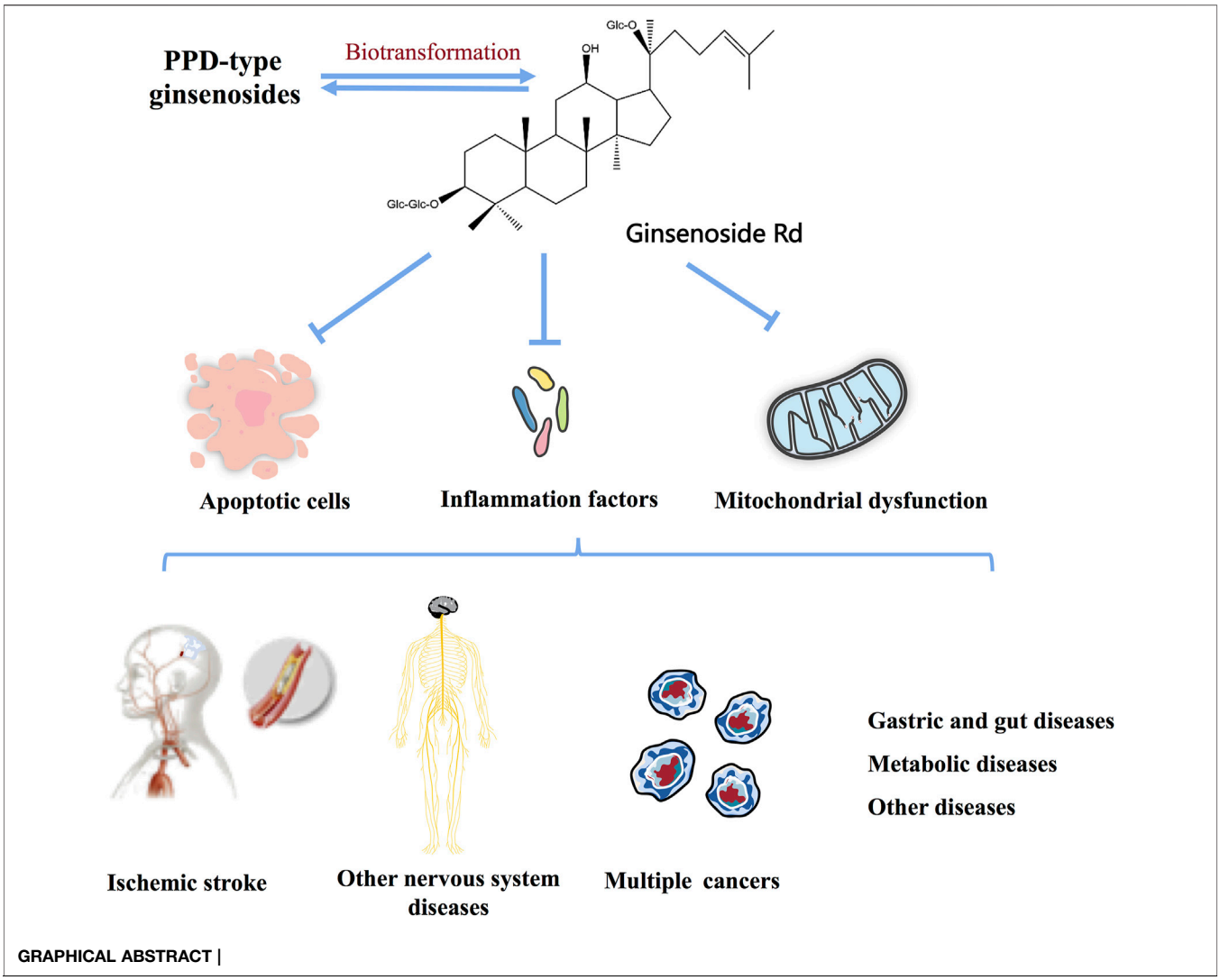

GRAPHICAL ABSTRACT |

(Xu et al., 2021; Yi, 2021), anticancer (Zhang et al., 2021a), and anti-viral (Kang et al., 2021), regulate immunity (Kang et al., 2021), metabolism (Wang et al., 2021a), and improve cardiovascular system (Wang et al., 2021b; Sarhene et al., 2021) and nervous system (Brioschi Guevara et al., 2021) function, whereas most attention has been focused on the ginsenoside Rd.

Ginsenoside Rd, a natural compound extracted from the root of *Panax ginseng* C.A. Mey., is one of the protopanaxadiol (PPD)-type ginsenosides, while the proportion of ginsenoside Rd in ginseng is very low (Liu et al., 2020a). Interestingly, the promising effects of the pretreatment and treatment of ginsenoside Rd on neurological diseases, cancer, gastrointestinal disease, and metabolic diseases have been studied extensively in *in vivo* and *in vitro* models (Guo et al., 2021; Chen et al., 2022; Zhou et al., 2022).

Existing studies related to ginsenoside Rd have shown that various ginsenosides, such as Rb1, Rb2, and Rc, can be transformed into ginsenoside Rd after absorption and metabolism *in vivo* (Park et al., 2010; Shin and Oh, 2016). In addition, Rd can be prepared in a variety of ways based on the in-depth study of biotransformation and the development of modern fermentation technology (He et al., 2019). Based on the above results, we summarized the biotransformation process of other ginsenosides into Rd, thereby hoping to play a positive role in the large-scale industrial production of Rd. In this study, the biotransformation sources, pharmacokinetics, pharmacological effects, and molecular mechanisms of ginsenoside Rd on various systemic diseases in recent years were reviewed, and their therapeutic potential was discussed.

BIOTRANSFORMATION OF GINSENOSIDE RD

Multiple studies have confirmed that ginsenosides can be transformed into ginsenoside Rd using enzymes and bacterial communities and can promote the transformation of ginsenoside

TABLE 1 | Summary of the biotransformation of ginsenoside Rd.

References	Conversion	Source	Enzyme	Optimal conditions	Conversion ratio (%)
Akter and Huq, (2018)	Rb1 to Rd	*Paenibacillus*	MAH-16T	pH 5.0-7.0, 20-40°C	
Fang et al. (2020)	Rb1 to Rd		Pectinase	pH 6, 52.5°C	46.15
Renchinkhand et al. (2020)	Rb1 to Rd	*Dekkera anomala* YAE-1	β-glucosidase	pH 5.0, 40°C, 48 h	
Renchinkhand et al. (2017)	Rb1 to Rd	*Paenibacillus* sp. MBT213	β-glucosidase	pH7.0, 35°C, 14 days	
Hong et al. (2012)	Rb1 to Rd	*Flavobacterium johnsoniae*	β-glucosidase	pH 6.0, 37°C	
Quan et al. (2011)	Rb1 to XVII、Rd to F2 to CK	*Leuconostoc mesenteroides* DC102	Glucosidase	pH6.0–8.0, 30°C, 72 h	
Zhong et al. (2016)	Rb1 to Rd	*Lactobacillus brevis*	β-glucosidase	pH 7.0, 30°C	69
Feng et al. (2016)	Rb1 to Rd	*Aspergillus niger*	TH-10a	pH 5.0, 32°C, 48 h	86
Ye et al. (2010)	Rb1 to Rd	*Paecilomyces bainier* 229-7	β-glucosidase	pH5.0, 28°C, 72 h	89-94.9
Ye et al. (2012)	Rb1 to Rd	*Paecilomyces bainier* 229-7	External calcium regulated β-glucosidase	pH5.0, 28°C, 72 h	92.44
Son et al. (2008)	Rb1 to Rd	*Thermus caldophilus*	β-glucosidase	pH 5.0, 75°C, 18 h	80
Kim et al. (2013a)	Rb1 to Rd	*Microbacterium trichothecenolyticum*	*M.trichothecenolyticum* KCTC 19343	30°C, 24 h	
Zhao et al. (2009)	Rb1 to Rd	*Cladosporium fulvum*	β-glucosidase	pH 5.0, 37°C, 8 days	86
Lin et al. (2015)	Rb1 to Rd	*Aspergillus versicolor* LFJ1403	β-glucosidase	PH 5.0, 30°C, 96 h	85
Shin et al. (2013)	Rc to Rd	*Caldicellulosiruptor saccharolyticus* DSM 8903	α-L-arabinofuranosidase	pH 5.5, 80°C, 30 min	100
Xie et al. (2016a)	Rc to Rd	*Thermotoga thermarum* DSM5069	α-L-arabinofuranosidase	pH 5.0, 85°C, 60 min	99.4
Liu et al. (2013)	Rc to Rd	*Leuconostoc* sp. strain 22-3	α-L-arabinofuranosidase	pH 6.0, 30°C, 20 min	
Zhang et al. (2021b)	Rc to Rd	*Bacillus subtilis* Str. 168	α-L-arabinofuranosidase	pH 5, 40°C, 24 h	90
Kim et al. (2020)	Rb2 to Rd	*Blastococcus saxobsidens*	α-L-arabinopyranosidase	pH 7.0, 40°C, 1 h	
Jung et al. (2014)	F2 to Rd	Ginseng UDP-glycosyltransferases	UDP-glycosyltransferases 94Q2		

Rd into other metabolites (He et al., 2019). We summarized the precursors, metabolites, and transformation conditions of ginsenoside Rd (**Table 1**) (**Figure 1**).

Ginsenoside Rd can be synthesized from ginsenoside Rb1 by the hydrolysis of glucose at C-20 (Akter and Huq, 2018). The β-glucosidase produced by pectinase (Fang et al., 2020), *Dekkera anomala* YAE-1 (Renchinkhand et al., 2020), *Paenibacillus* sp. MBT213 (Renchinkhand et al., 2017), *Flavobacterium johnsoniae* (Hong et al., 2012), *Leuconostoc mesenteroides* DC102 (Quan et al., 2011), and *Lactobacillus brevis* (Zhong et al., 2016) is able to hydrolyze ginsenoside Rb1 (Rb1) and convert it to ginsenoside Rd during the fermentation of the ginseng. In addition, *Aspergillus niger* strain TH-10 (Feng et al., 2016), *Paecilomyces bainier* 229-7 (Ye et al., 2010; Ye et al., 2012), *Thermus caldophilus* GK24 (Son et al., 2008), *Microbacterium trichothecenolyticum* (Kim et al., 2013a), *Cladosporium fulvum* (Zhao et al., 2009), and *Aspergillus versicolor* (Lin et al., 2015) have shown similar effects as those of hydrolases in Rb1.

The *α-L-arabinosidase* (AbpBs) from *Caldicellulosiruptor saccharolyticus* (Shin et al., 2013), *Thermotoga thermarum* DSM 5069 (Xie et al., 2016a), *Leuconostoc* sp. 22-3 (Liu et al., 2013), and *Bacillus subtilis* (Zhang et al., 2021b) converts ginsenoside Rc (Rc) into ginsenoside Rd by attacking the C-20 position of α-linked arabinoside, thereby releasing arabinose (Liu et al., 2013; Zhang et al., 2021b). AbpBs can promote the biotransformation of ginsenoside Rb2 (Rb2) to ginsenoside Rd by attacking C-20, thereby releasing arabinoside (Kim et al., 2020). In addition, enzymes PgUGT74AE2 and PgUGT94Q2, which participate in ginsenoside biosynthesis, transfer two glucose groups from UDP-glucose (UDP-Glc) to the C3 hydroxyl group of ginsenoside compound K (CK) to form ginsenoside Rd (Jung et al., 2014).

β-glucosidase cleaves the glycoside at the C-3 position of ginsenoside Rd and produces the ginsenoside compound CK (Renchinkhand et al., 2020). Ginsenoside M1 is formed by the hydrolysis of the C-3 glucose group in ginsenoside Rd by snailase (Renchinkhand et al., 2017).

PHARMACOKINETICS

Intestinal flora can promote the metabolic transformation of ginseng extract and Rb1 into ginsenoside Rd in rats and can enter the blood for absorption in rats (Kim et al., 2014a). Ginsenoside Rd is distributed in various organs, with the highest content in the lungs, followed by the liver, kidney, heart, and intestine, and the lowest content in the brain (Sun et al., 2012). After taking urine 0–24 h after oral administration and intravenous administration, liquid chromatography-mass spectrometry (LC-MS) is used to confirm that oxidation and

TABLE 2 | Summary of the neuroprotective effects and mechanism of ginsenoside Rd in animal and cell models.

References	Diseases	Inducer	Experimental model	Effects	Mechanism
Zhang et al. (2013a)	Ischemic stroke	MCAO	Male SD rats	GLT-1, PKB/Akt, p-ERK1/2↑ Glutamate↓	Glutamate metabolism
Zhang et al. (2012a)	Ischemic stroke	Glutamate, NMDA	Primary hippocampal cell cultures from SD rat embryos	TUNEL-positive cells, caspase-3, Ca^{2+}↓	Ca^{2+}, apoptosis
Xie et al. (2016b)	Stroke	OGD/Transient MCAO	Adult male primary cortical neuron cells/SD rats	Infarct volume, NR2B subunit, p-Ser-1303, p-Tyr-1472, p-Tyr-1480↓	Hyperphosphorylation of neurons
Zhang et al. (2020a)	Ischemic stroke	OGD/MCAO, CsA	Primary cortical neurons cells, HEK293 cells/Adult male SD rats	Ca^{2+}, NMDA receptor currents, caspase3↓	Apoptosis
Zhang et al. (2012b)	Ischemic stroke	MCAO	Male SD rats	ASIC2a↑ TRPM7, ASIC1a↓	Ca^{2+} overload
Ye et al. (2011b)	Transient ischemic stroke	MCAO	Male SD rats, isolated mitochondria	ETC, aconitase, MMP, Pyruvate↑ ROS, Lactate, caspase-3, Cyto C, AIF↓	Mitochondrial dysfunction, apoptosis
Yang et al. (2016)	Ischemic stroke	MCAO	Male SD rats	NEIL1, NEIL3↑ Cleaved caspase-3↓	mtDNA and nDNA damages, apoptosis
Hu et al. (2013)	Cerebral ischemia	MCAO	Adult male SD rats	PARP-1, NF-κB, AIF↓	Apoptosis, inflammation
Ye et al. (2009)	Cerebral ischemic injury	OGD	Primary hippocampal neurons cells	GSH, GPX,SOD,CAT,MMP↑ ROS, MDA,LDH, GSSG↓	Oxidative stress, apoptosis
Ye et al. (2011c)	Transient focal ischemia in the aged brain	MCAO	Male C57BL/6 mice	Mitochondrial complex, MMP, CAT, SOD, GPX, GST↑ MDA, protein carbonyl concentration, ROS, mitochondrial aconitase↓	Mitochondrial dysfunction oxidative stress
Zhang et al. (2014)	Ischemic stroke	OGD/MCAO	Primary culture of neurons/Male SD rats	p-AKT, GSK-3β↑ p-tau, S199/202, PHF-1↓	p-tau
Liu et al. (2015a)	Stroke	OGD/R/Transient MCAO followed by reperfusion	PC12 cells/Male SD rats	p-AKT, p-ERK, VEGF, BDNF↑	Apoptosis
Hou et al. (2017)	TMT intoxication	Trimethyltin	Primary hippocampal neuron/Male ICR mice	Bcl-2↑ Bax, caspase-3↓	Apoptosis
Ye et al. (2011d)	Transient ischemic stroke	MCAO	Male SD rats	CAT, SOD 1 and 2, GR, GSH/GSSG↑ 2,3- and 2,5-DHBA, 8-OHdG positive cells, 4-HNE, MDA, AGEs↓	Oxidative stress, inflammation
Zhang et al. (2020b)	Transient forebrain ischemia	MCAO	Male SD rats	IκB-α↑ 20S proteasome, NF-κB, p65, matrix MMP-9↓	Inflammation
Zhang et al. (2016)	Ischemic stroke	OGD or LPS/MCAO	BV2 cells/Adult male SD rats	IL-1β, IL-6, TNF-α, IFN-γ, p-IκBα↓	Inflammation
Wu et al. (2016)	Ischemic stroke	NGF	PC12 cells	p-ERK1/2, p-AKT GAP-43↑	NGF
Ye et al. (2008)	Oxidative damage	H_2O_2	PC12 cells	SOD, GPX, MMP↑ LDH, ROS, MDA,↓	Oxidative stress, mitochondrial dysfunction
Ren et al. (2021)	GBS	Peripheral nerve antigen $P0_{180–199}$ peptide, Pertussis toxin (PTX)	Male C57 BL/6 mice	Non-classical $Ly6C^{lo}$ monocytes Nr4a1↑ IL-12, IL-1β, TNF- α, IL-6, $CD45+Ly6G^{+}$↓	Immunization, inflammation
Liu et al. (2015b)	Parkinson disease	MPP^{+}	SH-SY5Y cells/C57BL/6J mice	SOD, GPX, MMP, complex I, ATP, Bcl-2, p-Akt↑ LDH, ROS, MDA, Bax↓	Oxidative stress, mitochondrial dysfunction
Liu et al. (2015c)	Alzheimer's disease	$Aβ_{25-35}$	Primary cultured hippocampal neurons cells	SOD, GSH-Px, Bcl-2 mRNA↑ ROS, Bax mRNA, Caspase-3, Cyt C mRNA↓	Oxidative stress, Neuronal apoptosis
Liu et al. (2015d)	Alzheimer's disease		APP transgenic mice	IL-1β, IL-6, TNF-α, S100β mRNA, NF-κB p65↓ IL-10↑	Inflammation
Kim et al. (2014b)	Neurodegenerative diseases		Neuro2a cells	ChAT, VAChT, ACh, MAP-2, p75, p21, TrkA↑	Cholinergic markers
Li et al. (2013)	Alzheimer's disease		APP transgenic mice	Ser9, PP-2A↑	p-tau

(Continued on following page)

TABLE 2 | (*Continued*) Summary of the neuroprotective effects and mechanism of ginsenoside Rd in animal and cell models.

References	Diseases	Inducer	Experimental model	Effects	Mechanism
				GSK-3β, Tyr216↓	
Li et al. (2011a)	Alzheimer's disease	Okadaic Acid	Adult male SD rats/ Cortical neurons cells	PP-2A↑ Tau↓	Tau
Li et al. (2021)	Alzheimer's disease		APP transgenic mice	P35↑ Tau, P25↓	p-tau
Yan et al. (2017)	Alzheimer's disease	Ovariectomy/Inhibitor	Adult female rats/HT22 hippocampal neuronal cells	BACE1, Aβ↓ sAPPα, ADAM↑	Activating estrogen-like activity
Zhu et al. (2014)	Multiple sclerosis	Experimental autoimmune encephalomyelitis	6-8 weeks female C57 BL/6 mice	IL-4, BDNF, NGF↑ IFN-γ↓	Blood–brain barrier, inflammation
Jin et al. (2020a)	Multiple sclerosis	Experimental autoimmune encephalomyelitis	Splenocyte/6-8 weeks C57BL/6 mice	TGF-β, IL-10, Treg, Foxp3↑ IL-6, IL-17, RORγt, Jak1, Jak2,STAT↓	Inflammation, autoimmunity
Cong and Chen, (2016)	Spinal cord injury	T8 laminectomy and a spinal contusion injury	Adult female SD rats	MDA, TNF-α, IL-1β, IL-6, Bax, GSK, SOD, Bcl-2↑ cleaved-caspase 3, p-ERK, p-JNK, p-p38↓	Oxidative stress, inflammation, apoptosis
Zhou et al. (2014)	Paraplegia	Ca^{2+}	Isolated spinal cord mitochondria/Male C57BL/6J mice	p-AKT, p-ERK↑ Cyto C↓	Mitochondrial dysfunction
Wang et al. (2014)	Delayed paralysis	Occlusion of the abdominal aorta for 1 h	Female SD rats	Caspase 3, ASK1, JNK↓	Apoptosis
Wang et al. (2020)	Cognitive impairment	Respiration in a transparent plexiglas restrainer with many air holes to for 10 h	Male C57BL/6J mice	SOD, CAT, GSH, GPX, p-PI3K, p-CREB, BDNF, TrkB↑ TNF-α, IL-6, p-AKT↓	Oxidative stress, inflammation, neurotrophic factors
Wang et al. (2013a)		Lead (Pb) exposure	Retired breeder SD rats	IL-1β, IL-6, TNF-α↓	Inflammation

Abbreviations: CsA, cyclosporin A; ETC, mitochondrial electron transport chain; CAT, catalase; SOD, superoxide dismutase; GPX, glutathione peroxidase; GR, glutathione reductase; GSH, glutathione; GSSG, glutathione disulfide; 8-OHdG, 8-hydroxy-deoxyguanosine; 4-HNE, 4-hydroxynonenal; MDA, malondialdehyde; AGEs, advanced glycosylation end products; NGF, nerve growth factor; PTX, pertussis toxin; Nr4a1, nuclear receptor subfamily 4 group A member 1; ChAT, choline acetyltransferase; VAChT, vesicular acetylcholine transporter; ACh, acetylcholine.

glycosylation (Yang et al., 2006a; Yang et al., 2007a) are the main metabolic pathways of ginsenoside Rd in rats. The absolute bioavailability of Rd in dogs is 0.26% (Wang et al., 2007). As in clinical trials, ginsenoside Rd shows linear pharmacokinetics, is well tolerated in the dose range of 10–75 mg after an intravenous administration, and is slowly cleared from plasma, and the elimination rate does not change after repeated administration (Zeng et al., 2010).

GINSENOSIDE RD TARGETS MULTIPLE DISEASES

Ischemic Stroke

In ischemic stroke, ginsenoside Rd plays a neuroprotective role by restoring mitochondrial function, reducing neuronal apoptosis, and eliminating neuroinflammation (**Figure 2**). As for the therapeutic window study, ginsenoside Rd shows an obvious neuroprotective effect in the middle cerebral artery occlusion (MCAO) model (Ye et al., 2011a). Importantly, the results of a clinical trial showed that ginsenoside Rd has a positive effect on the prognosis of acute ischemic stroke (Liu et al., 2012).

In Ca^{2+} influx and mitochondrial dysfunction, ginsenoside Rd, a potential Ca^{2+} channel blocker (Li et al., 2010), significantly reduces the burst of glutamate by increasing the expression of glutamate transporter-1 (GLT-1) and inhibits the channels of Ca^{2+} influx (Zhang et al., 2013a) to protect the rat hippocampal neurons (Zhang et al., 2012a). Similar to a calcineurin inhibitor, ginsenoside Rd exerts a neuroprotective effect by inhibiting the elevation of N-methyl-D-aspartate (NMDA) receptors and the hyperphosphorylation of the N-methyl-D-aspartate receptor 2B (NR2B) subunit in the MCAO model and oxygen–glucose deprivation (OGD) cultured neurons (Xie et al., 2016b; Zhang et al., 2020a). Ginsenoside Rd pretreatment exerts neuroprotective effects by inhibiting the Ca^{2+} overload and specificity attenuated the expression of transient receptor potential melastatin (TRPM) 7 and acid-sensing ion channel (ASIC) 1a while promoting ASIC2a expression following focal ischemia (Zhang et al., 2012b). Remarkably, the results of a clinical trial based on Ca^{2+} disorder and subsequent neurotoxicity induced by acuteischemic stroke, ginsenoside Rd can be considered a calcium channel antagonist and a neuroprotectant (Liu et al., 2009). As for mitochondrial dysfunction, ginsenoside Rd markedly protects the mitochondria, as indicated by regulating enzyme activity, reducing mitochondrial hydrogen peroxide production and depolarizing mitochondrial membrane potential (MMP), decreasing reactive oxygen species (ROS) production in isolated mitochondria from Sprague–Dawley (SD) rats (Ye et al., 2011b), and reducing the mitochondrial DNA (mtDNA) and nuclear DNA (nDNA) damage and cell apoptosis in MCAO-induced ischemic stroke model (Hu et al., 2013; Yang et al., 2016).

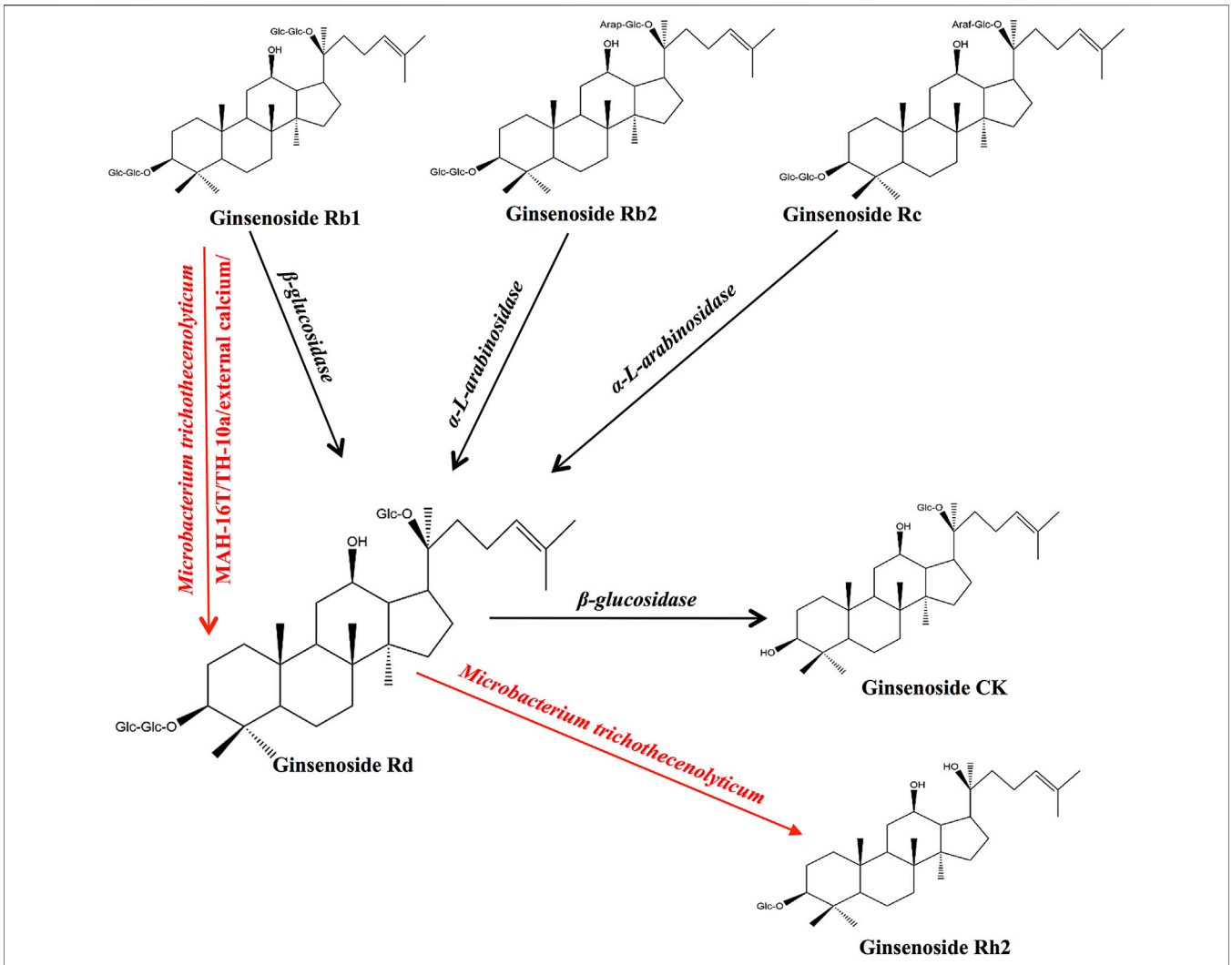

FIGURE 1 | Biotransformation and pharmacokinetics of ginsenoside Rd *in vivo*.

These findings are also confirmed in primary cultured hippocampal neuron cells (Ye et al., 2009). In addition, in elderly stroke mice, ginsenoside Rd can play an equivalent neuroprotective role in elderly transient focal ischemic mice by regulating lipid peroxide accumulation, mitochondrial complex activity, and MMP (Ye et al., 2011c).

As far as apoptosis is concerned, ginsenoside Rd may reduce cerebral ischemia-induced tau phosphorylation by decreasing the activity of glycogen synthase kinase-3β (GSK-3β) and enhancing the activity of protein kinase B (PKB/AKT) (Zhang et al., 2014). In PC12 cells with OGD/reperfusion (OGD/R) and SD rats with ischemia/reperfusion (I/R) injury, ginsenoside Rd significantly limits the expression of vascular endothelial growth factor (VEGF), brain-derived neurotrophic factor (BDNF), and the phosphatidylinositol 3-kinase (PI3K)/AKT and ERK1/2 pathways (Liu et al., 2015a). As a neuroprotective agent ginsenoside Rd also prevents trimethyltin (TMT)-induced neurotoxicity and significantly reduces neuronal loss in TMT-induced hippocampal dysfunction and active astrocytes via regulation of B-cell lymphoma-2 (Bcl-2), Bcl-2-like protein 4, and caspase-3 (Hou et al., 2017). Taken together, ginsenoside Rd has neuroprotective effects via mitogen-activated protein kinase (MAPK)/ERK-, PI3K/AKT, PI3K/AKT/GSK-3β, and ERK1/2-dependent pathways.

For inflammation, ginsenoside Rd inhibits ischemic stroke-indeced neuronal death and inflammation by inhibiting cleaved poly adenosine diphosphate-ribose polymerase-1(PARP-1) activity, levels of poly (ADP-ribose), sequential apoptosis-inducing factor (AIF) translocation, and nuclear factor kappa-light-chain-enhancer of activated B cells (NF-κB) nuclear accumulation (Hu et al., 2013). Postischemic syntheses of two damaging enzymes, cyclooxygenase-2 (COX-2) and inducible nitric oxide synthase (iNOS), are also significantly inhibited by ginsenoside Rd treatment. Ginsenoside Rd reduces free radical generation during I/R and suppresses oxidative damage and inflammatory injury (Ye et al., 2011d). As a proteasome-related compound, ginsenoside Rd protects against MCAO-induced ischemic brain injury by inhibiting the proteasome

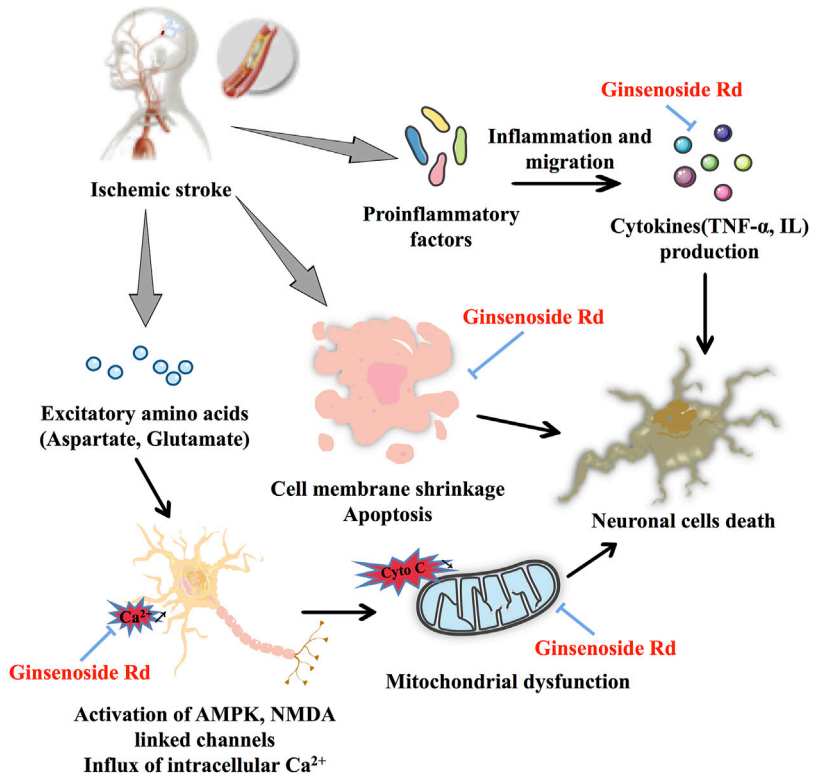

FIGURE 2 | Protective effect of ginsenoside Rd on ischemic stroke.

activity and NF-κB/matrix metalloproteinase-9 (MMP-9) signal pathway (Zhang et al., 2020b). Ginsenoside Rd inhibits MCAO-induced microglial activation, decreases the expression levels of nuclear factor of kappa light polypeptide gene enhancer in B cell inhibitor, alpha (IκBα) phosphorylation and NF-κB nuclear translocation within a short time, and has fewer side effects than glucocorticoids (Zhang et al., 2016).

Other Nervous System Diseases

Ginsenoside Rd has a significant neuroprotective effect on a variety of neurological diseases, which may be related to its promotion of stem cell proliferation (Shi et al., 2005) and differentiation into astrocytes (Lin et al., 2012). Ginsenoside Rd may promote neurite outgrowth by upregulating growth-associated protein of 43 kDa (GAP-43) expression via ERK- and ARK-dependent signaling pathways in NGF-induced PC12 cells (Wu et al., 2016).

In H_2O_2-induced PC12 cells, ginsenoside Rd, as a neuroprotective agent, has neuroprotective effects on neurodegenerative diseases (Ye et al., 2008). In the converting monocyte phenotype and macrophages of the Guillain–Barre syndrome (GBS) mouse model, ginsenoside Rd attenuates experimental autoimmune neuritis (Ren et al., 2021). Ginsenoside Rd can regulate MMP by decreasing intracellular ROS and enhancing the activity of antioxidant enzymes and mitochondrial complex, thereby increasing intracellular ATP levels and ultimately reducing 1-methyl-4-phenylpyridinium (MPP^+)-induced cell death in Parkinson's disease (PD) (Liu et al., 2015b). Meanwhile, in the $A\beta_{25-35}$-induced neuronal damage model, apoptosis and oxidative stress are ameliorated by ginsenoside Rd by regulating antioxidant capacity and the production of apoptotic proteins (Liu et al., 2015c). Learning and memory abilities can be improved in ginsenoside Rd-pretreated APP transgenic mice by significantly suppressing the NF-κB pathway to reduce the generation of proinflammatory factors (Liu et al., 2015d). Ginsenoside Rd-mediated neuroprotective effects against Alzheimer's disease (AD) progression play a significant role in Neuro2a cells (Kim et al., 2014b). Ginsenoside Rd pretreatment can inhibit tau protein phosphorylation by maintaining a balance of GSK-3β, cyclin-dependent kinase 5 (CDK5/P25), and protein phosphatase 2A (PP-2A) (Li et al., 2013) to inhibit tau phosphorylation of tau protein at Ser199/202, Ser396, or Ser404 in okadaic acid-induced rats, APP transgenic mice, and cortical neurons to increase PP-2A activity for protection against AD (Li et al., 2011a; Li et al., 2021), respectively. Moreover, ginsenoside Rd increases the soluble amyloid-β precursor protein α (sAPPα) level and reduces extracellular Aβ to enhance the cognitive and memory functions of ovariectomy rats (Yan et al., 2017).

In experimental autoimmune encephalomyelitis, ginsenoside Rd exerts a neuroprotective role by regulating the immune response and inflammatory reaction via a signal pathway of IFN-g/IL-4, BDNF/NGF (Zhu et al., 2014), and Foxp3/RORγt/JAK2/STAT3 (Jin et al., 2020a). In spinal cord injury (SCI) models, ginsenoside Rd shows

TABLE 3 | Summary of the effects and mechanisms of ginsenoside Rd on cell and animal models of multiple cancers.

References	Diseases	Experimental model	Effects	Mechanism
Tian et al. (2020)	Gastric cancer	MKN-45, SGC-7901 cells	Caspase-3, caspase-9↑ Cyclin D1↓	Apoptosis
Kim et al. (2013b)	Gastric cancer	AGS cells	Caspase-3, caspase8, PARP↑	Apoptosis
Chian et al. (2019)	NSCLC	A549 NSCLC cells	NRF2↓	Proliferation
Gu et al. (2019)	Glioblastoma	U251 cells	Caspase-3↑ Bcl-2, hTERT↓	Apoptosis
Liu et al. (2020b)	Glioblastoma	U251 cells, H4 (HTB148) cells, U87 MG cells	miR-144-5p, TLR2↑ Toll-like receptor 2↓	Proliferation
Phi et al. (2019)	Colorectal cancer	Human CRC cell, HT29 cells/SW620, NSG mice	Smad2↓	Apoptosis
Zhang et al. (2017)	Breast cancer	HUVECs, MDA-MB-231 cells/Athymic nude mice	Bax, caspase-3, HIF1-α↑ Bcl-2↓	Apoptosis
Kim, (2013)	Breast cancer	AGS cells, MCF-7 cells	Caspase-3↑	Apoptosis
Wang et al. (2016)	Breast cancer	4T1 cells, MDA-MB-231cells/Female BALB/c mice	Smad2↑ miR-18a↓	Attenuates metastasis
Pokharel et al. (2010)	Breast cancer	MCF-7/ADR cells	MDR1↓	Resistance
Yang et al. (2006b)	Cervical cancer	HeLa cells	Bax↑ Bcl-2↓	Apoptosis
Yang et al. (2021a)	Hepatocellular carcinoma	HepG2 cells/Male BALB/c nude mice		Proliferation, apoptosis
Yoon et al. (2012)	Hepatocellular carcinoma	HepG2 cells	MMP-1, MMP-2, MMP-7↓	Blocking MAPK signaling and inducing the formation of focal adhesions

anti-inflammatory effects consistent with dexamethasone that could significantly decrease the biomarkers of apoptosis, inflammation, oxidative damage factor, and repaired damaged mitochondria; particularly, there is no obvious difference in terms of dexamethasone in anti-inflammatory (Zhou et al., 2014; Cong and Chen, 2016), and these effects depended on the ASK1/JNK pathway (Wang et al., 2014). In the pathology of noise-induced hearing loss (NIHL), ginsenoside Rd could alleviate the apoptosis and oxidative stress damage on neuron cells by activating the SIRT1/PGC-1α signaling pathway (Chen et al., 2020). In addition, ginsenoside Rd treatment effectively eliminates the oxidative injury and the production of proinflammatory factors and peroxides in the chronic restraint stress (CRS) paradigm (Wang et al., 2020). Ginsenoside Rd pretreatment may be neuroprotective in old rats following acute Pb exposure through limited microglial activation and maintained neural stem cell proliferation (Wang et al., 2013a).

To summarize, ginsenoside Rd can play a significant role in neuron damage by inhibiting the production of excitatory amino acids, reducing the intracellular Ca^{2+} influx mediated by the NMDA pathway, changing the neurotoxicity of Ca^{2+} to mitochondrial function damage, and regulating apoptosis-inducing and neuroinflammatory factors (**Table 2**).

Cancer

As indicated in **Table 3** and **Figure 3**, ginsenoside Rd can inhibit the proliferation of various cancer cells by participating in the apoptotic pathway. As a potential therapeutic and specific 26S proteasome inhibitor, ginsenoside Rd plays an important role in anticancer therapy by targeting 26S proteasome (Chang et al., 2008).

Ginsenoside Rd can appreciably inhibit the proliferation of gastric cancer cells and can stimulate apoptosis by downregulating cyclin D1, thereby inducing cell cycle arrest in the G0/G1 phase and enhancing the expression of caspase-3 and caspase-9 and the ratio of Bax/Bcl-2 (Tian et al., 2020). After heat processing, the anticancer activity of deglycosylated Rd could be improved via the apoptotic pathway for AGS cells (Kim et al., 2013b).

In non-small-cell lung cancer (NSCLC), ginsenoside Rd, as a therapeutic drug, inhibits the nuclear factor erythroid 2-associated factor 2 (NRF2) pathway, and the synergistic effect of ginsenoside Rd in A549 and cisplatin (DDP)-resistant A549 cell lines (A549/DDP) can be weakened by knocking out NRF2 (Chian et al., 2019). As for glioblastoma, ginsenoside Rd decreases the proliferation of human glioma U251 cells and promotes apoptosis by downregulating the expression of hTERT and Bcl-2, upregulating the expression of the caspase-3 level, and inhibiting the telomerase activity of U251 cells (Gu et al., 2019). Ginsenoside Rd inhibits the proliferation and migration of glioblastoma cells by decreasing the expression of tumor-suppressor Mir-144-5p and promoting the expression of the target of Mir-144-5p toll-like receptor 2 (Liu et al., 2020b). In colorectal cancer cells, ginsenoside Rd, a therapeutic agent, targets epidermal growth factor receptor (EGFR)/SOX2 signaling (Phi et al., 2019).

Ginsenoside Rd also plays a crucial role in breast cancer. In MDA-MB-231 cell xenografted mice, ginsenoside Rd treatment inhibits the activation of PI3K, AKT, mammalian target of rapamycin (mTOR), and p70S6K in cells and decreases the expression of hypoxia-inducible factor 1-α (HIF1-α) (Zhang et al., 2017). In MCF-7 cells, ginsenoside Rd inhibits the proliferation of

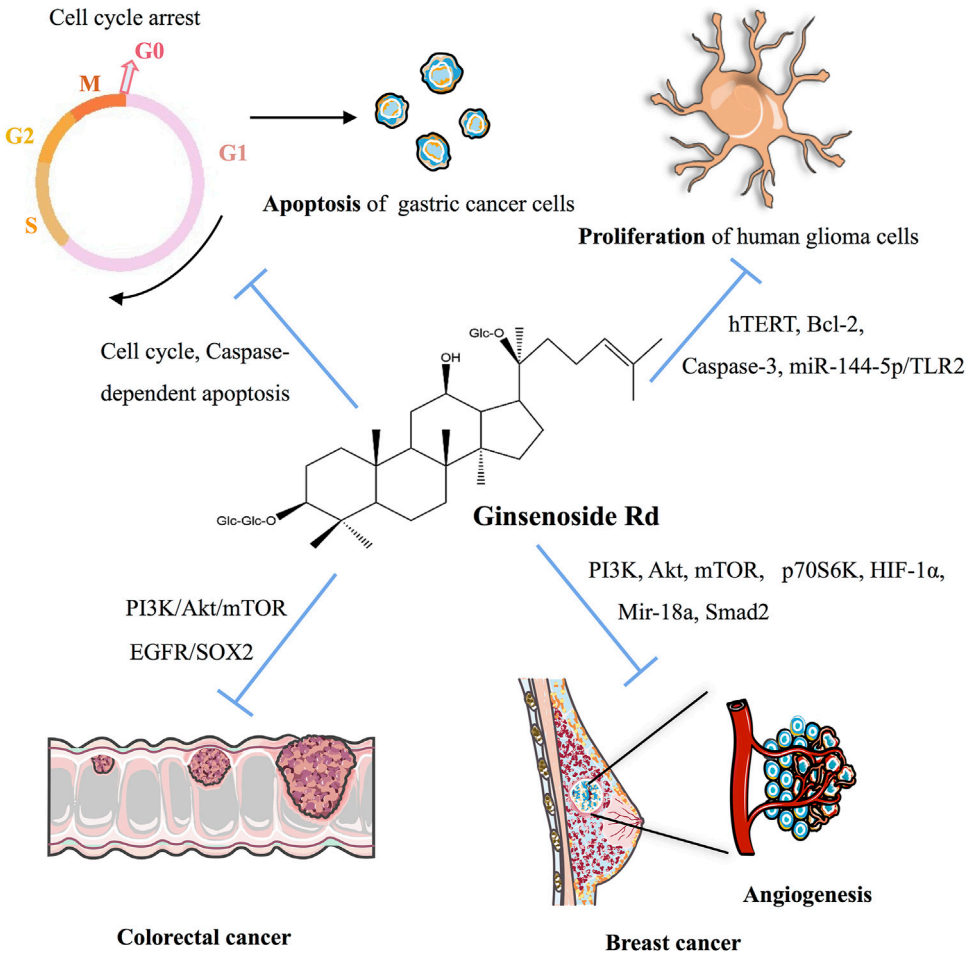

FIGURE 3 | Molecular mechanism of ginsenoside Rd on anticancer activity in multiple cancers.

MCF-7 cells by enhancing caspase-3 activity, mitochondrial depolarization, and sub-G1 populations (Kim, 2013). In 4T1 cells, the expression of Mir-18a and Smad2 decreases with ginsenoside Rd treatment (Wang et al., 2016). Furthermore, ginsenoside Rd promotes the ubiquitination of MDR1 and inhibits doxorubicin resistance in MCF-7/ADR cells (Pokharel et al., 2010). In cervical cancer, ginsenoside Rd treatment in HeLa cells upregulates Bax expression, downregulates Bcl-2 expression, decreases the mitochondrial transmembrane potential, activates the caspase-3 pathway, significantly inhibits proliferation, and induces apoptosis (Yang et al., 2006b).

Finally, in HepG2 cells and the HepG2 cell-injected nude mice-induced hepatocellular carcinoma model, the combination of CA4P and ginsenoside Rd has synergistic antitumor effects via the PI3K/AKT/mTOR signaling pathway-related inhibition of HIF-1α (Yang et al., 2021a). HepG2 cells treated with ginsenoside Rd noticeably promoted matrix metalloproteinases' (MMPs) activation, and MAPK signaling pathways were involved in cancer cell migration, thereby suggesting that ginsenoside Rd inhibits the activity of HepG2 cells in a dose-dependent and time-dependent manner (Yoon et al., 2012).

Gastric and Gut

In a sodium dextran sulfate (DSS)-induced colitis model, ginsenoside Rd reduces DSS-induced colonic pathology via the adenosine 5′-monophosphate-activated protein kinase/Unc-51 like autophagy activating kinase 1 (AMPK/ULK1)-induced autophagy signaling pathway and the inhibition of the production of proinflammatory cytokines (IL-1β, TNF-α, and IL-6) in serum and colon tissues (Liu et al., 2018). In irradiation-induced intestinal epithelial cells, ginsenoside Rd reduces apoptosis by activating a pathway of PI3K/AKT, inactivates MEK, and inhibits a mitochondria/caspase pathway (Tamura et al., 2008). Meanwhile, in 2,4,6-trinitrobenzenesulfonic acid (TNBS)-induced ulcerative colitis model, ginsenoside Rd showed obvious anti-inflammatory activity by inhibiting neutrophil infiltration, regulating apoptosis signal and oxidative stress (Yang et al., 2012a), reduced the accumulation of leukocytes, and downregulated multiple proinflammatory cytokines (Yang et al., 2012b).

Metabolic Diseases

Laboratory data of ginsenoside Rd suggest that it has effects on multiple metabolic diseases. The browning of white adipose tissue

induced by cold stress and cAMP levels are increased by ginsenoside Rd. In particular, Rd alleviates obesity and insulin resistance by upregulating thermogenesis through the cAMP/protein kinase A (PKA) signaling pathway (Yao et al., 2020). In fast-food diet-induced non-alcoholic fatty liver disease (NAFLD), fermented ginsenoside Rd with *Cordyceps militaris* regulates lipid metabolism and the inflammatory response via mTORC1 signaling (Choi et al., 2019). Ginsenoside Rd inhibits the progress of the death of islet transplantation by decreasing the apoptosis of the islet cells (Kaviani et al., 2019). In the atherosclerosis process, ginsenoside Rd decreases oxidized low-density lipoprotein (Ox-LDL) and cholesterol by inhibiting Ca^{2+} influx (Li et al., 2011b). In diabetic db/db mice and mesangial cells, pectin-lyase-modified ginsenoside Rd relieves diabetic nephropathy via alleviated ROS production (Jung et al., 2021).

Other Diseases

Ginsenoside Rd has positive effects on skin injury, osteoporosis, kidney injury, vessel injury, heart injury, lung injury, aging, and inflammation. In animal wound models, ginsenoside Rd significantly increases wound healing by promoting the proliferation and migration level of keratinocyte progenitor cells (KPCs) and human dermal fibroblasts (HDFs) (Kim et al., 2013c). Ginsenoside Rd also has a positive effect on rejection caused by a transplant skin allograft (Wang et al., 2012a). Beyond that, ginsenoside Rd, as an antiosteoporotic agent, promotes differentiation and mineralization in osteoblastic MC3T3-E1 cells (Kim et al., 2012). In animal models of renal I/R injury and cultured proximal tubule cells, ginsenoside Rd has a protective effect by inhibiting inflammation and regulating biochemical indexes of renal function (Yokozawa et al., 1998; Ren et al., 2016). In addition, ginsenoside Rd downregulates NF-κB and the expression of iNOS and COX-2 in lipopolysaccharide (LPS)-induced Institute of Cancer Research (ICR) mice, and RAW264.7 cells were suppressed (Kim et al., 2013d). In the nicotine-induced vascular endothelial injury model, ginsenoside Rd plays an important role in the prevention of cardiovascular diseases via participation in NO signaling and regulates platelet and vascular function (Zhang et al., 2020c). Ginsenoside Rd upregulates Cyto C release and caspase-9/caspase-3 activation and decreases the MMP and the ratio of Bcl-2/Bax via the mitochondria-dependent pathway in H_2O_2-induced apoptosis in basilar artery smooth muscle cells (BASMCs) (Li et al., 2012). Furthermore, ginsenoside Rd could relieve the cisplatin-induced kidney injury (Yokozawa and Liu, 2000; Yokozawa and Dong, 2001) and kidney proximal tubules cephaloridine injury under cephaloridine treatment (Yokozawa and Dong, 2001). In an adrenocorticotrophic hormone (ACTH)–induced corticosterone secretion cell model, ginsenoside Rd inhibits ACTH-induced corticosterone production by inhibiting the MC2R-cAMP/PKA/cyclic AMP response element binding (CREB) pathway in adrenocortical cells (Jin et al., 2020b). In myocardial I/R-induced rats and simulated I/R-induced primary neonatal rat cardiomyocyte models, ginsenoside Rd promotes cardioprotection via the activation of AKT/GSK-3b signaling (Wang et al., 2013b). In addition, ginsenoside Rd can protect against LPS-induced acute lung injury by inhibiting the PI3K/AKT signaling pathway (Yang et al., 2021b). Other studies have indicated that ginsenoside Rd can significantly enhance the survival time of *Caenorhabditis elegans* via lipid metabolism and the activation of the stress response signaling pathway (Yu et al., 2021) and can alleviate the oxidative damage caused by aging in senescence-accelerated mice (Yokozawa et al., 2004). Finally, the anti-inflammatory activity of ginsenoside Rd is well documented, is considered to be associated with its antioxidant effects (Kim et al., 2007; Zhang et al., 2013b), and selectively produces prostaglandin E2 (PGE2) by activating the CCAAT/enhancer binding protein (C/EBP) and CREB to express COX-2 (Jeong et al., 2007). Ginsenoside Rd exerts anti-inflammation effects in carrageenan-induced inflammation rats via the inhibition of the NF-κB signaling pathway (Wang et al., 2012b) and in ovalbumin-induced allergic rhinitis mice by regulating multiple inflammatory factors (Kim et al., 2019) and elicits a Th1 and Th2 immune responses (Yang et al., 2007b). Ginsenoside Rd enhances the Th1 response to surface mannan extract in mice, which protects mice from disseminated *candida* infection by stimulating higher titers of Th1 antibodies and a Th1-dominated immune response (Han and Rhew, 2013).

CONCLUSION AND PERSPECTIVE

As a widely used herbal medicine, ginseng appears in the form of dietary supplements nowadays. Available evidence suggests that the antiapoptotic, antioxidant, and anti-inflammatory activities, which suppress the calcium influx of ginsenoside Rd, may have an important role in the neuroprotective and anticancer effects. Ginsenoside Rd play a crucial role in neuroprotective, anticancer effects, metabolism, and other diseases by regulating PI3K/AKT, inhibiting Cyto C released and caspase activation, and regulating the release of inflammatory factors, which play a crucial role in neuroprotective, anticancer effects, metabolism, and other diseases.

In addition, ginsenoside Rd has potential therapeutic effects on regulating metabolism and in multiorgan protection. However, attributable to the shortage of clinical studies on ginsenoside Rd, it is difficult to make a clear decision. In addition to exploring its various activities, it is suggested to verify existing activities in a deeper mechanism, design clinical trials to prove its safety and effectiveness, and obtain a more extensive clinical application.

AUTHOR CONTRIBUTIONS

JnL, QH, and YY collected, analyzed, and reviewed the literature and wrote the main manuscript; PJ, JC, ME, ZZ, HQ, JaL, and ZC added/checked references and assembled figures/tables; DZ and LZ revised the manuscript; and XL and LZ designed and supervised the final version of the manuscript. All authors have read and agreed to the published version of the manuscript.

FUNDING

This work was supported by the National Natural Science Foundation of China (U19A2013, 82104432), the National Key Research and Development Program of China (2017YFC1702103), and the Science and Technology Development Plan Project of Jilin Province (202002053JC, 20200201419JC).

REFERENCES

Akter, S., and Huq, M. A. (2018). Biological Synthesis of Ginsenoside Rd Using Paenibacillus Horti Sp. Nov. Isolated from Vegetable Garden. *Curr. Microbiol.* 75, 1566–1573. doi:10.1007/s00284-018-1561-6

Brioschi Guevara, A., Bieler, M., Altomare, D., Berthier, M., Csajka, C., Dautricourt, S., et al. (2021). Protocols for Cognitive Enhancement. A User Manual for Brain Health Services-Part 5 of 6. *Alz Res. Ther.* 13, 172. doi:10.1186/s13195-021-00844-1

Chang, T. L., Ding, H. Y., and Kao, Y. W. (2008). Role of Ginsenoside Rd in Inhibiting 26S Proteasome Activity. *J. Agric. Food Chem.* 56, 12011–12015. doi:10.1021/jf801427e

Chen, X. M., Ji, S. F., Liu, Y. H., Xue, X. M., Xu, J., Gu, Z. H., et al. (2020). Ginsenoside Rd Ameliorates Auditory Cortex Injury Associated with Military Aviation Noise-Induced Hearing Loss by Activating SIRT1/PGC-1α Signaling Pathway. *Front. Physiol.* 11, 788. doi:10.3389/fphys.2020.00788

Chen, Y. Y., Liu, Q. P., An, P., Jia, M., Luan, X., Tang, J. Y., et al. (2022). Ginsenoside Rd: A Promising Natural Neuroprotective Agent. *Phytomedicine* 95, 153883. doi:10.1016/j.phymed.2021.153883

Chian, S., Zhao, Y., Xu, M., Yu, X., Ke, X., Gao, R., et al. (2019). Ginsenoside Rd Reverses Cisplatin Resistance in Non-small-cell Lung Cancer A549 Cells by Downregulating the Nuclear Factor Erythroid 2-related Factor 2 Pathway. *Anticancer Drugs* 30, 838–845. doi:10.1097/CAD.0000000000000781

Choi, S. Y., Park, J. S., Shon, C. H., Lee, C. Y., Ryu, J. M., Son, D. J., et al. (2019). Fermented Korean Red Ginseng Extract Enriched in Rd and Rg3 Protects against Non-alcoholic Fatty Liver Disease through Regulation of mTORC1. *Nutrients* 11. doi:10.3390/nu11122963

Cong, L., and Chen, W. (2016). Neuroprotective Effect of Ginsenoside Rd in Spinal Cord Injury Rats. *Basic Clin. Pharmacol. Toxicol.* 119, 193–201. doi:10.1111/bcpt.12562

Fang, H., Wei, Y., Li, Y., and Zhou, G. (2020). One-Pot Process for the Production of Ginsenoside Rd by Coupling Enzyme-Assisted Extraction with Selective Enzymolysis. *Biol. Pharm. Bull.* 43, 1443–1447. doi:10.1248/bpb.b19-01127

Feng, L., Xu, C., Li, Z., Li, J., Dai, Y., Han, H., et al. (2016). Microbial Conversion of Ginsenoside Rd from Rb1 by the Fungus Mutant Aspergillus niger Strain TH-10a. *Prep. Biochem. Biotechnol.* 46, 336–341. doi:10.1080/10826068.2015.1031391

Gu, B., Wang, J., Song, Y., Wang, Q., and Wu, Q. (2019). The Inhibitory Effects of Ginsenoside Rd on the Human Glioma U251 Cells and its Underlying Mechanisms. *J. Cell Biochem.* 120, 4444–4450. doi:10.1002/jcb.27732

Guo, Y. X., Zhang, Y., Gao, Y. H., Deng, S. Y., Wang, L. M., Li, C. Q., et al. (2021). Role of Plant-Derived Natural Compounds in Experimental Autoimmune Encephalomyelitis: A Review of the Treatment Potential and Development Strategy. *Front. Pharmacol.* 12, 639651. doi:10.3389/fphar.2021.639651

Han, Y., and Rhew, K. Y. (2013). Ginsenoside Rd Induces Protective Anti-Candida Albicans Antibody through Immunological Adjuvant Activity. *Int. Immunopharmacol.* 17, 651–657. doi:10.1016/j.intimp.2013.08.003

He, Y., Hu, Z., Li, A., Zhu, Z., Yang, N., Ying, Z., et al. (2019). Recent Advances in Biotransformation of Saponins. *Molecules* 24. doi:10.3390/molecules24132365

Hong, H., Cui, C. H., Kim, J. K., Jin, F. X., Kim, S. C., and Im, W. T. (2012). Enzymatic Biotransformation of Ginsenoside Rb1 and Gypenoside XVII into Ginsenosides Rd and F2 by Recombinant β-glucosidase from Flavobacterium Johnsoniae. *J. Ginseng Res.* 36, 418–424. doi:10.5142/jgr.2012.36.4.418

Hou, J., Xue, J., Lee, M., and Sung, C. (2017). Ginsenoside Rd as a Potential Neuroprotective Agent Prevents Trimethyltin Injury. *Biomed. Rep.* 6, 435–440. doi:10.3892/br.2017.864

Hu, G., Wu, Z., Yang, F., Zhao, H., Liu, X., Deng, Y., et al. (2013). Ginsenoside Rd Blocks AIF Mitochondrio-Nuclear Translocation and NF-Kb Nuclear Accumulation by Inhibiting poly(ADP-Ribose) Polymerase-1 after Focal Cerebral Ischemia in Rats. *Neurol. Sci.* 34, 2101–2106. doi:10.1007/s10072-013-1344-6

Jeong, H. G., Pokharel, Y. R., Han, E. H., and Kang, K. W. (2007). Induction of Cyclooxygenase-2 by Ginsenoside Rd via Activation of CCAAT-Enhancer Binding Proteins and Cyclic AMP Response Binding Protein. *Biochem. Biophys. Res. Commun.* 359, 51–56. doi:10.1016/j.bbrc.2007.05.034

Jin, B., Zhang, C., Geng, Y., and Liu, M. (2020). Therapeutic Effect of Ginsenoside Rd on Experimental Autoimmune Encephalomyelitis Model Mice: Regulation of Inflammation and Treg/Th17 Cell Balance. *Mediat. Inflamm.* 2020, 8827527. doi:10.1155/2020/8827527

Jin, W., Ma, R., Zhai, L., Xu, X., Lou, T., Huang, Q., et al. (2020). Ginsenoside Rd Attenuates ACTH-Induced Corticosterone Secretion by Blocking the MC2R-cAMP/PKA/CREB Pathway in Y1 Mouse Adrenocortical Cells. *Life Sci.* 245, 117337. doi:10.1016/j.lfs.2020.117337

Jung, E., Pyo, M. K., and Kim, J. (2021). Pectin-Lyase-Modified Ginseng Extract and Ginsenoside Rd Inhibits High Glucose-Induced ROS Production in Mesangial Cells and Prevents Renal Dysfunction in Db/db Mice. *Molecules* 26. doi:10.3390/molecules26020367

Jung, S. C., Kim, W., Park, S. C., Jeong, J., Park, M. K., Lim, S., et al. (2014). Two Ginseng UDP-Glycosyltransferases Synthesize Ginsenoside Rg3 and Rd. *Plant Cell Physiol.* 55, 2177–2188. doi:10.1093/pcp/pcu147

Kang, N., Gao, H., He, L., Liu, Y., Fan, H., Xu, Q., et al. (2021). Ginsenoside Rb1 Is an Immune-Stimulatory Agent with Antiviral Activity against Enterovirus 71. *J. Ethnopharmacol.* 266, 113401. doi:10.1016/j.jep.2020.113401

Kaviani, M., Keshtkar, S., Azarpira, N., Hossein Aghdaei, M., Geramizadeh, B., Karimi, M. H., et al. (2019). Cytoprotective Effects of Ginsenoside Rd on Apoptosis-Associated Cell Death in the Isolated Human Pancreatic Islets. *EXCLI J.* 18, 666–676. doi:10.17179/excli2019-1698

Kim, B. J. (2013). Involvement of Melastatin Type Transient Receptor Potential 7 Channels in Ginsenoside Rd-Induced Apoptosis in Gastric and Breast Cancer Cells. *J. Ginseng Res.* 37, 201–209. doi:10.5142/jgr.2013.37.201

Kim, D. H., Chung, J. H., Yoon, J. S., Ha, Y. M., Bae, S., Lee, E. K., et al. (2013). Ginsenoside Rd Inhibits the Expressions of iNOS and COX-2 by Suppressing NF-Kb in LPS-Stimulated RAW264.7 Cells and Mouse Liver. *J. Ginseng Res.* 37, 54–63. doi:10.5142/jgr.2013.37.54

Kim, D. Y., Park, Y. G., Quan, H. Y., Kim, S. J., Jung, M. S., and Chung, S. H. (2012). Ginsenoside Rd Stimulates the Differentiation and Mineralization of Osteoblastic MC3T3-E1 Cells by Activating AMP-Activated Protein Kinase via the BMP-2 Signaling Pathway. *Fitoterapia* 83, 215–222. doi:10.1016/j.fitote.2011.10.017

Kim, H., Kim, J. H., Lee, P. Y., Bae, K. H., Cho, S., Park, B. C., et al. (2013). Ginsenoside Rb1 Is Transformed into Rd and Rh2 by Microbacterium Trichothecenolyticum. *J. Microbiol. Biotechnol.* 23, 1802–1805. doi:10.4014/jmb.1307.07049

Kim, H. I., Kim, J. K., Kim, J. Y., Han, M. J., and Kim, D. H. (2019). Fermented Red Ginseng and Ginsenoside Rd Alleviate Ovalbumin-Induced Allergic Rhinitis in Mice by Suppressing IgE, Interleukin-4, and Interleukin-5 Expression. *J. Ginseng Res.* 43, 635–644. doi:10.1016/j.jgr.2019.02.006

Kim, J. H., Oh, J. M., Chun, S., Park, H. Y., and Im, W. T. (2020). Enzymatic Biotransformation of Ginsenoside Rb2 into Rd by Recombinant α-L-Arabinopyranosidase from Blastococcus Saxobsidens. *J. Microbiol. Biotechnol.* 30, 391–397. doi:10.4014/jmb.1910.10065

Kim, K. A., Yoo, H. H., Gu, W., Yu, D. H., Jin, M. J., Choi, H. L., et al. (2014). Effect of a Soluble Prebiotic Fiber, NUTRIOSE, on the Absorption of Ginsenoside Rd in Rats Orally Administered Ginseng. *J. Ginseng Res.* 38, 203–207. doi:10.1016/j.jgr.2014.03.003

Kim, M. S., Yu, J. M., Kim, H. J., Kim, H. B., Kim, S. T., Jang, S. K., et al. (2014). Ginsenoside Re and Rd Enhance the Expression of Cholinergic Markers and Neuronal Differentiation in Neuro-2a Cells. *Biol. Pharm. Bull.* 37, 826–833. doi:10.1248/bpb.b14-00011

Kim, N. D., Pokharel, Y. R., and Kang, K. W. (2007). Ginsenoside Rd Enhances Glutathione Levels in H4IIE Cells via NF-kappaB-dependent Gamma-Glutamylcysteine Ligase Induction. *Pharmazie* 62, 933–936.

Kim, W. K., Song, S. Y., Oh, W. K., Kaewsuwan, S., Tran, T. L., Kim, W. S., et al. (2013). Wound-healing Effect of Ginsenoside Rd from Leaves of Panax Ginseng via Cyclic AMP-dependent Protein Kinase Pathway. *Eur. J. Pharmacol.* 702, 285–293. doi:10.1016/j.ejphar.2013.01.048

Kim, Y. J., Yamabe, N., Choi, P., Lee, J. W., Ham, J., and Kang, K. S. (2013). Efficient Thermal Deglycosylation of Ginsenoside Rd and its Contribution to the Improved Anticancer Activity of Ginseng. *J. Agric. Food Chem.* 61, 9185–9191. doi:10.1021/jf402774d

Li, J., Xie, Z. Z., Tang, Y. B., Zhou, J. G., and Guan, Y. Y. (2011). Ginsenoside-Rd, a Purified Component from Panax Notoginseng Saponins, Prevents Atherosclerosis in apoE Knockout Mice. *Eur. J. Pharmacol.* 652, 104–110. doi:10.1016/j.ejphar.2010.11.017

Li, L., Li, T., Tian, X., and Zhao, L. (2021). Ginsenoside Rd Attenuates Tau Phosphorylation in Olfactory Bulb, Spinal Cord, and Telencephalon by

Regulating Glycogen Synthase Kinase 3β and Cyclin-dependent Kinase 5. *Evid. Based Complement. Altern. Med.* 2021, 4485957. doi:10.1155/2021/4485957

Li, L., Liu, J., Yan, X., Qin, K., Shi, M., Lin, T., et al. (2011). Protective Effects of Ginsenoside Rd against Okadaic Acid-Induced Neurotoxicity *In Vivo* and *In Vitro*. *J. Ethnopharmacol.* 138, 135–141. doi:10.1016/j.jep.2011.08.068

Li, L., Liu, Z., Liu, J., Tai, X., Hu, X., Liu, X., et al. (2013). Ginsenoside Rd Attenuates Beta-Amyloid-Induced Tau Phosphorylation by Altering the Functional Balance of Glycogen Synthase Kinase 3beta and Protein Phosphatase 2A. *Neurobiol. Dis.* 54, 320–328. doi:10.1016/j.nbd.2013.01.002

Li, S. Y., Wang, X. G., Ma, M. M., Liu, Y., Du, Y. H., Lv, X. F., et al. (2012). Ginsenoside-Rd Potentiates Apoptosis Induced by Hydrogen Peroxide in Basilar Artery Smooth Muscle Cells through the Mitochondrial Pathway. *Apoptosis* 17, 113–120. doi:10.1007/s10495-011-0671-4

Li, X. Y., Liang, J., Tang, Y. B., Zhou, J. G., and Guan, Y. Y. (2010). Ginsenoside Rd Prevents Glutamate-Induced Apoptosis in Rat Cortical Neurons. *Clin. Exp. Pharmacol. Physiol.* 37, 199–204. doi:10.1111/j.1440-1681.2009.05286.x

Lin, F., Guo, X., and Lu, W. (2015). Efficient Biotransformation of Ginsenoside Rb1 to Rd by Isolated Aspergillus versicolor, Excreting β-glucosidase in the Spore Production Phase of Solid Culture. *Ant. Van Leeuwenhoek* 108, 1117–1127. doi:10.1007/s10482-015-0565-5

Lin, T., Liu, Y., Shi, M., Liu, X., Li, L., Liu, Y., et al. (2012). Promotive Effect of Ginsenoside Rd on Proliferation of Neural Stem Cells *In Vivo* and *In Vitro*. *J. Ethnopharmacol.* 142, 754–761. doi:10.1016/j.jep.2012.05.057

Liu, C., Wang, J., Yang, Y., Liu, X., Zhu, Y., Zou, J., et al. (2018). Ginsenoside Rd Ameliorates Colitis by Inducing P62-Driven Mitophagy-Mediated NLRP3 Inflammasome Inactivation in Mice. *Biochem. Pharmacol.* 155, 366–379. doi:10.1016/j.bcp.2018.07.010

Liu, G. M., Lu, T. C., Sun, M. L., Jia, W. Y., Ji, X., and Luo, Y. G. (2020). Ginsenoside Rd Inhibits Glioblastoma Cell Proliferation by Up-Regulating the Expression of miR-144-5p. *Biol. Pharm. Bull.* 43, 1534–1541. doi:10.1248/bpb.b20-00338

Liu, H., Lu, X., Hu, Y., and Fan, X. (2020). Chemical Constituents of Panax Ginseng and Panax Notoginseng Explain Why They Differ in Therapeutic Efficacy. *Pharmacol. Res.* 161, 105263. doi:10.1016/j.phrs.2020.105263

Liu, J., Yan, X., Li, L., Li, Y., Zhou, L., Zhang, X., et al. (2015). Ginsenoside Rd Improves Learning and Memory Ability in APP Transgenic Mice. *J. Mol. Neurosci.* 57, 522–528. doi:10.1007/s12031-015-0632-4

Liu, J. F., Yan, X. D., Qi, L. S., Li, L., Hu, G. Y., Li, P., et al. (2015). Ginsenoside Rd Attenuates Aβ25-35-Induced Oxidative Stress and Apoptosis in Primary Cultured Hippocampal Neurons. *Chem. Biol. Interact.* 239, 12–18. doi:10.1016/j.cbi.2015.06.030

Liu, Q. M., Jung, H. M., Cui, C. H., Sung, B. H., Kim, J. K., Kim, S. G., et al. (2013). Bioconversion of Ginsenoside Rc into Rd by a Novel α-L-arabinofuranosidase, Abf22-3 from Leuconostoc Sp. 22-3: Cloning, Expression, and Enzyme Characterization. *Ant. Van Leeuwenhoek* 103, 747–754. doi:10.1007/s10482-012-9856-2

Liu, X., Wang, L., Wen, A., Yang, J., Yan, Y., Song, Y., et al. (2012). Ginsenoside-Rd Improves Outcome of Acute Ischaemic Stroke - a Randomized, Double-Blind, Placebo-Controlled, Multicenter Trial. *Eur. J. Neurol.* 19, 855–863. doi:10.1111/j.1468-1331.2011.03634.x

Liu, X., Xia, J., Wang, L., Song, Y., Yang, J., Yan, Y., et al. (2009). Efficacy and Safety of Ginsenoside-Rd for Acute Ischaemic Stroke: a Randomized, Double-Blind, Placebo-Controlled, Phase II Multicenter Trial. *Eur. J. Neurol.* 16, 569–575. doi:10.1111/j.1468-1331.2009.02534.x

Liu, X. Y., Zhou, X. Y., Hou, J. C., Zhu, H., Wang, Z., Liu, J. X., et al. (2015). Ginsenoside Rd Promotes Neurogenesis in Rat Brain after Transient Focal Cerebral Ischemia via Activation of PI3K/Akt Pathway. *Acta Pharmacol. Sin.* 36, 421–428. doi:10.1038/aps.2014.156

Liu, Y., Zhang, R. Y., Zhao, J., Dong, Z., Feng, D. Y., Wu, R., et al. (2015). Ginsenoside Rd Protects SH-Sy5y Cells against 1-Methyl-4-Phenylpyridinium Induced Injury. *Int. J. Mol. Sci.* 16, 14395–14408. doi:10.3390/ijms160714395

Park, C. S., Yoo, M. H., Noh, K. H., and Oh, D. K. (2010). Biotransformation of Ginsenosides by Hydrolyzing the Sugar Moieties of Ginsenosides Using Microbial Glycosidases. *Appl. Microbiol. Biotechnol.* 87, 9–19. doi:10.1007/s00253-010-2567-6

Phi, L. T. H., Sari, I. N., Wijaya, Y. T., Kim, K. S., Park, K., Cho, A. E., et al. (2019). Ginsenoside Rd Inhibits the Metastasis of Colorectal Cancer via Epidermal Growth Factor Receptor Signaling Axis. *IUBMB Life* 71, 601–610. doi:10.1002/iub.1984

Pokharel, Y. R., Kim, N. D., Han, H. K., Oh, W. K., and Kang, K. W. (2010). Increased Ubiquitination of Multidrug Resistance 1 by Ginsenoside Rd. *Nutr. Cancer* 62, 252–259. doi:10.1080/01635580903407171

Quan, L. H., Piao, J. Y., Min, J. W., Kim, H. B., Kim, S. R., Yang, D. U., et al. (2011). Biotransformation of Ginsenoside Rb1 to Prosapogenins, Gypenoside XVII, Ginsenoside Rd, Ginsenoside F2, and Compound K by Leuconostoc Mesenteroides DC102. *J. Ginseng Res.* 35, 344–351. doi:10.5142/jgr.2011.35.3.344

Ren, K., Jin, C., Ma, P., Ren, Q., Jia, Z., and Zhu, D. (2016). Ginsenoside Rd Alleviates Mouse Acute Renal Ischemia/reperfusion Injury by Modulating Macrophage Phenotype. *J. Ginseng Res.* 40, 196–202. doi:10.1016/j.jgr.2015.12.003

Ren, K., Li, S., Ding, J., Zhao, S., Liang, S., Cao, X., et al. (2021). Ginsenoside Rd Attenuates Mouse Experimental Autoimmune Neuritis by Modulating Monocyte Subsets Conversion. *Biomed. Pharmacother.* 138, 111489. doi:10.1016/j.biopha.2021.111489

Renchinkhand, G., Cho, S. H., Park, Y. W., Song, G. Y., and Nam, M. S. (2020). Biotransformation of Major Ginsenoside Rb1 to Rd by Dekkera Anomala YAE-1 from Mongolian Fermented Milk (Airag). *J. Microbiol. Biotechnol.* 30, 1536–1542. doi:10.4014/jmb.2004.04022

Renchinkhand, G., Cho, S. H., Urgamal, M., Park, Y. W., Nam, J. H., Bae, H. C., et al. (2017). Characterization of Paenibacillus Sp. MBT213 Isolated from Raw Milk and its Ability to Convert Ginsenoside Rb1 into Ginsenoside Rd from Panax Ginseng. *Korean J. Food Sci. Anim. Resour.* 37, 735–742. doi:10.5851/kosfa.2017.37.5.735

Sarhene, M., Ni, J. Y., Duncan, E. S., Liu, Z., Li, S., Zhang, J., et al. (2021). Ginsenosides for Cardiovascular Diseases; Update on Pre-clinical and Clinical Evidence, Pharmacological Effects and the Mechanisms of Action. *Pharmacol. Res.* 166, 105481. doi:10.1016/j.phrs.2021.105481

Shi, Q., Hao, Q., Bouissac, J., Lu, Y., Tian, S., and Luu, B. (2005). Ginsenoside-Rd from Panax Notoginseng Enhances Astrocyte Differentiation from Neural Stem Cells. *Life Sci.* 76, 983–995. doi:10.1016/j.lfs.2004.07.026

Shin, K. C., Lee, G. W., and Oh, D. K. (2013). Production of Ginsenoside Rd from Ginsenoside Rc by α-L-arabinofuranosidase from Caldicellulosiruptor Saccharolyticus. *J. Microbiol. Biotechnol.* 23, 483–488. doi:10.4014/jmb.1211.11012

Shin, K. C., and Oh, D. K. (2016). Classification of Glycosidases that Hydrolyze the Specific Positions and Types of Sugar Moieties in Ginsenosides. *Crit. Rev. Biotechnol.* 36, 1036–1049. doi:10.3109/07388551.2015.1083942

Son, J. W., Kim, H. J., and Oh, D. K. (2008). Ginsenoside Rd Production from the Major Ginsenoside Rb(1) by Beta-Glucosidase from Thermus Caldophilus. *Biotechnol. Lett.* 30, 713–716. doi:10.1007/s10529-007-9590-4

Sun, D., Wang, B., Shi, M., Zhang, Y. X., Zhou, L. F., Liu, Z. R., et al. (2012). Pharmacokinetic, Tissue Distribution and Excretion of Ginsenoside-Rd in Rodents. *Phytomedicine* 19, 369–373. doi:10.1016/j.phymed.2011.08.061

Tamura, T., Cui, X., Sakaguchi, N., and Akashi, M. (2008). Ginsenoside Rd Prevents and Rescues Rat Intestinal Epithelial Cells from Irradiation-Induced Apoptosis. *Food Chem. Toxicol.* 46, 3080–3089. doi:10.1016/j.fct.2008.06.011

Tian, Y. Z., Liu, Y. P., Tian, S. C., Ge, S. Y., Wu, Y. J., and Zhang, B. L. (2020). Antitumor Activity of Ginsenoside Rd in Gastric Cancer via Up-Regulation of Caspase-3 and Caspase-9. *Pharmazie* 75, 147–150. doi:10.1691/ph.2020.9931

Wang, B., Feng, G., Tang, C., Wang, L., Cheng, H., Zhang, Y., et al. (2013). Ginsenoside Rd Maintains Adult Neural Stem Cell Proliferation during Lead-Impaired Neurogenesis. *Neurol. Sci.* 34, 1181–1188. doi:10.1007/s10072-012-1215-6

Wang, B., Zhu, Q., Man, X., Guo, L., and Hao, L. (2014). Ginsenoside Rd Inhibits Apoptosis Following Spinal Cord Ischemia/reperfusion Injury. *Neural Regen. Res.* 9, 1678–1687. doi:10.4103/1673-5374.141802

Wang, F., Park, J. S., Ma, Y., Ma, H., Lee, Y. J., Lee, G. R., et al. (2021). Ginseng Saponin Enriched in Rh1 and Rg2 Ameliorates Nonalcoholic Fatty Liver Disease by Inhibiting Inflammasome Activation. *Nutrients* 13. doi:10.3390/nu13030856

Wang, H., Jiang, N., Lv, J., Huang, H., and Liu, X. (2020). Ginsenoside Rd Reverses Cognitive Deficits by Modulating BDNF-dependent CREB Pathway in Chronic Restraint Stress Mice. *Life Sci.* 258, 118107. doi:10.1016/j.lfs.2020.118107

Wang, L., Zhang, Y., Chen, J., Li, S., Wang, Y., Hu, L., et al. (2012). Immunosuppressive Effects of Ginsenoside-Rd on Skin Allograft Rejection in Rats. *J. Surg. Res.* 176, 267–274. doi:10.1016/j.jss.2011.06.038

Wang, L., Zhang, Y., Wang, Z., Li, S., Min, G., Wang, L., et al. (2012). Inhibitory Effect of Ginsenoside-Rd on Carrageenan-Induced Inflammation in Rats. *Can. J. Physiol. Pharmacol.* 90, 229–236. doi:10.1139/y11-127

Wang, P., Du, X., Xiong, M., Cui, J., Yang, Q., Wang, W., et al. (2016). Ginsenoside Rd Attenuates Breast Cancer Metastasis Implicating Derepressing microRNA-18a-Regulated Smad2 Expression. *Sci. Rep.* 6, 33709. doi:10.1038/srep33709

Wang, Q., Fu, W., Yu, X., Xu, H., Sui, D., and Wang, Y. (2021). Ginsenoside Rg2 Alleviates Myocardial Fibrosis by Regulating TGF-β1/Smad Signalling Pathway. *Pharm. Biol.* 59, 106–113. doi:10.1080/13880209.2020.1867197

Wang, W., Wang, G. J., Xie, H. T., Sun, J. G., Zhao, S., Jiang, X. L., et al. (2007). Determination of Ginsenoside Rd in Dog Plasma by Liquid Chromatography-Mass Spectrometry after Solid-phase Extraction and its Application in Dog Pharmacokinetics Studies. *J. Chromatogr. B Anal. Technol. Biomed. Life Sci.* 852, 8–14. doi:10.1016/j.jchromb.2006.12.046

Wang, Y., Li, X., Wang, X., Lau, W., Wang, Y., Xing, Y., et al. (2013). Ginsenoside Rd Attenuates Myocardial Ischemia/reperfusion Injury via Akt/GSK-3β Signaling and Inhibition of the Mitochondria-dependent Apoptotic Pathway. *PLoS One* 8, e70956. doi:10.1371/journal.pone.0070956

Wu, S. D., Xia, F., Lin, X. M., Duan, K. L., Wang, F., Lu, Q. L., et al. (2016). Ginsenoside-Rd Promotes Neurite Outgrowth of PC12 Cells through MAPK/ERK- and PI3K/AKT-dependent Pathways. *Int. J. Mol. Sci.* 17. doi:10.3390/ijms17020177

Xie, J., Zhao, D., Zhao, L., Pei, J., Xiao, W., Ding, G., et al. (2016). Characterization of a Novel Arabinose-Tolerant α-L-arabinofuranosidase with High Ginsenoside Rc to Ginsenoside Rd Bioconversion Productivity. *J. Appl. Microbiol.* 120, 647–660. doi:10.1111/jam.13040

Xie, Z., Shi, M., Zhang, C., Zhao, H., Hui, H., and Zhao, G. (2016). Ginsenoside Rd Protects against Cerebral Ischemia-Reperfusion Injury via Decreasing the Expression of the NMDA Receptor 2B Subunit and its Phosphorylated Product. *Neurochem. Res.* 41, 2149–2159. doi:10.1007/s11064-016-1930-0

Xu, X. F., Qu, W. J., Jia, Z., Han, T., Liu, M. N., Bai, Y. Y., et al. (2021). Effect of Cultivation Ages on Anti-inflammatory Activity of a New Type of Red Ginseng. *Biomed. Pharmacother.* 136, 111280. doi:10.1016/j.biopha.2021.111280

Yan, X., Hu, G., Yan, W., Chen, T., Yang, F., Zhang, X., et al. (2017). Ginsenoside Rd Promotes Non-amyloidogenic Pathway of Amyloid Precursor Protein Processing by Regulating Phosphorylation of Estrogen Receptor Alpha. *Life Sci.* 168, 16–23. doi:10.1016/j.lfs.2016.11.002

Yang, B., Wang, R., Ji, L. L., Li, X. P., Li, X. H., Zhou, H. G., et al. (2021). *Exploration of the Function of Ginsenoside RD Attenuates Lipopolysaccharide-Induced Lung Injury: A Study of Network Pharmacology and Experimental Validation*. Augusta, Ga: Shock.

Yang, L., Deng, Y., Xu, S., and Zeng, X. (2007). *In Vivo* pharmacokinetic and Metabolism Studies of Ginsenoside Rd. *J. Chromatogr. B Anal. Technol. Biomed. Life Sci.* 854, 77–84. doi:10.1016/j.jchromb.2007.04.014

Yang, L., Xu, S. J., Zeng, X., Liu, Y. M., Deng, S. G., Wu, Z. F., et al. (2006). Determination of Ginsenoside Rd and its Metabolites in Rat Urine by LC-MS. *Yao Xue Xue Bao* 41, 742–746.

Yang, L. X., Zhang, X., and Zhao, G. (2016). Ginsenoside Rd Attenuates DNA Damage by Increasing Expression of DNA Glycosylase Endonuclease VIII-like Proteins after Focal Cerebral Ischemia. *Chin. Med. J. Engl.* 129, 1955–1962. doi:10.4103/0366-6999.187851

Yang, X., Gao, M., Miao, M., Jiang, C., Zhang, D., Yin, Z., et al. (2021). Combining Combretastatin A4 Phosphate with Ginsenoside Rd Synergistically Inhibited Hepatocellular Carcinoma by Reducing HIF-1α via PI3K/AKT/mTOR Signalling Pathway. *J. Pharm. Pharmacol.* 73, 263–271. doi:10.1093/jpp/rgaa006

Yang, X. L., Guo, T. K., Wang, Y. H., Gao, M. T., Qin, H., and Wu, Y. J. (2012). Therapeutic Effect of Ginsenoside Rd in Rats with TNBS-Induced Recurrent Ulcerative Colitis. *Arch. Pharm. Res.* 35, 1231–1239. doi:10.1007/s12272-012-0714-6

Yang, X. L., Guo, T. K., Wang, Y. H., Huang, Y. H., Liu, X., Wang, X. X., et al. (2012). Ginsenoside Rd Attenuates the Inflammatory Response via Modulating P38 and JNK Signaling Pathways in Rats with TNBS-Induced Relapsing Colitis. *Int. Immunopharmacol.* 12, 408–414. doi:10.1016/j.intimp.2011.12.014

Yang, Z., Chen, A., Sun, H., Ye, Y., and Fang, W. (2007). Ginsenoside Rd Elicits Th1 and Th2 Immune Responses to Ovalbumin in Mice. *Vaccine* 25, 161–169. doi:10.1016/j.vaccine.2006.05.075

Yang, Z. G., Sun, H. X., and Ye, Y. P. (2006). Ginsenoside Rd from Panax Notoginseng Is Cytotoxic towards HeLa Cancer Cells and Induces Apoptosis. *Chem. Biodivers.* 3, 187–197. doi:10.1002/cbdv.200690022

Yao, L., Han, Z., Zhao, G., Xiao, Y., Zhou, X., Dai, R., et al. (2020). Ginsenoside Rd Ameliorates High Fat Diet-Induced Obesity by Enhancing Adaptive Thermogenesis in a cAMP-dependent Manner. *Obes. (Silver Spring)* 28, 783–792. doi:10.1002/oby.22761

Ye, L., Zhang, C., Li, J., Shi, X., and Feng, M. (2012). Effects of External Calcium on the Biotransformation of Ginsenoside Rb1 to Ginsenoside Rd by Paecilomyces Bainier 229-7. *World J. Microbiol. Biotechnol.* 28, 857–863. doi:10.1007/s11274-011-0882-4

Ye, L., Zhou, C. Q., Zhou, W., Zhou, P., Chen, D. F., Liu, X. H., et al. (2010). Biotransformation of Ginsenoside Rb1 to Ginsenoside Rd by Highly Substrate-Tolerant Paecilomyces Bainier 229-7. *Bioresour. Technol.* 101, 7872–7876. doi:10.1016/j.biortech.2010.04.102

Ye, R., Han, J., Kong, X., Zhao, L., Cao, R., Rao, Z., et al. (2008). Protective Effects of Ginsenoside Rd on PC12 Cells against Hydrogen Peroxide. *Biol. Pharm. Bull.* 31, 1923–1927. doi:10.1248/bpb.31.1923

Ye, R., Kong, X., Yang, Q., Zhang, Y., Han, J., Li, P., et al. (2011). Ginsenoside Rd in Experimental Stroke: Superior Neuroprotective Efficacy with a Wide Therapeutic Window. *Neurotherapeutics* 8, 515–525. doi:10.1007/s13311-011-0051-3

Ye, R., Kong, X., Yang, Q., Zhang, Y., Han, J., and Zhao, G. (2011). Ginsenoside Rd Attenuates Redox Imbalance and Improves Stroke Outcome after Focal Cerebral Ischemia in Aged Mice. *Neuropharmacology* 61, 815–824. doi:10.1016/j.neuropharm.2011.05.029

Ye, R., Li, N., Han, J., Kong, X., Cao, R., Rao, Z., et al. (2009). Neuroprotective Effects of Ginsenoside Rd against Oxygen-Glucose Deprivation in Cultured Hippocampal Neurons. *Neurosci. Res.* 64, 306–310. doi:10.1016/j.neures.2009.03.016

Ye, R., Yang, Q., Kong, X., Han, J., Zhang, X., Zhang, Y., et al. (2011). Ginsenoside Rd Attenuates Early Oxidative Damage and Sequential Inflammatory Response after Transient Focal Ischemia in Rats. *Neurochem. Int.* 58, 391–398. doi:10.1016/j.neuint.2010.12.015

Ye, R., Zhang, X., Kong, X., Han, J., Yang, Q., Zhang, Y., et al. (2011). Ginsenoside Rd Attenuates Mitochondrial Dysfunction and Sequential Apoptosis after Transient Focal Ischemia. *Neuroscience* 178, 169–180. doi:10.1016/j.neuroscience.2011.01.007

Yi, Y. S. (2021). New Mechanisms of Ginseng Saponin-Mediated Anti-inflammatory Action via Targeting Canonical Inflammasome Signaling Pathways. *J. Ethnopharmacol.* 278, 114292. doi:10.1016/j.jep.2021.114292

Yokozawa, T., and Dong, E. (2001). Role of Ginsenoside-Rd in Cisplatin-Induced Renal Injury: Special Reference to DNA Fragmentation. *Nephron* 89, 433–438. doi:10.1159/000046116

Yokozawa, T., Liu, Z. W., and Dong, E. (1998). A Study of Ginsenoside-Rd in a Renal Ischemia-Reperfusion Model. *Nephron* 78, 201–206. doi:10.1159/000044911

Yokozawa, T., and Liu, Z. W. (2000). The Role of Ginsenoside-Rd in Cisplatin-Induced Acute Renal Failure. *Ren. Fail* 22, 115–127. doi:10.1081/jdi-100100858

Yokozawa, T., and Owada, S. (1999). Effect of Ginsenoside-Rd in Cephaloridine-Induced Renal Disorder. *Nephron* 81, 200–207. doi:10.1159/000045277

Yokozawa, T., Satoh, A., and Cho, E. J. (2004). Ginsenoside-Rd Attenuates Oxidative Damage Related to Aging in Senescence-Accelerated Mice. *J. Pharm. Pharmacol.* 56, 107–113. doi:10.1211/0022357022449

Yoon, J. H., Choi, Y. J., Cha, S. W., and Lee, S. G. (2012). Anti-metastatic Effects of Ginsenoside Rd via Inactivation of MAPK Signaling and Induction of Focal Adhesion Formation. *Phytomedicine* 19, 284–292. doi:10.1016/j.phymed.2011.08.069

Yu, X., Li, H., Lin, D., Guo, W., Xu, Z., Wang, L., et al. (2021). Ginsenoside Prolongs the Lifespan of *C. elegans* via Lipid Metabolism and Activating the Stress Response Signaling Pathway. *Int. J. Mol. Sci.* 22. doi:10.3390/ijms22189668

Zeng, X., Deng, Y., Feng, Y., Liu, Y., Yang, L., Huang, Y., et al. (2010). Pharmacokinetics and Safety of Ginsenoside Rd Following a Single or Multiple Intravenous Dose in Healthy Chinese Volunteers. *J. Clin. Pharmacol.* 50, 285–292. doi:10.1177/0091270009344334

Zhang, B., Hu, X., Wang, H., Wang, R., Sun, Z., Tan, X., et al. (2020). Effects of a Dammarane-type Saponin, Ginsenoside Rd, in Nicotine-Induced Vascular Endothelial Injury. *Phytomedicine* 79, 153325. doi:10.1016/j.phymed.2020.153325

Zhang, C., Du, F., Shi, M., Ye, R., Cheng, H., Han, J., et al. (2012). Ginsenoside Rd Protects Neurons against Glutamate-Induced Excitotoxicity by Inhibiting Ca(2+) Influx. *Cell Mol. Neurobiol.* 32, 121–128. doi:10.1007/s10571-011-9742-x

Zhang, C., Liu, X., Xu, H., Hu, G., Zhang, X., Xie, Z., et al. (2020). Protopanaxadiol Ginsenoside Rd Protects against NMDA Receptor-Mediated Excitotoxicity by Attenuating Calcineurin-Regulated DAPK1 Activity. *Sci. Rep.* 10, 8078. doi:10.1038/s41598-020-64738-2

Zhang, E., Shi, H., Yang, L., Wu, X., and Wang, Z. (2017). Ginsenoside Rd Regulates the Akt/mTOR/p70S6K Signaling Cascade and Suppresses Angiogenesis and Breast Tumor Growth. *Oncol. Rep.* 38, 359–367. doi:10.3892/or.2017.5652

Zhang, G., Xia, F., Zhang, Y., Zhang, X., Cao, Y., Wang, L., et al. (2016). Ginsenoside Rd Is Efficacious against Acute Ischemic Stroke by Suppressing Microglial Proteasome-Mediated Inflammation. *Mol. Neurobiol.* 53, 2529–2540. doi:10.1007/s12035-015-9261-8

Zhang, H., Park, S., Huang, H., Kim, E., Yi, J., Choi, S. K., et al. (2021). Anticancer Effects and Potential Mechanisms of Ginsenoside Rh2 in Various Cancer Types (Review). *Oncol. Rep.* 45. doi:10.3892/or.2021.7984

Zhang, R., Tan, S. Q., Zhang, B. L., Guo, Z. Y., Tian, L. Y., Weng, P., et al. (2021). Two Key Amino Acids Variant of Alpha-L-Arabinofuranosidase from Bacillus Subtilis Str. 168 with Altered Activity for Selective Conversion Ginsenoside Rc to Rd. *Molecules* 26, 1733. doi:10.3390/molecules26061733

Zhang, X., Liu, X., Hu, G., Zhang, G., Zhao, G., and Shi, M. (2020). Ginsenoside Rd Attenuates Blood-Brain Barrier Damage by Suppressing Proteasome-Mediated Signaling after Transient Forebrain Ischemia. *Neuroreport* 31, 466–472. doi:10.1097/WNR.0000000000001426

Zhang, X., Shi, M., Bjørås, M., Wang, W., Zhang, G., Han, J., et al. (2013). Ginsenoside Rd Promotes Glutamate Clearance by Up-Regulating Glial Glutamate Transporter GLT-1 via PI3K/AKT and ERK1/2 Pathways. *Front. Pharmacol.* 4, 152. doi:10.3389/fphar.2013.00152

Zhang, X., Shi, M., Ye, R., Wang, W., Liu, X., Zhang, G., et al. (2014). Ginsenoside Rd Attenuates Tau Protein Phosphorylation via the PI3K/AKT/GSK-3β Pathway after Transient Forebrain Ischemia. *Neurochem. Res.* 39, 1363–1373. doi:10.1007/s11064-014-1321-3

Zhang, Y., Zhou, L., Zhang, X., Bai, J., Shi, M., and Zhao, G. (2012). Ginsenoside-Rd Attenuates TRPM7 and ASIC1a but Promotes ASIC2a Expression in Rats after Focal Cerebral Ischemia. *Neurol. Sci.* 33, 1125–1131. doi:10.1007/s10072-011-0916-6

Zhang, Y. X., Wang, L., Xiao, E. L., Li, S. J., Chen, J. J., Gao, B., et al. (2013). Ginsenoside-Rd Exhibits Anti-inflammatory Activities through Elevation of Antioxidant Enzyme Activities and Inhibition of JNK and ERK Activation *In Vivo*. *Int. Immunopharmacol.* 17, 1094–1100. doi:10.1016/j.intimp.2013.10.013

Zhao, X., Wang, J., Li, J., Fu, L., Gao, J., Du, X., et al. (2009). Highly Selective Biotransformation of Ginsenoside Rb1 to Rd by the Phytopathogenic Fungus Cladosporium Fulvum (Syn. Fulvia Fulva). *J. Ind. Microbiol. Biotechnol.* 36, 721–726. doi:10.1007/s10295-009-0542-y

Zhong, F. L., Ma, R., Jiang, M., Dong, W. W., Jiang, J., Wu, S., et al. (2016). Cloning and Characterization of Ginsenoside-Hydrolyzing β-Glucosidase from Lactobacillus Brevis that Transforms Ginsenosides Rb1 and F2 into Ginsenoside Rd and Compound K. *J. Microbiol. Biotechnol.* 26, 1661–1667. doi:10.4014/jmb.1605.05052

Zhou, J. S., Wang, J. F., He, B. R., Cui, Y. S., Fang, X. Y., Ni, J. L., et al. (2014). Ginsenoside Rd Attenuates Mitochondrial Permeability Transition and Cytochrome C Release in Isolated Spinal Cord Mitochondria: Involvement of Kinase-Mediated Pathways. *Int. J. Mol. Sci.* 15, 9859–9877. doi:10.3390/ijms15069859

Zhou, S., Ji, Y., Yao, H., Guo, H., Zhang, Z., Wang, Z., et al. (2022). Application of Ginsenoside Rd in Periodontitis with Inhibitory Effects on Pathogenicity, Inflammation, and Bone Resorption. *Front. Cell Infect. Microbiol.* 12, 813953. doi:10.3389/fcimb.2022.813953

Zhu, D., Liu, M., Yang, Y., Ma, L., Jiang, Y., Zhou, L., et al. (2014). Ginsenoside Rd Ameliorates Experimental Autoimmune Encephalomyelitis in C57BL/6 Mice. *J. Neurosci. Res.* 92, 1217–1226. doi:10.1002/jnr.23397

Conflict of Interest: The authors declare that the research was conducted in the absence of any commercial or financial relationships that could be construed as a potential conflict of interest.

Publisher's Note: All claims expressed in this article are solely those of the authors and do not necessarily represent those of their affiliated organizations or those of the publisher, the editors, and the reviewers. Any product that may be evaluated in this article or claim that may be made by its manufacturer is not guaranteed or endorsed by the publisher.

GLOSSARY

PPD protopanaxadiol
LC-MS liquid chromatography-mass spectrometry
MCAO middle cerebral artery occlusion
GLT-1 glutamate transporter-1
NMDA N-methyl-D-aspartate
NR2B N-methyl-D-aspartate receptor 2B
OGD oxygen–glucose deprivation
TRPM transient receptor potential melastatin
ASIC acid-sensing ion channel
MMP mitochondrial membrane potential
ROS reactive oxygen species
SD Sprague–Dawley
mtDNA mitochondrial DNA
nDNA nuclear DNA
PKB protein kinase Bprotein kinase B
GSK-3β glycogen synthase kinase-3β
PKB protein kinase Bprotein kinase B
OGD/R oxygen–glucose deprivation/reperfusion
I/R ischemia/reperfusion
VEGF vascular endothelial growth factor
BDNF brain-derived neurotrophic factor
PI3K phosphatidylinositol 3-kinase
TMT trimethyltin
Bcl-2 B-cell lymphoma-2
MAPK mitogen-activated protein kinase
PARP-1 poly adenosine diphosphate-ribose polymerase-1
AIF apoptosis-inducing factor
NF-κB nuclear factor kappa-light-chain-enhancer of activated B cells
COX-2 cyclooxygenase-2
iNOS inducible nitric oxide synthase
MMP-9 matrix metalloproteinase-9
IκBα nuclear factor of kappa light polypeptide gene enhancer in B cells inhibitor, alpha
GAP-43 growth-associated protein of 43 kDa
GBS Guillain–Barre syndrome
MPP+ 1-methyl-4-phenylpyridinium
PD Parkinson's disease
AD Alzheimer's disease
CDK5/P25 cyclin dependent Kinase 5
PP-2A protein phosphatase 2A
sAPPα soluble amyloid-β precursor protein α
SCI spinal cord injury
NIHL noise-induced hearing loss
CRS chronic restraint stress
NSCLC non-small-cell lung cancer
NRF2 nuclear factor erythroid 2-associated factor 2
DDP cisplatin
EGFR epidermal growth factor receptor
mTOR mammalian target of rapamycin
HIF1-α hypoxia-inducible factor 1-α
MMPs matrix metalloproteinases
DSS sodium dextran sulfate
AMPK adenosine 5′-monophosphate-activated protein kinase
ULK1 Unc-51 like autophagy activating kinase 1
TNBS trinitrobenzenesulfonic acid
PKA protein kinase A
NAFLD non-alcoholic fatty liver disease
Ox-LDL oxidation low lipoprotein
KPCs keratinocyte progenitor cells
HDFs human dermal fibroblasts
LPS lipopolysaccharides
ICR Institute of Cancer Research
BASMCs basilar artery smooth muscle cells
ACTH adrenocorticotrophic hormone
PGE2 prostaglandin E2
C/EBP CCAAT/enhancer binding protein
CREB cyclic AMP response element binding protein

frontiers | Frontiers in Pharmacology

TYPE Original Research
PUBLISHED 30 August 2022
DOI 10.3389/fphar.2022.915535

OPEN ACCESS

EDITED BY
Shuai Ji,
Xuzhou Medical University, China

REVIEWED BY
Liqin Ding,
Tianjin University of Traditional Chinese Medicine, China
Olimpio Montero,
Spanish National Research Council (CSIC), Spain
Lin Qiyan,
Shanghai University of Traditional Chinese Medicine, China

*CORRESPONDENCE
Dong Shang,
shangdong@dmu.edu.cn
Dan Yuan,
yuandan_kampo@163.com

SPECIALTY SECTION
This article was submitted to Ethnopharmacology, a section of the journal Frontiers in Pharmacology

RECEIVED 08 April 2022
ACCEPTED 06 July 2022
PUBLISHED 30 August 2022

CITATION
Qu J, Chen Q, Wei T, Dou N, Shang D and Yuan D (2022), Systematic characterization of Puerariae Flos metabolites in vivo and assessment of its protective mechanisms against alcoholic liver injury in a rat model. *Front. Pharmacol.* 13:915535. doi: 10.3389/fphar.2022.915535

Systematic characterization of Puerariae Flos metabolites *in vivo* and assessment of its protective mechanisms against alcoholic liver injury in a rat model

Jialin Qu[1], Qiuyue Chen[2], Tianfu Wei[1], Ning Dou[2], Dong Shang[1]* and Dan Yuan[2]*

[1]Clinical Laboratory of Integrative Medicine, The First Affiliated Hospital of Dalian Medical University, Dalian, China, [2]Department of Traditional Chinese Medicine, Shenyang Pharmaceutical University, Shenyang, China

Puerariae Flos, a representative homology plant of medicine and food for alcoholism, has a long history of clinical experience and remarkable curative effect in the treatment of alcoholic liver disease (ALD). However, its effective forms and hepatoprotective mechanisms remain unknown. In the present study, a strategy based on UPLC-QTOF MS combined with mass defect filtering technique was established for comprehensive mapping of the metabolic profile of PF in rat plasma, urine, bile, and feces after oral administration. Furthermore, the absorbed constituents into plasma and bile with a relatively high level were subjected to the network analysis, functional enrichment analysis, and molecular docking to clarify the potential mechanism. Finally, the therapeutic effect of PF on ALD and predicted mechanisms were further evaluated using a rat model of alcohol-induced liver injury and Western blot analysis. In total, 25 prototype components and 82 metabolites, including 93 flavonoids, 13 saponins, and one phenolic acid, were identified or tentatively characterized *in vivo*. In addition, glucuronidation, sulfation, methylation, hydroxylation, and reduction were observed as the major metabolic pathways of PF. The constructed compound–target–pathway network revealed that 11 absorbed constituents associated with the 16 relevant targets could be responsible for the protective activity of PF against ALD by regulating nine pathways attributable to glycolysis/gluconeogenesis, amino acid metabolism, and lipid regulation as well as inflammation and immune regulation. In addition, four active ingredients (6″-O-xylosyltectoridin, genistein-7-glucuronide-4′-sulfate, tectoridin-4′-sulfate, and 6″-O-xylosyltectoridin-4′-sulfate) as well as two target genes (MAO-A and

Abbreviations: ACOX1, peroxisomal acyl-coenzyme A oxidase 1; ALDH2, aldehyde dehydrogenase; ALOX12, polyunsaturated fatty acid lipoxygenase ALOX12; ALOX15, polyunsaturated fatty acid lipoxygenase ALOX15; CHKB, choline/ethanolamine kinase; GOT2, aspartate aminotransferase; HSP90AA1, heat shock protein HSP 90-alpha; HSP90B1, endoplasmin; LDHB, L-lactate dehydrogenase B chain; MAO-A, amine oxidase (flavin-containing) A; MIF, macrophage migration inhibitory factor; PPAR-α, peroxisome proliferator–activated receptor alpha; PTGS1, prostaglandin G/H synthase 1; TNF, tumor necrosis factor; TPI1, triosephosphate isomerase; TYR, tyrosinase; UPLC, ultra-performance liquid chromatography.

PPAR-α) were screened and validated to play a crucial role with a good molecular docking score. The present results not only increase the understanding on the effective form and molecular mechanisms of PF-mediated protection against ALD but also promote better application of PF as a supplement food and herbal medicine for the treatment of ALD.

KEYWORDS

Puerariae Flos, metabolic profile, alcoholic liver disease, bioinformatics, PPAR-α, MAO-A

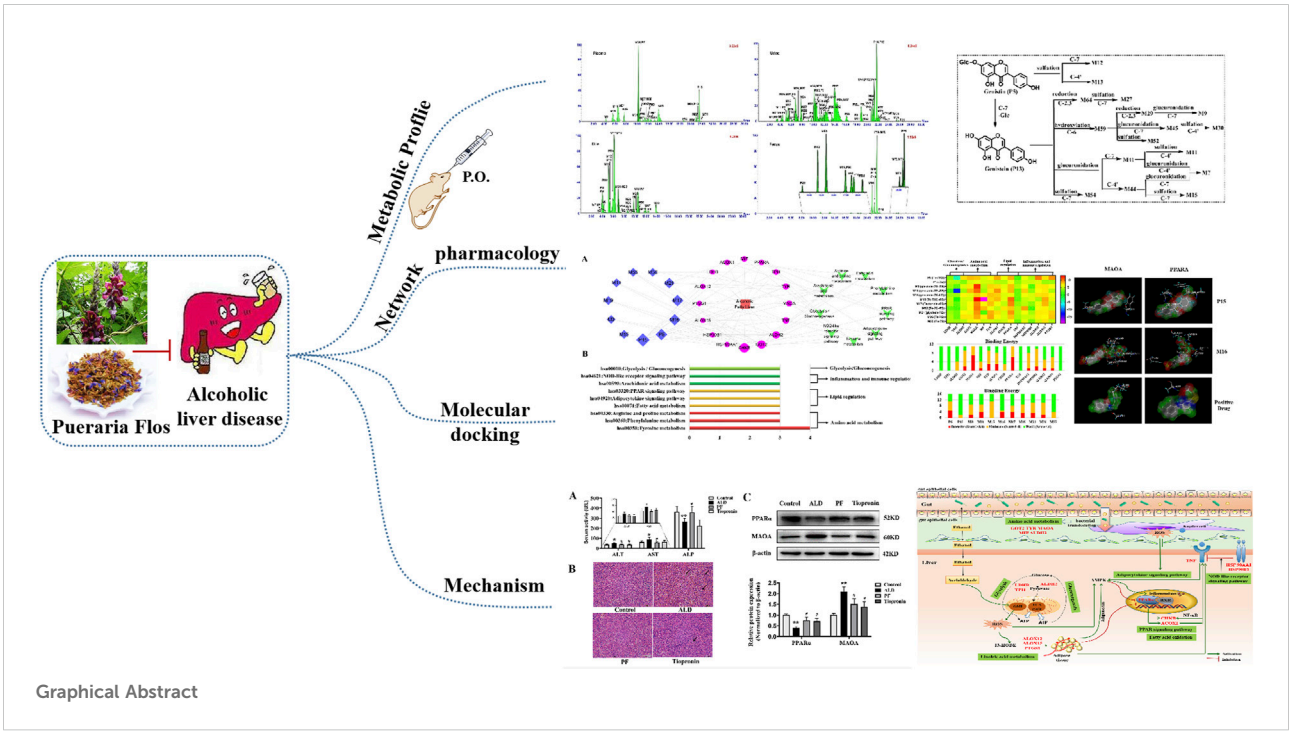

Graphical Abstract

Highlights

➢ Metabolic profile of Puerariae Flos (PF) extracts *in vivo* was firstly mapped.
➢ Phase II conjugated metabolites of isoflavonoids may be the effective forms responsible for the hepatoprotective effects of PF.
➢ PPAR-α and MAO-A involved in lipid regulation and amino acid metabolism were screened and validated to play a crucial role in the treatment of PF on alcoholic liver disease (ALD).
➢ A comprehensive mechanism for the multi-target and multi-pathway effects of PF on ALD was proposed.

1 Introduction

With the development of social economy, alcohol drinkers have been increasing in recent years. Alcohol abuse and alcoholism have emerged as common public health problems all round the world (Addolorato et al., 2016). As an important organ responsible for alcohol metabolism, the liver is the main target organ for alcohol toxicity. Accordingly, the incidence rate of alcoholic liver disease (ALD) caused by long-term heavy drinking is increasing year by year (Mathurin and Bataller, 2015). Therefore, exploring the effective treatment of ALD has become a particularly important issue which captures the attention of academic research. At present, the treatment of ALD largely relies on three medications or health products, namely, synthetic alcohol dehydrogenase inhibitor fomepizole (González-Santiago et al., 2009), commercial plant extracts of Camette *Silybum marianum* (L.) Gaertn. (Milk Thistle) and hydrodol tablets imported from Denmark and Australia (Rambaldi et al., 2005; Abenavoli et al., 2010), and an extract of oyster powder known as the Haiwang Jinzun tablet. However, their application is restricted due to side effects (hypotension, slow heartbeat, etc.), high price that depends on import, and

safety problems incurred by the influence of fresh storage and marine pollution on raw materials. Overall, the drugs for treatment of ALD enjoy huge market capacity and potential in two respects. First, it has a stable and huge beneficiary population. Second, it is in a situation where imported drugs are dominant and domestic new drugs are obviously scarce.

There have been some records of "alcohol injury," "alcohol jaundice," and "alcoholism" in ancient Chinese medicine books for a long time. As an important part of traditional Chinese medicine, some ethnic and edible medicines have rich clinical experience and remarkable curative effect in the treatment of ALD, and they are valuable and prospective for drug research and development. Puerariae Flos (PF), known as "Ge-hua" in Chinese, is botanically from the dried flowers of *Pueraria montana* var. *thomsonii* (Benth.) M.R. Almeida or *P. montana* var. *lobata* (Willd.) Maesen and S.M. Almeida ex Sanjappa & Predeep. As a homology plant of medicine and food, it has been traditionally used to relieve toxic symptoms caused by excessive alcohol consumption, such as hangover, nausea, headache, and red face in China, Japan, and Korea for over 1,500 years (National Administration of Traditional Chinese Medicine "Chinese Materia Medica" Editorial Committee, 1999). Consequently, PF has been considered as the most representative antidote in traditional medicine. In clinical application, compound preparations such as Gehua Jiecheng Decoction (葛花解酲汤) and Jiusuyu (酒速愈) are its main forms, which have regulatory and protective effect on the nervous system and the liver caused by alcohol. Meanwhile, diet therapy is also the embodiment of the clinical application of PF. Products of medicine food homology including functional slimming food—PILLBOX Onaka, PF tea, and beverage have become increasingly popular among Asian people. Recent pharmacological studies showed that extracts and compounds from PF possessed various bioactivities, such as hepatoprotective (Xiong et al., 2010), hypoglycemic (Lee et al., 2000), hypolipidemic (Lee et al., 2000), estrogenic (Shin et al., 2006), and anti-inflammatory effects (Yuan et al., 2009). With respect to the chemical constituents of PF, more than 80 compounds have been isolated and identified to date (Qu, 2014), among which, isoflavanoids and triterpenoid saponins are two major types of constituents and play important roles in its pharmacological effects. In addition, five isoflavanoids kakkalide, irisolidone, 6″-O-xylosyltectoridin, tectoridin, and tectorigenin have been proved for potential medicinal values and regarded as important phytochemical markers for quality evaluation and differentiation between species under PF (Lu et al., 2013).

According to the concept of "effective forms" and "additive effect" of pharmacodynamics substances of TCMs, only the constituents and/or metabolites that are successfully assimilated into the circulatory system and maintain a considerable concentration level by additive effect in target organs may exert curative effects. In the past decade, the metabolism of PF isoflavanoids *in vitro* has been reported by some scholars (Hirayama et al., 2011). Our research group have also been devoting our efforts toward their ADME (absorption, distribution, metabolism, and elimination) characteristic by column separation, ultra-performance liquid chromatography/quadrupole time-of-flight mass spectrometry (UPLC-QTOF-MS), and NMR spectroscopy (Bai et al., 2010; Bai et al., 2011a; Bai et al., 2011b; Qu et al., 2012; Wang H. et al., 2013; Wang S. et al., 2013; Zhang et al., 2013; Qu et al., 2014; Shi et al., 2015; Zhang et al., 2015). A total of ten urinary and biliary metabolites have been isolated and structurally identified, and the plasma pharmacokinetics as well as urinary and biliary excretion of the conjugated metabolites was also determined in rats after oral administration. The results indicated that glucuronidation and/or sulfation after deglycosylation at the C-7 position was the major metabolic pathway of isoflavanoids from PF *in vivo*. In addition, kaikasaponin III, soyasaponin I, and kakkasaponin I were the most abundant saponins in PF and showed powerful protective effects against liver damage in the previous study, which are also responsible for the overall curative effects of PF (Kinjo et al., 1999). However, to the best of our knowledge, no reports have described the global metabolic profile of triterpenoid saponins or whole plant extract of PF *in vivo*. Moreover, pharmacological mechanisms and bioactive components of PF for the treatment of ALF are still not clear.

In this study, the absorbed and excreted prototypes and metabolites of the extract of *Pueraria montana* var. *thomsonii* (Benth.) M.R. Almeida in rat plasma, urine, bile, and feces were first characterized by UPLC-QTOF MS. Furthermore, with subsequent visualization of "ingredient–target–pathway–disease" association network constructed by using a network analysis and the binding interactions between key ingredients with targets performed by molecular docking simulation, the potential active components and underlying pharmacological mechanisms for the effect of PF on ALD were explored. Furthermore, the predicted key targets of PF against ALD were validated in an alcohol-induced liver injury rat model, which would promote better application of PF, which is a medical resource for developing a supplement food or an herbal medicine for the treatment of ALD (Graphic abstract).

2 Materials and methods

2.1 Chemicals, reagents, and materials

Puerariae Flos (Batch No. 161001) collected from Anhui Province was purchased from the Tong Ren Tang TCM store (Shenyang, Liaoning Province, China) in October 2017 and was authenticated as the flower of *Pueraria montana* var. *thomsonii* (Benth.) M.R. Almeida by Prof. Dan Yuan (Department of Traditional Chinese Medicine, Shenyang Pharmaceutical University). A voucher specimen was deposited at the authors' laboratory. The reference compounds daidzein (16, Cat. No. NH010102) and luteolin (20, Cat. No. JOT-10088) were

purchased from Funakoshi Co., Ltd. (Tokyo, Japan) and Chengdu Pufei De Biotech Co., Ltd. (Chengdu, China), respectively.

Moreover, 6″-O-xylosyltectoridin (10), tectoridin (12), genistein (23), tectorigenin (25), and irisolidone (32) were isolated from the extracts of the flowers of *Pueraria montana* var. *thomsonii* (Benth.) M.R. Almeida or *Pueraria lobate* (Willd.) Ohwi. in our previous studies (Yuan et al., 2009). The purities of these compounds evaluated using a HPLC photodiode array detector (PDA) were more than 95%.

HPLC-grade acetonitrile, methanol, and formic acid were supplied by Fisher Scientific Company Inc. (Fairlawn, NJ). Ultra-pure water (18.2 MΩ) was prepared using a Milli-Q water purification system (Millipore, Milford, MA, United States). All other reagents were of analytical grade and purchased from Shandong Yuwang Pharmaceutical Co., Ltd.(Yucheng, Shandong Province, China).

Rabbit monoclonal antibodies against peroxisome proliferator–activated receptor α (PPAR-α, Cat. No. ab126285), monoamine oxidase type A (MAO-A, Cat. No. A4105), and β-actin (Cat. No. AC026) were obtained from Abcam (Cambridge, MA, United States) and ABclonal Inc, (Wuhan, Hubei Province, China), respectively. A protein extraction kit was purchased from KeyGen Biotech Co., Ltd. (Nanjing, Jiangsu Province, China).

2.2 Preparation of Puerariae Flos extracts

Dried flowers of *Pueraria montana* var. *thomsonii* (Benth.) M.R. Almeida (1 kg) were weighed accurately and reflux-extracted twice with 80% EtOH (1:12 and then 1:10, w/v) for 1 h each time. After filtering with a six-layer absorbent gauze, the two filtered extracts were combined, concentrated under vacuum to 1 L (equal to 1 g crude herb/mL), and finally transformed into a freeze-dried powder.

Now, 50 mg of prepared powder was dissolved again with 10 ml of methanol/water (8:2, v/v) and extracted for 30 min under ultrasound. After centrifugation at 13,000 rpm for 10 min at 4°C and filtration through a 0.22-μm filter, 1.0 μL of filtrate was injected to UHPLC-QTOF MS for a qualitative analysis.

To calculate the administered dose, the contents of the three major ingredients were quantitatively determined by reported HPLC-UV using an external standard method (Zhang et al., 2009). The results indicated that the contents of 6″-O-xylosyltectoridin (10), tectoridin (12), and tectorigenin (25) in the extract were 112.5, 96.64, and 19.81 mg/g, respectively.

2.3 Sample collection and pretreatment *in vivo*

A total of nine male Sprague–Dawley rats (200 ± 20 g body weight and about 6- to 8-week-old) purchased from the animal center of Shenyang Pharmaceutical University were maintained in ambient houses (22 ± 2°C) with a 12-h light/12-h dark cycle. For acclimatization, rats were allowed soy-free food and water *ad libitum* in metabolic cages for 1 week before the experiments. The animals were divided into three groups at random: a dosed plasma collection group ($n = 3$), a dosed urine and feces collection group ($n = 3$), and a dosed bile collection group ($n = 3$). All animals were fasted for 12 h before the experiments and provided with free access to water and sugar over the period of sample collection. PF extracts were suspended in a 0.5% carboxy-methyl cellulose sodium salt aqueous solution with a concentration of 0.11 g/ml and administered by oral gavage at a dose of 1.1 g/kg body weight (equivalent to 200 mg tectoridin per kg) to rats. All experimental protocols were approved by the Ethics Review Committee for Animal Experimentation of Shenyang Pharmaceutical University (License number: SCXK (Liao) 2015-0001).

Serial blood samples (approximately 0.5 ml) were collected from the suborbital vein and placed in heparinized polythene tubes at 0, 0.5, 1, 1.5, 2, 3, 4, and 8 h after oral administration and then immediately centrifuged at 3,500 rpm for 10 min at 4°C to obtain plasma. Urine and bile samples were, respectively, collected at 0–2, 2–4, 4–8, 8–12, and 12–24 h after the dosing. Feces samples were collected at 0–12 and 12–24 h and then left in a cool and dry place to dry. The collected plasma, urine, and bile samples were mixed and pretreated using solid phase extraction, while the feces samples were extracted with ultrasound in methanol/water (75:25, v/v), according to our previous method (Zhang et al., 2013).

2.4 UPLC-QTOF MS analysis

The condition of chromatographic separation and mass detection was almost the same as those reported in the literature (Qu et al., 2014). Water containing 0.2% formic acid (solvent system A) and acetonitrile containing 0.2% formic acid (solvent system B) served as the mobile phase. The only difference is the change of elution gradient, which is listed as follows: 0–1 min, 5%–8% B; 1–8 min, 8%–13% B; 8–9.5 min, 13%–15% B; 9.5–11.5 min, 15% B; 11.5–14 min, 15%–16% B; 14–18 min, 16%–17% B; 18–30 min, 17%–65% B; 30–30.5 min, 65%–99% B; and 30.5–30.6 min, 99%–5% B.

2.5 Network analysis

2.5.1 Identification of candidate targets of absorbed constituents and ALD

After identifying the absorbed and excreted ingredients of PF *in vivo* by UPLC-QTOF MS/MS, the chemical structure of absorbed constituents in plasma and bile with relative content higher than 3% was obtained as a SDF format by using ChemBioDraw Ultra 12.0 software, and then it was submitted

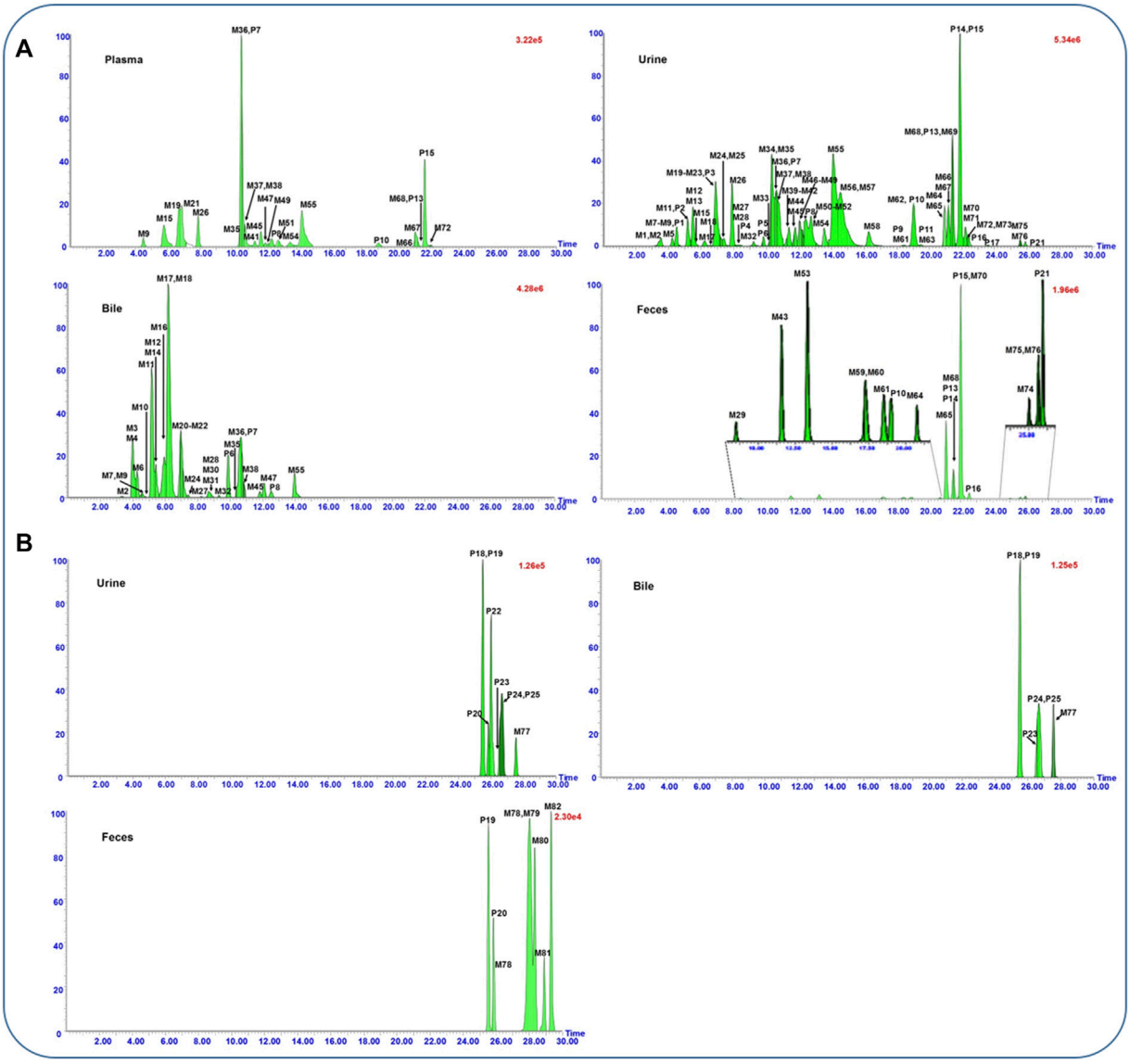

FIGURE 1
UPLC-QTOF/MS extracted ion chromatograms of flavonoid- **(A)** and saponin- **(B)** related metabolites in rat plasma, urine, bile, and feces samples after oral administration of the flower of *Pueraria montana* var. *thomsonii* (Benth.) M.R. Almeida extract.

to the Swiss Target Prediction platform (http://www.swisstargetprediction.ch/) to predict the most probable protein targets. The official gene names of top 100 targets with high matching degrees were selected for subsequent analysis. The targets associated with "alcoholic liver disease" were acquired from OMIM, TTD, CTD, GAD, DisGeNET, and GeneCards databases.

2.5.2 The protein–protein interaction network analysis

The Search Tool for the Retrieval of Interacting Genes (STRING) database (https://string-db.org/) provides predicted PPI information as well as the data which have been experimentally confirmed. The version 11.0 of STRING was applied to acquire the PPI information, with the species limited to "*Homo sapiens*" and a confidence score > 0.9. These PPI targets were defined as core targets for further analysis.

2.5.3 Enrichment analysis

The KEGG pathway analysis was performed by Database for Annotation, Visualization, and Integrated Discovery (DAVID, https://david.ncifcrf.gov/home.jsp, ver. 6.8) to find the signaling pathways related to candidate targets, and then the ALD-related pathways were selected.

2.5.4 Network construction and analysis

The absorbed constituent–target–pathway–disease network was constructed by using the network visualization software Cytoscape 3.2.1, which supplies a method for data integration, analysis, and visualization for a complicated network analysis. In the network plot, a "node" signifies an ingredient, target, or pathway, and an "edge" represents the interaction among different targets. The "degree" of a node agreed with the number of its connected edges.

2.6 Molecular docking and dynamics

The Surflex docking program in Sybyl X2.0 was utilized to evaluate the binding energies and interactions between key active compounds and targets. The crystallographic structures of 16 target proteins were retrieved from the RCSB Protein Data Bank database (http://www.rcsb.org). The binding energy could be accomplished by the formation of binding pockets after preparation of ligands and receptors by removal of water molecules and original ligands, addition of hydrogen atoms, and repairmen of amino acids. "Total Score" was used as the indicator and positive correlation with docking preference. A score ≥ 4 was considered meaningful, which mean that there was a binding between the constituents and the targets.

2.7 Experimental validations of the pharmacological effects and the molecular mechanisms of PF against ALD

SD rats were randomly divided into four groups, including control group, alcoholic liver injury (ALD) model group, PF treatment (1.1 g·kg^{-1}) group, and tiopronin treatment (60 mg·kg^{-1}) group (n = 10 in each group). The medicine-treated rats were pretreated with PF extracts or tiopronin by intragastric administration twice daily for 1 week before the first dose of ethanol and at 1 h before each administration of ethanol doses for 4 weeks, whereas the rats in the control and model groups were given equivalent volume of 0.5% sodium carboxymethylcellulose. Except for the control group, the ALD model group was simultaneously induced by orally feeding 56% Erguotou wine (10 ml/kg/d) by gavage for 4 weeks.

Furthermore, 12 h after the final administration, blood was collected and centrifuged at 3,000 r/min for 15 min to obtain serum. Liver tissues were harvested and divided into two parts: one was fixed in 4% paraformaldehyde for histological observation and another was immediately stored in −80°C for the subsequent protein validation experiments.

The levels of alanine transaminase (ALT), aspartate transaminase (AST), and alkaline phosphatase (ALP) in the serum were measured using an automatic biochemistry analyzer (Hitachi, 7600-020, Tokyo, Japan). The middle lobe of liver tissues was collected, sectioned, and fixed in 4% paraformaldehyde for at least 24 h. After being dehydrated in ethanol and embedded in paraffin, a series of paraffin sections (5 μm) were stained with hematoxylin-eosin (H&E) for histopathological examination.

The liver tissues were lysed with a lysis buffer containing 1% PMSF, phosphatase inhibitors, and protease inhibitors and incubated in an ice bath for 30 min to extract total protein. The concentration of the extracted protein was measured by using the BCA quantitative method. Equal amount of protein was electrophoretically separated by 10% SDS-PAGE. After electrophoresis, the protein was transferred on PVDF membranes and then blocked in 5% milk with TBST for 2 h. The membranes were immersed in primary antibody of PPAR-α (1:1,000 dilution), MAO-A (1:1,000 dilution), and β-actin (1: 50,000 dilution), respectively, at 4°C overnight; the next day, they were incubated with horseradish peroxidase–conjugated secondary antibody at room temperature for 2 h. Protein bands were detected with ECL Plus chemiluminescence reagent and quantified using ImageJ software (National Institutes of Health, USA). The values for each target protein were normalized to β-actin.

2.8 Statistical analysis

All values were expressed as mean ± standard deviation (SD). Differences between different groups were analyzed with one-way analysis of variance (ANOVA) using GraphPad Prism 8.0.1. The value of $p < 0.05$ was considered as statistically significant.

3 Results

3.1 Identification of PF metabolites *in vivo*

In order to identify the *in vivo* metabolites in rats, a total of 43 chemical constituents, including 22 isoflavonoids, 14 saponins, six flavonoids, and one phenolic acid were first identified or tentatively characterized in PF extracts by UPLC-QTOF MS based on our previous literatures (Lu et al., 2013) (Supplementary Figure S1, Supplementary Table S1). Consequently, the extracted ion chromatograms (EICs) were adopted to reduce the endogenous interferences from complex biological matrices and increase the sensitivity by using Metabolynx™ software combined with mass defect filtering (MDF) technique.

In total, 25 prototype components and 82 metabolites, including 93 flavonoids, 13 saponins, and one phenolic acid, were obtained by comparing the extraction ion chromatograms of dosed rat biosamples (Figure 1) with control biosamples

TABLE 1 Characterization of the metabolites in rat after oral administration of *P. montana* var. *thomsonii* (Benth.) M. R. Almeida extract by UHPLC-QTOF MS.

No.	t_R	Formula	$(M-H)^-$				Identification[a]	Relative content (%)[b]			
	(min)		Calculated	Observed	PPM	MS/MS fragments		P	U	B	F
M1	3.26	$C_{28}H_{30}O_{18}$	653.1354	653.1315	−5.97	477,301,286	Dihydrotectorigenin-7G-4′G	—	0.03	—	—
M2	3.53	$C_{28}H_{28}O_{18}$	651.1197	651.1194	−0.46	475,299,284	Tectorigenin-7G-4′G	—	0.50	0.16	—
M3	3.98	$C_{22}H_{20}O_{14}S$	539.0496	539.0497	0.19	363,283,268	Glycitein-7G-4′-S	—	—	5.90	—
M4	4.1	$C_{28}H_{30}O_{17}$	637.1405	637.1406	0.16	461,299,284	Tectoridin-7G	—	—	0.84	—
M5	4.2	$C_{22}H_{22}O_{13}$	493.0982	493.097	−2.43	317,301,286	8-OH-Dihydrotectorigenin-7G	—	0.34	—	—
M6	4.26	$C_{22}H_{22}O_{13}S$	525.0703	525.0704	0.19	445,283,268	Glycitin-4′S	—	—	2.92	—
M7	4.44	$C_{27}H_{26}O_{17}$	621.1092	621.1105	2.09	445,269,133	Genistein-7G-4′G	—	0.17	0.18	—
M8	4.45	$C_{22}H_{22}O_{13}$	493.0982	493.0974	−1.62	317,302	Dihydro-irilin D-7G	—	0.29	—	—
M9	4.51	$C_{21}H_{20}O_{12}$	463.0877	463.0861	−3.46	287,259	6-OH-Dihydrogenistein-7G	1.18	0.44	0.28	—
P1	4.69	$C_{21}H_{22}O_{11}$	449.1084	449.1083	−0.22	287,269	Dihydrokaempferol-7-O-glucoside	—	0.03	—	—
M10	4.76	$C_{28}H_{30}O_{17}$	637.1405	637.1455	7.85	461,299,284	Tectoridin-4′G	—	—	0.06	—
M11	5.16	$C_{21}H_{18}O_{14}S$	525.0339	525.0337	−0.38	349,269,133	Genistein-7G-4′S	—	1.27	15.57	—
P2	5.3	$C_{27}H_{30}O_{15}$	593.151	593.1499	−1.85	285,151	Nicotiflorin	—	0.02	—	—
M12	5.38	$C_{21}H_{20}O_{13}S$	511.0546	511.0534	−2.35	431,269,133	Genistin-7S	—	0.08	2.36	—
M13	5.48	$C_{16}H_{14}O_{10}S$	397.0229	397.0228	−0.25	317,301,286	8-OH-Dihydrotectorigenin-7S	—	1.86	—	—
M14	5.53	$C_{22}H_{22}O_{14}S$	541.0652	541.0621	−5.73	461,299,284	Tectoridin-7S	—	—	0.26	—
M15	5.79	$C_{21}H_{18}O_{14}S$	525.0339	525.0361	4.19	349,269,133	Genistein-7S-4′G	6.05	0.02	—	—
M16	5.92	$C_{27}H_{30}O_{18}S$	673.1075	673.1075	0.00	379,299,284	6″-O-Xylosyltectoridin-4′S	—	—	6.52	—
M17	6.21	$C_{22}H_{22}O_{14}S$	541.0652	541.0643	−1.66	461,299,284	Tectoridin-4′S	—	0.34	31.08	—
M18	6.56	$C_{28}H_{28}O_{19}$	667.1147	667.1157	1.50	491,315,300	Irilin D-7G-4′G	—	0.04	0.04	—
M19	6.71	$C_{22}H_{20}O_{15}S$	555.0445	555.0441	−0.72	379,299,284	Tectorigenine-7G-4′S	12.17	22.71	—	—
M20	6.87	$C_{22}H_{20}O_{16}S$	571.0394	571.0394	0.00	395,315,299,284	8-OH-Tectorigenine-7G-4′S	—	2.48	4.65	—
M21	6.89	$C_{22}H_{20}O_{11}$	459.0927	459.0915	−2.61	283,268	Glycitein-7G	3.61	2.03	4.49	—
M22	7.14	$C_{22}H_{22}O_{15}S$	557.0601	557.0587	−2.51	477,301,286	Dihydrotectorigenine-7G-4′S	—	0.35	0.83	—
M23	7.17	$C_{16}H_{12}O_{11}S_2$	442.9743	442.9748	1.13	363,283,268	Glycitein-7S-4′S	—	0.02	—	—
P3	7.28	$C_{22}H_{22}O_{10}$	445.1135	445.1136	0.22	283,268,239	Glycitin	—	0.04	—	—
M24	7.37	$C_{22}H_{20}O_{11}$	459.0927	459.0922	−1.09	283,268	Glycitein-4′G	—	0.11	0.15	—
M25	7.4	$C_{22}H_{20}O_{13}$	491.0826	491.0817	−1.83	315,299,284	8-OH-Tectorigenine-7G	—	0.14	—	—
M26	7.88	$C_{16}H_{14}O_6$	301.0712	301.0716	−0.66	286,257	Dihydrotectorigenin	4.40	2.94	—	—
M27	8.1	$C_{15}H_{12}O_8S$	351.0175	351.0158	−4.84	271,253,225	Dihydrogenistein-7S	—	0.02	0.14	—
M28	8.36	$C_{16}H_{12}O_{12}S_2$	458.9692	458.9671	−4.58	379,299,284	Tectorigenin-7S-4′S	—	0.10	0.05	—
M29	8.5	$C_{15}H_{12}O_6$	287.0556	287.0561	1.74	259	6-OH-Dihydrogenistein	—	—	—	0.13
M30	8.67	$C_{21}H_{18}O_{15}S$	541.0288	541.0308	3.70	461,285,133	6-OH-Genistein-7G-4′S	—	—	0.80	—
M31	8.84	$C_{21}H_{20}O_{13}S$	511.0546	511.0535	−2.15	431,269,133	Genistin-4′S	—	—	0.20	—
P4	9.02	$C_{27}H_{30}O_{16}$	609.1456	609.1415	−6.73	301,285	Rutin	—	0.01	—	—
M32	9.21	$C_{22}H_{20}O_{16}S$	571.0394	571.0386	−1.40	395,315,300	Irilin D-7G-4′S	—	0.24	0.21	—
P5	9.75	$C_{21}H_{20}O_{10}$	431.0978	431.0961	−3.94	269,133	Genistin	—	0.02	—	—
P6 [c]	9.82	$C_{27}H_{30}O_{15}$	593.1506	593.1506	0.00	299,284,255	6″-O-Xylosyltectoridin	—	0.40	4.07	—
M33	10.15	$C_{22}H_{20}O_{11}$	459.0927	459.0925	−0.44	283,268	Biochanin A-7G	—	0.16	—	—
M34	10.27	$C_{16}H_{12}O_{10}S$	395.0073	395.0063	−2.53	315,299,284	8-OH-Tectorigenin-7S	—	0.19	—	—
M35	10.44	$C_{16}H_{12}O_8S$	363.0175	363.0197	6.06	283,268	Glycitein-7S	0.31	4.26	0.84	—
M36	10.56	$C_{22}H_{20}O_{12}$	475.0877	475.0863	−2.95	299,284	Tectorigenine-7G	31.64	3.25	8.23	—
P7 [c]	10.62	$C_{22}H_{22}O_{11}$	461.1084	461.1076	−1.73	299,284,255	Tectoridin	0.71	0.52	1.55	—
M37	10.74	$C_{16}H_{12}O_8S$	363.0175	363.0174	−0.28	283,268	Glycitein-4′S	2.90	0.74	—	—

(Continued on following page)

TABLE 1 (*Continued*) Characterization of the metabolites in rat after oral administration of *P. montana* var. *thomsonii* (Benth.) M. R. Almeida extract by UHPLC-QTOF MS.

No.	t_R	Formula	$(M-H)^-$				Identification[a]	Relative content (%)[b]			
	(min)		Calculated	Observed	PPM	MS/MS fragments		P	U	B	F
M38	10.8	$C_{22}H_{20}O_{12}$	475.0877	475.0843	−7.16	299,284	Tectorigenine-4′G	1.27	2.26	1.00	—
M39	11.24	$C_{22}H_{20}O_{13}$	491.0826	491.0819	−1.43	315,300	Irilin D-7G	—	0.16	—	—
M40	11.26	$C_{16}H_{12}O_8S$	363.0175	363.0181	1.65	283,268	Biochanin A-7S	—	0.30	—	—
M41	11.39	$C_{21}H_{18}O_{11}$	445.0771	445.0743	−6.29	269,133	Genistein-7G	0.80	0.80	—	—
M42	11.47	$C_{15}H_{10}O_8S$	349.0018	348.9996	−6.30	269,151	6-OH-Daidzein-7S	—	0.05	—	—
M43	11.58	$C_{15}H_{12}O_5$	271.0606	271.0599	−2.58	253,225	6-OH-Dihydrodaidzein	—	—	—	0.88
M44	11.68	$C_{21}H_{18}O_{11}$	445.0771	445.0769	−0.45	269,133	Genistein-4′G	—	0.28	—	—
M45	11.76	$C_{21}H_{18}O_{12}$	461.0720	461.0714	−1.30	285,133	6-OH-Genistein-7G	2.42	0.76	0.62	—
M46	12.02	$C_{16}H_{14}O_{10}S$	397.0229	397.0219	−2.52	317,302	Dihydroirilin D-7S	—	0.27	—	—
M47	12.04	$C_{23}H_{22}O_{13}$	505.0982	505.0963	−3.76	329,313,298,283,255	8-OH-Irisolidone-7G	0.55	1.11	1.53	—
M49	12.24	$C_{22}H_{22}O_{12}$	477.1033	477.1028	−1.05	301,286	Dihydrotectorigenin-7G	—	0.16	—	—
leftM48	12.24	$C_{16}H_{14}O_{10}S$	397.0229	397.0212	−4.28	317,302	Dihydroirilin D-4′S	0.39	0.64	—	—
P8	12.43	$C_{21}H_{20}O_{11}$	447.0927	447.0971	9.84	285,267	6-Hydroxygenistein-7-O-glucoside	1.56	0.28	0.84	—
M50	12.75	$C_{22}H_{20}O_{12}$	475.0877	475.0872	−1.05	299,284,255	6-OH-Biochanin A-6G	—	1.25	—	—
M51	12.86	$C_{16}H_{14}O_9S$	381.028	381.0269	−2.89	301,286	Dihydrotectorigenin-7S	1.51	2.50	—	—
M52	13.03	$C_{15}H_{10}O_9S$	364.9967	364.9967	0.00	285,257	6-OH-Genistein-7S	—	0.19	—	—
M53	13.34	$C_{15}H_{10}O_5$	269.045	269.0448	−0.74	151	6-OH-Daidzein	—	—	—	1.35
M54	14.08	$C_{15}H_{10}O_8S$	349.0018	348.9989	−8.31	269,133	Genistein-7S	0.93	1.34	—	—
M55	14.2	$C_{16}H_{12}O_9S$	379.0124	379.0116	−2.11	299,284	Tectorigenin-7S	12.10	8.75	2.64	—
M56	14.53	$C_{16}H_{12}O_9S$	379.0124	379.0133	2.37	299,284	Tectorigenin-4′S	—	6.97	—	—
M57	15.01	$C_{16}H_{12}O_{10}S$	395.0073	395.0068	−1.27	315,300	Irilin D-7S	—	1.00	—	—
M58	16.23	$C_{17}H_{14}O_{10}S$	409.0229	409.0227	−0.49	329,313,298,283	8-OH-Irisolidone-7S	—	1.26	—	—
M59	17.19	$C_{15}H_{10}O_6$	285.0399	285.0392	−2.46	257,229	6-OH-Genistein	—	—	—	0.26
M60	17.26	$C_{16}H_{12}O_7$	315.0505	315.0511	1.90	299,284,255	8-OH-Tectorigenin	—	—	—	0.47
P9	18.44	$C_{16}H_{12}O_7$	315.0505	315.0483	−6.98	300	Irilin D	—	0.06	—	—
M61	18.49	$C_{16}H_{14}O_5$	285.0763	285.076	−1.05	270	Dihydroglycitein	—	0.03	—	0.54
P10	19.02	$C_{16}H_{12}O_5$	283.0606	283.0614	2.83	268	Glycitein	0.68	2.62	—	0.45
M62	19.02	$C_{23}H_{22}O_{13}$	505.0982	505.0937	−8.91	329,314	Iristectorigenin A-7G	—	0.27	—	—
P11 [c]	19.47	$C_{15}H_{10}O_6$	285.0399	285.0382	−5.96	133	Luteolin	—	0.09	—	—
M63	19.86	$C_{17}H_{16}O_6$	315.0869	315.0845	−7.62	300,285,257	Dihydroirisolidone	—	0.01	—	—
P12	20.13	$C_8H_8O_4$	167.0344	167.0345	0.60	108	Vanillic acid	0.51	0.04	—	—
M64	20.72	$C_{15}H_{12}O_5$	271.0606	271.0589	−6.27	253,225	Dihydrogenistein	—	0.14	—	0.26
M65	20.92	$C_{16}H_{14}O_6$	301.0712	301.0711	−0.66	286,257	6-OH-Dihydrobiochanin A	—	1.67	—	21.96
M66	21.14	$C_{17}H_{14}O_{10}S$	409.0229	409.0215	−3.42	329,314	Iristectorigenin A-7S	0.43	0.54	—	—
M67	21.3	$C_{17}H_{14}O_9S$	393.028	393.0269	−2.80	313,298,283,255	Irisolidone-7S	1.85	1.42	—	—
M68	21.41	$C_{16}H_{12}O_6$	299.0556	299.0553	−1.00	284,255	Isotectorigenin	0.25	1.80	—	5.69
P13 [c]	21.43	$C_{15}H_{10}O_5$	269.045	269.0451	0.37	133	Genistein	0.59	3.02	—	2.74
M69	21.59	$C_{23}H_{24}O_{12}$	491.119	491.1167	−4.68	315,300,285	Dihydroirisolidone-7G	—	0.03	—	—
P14	21.74	$C_{15}H_{10}O_5$	269.045	269.0452	0.74	151	Apigenin	—	0.30	—	0.39
P15 [c]	21.87	$C_{16}H_{12}O_6$	299.0556	299.0548	−2.68	284,255	Tectorigenin	11.07	9.11	—	57.87
M70	22.13	$C_{17}H_{14}O_7$	329.0661	329.0678	5.17	313,298,283,255	8-OH-Irisolidone	—	0.05	—	0.21
M71	22.2	$C_{23}H_{22}O_{12}$	489.1033	489.1028	−1.02	313,298,283,255	Irisolidone-7G	—	0.68	—	—
M72	22.24	$C_{18}H_{16}O_6$	327.0869	327.0883	4.28	313,298,283,255	4′,7-Di-methyltectorigenin	0.14	0.01	—	—

(Continued on following page)

TABLE 1 (*Continued*) Characterization of the metabolites in rat after oral administration of *P. montana* var. *thomsonii* (Benth.) M. R. Almeida extract by UHPLC-QTOF MS.

No.	t_R (min)	Formula	$(M-H)^-$				Identification[a]	Relative content (%)[b]			
			Calculated	Observed	PPM	MS/MS fragments		P	U	B	F
M73	22.3	$C_{16}H_{12}O_6$	299.0556	299.0554	−0.67	284,255	6-OH-Biochanin A	—	0.35	—	—
P16	22.42	$C_{17}H_{14}O_7$	329.0661	329.066	−0.30	314	Iristectorigenin A	—	0.24	—	1.55
P17	23.6	$C_{16}H_{12}O_4$	267.0657	267.066	1.12	252	Formononetin	—	0.04	—	—
M74	25.03	$C_{16}H_{14}O_5$	285.0763	285.0751	−4.21	270	Dihydrobiochanin A	—	—	—	0.13
P18	25.47	$C_{47}H_{76}O_{17}$	911.5004	911.4987	−1.87	765,615,457,437	Astragaloside VIII	—	0.04	0.14	—
P19	25.52	$C_{48}H_{78}O_{18}$	941.511	941.5088	−2.34	795,615,457,437	Soyasaponin I	—	0.15	0.36	0.76
M75	25.56	$C_{17}H_{14}O_6$	313.0712	313.072	−0.66	298,283,255	Isoirisolidone	—	0.04	—	0.13
M76	25.69	$C_{16}H_{12}O_5$	283.0606	283.0605	−0.35	268	Biochanin A	—	0.21	—	0.25
P20	25.86	$C_{47}H_{76}O_{17}$	911.5004	911.5	−0.44	765,615,457,437	Soyasaponin II	—	0.04	—	0.29
P21 [c]	25.89	$C_{17}H_{14}O_6$	313.0712	313.0714	0.64	298,283,255	Irisolidone	—	0.16	—	0.64
P22	26.01	$C_{48}H_{78}O_{17}$	925.5161	925.517	0.97	779,599,441,439	Kaikasaponin III	—	0.16	—	—
P23	26.57	$C_{42}H_{68}O_{13}$	779.4582	779.4576	−0.77	617,439	Kaikasaponin I	—	0.05	0.13	—
P24	26.66	$C_{47}H_{76}O_{16}$	895.5055	895.5039	−1.79	599,441,439	Kakkasapnin I	—	0.05	0.11	—
P25	26.75	$C_{47}H_{76}O_{16}$	895.5055	895.5021	−3.80	599,441,439	Baptisiasaponin I	—	0.05	0.10	—
M77	27.54	$C_{41}H_{66}O_{12}$	749.4476	749.4461	−2.00	587,411,409	Demethyl-22-dehydroxyl-kaikasaponin I	—	0.03	0.16	—
M78	27.92	$C_{36}H_{60}O_9$	635.4159	635.4177	2.83	459,438	Reduct-soyasapogenol B-3-β-D-glucuronide	—	—	—	0.14
M79	28.03	$C_{31}H_{50}O_3$	469.3682	469.3668	−2.98	455,439,437	Methyl-soyasapogenol E	—	—	—	1.48
M80	28.32	$C_{30}H_{48}O_5$	487.3423	487.3398	−5.13	471,455,439	1, 21-Dihydroxyl-soyasapogenol E	—	—	—	0.55
M81	28.89	$C_{37}H_{62}O_9$	649.4316	649.4307	−1.39	473,459,441,439	Methyl-reduct-soyasapogenol B-3-β-D-glucuronide	—	—	—	0.23
M82	29.31	$C_{30}H_{50}O_4$	473.3631	473.3635	0.85	457,437	1-Hydroxyl-soyasapogenol B	—	—	—	0.65

[a]G, glucuronide; S, sulfate; and OH, hydroxylation.
[b]P, plasma samples; U, urine samples; B, bile samples; and F, fecal samples.
[c]Components identified with reference compounds comparison.

(Supplementary Figure S2). In addition, the peak area of each absorbed constituent was also recorded automatically using the MetaboLynx™ system. After summarizing the peak area of all constituents, the percentage calculated by the ratio of their peak area to the total peak area in each biological sample was described as relative content. The detail data of identified results are listed in Table 1. These compounds could be generally divided into two categories, namely, flavonoid- and saponin-related metabolites.

3.1.1 Metabolites associated with flavonoids

A total of 93 flavonoids and their metabolites were screened out from the dosed samples, with 16 of them elucidated as prototypes and others assigned as metabolites. Among the prototypes, eight components that were almost consistent with our previous study belonged to aglycones (P9~P11, P13~P17, and P21) and glycosides (P1~P8), respectively. In addition, five (P7~P8, P10, P13, and P15), 25 (P1~P25), three (P6~P8), and six (P10, P13~P16, and P21) prototype components were observed separately in rat plasma, urine, bile, and feces samples. As for the metabolites, glucuronidation, sulfation, methylation, hydroxylation, and reduction were their major metabolic pathways. 76 metabolites, including 24 sulfates, 21 glucuronides, 17 aglycones, eight glucuronide–sulfates, four diglucuronides, and two disulfates were identified (Figure 1A).

As for the aglycone skeleton, MS^2 spectra with high energy showed characteristic $^{1,3}A^-$ and $^{1,3}B^-$ ions origin from a retro-Diels-Alder (RDA) cleavage of the C ring as well as losses of CH_3 (15 Da), O (16 Da), H_2O (18 Da), CO (28 Da), CO_2 (44 Da), and/or combination of the fragments mentioned before. Meanwhile, the reduction at 2,3-double bond of the C ring and rearrangement between C-6 and C-8 positions were also common in the *in vivo* metabolic pathway of PF flavonoids according to the related literature (Bai et al., 2010; Bai et al., 2011a). Correspondingly, the metabolic pathway of flavonoids

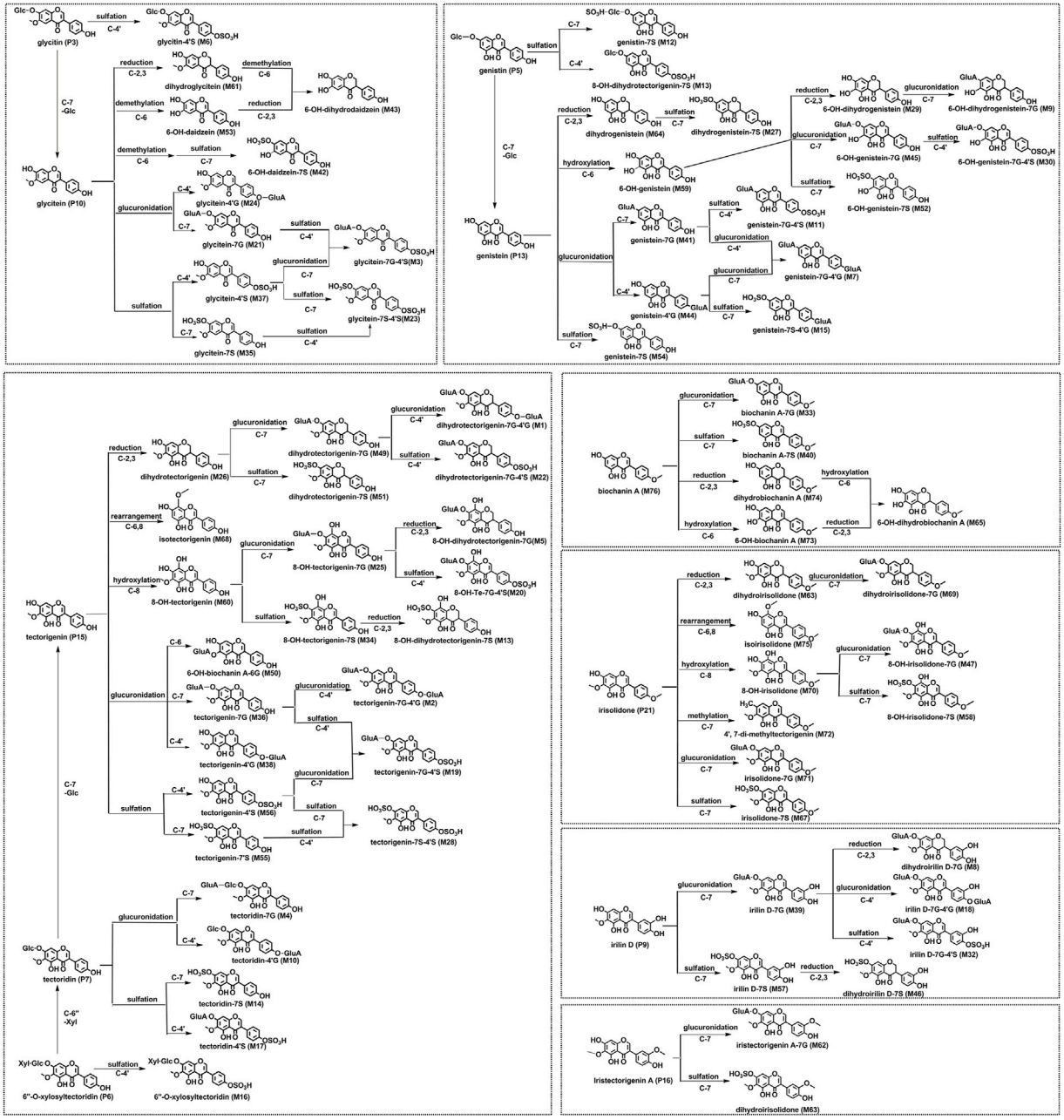

FIGURE 2
Proposed metabolic pathways of flavonoid-related metabolites in rats after oral administration of the flower of *Pueraria montana* var. *thomsonii* (Benth.) M. R. Almeida extract.

from PF *in vivo* was outlined, as shown in Figure 2. The results indicated that irilin D (P9), glycitein (P10), genistein (P13), tectorigenin (P15), iristectorigenin A (P16), and irisolidone (P21), which were the aglycone of flavonoids constituent in PF extracts, were the key prototype components in the metabolic process.

3.1.2 Metabolites associated with saponins

Triterpenoid saponins found in PF are another major group of bioactive components. In addition, 13 saponins, sharing a basic chemical skeleton but with different moieties at C-3, C-22, and C-28, were identified and tentatively characterized based on

their mass spectra and literature reports (Gao et al., 2007; Liang et al., 2014; Yu et al., 2016) (Figure 1B).

Compounds P18~P20, M78, and M81~M82 could be grouped because they possess the same aglycone soyasapogenol B ($C_{30}H_{50}O_3$) as the aglycone, and they presented similar fragmentation pathways. P18 and P20 with precursor ions detected at *m/z* 911 $(M-H)^-$ are a pair of isomeric with an identical elemental composition of $C_{47}H_{76}O_{17}$. Both displayed a series of characteristic fragment ions at *m/z* 765, 615, 457, and 437 by simultaneously losing sugar units including 146 Da (rhamonose), 132 Da (arabinose, xylose), 176 Da (glucuronosyl), and 18 Da (H_2O) at the site of C-3. They were ascribed to astragaloside VIII and soyasaponin II, respectively (Lu et al., 2013). Similarly, P19 was identified as soyasaponin I according to our previous reports (Lu et al., 2013). The metabolites M78 and M81 exhibited the protonated molecular ion at *m/z* 635.4177 ($C_{36}H_{60}O_9$) and *m/z* 649.4307 ($C_{37}H_{62}O_9$), which were 2Da (2H) and 16 Da (CH_2+2H) higher than that of the soyasapogenol B-3-β-D-glucuronide, suggesting that both were reduced and methylated metabolites. The reduction at 12,13-double bond of the C ring is a metabolic pathway for saponins such as α-hederin (Liang et al., 2014), which was also reduced to hydrogenated metabolite in rat feces by the gut microflora. Accordingly, M78 and M81 were tentatively identified as reduct-soyasapogenol B-3-β-D-glucuronide and methyl-reduct-soyasapogenol B-3-β-D-glucuronide based on the aforementioned researches. Similarly, M82 with *m/z* 473.3635 ($C_{30}H_{50}O_4$) was 16 Da (O) higher than that of aglycone, which was identified as 1-hydroxyl-soyasapogenol B because C-1 was the active site according to the related research (Yu et al., 2016).

P22~P25 and M77 could be grouped because they possess the same aglycone sophoradiol. P22~P25 were identified as kaikasaponin III, kaikasaponin I, kakkasaponin I, and baptisiasaponin I by comparison with the identified constituent in PF extracts, respectively (Lu et al., 2013). M77 exhibited a protonated molecular ion at m/z 749.4461 ($C_{41}H_{66}O_{12}$), which was 30 Da (-CH_2-O) lower than that of kakkasaponin I (P23). Thus, it was demethylated and dehydroxylated metabolite of P23. Since there is only one hydroxyl substituted at C-22, M77 was deduced as dimethyl-22-dehydroxyl-kakkasaponin I. Analogously, M79 and M80 were identified as methylated and C1, C21-dihydroxyl of aglycone soyasapogenol E based on the similar metabolic pathway of saikosaponin G and glycyrrhetinic acid (Gao et al., 2007; Yu et al., 2016).

3.3 Compound–target–pathway network construction

In order to understand important effective components, the relative content of each metabolite was calculated by area normalization and expressed as the percentage of its peak area to the total peak areas in each kind of biosamples (Table 1). A total of 13 candidate components that detected in rat plasma and/or bile samples with relative content more than 3% were screened for the further network analysis. In all, 104 protein targets associated with the 13 constituents were retrieved from the Swiss Target Prediction platform after eliminating the overlaps, and a component–target network was constructed (Figure 3A). Their detail information is shown in Supplementary Table S2. Similarly, 5338 ALD-related targets obtained from OMIM, TTD, CTD, GAD, DisGeNET, and GeneCards databases were collected after searching, integrating, and de-duplicating steps (Supplementary Table S3).

To acquire the candidate targets of PF against ALD, aforementioned constituent targets and disease targets were intersected, and 88 intersection targets were obtained (Figure 3B). Then the protein–protein interaction (PPI) analysis aiming at more crucial targets was carried out based on the aforementioned 88 targets by using the STRING database. Accordingly, 47 candidate targets with confidence scores greater than 0.9 were screened out (Figure 3C) and subjected to the KEGG pathway enrichment to elucidate their molecular mechanisms. As a result, nine signaling pathways (excluded cancer pathways) were involved and enriched from 16 of 47 targets (Figure 3D), which could be sorted into four groups according to their biological functions: (1) glycolysis/gluconeogenesis-related targets (LDHB, TPI1, and ALDH2); (2) amino acid metabolism–related targets (ALDH2, GOT2, MAOA, MIF, and TYR); (3) lipid regulation–related targets (ALDH2, ACOX1, CHKB, PPARA, and TNF); and (4) inflammation and immune regulation–related targets (TNF, HSP90AA1, HSP90B1, ALOX12, ALOX15, and PTGS1). Furthermore, we mapped the 16 targets into components and obtained 11 absorbed components (P6, P15, M3, M11, M15~M17, M19, M21, M36, and M55) (Figure 3D).

3.4 Molecular docking

A docking analysis was performed to evaluate the relationship between the active components and potential targets that were predicted by the network analysis. The aforementioned absorbed 11 ingredients were selected as candidate components to dock with the 16 relevant targets that were screened by the network analysis. Consequently, a heat map performed by GraphPad 8.0 software was present for intuitively describing the receptor–ligand interactions.

Based on the heat map (Figure 4A), the interactions of 11 components with 16 selective targets were ranked as intensive binding (>8.0), moderate binding (6.0–8.0), and weak binding (<6.0). Here, 8.0 was set as the cutoff value to screen the potential active components against ALD. As a result, 6″-O-xylosyltectoridin (P6) and three metabolites genistein-7-

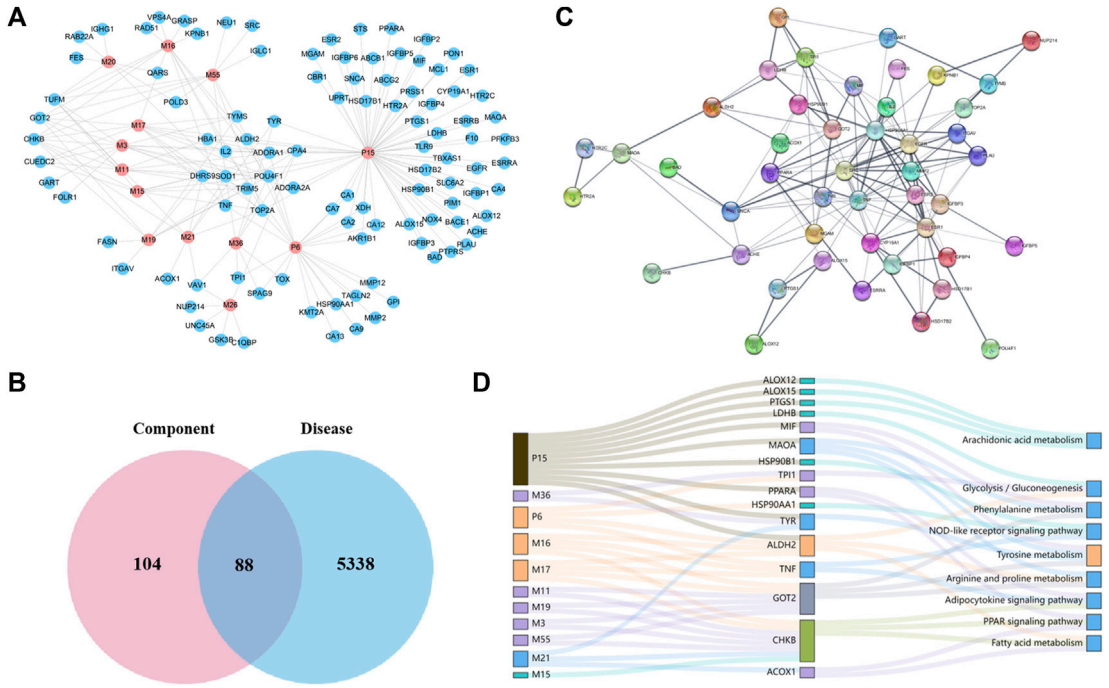

FIGURE 3
Network construction and correlation analysis. **(A)** Distribution characteristic of 13 candidate-absorbed components and their predicted targets; **(B)** Venn analysis of targets between 13 candidate components and ALD; **(C)** PPI network of 47 merged targets according to the STRING database; **(D)** interaction network of absorbed constituents, candidate targets, and enriched pathways. A node stands for a constituent (left), a target (middle), or a pathway (right); the interactions of two nodes were represented by a line, and the bigger size of a node, the higher the degree.

glucuronide-4′-sulfate (M11), tectoridin-4′-sulfate (M17), and 6″-O-xylosyltectoridin-4′-sulfate (M16) showed better binding ability with more than three intensive values, while weak or no inhibition effects were observed to the prototype tectorigenin (P15). As for targets, monoamine oxidase type A (MAO-A) and peroxisome proliferator–activated receptor α (PPAR-α), which rank the top two places in binding ability, contained seven and six values more than the cutoff and revealed close correlations with PF absorbed components. Among them, the interaction between MAO-A and compounds M3, M11, and M16 and PPAR-α and M16 presented the best performance. P15 and M16 were selected as representative prototype components and metabolites, respectively. Their binding mode in the active site of MAO-A and PPAR-α has been shown in a three-dimensional pattern in Figure 4B.

As for MAO-A, P15 showed two H-bond interactions with PHE208 and ALA68, which were C-7 and C-4′ phenolic hydroxyls on the A and B rings, respectively. M16 showed eight H-bond interactions as follows: four hydroxyl groups on glucose with Gly443, Gly49, ARG51, and THR52; three hydroxyl groups on xylose with THR435, SER24, and ALA27; and a phenolic hydroxyl at C-4′ on the B ring with GLN215. While Gly443 and ILE23 were involved in the N-H Bond interactions with a representative MAO-A inhibitor moclobemide, the former was also the connection site of M16 with MAO-A.

Along the similar lines, interaction between P15 and PPAR-α showed three H-bond interactions, a phenolic hydroxyl, and a carbonyl group from the isoflavonoid skeleton with ASN219; a methoxy group and a phenolic hydroxyl on the A ring with ALA333; and a methoxy group on the A ring with TYR334. Similarly, M16 showed five H-bond interactions, two phenolic hydroxyls with ASN219 and ALA333, and three hydroxyl groups on glucose and xylose with THR279, Glu286, and Gly335. In addition, the interaction of C-4′-sulfate with TYR 279 was also observed. As the positive comparison, PPAR-α agonist WY14643 shared the same residue ALA333 with P15 and M16, which was the active site for the treatment on ALD. Collectively, the docking results above showed that glycosylation or sulfation increased the binding activity comparison with the prototype.

3.5 Experimental validations of the pharmacological effects and the molecular mechanisms of PF against ALD

We further verified the pharmacological effects and the prediction mechanisms of PF against ALD based on the rat model. As shown in Figure 5A, ALT and AST levels were

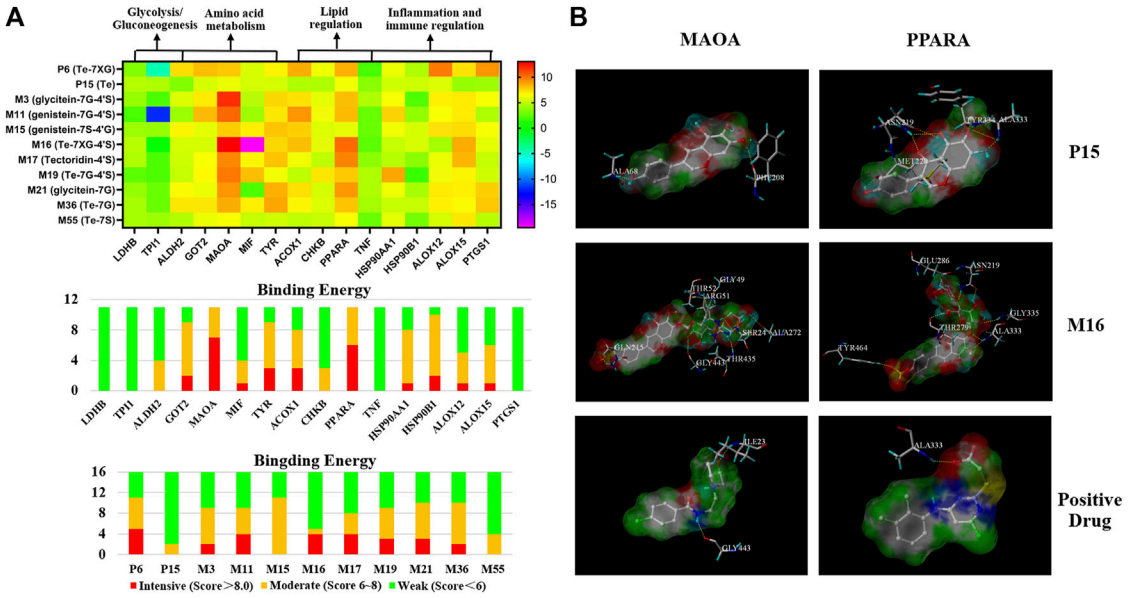

FIGURE 4
Binding interaction between the active metabolites and potential targets predicted by network analysis. **(A)** Binding energy between 11 constituents with 16 targets performed by docking. **(B)** Binding mode of tectorigenin (P15), 6″-O-xylosyltectoridin-4′-sulfate (M16), and positive drug with MAO-A and PPAR-α. (Compounds are presented with the thick stick style; hydrogen bonding interactions are expressed by yellow dotted lines. Amino acid residues which form H-bonds are presented by thin line and labeled with residue sequence.)

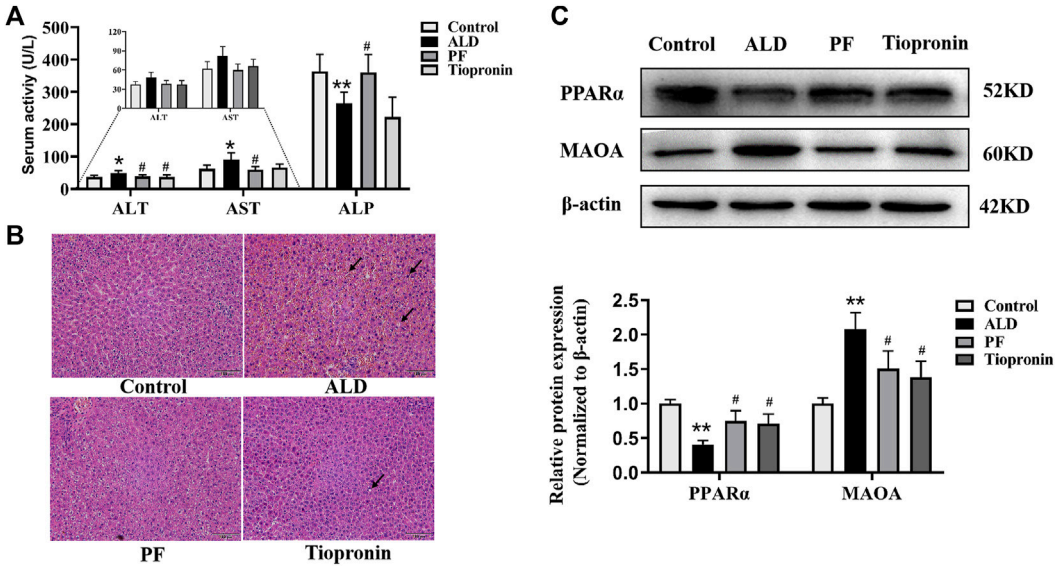

FIGURE 5
Protective effect of PF on ethanol induced rat liver injury. **(A)** Serum ALT, AST and ALP were measured using the automatic biochemistry analyzer. **(B)** Histological changes were observed using H&E staining (100×). The arrow indicates swelling and nuclear deviation, red blood cells overflow, or lipid vacuolation. **(C)** Effects of PF on PPAR-α and MAO-A protein levels in liver tissue based on the Western blotting assay. Data are presented as the mean ± SD (n = 3), *p < 0.05 and **p < 0.01 vs. control group. $^{\#}p$ < 0.05 vs. model group.

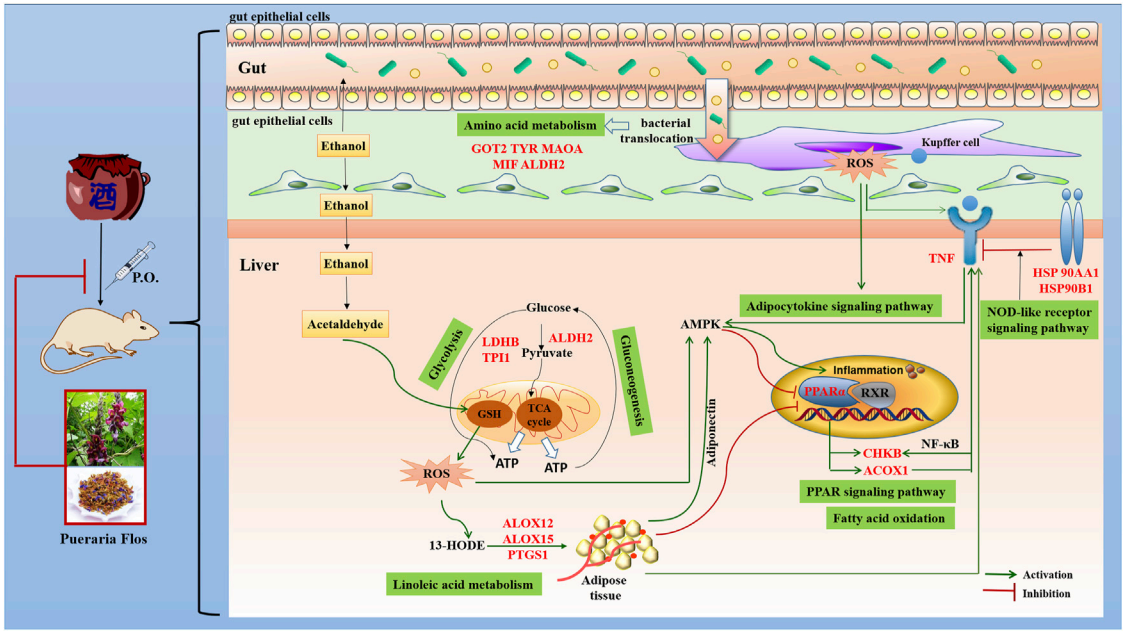

FIGURE 6
Potential molecular mechanism of PF acting on ALD.

enhanced in the ethanol-treated group in comparison with the control group whereas that of ALP decreased significantly ($p < 0.05$). Conversely, supplementation of PF could effectively reduce the activities of AST and ALT as well as increase the level of ALP ($p < 0.05$). Similarly, tiopronin reduced the content of ALT ($p < 0.05$), while there was no statistical difference in the AST and ALP activities ($p > 0.05$). H&E staining results indicated that PF and tiopronin markedly alleviated ethanol-triggered microvesicular steatosis with mild swelling and nuclear deviation and red blood cells overflow as well as certain lipid vacuolation in hepatocytes (Figure 5B).

To validate whether the targets MAO-A and PPAR-α were involved in the protective effect of ALD by PF, their protein levels in the liver tissues were examined. As shown in Figure 5C, the expression levels of MAO-A and PPAR-α protein respectively increased and decreased in the ALD model rats, compared to the normal control group ($p < 0.01$). As hypothesized, treatment with PF significantly recovered the protein expression of MAO-A and PPAR-α compared to the model group ($p < 0.05$). Notably, the effect of PF was approximately equal to that of tiopronin. The verification results are consistent with the network prediction results.

4 Discussion

In general, PF is given as a tea drink or compounded preparations with other herbal medicines by oral administration in the daily life or clinic therapy. Thus, exploring the constituents absorbed and excreted *in vivo* can narrow the screening scope of effective forms and build a foundation for the follow-up mechanism research of PF in treating various diseases. In the present study, a global metabolic profile of PF including the identification and classification was provided by detecting the metabolites in rat plasma, urine, bile, and feces after oral administration owing to high sensitivity of the UPLC-QTOF MS system. Moreover, the relative content of the prototypes and metabolites in the four biological samples were determined to evaluate the contribution of different metabolic reactions *in vivo*. As shown in Table 1, two categories of the parent compounds and related metabolites, including flavonoids and saponins, were observed in rat biological samples. The saponins were only detected in urine and feces in the form of prototypes or metabolites that were produced from phase I metabolism, such as hydroxylation, dehydroxylation, methylation, demethylation, and reduction. The flavonoids were generally speculated to be the bioactive components, and the effective forms should be absorbed into blood with appropriate concentrations.

If we evaluate the contribution of different metabolic reactions to the metabolite formation according to their number and relative content, we could find that sulfation and glucuronidation are both major metabolic reactions for PF flavonoids. The route of *in vivo* metabolism or biotransformation for flavonoids is a process to transform them into more hydrophilic metabolites, which not only

enhanced their oral absorption and bioavailability but also enhanced the excretion from the body *via* the bile and urine. O'Leary et al. (2003) demonstrated that the isoflavone conjugates formed at intestinal are easy to be transported into the hepatocytes and then excreted into the bile. Moreover, hepatic uptake and efflux transporters on the basolateral membrane participate in drug elimination, which can facilitate endogenous compounds and metabolites with poor membrane permeability to transport into hepatocytes (Funk, 2008). Except for some conjugated metabolites that were eluted in bile, deconjugated by intestinal microflora, and excreted to feces, the others were reabsorbed *in vivo* and then underwent enterohepatic circulation. Therefore, the metabolites with higher relative content in bile were also selected for a follow-up mechanism analysis.

The network analysis combined with the docking analysis revealed that 6″-O-xylosyltectoridin (P6) and three metabolites genistein-7-glucuronide-4′-sulfate (M11), tectoridin-4′-sulfate (M17), and 6″-O-xylosyltectoridin-4′-sulfate (M16) may be the effective forms in the treatment of PF on ALD. The latter three belong to conjugated metabolites. Over the past two decades, several studies showed that glucuronides, sulfates, or bis-conjugates were the major existent form of flavonoids in systemic circulation and closely associated with their pharmacological actions. Our previous study found that tectorigenin-7S (M55) and tectorigenin-7G (M36) exhibited stronger inhibitory activity against aldose reductase than tectorigenin (P15) (Qu et al., 2014). In addition, several flavonoids conjugates, such as daidzein-7-glucuronide-4′-sulfate; daidzein-4′,7-disulfate; apigenin-7-*O*-glucuronide; quercetin-3-*O*-glucuronide; quercetin-4′-*O*-glucuronide; quercetin-3′-*O*-sulfate; and luteolin-7-*O*-glucuronide, have also been proved to possess some pharmacological activities, including anti-inflammatory (Min et al., 2009), anti-oxidative (Moon et al., 2001), antitumor (Chuang et al., 2016), and triglyceride-lowering effects (Eseberri et al., 2019). Therefore, these Phase II metabolites may be responsible for the pharmacological and medicinal properties of flavonoids *in vivo*, and the conjugation site should be considered as their benefit for structural modification.

When compare the difference in connecting targets, 6″-O-xylosyltectoridin (**P6**), 6″-O-xylosyltectoridin-4′-sulfate (M16), and tectoridin-4′-sulfate (M17) were strongly associated with fatty acid metabolism, adipocytokine signaling pathway, arginine and proline metabolism, NOD-like receptor signaling pathway, and glycolysis/gluconeogenesis *via* targeting ALDH2 and TNF. 6″-O-xylosyltectoridin (P6) was also involved in the NOD-like receptor signaling pathway and glycolysis/gluconeogenesis *via* regulating the candidate targets HSP90A1 and TPI1. Remarkably, GOT2 and CHKB, involved in the regulation of lipid and amino acid metabolism, were only found to be related with the metabolites genistein-7G-4′S (M11), 6″-O-xylosyltectoridin-4′-sulfate (M16), and tectoridin-4′S (M17). These results showed that the protective role of PF depended on the interacting and synergetic of both prototypes and metabolites. The prototypes are more likely to act on glycolysis/gluconeogenesis as well as inflammation and immune regulation, while the metabolites are highly involved in regulation of lipid and amino acid metabolism.

ALD is characterized by oxidative stress, inflammation, and disturbance of hepatocyte metabolism as well as bacterial translocation (Louvet and Mathurin, 2015). In the present study, the KEGG enrichment analysis showed that the targets were regulated by 16 genes correlated with multiple biological processes inclusive of nine pathways, which were interacting and synergetic. Combined with docking results, the regulation of lipid and amino acid metabolism should highly involve in the protective effect of PF against ALD (Figure 6).

Growing evidence has demonstrated that the development of ALD is associated with disturbance of lipid regulation. Fatty acid metabolism (hsa00071), adipocytokine signaling pathway (hsa04920), and PPAR signaling pathway (hsa03320), selected on the basis of the enrichment by five genes ACOX1, CHKB, ALDH2, PPARA, and TNF, participate in the lipid regulation process of PF. Peroxisome proliferator–activated receptor α (PPAR-α), a key nuclear transcription factor abundantly expressed in the liver, plays a major role in lipid metabolism regulation. Several studies reported that PPAR-α agonists were expected to be a treatment for ALD by reducing oxidative stress, regulating fatty acid synthesis and oxidation, inhibiting the production and release of inflammatory and profibrogenic factors, and alleviating liver tissue damage (Kersten, 2014). As the target genes of PPAR-α, the expression of peroxisomal acyl-coenzyme A oxidase 1 (ACOX1) and choline/ethanolamine kinase (CHKB) through fatty acid oxidation will be reduced, and the accumulation of triglyceride in the liver and the content of TNF-α in serum was accordingly increased in the development and progression of ALD. Concordantly, increased TNF affects the expression of CHKB through the NF-kB pathway and induces inflammation, which aggravates the course of disease.

Abnormal amino acid metabolism, including tyrosine metabolism (hsa00350), phenylalanine metabolism (hsa00360), and arginine and proline metabolism (hsa00330), is closely related to intestinal flora metabolism, and bacterial translocation from the gut microbiota into the portal blood stream is an important driver of ALD (Vassallo et al., 2015). MAO-A, a mitochondrial enzyme, exists mainly in the human liver, kidney, small intestine, and nerve tissues and could remove the metabolites of tyrosine and phenylalanine by oxidative deamination. It had been closely associated with neurological and psychiatric disorders due to its degradation of catecholamine neurotransmitter. Recent studies provide insights into the application of MAO-A as a novel predictor of clinical outcomes that MAO-A expression was negatively correlated with the alcohol consumption level and hepatocellular carcinoma (Cervera-Juanes et al., 2016). Increasing MAO-A expression or enzyme activity may be a new approach that can be used for ALD treatment. In addition, researchers

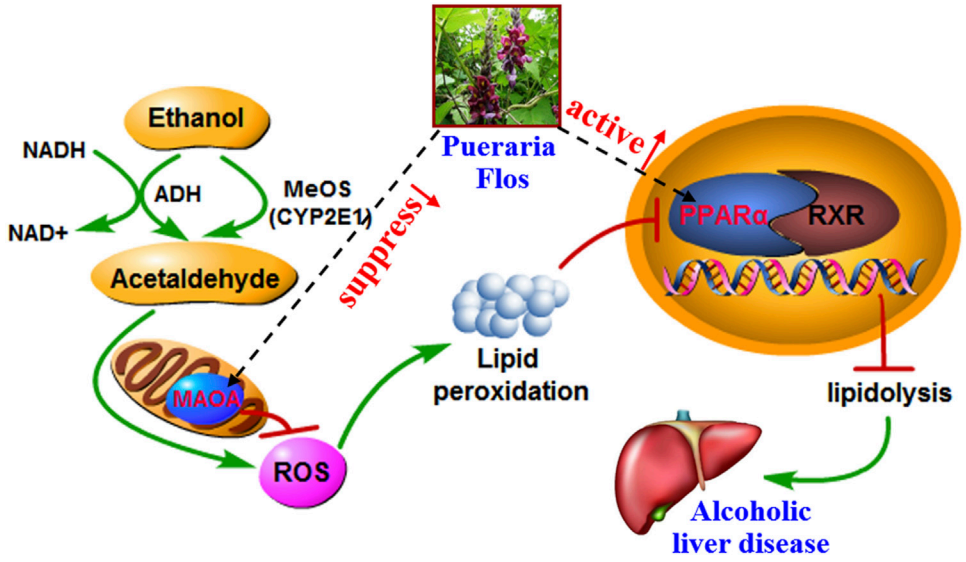

FIGURE 7
Overview of potential mechanisms underlying the protective effects of PF on alcohol-induced liver injury.

founded that ALDH2, aldehyde dehydrogenase located in mitochondria, was the downstream gene of MAO-A. A link between capacity to reduce alcohol consumption and increased liver ratio of MAO to ALDH2 has been established by using an animal model (Cervera-Juanes et al., 2016). Other targets, such as GOT2, TYR, and MIF, are also involved in the gut bacterial pathway for dopamine and tyrosine metabolism, which affect the intestinal permeability and bacterial translocation.

An increasing number of studies have shown that inflammation and immune regulation was also critical for the progression of ALD. Heat shock protein 90 (hsp90), an emerging therapeutic target in ALD, was a main effector in the NOD-like receptor signaling pathway (hsa04621). It is involved in initiation of the early phases of ER stress contributing to stimulation and accumulation of hepatic lipids (Ambade et al., 2014). Hsp90 inhibitors could alleviate serum ALT, endotoxin, and pro-inflammatory cytokines such as TNF-α in acute and chronic alcoholic liver injury and regulating PPAR-α to influence fatty acid oxidation and synthesis. In addition, ALOX12, ALOX15, and PTGS1, which catalyze the generation of leukotrienes and prostaglandins by arachidonic acid metabolism (hsa00590), also participate in the processes of ALD through activation of inflammatory responses (Zhang et al., 2017). Their chemical inhibitors have been confirmed to significantly alleviate alcohol-induced oxidative stress, lipid accumulation, and liver damage. In addition, LDHB, TPI1, and ALDH2, which act as master regulatory genes of glycolysis/gluconeogenesis (hsa00010) due to the increased cells' need for oxygen by chronic alcohol consumption, also play a vital role in the treatment of PF in ALD.

In this study, the bioinformatic method was combined to elucidate the active components and mechanism of PF in the treatment of ALD. Some of the predicted results are confirmed by *in vivo* experiments, which preliminarily prove the scientific nature of this method. In addition, some of the compound–target–pathway interactions predicted by the network analysis have also been confirmed in the previous studies. For example, protective effects of genistein against chronic alcohol-induced liver injury in mice were related to regulate expression of inflammatory-related factors TNFα, NF-κB, and PTGS1 (Zhao et al., 2016). Tectoridin, a characteristic isoflavone glycoside found in PF and *Belamcanda* chinensis (L.) DC., could protect against ethanol-induced liver steatosis mainly by modulating the disturbance of the PPAR-α pathway and ameliorating the mitochondrial function (Xiong et al., 2010). In addition, attenuated alcoholism by daidzin has been proved to be associated with the liver mitochondrial MAO–ALDH2 pathway (Ambade et al., 2014). However, other constituents and targets especially conjugated metabolites predicted in the present study still need to be validated in the follow-up study.

There are still two shortcomings in this study. On the one hand, benchwork assessing affinity using several technologies such as the surface plasmon resonance biosensor should be combined with a docking analysis to evaluate and validate the importance of relative compounds and targets. As our research focus on the *in vivo* metabolites, the phase II metabolites including glucuronides, sulfates, and/or bis-conjugates that account for the most part were difficult to isolate due to their exclusivity distribution in the biological matrix rather than the plant kingdom. Therefore, the absence of metabolite references

restricted further affinity evaluation. On the other side, the single dose in the present study was chosen to continue and compare with our previous metabolism research, which determined the pharmacokinetic parameters of tectoridin and tectorigenin after oral administration at dosages of 200 and 130 mg/kg, respectively (Qu et al., 2012; Wang S. et al., 2013). However, three dosages (low, middle, and high) should be set to reflect the dose–effect relationship more scientifically in the pharmacological research. These deficiencies will be improved in our subsequent studies.

5 Conclusion

The present study has developed a sensitive and rapid method for the separation and identification of the absorbed constituents and metabolites of PF *in vivo* for the first time. Glucuronidation, sulfation, methylation, hydroxylation, and reduction are the major metabolic reactions. Furthermore, the constructed absorbed constituent–target–pathway–disease network and the docking analysis revealed that phase II metabolites may play more important roles in the PF-mediated protection against ALD. Also, the protective effects and predicted mechanism associated with decreased and elevated expression of MAO-A and PPAR-α in rat ALD models were also validated (Figure 7). However, the absence of metabolite references restricted the reliability of predicted conclusions about importance of key metabolites. In the future, we will try to purify the glucuronides, sulfates, and/or bis-conjugated metabolites and employed the benchwork assay to obtain the affinity and Michaelis constant of active compounds bound to key targets, which make the research more credible.

Data availability statement

The datasets presented in this study can be found in online repositories. The names of the repository/repositories and accession number(s) can be found in the article/Supplementary Material.

Ethics statement

The animal study was reviewed and approved by the Ethics Review Committee for Animal Experimentation of Shenyang Pharmaceutical University (License number: SCXK (Liao) 2015-0001).

Author contributions

JQ: experimental works, project administration, data curation, and writing—original draft. QC: experimental works and data curation. TW: bioinformatic investigation of the network analysis and molecular docking. ND: experimental works. DS: writing—review and editing. DY: research design and supervision and writing—review and editing.

Funding

This work was financially supported by grants from the National Natural Science Foundation of China (No. 81703675); China Postdoctoral Science Foundation (2021M692398); Natural Science Foundation of Liaoning Province (No. 2019-ZD-0631); Distinguished Professor Foundation in 2011 from Liaoning Province China (No. 511260); and the Leading Talent of Hundred, Thousand and Ten Thousand Project of Xingliao Gifted Person Program of Liaoning Province (No. XLYC1905013).

Conflict of interest

The authors declare that the research was conducted in the absence of any commercial or financial relationships that could be construed as a potential conflict of interest.

Publisher's note

Supplementary material

The Supplementary Material for this article can be found online at: https://www.frontiersin.org/articles/10.3389/fphar.2022.915535/full#supplementary-material

SUPPLEMENTARY FIGURE S1
Representative base peak chromatogram (BPC) of seven mixed reference compounds **(A)** and PF extract **(B)** in the negative ion mode. See Supplementary Table 1 for the peak numbers, and see section 2.4 UPLC-QTOF MS analysis for UPLC-QTOF MS conditions.

SUPPLEMENTARY FIGURE S2
Extracted ion chromatograms of all identified metabolites in blank biosamples determined by UPLC-QTOF MS analysis.

SUPPLEMENTARY TABLE S1
Compounds identified from the flower of *Pueraria montana* var. *thomsonii* (Benth.) M.R. Almeida extract by the UPLC-QTOF/MS method.

SUPPLEMENTARY TABLE S2
Potential targets of 13 absorbed constituents from Puerariae Flos.

SUPPLEMENTARY TABLE S3
Therapeutic targets of alcoholic fatty liver.

References

Abenavoli, L., Capasso, R., Milic, N., and Capasso, F. (2010). Milk thistle in liver diseases: Past, present, future. *Phytother. Res.* 24 (10), 1423–1432. doi:10.1002/ptr.3207

Addolorato, G., Mirijello, A., Barrio, P., and Gual, A. (2016). Treatment of alcohol use disorders in patients with alcoholic liver disease. *J. Hepatol.* 65 (3), 618–630. doi:10.1016/j.jhep.2016.04.029

Ambade, A., Catalano, D., Lim, A., Kopoyan, A., Shaffer, S. A., Mandrekar, P., et al. (2014). Inhibition of heat shock protein 90 alleviates steatosis and macrophage activation in murine alcoholic liver injury. *J. Hepatol.* 61 (4), 903–911. doi:10.1016/j.jhep.2014.05.024

Bai, X., Qu, J. L., Liu, J., Sun, J. H., and Yuan, D. (2011a). Isolation and identification of urinary metabolites of tectoridin in rats. *J. Asian Nat. Prod. Res.* 13 (7), 604–610. doi:10.1080/10286020.2011.578069

Bai, X., Qu, J. L., Lu, J., Kano, Y., and Yuan, D. (2011b). Pharmacokinetics of kakkalide and its main metabolites in rat plasma determined by HPLC-DAD and LC-MS^n. *J. Chromatogr. B Anal. Technol. Biomed. Life Sci.* 879 (5–6), 395–402. doi:10.1016/j.jchromb.2010.12.025

Bai, X., Xie, Y. Y., Liu, J., Qu, J. L., Kano, Y., Yuan, D., et al. (2010). Isolation and identification of urinary metabolites of kakkalide in rats. *Drug Metab. Dispos.* 38 (2), 281–286. doi:10.1124/dmd.109.028555

Cervera-Juanes, R., Wilhem, L. J., Park, B., Lee, R., Locke, J., Helms, C., et al. (2016). MAOA expression predicts vulnerability for alcohol use. *Mol. Psychiatry* 21 (4), 472–479. doi:10.1038/mp.2015.93

Chuang, C. H., Yeh, C. L., Yeh, S. L., Lin, E. S., Wang, L. Y., Wang, Y. H., et al. (2016). Quercetin metabolites inhibit MMP-2 expression in A549 lung cancer cells by PPAR-γ associated mechanisms. *J. Nutr. Biochem.* 33, 45–53. doi:10.1016/j.jnutbio.2016.03.011

Eseberri, I., Miranda, J., Lasa, A., Mosqueda-Solís, A., González-Manzano, S., Santos-Buelga, C., et al. (2019). Effects of quercetin metabolites on triglyceride metabolism of 3T3-L1 preadipocytes and mature adipocytes. *Int. J. Mol. Sci.* 20 (2), 264. doi:10.3390/ijms20020264

Funk, C. (2008). The role of hepatic transporters in drug elimination. *Expert Opin. Drug Metab. Toxicol.* 4 (4), 363–379. doi:10.1517/17425255.4.4.363

Gao, K., Yu, W., Yang, J., and Duan, X. H. (2007). CYP3A1/2 and 2C9/10 in rat liver microsomes mediate 22α- and 24-hydroxylation of 18α-glycyrrhetic acid. *Chin. J. Clin. Pharmacol. Ther.* 12 (11), 1255–1260.

González-Santiago, O., and Garza-Ocañas, L. (2009). Fomepizole for toxic alcohol poisoning. *N. Engl. J. Med.* 361 (12), 1213–1214. doi:10.1056/NEJMc091309

Hirayama, K., Matsuzuka, Y., Kamiya, T., Ikeguchi, M., Takagaki, K., Itoh, K., et al. (2011). Metabolism of isoflavones found in the Pueraria thomsonii flower by human intestinal microbiota. *Biosci. Microflora* 30 (4), 135–140. doi:10.12938/bifidus.30.135

Kersten, S. (2014). Integrated physiology and systems biology of PPARα. *Mol. Metab.* 3 (4), 354–371. doi:10.1016/j.molmet.2014.02.002

Kinjo, J., Aoki, K., Okawa, M., Shii, Y., Hirakawa, T., Nohara, T., et al. (1999). HPLC profile analysis of hepatoprotective oleanene-glucuronides in Puerariae Flos. *Chem. Pharm. Bull.* 47 (5), 708–710. doi:10.1248/cpb.47.708

Lee, K. T., Sohn, I. C., Kim, D. H., Choi, J. W., Kwon, S. H., Park, H. J., et al. (2000). Hypoglycemic and hypolipidemic effects of tectorigenin and kaikasaponin III in the streptozotocin-lnduced diabetic rat and their antioxidant activity *in vitro*. *Arch. Pharm. Res.* 23 (5), 461–466. doi:10.1007/BF02976573

Liang, Q. D., He, M. Z., Ouyang, H., Huang, W. P., Guo, Y. C., Feng, Y. L., et al. (2014). Analysis on *in vivo* metabolites of α-hederin in rats by UPLC-MS/MS. *Chin. Traditional Herb. Drugs* 45 (13), 1883–1888. doi:10.7501/j.issn.0253-2670.2014.13.014

Louvet, A., and Mathurin, P. (2015). Alcoholic liver disease: Mechanisms of injury and targeted treatment. *Nat. Rev. Gastroenterol. Hepatol.* 12 (4), 231–242. doi:10.1038/nrgastro.2015.35

Lu, J., Xie, Y. Y., Tan, Y., Qu, J. L., Matsuda, H., Yoshikawa, M., et al. (2013). Simultaneous determination of isoflavones, saponins and flavones in Flos Puerariae by ultra performance liquid chromatography coupled with quadrupole time-of flight mass spectrometry. *Chem. Pharm. Bull.* 61 (9), 941–951. doi:10.1248/cpb.c13-00271

Mathurin, P., and Bataller, R. (2015). Trends in the management and burden of alcoholic liver disease. *J. Hepatol.* 62 (1), S38–S46. doi:10.1016/j.jhep.2015.03.006

Min, Y. S., Yim, S. H., Bai, K. L., Choi, H. J., Jeong, J. H., Song, H. J., et al. (2009). The inhibitory effect of quercetin-3-O-β-D-glucuronopyranoside on gastritis and reflux esophagitis in Rats. *Korean J. Physiol. Pharmacol.* 13 (4), 295–300. doi:10.4196/kjpp.2009.13.4.295

Moon, J. H., Tsushida, T., Nakahara, K., and Terao, J. (2001). Identification of quercetin 3-O-β-D-glucuronide as an antioxidative metabolite in rat plasma after oral administration of quercetin. *Free Radic. Biol. Med.* 30 (11), 1274–1285. doi:10.1016/s0891-5849(01)00522-6

National Administration of Traditional Chinese Medicine "Chinese Materia Medica" Editorial Committee (1999). *Chinese Materia Medica*. fourth ed. Shanghai: Shanghai Scientific & Technical Publishers, 619–620.

O'Leary, K. A., Day, A. J., Needs, P. W., Mellon, F. A., O'Brien, N. M., Williamson, G., et al. (2003). Metabolism of quercetin-7- and quercetin-3-glucuronides by an *in vitro* hepatic model: The role of human β-glucuronidase, sulfotransferase, catechol-O-methyltransferase and multi-resistant protein 2 (MRP2) in flavonoid metabolism. *Biochem. Pharmacol.* 65 (3), 479–491. doi:10.1016/S0006-2952(02)01510-1

Qu, J. L., Gao, J., Sun, J. H., Zhang, L., Makino, T., and Yuan, D. (2012). Pharmacokinetics of conjugated metabolites in rat plasma after oral administration of tectoridin. *J. Chromatogr. B Anal. Technol. Biomed. Life Sci.* 902, 61–69. doi:10.1016/j.jchromb.2012.06.017

Qu, J. L. (2014). *Studies on chemical constituents of flower of Puerariae thomsonii Benth. and metabolism of tectoridin in rats*. Doctorate Dissertation (Shenyang, China: Shenyang Pharmaceutical University).

Qu, J. L., Wu, Z. Z., Gao, J., Wen, H., Wang, T., Yuan, D., et al. (2014). Excretion of tectoridin metabolites in rat urine and bile orally administrated at different dosages and their inhibitory activity against aldose reductase. *Fitoterapia* 99, 99–108. doi:10.1016/j.fitote.2014.09.009

Rambaldi, A., Jacobs, B. P., Iaquinto, G., and Gluud, C. (2005). Milk thistle for alcoholic and/or Hepatitis B or C liver diseases--a systematic Cochrane hepato-biliary group review with meta-analyses of randomized clinical trials. *Am. J. Gastroenterol.* 100 (11), 2583–2591. doi:10.1111/j.1572-0241.2005.00262.x

Shi, Z. M., Zhang, G. Z., Zhao, L. Z., Wang, S., Kano, Y., and Yuan, D. (2015). Excretion of tectorigenin in rat urine orally administrated at different dosages by ultra-performance liquid chromatography coupled to quadrupole time-of-flight mass spectrometry. *Eur. J. Drug Metab. Pharmacokinet.* 40 (3), 255–266. doi:10.1007/s13318-014-0202-0

Shin, J. E., Bae, E. A., Lee, Y. C., Ma, J. Y., and Kim, D. H. (2006). Estrogenic effect of main components kakkalide and tectoridin of Puerariae Flos and their metabolites. *Biol. Pharm. Bull.* 29 (6), 1202–1206. doi:10.1248/bpb.29.1202

Vassallo, G., Mirijello, A., Ferrulli, A., Antonelli, M., Landolfi, R., Gasbarrini, A., et al. (2015). Review article: Alcohol and gut microbiota - the possible role of gut microbiota modulation in the treatment of alcoholic liver disease. *Aliment. Pharmacol. Ther.* 41 (10), 917–927. doi:10.1111/apt.13164

Wang, H., Bai, X., Sun, J. H., Kano, Y., Makino, T., Yuan, D., et al. (2013a). Metabolism and excretion of kakkalide and its metabolites in rat urine, bile, and feces as determined by HPLC/UV and LC/MS/MS. *Planta Med.* 79 (16), 1552–1557. doi:10.1055/s-0033-1350832

Wang, S., Gong, T. X., Lu, J., Kano, Y., and Yuan, D. (2013b). Simultaneous determination of tectorigenin and its metabolites in rat plasma by ultra-performance liquid chromatography/quadrupole time-of-flight mass spectrometry. *J. Chromatogr. B Anal. Technol. Biomed. Life Sci.* 933, 50–58. doi:10.1016/j.jchromb.2013.06.009

Xiong, Y., Yang, Y. Q., Yang, J., Chai, H. Y., Li, Y., Yang, J., et al. (2010). Tectoridin, an isoflavone glycoside from the flower of Pueraria lobata, prevents acute ethanol-induced liver steatosis in mice. *Toxicology* 276 (1), 64–72. doi:10.1016/j.tox.2010.07.007

Yu, P., Qiu, H., Wang, M., Tian, Y., Zhang, Z., Song, R., et al. (2016). *In vitro* metabolism study of saikosaponin d and its derivatives in rat liver microsomes. *Xenobiotica.* 47 (1), 11–19. doi:10.3109/00498254.2016.1163753

Yuan, D., Xie, Y. Y., Bai, X., Wu, X., Yang, J. Y., Wu, C. F., et al. (2009). Inhibitory activity of isoflavones of Pueraria flowers on nitric oxide production from lipopolysaccharide-activated primary rat microglia. *J. Asian Nat. Prod. Res.* 11 (6), 471–481. doi:10.1080/10286020902819822

Zhang, G. F., Wu, X., Bai, X., Kano, Y., Uno, T., and Yuan, D. (2009). Simultaneous determination of four isoflavone compounds in flowers of Pueraria lobata by HPLC. *J. Shenyang Pharm. Univ.* 26 (1), 43–47.

Zhang, G. Z., Gong, T. X., Kano, Y., and Yuan, D. (2013). Metabolic profile of irisolidone in rats obtained by ultra-high performance liquid chromatography/quadrupole time-of-flight mass spectrometry. *J. Chromatogr. B Anal. Technol. Biomed. Life Sci.* 941, 1–9. doi:10.1016/j.jchromb.2013.09.033

Zhang, G. Z., Qi, W., Xu, L. Y., Kano, Y., and Yuan, D. (2015). Pharmacokinetics of irisolidone and its main metabolites in rat plasma determined by ultra-performance liquid chromatography/quadrupole time-of-flight mass spectrometry. *J. Chromatogr. B Anal. Technol. Biomed. Life Sci.* 1005, 23–29. doi:10.1016/j.jchromb.2015.09.040

Zhang, W. L., Zhong, W., Sun, Q., Sun, X. G., and Zhou, Z. X. (2017). Hepatic overproduction of 13-HODE due to ALOX15 upregulation contributes to alcohol-induced liver injury in mice. *Sci. Rep.* 7 (1), 8976. doi:10.1038/s41598-017-02759-0

Zhao, L., Wang, Y., Liu, J., Wang, K., Guo, X. X., Ji, B. P., et al. (2016). Protective effects of genistein and puerarin against chronic alcohol-induced liver injury in mice via antioxidant, anti-inflammatory, and anti-apoptotic mechanisms. *J. Agric. Food Chem.* 64 (38), 7291–7297. doi:10.1021/acs.jafc.6b02907

frontiers | Frontiers in Pharmacology

TYPE Original Research
PUBLISHED 16 September 2022
DOI 10.3389/fphar.2022.926134

OPEN ACCESS

EDITED BY
Bingyou Yang,
Heilongjiang University of Chinese Medicine, China

REVIEWED BY
Jiabao Liao,
Yunnan University of Traditional Chinese Medicine, China
Chih-Yuan Ko,
The Second Affiliated Hospital of Fujian Medical University, China
Chan-Yen Kuo,
Taipei Tzu Chi Hospital, Taiwan

*CORRESPONDENCE
Dongqiang Wang,
wdqklm@sina.com

SPECIALTY SECTION
This article was submitted to Ethnopharmacology, a section of the journal Frontiers in Pharmacology

RECEIVED 22 April 2022
ACCEPTED 31 August 2022
PUBLISHED 16 September 2022

CITATION
He W, Xi Q, Cui H, Zhang P, Huang R, Wang T and Wang D (2022), Liang-Ge decoction ameliorates acute lung injury in septic model rats through reducing inflammatory response, oxidative stress, apoptosis, and modulating host metabolism.
Front. Pharmacol. 13:926134.
doi: 10.3389/fphar.2022.926134

Liang-Ge decoction ameliorates acute lung injury in septic model rats through reducing inflammatory response, oxidative stress, apoptosis, and modulating host metabolism

Wenju He[1], Qiang Xi[2], Huantian Cui[3], Pingping Zhang[1], Rui Huang[4], Taihuan Wang[4] and Dongqiang Wang[1]*

[1]Department of Integration of Traditional Chinese and Western Medicine, First Central Hospital Affiliated to Nankai University, Tianjin First Central Hospital, Tianjin, China, [2]Department of Practice and Education, Tianjin University of Traditional Chinese Medicine, Tianjin, China, [3]Shandong Provincial Key Laboratory of Animal Cell and Developmental Biology, School of Life Sciences, Shandong University, Qingdao, China, [4]Department of Graduate School, Tianjin University of Traditional Chinese Medicine, Tianjin, China

Liang-Ge decoction (LG) has been used in the treatment of early stage of spesis and can ameliorate sepsis-associated lung injury. However, the mechanism of LG on sepsis-associated lung injury remains unknown. In this study, we established a rat model of sepsis-associated lung injury using the cecal ligation and puncture (CLP) method, and investigated the therapeutic effects of LG on lung injury in rats with sepsis. In addition, the anti-inflammatory, anti-oxidative and anti-apoptotic effects of LG on sepsis-associated lung injury model rats were evaluated. Besides, untargeted metabolomics was used to investigate the regulation of metabolites in rats with sepsis-associated lung injury after LG treatment. Our results showed that LG could decrease the wet/dry (W/D) ratio in lung and the total cell count and total protein concentration in bronchoalveolar lavage fluid (BALF) in septic model rats. Hematoxylin and eosin (HE) staining showed that LG reduced the infiltration of pro-inflammatory cells in lung. In addition, LG treatmment down-regulated the gene and protein expression of pro-inflammatory cytokins in lung tissue and BALF. The activities of superoxide dismutase (SOD) and glutathione peroxidase (GSH-Px) were increased and the level of methane dicarboxylic aldehyde (MDA) was decreased in lung tissue homogenate in septic model rats after LG treament. Moreover, the numbers of apoptotic cells in lung were reduced and the activity of lactic dehydrogenase (LDH) in BALF was decreased in septic model rats after LG treament. Untargeted metabolomics analysis showed that LG treatment affected the levels of 23 metabolites in lung in septic model rats such as citric acid, methionine, threonine, alpha-ketoglutaric acid, and inositol, these metabolites were associated with the glycine, serine and threonine metabolism, cysteine and methionine metabolism, inositol phosphate metabolism and citrate cycle (TCA cycle)

pathways. In conclusion, our study demonstrated the therapeutic effetcts of LG on sepsis-associated lung injury model rats. Moreover, LG could inhibit the inflammatory response, oxidative stress, apoptosis and regulate metabolites related to glycine, serine and threonine metabolism, cysteine and methionine metabolism, inositol phosphate metabolism and TCA cycle in lung in sepsis-associated lung injury model rats.

KEYWORDS

liang-Ge decoction, sepsis-associated lung injury, inflammatory response, oxidative stress, apoptosis, untargeted metabolomics

Introduction

Sepsis is a systemic disease caused by infection that can involve numerous organs, such as the lung, kidney, heart, brain, and gastrointestinal (GI) tract. Besides, the consequent multiple organ dysfunction syndromes are the main cause of death in patients with sepsis (Xia et al., 2021). During the progression of sepsis, lung is the first and most common organ to be damaged (Wang et al., 2019; Xu et al., 2020). If patients do not receive timely and effective treatment, their condition often deteriorates rapidly into severe respiratory failure (Johnson and Matthay, 2010), which can be life threatening. Studies have shown that 40%–68.2% of adults with sepsis are accompanied by lung injury (Cecconi et al., 2018). With the widespread use of antibiotics, which has resulted in widespread drug resistance, the treatment of sepsis-associated lung injury is becoming increasingly challenging (Johnson and Matthay, 2010). Therefore, it is crucial to develop practical interventions to improve sepsis-associated lung injury.

Many studies have demonstrated the protective effects of traditional Chinese medicine (TCM) on sepsis-associated lung injury. Qing-Wen-Bai-Du decoction could improve acute lung injury and ameliorate the coagulation disorders in septic model rats (Jia et al., 2022). Xue-Bi-Jing injection could ameliorate acute lung injury in septic model rats through improving lung permeability and inhibiting inflammatory response (Liu et al., 2014). Si-Ni decoction could alleviate lung injury in cecal ligation and puncture (CLP)-induced septic model mice through modulating the gut microbiota (Wang et al., 2020). Ba-Bao-Dan treatment reduced the inflammatory response in septic model mice through inhibiting the activation of NOD-like receptor protein 3 (NLRP3)-mediated inflammasome (Li et al., 2022). Illustrating the protective mechanisms of TCM on sepsis-associated lung injury can contribute to the modernization of TCM.

Alterations in the levels of metabolites have been closely correlated with several pathological states, such as inflammation, tissue injury, apoptosis, and oxidative stress. With the use of untargeted metabolomics, it is possible to study the changes in metabolite levels during disease development. It was found that similar alterations in metabolic levels also occurred during sepsis development. In patients with sepsis, the serum levels of glucose, glycine, 3-hydroxybutyrate, creatinine, and glycoprotein acetyls are significantly increased, whereas those of citrate and histidine are significantly decreased compared with healthy subjects (Jaurila et al., 2020). Other studies have also demonstrated a correlation between the total glutathione, adenosine, phosphatidylserine, and sphingomyelin levels, and the development of sepsis-associated lung injury (Stringer et al., 2011). Moreover, adipose tissue-derived mesenchymal stem cells can suppress the inflammatory responses in the lungs of septic rats by regulating the levels of acetylcholine, spermine, phenylalanine, and threonine (Cui J. et al., 2020). Furthermore, mangiferin can improve lung injury caused by sepsis by inhibiting oxidative stress and regulating the lipid metabolism and energy biosynthesis (Wang et al., 2018; Xu et al., 2020).

Liang-Ge decoction (LG) is composed of *Rheum palmatum* L. [Polygonaceae; Rhei radix et rhizoma], *Citrullus lanatus* (Thunb.) Matsum. and Nakai [Cucurbitaceae; Mirabilitum praeparatum], *Glycyrrhiza glabra* L. [Fabaceae; Glycyrrhizae radix et rhizoma], *Gardenia jasminoides* J. Ellis [Rubiaceae; Gardeniae fructus praeparatus], *Mentha canadensis* L. [Lamiaceae; Menthae haplocalycis herba], *Scutellaria baicalensis* Georgi [Lamiaceae; Scutellariae radix], *Forsythia suspensa* (Thunb). Vahl [Oleaceae; Forsythiae fructus], and *Lophatherum gracile* Brongn. [Poaceae; Lophatheri herba], and can be used for treating the early stage of sepsis. Clinical study revealed that combination treatment of LG and western therapy could significantly suppress the inflammatory response and reduce platelet activation/thrombocytopenia in spetic petients (Wang et al., 2011). A study has demonstrated that LG can inhibit the inflammatory response in septic model mice (Yang et al., 2019); however, the mechanism of action of LG to improve the symptoms of sepsis-associated lung injury remains unclear. In this study, we established a rat model of sepsis-associated lung injury using the CLP method, and investigated the therapeutic effects of LG on lung injury in rats with sepsis. In addition, the anti-inflammatory, anti-oxidative and anti-apoptotic effects of LG on sepsis-associated lung injury model rats were evaluated. Besides,

untargeted metabolomics was used to investigate the regulation of metabolites in rats with sepsis-associated lung injury after LG treatment.

Material and methods

Reagents

Terminal deoxynucleotidyl transferase deoxyuridine triphosphate (dUTP) nick end labeling (TUNEL) staining kit was purchased from Kaiji Biotechnology Co., Ltd. (Jiangsu, China). Enzyme-linked immunosorbent assay (ELISA) kits of rat interleukin (IL)-1β, IL-6 and umor necrosis factor alpha (TNF-α) were obtained from Shanghai Bluegene Biotech Co., Ltd. (Shanghai, China). Total protein, superoxide dismutase (SOD), methane dicarboxylic aldehyde (MDA), glutathione peroxidase (GSH-Px) and lactic dehydrogenase (LDH) assay kits were purchased from Nanjing Jiancheng Biological Engineering Institute (Nanjing, China). RNA extraction, first-strand cDNA reverse transcription, polymerase chain reaction (PCR) kits and primers were purchased from TianGen Biotechnology Co., Ltd. (Beijing, China).

Laboratory animals

Seventy-five male Sprague Dawley rats weighing 200 ± 20 g each were obtained from Beijing Huafukang Biotechnology Co., Ltd. They were acclimatized in a quiet environment for one week with a relative humidity of 55%–60%. Adequate clean water was provided to the animals, and they were fed freely. The experiment was approved by the Ethics Committee of Tianjin First Central Hospital.

Generation of a septic rat model

An animal model of sepsis was generated using the CLP method (Dejager et al., 2011). A 12-h fast for food and water was performed before surgery. The skin of the anterior mid-abdomen of the rats was shaved after the application of anesthesia with isoflurane gas. This skin was then disinfected and a 2-cm incision was made in the mid-abdomen. After removing the cecum, the mesentery and cecum were freed, and the end of the cecum was ligated at a site 5 mm away from the ileocecal region using a 3–0 surgical suture; then, a syringe needle (20 G) was used to perform a through-hole puncture twice at a site located approximately 0.8–1 cm away from the intestinal wall on both sides of the distal appendiceal root of the ligature, from where a small amount of intestinal content was squeezed out. Subsequently, a 3 mm× 0.5 mm× 30 mm surgical drain was placed in the cecum through-hole puncture, after which the cecum was placed back into the abdominal cavity and the incision was sutured.

Preparation of Liang-Ge decoction

LG was firstly recorded in "Prescriptions People's Welfare Pharmacy" in Song Dynasty and was prepared based on the description in "Prescriptions People's Welfare Pharmacy." Briefly, 6 g of *R. palmatum* L. [Polygonaceae; Rhei radix et rhizoma] (Batch No. 210115), 10 g of *Citrullus lanatus* (Thunb.) Matsum. and Nakai [Cucurbitaceae; Mirabilitum praeparatum] (Batch No. 210312), 6 g of *G. glabra* L. [Fabaceae; Glycyrrhizae radix et rhizoma] (Batch No. 210327), 10 g of *G. jasminoides* J. Ellis [Rubiaceae; Gardeniae fructus praeparatus] (Batch No. 211203), 6 g of *M. canadensis* L. [Lamiaceae; Menthae haplocalycis herba] (Batch No. 201127), 10 g of *S. baicalensis* Georgi [Lamiaceae; Scutellariae radix] (Batch No. 210708), 20 g of *F. suspensa* (Thunb). Vahl [Oleaceae; Forsythiae fructus] (Batch No. 210319), and 10 g of *L. gracile* Brongn. [Poaceae; Lophatheri herba] (Batch No. 210521) were weighed and soaked with an eight-fold volume of water (624 ml) for 30 min. The mixture was decocted for 30 min and filtered. The filtrate was stored separately. The dregs were then mixed with eight-fold volume of water (624 ml) for the second extraction. About 150 ml of filtrates each time were obtained and combined. Then, the combined filtrates (300 ml) were evaporated to about 50 ml (1.59 g of crude herb/ml). Then, the evaporated LG extraction was the diluted into 0.39 g/ml, and 0.78 g/ml, respectively. All herbs were obtained from Tianjin traditional Chinese Medicine prepared pieces Co., Ltd. and authenticated by pharmacist of the Tianjin First Central Hospital. The voucher specimen of herbs were deposited at the Department of Integration of Traditional Chinese and Western Medicine in Tianjin First Central Hospital.

Quality control of LG was performed using Ultra performance liquid chromatography (UPLC; ACQUITY UPLC®, United States) coupled with Xevo G2 quadrupole-timeof-flight (Q-TOF) mass spectrometer (MS; Waters Corp.Milford, MA, United States) systems based on our previous established protocol (Xie et al., 2021).

Experimental groups and drug administration protocol

Seventy-five rats were selected and randomly and equally divided into the following groups: Sham, model, LG low-dose, LG middle-dose, and LG high-dose groups. Rats from model,

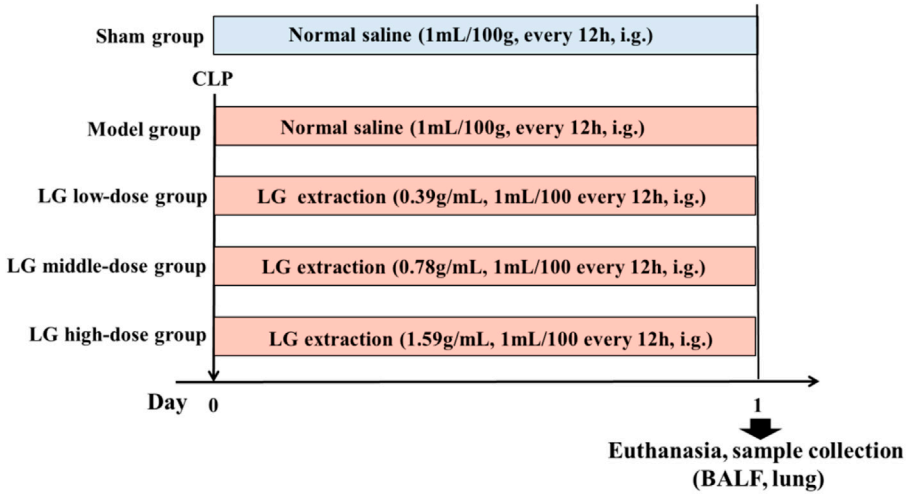

FIGURE 1
Grouping and dosing regimen. LG: Liang-Ge decoction, BALF: bronchoalveolar lavage fluid.

LG low-dose, LG middle-dose, and LG high-dose groups received CLP to establish the sepsis model. In contrast, rats in the sham group only had their abdominal wall incised and sutured without receiving CLP. After modeling, the rats in the Sham and model groups were administered with 1 ml/100 g of saline intragastrically, and the rats in the LG low-, middle-, and high-dose groups were administered with 0.39 g/ml, 0.78 g/ml, and 1.59 g/ml of LG extractions every 12 h, respectively (Figure 1). The gavage amount of LG extraction was 1 ml/100 g. The dosage of LG for rats was calculated using the animal dose conversion formula based on the daily human dose, with a conversion coefficient of 6. The amount used for the middle-dose LG rats group represents the human equivalent dose using the following formula: middle-dose LG = 78 g (the total raw materials)/60 kg (human weight) × 6 (conversion coefficient).

Collection of bronchoalveolar lavage fluid bronchoalveolar lavage fluid

After 24 h of drug administration, the thoracic cavity of the rat was opened and the cervical trachea was exposed layer by layer. A Lanz incision was made on the trachea of the rats, and a rat lavage needle was inserted into the lower end of the right main bronchus. The trachea and rat lavage needle were ligated using surgical sutures. Then, the left hilus of the rat's lung was firmly ligated with surgical sutures, to ensure that the left lung was in an airtight state. Using a syringe, 5 ml of saline was withdrawn and connected to the lavage needle that was ligated in the cervical trachea, and saline was slowly injected into the right lung of the rats. Saline was left in the alveoli for 15–30 s and then gently sucked back to withdraw the BALF; the saline was closely observed for exudation during the lavage. This injection and withdrawal procedure was repeated thrice, and a total of approximately 10 ml of BALF was withdrawn from each rat.

Lung wet-to-dry wet/dry weight ratio

Twenty-four hours after model generation and drug administration, the left lung of the rats, which had not been lavaged, was collected after collecting BALF from each group. The wet mass (W) of the left lung was weighed, and the organ was dried in a constant temperature incubator at 80°C for 48 h, until the lung weight no longer decreased; the lung was then weighed and the value was used as the lung dry weight (D). The W/D ratio of lung tissue was then calculated.

Total cell count and protein concentration assay of the bronchoalveolar lavage fluid

The BALF was centrifuged at 3,000 rpm/min at 4°C for 10 min, and the cell precipitate and supernatant were collected separately. The total cell count in the BALF precipitate was assessed using a cell-counting plate. The total protein concentration in the BALF supernatant was measured using a bicinchoninic acid (BCA) total protein concentration assay kit.

TABLE 1 Primer sequences of target genes for rats.

Genes	Primer sequence (5′-3′)
β-actin	Forward: CTTCCAGACACGCCATCATG
	Reverse: TGGTGATGGCGTAGAACAGT
IL-1β	Forward: GGGATGATGACGACCTGCTA
	Reverse: TGTCGTTGCTTGTCTCTCCT
IL-6	Forward: CTCATTCTGTCTCGAGCCCA
	Reverse: TGAAGTAGGGAAGGCAGTGG
TNF-α	Forward: GAGCACGGAAAGCATGATCC
	Reverse: TAGACAGAAGAGCGTGGTGG

IL, interleukin; TNF-α, tumor necrosis factor alpha.

Pathological staining

Twenty-four hours after model generation and drug administration, the rats were sacrificed and the lung tissues of each group were collected, fixed in a formalin solution, embedded in paraffin, cut into 3-μm sections, routinely stained with hematoxylin and eosin (HE), and sealed with neutral balsam. The pathological changes in each group of rats were observed under a light microscope. The inflammation score of HE staining was evaluated baed on the previous study (Cui Y. et al., 2020). In addition, the level of apoptosis in lung tissue was observed using terminal deoxynucleotidyl transferase deoxyuridine triphosphate (dUTP) nick end labeling (TUNEL) staining. The positive expression area was quantified using Image-Pro Plus 6.0, and the TUNEL positive area was calculated based on the integrated optical density (IOD) and total area using the following formula: TUNEL positive area (%) = IOD/total area *100%

Enzyme-linked immunosorbent assay

The levels of the inflammatory cytokines IL-6, IL-1β, and TNF-α in the BALF supernatant were measured based on the instructions of the ELISA kits.

Quantitative polymerase chain reaction

Total RNA was extracted from the stored frozen lung tissues using an RNA extraction kit (TianGen Biotechnology Co., Ltd. Beijing, China). After testing the purity and concentration of the RNA, it was reverse transcribed into cDNA and used in real-time PCR to detect the expression of the *IL-6*, *IL-1β*, and *TNF-α* mRNAs in liver tissues. The relative expression of the mRNAs was calculated based on the $2^{-\triangle\triangle CT}$ quantification method using *β-actin* as a loading control. The primer sequences were designed by TianGen Biotechnology Co., Ltd. Beijing, China (Table 1).

Detection of biochemical indicators

The supernatant of BALF was collected the protein levels in the lung tissue homogenate were determined using the BCA kit. Moreover, the activities of SOD and GSH-Px and the level of MDA in the lung tissue homogenate and the activity of LDH in BALF were measured based on the instructions of the kit.

Untargeted metabolomics

A 100 mg sample of lung tissue was added to 500 μl of 80% methanol solution, vortexed, and shaken, and then left to stand in an ice bath for 5 min. Subsequently, the sample was centrifuged at 15,000 × *g* at 4°C for 20 min. The supernatant was collected and diluted with water to 53% methanol, followed by centrifugation at 15,000 g at 4°C for 20 min. The supernatant was collected to obtain a tissue homogenate, in which the level of metabolites was detected by liquid chromatography–mass spectrometry according to the specific detection method and analysis reported previously by the group (Xie et al., 2021, Supplementary materials).

Statistical processing

The experimental results were analyzed using the SPSS Statistics 20.0 statistical software, and the measurement data were expressed as mean ± standard deviation. A *t*-test and a one-way analysis of variance with Tukey's HSD (honest significant difference) post-hoc test were used for the comparison of means among multiple groups. Significance was set at $p < 0.05$.

Results

Identification of main compounds in LG by UPLC-MS analysis

Geniposide, menthol, isoorientin, baicalin, forsythin, forsythoside A, emodin and liquiritin were used as the reference standards to validate the main compounds in LG. The detailed information of these compounds were shown in Supplementary Figure S1. The typical based peak intensity (BPI) chromatograms of LG and these reference standards were shown in Supplementary Figure S2. The characteristic fragment ions of these compounds were shown in Supplementary Table S1. Emodin in *R. palmatum* L. [Polygonaceae; Rhei radix et rhizoma], liquiritin in *G. glabra* L. [Fabaceae; Glycyrrhizae radix et rhizoma], geniposide in *G. jasminoides* J. Ellis [Rubiaceae; Gardeniae fructus praeparatus], menthol in *M. canadensis* L. [Lamiaceae; Menthae haplocalycis herba], baicalin in *S. baicalensis* Georgi [Lamiaceae; Scutellariae

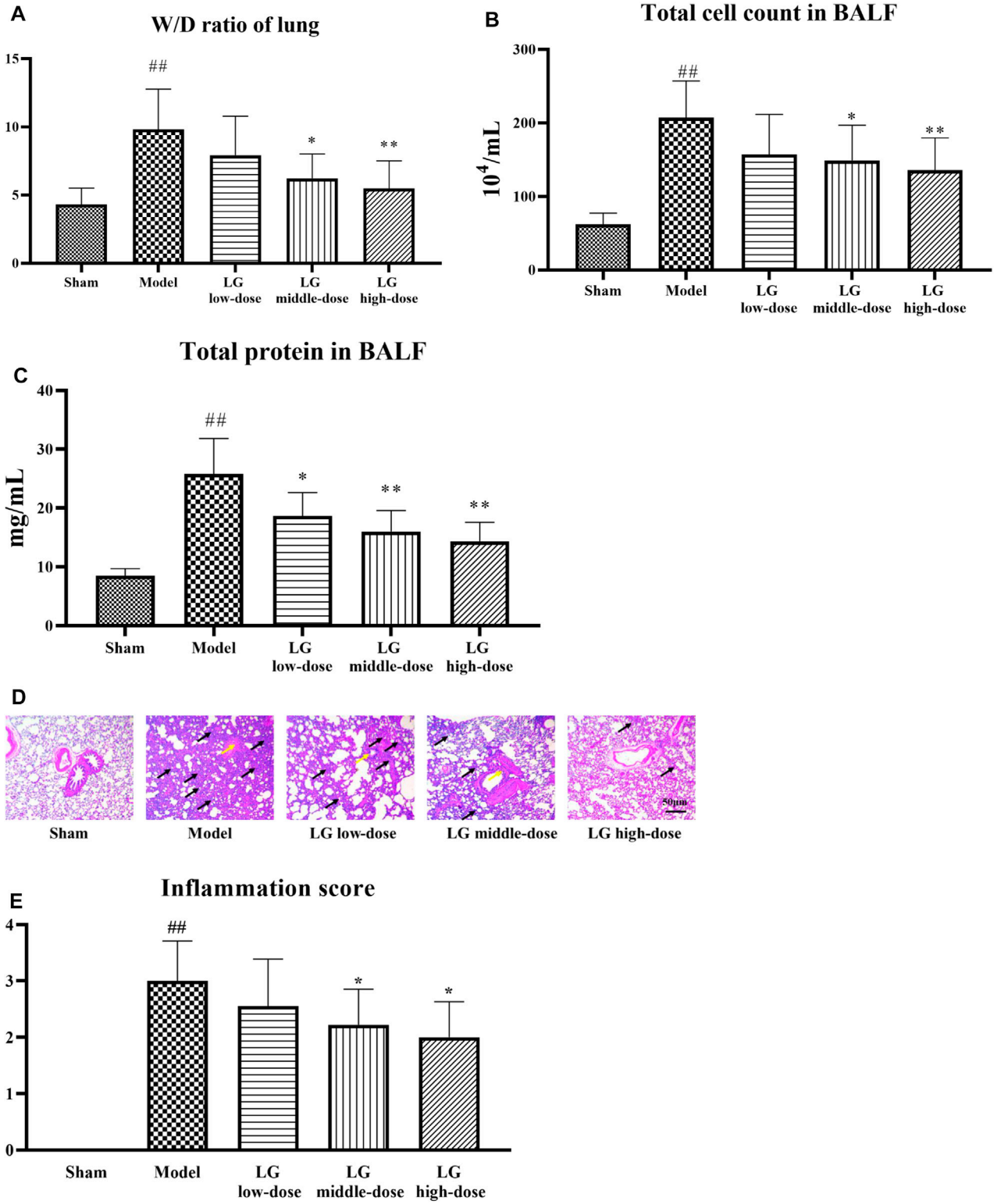

FIGURE 2
LG treatment alleviated acute lung injury in septic model rats. **(A)** LG decreased the W/D ratio in lung. **(B)** LG treatment decreased the total cell count in BALF. **(C)** LG treatment decreased the total protein concentration in BALF. **(D,E)** HE staining indicated that LG treatment alleviated the pathological changes and decreased the inflammation score in lung (100×), black arrows indicated in infiltratiion of inflammatory cells and yellow arrows indicated the damage of bronchial structure. W/D: wet/dry, HE: hematoxylin and eosin. Sham group (n = 15), Model group (n = 8), LG low-dose group (n = 9), LG middle-dose group (n = 9), LG high-dose group (n = 10) ##: $p < 0.01$ compared with the sham group; *: $p < 0.05$ compared with the model group; **: $p < 0.01$ compared with the model group.

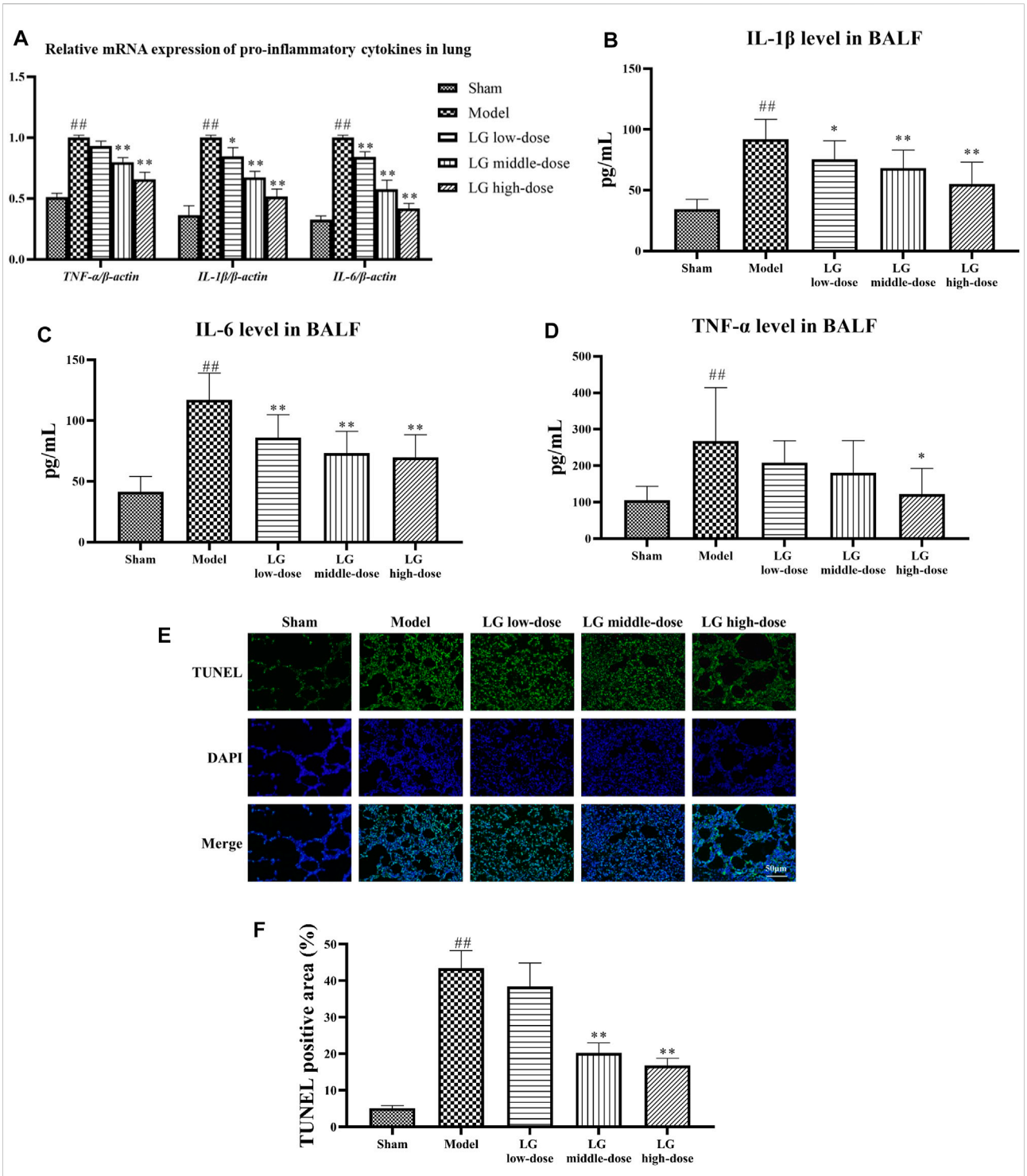

FIGURE 3
LG treatment reduced the inflammatory response and apoptosis in lung. **(A)** qPCR showed that LG treatment down-regulated the mRNA expression of *IL-6*, *IL-1β*, and *TNF-α* in lung. **(B–D)** LG treatment decreased the levels of IL-1β **(B)**, IL-6 **(C)** and TNF-α **(D)** in BALF. **(E,F)** TUNEL staining indicated that LG treatment decreased the proportions of apoptotic cells in lung (100×). TUNEL: terminal deoxynucleotidyl transferase deoxyuridine triphosphate (dUTP) nick end labeling. Sham group (n = 15), Model group (n = 8), LG low-dose group (n = 9), LG middle-dose group (n = 9), LG high-dose group (n = 10) ##: $p < 0.01$ compared with the sham group; *: $p < 0.05$ compared with the model group; **: $p < 0.01$ compared with the model group.

radix], forsythin and forsythoside A in *F. suspensa* (Thunb.) Vahl [Oleaceae; Forsythiae fructus], and isoorientin in *L. gracile* Brongn [Poaceae; Lophatheri herba]. Were identified as the preeminent compounds in LG.

Therapeutic effects of Liang-Ge decoction on sepsis-associated lung injury model rats

After 24 h of drug administration for modeling, 15 rats in sham group, 8 rats in the model group, 9 rats in LG low-dose group, 9 rats in LG middle-dose group, 10 rats in LG high-dose group were survived. The W/D ratio of lung tissue, total cell count and total protein level in BALF were significantly increased in model group compared with the sham group ($p < 0.01$, respectively). Middle- and high-dose treatment of LG reduced the W/D ratio of lung tissue and total cell count in BALF in septic model rats ($p < 0.05$ and $p < 0.01$, respectively). In addition, the total protein levels in BALF were lower in LG low-dose ($p < 0.05$), LG middle-dose ($p < 0.01$) and LG high-dose ($p < 0.01$) groups compared with that in the model group (Figures 2A–C). Lung HE staining results showed intact bronchial epithelial structure, normal interalveolar septum, absence of interstitial edema in the lungs, and absence of significant inflammatory cell exudates in the sham group. In the model group, bronchial epithelial structure was no longer intact and infiltration by a considerable number of inflammatory cells could be observed. Treatment with low-, middle- and high-dose LG significantly improved pathological changes in lung from septic model rats (Figure 2D). Likewise, the inflammation score of HE staining was higher in model group than that in the control group and the inflammation score was lower in LG middle-dose ($p < 0.05$) and LG high-dose ($p < 0.05$) groups compared with that in the model group (Figure 2E).

Effects of Liang-Ge decoction on inflammatory response, oxidative stress and apoptosis in lung in sepsis-associated lung injury model rats

The anti-inflammatory effects of LG on sepsis-associated lung injury model rats were studied by investigating the gene and protein expressions of pro-inflammatory cytokines in lung and BALF. qPCR analysis showed that the mRNA expressions of *IL-6*, *IL-1β*, and *TNF-α* in lung tissue were up-regulated in model group compared with those in the sham group ($p < 0.01$, respectively). Compared with the model group, the mRNA expressions of *IL-1β* and *IL-6* were down-regulated in LG low-dose ($p < 0.05$ and $p < 0.01$, respectively), LG middle-dose ($p < 0.01$, respectively) and LG high-dose ($p < 0.01$, respectively) groups. The mRNA expression of *TNF-α* was lower in LG middle-dose and LG high-dose ($p < 0.01$, respectively) groups compared with the model group (Figure 3A). Likewise, ELISA results showed that the levels of IL-6, IL-1β, and TNF-α in BALF were increased in model group compared with those in the sham group ($p < 0.01$, respectively). Compared with the model group, the levels of IL-1β and IL-6 were lower in LG low-dose ($p < 0.05$ and $p < 0.01$, respectively), LG middle-dose ($p < 0.01$, respectively) and LG high-dose ($p < 0.01$, respectively) groups (Figures 3B,C). The level of TNF-α was decreased in LG high-dose groups compared with the model group ($p < 0.05$, Figure 3D).

Furthermore, the anti-oxidative effects of LG were evaluated by measuring the activities of SOD and GSH-Px and the level of MDA in lung tissue homogenates. The activities of SOD and GSH-Px were lower and the level of MDA was increased in model group compared with those in the sham group ($p < 0.01$, respectively). Compared with the model group, treatment with middle- and high-dose LG significantly elevated the activities of SOD ($p < 0.05$ and $p < 0.01$, respectively) and GSH-Px ($p < 0.05$ and $p < 0.01$, respectively) in lung tissue homogenates. The MDA level was lower in LG high-dose group compared with the model group ($p < 0.05$, Table 2).

The anti-apoptotic effects of LG were then studied using TUNEL staining and by measuring the activity of LDH in BALF. TUNEL staining showed that the TUNEL positive area in model group were increased compared with the sham group ($p < 0.01$), whereas the TUNEL positive area in LG middle-dose and LG high-dose groups were decreased compared with the model group ($p < 0.01$, respectively, Figures 3E,F). Besides, the activity of LDH was increased in model group compared with the sham group ($p < 0.01$). Treatment with middle- and high-dose LG reduced the activity of LDH compared with the model group ($p < 0.01$, respectively, Table 3).

Taken together, high-dose of LG treatment showed significant therapeutic, anti-inflammatory, anti-oxidative and anti-apoptotic effects on sepsis-associated lung injury model rats. Therefore, LG high-dose group was selected for further untargeted metabolomics study to elucidate the metabolic modulatory mechanisms of LG on sepsis-associated lung injury.

Effects of Liang-Ge decoction on metabolite levels in lung in sepsis-associated lung injury model rats

We further used untargeted metabolomics to study the changes of metabolites in lung sepsis-associated lung injury model rats after LG treatment. The principle component analysis (PCA) plot showed that the sham and model groups were well differentiated and that the model and LG high-dose group were also well differentiated (Figure 4A). To identify differentially expressed metabolites, partial least-squares discriminant analysis (PLS-DA) was used and the explanatory

TABLE 2 Acitivities of SOD and GSH-Px and level of MDA in lung tissue homogenates after LG treatment.

Group	SOD (U/mgprot)	MDA (nmol/mgprot)	GSH-Px (U/mgprot)
Sham	55.70 ± 14.92	1.73 ± 0.62	20.75 ± 3.80
Model	25.22 ± 15.6$^{\#\#}$	3.85 ± 1.35$^{\#\#}$	8.04 ± 4.58$^{\#\#}$
LG low-dose	34.56 ± 6.62	3.24 ± 1.35	12.22 ± 3.54
LG middle-dose	42.16 ± 13.07*	3.01 ± 1.03	12.37 ± 3.42*
LG high-dose	46.66 ± 13.62**	2.60 ± 0.62*	16.12 ± 3.88**

SOD, superoxide dismutase; MDA, methane dicarboxylic aldehyde; GSH-Px, glutathione peroxidase. Sham group (n = 15), Model group (n = 8), LG, low-dose group (n = 9), LG, middle-dose group (n = 9), LG, high-dose group (n = 10) $^{\#\#}p < 0.01$ compared with the sham group; $^{*}p < 0.05$ compared with the model group; $^{**}p < 0.01$ compared with the model group.

TABLE 3 Activity of LDH in BALF after LG treatment.

Group	LDH (U/mL)
Sham	4.37 ± 0.82
Model	31.27 ± 8.42$^{\#\#}$
LG low-dose	25.36 ± 4.24
LG middle-dose	21.25 ± 2.69**
LG high-dose	15.2 ± 1.61**

LDH, lactic dehydrogenase; Sham group (n = 15), Model group (n = 8), LG, low-dose group (n = 9), LG, middle-dose group (n = 9), LG, high-dose group (n = 10) ##: $p <$ 0.01 compared with the sham group; $^{**}p < 0.01$ compared with the model group.

power (R^2) and predictive power (Q^2) of PLS-DA model were accessed. Compared with the sham group, the model group had an R^2 = 0.79 and a Q^2 = −0.78, whereas LG high-dose group had an R^2 = 0.83 and a Q^2 = −0.78 compared with the model group (Figures 4B–E). These results showed that the model was stable and had good predictive power.

The following three criteria were used to screen for differentially expressed metabolites: $p < 0.05$ and VIP >1.0, fold change (FC) > 1.20 or FC < 0.80 (between sham and model group or between model and LG high-dose group), where 28 differentially expressed metabolites were identified in total (Table 4). Compared with those in the sham group, the levels of citric acid, glycocholic acid, hydroxyproline, cytidine, 2-deoxyuridine, uracil, cytosine, L-isoleucine, and DL-serine were significantly increased while those of cholesterol, 2-deoxycytidine, nicotinic acid, glutathione, oleanolic acid, nicotinamide, methionine, chenodeoxycholic acid, cholic acid, inositol, alpha-ketoglutaric acid and hippuric acid were significantly decreased in the model group. Levels of hippuric acid, alpha-ketoglutaric acid, inositol, cholic acid, chenodeoxycholic acid, methionine, oleanolic acid, nicotinic acid, L-ascorbate, threonine, D-proline and D-(+)-tryptophan were significantly increased in the LG high-dose group compared with those in the model group while those of DL-serine, DL-malic acid, taurodeoxycholic acid, L-isoleucine, inosine, cytosine, 2-deoxyuridine, cytidine, hydroxyproline, glycocholic acid and citric acid were significantly decreased in the LG high-dose group (Table 4).

Pathway analysis of differential metabolites

The MetaboAnalyst platform was used for metabolic pathway enrichment analysis of differentially expressed metabolites together with the KEGG database. Differential metabolic pathways were selected based on a pathway impact >0.05 and $p < 0.05$ (Xie et al., 2021). Differential metabolic pathways between the sham group and model group included glycine, serine and threonine metabolism, cysteine and methionine metabolism, nicotinate and nicotinamide metabolism, pyrimidine metabolism, inositol phosphate metabolism, citrate cycle (TCA cycle) (Figure 4F). Differential metabolic pathways between the model group and the LG high-dose group included glycine, serine and threonine metabolism, cysteine and methionine metabolism, inositol phosphate metabolism, TCA cycle, tryptophan metabolism and aminoacyl-tRNA biosynthesis (Figure 4G). Among these pathways, glycine, serine and threonine metabolism, cysteine and methionine metabolism, inositol phosphate metabolism and TCA cycle were pathways common to the sham, model, and LG high-dose groups.

Discussion

In this study, we used CLP to generate a rat model of sepsis. Our results showed that the W/D ratio of the lung tissues in the model group rats was increased, along with the increase of total cell count and protein levels in the BALF, suggesting increased permeability of the lung tissues in the model group rats. The results of the pathological staining revealed a significant inflammatory cell infiltration in the lung tissue of the model group rats, which was accompanied by bronchial epithelial cell injury. These changes were consistent with the pathological changes of sepsis-associated lung injury (Jia et al., 2022). LG significantly reduced the permeability of the lung tissues in rats with sepsis-associated lung injury and improved the pathological changes detected in the lung tissues.

Our results also showed that LG downregulated the expression of the pro-inflammatory cytokines IL-6, IL-1β, and

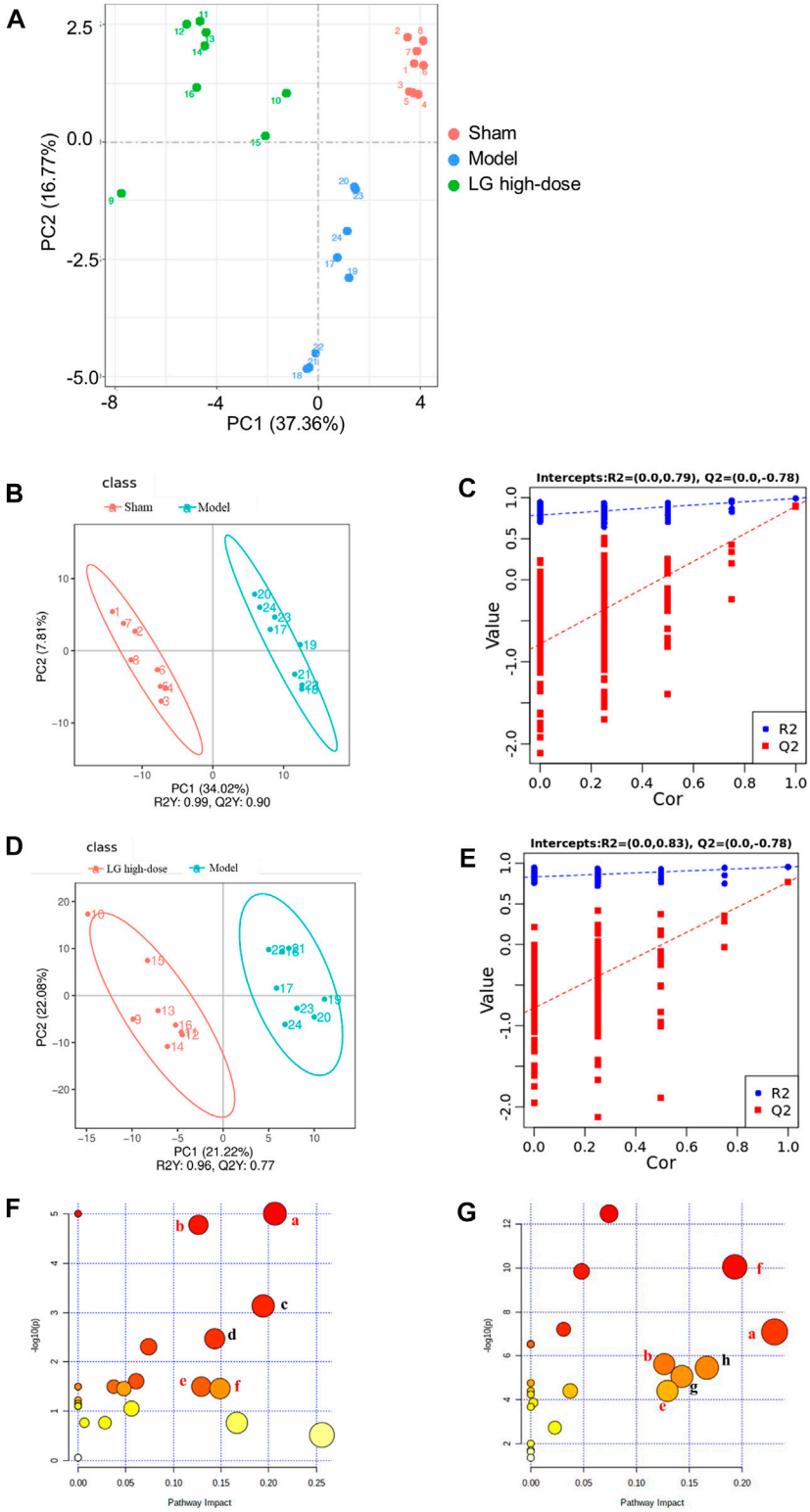

FIGURE 4
LG treatment modulated the metabolites in lung in sepsis-associated lung injury model rats. **(A)** Scores plots of PCA among each group. **(B,C)** Scores plots of PLS-DA between the sham and model groups and the corresponding coefficient of loading plots. **(D,E)** Scores plots of PLS-DA between the model and LG high-dose groups and the corresponding coefficient of loading plots. **(F,G)** Summary of pathway analysis between sham and model groups **(F)** and between model and LG high-dose groups **(G)**, the common pathways have been marked in red. **(A)** Glycine, serine and threonine metabolism; **(B)** Cysteine and methionine metabolism; **(C)** Nicotinate and nicotinamide metabolism; **(D)** Pyrimidine metabolism; **(E)** Inositol phosphate metabolism; **(F)** Citrate cycle (TCA cycle); **(G)** Tryptophan metabolism; **(H)** Aminoacyl-tRNA biosynthesis. Sham, model, and LG high-dose groups (n = 8 per group). PCA: principle component analysis, PLS-DA: partial least-squares discriminant analysis.

TABLE 4 Differential metabolites in lung in sepsis-associated lung injury model rats after the treatment of LG.

No.	Formula	RT [min]	m/z	Metabolites	VIP		FC		Trend		Pathway
					M vs. S	L vs. M	M vs. S	L vs M	M vs. S	L vs. M	
1	$C_6H_8O_7$	2.08	191.02	Citric acid	1.88	1.41	3.62	0.18	↑##	↓**	f
2	$C_{26}H_{43}NO_6$	6.73	464.30	Glycocholic acid	1.97	1.02	4.77	0.36	↑##	↓**	
3	$C_9H_9NO_3$	5.34	178.05	Hippuric acid	2.01	1.11	0.23	1.93	↓##	↑*	
4	$C_5H_6O_5$	1.37	145.01	alpha-Ketoglutaric acid	1.63	1.62	0.55	4.84	↓##	↑**	f
5	$C_6H_{12}O_6$	1.45	179.06	Inositol	1.43	1.55	0.68	5.61	↓#	↑**	e
6	$C_{24}H_{40}O_5$	6.60	407.28	Cholic acid	1.38	1.16	0.28	2.97	↓#	↑**	
7	$C_{24}H_{40}O_4$	6.91	437.29	Chenodeoxycholic Acid	1.18	0.52	0.39	1.89	↓#	↑*	
8	$C_5H_9NO_3$	1.30	132.07	Hydroxyproline	1.86	0.62	3.91	0.15	↑##	↓**	
9	$C_5H_{11}NO_2S$	5.30	150.06	Methionine	1.02	2.00	0.57	2.27	↓##	↑**	b, h
10	$C_6H_6N_2O$	1.89	123.06	Nicotinamide	1.52	0.46	0.27	1.53	↓##	↑	c
11	$C_{30}H_{48}O_3$	9.46	439.35	Oleanolic acid	1.51	1.02	0.57	3.19	↓##	↑**	
12	$C_9H_{13}N_3O_5$	1.38	244.09	Cytidine	1.21	0.78	2.17	0.28	↑##	↓**	d
13	$C_{10}H_{17}N_3O_6S$	1.38	308.09	Glutathione	1.32	0.48	0.58	1.52	↓#	↑	
14	$C_9H_{12}N_2O_5$	6.21	229.08	2-Deoxyuridine	1.42	0.29	3.09	0.23	↑#	↓*	d
15	$C_4H_4N_2O_2$	1.79	113.03	Uracil	1.30	0.86	1.99	0.55	↑#	↓	d
16	$C_4H_5N_3O$	1.38	112.05	Cytosine	1.13	0.35	1.98	0.47	↑##	↓**	
17	$C_6H_5NO_2$	1.74	124.04	Nicotinic Acid	1.21	1.75	0.46	2.49	↓#	↑*	c
18	$C_9H_{13}N_3O_4$	1.82	228.10	2-Deoxycytidine	1.07	0.38	0.53	1.82	↓#	↑	d
19	$C_{27}H_{46}O$	8.18	387.36	Cholesterol	1.22	0.39	0.56	1.68	↓##	↑	
20	$C_6H_8O_6$	5.50	177.04	l-Ascorbate	0.18	1.64	0.96	1.65	↓	↑**	
21	$C_{10}H_{12}N_4O_5$	5.04	269.09	Inosine	0.22	1.80	1.16	0.44	↑	↓**	
22	$C_6H_{13}NO_2$	3.01	132.10	l-Isoleucine	1.04	1.43	1.31	0.64	↑#	↓**	h
23	$C_4H_9NO_3$	1.31	120.07	Threonine	0.62	1.38	0.79	4.20	↓	↑**	a, h
24	$C_5H_9NO_2$	1.37	116.07	D-Proline	0.71	1.14	0.70	1.79	↓	↑**	
25	$C_{26}H_{45}NO_6S$	7.13	500.30	Taurodeoxycholic Acid	0.24	1.44	1.35	0.35	↑	↓**	
26	$C_4H_6O_5$	1.67	133.01	DL-Malic acid	0.61	1.30	1.21	0.35	↑	↓**	f
27	$C_{11}H_{12}N_2O_2$	5.13	157.08	D-(+)-Tryptophan	0.62	1.43	0.85	2.99	↓	↑**	g, h
28	$C_3H_7NO_3$	1.29	106.05	DL-Serine	1.05	1.59	2.11	0.23	↑##	↓**	a, b, h

RT, retention time; VIP, variable importance of projection; FC: fold change; $^{\#}p < 0.05$ as compared to the control group; $^{\#\#}p < 0.01$ as compared to the control group; $^{*}p < 0.05$ as compared to the model group; $^{**}p < 0.01$ as compared to the model group; ↑content increased; ↓content decreased; vs. S, sham group; M, model group; L: LG, high-dose group. a, Glycine, serine and threonine metabolism; b, Cysteine and methionine metabolism; c, Nicotinate and nicotinamide metabolism; d, Pyrimidine metabolism; e, Inositol phosphate metabolism; f, Citrate cycle (TCA, cycle); g, Tryptophan metabolism; h, Aminoacyl-tRNA, biosynthesis. Sham, model, and LG, high-dose groups ($n = 8$ per group). $^{\#}p < 0.05$ compared with the sham group; $^{\#\#}p < 0.01$ compared with the sham group; $^{*}p < 0.05$ compared with the model group; $^{**}p < 0.01$ compared with the model group.

TNF-α in lung tissues, and decreased the levels of these cytokines in the BALF. The overactivation of inflammatory responses is an important pathological process in the early stages of sepsis, and these responses induced by infection and injury are initially protective, but can severely damage lung tissues when the stimulus is too intense and cytokine production is excessive (Jianjun et al., 2018). Studies have shown that the levels of pro-inflammatory cytokines, such as those of IL-6, IL-1β, and TNF-α, significantly increase in rats from 6 to 48 h after CLP treatment (Zafrani et al., 2012; Jia et al., 2021).

In addition, oxidative stress is among the pathological manifestations of lung injury in sepsis. Bacterial infection can directly cause excessive reactive oxygen species (ROS) production in lung tissues, and the high levels of inflammatory cytokines can also promote ROS production; in turn, these ROS can damage membrane structures in lung tissue cells through oxidative reactions (Tripathi et al., 2018). Our results showed that LG increased the activity of SOD and GSH-Px and decreased MDA levels in lung tissues. MDA is a lipid peroxidation end product that is cytotoxic and its level is positively correlated with the degree of oxidative stress (Tsikas, 2017). SOD and GSH-Px are important antioxidant enzymes that scavenge ROS from cells (Olsvik et al., 2005); SOD promotes the conversion of ROS to H_2O_2, which is subsequently converted to H_2O and O_2 under the effect of GSH-Px. The increased activity of SOD and GSH-Px

protects the lung tissues from oxidative stress injury (Liu et al., 2022).

Bacterial infection can directly lead to alveolar epithelial cell necrosis and apoptosis, and the excessive inflammatory responses and oxidative stress induced by infection can also aggravate alveolar cell damage, which in turn can impair the barrier function of lungs and alter the permeability of lung tissues. LG reduces the activity of LDH in the BALF. LDH is an important regulatory enzyme of anaerobic glycolysis and gluconeogenesis. The disruption of the cell membrane structure causes LDH release; thus, the detection of LDH can reflect cell injury (Laganá et al., 2019). In addition, we used TUNEL staining to observe apoptosis in lung tissues. After apoptosis, the chromosomes break, producing a large number of sticky 3′-OH ends. TUNEL staining is a method that is commonly used to detect apoptotic cells via terminal deoxynucleotidyl transferase to label the sticky 3′-OH ends of DNA with derivatives formed from dUTP and fluorescein (Mirzayans and Murray, 2020). The results of TUNEL staining showed a decrease in the number of apoptotic cells in lung tissues after the LG intervention.

Next, we investigated the effect of LG on metabolites in the lung tissues of rats with sepsis-associated lung injury using untargeted metabolomics. A PCA and PLS-DA revealed significant changes in lung tissue metabolism in the model and sham groups, with the lung tissue metabolism in rats with sepsis-associated lung injury being significantly affected after treatment with LG. A further differential metabolite analysis showed that LG affected the levels of 23 metabolites in lung such as citric acid, methionine, threonine, alpha-ketoglutaric acid, and inositol. A metabolic pathway analysis of the differential metabolites using MetaboAnalyst showed that glycine, serine and threonine metabolism, cysteine and methionine metabolism, inositol phosphate metabolism and TCA cycle pathways were the common pathways showing differences between the sham and model groups and between the model and LG high-dose groups, suggesting that LG plays a role in the treatment of sepsis-associated lung injury by regulating the metabolites in these pathways.

Glycine, serine, and threonine metabolism

Our results showed that the LG intervention reduced DL-serine levels and increased threonine levels in the glycine, serine, and threonine metabolism pathway in the lung tissues of rats with sepsis-associated lung injury. Amino acid metabolism is closely related to immune cell activation in inflammatory responses. Serine belongs to the one-carbon unit amino acids and plays an important role in cellular nucleotide synthesis (Yang et al., 2019; Yang and Vousden, 2016). In a lipopolysaccharide-induced macrophage model, serine supplementation promoted IL-1β secretion, whereas the inhibition of serine metabolism reduced IL-1β production in a sepsis model, while improving survival in septic mice (Rodriguez et al., 2019). The inhibition of IL-1β production by LG in rats with sepsis-associated lung injury may be associated with a decrease of serine levels in macrophages; however, this needs to be confirmed in additional *in vitro* studies. Threonine is an essential amino acid and an important nutrient for the body and can be converted to acetyl-CoA to enter the TCA cycle and provide energy to the body (Tang et al., 2021). The role of threonine in sepsis has not been reported, and the relationship between the increased threonine levels after treatment with LG and improved sepsis-associated lung injury warrants further study.

Cysteine and methionine metabolism

Our results showed that the LG intervention reduced DL-serine levels and increased methionine levels in the cysteine and methionine metabolism pathway in the lung tissues of rats with sepsis-associated lung injury. The relationship between serine and sepsis-associated lung injury has been discussed previously in this study. Methionine can be converted from serine, which plays an important regulatory role in cell survival (Lee et al., 2015). An *in vitro* study found that methionine deficiency caused apoptosis and cell-cycle arrest (Song et al., 2021). LG may inhibit the inflammatory responses and apoptosis of lung tissue by promoting the conversion of serine to methionine.

Inositol phosphate metabolism

Our results showed that the LG intervention increased inositol levels in the inositol phosphate metabolism pathway in the lung tissues of rats with sepsis-associated lung injury. Inositol is an important nutrient that promotes cell survival and proliferation and is also used as a drug in the alleviation of respiratory distress syndrome (RDS), Alzheimer's disease, etc. (Bizzarri et al., 2016). An ensuing shamled clinical study found that supplementation with inositol in preterm infants presenting with RDS significantly improved clinical symptoms and reduced the incidence of sepsis in the affected children (Howlett et al., 2019). In addition, an *in vitro* study found that Myo-inositol, which is an inositol derivative, protects cells from oxidative stress injury (Ponchia et al., 2021). Similarly, one study found that *in vitro* intervention using Myo-inositol combined with ethanolamine significantly alleviated H_2O_2-induced oxidative stress injury in cells (Sibomana et al., 2019). Therefore, the effect of LG in ameliorating oxidative stress in sepsis-associated lung injury may be related to the increase in inositol levels in the inositol phosphate metabolism pathway.

TCA cycle

Our results showed that LG increased the level of alpha-ketoglutaric acid and decreased those of citric acid and DL-malic acid in the TCA cycle in the lung tissues of rats with sepsis-associated lung injury. The TCA cycle is the most efficient way for the body to oxidize carbohydrates for energy and is the hub for the metabolic liaison and transformation of carbohydrates, lipids, and amino acids. A recent study showed that the reprogramming of glucose metabolism is closely related to macrophage polarization (Russo et al., 2021). Moreover, an *in vitro* study revealed that alpha-ketoglutaric acid inhibits M1-type macrophage polarization and reduces the production of the pro-inflammatory cytokines IL-1β, IL-6, and TNF-α by inhibiting nuclear factor kappa B (NF-κB) pathway activation, and also promotes M2-type macrophage polarization by activating Jumonji domain-containing protein D3 (JMJD3) (Pu-Ste et al., 2017). In contrast, citric acid and DL-malic acid levels were significantly increased in activated macrophages (Viola et al., 2019). Citric acid promotes macrophage activation, which in turn induces inflammatory responses (Viola et al., 2019). Interestingly, a recent study found that the citrate/malate exchange on macrophage mitochondria plays an important role in regulating macrophage activation and the secretion of inflammatory mediators (Palmieri et al., 2015). The reprogramming of carbohydrate metabolism in macrophages through its regulation provides a novel strategy for inhibiting the development of inflammatory responses. Melatonin can inhibit the development of inflammatory responses by increasing the levels of alpha-ketoglutaric acid in macrophages (Liu et al., 2017).

In conclusion, our study demonstrated the therapeutic effetcts of LG on sepsis-associated lung injury model rats. Moreover, LG could inhibit the inflammatory response, oxidative stress and apoptosis and regulate metabolites related to glycine, serine and threonine metabolism, cysteine and methionine metabolism, inositol phosphate metabolism and TCA cycle in lung in sepsis-associated lung injury model rats. This study is the first to screen the differential metabolites of LG on CLP-induced sepsis-associated lung injury model. In addition, our study revealed significant anti-inflammatory, anti-oxidative and anti-apoptotic potentials of LG. Based on the close relationship between host metabolism and pathological processes such as inflammatory response, oxidative stress and apoptosis, our further studies should be carried out using *in vivo* and *in vitro* model to construct a metabolism-downstream pathway regulatory network of LG and its active components on sepsis-associated lung injury model.

Data availability statement

The original contributions presented in the study are included in the article/Supplementary Material, further inquiries can be directed to the corresponding author.

Ethics statement

The experiment was approved by the Ethics Committee of Tianjin First Central Hospital.

Author contributions

WH carried out the experiments and manuscript writing. QX, HC, PZ, RH, and TW provided experimental help, and performed data analysis and result interpretation. DW provided ideas and technical guidance for the whole work. All authors contributed to the article and approved the submitted version.

Funding

This work was supported by the National Science Foundation of China (No. 81973800); Youth Scientific Research of Tianjin Administration of Traditional Chinese Medicine (No. 2019099); spring Seedling of Tianjin First Central Hospital (No. 2019CM5); Research Projects in Key Rreas of Traditional Chinese medicine in Tianjin (No. 2017006, 2022007).

Conflict of interest

The authors declare that the research was conducted in the absence of any commercial or financial relationships that could be construed as a potential conflict of interest.

Publisher's note

Supplementary material

The Supplementary Material for this article can be found online at: https://www.frontiersin.org/articles/10.3389/fphar.2022.926134/full#supplementary-material

References

Bizzarri, M., Fuso, A., Dinicola, S., Cucina, A., and Bevilacqua, A. (2016). Pharmacodynamics and pharmacokinetics of inositol(s) in health and disease. *Expert Opin. Drug Metab. Toxicol.* 12 (10), 1181–1196. doi:10.1080/17425255.2016.1206887

Cecconi, M., Evans, L., Levy, M., and Rhodes, A. (2018). Sepsis and septic shock. *Lancet* 392 (10141), 75–87. doi:10.1016/s0140-6736(18)30696-2

Cui, J., Gao, J., Li, Y., Fan, T., Qu, J., Sun, Y., et al. (2020). Andrographolide sulfate inhibited NF-κB activation and alleviated pneumonia induced by poly I:C in mice. *J. Pharmacol. Sci.* 144 (4), 189–196. doi:10.1016/j.jphs.2020.08.005

Cui, Y., Liu, S., Zhang, X., Ding, X., Duan, X., Zhu, Z., et al. (2020). Metabolomic analysis of the effects of adipose-derived mesenchymal stem cell treatment on rats with sepsis-induced acute lung injury. *Front. Pharmacol.* 11, 902. doi:10.3389/fphar.2020.00902

Dejager, L., Pinheiro, I., Dejonckheere, E., and Libert, C. (2011). Cecal ligation and puncture: The gold standard model for polymicrobial sepsis? *Trends Microbiol.* 19 (4), 198–208. doi:10.1016/j.tim.2011.01.001

Howlett, A., Ohlsson, A., and Plakkal, N. (2019). Inositol in preterm infants at risk for or having respiratory distress syndrome. *Cochrane Database Syst. Rev.* 2020 (1), CD000366. doi:10.1002/14651858.cd000366.pub4

Jaurila, H., Koivukangas, V., Koskela, M., Gäddnäs, F., Myllymaa, S., Kullaa, A., et al. (2020). 1H NMR based metabolomics in human sepsis and healthy serum. *Metabolites* 10 (2), 70. doi:10.3390/metabo10020070

Jia, B. T., Wu, Y. L., Liao, J. B., He, W., Wang, D., Chen, F., et al. (2022). Effects of Qingwen Baidu decoction on coagulation and multiple organ injury in rat models of sepsis. *Tradit. Med. Res.* 7 (3), 25. doi:10.53388/TMR20220315269

Jia, C.-M., Zhang, F.-W., Wang, S.-J., Wang, W., and Li, Y. (2021). Tea polyphenols prevent sepsis-induced lung injury via promoting translocation of DJ-1 to mitochondria. *Front. Cell Dev. Biol.* 9, 622507. doi:10.3389/fcell.2021.622507

Jianjun, X., Caijiao, L., Zhengjun, L., Peng, Z., Hailei, G., and Tingting, W. (2018). Schizandrin B protects LPS-induced sepsis via TLR4/NF-κB/MyD88 signaling pathway. *Am. J. Transl. Res.* 10 (4), 1155.

Johnson, E. R., and Matthay, M. A. (2010). Acute lung injury: Epidemiology, pathogenesis, and treatment. *J. Aerosol Med. Pulm. Drug Deliv.* 23 (4), 243–252. doi:10.1089/jamp.2009.0775

Laganá, G., Barreca, D., Calderaro, A., and Bellocco, E. (2019). Lactate dehydrogenase inhibition: Biochemical relevance and therapeutical potential. *Curr. Med. Chem.* 26 (18), 3242–3252. doi:10.2174/0929867324666170209103444

Lee, B. C., Kaya, A., and Gladyshev, V. N. (2015). Methionine restriction and life-span control. *Ann. N. Y. Acad. Sci.* 1363 (1), 116–124. doi:10.1111/nyas.12973

Li, Y. F., Sheng, H. D., Qian, J., and Wang, Y. (2022). The Chinese medicine babaodan suppresses LPS-induced sepsis by inhibiting NLRP3-mediated inflammasome activation. *J. Ethnopharmacol.* 292, 115205. doi:10.1016/j.jep.2022.115205

Liu, M. W., Wang, Y. H., Qian, C. Y., and Li, H. (2014). Xuebijing exerts protective effects on lung permeability leakage and lung injury by upregulating Toll-interacting protein expression in rats with sepsis. *Int. J. Mol. Med.* 34 (6), 1492–1504. doi:10.3892/ijmm.2014.1943

Liu, Z., Gan, L., Zhang, T., Ren, Q., and Sun, C. (2017). Melatonin alleviates adipose inflammation through elevating α-ketoglutarate and diverting adipose-derived exosomes to macrophages in mice. *J. Pineal Res.* 64 (1), e12455. doi:10.1111/jpi.12455

Liu, Z., Gao, J., Ye, X., Wang, C., and Zhao, B. (2022). Endogenous sulfur dioxide improves the survival rate of sepsis by improving the oxidative stress response during lung injury. *Oxid. Med. Cell. Longev.* 2022, 6339355–6339359. doi:10.1155/2022/6339355

Mirzayans, R., and Murray, D. (2020). Do TUNEL and other apoptosis assays detect cell death in preclinical studies? *Int. J. Mol. Sci.* 21 (23), 9090. doi:10.3390/ijms21239090

Olsvik, P. A., Kristensen, T., Waagbø, R., Rosseland, B. O., Tollefsen, K.-E., Baeverfjord, G., et al. (2005). mRNA expression of antioxidant enzymes (SOD, CAT and GSH-Px) and lipid peroxidative stress in liver of Atlantic salmon (*Salmo salar*) exposed to hyperoxic water during smoltification. *Comp. Biochem. Physiol. C. Toxicol. Pharmacol.* 141 (3), 314–323. doi:10.1016/j.cbpc.2005.07.009

Palmieri, E. M., Spera, I., Menga, A., Infantino, V., Porcelli, V., Iacobazzi, V., et al. (2015). Acetylation of human mitochondrial citrate carrier modulates mitochondrial citrate/malate exchange activity to sustain NADPH production during macrophage activation. *Biochim. Biophys. Acta* 1847 (8), 729–738. doi:10.1016/j.bbabio.2015.04.009

Ponchia, R., Bruno, A., Renzi, A., Landi, C., Shaba, E., Luongo, F. P., et al. (2021). Oxidative stress measurement in frozen/thawed human sperm: The protective role of an *in vitro* treatment with myo-inositol. *Antioxidants* 11 (1), 10. doi:10.3390/antiox11010010

Pu-Ste, L., Haiping, W., Xiaoyun, L., Tung, C., Tony, T., Stefan, C., et al. (2017). α-ketoglutarate orchestrates macrophage activation through metabolic and epigenetic reprogramming. *Nat. Immunol.* 18 (9), 985–994. doi:10.1038/ni.3796

Rodriguez, A. E., Ducker, G. S., Billingham, L. K., Martinez, C. A., Mainolfi, N., Suri, V., et al. (2019). Serine metabolism supports macrophage IL-1β production. *Cell Metab.* 29 (4), 1003–1011. e4. doi:10.1016/j.cmet.2019.01.014

Russo, S., Kwiatkowski, M., Govorukhina, N., Bischoff, R., and Melgert, B. N. (2021). Meta-inflammation and metabolic reprogramming of macrophages in diabetes and obesity: The importance of metabolites. *Front. Immunol.* 12, 746151. doi:10.3389/fimmu.2021.746151

Sibomana, I., Grobe, N., DelRaso, N. J., and Reo, N. V. (2019). Influence of *myo*-inositol Plus ethanolamine on plasmalogens and cell viability during oxidative stress. *Chem. Res. Toxicol.* 32 (2), 265–284. doi:10.1021/acs.chemrestox.8b00280

Song, B., Zeng, Q., Liu, Y., and Wu, B. (2021). Effect of methionine deficiency on the apoptosis and cell cycle of kidney in broilers. *Res. Vet. Sci.* 135, 228–236. doi:10.1016/j.rvsc.2019.09.013

Stringer, K. A., Serkova, N. J., Karnovsky, A., Guire, K., Paine, R., and Standiford, T. J. (2011). Metabolic consequences of sepsis-induced acute lung injury revealed by plasma ^{1}H-nuclear magnetic resonance quantitative metabolomics and computational analysis. *Am. J. Physiol. Lung Cell. Mol. Physiol.* 300 (1), L4–L11. doi:10.1152/ajplung.00231.2010

Tang, Q., Tan, P., Ma, N., and Ma, X. (2021). Physiological functions of threonine in animals: Beyond nutrition metabolism. *Nutrients* 13 (8), 2592. doi:10.3390/nu13082592

Tripathi, J. K., Sharma, A., Sukumaran, P., Sun, Y., Mishra, B. B., Singh, B. B., et al. (2018). Oxidant sensor cation channel TRPM2 regulates neutrophil extracellular trap formation and protects against pneumoseptic bacterial infection. *FASEB J.* 32 (12), 6848–6859. doi:10.1096/fj.201800605

Tsikas, D. (2017). Assessment of lipid peroxidation by measuring malondialdehyde (MDA) and relatives in biological samples: Analytical and biological challenges. *Anal. Biochem.* 524, 13–30. doi:10.1016/j.ab.2016.10.021

Viola, A., Munari, F., Sánchez-Rodríguez, R., Scolaro, T., and Castegna, A. (2019). The metabolic signature of macrophage responses. *Front. Immunol.* 10, 1462. doi:10.3389/fimmu.2019.01462

Wang, B., Wang, Y. Q., Cao, S. H., and Liang, Y. (2011). Platelet parameters and platelet toll-like receptor 4 (TLR4) expression in patients with sepsis, and the effect of a joint treatment-plan integrating traditional Chinese and Western medicine: A clinical study. *Zhongguo Wei Zhong Bing Ji Jiu Yi Xue* 23 (10), 616–620. doi:10.3760/cma.j.issn.1003-0603.2011.10.014

Wang, W., Chen, Q., Yang, X., Wu, J., and Huang, F. (2020). Sini decoction ameliorates interrelated lung injury in septic mice by modulating the composition of gut microbiota. *Microb. Pathog.* 140, 103956. doi:10.1016/j.micpath.2019.103956

Wang, Y.-M., Ji, R., Chen, W.-W., Huang, S.-W., Zheng, Y.-J., Yang, Z.-T., et al. (2019). Paclitaxel alleviated sepsis-induced acute lung injury by activating MUC1 and suppressing TLR-4/NF-κB pathway. *Drug Des. devel. Ther.* 13, 3391–3404. doi:10.2147/dddt.s222296

Wang, Y., Liu, Y., Cao, Q., Shi, X., Lu, H., Gao, S., et al. (2018). Metabolomic analysis for the protective effects of mangiferin on sepsis-induced lung injury in mice. *Biomed. Chromatogr.* 32 (6), e4208. doi:10.1002/bmc.4208

Xia, Y., Cao, Y., Sun, Y., Hong, X., Tang, Y., Yu, J., et al. (2021). Calycosin alleviates sepsis-induced acute lung injury via the inhibition of mitochondrial ROS-mediated inflammasome activation. *Front. Pharmacol.* 12, 690549. doi:10.3389/fphar.2021.690549

Xie, X., Liao, J., Ai, Y., Gao, J., Zhao, J., Qu, F., et al. (2021). Pi-dan-jian-qing decoction ameliorates type 2 diabetes mellitus through regulating the gut microbiota and serum metabolism. *Front. Cell. Infect. Microbiol.* 11, 748872. doi:10.3389/fcimb.2021.748872

Xu, H., Qi, Q., and Yan, X. (2020). Myricetin ameliorates sepsis-associated acute lung injury in a murine sepsis model. *Naunyn. Schmiedeb. Arch. Pharmacol.* 394 (1), 165–175. doi:10.1007/s00210-020-01880-8

Yang, H., Lu, Z., Huo, C., Chen, Y., Cao, H., Xie, P., et al. (2019). Liang-Ge-San, a classic traditional Chinese medicine formula, attenuates lipopolysaccharide-induced acute lung injury through up-regulating miR-21. *Front. Pharmacol.* 10, 1332. doi:10.3389/fphar.2019.01332

Yang, M., and Vousden, K. H. (2016). Serine and one-carbon metabolism in cancer. *Nat. Rev. Cancer* 16 (10), 650–662. doi:10.1038/nrc.2016.81

Zafrani, L., Gerotziafas, G., Byrnes, C., Hu, X., Perez, J., Lévi, C., et al. (2012). Calpastatin controls polymicrobial sepsis by limiting procoagulant microparticle release. *Am. J. Respir. Crit. Care Med.* 185 (7), 744–755. doi:10.1164/rccm.201109-1686oc

frontiers | Frontiers in Pharmacology

TYPE Original Research
PUBLISHED 04 October 2022
DOI 10.3389/fphar.2022.924251

OPEN ACCESS

EDITED BY
Qi Wang,
Harbin Medical University, China

REVIEWED BY
Xiaolong Wang,
Temple University, United States
Yun K. Tam,
Sinoveda Canada Inc., Canada

*CORRESPONDENCE
Xuelin Zhou,
peterxlzhou@gmail.com,
zhouxuelin@ccmu.edu.cn

SPECIALTY SECTION
This article was submitted to Ethnopharmacology, a section of the journal Frontiers in Pharmacology

RECEIVED 20 April 2022
ACCEPTED 06 September 2022
PUBLISHED 04 October 2022

CITATION
Qiang Y, Bai L, Tian S, Ma Y, Xu P, Cheng M, Wu Y, Li X, Xue M and Zhou X (2022), Daidzein is the in vivo active compound of Puerariae Lobatae Radix water extract for muscarinic receptor-3 inhibition against overactive bladder. *Front. Pharmacol.* 13:924251. doi: 10.3389/fphar.2022.924251

Daidzein is the *in vivo* active compound of Puerariae Lobatae Radix water extract for muscarinic receptor-3 inhibition against overactive bladder

Yining Qiang[1], Lu Bai[1], Shuran Tian[1], Yi Ma[1], Pingxiang Xu[1,2], Mingchang Cheng[1], Yi Wu[1], Xiaorong Li[1,2], Ming Xue[1,2] and Xuelin Zhou[1,2]*

[1]Department of Pharmacology, School of Basic Medical Sciences, Capital Medical University, Beijing, China, [2]Beijing Engineering Research Center for Nerve System Drugs, Beijing, China

Background: In the previous study, Puerariae Lobatae Radix (named Gegen in Chinese) water extract attenuated M3 receptor agonist carbachol-induced detrusor contraction after 3-week oral administration in a hypertension-associated OAB (overactive bladder) model. This research aimed to investigate the active ingredients from Gegen water extract against OAB.

Methods: Bioassay-guided fractionation was performed by using preparative HPLC for fast isolation of fractions followed by screening their *ex vivo* activity through carbachol-induced bladder strip contraction assay. Chemicals in each active fraction were analyzed by HPLC-UV. Urine metabolites were quantified by LC-MS/MS after sub-acute administration. Thermal shift assay with the recombinant human M3 receptor protein was performed, and molecular docking analysis was used for molecular modelling of M3 receptor inhibition.

Results: Bioassay-guided fractionation results for isolating M3 receptor inhibitors indicated that four compounds were identified as active ingredients of Gegen water extract, and their inhibition potency on carbachol-induced detrusor contraction was ranked in descending order according to their inhibition concentrations as follows: genistein > daidzein > biochanin A >> puerarin. Daidzein in urine reached an *ex vivo* effective concentration to inhibit detrusor contraction, but others did not. Daidzein concentration-dependently increased the melt temperature (*Tm*) of recombinant human M3 receptor protein with a positive binding (ΔTm = 2.12 °C at 100 μg/ml). Molecular docking analysis showed that daidzein can potently bind to the ligand binding pocket of the M3 receptor via hydrogen bonding.

Abbreviations: OAB, overactive bladder; HPLC, high-performance liquid chromatography; SHR, spontaneously hypertensive rats; UV, ultraviolet; MS, mass spectrum; TQS, triple quadrupoles; *Tm*, melt temperature; MRM, multiple reaction monitoring.

Conclusion: Puerarin and its derivatives were pro-drugs, and daidzein was their *in vivo* active form via M3 receptor inhibition for treating OAB.

KEYWORDS

overactive bladder, Puerariae Lobatae Radix, *in vivo* active components, bioassay-guided fractionation, muscarinic receptor inhibition

Highlights

- The major components of Gegen water extract were isoflavone glycosides (puerarin and its derivatives), but their aglycones were the potent M3 receptor inhibitors as found by bioassay-guided fractionation.
- The contents of aglycones (e.g., daidzein) as the major urine metabolites were quantified by LC-MS/MS.
- Daidzein can bind to recombinant human M3 receptor as revealed by thermal shift assay, but peurarin did not.
- Puerarin and its derivatives were pro-drugs.

1 Introduction

Overactive bladder (OAB), a common disease, is defined as a kind of clinical syndrome followed by urinary dysfunction and urgency, with or without incontinence, often accompanied by increased urinary frequency and nocturia (White and Iglesia, 2016). It could seriously affect the patients' quality of life and disturb their normal sociality, and it is so-called "social cancer." The global prevalence of OAB was about 9–43% in women and 7–27% in men (Milsom et al., 2014; Przydacz et al., 2020). Clinical investigation showed that OAB gradually increased with ageing, and the overall prevalence rate of people over 40 years old in China was 11.3% (Chen et al., 2015; Zhu et al., 2015). The pathogenesis of OAB is generally believed to be the result of many factors. At present, one of the main pathogenesis theories of OAB is myogenic, which includes an abnormal excitation of bladder smooth muscle (Andersson et al., 2015).

Selective muscarinic receptor-3 (M3) inhibitors (e.g., solifenacin and darifenacin) are the first-line drugs for treating OAB in clinics (Zinner et al., 2006). However, side effects such as dry mouth and constipation become serious after their long-term use (Yang et al., 2021). The M3 receptor is located in the bladder mainly for controlling detrusor contraction, which is activated by urothelium-released acetylcholine. Thus, drugs in urine possibly act on urothelium for OAB treatment (Ito et al., 2016). Bladder infusion refers to injecting drugs directly into the bladder through a catheter to maximize their local effects. Intravesical administration of oxybutynin hydrochloride, an anti-muscarinic drug, is a potential second-line treatment for patients that cannot tolerate oral anticholinergic drugs (Shen et al., 2022). However, its intravesical delivery still needs a frequent and cumbersome process in clinics. Therefore, it is urgent to develop an alternative treatment with low side effects for treating OAB.

As a common functional food and well-tolerated medicinal herb, Puerariae Lobatae Radix (named Gegen in Chinese) has been used for medicinal purposes and daily soup for hundreds of years in China and other regions of East Asia. Gegen is honored as "longevity powder" or "Asian ginseng" due to its high nutritional values and high safety (Zhang et al., 2020). The major components in Gegen water extract are isoflavone glycosides such as puerarin (daidzein-8-C-glucoside) and its glycosides, daidzin (daidzein-7-O-glucoside), and genistin (genistein-7-O-glucoside), and the contents of liposoluble aglycones like daidzein were low due to water extraction (Figure 1) (Zhang H. et al., 2019). Gegen and its major component puerarin have been reported for their relaxation effect through different mechanisms on the basilar artery (Prasain et al., 2004), pulmonary arterial smooth muscle (Zhang X. et al., 2019), and microvessels (Deng et al., 2012). In the previous study, the *ex vivo* analysis of detrusor functions showed that after 3-week oral administration, Gegen water extract at 300 mg/kg, a clinical equivalent dose, decreased detrusor tonic contraction and phasic frequency stimulated by muscarinic receptor agonist carbachol; meanwhile, it was also able to reduce tonic contraction caused by electric field stimulation (Zhou et al., 2016). These results indicated that Gegen water extract could improve detrusor overactivity through anti-muscarinic mechanisms. However, it was still unknown which compounds were responsible for this inhibition on muscarinic receptor.

Pharmacokinetics and metabolism of major compounds in Gegen water extract have been reported. After oral administration of Gegen water extract containing low content of aglycones (Puerarin: daidzin: daidzein = 6.42:1:0.14, w/w/w ratio), it was reported that plasma AUCs of puerarin and daidzein were 15.1 μg·h/mL and 4·4 μg·h/mL, respectively, showing that daidzein was its major metabolites in plasma (Wei et al., 2020). The contents of chemicals in the urine after sub-acute treatment of Gegen water extract were still unknown, although there was a report for its urine metabolite profile. Similar to intravesical oxybutynin, pro-drugs and metabolites of Gegen water extract in the urine probably acted on M3 receptors in the bladder wall if their concentrations can meet the threshold of their inhibitory effects. Hence, our study aimed to identify the pharmacological compounds from Gegen water extract that were responsible for the inhibition of muscarinic receptor-3 against OAB.

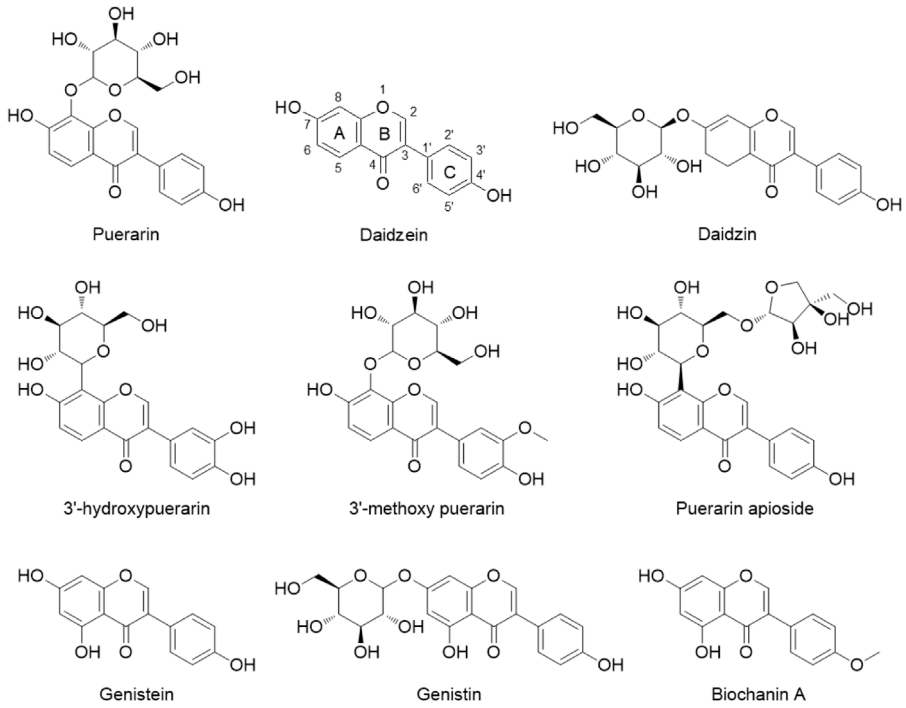

FIGURE 1
Structures of the major components in Gegen water extract.

2 Methods and materials

2.1 Chemicals and materials

Commercially obtained standards (purity >98%; HPLC grade) of puerarin, 3′-hydroxypuerarin, 3′-methoxy puerarin, puerarin apioside, genistin, daidzein, and genistein were purchased from Chengdu Chroma Co. (Chengdu, China). Carbachol, SYPRO Orange protein stain (5000x), and other unspecified chemicals were purchased from Sigma-Aldrich Co. LLC (St. Louis, MO, United States). Darifenacin hydrobromide was provided by Amandas (Shanghai, China). Full-length recombinant human M3 muscarinic acetylcholine receptor membrane preparation was provided by Millipore Co. (Merck KGaA, Darmstadt, Germany). The composition used for preparing Krebs' solution was as follows: NaCl, 119 mM; KCl, 4.6 mM; $MgCl_2$, 1.2 mM; NaH_2PO_4, 1.2 mM; $NaHCO_3$, 15 mM; $CaCl_2$, 1.5 mM; and D-glucose, 11 mM.

2.2 Herbal extraction

The dried root of Pueraria lobata (Willd.) Ohwi (harvested in Henan Province; Lot No. 17072102) was purchased from Beijing Lvye Pharmaceutical Co (Beijing, China). According to Chinese Pharmacopoeia v.2015, the supplier chemically authenticated the raw herb with reference herb and chemical marker puerarin using thin-layer chromatography, showing its good quality as required. The raw materials (400 g) were extracted by boiling with water (4 L) for an hour and repeated once. After filtering, the supernatant was collected and subjected to freeze-drying for the dried extract, which was stored in the desiccator before use.

2.3 Chemical profile of Gegen water extract

The chemical composition of Gegen water extract was analyzed via the Agilent 1100 Infinity HPLC-UV system (Santa Clara, CA, United States) after the dried powder was dissolved in water and filtered using a 0.45-μm filter according to our previous study (Zhou et al., 2016). The content of each compound in Gegen water extract was listed as follows (mean ± SEM): puerarin, 221.3 ± 8.34 μg/mg; daidzein, 8.07 ± 0.01 μg/mg; 3′-methoxypuerarin, 39.59 ± 0.81 μg/mg; 3′-hydroxypuerarin, 72.98 ± 3.10 μg/mg; puerarin apioside, 64.29 ± 2.78 μg/mg; and daidzin, 41.03 ± 1.32 μg/mg (Supplementary Figures S1A and S1B).

2.4 Animals

The nine-week-old male spontaneously hypertensive rats (SHRs) were provided by Beijing Charles River Laboratory

Animal Technology Co., Ltd. To lower the estrogen effect of Gegen isoflavones, male rats were used in this study. All experiments were approved by the Animal Ethics Committee of Capital Medical University (Approved Ethics Number AEEI-2018-098). Animals got free access to soybean-free chow (Beijing Ke-Ao-Xie-Li Co., China) and water for 3 weeks during drug treatment.

2.5 Carbachol-induced bladder strip contraction for *ex vivo* activity screening

SHRs were sacrificed with carbon dioxide, and the whole bladder was immediately isolated to prepare detrusor strips in Krebs' solution. Then, the strips were placed in a PanLab organ bath (Harvard Apparatus, Holliston, Massachusetts, United States) full of bubbling Krebs' solution at 37°C. After stimulation with high-potassium solution, the strips were washed with Krebs' solution three times. When the strips were incubated in Krebs' solution until the tension was set at about 1.5 g, 0.1% DMSO was added for a 10-min incubation as a control, and then the muscle strip was stimulated to shrink by adding muscarinic agonist carbachol (10 μM), which is used for determinization of M3 receptor function in the bladder strip (Liang and Leung, 2012). Between two stimulations, the strips were washed out and balanced for 15 min. The contraction force of the bladder strip was recorded. After the experiment, detrusor strips were collected, dried, and weighed for data normalization. Data were recorded and analyzed using LabChart software (version 8.0).

2.6 Bioassay-guided fractionation

Bioassay-guided fractionation was performed by using preparative HPLC for fast isolation of fractions and carbachol-induced bladder strip contraction for *ex vivo* activity screening. Briefly, 10 g of Gegen water extract was totally dissolved in 10 ml of double distilled water and then mixed with 190 ml of ethanol. The mixture was put on the magnetic agitator for stirring and performed ultrasonication for 30 min to precipitate the fiber and protein, etc. After being filtered through a 0.45-μm filter membrane, the purified filtrate was transferred into a 250-ml flask. The liquid was drained using a rotary evaporator at 60°C and a rotating speed of 110 rpm under vacuum, and the dried samples were collected. The dried extract was totally dissolved in methanol (5 ml) and filtered through a 0.45-μm filter membrane into the sample vial for injection to the Agilent 1260 preparative HPLC. An Agilent Zorbax Eclipse XDB-C18 preparative column (21.2 × 150 mm, 5 μm) was used, and the flow rate was set at 20 ml/min. The fractionation was performed through two different mobile phases. The mobile phase for the first fractionation consisted of solution A (distilled water) and solution B (acetonitrile) with the following gradient: 10–12.5% B from 0 to 10 min; 12.5–15% B from 10 to 15 min; 15–60% B from 15 to 20 min; 60–90% B from 20 to 25 min; and 90% B from 25 min to 30 min. The mobile phase for the second fractionation consisted of solution A (distilled water) and solution B (acetonitrile) with the following gradient: 10–30% B from 0 to 10 min; 30% B from 10 to 15 min; 30–60% B from 15 to 20 min; and 90% B from 20 min to 30 min.

The relevant components were separated and enriched according to their chemical profiles in HPLC chromatograms using the Agilent 1100 HPLC system. The HPLC mobile phase consisted of solution A (0.1% acetic acid) and solution B (acetonitrile) with the following gradient: 10–12.5% B from 0 to 20 min; 12.5–15% B from 20 to 30 min; 15–60% B from 30 to 40 min; and 60–90% B from 40 min to 45 min. The HPLC elution was performed using an Alltima HPLC C18 column (250 mm × 4.6 mm, 5 μm) guarded using a guard column with the same stationary phase. The column was maintained at room temperature, and the flow rate was set at 1 ml/min. The UV absorbance was detected at 254 nm, and the injection volume was 10 μl. The fractions with similar HPLC-UV profiles were combined and transferred into the 250-ml flask for rotary evaporation to collect dried fractions using the same temperature and speed as mentioned previously.

Detrusor strips were isolated from SHRs and placed in the organ bath as mentioned previously, and then inhibitory activities of different fractions at 100 μg/ml were tested under carbachol (10 μM)-stimulated detrusor contraction. The chemical profiles of potent fractions were analyzed by HPLC-UV at 254 nm with authentic compounds. After confirming potent compounds in each fraction, the concentration-dependent inhibitory effect of each potent compound (6.25-50 or 100 μg/ml in 0.1% DMSO-Krebs' solution) against carbachol (10 μM)-induced detrusor contraction was performed. Darifenacin (12.5–200 ng/ml) served as a positive control.

2.7 Determination of urine metabolites

When the last dose of Gegen water extract (300 mg/kg) in a 3-week treatment was given to SHRs, conscious rats were put into the metabolic cages with free access to water. Urine samples were collected into ice-cold 15-ml Falcon tubes every 2 h and up to a total of 8 h, and the tubes were cooled by ice to prevent bacteria proliferation and water evaporation during collection. The urine of each rat was first centrifuged at 13,000 rpm at 4°C for 10 min, and the supernatant was collected. Then, 50 μl of urine and 150 μl of methanol were added into the centrifuge tube for fully precipitating protein and then centrifuged at 13,000 rpm and 4°C for 10 min to collect the supernatant for sample analysis via UPLC-MS/MS.

Urine metabolites were analyzed by ultra-performance liquid chromatography (UPLC, Waters) coupled with a Xevo-TQS mass spectrometer (Waters) using the Acquity UPLC HSS T3 column (2.1 mm × 150 mm, 1.8 μm). The mobile phase flow rate was 0.4 ml/min and consisted of 0.1% formic acid in water (A) and acetonitrile (B). The gradient profile was set as follows: 10–40% B from 0 to 11 min; and 40–80% B from 11 to 15 min. The parameters for mass spectrometry were as follows: capillary, 2.5 kV for negative mode; sampling cone, 34 V; source offset, 80 V; cone gas flow, 150 L/h; desolvation gas flow, 650 L/h; and desolvation temperature, 350°C. Samples were kept at 4°C in the sample manager, and the column was maintained at 40°C. Extracted ion chromatograms were used to quantify puerarin (m/z 414.94→266.9), daidzein (m/z 252.96→90.91), genistein (m/z 268.96→132.93), and biochanin A (m/z 282.98→267.91) in the ESI negative-ion mode. According to the peak area and respective concentrations, the linear ranges of puerarin, daidzein, genistein, and biochanin A were 0.78–50 μg/ml, 0.78-50 μg/ml, 0.16–10 μg/ml, and 6.25–400 ng/ml, respectively (R^2 > 0.99). The precision and accuracy of the quantitation were satisfied according to FDA Bioanalytical Method Validation Guidance for Industry. Total ion chromatograms including retention times and MRM masses are shown in Supplementary Figure S2.

2.8 Thermal shift assay for the potential binding to M3 receptor

A thermal shift assay was performed to measure the binding of ligands to a recombinant human M3 receptor as modified from the previous study (Huynh and Partch, 2015). Briefly, after optimization of protein and dye concentrations, the M3 receptor protein (0.025 mg/ml) was incubated with different concentrations of tested compounds (0–100 μg/ml in 1% DMSO) in an 18 μl volume of ice-cold PBS for 2 h. Then, SYPRO Orange protein stain (2 μl; 8x as the final concentration diluted from original 5000x with PBS) was added, and the melt curve was detected using the Applied Biosystems QuantStudio5 real-time PCR system under the following conditions: ramp speed, standard; excitation wavelength at 470 nm (Reporter: FAM), and emission wavelength at 586 nm (Quencher: TAMRA) with no passive reference; an initial 2-min hold at 25°C (ramp rate, 1.6°C/s), ramping up in increments of 0.05°C/s to a final temperature of 99°C. Melt temperatures (*T*m) were calculated using Protein Thermal Shift software v.1.4 (Applied Biosystems, Thermo, United States). The change in melt temperature (Δ*T*m) was equal to the *T*m of control (1% DMSO) subtracted from the *T*m of the tested compound. Δ*T*m higher than 2°C was considered a positive interaction between the ligand and receptor protein (Huynh and Partch, 2015).

2.9 Molecular docking analysis for molecular modelling

To better understand the binding affinity of chemicals to the M3 receptor and comprehensively explain the structure–activity relationship of these isoflavones, molecular docking was performed for modelling. AutoDock Vina v.1.0.2 software was used for the molecular docking analysis, and the software parameters were set by default (Trott and Olson, 2010). The protein crystal structure of the M3 receptor was selected from the Protein Data Bank. The molecular docking conformation was further optimized by selecting the binding mode of the compound to the M3 receptor (PDB ID 5ZHP) with the lowest binding free energy (Liu et al., 2018). The crystal structure of the M3 receptor was used to conduct virtual docking of the aforementioned compounds, and the potential active chemical components were determined by comparison with the positive control (crystal ligand 9EC). Simulation results were output and illustrated by LigPlot + v.2.2 (http://www.ebi.ac.uk/thornton-srv/software/LIGPLOT/) (Laskowski and Swindells, 2011) and PyMOL Molecular Graphics System (da Silva Giotto et al., 1998) v.1.3 (Schrödinger, LLC, New York City, United States), respectively.

2.10 Data analysis

Data were represented as mean ± standard error of mean (SEM). A non-linear regression analysis was used to calculate the IC_{50} value by using Prism version 5.0 (GraphPad Software, CA, United States). Data were analyzed by one-tailed student *t*-test. When the *p*-value was less than 0.05, the difference was considered statistically significant.

3 Results and discussion

3.1 Bioassay-guided fractionation

To confirm the potent M3 receptor inhibitors in Gegen water extract, bioassay-guided fractionation was performed by using preparative HPLC and *ex vivo* detrusor contraction assay. The schematic diagram of fractionation is shown in Figure 2. For the first fractionation by the preparative HPLC, 30 fractions were attained from the elution at each minute and combined into 8 fractions according to their similar HPLC-UV chromatograms. Then, these 8 fractions were dried by rotary evaporation as mentioned previously and subjected to *ex vivo* pharmacological tests, respectively (Supplementary Figures S1C and S1D).

Fraction F1-5 (combined tubes 9–12 of first fractionation) with an inhibition rate of 14% contained puerarin, 3′-methoxypuerarin, and puerarin apioside, which were identified by authentic standards.

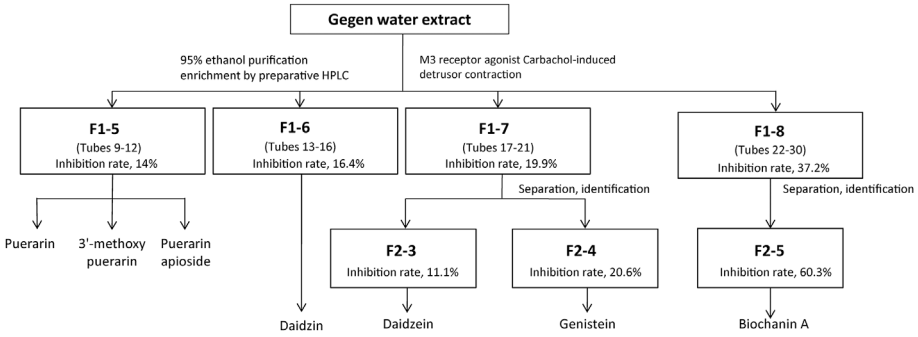

FIGURE 2
Schematic diagram indicates the fast isolation of active fractions from Gegen water extract using bioassay-guided fractionation with preparative HPLC. Active fractions were selected for further fractionation.

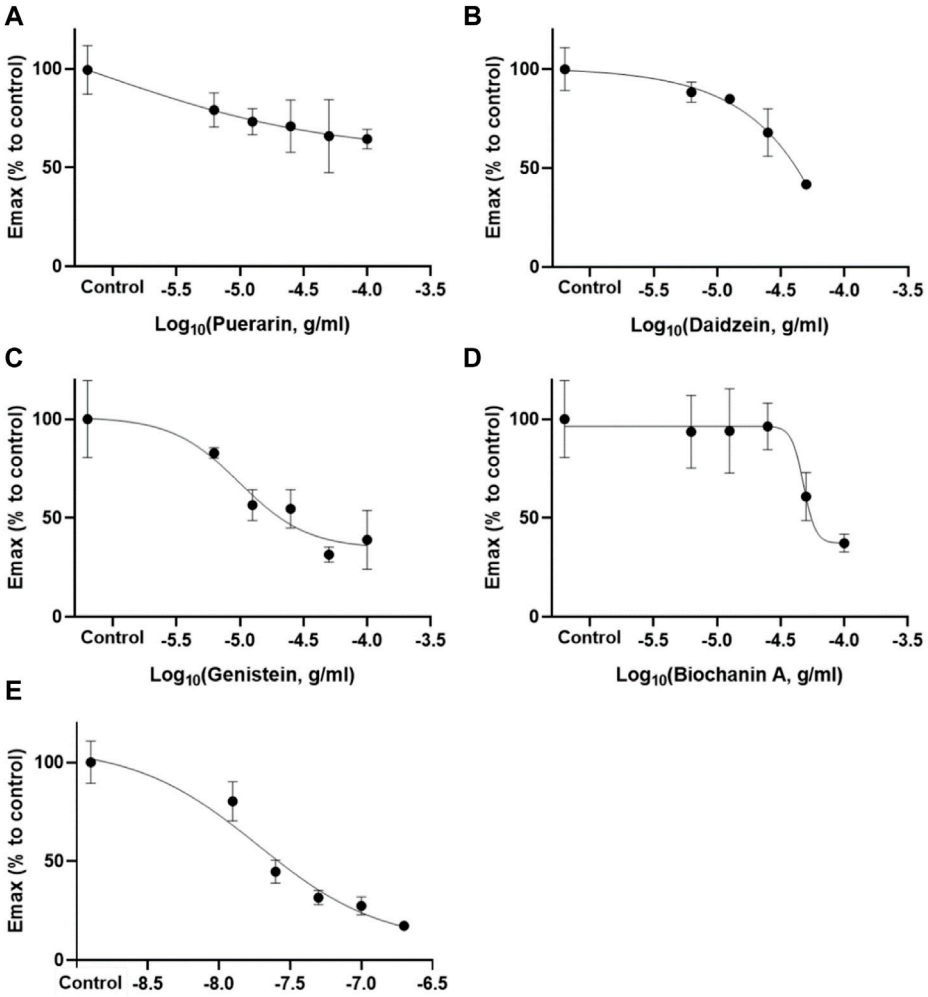

FIGURE 3
Inhibitory effects of puerarin **(A)**, daidzein **(B)**, genistein **(C)**, and biochanin A **(D)** at different concentrations (6.25–50 or 100 μg/ml) against carbachol (10 μM)-induced detrusor contraction (Mean ± SEM; n = 3). Darifenacin **(D)** (12.5–200 ng/ml) served as the positive control.

TABLE 1 Inhibition values of active compounds isolated from Gegen water extract on carbachol-induced detrusor contraction (Mean ± SEM, n = 3).

Compound	IC_{50} value (μg/ml)	IC_{10} value (μg/ml)
Daidzein	40.27 ± 0.46	8.15 ± 1.85
Puerarin	ND	2.90 ± 2.11
Genistein	18.57 ± 11.20	5.05 ± 0.58
Biochanin A	57.07 ± 12.47	34.94 ± 6.75
Darifenacin[a]	0.0293 ± 0.0047	0.0076 ± 0.0013

[a]positive control. ND: not determined.

Fraction F1-6 (combined tubes 13–16 of first fractionation) was identified as a daidzin-rich fraction with an inhibition rate of 16.4%. According to the composition of the mobile phase, Fraction F1-7 (combined tubes 17–21 of first fractionation) was separated into F2-3 (tube 4 of second fractionation) and F2-4 (tube 5 of second fractionation), which were identified as a daidzein-rich fraction (inhibition rate: 11.1%) and a genistein-rich fraction (inhibition rate: 20.6%), respectively (Supplementary Figures S1E and S1F).

Fraction F2-5 (combined tubes 6–30 of second fractionation) significantly inhibited carbachol-induced detrusor contraction, which suggested that F2-5 contained active substances with an inhibition rate of 60.3%. According to the retention time of authentic standard in the HPLC-UV chromatograms, biochanin A was one of the compounds in Fraction F2-5 (Supplementary Figure S1G).

3.2 Inhibition activity of potent active compounds

According to the retention times of the pure compounds, the major components in each active fraction were identified. Seven compounds were identified, and their inhibition potency on carbachol-induced detrusor contraction was ranked in descending order according to their IC values as follows: genistein (IC_{50} = 18.57 ± 11.20 μg/ml) > daidzein (IC_{50} = 40.27 ± 0.46 μg/ml) > biochanin A (IC_{50} = 57.07 ± 12.47 μg/ml) >> puerarin (IC_{10} = 2.90 ± 2.11 μg/ml) (Figure 3 and Table 1). 3′-Hydroxypuerarin (remaining activity at 100 μg/ml: 82.3 ± 1.8%), 3′-methoxypuerarin (remaining activity at 100 μg/ml: 80.1 ± 3.4%), and puerarin apioside (remaining activity at 100 μg/ml: 89.3 ± 9.2%) showed weak inhibition. Compared with the high inhibition rate of the positive control (darifenacin), biochanin A, daidzein, and genistein showed strong inhibitory effects. It has been reported that genistein was a potent inhibitor against carbachol stimulation in the previous study (Di Salvo et al., 1993), which is consistent with our current results. This is the first time to report the inhibitory activity of biochanin A on M3 receptor.

3.3 Quantitation of major metabolites in urine

Muscarinic receptor 3 exists in bladder urothelium and sub-urothelial myofibroblasts, suggesting that active chemicals in urine could act on the M3 receptor in urothelial sensory function. The main urine metabolites after oral administration of Gegen water extract were daidzein and other isoflavone glycosides, and the highest concentration of each compound at 4 h was determined as follows (Mean ± SEM): puerarin, 10.280 ± 2.475 μg/ml; daidzein, 15.877 ± 9.303 μg/ml; genistein, 1.410 ± 1.003 μg/ml; and biochanin A, 0.085 ± 0.057 μg/ml (Table 2 and Figure 4). Our results were consistent with the previous study, which showed that daidzein was one of the major urine components of Gegen water extract in a clinical trial (Prasain et al., 2004; Jung et al., 2014; Shang et al., 2017). The content of daidzein in urine reached its IC_{10} value; thus, daidzein in urine could have a direct effect on reducing detrusor contraction with 15% inhibition at 12.5 μg/ml on M3 receptor *ex vivo* ($p < 0.05$). In addition, Gegen water extract did not alter the expression of the M3 receptor as detected by immunochemistry (Supplementary Figure S3).

The literature showed that the bioavailability of glycoside compounds is low, but isoflavone glycosides such as puerarin (daidzein-8-C-glucoside) and daidzin (daidzein 7-O-glucoside) can be biotransformed into aglycones including daidzein by gut microbiota (Nakamura et al., 2020). Since aglycones were produced from *in vivo* metabolization and considering the decrease of puerarin and its glycosides while daidzein's amount increased, the results indicated that puerarin and its glycosides probably acted as pro-drugs for M3 receptor inhibition. Although biochanin A and genistein were potent inhibitors for carbachol-induced detrusor contraction among these isoflavones, their amounts in Gegen water extract and urine were too low (less than 0.1%). Thus, for the *in vivo* inhibition against the M3 receptor, daidzein was the major active form for OAB, while puerarin, its glycosides, and daidzin were the pro-drugs.

Isoflavones such as daidzein have been reported in several studies through different mechanisms such as hormone replacement (Waetjen et al., 2013), anti-oxidant, and anti-inflammatory (Wu et al., 2018). Thus, our study provided more information on isoflavone-rich herbs in treating OAB with different etiology characteristics.

3.4 Thermal shift assay

As suggested by the supplier, the recombinant human M3 receptor protein can bind potent antagonists and be used for inhibitor screening. This membrane fraction contains BSA and glycerin; thus, daidzein was first checked for its possible binding

TABLE 2 Contents of major urine metabolites after oral administration of Gegen water extract in SHR detected by LC-MS/MS (Mean ± SEM; n = 8).

Compounds	Content (μg/ml)			
	2 h	4 h	6 h	8 h
Puerarin	6.378 ± 0.897	10.280 ± 2.475	3.309 ± 0.325	2.207 ± 0.164
Daidzein	4.403 ± 1.002	15.877 ± 9.303	8.128 ± 2.664	14.425 ± 5.141
Genistein	0.517 ± 0.138	1.410 ± 1.003	0.327 ± 0.098	0.342 ± 0.035
Biochanin A	0.026 ± 0.007	0.085 ± 0.057	0.030 ± 0.014	0.028 ± 0.005

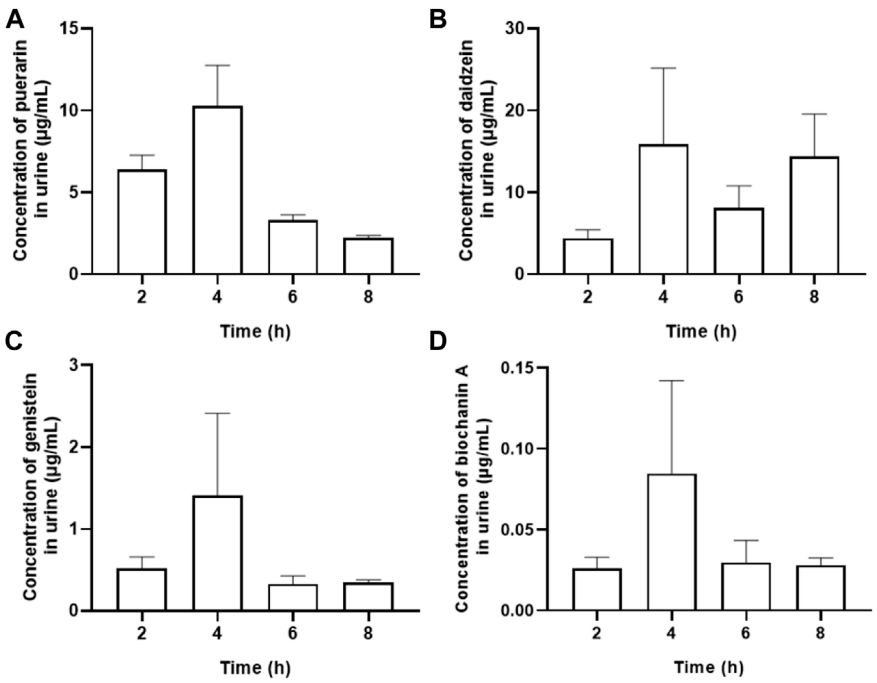

FIGURE 4
Contents of major urine metabolites including peurarin **(A)**, daidzein **(B)**, genistein **(C)** and biochanin A **(D)** after oral administration of Gegen water extract in SHR as detected by LC-MS/MS (Mean ± SEM; n = 8).

to BSA. As a result, Δ*T*m of daidzein at 100 μg/ml was about 0.58°C in PBS solution containing BSA and glycerin at the same concentrations as the recombinant human M3 receptor protein. Furthermore, as shown in Figure 5A, daidzein at 100 μg/ml shifted the melt curve and increased the *T*m value of the human M3 receptor protein from 64.17 ± 0.37°C to 66.29 ± 0.38°C ($p < 0.01$). Since Δ*T*m was 2.12°C, daidzein was positively bound to the human M3 receptor protein as suggested (Huynh and Partch, 2015). In Figure 5B, daidzein concentration-dependently increased the *T*m values with an EC_{50} of 15.8 μg/ml at 65.3°C. *In vitro* thermal shift assay with the M3 receptor protein showed that daidzein was much more potent than the *ex vivo* detrusor contraction. At the same time, the *T*m value of the human M3 receptor protein interacted with puerarin at 100 μg/ml was 64.92 ± 0.03°C, showing its very weak binding to the M3 receptor protein.

3.5 Molecular docking analysis

Molecular docking results show that biochanin A, daidzein, genistein, 3′-hydroxypuerarin, 3′-methoxypuerarin, puerarin, daidzin, genistin, and puerarin apioside bound to the M3 receptor crystal structure (PDB ID 5ZHP) with different affinities (Table 3). However, only biochanin A, daidzein, and genistein showed potent binding free energy to the M3 receptor with a binding free energy lower than −7 kcal/mol (a basic

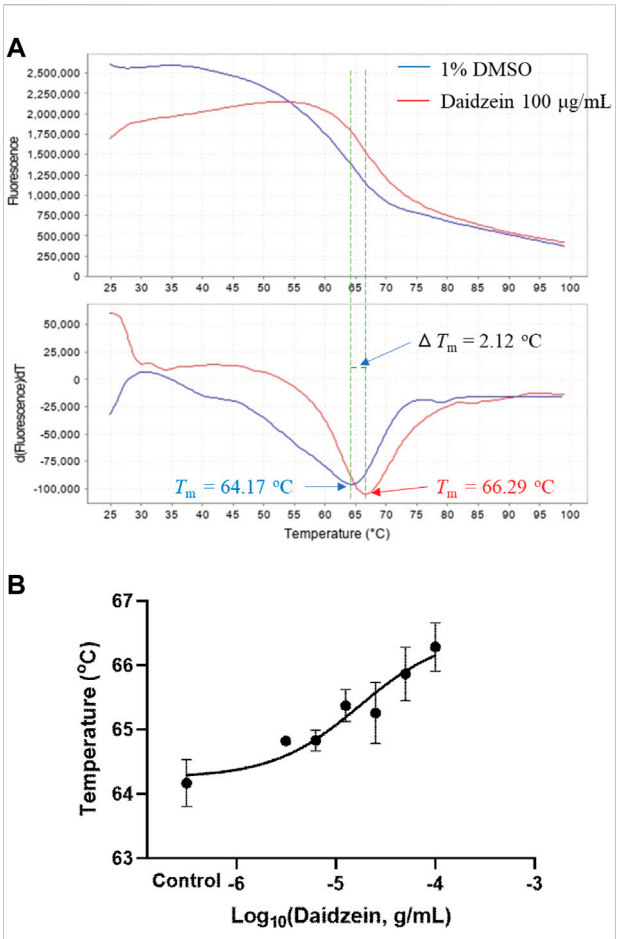

FIGURE 5
Ligand screening with the recombinant human M3 receptor protein as detected by thermal shift assay. **(A)** Representative fluorescence melt curve (upper) and derivative melt curve (lower) containing mean melt temperatures (*Tm*) of the M3 receptor protein with or without daidzein (100 μg/ml), showing that binding of daidzein increased the thermal stability of the M3 receptor protein with Δ*Tm* > 2 °C. **(B)** Daidzein (3.125–100 μg/ml) concentration-dependently increased the melt temperatures of the M3 receptor protein. Data are presented as Mean ± SEM (n = 3). DMSO (1%) served as the vehicle control.

binding free energy for the positive ligand–receptor interaction), which was consistent with the *ex vivo* results.

For docking simulation, the 3D conformation of the newly docked 9EC was highly consistent with the 3D conformation of the original co-crystal compound, indicating the high accuracy of this molecular docking (Figure 6A). Two-dimensional conformation analysis revealed that crystallized ligand 9EC strongly interacted with Asn507 through H-bonding at a distance of 2.87 Å and hydrophobic interactions with TRP199, PHE239, TYR506, ASP147, and TYR148, etc., and re-docked 9EC showed similar interactions (Figure 6B). Biochanin A, daidzein, and genistein have strong interactions with amino acid residues in the M3 receptor. For daidzein, its hydroxyl group in Ring C

TABLE 3 Binding affinities (logarithm) of major components in Gegen water extract to the binding pocket of M3 receptor (PDB ID 5ZHP chain B).

Ligand	Binding free energy (kcal/mol)
9EC[a]	−11.5
Biochanin A	−9.6
Daidzein	−9.3
Genistein	−9.1
3′-Hydroxypuerarin	−5.7
3′-Methoxypuerarin	−5.0
Puerarin	−4.7
Daidzin	−2.8
Genistin	−2.8
Puerarin apioside	1.5

[a]M3 receptor (PDB ID 5ZHP) co-crystallized ligand 9EC: (1R,2R,4S,5S,7s)-7-({[4-fluoro-2-(thiophen-2-yl)phenyl]carbamoyl}oxy)-9,9-dimethyl-3-oxa-9-azatricyclo [3.3.1.0~2,4~]nonan-9-ium.

interacted with Thr231 and Ala235 through H-bonding (Figure 6C). For genistein, the ether group in Ring B interacted with TYR506 through H-bonding (Figure 6D). For biochanin A, hydroxyl groups at C-5 and C-7 in Ring A interacted with ALA235, THR231, and TYR506 through H-bonding, respectively, as did the ketone group in Ring B, which interacted with TYR148 (Figure 6E).

3.6 Structure–activity relationship

According to the inhibitory activities (IC values) of tested compounds on *ex vivo* carbachol-induced detrusor contraction as shown in Table 3, structure–activity relationships of isoflavones and their glycosides tested in the current study were analyzed and summarized as follows: first of all, puerarin (daidzein-8-C-glucoside) and its derivatives have lower inhibitory activities among these compounds. Substitution with a methoxyl group or hydroxyl group at C-3′ in Ring C could reduce M3 receptor inhibition, as well as substitution by glucose or apioside in Ring A. This is probably due to the reduced binding affinity to the active pocket of the M3 receptor. For instance, 3′-methoxypuerarin (inhibition rate at 100 μg/ml: 19.89 ± 3.38%) containing a methoxyl group and 3′-hydroxypuerarin (inhibition rate at 100 μg/ml: 17.75 ± 1.75%) at C-3′ showed weaker inhibitory activity than puerarin (inhibition rate at 100 μg/ml: 33.83 ± 3.05%). Genistin (Genistein-7-O-glucoside) (IC_{50} > 100 μg/ml) containing glucose and puerarin apioside containing apioside (inhibition rate at 100 μg/ml: 10.7 ± 9.24%) in Ring A showed weak inhibition on the M3 receptor. Second, when compared to daidzein (IC_{50}: 40.27 ± 0.46 μg/ml), puerarin (inhibition rate at 100 μg/ml: 33.83 ± 3.05%)

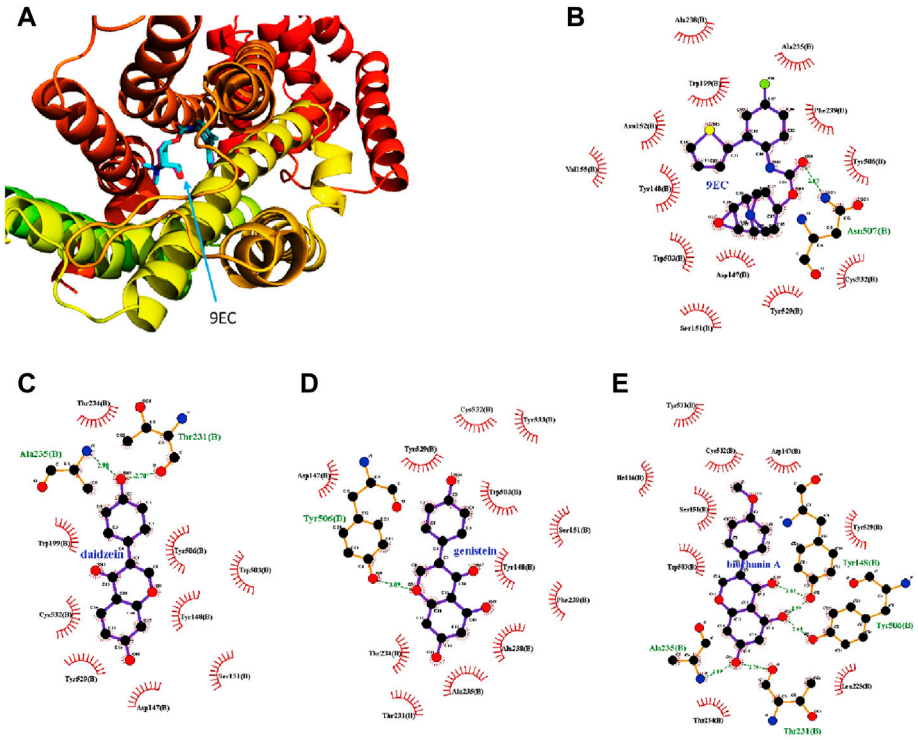

FIGURE 6
Molecular docking analysis indicates the best binding positions of the ligands with the lowest binding free energy in the ligand binding pocket of the M3 receptor (PDB ID 5ZHP chain B). The three-dimensional diagram illustrates the interactions of redocked 9EC (purple sticks) and the crystallized one (blue sticks) with the M3 receptor with the same binding position **(A)** which shows the high accuracy of the current docking method. The two-dimensional diagrams show the interactions of 9EC **(B)**, daidzein **(C)**, genistein **(D)**, and biochanin A **(E)** with the amino acid residues in the binding pocket of the M3 receptor. The spoked arcs show amino acid residues providing nonbonded interactions with the ligand. Green arrows with respective distances represent H-bonding between ligands and specific amino acid residues.

with substitution by glucuronic acid at C-5 in Ring A showed a weaker inhibitory effect on the M3 receptor; without substitution at C-8 in Ring A, daidzein (IC_{50}: 40.27 ± 0.46 μg/ml) showed a stronger inhibitory activity. Compounds substituted with a hydroxyl group at Ring A showed stronger M3 receptor inhibition, which is probably due to the interaction with amino acid residues in the binding pocket of the M3 receptor. For example, the substitution of a hydroxyl group at the C-5 site in Ring A increased the inhibitory effect. Genistein (5-hydroxyl daidzein) (IC_{50}: 18.57 ± 11.20 μg/ml) showed the strongest inhibitory effects among these compounds, whose substitution with the hydroxyl group at the C-5 site provided stronger binding to the M3 receptor when the ether group in Ring B interacted with TYR506 through a hydrogen bond. However, the substitution of a methoxyl group instead of a hydroxyl group at the C-4′ site in Ring C reduced the inhibitory activity. Biochanin A (genistein 4′-methyl ether) (IC_{50}: 57.07 ± 12.47 μg/ml) with a methoxyl group showed a weaker inhibitory activity than genistein.

4 Conclusion

As pro-drugs, puerarin, its derivatives, and daidzin were the major chemical components of Gegen water extract, and daidzein was their major *in vivo* active form for M3 receptor inhibition against OAB at the threshold concentration in urine. It could probably act on the bladder wall since it reached an effective concentration in urine. Biochanin A and genistein were much more potent, but their contents were too low for the pharmacological effect of Gegen water extract. Due to the threshold effects of daidzein, other molecular mechanisms should be revealed to fully understand the underlying mechanisms of Gegen water extract against OAB in the future.

Data availability statement

The original contributions presented in the study are included in the article/Supplementary Material; further inquiries can be directed to the corresponding author.

Ethics statement

The animal study was reviewed and approved by the Animal Ethics Committee of Capital Medical University.

Author contributions

YQ: methodology, writing—original draft, formal analysis, and visualization. LB: methodology. YM: methodology. PX: methodology. MC: validation. YW: methodology. XL: supervision. MX: supervision. XZ: conceptualization, methodology, writing—review and editing, project administration, and funding acquisition.

Funding

This study was financially supported by the National Natural Science Foundation of China (No. 81703796).

Conflict of interest

The authors declare that the research was conducted in the absence of any commercial or financial relationships that could be construed as a potential conflict of interest.

Publisher's note

All claims expressed in this article are solely those of the authors and do not necessarily represent those of their affiliated organizations, or those of the publisher, the editors, and the reviewers. Any product that may be evaluated in this article, or claim that may be made by its manufacturer, is not guaranteed or endorsed by the publisher.

Supplementary material

The Supplementary Material for this article can be found online at: https://www.frontiersin.org/articles/10.3389/fphar.2022.924251/full#supplementary-material

References

Andersson, K. E., Nomiya, M., and Yamaguchi, O. (2015). Chronic pelvic ischemia: Contribution to the pathogenesis of lower urinary tract symptoms (luts): A new target for pharmacological treatment? *Low. Urin. Tract. Symptoms* 7, 1–8. doi:10.1111/luts.12084

Chen, Y., Yu, W., Yang, Y., Duan, J., Xiao, Y., Zhang, X., et al. (2015). Association between overactive bladder and peri-menopause syndrome: A cross-sectional study of female physicians in China. *Int. Urol. Nephrol.* 47, 743–749. doi:10.1007/s11255-015-0948-6

da Silva Giotto, M. T., Garratt, R. C., Oliva, G., Mascarenhas, Y. P., Giglio, J. R., Cintra, A. C., et al. (1998). Crystallographic and spectroscopic characterization of a molecular hinge: Conformational changes in bothropstoxin I, a dimeric lys49-phospholipase A2 homologue. *Proteins* 30, 442–454. doi:10.1002/(sici)1097-0134(19980301)30:4<442::aid-prot11>3.0.co;2-i

Deng, Y., Ng, E. S., Yeung, J. H., Kwan, Y. W., Lau, C. B., Koon, J. C., et al. (2012). Mechanisms of the cerebral vasodilator actions of isoflavonoids of Gegen on rat isolated basilar artery. *J. Ethnopharmacol.* 139, 294–304. doi:10.1016/j.jep.2011.11.021

Di Salvo, J., Steusloff, A., Semenchuk, L., Satoh, S., Kolquist, K., and Pfitzer, G. (1993). Tyrosine kinase inhibitors suppress agonist-induced contraction in smooth muscle. *Biochem. Biophys. Res. Commun.* 190, 968–974. doi:10.1006/bbrc.1993.1144

Huynh, K., and Partch, C. L. (2015). Analysis of protein stability and ligand interactions by thermal shift assay. *Curr. Protoc. Protein Sci.* 79, 28–29. doi:10.1002/0471140864.ps2809s79

Ito, Y., Kashiwabara, M., Yoshida, A., Hikiyama, E., Onoue, S., and Yamada, S. (2016). Muscarinic receptor binding in rat bladder urothelium and detrusor muscle by intravesical solifenacin. *Biol. Pharm. Bull.* 39, 1167–1171. doi:10.1248/bpb.b16-00194

Jung, H. R., Kim, S. J., Ham, S. H., Cho, J. H., Lee, Y. B., and Cho, H. Y. (2014). Simultaneous determination of puerarin and its active metabolite in human plasma by UPLC-MS/MS: Application to a pharmacokinetic study. *J. Chromatogr. B Anal. Technol. Biomed. Life Sci.* 971, 64–71. doi:10.1016/j.jchromb.2014.09.015

Laskowski, R. A., and Swindells, M. B. (2011). LigPlot+: Multiple ligand-protein interaction diagrams for drug discovery. *J. Chem. Inf. Model.* 51, 2778–2786. doi:10.1021/ci200227u

Liang, W., and Leung, P. C. (2012). Variations in carbachol- and ATP-induced contractions of the rat detrusor: Effects of gender, mucosa and contractile direction. *Int. Urol. Nephrol.* 44, 1641–1648. doi:10.1007/s11255-012-0287-9

Liu, H., Hofmann, J., Fish, I., Schaake, B., Eitel, K., Bartuschat, A., et al. (2018). Structure-guided development of selective M3 muscarinic acetylcholine receptor antagonists. *Proc. Natl. Acad. Sci. U. S. A.* 115, 12046–12050. doi:10.1073/pnas.1813988115

Milsom, I., Coyne, K. S., Nicholson, S., Kvasz, M., Chen, C. I., and Wein, A. J. (2014). Global prevalence and economic burden of urgency urinary incontinence: A systematic review. *Eur. Urol.* 65, 79–95. doi:10.1016/j.eururo.2013.08.031

Nakamura, K., Zhu, S., Komatsu, K., Hattori, M., and Iwashima, M. (2020). Deglycosylation of the isoflavone C-glucoside puerarin by a combination of two recombinant bacterial enzymes and 3-oxo-glucose. *Appl. Environ. Microbiol.* 86, e00607–e00620. doi:10.1128/AEM.00607-20

Prasain, J. K., Jones, K., Brissie, N., Moore, R., Wyss, J. M., and Barnes, S. (2004). Identification of puerarin and its metabolites in rats by liquid chromatography-tandem mass spectrometry. *J. Agric. Food Chem.* 52, 3708–3712. doi:10.1021/jf040037t

Przydacz, M., Golabek, T., Dudek, P., Lipinski, M., and Chlosta, P. (2020). Prevalence and bother of lower urinary tract symptoms and overactive bladder in Poland, an Eastern European Study. *Sci. Rep.* 10, 19819. doi:10.1038/s41598-020-76846-0

Shang, Z., Xin, Q., Zhao, W., Wang, Z., Li, Q., Zhang, J., et al. (2017). Rapid profiling and identification of puerarin metabolites in rat urine and plasma after oral administration by UHPLC-LTQ-Orbitrap mass spectrometer. *J. Chromatogr. B Anal. Technol. Biomed. Life Sci.* 1068-1069, 180–192. doi:10.1016/j.jchromb.2017.10.038

Shen, S. H., Jia, X., Peng, L., Zeng, X., Shen, H., and Luo, D. Y. (2022). Intravesical oxybutynin therapy for patients with neurogenic detrusor overactivity: A systematic review and meta-analysis. *Int. Urol. Nephrol.* 54, 737–747. doi:10.1007/s11255-022-03129-0

Trott, O., and Olson, A. J. (2010). AutoDock Vina: Improving the speed and accuracy of docking with a new scoring function, efficient optimization, and multithreading. *J. Comput. Chem.* 31, 455–461. doi:10.1002/jcc.21334

Waetjen, L. E., Leung, K., Crawford, S. L., Huang, M. H., Gold, E. B., Greendale, G. A., et al. (2013). Relationship between dietary phytoestrogens and development of urinary incontinence in midlife women. *Menopause* 20, 428–436. doi:10.1097/gme.0b013e3182703c9c

Wei, L., Zhu, P., Chen, X., Wang, Y., and Xu, Y. (2020). An ultra high performance liquid chromatography with tandem mass spectrometry method for simultaneous determination of thirteen components extracted from Radix Puerariae in rat plasma and tissues: Application to pharmacokinetic and tissue distribution study. *J. Sep. Sci.* 43, 418–437. doi:10.1002/jssc.201900824

White, N., and Iglesia, C. B. (2016). Overactive bladder. *Obstet. Gynecol. Clin. North Am.* 43, 59–68. doi:10.1016/j.ogc.2015.10.002

Wu, K. C., Chiang, B. J., Tsai, W. H., Chung, S. D., and Chien, C. T. (2018). I-Tiao-Gung extract through its active component daidzin improves cyclophosphamide-induced bladder dysfunction in rat model. *Neurourol. Urodyn.* 37, 2560–2570. doi:10.1002/nau.23815

Yang, N., Wu, Q., Xu, F., and Zhang, X. (2021). Comparisons of the therapeutic safety of seven oral antimuscarinic drugs in patients with overactive bladder: A network meta-analysis. *J. Int. Med. Res.* 49, 3000605211042994. doi:10.1177/03000605211042994

Zhang, G., Liu, J., Gao, M., Kong, W., Zhao, Q., Shi, L., et al. (2020). Tracing the edible and medicinal plant Pueraria Montana and its products in the marketplace yields subspecies level distinction using DNA barcoding and DNA metabarcoding. *Front. Pharmacol.* 11, 336. doi:10.3389/fphar.2020.00336

Zhang, H., Hu, X., Qiao, M., Li, Y., Cao, S., Ding, L., et al. (2019). Simultaneous determination of five isoflavones in rat plasma by LC-MS/MS: Comparative pharmacokinetic characteristics of Puerariae lobatae radix in normal and type 2 diabetic rats. *J. Sep. Sci.* 42, 2592–2601. doi:10.1002/jssc.201900341

Zhang, X., Liu, Q., Zhang, C., Sheng, J., Li, S., Li, W., et al. (2019). Puerarin prevents progression of experimental hypoxia-induced pulmonary hypertension via inhibition of autophagy. *J. Pharmacol. Sci.* 141, 97–105. doi:10.1016/j.jphs.2019.09.010

Zhou, X., Lam, W. P., Tang, H. C., Koon, C. M., Cheng, L., Lau, C. B., et al. (2016). Effects of Gegen (Puerariae lobatae Radix) water extract on improving detrusor overactivity in spontaneously hypertensive rats. *Phytomedicine* 23, 672–678. doi:10.1016/j.phymed.2016.03.002

Zhu, L., Cheng, X., Sun, J., Lv, S., Mei, S., Chen, X., et al. (2015). Association between menopausal symptoms and overactive bladder: A cross-sectional questionnaire survey in China. *PLoS One* 10, e0139599. doi:10.1371/journal.pone.0139599

Zinner, N., Susset, J., Gittelman, M., Arguinzoniz, M., Rekeda, L., and Haab, F. (2006). Efficacy, tolerability and safety of darifenacin, an M(3) selective receptor antagonist: An investigation of warning time in patients with OAB. *Int. J. Clin. Pract.* 60, 119–126. doi:10.1111/j.1368-5031.2005.00770.x

frontiers | Frontiers in Pharmacology

TYPE Original Research
PUBLISHED 04 October 2022
DOI 10.3389/fphar.2022.995641

OPEN ACCESS

EDITED BY
Bingyou Yang,
Heilongjiang University of Chinese Medicine, China

REVIEWED BY
Yun K. Tam,
Sinoveda Canada Inc., Canada
Wei Dong Chen,
Anhui University of Chinese Medicine, China
Yhiya Amen,
Mansoura University, Egypt

*CORRESPONDENCE
Feng Xu,
xufeng_pharm@163.com
Shao-Qing Cai,
sqcai@hsc.pku.edu.cn

SPECIALTY SECTION
This article was submitted to Ethnopharmacology, a section of the journal Frontiers in Pharmacology

RECEIVED 16 July 2022
ACCEPTED 29 August 2022
PUBLISHED 04 October 2022

CITATION
Zhang J, Lv Y, Zhang J, Shi W-J, Guo X-Y, Xu J-J, Wang P-P, Chen X-T, Xiang L-H, Xu F, Wang X and Cai S-Q (2022), Metabolism of Paeoniae Radix Rubra and its 14 constituents in mice. *Front. Pharmacol.* 13:995641. doi: 10.3389/fphar.2022.995641

Metabolism of Paeoniae Radix Rubra and its 14 constituents in mice

Jing Zhang, Yang Lv, Jing Zhang, Wen-Jin Shi, Xu-Yan Guo, Jing-Jing Xu, Peng-Pu Wang, Xue-Tai Chen, Lin-Han Xiang, Feng Xu*, Xuan Wang and Shao-Qing Cai*

State Key Laboratory of Natural and Biomimetic Drugs, School of Pharmaceutical Sciences, Peking University, Beijing, China

Objective: Paeoniae Radix Rubra (PRR) is a commonly used traditional Chinese medicine with the effects of clearing away heat, cooling the blood, and relieving blood stasis. To 1) elucidate the metabolites and metabolic pathways of PRR and its 14 main constituents in mice and 2) reveal the possible origins of the known effective forms of PRR and their isomers, the metabolism of PRR in mice was systematically studied for the first time.

Methods: PRR and its 14 constituents were administered to mice by gavage once a day for seven consecutive days, respectively. All urine and feces were collected during the 7 days of dosing, and blood was collected at 1 h after the last dose. Metabolites were detected and identified using high performance liquid chromatography with diode array detector and combined with electrospray ionization ion trap time-of-flight multistage mass spectrometry (HPLC-DAD-ESI-IT-TOF-MS^n).

Results: In total, 23, 16, 24, 17, 18, 30, 27, 17, 22, 17, 33, 3, 8, 24, and 31 metabolites of paeoniflorin, albiflorin, oxypaeoniflorin, benzoylpaeoniflorin, hydroxybenzoylpaeoniflorin, benzoyloxypaeoniflorin, galloylpaeoniflorin, lactiflorin, epicatechin gallate, catechin gallate, catechin, ellagic acid, 3,3′-di-*O*-methylellagic acid, methylgallate, and PRR were respectively identified in mice; after eliminating identical metabolites, a total of 195 metabolites remained, including 8, 11, 25, 17, 18, 30, 27, 17, 21, 17, 1, 2, 8, 20, and 20 newly identified metabolites, respectively. The metabolic reactions of PRR and its 14 main constituents in mice were primarily methylation, hydrogenation, hydrolysis, hydroxylation, glucuronidation, and sulfation.

Abbreviations: A, albiflorin; B, benzoylpaeoniflorin; BO, benzoyloxypaeoniflorin; BPCs, base peak chromatograms; C, catechin; CDL, curved desolvation line; CG, catechin gallate; CID, relative collision-induced dissociation; d, day; DEA, 3,3′-di-*O*-methylellagic acid; EA, ellagic acid; ECG, epicatechin gallate; EICs, extracted ion chromatograms; Err., error.; ESI, electrospray ionization; G, galloylpaeoniflorin; HPLC, high-performance liquid chromatography; HPLC-ESI-IT-TOF-MS^n, high performance liquid chromatography with diode array detector and combined with electrospray ionization ion trap time-of-flight multistage mass spectrometry; L, lactiflorin; Meas., measured; MG, methyl gallate; NLRP3, NOD-like receptor thermal protein domain associated protein 3; O, oxypaeoniflorin; OB, hydroxybenzoylpaeoniflorin; P, paeoniflorin; PRR. Paeoniae Radix Rubra; t_R, retention time.

Conclusion: We elucidated the metabolites and metabolic pathways of PRR and its 14 constituents (e.g., paeoniflorin, catechin, ellagic acid, and gallic acid) in mice and revealed the possible origins of the 10 known effective forms of PRR and their isomers. The findings are of great significance to studying the mechanism of action and quality control of PRR.

KEYWORDS

Paeoniae Radix Rubra, paeoniflorin, catechin, ellagic acid, methylgallate, *in vivo* metabolism

1 Introduction

The effective forms of traditional Chinese medicines can be the original constituents or the active metabolites produced *in vivo* (Xu et al., 2022). The metabolism of traditional Chinese medicines is the key link between their phytochemistry *in vitro* and their pharmacological activity *in vivo*. Therefore, studying the metabolism of traditional Chinese medicines is crucial to understanding the forms of the medicine that exist and are active *in vivo* along with the mechanisms of action of traditional Chinese medicines.

Paeoniae Radix Rubra (PRR), obtained from the dried roots of *Paeonia lactiflora* Pall. or *Paeonia veitchii* Lynch, is a commonly used traditional Chinese medicine with the effects of clearing away heat, cooling the blood, and relieving blood stasis (Zhao et al., 2021). PRR has many pharmacological effects, such as preventing liver fibrosis, curing jaundice, improving cholestasis in rats, relieving inflammation, and improving myocardial infarction, hypertrophy, and fibrosis (Tan et al., 2020).

The constituents of PRR have various structures, with the primary ones being monoterpene glycosides, tannins, flavonoids, and triterpenes (Yan et al., 2018). Monoterpene glycosides include paeoniflorin, albiflorin, oxypaeoniflorin, benzoylpaeoniflorin, hydroxybenzoylpaeoniflorin, benzoyloxypaeoniflorin, galloylpaeoniflorin, and lactiflorin. Tannins include ellagic acid and 3,3′-di-*O*-methylellagic acid. Catechins include catechin, catechin gallate, and epicatechin gallate. Gallic acids include methylgallate.

Among the 14 constituents mentioned above, 11 (all but hydroxybenzoylpaeoniflorin, benzoyloxypaeoniflorin, and lactiflorin) exhibit various biological activities. For example, paeoniflorin (the main active constituent of PRR) shows good anti-inflammatory, immunomodulatory, and anti-tumor effects (Zhao et al., 2021). Albiflorin has the function of soothing the liver and relieving depression (Zhao et al., 2018). Oxypaeoniflorin can prevent acute lung injury caused by lipopolysaccharides in mice (Fan et al., 2021). Benzoylpaeoniflorin exhibits anti-allergic activity, making it a potential candidate drug for the treatment of allergic diseases (Zhong et al., 2021). Galloylpaeoniflorin can relieve osteoporosis following oophorectomy (Liu et al., 2021b). Ellagic acid reduces the toxicity of diclofenac in rat hepatocytes by enhancing the activity of antioxidant enzymes such as catalase (Hatefi-Hesari et al., 2021). 3,3′-Di-*O*-methylellagic acid significantly reduces retinal vasodilation caused by high glucose levels in juvenile zebrafish (Lee et al., 2018). Methylgallate improves potassium oxazinate-induced kidney damage in mice with hyperuricemia nephropathy by inhibiting the NOD-like receptor thermal protein domain associated protein 3 (NLRP3) pathway, thereby producing a renal protective effect (Liu et al., 2021a). Catechin protects rat cardiomyocytes against hypoxic damage (Fang et al., 2018) and also exerts an anti-inflammatory effect (Syed Hussein et al., 2015). Both catechin gallate and epicatechin gallate have significant anti-inflammatory and anti-proliferative activities (Kurbitz et al., 2011). Catechin gallate inhibits catechol methylation in rat hepatocyte cytoplasm and hepatocyte cultures by inhibiting the activity of catechol oxymethyltransferase (Kadowaki et al., 2005).

In a previous study, we found that only four of the 21 forms of PRR that can effectively treat toxic heat and blood stasis were the original constituents; the other 17 were metabolites (Xu et al., 2022). The four original constituents were paeoniflorin (C1), oxypaeoniflorin (C2), desbenzoylpaeoniflorin isomer (C3), and 3,7/8-dimethylellagic acid (C4), and the 17 metabolites were 3′-*O*-methyl (epi) catechin 5-*O*-glucuronide (C5), 3-hydroxy phenylpropionic acid sulfate (C6), 3-hydroxy-4-methoxy-phenylpropionic acid sulfate (C7), 3/4-hydroxy benzoic acid sulfate (C8), $C_{10}H_{18}O_2$ glucuronide (C9-C15), $C_{10}H_{18}O_4$ glucuronide (C16), $C_{10}H_{14}O_3$ glucuronide (C17), 3-methoxy-4-hydroxy-phenylpropionic acid sulfate (C18), $C_8H_8O_3$ glucuronide (C19, C20), and benzoyl glucuronide (C21). Of them, C9–C17, C19, C20, and M23 are derived from paeoniflorin; C5–C7, C18, and C21 are possibly derived from catechins; and C8 is possibly derived from catechins or gallic acids (Liang et al., 2013).

In this study, we systematically explored the metabolism of PRR and its 14 constituents with four structure types (paeoniflorins, catechins, gallic acids, and ellagic acids) in mice. The objectives of the study were to 1) elucidate the metabolites and metabolic pathways of PRR and its 14 main constituents in mice, 2) determine the possible origins of the metabolites of PRR, and 3) clarify whether these compounds can be converted into the recognized effective forms *in vivo*. The findings are helpful for further elucidating the forms of PRR that exist *in vivo* and identifying the effective forms of PRR. The

findings are also of great significance for studying the mechanisms of action and quality control of PRR.

2 Materials and methods

2.1 Medicinal materials and reagents

PRR was purchased from Baohua, a dealer of Chinese herbal medicines in Xunke County, Heilongjiang Province (Sample No. 6524). The medicine was identified as the dried roots of *Paeonia lactiflora* Pall. by Professor Shao-Qing Cai from Peking University School of Pharmaceutical Sciences. A voucher sample (No. 6524) was stored in the Herbarium of Peking University School of Pharmaceutical Sciences.

Paeoniflorin (Lot No. PS010957), albiflorin (Lot No. PS011455), oxypaeoniflorin (Lot No. PS010199), benzoylpaeoniflorin (Lot No. PS000157), hydroxyben zoylpaeoniflorin (Lot No. PS000693), benzoyloxypaeoniflorin (Lot No. PS012411), galloylpaeoniflorin (Lot No. PS010194), epicatechin gallate (Lot No. PS000163), catechin gallate (Lot No. PS010638) and 3,3′-di-*O*-methylellagic acid (Lot No. PS 22960025) were purchased from Chengdu Push Biotechnology Co., Ltd. (Chengdu, China). Catechin (Lot No. P21J11F 118,380) and methylgallate (Lot No. L19D5Y1) were obtained from Shanghai Yuanye Biotechnology Co., Ltd. (Shanghai, China). Lactiflorin (Lot No. MUST-21041202) and ellagic acid (Lot No. KN 960133) were purchased from Chengdu Must Biotechnology Co., Ltd. (Chengdu, China). The purity of all reference substances was greater than 95.0%, as indicated by high-performance liquid chromatography (HPLC; 254 nm). Formic acid (Lot No. 212271), acetonitrile (Lot No. F21LAL 202), and methanol (Lot No. 206409), all HPLC grade, were purchased from Thermo Fisher Scientific, Inc. (Waltham, MA, United States). HPLC-grade ethanol (Lot No. 32061) was purchased from Fuchen (Tianjin) Chemical Reagents Co., Ltd. (Tianjin, China). Sodium carboxymethyl cellulose (Lot No. A18105) was purchased from Sinopharm Chemical Reagents Co., Ltd. (Shanghai, China). Ultrapure water was prepared using a Milli-Q Integral 3 ultrapure water machine (Millipore, Billerica, MA, United States).

2.2 Preparation and qualitative analysis of the lyophilized powder of PRR decoction

The lyophilized powder of PRR decoction was prepared as described previously (Liang et al., 2013). Each Gram of the lyophilized powder was equivalent to 2.63 g of the crude drug. The constituents in the lyophilized powder of the PRR decoction were identified by high performance liquid chromatography with diode array detector and combined with electrospray ionization ion trap time-of-flight multistage mass spectrometry (HPLC-DAD-ESI-IT-TOF-MS^n) with reference to the mass spectral data of the reference substances or the relevant literature (Supplementary Figure S1).

2.3 Animal and metabolic studies

Forty-eight ICR mice (male, 30 ± 2 g) were purchased from the Department of Laboratory Animal Sciences at the Peking University Health Science Center and randomized into one control group and 15 dosing groups (14 compound-dosed groups and one PRR decoction-dosed group) with three mice in each group. All mice were housed in mouse metabolism cages. The experiment lasted for 10 days. After adapting for the first 3 days, the mice were dosed by gavage once per day for the following 7 days. In the 14 compound-dosed groups, the dose was 40 mg/kg mouse weight, while the dose in the decoction-dosed group was 70 mg of lyophilized powder of PRR decoction per kg mouse weight (equivalent to 200 mg/kg of PRR crude drug). All compounds and the lyophilized powder of PRR decoction were suspended in 0.5% sodium carboxymethyl cellulose solution, and the dose volume was approximately 0.2 ml for each mouse. The control group was given the same volume of 0.5% sodium carboxymethyl cellulose solution. The mice were maintained in an environment at 22 ± 2°C (relative humidity 50 ± 5%) and allowed to eat and drink *ad libitum*. All animal experiments were approved by the Animal Ethics Committee of Peking University Health Science Center (approval number: LA2019117).

2.4 Collection and preparation of samples

2.4.1 Collection of samples

All urine and feces were collected during the 7 days of dosing. One hour after the last dosing by gavage, the blood was collected into 1.5-ml heparin sodium-containing tubes by excising the eyeballs. All samples were stored in a refrigerator at −20°C prior to use.

2.4.2 Preparation of urine, feces, and plasma samples

All urine, feces, and plasma samples from the same group were pooled, resulting in 16 urine, 16 feces, and 16 plasma samples. Each urine sample was centrifuged at 8,000 rpm at 4°C for 15 min. The supernatant was harvested, concentrated, and dried at 55°C followed by the addition of 10 ml of methanol and ultrasonic extraction for 30 min. The extract was filtered, concentrated, and dried at 55°C. Each feces sample was dried at 50°C for 48 h and smashed followed by the addition of 30 ml of methanol and ultrasonic extraction for 30 min per round (three rounds of extraction). The extract was filtered, and the filtrates obtained from the three rounds of extraction were pooled, concentrated, and dried at 55°C

followed by the addition of 10 ml of methanol, ultrasonic extraction for 30 min, and centrifugation at 8,000 rpm and 4°C for 15 min. The supernatant was concentrated and dried at 55°C. The urine and feces samples (0.5 g each) were separately dissolved in 1 ml methanol. Each plasma sample was centrifuged at 5,000 rpm and 4°C for 15 min, and approximately 0.9 ml supernatant was collected for each group. After adding 4.5 ml methanol, the mixture was centrifuged at 5,000 rpm and 4°C for 15 min. The supernatant was blown with nitrogen and dried at 40°C followed by the addition of 0.5 ml methanol for reconstitution. All samples were filtered through a 0.22-μm membrane and stored at −20°C prior to further analysis.

2.5 Instruments and Conditions

HPLC-DAD-ESI-IT-TOF-MS^n analysis was performed using an HPLC instrument and an IT-TOF mass spectrometer connected to two LC-20AD pumps, an SIL-20AC autosampler, a CTO-20A column heater, an SPD-M20A photo-diode array (PDA) detector, and a CBM-20A system controller (Shimadzu, Kyoto, Japan). Data analysis was performed using LCMS Solution v.3.60, Formula Predictor v.1.2, and Accurate Mass Calculator (Shimadzu, Kyoto, Japan).

The chromatographic conditions were as follows: chromatographic column, Phenomenex Gemini C18 (250 mm × 4.6 mm, 5 μm); guard column, Phenomenex Security Guard (4 mm × 3.0 mm, 5.0 μm; Phenomenex, Torrance, CA, United States); column temperature, 40°C; injection volume, 10 μL; and flow rate, 1 ml/min. The mobile phase was 0.1% aqueous solution of formic acid (A) and acetonitrile (B). The mobile phase gradients were as follows: 0–12 min, 3% B; 12–33 min, 3%–8% B; 33–37.5 min, 8% B; 37.5–52.5 min, 8%–12% B; 52.5–82.5 min, 12%–25% B; 82.5–105 min, 25 %–60% B; 105–120 min, 60%–100% B; 120–130 min, 100% B. PDA detector: 200–700 nm. The mass spectrometry conditions were as follows: electrospray ionization (ESI), positive and negative ion mode; mass scan range, *m/z* 100–1,000 (MS), *m/z* 50–1,000 (MS^2 and MS^3); relative collision-induced dissociation (CID) energy, 50%; heater block temperature, 200°C; curved desolvation line (CDL) temperature, 200°C; detection voltage, 1.70 kV; interface voltage (+) 4.5 kV, (−) 3.5 kV; drying gas, nitrogen; and drying gas flow rate, 1.5 L/min.

2.6 Identification of the forms of PRR present *in vivo* (original constituents and metabolites)

The *in vivo* existence forms of PRR were identified as previously described (Liang et al., 2013). First, the base peak chromatograms (BPCs) of the samples from the dosing and control groups were compared to find the distinguishing peaks and tentatively determine the *in vivo* existence forms of PRR. Second, the extracted ion chromatograms (EICs) of the compounds in the dosing and control groups were compared to confirm the distinguishing peaks. The chromatographic peaks that appeared in the dosing groups but not in the control group were considered to represent the *in vivo* existence forms of PRR. Finally, the forms of PRR existing *in vivo* were analyzed structurally based on the obtained liquid chromatography-high resolution multi-stage mass spectrometry data combined with 1) the mass spectrometry data of reference substances, 2) the mass spectrometry fragmentation patterns, 3) the mass spectrometry fragmentation information reported in the literature, and 4) information obtained by searching the SciFinder database.

3 Results

In this study, 23, 16, 24, 17, 18, 30, 27, 17, 22, 17, 33, 3, 8, 24, and 31 metabolites of paeoniflorin (P), albiflorin (A), oxypaeoniflorin (O), benzoylpaeoniflorin (B), hydroxybenzoylpaeoniflorin (OB), benzoyloxypaeoniflorin (BO), galloylpaeoniflorin (G), lactiflorin (L), epicatechin gallate (ECG), catechin gallate (CG), catechin (C), ellagic acid (EA), 3,3′-di-O-methylellagic acid (DEA), methylgallate (MG), and PRR were respectively identified in mice. After identifying identical metabolites, a total of 195 metabolites remained (Table 1). The LC-MS^n data of the metabolites and the distributions of metabolites in urine, feces, and plasma of can be found in Supplementary Tables S1, S2.

In this study, the usual neutral losses in mass spectrometry were 30.01 Da (CH_2O), 14.01 Da (CH_2), 176.03 Da ($C_6H_8O_6$), 79.95 Da (SO_3), 81.97 Da (H_2SO_3), 43.99 Da (CO_2), 15.02 Da (CH_3•), 27.99 Da (CO), 42.01 Da (C_2H_2O), 46.01 Da (CH_2O_2), 104.01 Da (C_7H_4O), 122.04 Da ($C_7H_6O_2$), and 162.05 Da ($C_6H_{10}O_5$), indicating that a molecule which shows these neutral losses contains formaldehyde or methanyl, methyl, glucuronosyl, sulfonyl, sulfonyl, carboxy or lactone, methyl, carbonyl, acetyl, carboxy or lactone group, benzoyl, benzoyloxy, and hexosyl (more likely glucosyl) groups, respectively. In addition, the fragment ions at *m/z* 175.02 ($C_6H_7O_6$) and *m/z* 96.96 (SO_4H) indicate that the molecule contains glucuronosyl and sulfate groups.

3.1 Mass spectral features of the 14 reference substances

The mass spectral fragments and fragmentation pathways of the 14 reference substances are presented in Supplementary Table S3 and Supplementary Figure S2.

TABLE 1 Retention times (t_R) molecular formulae, and identities of 10 absorbed compounds and 195 metabolites of PRR and its 14 constituents in mice based on HPLC-ESI-IT-TOF-MS^n.

No.	t_R (min)	Formula	Meas. (Da)	Err (ppm)	P	A	O	B	OB	BO	G	L	ECG	CG	C	EA	DEA	MG	PRR	Identification
P0[a]	56.58	$C_{23}H_{28}O_{11}$	525.1590	−4.57	+	−	−	−	−	−	−	−	−	−	−	−	−	−	−	paeoniflorin
A0[a]	51.95	$C_{23}H_{28}O_{11}$	525.1597	−3.24	−	+	−	−	−	−	−	−	−	−	−	−	−	−	−	albiflorin
O0[a]	42.99	$C_{23}H_{28}O_{12}$	495.1501	−1.41	−	−	+	−	−	−	−	−	−	−	−	−	−	−	−	oxypaeoniflorin
OB0[a]	84.65	$C_{30}H_{32}O_{13}$	599.1726	−7.34	−	−	−	−	+	−	−	−	−	−	−	−	−	−	−	hydroxybenzoylpaeoniflorin
BO0[a]	87.12	$C_{30}H_{32}O_{13}$	599.1755	−2.5	−	−	−	−	−	+	−	−	−	−	−	−	−	−	−	benzoyloxypaeoniflorin
G0[a]	70.17	$C_{30}H_{32}O_{15}$	631.1633	−5.55	−	−	−	−	−	−	+	−	−	−	−	−	−	−	−	galloylpaeoniflorin
L0[a]	81.32	$C_{23}H_{26}O_{10}$	507.1508	0.00	−	−	−	−	−	−	−	+	−	−	−	−	−	−	−	lactiflorin
ECG0[a]	67.80	$C_{22}H_{18}O_{10}$	441.0827	0.00	−	−	−	−	−	−	−	−	+	−	−	−	−	−	−	epicatechin gallate
CG0[a]	70.36	$C_{22}H_{18}O_{10}$	441.0828	0.23	−	−	−	−	−	−	−	−	−	+	−	−	−	−	−	catechin gallate
DEA0[a]	90.97	$C_{16}H_{10}O_8$	329.0315	3.65	−	−	−	−	−	−	−	−	−	−	−	−	+	−	−	3,3′-di-*O*-methylellagic acid
M1[a]	56.58	$C_{23}H_{28}O_{11}$	525.1590	−4.57	−	−	+	+	+	−	+	−	−	−	−	−	−	−	−	paeoniflorin
M2[a]	42.53	$C_{23}H_{28}O_{12}$	495.1502	−1.21	+	−	−	−	+	+	−	−	−	−	−	−	−	−	−	oxypaeoniflorin
M3	77.90	$C_{10}H_{16}O_4$	199.0987	5.52	−	−	−	−	−	+	+	−	−	−	−	−	−	−	−	paeonimetabolin II isomer 1
M4	78.72	$C_{10}H_{16}O_4$	199.0978	1.00	−	−	−	−	−	−	−	−	−	−	−	−	−	−	+	paeonimetabolin II isomer 2
M5	80.91	$C_{10}H_{16}O_4$	199.0980	2.01	−	−	−	−	−	−	−	−	−	−	−	−	−	−	+	paeonimetabolin II isomer 3
M6	80.24	$C_{10}H_{16}O_4$	199.0970	−3.01	−	−	−	−	−	+	+	−	−	−	−	−	−	−	−	paeonimetabolin II isomer 4
M7	23.69	$C_{10}H_{16}O_7S$	279.0532	−4.30	−	+	−	−	−	−	−	−	−	−	−	−	−	−	−	paeonimetabolin II sulfate isomer 1
M8	31.89	$C_{10}H_{16}O_7S$	279.0525	−6.81	−	−	−	−	+	−	−	−	−	−	−	−	−	−	−	paeonimetabolin II sulfate isomer 2
M9	43.84	$C_{10}H_{16}O_7S$	279.0524	−7.17	−	+	−	−	−	−	−	−	−	−	−	−	−	−	−	paeonimetabolin II sulfate isomer 3
M10	49.22	$C_{10}H_{16}O_7S$	279.0523	−7.53	−	+	−	−	−	−	+	−	−	−	−	−	−	−	−	paeonimetabolin II sulfate isomer 4
M11	8.77	$C_{16}H_{24}O_{10}$	421.1361	2.14	−	+	−	−	−	−	−	−	−	−	−	−	−	−	−	desbenzoyl albiflorin isomer 1
M12	31.28	$C_{16}H_{24}O_{10}$	375.1266	−8.26	−	+	−	−	−	−	−	−	−	−	−	−	−	−	−	desbenzoyl albiflorin isomer 2
M13	10.08	$C_{16}H_{24}O_{10}$	421.1332	−4.75	−	+	−	−	−	−	−	−	−	−	−	−	−	−	−	desbenzoyl albiflorin isomer 3
M14	51.34	$C_{16}H_{24}O_{10}$	421.1333	−4.51	+	+	+	+	+	−	−	−	−	−	−	−	−	−	−	desbenzoylpaeoniflorin isomer 1
M15	52.97	$C_{16}H_{24}O_{10}$	421.1346	−1.42	+	+	+	+	+	+	+	+	−	−	−	−	−	−	−	desbenzoylpaeoniflorin isomer 2
M16	29.71	$C_{17}H_{26}O_{10}$	435.1485	−5.29	+	−	−	−	−	−	−	−	−	−	−	−	−	−	−	methyl desbenzoylpaeoniflorin isomer 1
M17	26.15	$C_{17}H_{26}O_{10}$	435.1477	−7.12	−	−	−	−	−	−	−	−	−	−	−	−	−	−	+	methyl desbenzoylpaeoniflorin isomer 2
M18	32.07	$C_{16}H_{22}O_{10}$	373.1146	1.61	+	−	+	+	+	+	+	−	−	−	−	−	−	−	−	paeonimetabolin I glucuronide isomer 1
M19	33.01	$C_{16}H_{22}O_{10}$	373.1145	1.34	−	−	+	+	+	+	+	−	−	−	−	−	−	−	−	paeonimetabolin I glucuronide isomer 2
M20	29.78	$C_{16}H_{22}O_{10}$	373.1123	−4.56	−	−	−	−	−	−	−	+	−	−	−	−	−	−	−	paeonimetabolin I glucuronide isomer 3
M21	28.88	$C_{16}H_{22}O_{10}$	373.1135	−1.34	−	−	−	−	−	−	−	+	−	−	−	−	−	−	−	paeonimetabolin I glucuronide isomer 4
M22	55.09	$C_{16}H_{22}O_{10}$	373.1133	−1.88	−	−	+	−	−	−	−	−	−	−	−	−	−	−	−	paeonimetabolin I glucuronide isomer 5
M23	24.88	$C_{10}H_{14}O_6S$	261.0437	−0.38	+	−	−	+	+	+	+	−	−	−	−	−	−	−	−	$C_{10}H_{14}O_3$ sulfate isomer 1

(Continued on following page)

10.3389/fphar.2022.995641

TABLE 1 (*Continued*) Retention times (t_R) molecular formulae, and identities of 10 absorbed compounds and 195 metabolites of PRR and its 14 constituents in mice based on HPLC-ESI-IT-TOF-MS^n.

No.	t_R (min)	Formula	Meas. (Da)	Err (ppm)	P	A	O	B	OB	BO	G	L	ECG	CG	C	EA	DEA	MG	PRR	Identification
M24	26.01	$C_{10}H_{14}O_6S$	261.0438	0.00	+	−	−	+	+	+	+	−	−	−	−	−	−	−	−	$C_{10}H_{14}O_3$ sulfate isomer 2
M25	28.75	$C_{10}H_{14}O_6S$	261.0423	−5.75	−	−	+	−	−	−	−	−	−	−	−	−	−	−	−	$C_{10}H_{14}O_3$ sulfate isomer 3
M26	29.29	$C_{10}H_{14}O_6S$	261.0423	−5.75	+	−	+	−	+	−	−	−	−	−	−	−	−	−	−	$C_{10}H_{14}O_3$ sulfate isomer 4
M27	34.56	$C_{10}H_{14}O_6S$	261.0429	−3.45	+	−	−	+	+	−	−	−	−	−	−	−	−	−	−	$C_{10}H_{14}O_3$ sulfate isomer 5
M28	37.82	$C_{10}H_{14}O_6S$	261.0432	−2.3	−	−	+	−	−	−	−	−	−	−	−	−	−	−	−	$C_{10}H_{14}O_3$ sulfate isomer 6
M29	24.33	$C_{16}H_{26}O_{10}$	377.1475	5.83	−	−	+	−	+	+	−	−	−	−	−	−	−	−	−	$C_{10}H_{18}O_4$ glucuronide isomer 1
M30	24.90	$C_{16}H_{26}O_{10}$	377.1443	−2.65	−	−	−	−	−	+	+	−	−	−	−	−	−	−	−	$C_{10}H_{18}O_4$ glucuronide isomer 2
M31	26.71	$C_{16}H_{26}O_{10}$	377.1463	2.65	+	−	+	+	+	+	+	−	−	−	−	−	−	−	−	$C_{10}H_{18}O_4$ glucuronide isomer 3
M32	30.81	$C_{16}H_{26}O_{10}$	377.1453	0.00	−	−	−	−	−	+	+	−	−	−	−	−	−	−	−	$C_{10}H_{18}O_4$ glucuronide isomer 4
M33	31.97	$C_{16}H_{26}O_{10}$	377.1437	−4.24	+	−	+	+	−	+	+	−	−	−	−	−	−	−	−	$C_{10}H_{18}O_4$ glucuronide isomer 5
M34	53.31	$C_{16}H_{26}O_{10}$	377.1443	−2.65	−	−	−	−	−	−	−	+	−	−	−	−	−	−	+	$C_{10}H_{18}O_4$ glucuronide isomer 6
M35	56.90	$C_{16}H_{28}O_{10}$	379.1614	1.05	−	−	−	−	−	+	+	−	−	−	−	−	−	−	−	$C_{10}H_{20}O_4$ glucuronide
M36	23.65	$C_{14}H_{16}O_9$	327.0731	2.75	−	+	−	−	−	−	−	−	−	−	−	−	−	−	−	$C_8H_8O_3$ glucuronide isomer 1
M37	31.11	$C_{14}H_{16}O_9$	327.0712	−3.06	−	+	−	−	−	+	+	−	−	−	−	−	−	−	−	$C_8H_8O_3$ glucuronide isomer 2
M38	32.32	$C_{14}H_{16}O_9$	327.0722	0.00	−	+	−	−	−	−	−	−	−	−	−	−	−	−	−	$C_8H_8O_3$ glucuronide isomer 3
M39	35.98	$C_{14}H_{16}O_9$	327.0707	−4.59	−	+	−	−	−	−	−	−	−	−	−	−	−	−	−	$C_8H_8O_3$ glucuronide isomer 4
M40	41.65	$C_{14}H_{16}O_9$	327.0696	−7.95	−	−	−	−	−	+	+	−	−	−	−	−	−	−	−	$C_8H_8O_3$ glucuronide isomer 5
M41	34.25	$C_{10}H_{18}O_6S$	265.0730	−7.92	−	−	+	−	−	−	−	−	−	−	−	−	−	−	−	2,6-dihydroxycineol sulfate isomer 1
M42	47.90	$C_{10}H_{18}O_6S$	265.0732	−7.17	+	−	+	−	+	−	−	−	−	−	−	−	−	−	−	2,6-dihydroxycineol sulfate isomer 2
M43	51.20	$C_{10}H_{18}O_6S$	265.0736	−5.66	+	−	+	+	+	−	−	−	−	−	−	−	−	−	−	2,6-dihydroxycineol sulfate isomer 3
M44	54.17	$C_{10}H_{18}O_6S$	265.0745	−2.26	+	−	+	+	−	−	−	−	−	−	−	−	−	−	−	2,6-dihydroxycineol sulfate isomer 4
M45	63.27	$C_{10}H_{18}O_6S$	265.0729	−8.30	+	+	+	+	+	+	+	−	−	−	−	−	−	−	−	2,6-dihydroxycineol sulfate
M46	83.48	$C_{10}H_{18}O_6S$	265.0739	−4.53	+	−	+	−	−	−	−	−	−	−	−	−	−	−	−	2,6-dihydroxycineol sulfate isomer 6
M47	85.97	$C_{10}H_{18}O_6S$	265.0733	−6.79	+	+	+	+	−	+	+	−	−	−	−	−	−	−	−	2,6-dihydroxycineol sulfate isomer 7
M48	111.38	$C_{10}H_{18}O_6S$	265.0740	−4.15	−	−	−	−	−	−	−	−	−	−	−	−	−	−	+	2,6-dihydroxycineol sulfate isomer 8
M49	128.78	$C_{10}H_{18}O_6S$	265.0753	0.75	−	−	−	−	−	−	−	−	−	−	−	−	−	−	+	2,6-dihydroxycineol sulfate isomer 9
M50	69.08	$C_{16}H_{26}O_9$	361.1522	4.98	−	−	−	−	−	−	−	−	−	−	−	−	−	−	+	paeonimetabolin II glucoside isomer 1
M51	71.20	$C_{16}H_{26}O_9$	361.1486	−4.98	−	−	−	−	−	−	−	−	−	−	−	−	−	−	+	paeonimetabolin II glucoside isomer 2
M52	70.28	$C_{16}H_{26}O_9$	361.1520	4.43	+	−	−	−	−	−	−	−	−	−	−	−	−	−	−	paeonimetabolin II glucoside isomer 3
M53	72.81	$C_{16}H_{26}O_9$	361.1508	1.11	−	−	−	−	−	−	−	−	−	−	−	−	−	−	+	paeonimetabolin II glucoside isomer 4
M54	66.15	$C_{16}H_{26}O_9$	361.1489	−4.15	−	−	−	−	−	+	+	−	−	−	−	−	−	−	−	paeonimetabolin II glucoside
M55	61.87	$C_{10}H_{20}O_6S$	267.0936	0.00	+	+	+	−	+	+	+	−	−	−	−	−	−	−	−	hydrogenated 2,6-dihydroxycineol sulfate isomer 1
M56	57.88	$C_{10}H_{20}O_6S$	267.0901	−2.62	−	−	−	−	−	−	−	−	−	−	−	−	−	−	+	hydrogenated 2,6-dihydroxycineol sulfate isomer 2

(Continued on following page)

10.3389/fphar.2022.995641

TABLE 1 (*Continued*) Retention times (t_R) molecular formulae, and identities of 10 absorbed compounds and 195 metabolites of PRR and its 14 constituents in mice based on HPLC-ESI-IT-TOF-MS^n.

No.	t_R (min)	Formula	Meas. (Da)	Err (ppm)	P	A	O	B	OB	BO	G	L	ECG	CG	C	EA	DEA	MG	PRR	Identification
M57	38.30	$C_{16}H_{24}O_9$	359.1318	−8.35	+	−	+	+	−	+	+	−	−	−	−	−	−	−	−	dehydrogenated 2,6-dihydroxycineol glucuronide isomer 1
M58	39.01	$C_{16}H_{24}O_9$	359.1343	−1.39	+	−	+	+	−	+	+	−	−	−	−	−	−	−	−	dehydrogenated 2,6-dihydroxycineol glucuronide isomer 2
M59	39.61	$C_{16}H_{24}O_9$	359.1342	−1.67	−	−	−	−	−	+	−	−	−	−	−	−	−	−	−	dehydrogenated 2,6-dihydroxycineol glucuronide isomer 3
M60	41.87	$C_{16}H_{24}O_9$	359.1322	−7.24	+	−	+	−	−	+	+	−	−	−	−	−	−	−	−	dehydrogenated 2,6-dihydroxycineol glucuronide isomer 4
M61	48.65	$C_{16}H_{24}O_9$	359.1333	−4.18	+	−	+	+	+	+	+	−	−	−	−	−	−	−	−	dehydrogenated 2,6-dihydroxycineol glucuronide
M62	49.63	$C_{16}H_{24}O_9$	359.1353	1.39	−	−	−	−	−	+	−	−	−	−	−	−	−	−	−	dehydrogenated 2,6-dihydroxycineol glucuronide isomer 5
M63	32.99	$C_7H_6O_8S$	248.9691	5.62	−	−	−	−	−	−	+	−	−	−	−	−	−	−	−	gallic acid sulfate
M64	42.42	$C_7H_6O_8S$	248.9719	3.21	−	−	−	−	−	−	+	−	−	−	−	−	−	−	−	gallic acid sulfate
M65	37.17	$C_9H_9NO_3$	178.0516	3.37	−	+	−	−	−	+	+	−	−	−	−	−	−	−	+	hippuric acid
M66	27.64	$C_9H_9NO_4$	194.0469	5.15	−	−	−	−	−	+	−	−	−	−	−	−	−	−	−	hydroxyhippuric acid
M67	29.07	$C_9H_9NO_4$	194.0459	0.00	−	−	−	−	−	+	−	−	−	−	−	−	−	−	−	hydroxyhippuric acid
M68	28.31	$C_{13}H_{14}O_9$	313.0547	−5.75	−	−	−	−	−	+	−	−	−	−	−	−	−	−	−	salicylic acid glucuronide
M69	71.03	$C_{23}H_{28}O_{10}$	509.1654	−2.16	−	−	−	−	−	−	−	+	−	−	−	−	−	−	−	hydrogenated lactiflorin
M70	63.56	$C_{23}H_{28}O_{10}$	509.1652	−2.55	−	−	−	−	−	−	−	+	−	−	−	−	−	−	+	hydrogenated lactiflorin isomer
M71	71.64	$C_{23}H_{28}O_{11}$	525.1598	−3.05	−	−	−	−	−	−	−	+	−	−	−	−	−	−	−	hydrogenated hydroxylated lactiflorin
M72	35.33	$C_{23}H_{28}O_{11}$	525.1635	4.00	−	−	−	−	−	−	−	−	−	−	−	−	−	−	+	hydrogenated hydroxylated lactiflorin isomer 1
M73	33.67	$C_{23}H_{28}O_{11}$	525.1624	1.90	−	−	−	−	−	−	−	−	−	−	−	−	−	−	+	hydrogenated hydroxylated lactiflorin isomer 2
M74	37.32	$C_{23}H_{28}O_{11}$	525.1624	1.90	−	−	−	−	−	−	−	−	−	−	−	−	−	−	+	hydrogenated hydroxylated lactiflorin isomer 3
M75	85.18	$C_{17}H_{18}O_8S$	381.0612	−1.05	−	−	−	−	−	−	−	+	−	−	−	−	−	−	−	hydrogenated deglycosylated lactiflorin sulfate isomer 1
M76	66.53	$C_{17}H_{18}O_8S$	381.0625	2.36	−	−	−	−	−	−	−	+	−	−	−	−	−	−	−	hydrogenated deglycosylated lactiflorin sulfate isomer 2
M77	84.31	$C_{17}H_{18}O_8S$	381.0622	1.57	−	−	−	−	−	−	−	+	−	−	−	−	−	−	−	hydrogenated deglycosylated lactiflorin sulfate isomer 3
M78	100.37	$C_{17}H_{18}O_8S$	381.0629	3.41	−	−	−	−	−	−	−	+	−	−	−	−	−	−	−	hydrogenated deglycosylated lactiflorin sulfate isomer 4
M79[a]	40.07	$C_{15}H_{14}O_6$	289.0706	−4.15	−	−	−	−	−	−	−	−	−	+	−	−	−	−	−	catechin
M80	71.09	$C_{15}H_{14}O_9S$	369.0295	2.44	−	−	−	−	−	−	−	−	+	−	−	−	−	−	−	epicatechin sulfate
M81	66.12	$C_{15}H_{14}O_9S$	369.0285	−0.27	−	−	−	−	−	−	−	−	−	+	−	−	−	−	−	catechin 5/7-*O*-sulfate isomer 1
M82	67.48	$C_{15}H_{14}O_9S$	369.0268	−4.88	−	−	−	−	−	−	−	−	−	+	−	−	−	−	−	catechin sulfate isomer 2
M83	72.48	$C_{15}H_{14}O_9S$	369.0280	−1.63	−	−	−	−	−	−	−	−	−	+	−	−	−	−	−	catechin sulfate isomer 3
M84	61.79	$C_{15}H_{14}O_9S$	369.0283	−0.81	−	−	−	−	−	−	−	−	−	−	+	−	−	−	−	catechin 5/7-*O*-sulfate isomer 2
M85	68.11	$C_{15}H_{14}O_9S$	369.0283	−0.81	−	−	−	−	−	−	−	−	−	−	+	−	−	−	−	catechin 3′/4′-*O*-sulfate isomer
M86	37.64	$C_{21}H_{22}O_{12}$	465.1038	0.00	−	−	−	−	−	−	−	−	−	−	+	−	−	−	−	catechin glucuronide isomer 1
M87	36.14	$C_{21}H_{22}O_{12}$	465.1008	−6.45	−	−	−	−	−	−	−	−	−	−	+	−	−	−	−	catechin glucuronide isomer 2
M88	32.94	$C_{21}H_{22}O_{12}$	465.1053	3.23	−	−	−	−	−	−	−	−	−	−	+	−	−	−	−	catechin glucuronide isomer 3
M89	66.43	$C_{21}H_{22}O_{15}S$	545.0599	−1.47	−	−	−	−	−	−	−	−	−	+	−	−	−	−	−	catechin glucuronide sulfate isomer 1

(Continued on following page)

10.3389/fphar.2022.995641

TABLE 1 (*Continued*) Retention times (t_R) molecular formulae, and identities of 10 absorbed compounds and 195 metabolites of PRR and its 14 constituents in mice based on HPLC-ESI-IT-TOF-MS^n.

No.	t_R (min)	Formula	Meas. (Da)	Err (ppm)	P	A	O	B	OB	BO	G	L	ECG	CG	C	EA	DEA	MG	PRR	Identification
M90	61.43	$C_{21}H_{22}O_{15}S$	545.0576	−5.69	–	–	–	–	–	–	–	–	–	–	+	–	–	–	–	catechin glucuronide sulfate isomer 2
M91	54.85	$C_{21}H_{22}O_{15}S$	545.0621	2.57	–	–	–	–	–	–	–	–	–	–	+	–	–	–	–	catechin glucuronide sulfate isomer 3
M92	83.80	$C_{15}H_{16}O_8S$	355.0485	−2.25	–	–	–	–	–	–	–	–	+	–	–	–	–	–	–	3-HPP-2-ol sulfate isomer 1
M93	85.03	$C_{15}H_{16}O_8S$	355.0475	−5.07	–	–	–	–	–	–	–	–	+	–	–	–	–	–	–	3-HPP-2-ol sulfate isomer 2
M94	79.52	$C_{15}H_{16}O_8S$	355.0473	−5.63	–	–	–	–	–	–	–	–	–	–	+	–	–	–	–	3-HPP-2-ol sulfate isomer 3
M95	40.82	$C_{12}H_{14}O_{12}S$	381.0138	1.31	–	–	–	–	–	–	–	–	+	+	–	–	–	–	–	pyrogallol-*O*-glucuronide sulfate isomer 1
M96	41.84	$C_{12}H_{14}O_{12}S$	381.0149	4.20	–	–	–	–	–	–	–	–	–	+	–	–	–	–	–	pyrogallol-*O*-glucuronide sulfate isomer 2
M97	50.13	$C_{11}H_{14}O_4$	209.0812	−3.35	–	–	–	–	–	–	–	–	+	–	–	–	–	–	–	5-(3,4-dihydroxyphenyl)-valeric acid
M98	69.82	$C_{11}H_{14}O_7S$	289.0386	−0.35	–	–	–	–	–	–	–	–	+	–	–	–	–	–	–	5-(3,4-dihydroxyphenyl)-valeric acid sulfate isomer 1
M99	125.97	$C_{11}H_{14}O_7S$	289.0400	4.50	–	–	–	–	–	–	–	–	–	–	+	–	–	–	–	5-(3,4-dihydroxyphenyl)-valeric acid sulfate isomer 2
M100	66.80	$C_{11}H_{14}O_7S$	289.0368	−6.57	–	–	–	–	–	–	–	–	–	–	+	–	–	–	–	5-(3,4-dihydroxyphenyl)-valeric acid sulfate isomer 3
M101	64.15	$C_{11}H_{14}O_8S$	305.0348	3.61	–	–	–	–	–	–	–	–	+	–	–	–	–	–	–	trihydroxy benzenepentanoic acid sulfate isomer 1
M102	60.56	$C_{11}H_{14}O_8S$	305.0316	−6.88	–	–	–	–	–	–	–	–	–	–	+	–	–	–	–	trihydroxy benzenepentanoic acid sulfate isomer 2
M103	79.45	$C_{11}H_{12}O_7S$	287.0251	2.44	–	–	–	–	–	–	–	–	+	+	–	–	–	–	–	5-(3,4-dihydroxyphenyl)-γ-valerolactone sulfate isomer 1
M104	72.89	$C_{11}H_{12}O_7S$	287.0243	4.18	–	–	–	–	–	–	–	–	+	–	–	–	–	–	–	5-(3,4-dihydroxyphenyl)-γ-valerolactone sulfate isomer 2
M105	77.34	$C_{11}H_{12}O_7S$	287.0227	−1.39	–	–	–	–	–	–	–	–	–	+	+	–	–	–	–	5-(3,4-dihydroxyphenyl)-γ-valerolactone sulfate isomer 3
M106	76.08	$C_{11}H_{12}O_7S$	287.0219	−4.18	–	–	–	–	–	–	–	–	–	–	+	–	–	–	–	5-(3,4-dihydroxyphenyl)-γ-valerolactone sulfate isomer 4
M107	46.82	$C_{17}H_{20}O_{10}$	383.1002	4.70	–	–	–	–	–	–	–	–	+	–	–	–	–	–	–	5-(3,4-dihydroxyphenyl)-γ-valerolactone glucuronide isomer 1
M108	47.38	$C_{17}H_{20}O_{10}$	383.1005	5.48	–	–	–	–	–	–	–	–	–	+	–	–	–	–	–	5-(3,4-dihydroxyphenyl)-γ-valerolactone glucuronide isomer 2
M109	76.97	C10H10O7S	273.0072	−0.73	–	–	–	–	–	–	–	–	+	+	–	–	–	–	–	ferulic acid sulfate
M110	87.39	$C_{11}H_{12}O_6S$	271.0286	1.48	–	–	–	–	–	–	–	–	+	–	–	–	–	–	–	5-(3-hydroxyphenyl)-γ-valerolactone sulfate isomer 1
M111	82.81	$C_{11}H_{12}O_6S$	271.0284	0.74	–	–	–	–	–	–	–	–	–	–	+	–	–	–	–	5-(3-hydroxyphenyl)-γ-valerolactone sulfate isomer 2
M112	78.53	$C_{23}H_{20}O_{10}$	455.0985	0.22	–	–	–	–	–	–	–	–	–	+	–	–	–	–	–	methyl catechin gallate
M113	99.94	$C_{15}H_{16}O_6$	291.0891	5.84	–	–	–	–	–	–	–	–	–	–	+	–	–	–	–	3,4-diHPP-2-ol
M114	95.61	$C_{15}H_{16}O_6$	291.0866	−2.75	–	–	–	–	–	–	–	–	–	–	–	–	–	–	+	3,4-diHPP-2-ol isomer 1
M115	98.62	$C_{15}H_{16}O_6$	291.0875	0.34	–	–	–	–	–	–	–	–	–	–	–	–	–	–	+	3,4-diHPP-2-ol isomer 2
M116	102.43	$C_{15}H_{16}O_6$	291.0863	−3.78	–	–	–	–	–	–	–	–	–	–	–	–	–	–	+	3,4-diHPP-2-ol isomer 3
M117	108.16	$C_{15}H_{16}O_6$	291.0885	3.78	–	–	–	–	–	–	–	–	–	–	–	–	–	–	+	3,4-diHPP-2-ol isomer 4
M118	110.64	$C_{15}H_{16}O_6$	291.0880	2.06	–	–	–	–	–	–	–	–	–	–	–	–	–	–	+	3,4-diHPP-2-ol isomer 5
M119	125.68	$C_{15}H_{16}O_6$	291.0882	2.75	–	–	–	–	–	–	–	–	–	–	–	–	–	–	+	3,4-diHPP-2-ol isomer 6
M120	95.25	$C_{21}H_{24}O_{15}S$	547.1477	3.66	–	–	–	–	–	–	–	–	–	+	–	–	–	–	–	3,4-diHPP-2-ol glucuronide sulfate
M121	67.91	$C_{21}H_{24}O_{14}S$	531.0796	−3.39	–	–	–	–	–	–	–	–	–	–	+	–	–	–	–	3-HPP-2-ol glucuronide sulfate

(Continued on following page)

10.3389/fphar.2022.995641

TABLE 1 (*Continued*) Retention times (t_R) molecular formulae, and identities of 10 absorbed compounds and 195 metabolites of PRR and its 14 constituents in mice based on HPLC-ESI-IT-TOF-MS^n.

No.	t_R (min)	Formula	Meas. (Da)	Err (ppm)	P	A	O	B	OB	BO	G	L	ECG	CG	C	EA	DEA	MG	PRR	Identification
M122	85.09	$C_{16}H_{16}O_9S$	383.0449	1.83	–	–	–	–	–	–	–	–	+	–	–	–	–	–	–	methyl catechin sulfate isomer 1
M123	82.21	$C_{16}H_{16}O_9S$	383.0456	3.65	–	–	–	–	–	–	–	–	–	+	–	–	–	–	–	methyl catechin sulfate isomer 2
M124	81.83	$C_{16}H_{16}O_9S$	383.0454	3.13	–	–	–	–	–	–	–	–	–	–	+	–	–	–	–	methyl catechin sulfate isomer 3
M125	75.73	$C_{16}H_{16}O_9S$	383.0458	4.18	–	–	–	–	–	–	–	–	–	–	+	–	–	–	–	methyl catechin sulfate isomer 4
M126	77.29	$C_{16}H_{16}O_9S$	383.0424	−4.70	–	–	–	–	–	–	–	–	–	–	+	–	–	–	–	methyl catechin sulfate isomer 5
M127	42.29	$C_{22}H_{24}O_{12}$	479.1165	−6.26	–	–	–	–	–	–	–	–	–	–	+	–	–	–	–	methyl catechin glucuronide isomer 1
M128	51.77	$C_{22}H_{24}O_{12}$	479.1171	−5.01	–	–	–	–	–	–	–	–	–	–	+	–	–	–	–	methyl catechin glucuronide isomer 2
M129	40.51	$C_{22}H_{24}O_{12}$	479.1198	0.63	–	–	–	–	–	–	–	–	–	–	+	–	–	–	–	methyl catechin glucuronide isomer 3
M130	55.14	$C_{22}H_{24}O_{15}S$	559.0763	0.00	–	–	–	–	–	–	–	–	–	–	+	–	–	–	–	methyl catechin glucuronide sulfate isomer 1
M131	53.57	$C_{22}H_{24}O_{15}S$	559.0735	−5.01	–	–	–	–	–	–	–	–	–	–	+	–	–	–	–	methyl catechin glucuronide sulfate isomer 2
M132	65.48	$C_{22}H_{24}O_{15}S$	559.0752	−1.97	–	–	–	–	–	–	–	–	–	–	+	–	–	–	–	methyl catechin glucuronide sulfate isomer 3
M133	81.08	$C_9H_8O_6S$	242.9965	−1.65	–	–	–	–	–	–	–	–	+	–	–	–	–	–	–	*m*-coumaric acid sulfate
M134	56.30	$C_7H_6O_6S$	216.9820	3.69	–	–	–	–	–	–	–	–	+	–	–	–	–	–	–	3/4-hydroxy benzonic acid sulfate isomer 1
M135	40.62	$C_7H_6O_6S$	216.9809	−1.38	–	–	–	–	–	–	–	–	–	–	–	–	–	–	+	3/4-hydroxy benzonic acid sulfate isomer 2
M136	126.14	$C_{15}H_8O_{11}S$	394.9707	−2.03	–	–	–	–	–	–	–	–	–	–	–	+	–	–	–	methyl ellagic acid sulfate isomer 1
M137	127.57	$C_{15}H_8O_{11}S$	394.9710	−1.27	–	–	–	–	–	–	–	–	–	–	–	+	–	–	–	methyl ellagic acid sulfate isomer 2
M138	127.83	$C_{13}H_8O_7S$	306.9927	2.93	–	–	–	–	–	–	–	–	–	–	–	–	+	–	–	urolithin A sulfate
M139	125.56	$C_{13}H_8O_6S$	290.9960	−3.09	–	–	–	–	–	–	–	–	–	–	–	+	+	–	–	urolithin B sulfate isomer 1
M140	129.13	$C_{13}H_8O_6S$	290.9959	−3.44	–	–	–	–	–	–	–	–	–	–	–	–	+	–	+	urolithin B sulfate isomer 2
M141	116.13	$C_{13}H_8O_6S$	290.9947	−7.65	–	–	–	–	–	–	–	–	–	–	–	–	–	–	+	urolithin B sulfate isomer 3
M142[a]	126.77	$C_{16}H_{10}O_8$	329.0300	−0.91	–	–	–	–	–	–	–	–	–	–	–	–	+	–	–	3,3′-di-*O*-methylellagic acid isomer
M143	128.12	$C_{16}H_{10}O_{11}S$	408.9866	−1.22	–	–	–	–	–	–	–	–	–	–	–	–	+	–	–	3,3′-di-*O*-methylellagic acid sulfate isomer 1
M144	126.52	$C_{16}H_{10}O_{11}S$	408.9867	−0.98	–	–	–	–	–	–	–	–	–	–	–	–	+	–	–	3,3′-di-*O*-methylellagic acid sulfate isomer 2
M145	73.88	$C_{22}H_{18}O_{14}$	505.0627	−2.18	–	–	–	–	–	–	–	–	–	–	–	–	+	–	–	3,3′-di-*O*-methylellagic acid glucuronide isomer 1
M146	74.73	$C_{22}H_{18}O_{14}$	505.0634	1.98	–	–	–	–	–	–	–	–	–	–	–	–	+	–	–	3,3′-di-*O*-methylellagic acid glucuronide isomer 2
M147	43.79	$C_8H_8O_8S$	262.9867	0.00	–	–	–	–	–	–	–	–	–	–	–	–	–	+	–	methyl gallate sulfate
M148	45.96	$C_8H_8O_8S$	262.9872	1.90	–	–	–	–	–	–	–	–	–	–	–	–	–	+	–	methyl gallate sulfate isomer 1
M149	59.29	$C_8H_8O_8S$	262.9850	−6.46	–	–	–	–	–	–	–	–	–	–	–	–	–	+	–	methyl gallate sulfate isomer 2
M150	61.06	$C_8H_8O_8S$	262.9867	0.00	–	–	–	–	–	–	–	–	–	–	–	–	–	+	–	methyl gallate sulfate isomer 3
M151	64.01	$C_8H_8O_8S$	262.9852	−5.70	–	–	–	–	–	–	–	–	–	–	–	–	–	+	–	methyl gallate sulfate
M152	84.88	$C_8H_8O_8S$	262.9862	−1.90	–	–	–	–	–	–	–	–	–	–	–	–	–	+	–	methyl gallate sulfate isomer 4
M153	88.43	$C_8H_8O_8S$	262.9854	−4.94	–	–	–	–	–	–	–	–	–	–	–	–	–	+	–	methyl gallate sulfate isomer 5
M154	125.33	$C_8H_8O_8S$	262.9864	−1.14	–	–	–	–	–	–	–	–	–	–	–	–	–	+	–	methyl gallate sulfate isomer 6

(Continued on following page)

10.3389/fphar.2022.995641

TABLE 1 (*Continued*) Retention times (t_R) molecular formulae, and identities of 10 absorbed compounds and 195 metabolites of PRR and its 14 constituents in mice based on HPLC-ESI-IT-TOF-MS^n.

No.	t_R (min)	Formula	Meas. (Da)	Err (ppm)	P	A	O	B	OB	BO	G	L	ECG	CG	C	EA	DEA	MG	PRR	Identification
M155	127.18	$C_8H_8O_8S$	262.9887	7.60	–	–	–	–	–	–	–	–	–	–	–	–	–	+	–	methyl gallate sulfate isomer 7
M156	36.25	$C_{14}H_{16}O_{11}$	359.0622	0.56	–	–	–	–	–	–	–	–	–	–	–	–	–	+	–	methyl gallate glucuronide isomer 1
M157	37.21	$C_{14}H_{16}O_{11}$	359.0620	0.00	–	–	–	–	–	–	–	–	–	–	–	–	–	+	–	methyl gallate glucuronide
M158	50.09	$C_{14}H_{16}O_{11}$	359.0597	−6.41	–	–	–	–	–	–	–	–	–	–	–	–	–	+	–	methyl gallate glucuronide isomer 2
M159	26.75	$C_{14}H_{16}O_{11}$	359.0618	−0.56	–	–	–	–	–	–	–	–	–	–	–	–	–	+	–	methyl gallate glucuronide isomer 3
M160	40.24	$C_{20}H_{24}O_{17}$	535.0949	1.50	–	–	–	–	–	–	–	–	–	–	–	–	–	+	–	methyl gallate diglucuronide isomer 1
M161	38.77	$C_{20}H_{24}O_{17}$	535.0943	0.37	–	–	–	–	–	–	–	–	–	–	–	–	–	+	–	methyl gallate diglucuronide isomer 2
M162	58.58	$C_{14}H_{16}O_{14}S$	439.0199	2.51	–	–	–	–	–	–	–	–	–	–	–	–	–	+	–	methyl gallate sulfate glucuronide
M163	42.90	$C_{15}H_{18}O_{11}$	373.0765	−2.95	–	–	–	–	–	–	–	–	–	–	–	–	–	+	–	methylated methyl gallate glucuronide isomer 1
M164	44.57	$C_{15}H_{18}O_{11}$	373.0773	−0.80	–	–	–	–	–	–	–	–	–	–	–	–	–	+	–	methylated methyl gallate glucuronide isomer 2
M165	43.71	$C_{15}H_{18}O_{11}$	373.0763	−3.48	–	–	–	–	–	–	–	–	–	–	–	–	–	+	–	methylated methyl gallate glucuronide isomer 3
M166	76.78	$C_9H_{10}O_8S$	277.0014	−3.61	–	–	–	–	–	–	–	–	–	–	–	–	–	+	–	methylated methyl gallate sulfate isomer 1
M167	96.53	$C_9H_{10}O_8S$	277.0015	−3.25	–	–	–	–	–	–	–	–	–	–	–	–	–	+	–	methylated methyl gallate sulfate isomer 2
M168	126.77	$C_9H_{10}O_8S$	277.0018	−2.17	–	–	–	–	–	–	–	–	–	–	–	–	–	+	–	methylated methyl gallate sulfate isomer 3
M169	126.98	$C_{10}H_{12}O_8S$	291.0165	−5.15	–	–	–	–	–	–	–	–	–	–	–	–	–	+	–	dimethylated methyl gallate sulfate
M170	81.24	$C_7H_8O_4S$	187.0064	−3.74	–	–	–	–	–	–	–	–	–	–	–	–	–	–	+	benzyl alcohol sulfate
M171	50.12	$C_8H_8O_6S$	230.9969	0.00	–	–	–	–	–	–	–	+	–	–	+	–	–	–	–	3/4-hydroxy phenylacetic acid sulfate isomer 1
M172	45.80	$C_8H_8O_6S$	230.9952	−5.19	–	–	–	–	–	–	–	+	–	–	–	–	–	–	–	3/4-hydroxy phenylacetic acid sulfate isomer 2
M173	46.27	$C_8H_8O_6S$	230.9953	−6.93	–	–	–	–	–	–	–	–	–	–	+	–	–	–	–	3/4-hydroxy phenylacetic acid sulfate isomer 3
M174	53.30	$C_8H_8O_6S$	230.9952	−7.36	–	–	–	–	–	–	–	–	+	+	–	–	–	–	–	3/4-hydroxy phenylacetic acid sulfate isomer 4
M175	48.15	$C_8H_8O_6S$	230.9962	−3.03	–	–	–	–	–	–	–	–	–	–	–	–	–	–	+	3/4-hydroxy phenylacetic acid sulfate isomer 5
M176	43.92	$C_8H_8O_6S$	230.9962	−3.03	–	–	–	–	–	–	–	–	–	–	–	–	–	–	+	3/4-hydroxy phenylacetic acid sulfate isomer 6
M177	127.45	$C_9H_{10}O_6S$	245.0129	1.63	–	–	–	–	–	–	–	+	–	–	–	–	–	–	–	3/4-hydroxy phenylpropionic acid sulfate isomer 1
M178	74.60	$C_9H_{10}O_6S$	245.0126	0.41	–	–	–	–	–	–	–	–	+	+	–	–	–	–	–	3/4-hydroxy phenylpropionic acid sulfate isomer 2
M179	70.97	$C_9H_{10}O_6S$	245.0117	−3.27	–	–	–	–	–	–	–	–	–	–	+	–	–	–	–	3/4-hydroxy phenylpropionic acid sulfate isomer 3
M180	69.45	$C_9H_{10}O_6S$	245.0109	−6.53	–	–	–	–	–	–	–	–	–	–	+	–	–	–	–	3/4-hydroxy phenylpropionic acid sulfate isomer 4
M181	55.54	$C_9H_{10}O_7S$	261.0059	−5.75	–	–	–	–	–	–	–	+	–	–	–	–	–	–	–	3,4-dihydroxy phenylpropionic acid sulfate isomer 1
M182	58.99	$C_9H_{10}O_7S$	261.0083	3.45	–	–	–	–	–	–	–	–	+	–	–	–	–	–	–	3,4-dihydroxy phenylpropionic acid sulfate isomer 2
M183	67.81	$C_9H_{10}O_7S$	261.0079	1.92	–	–	–	–	–	–	–	–	+	–	–	–	–	–	–	3,4-dihydroxy phenylpropionic acid sulfate isomer 3
M184	64.31	$C_9H_{10}O_7S$	261.0088	−5.36	–	–	–	–	–	–	–	–	–	–	+	–	–	–	–	3,4-dihydroxy phenylpropionic acid sulfate isomer 4
M185	40.17	$C_9H_{10}O_7S$	261.0082	3.07	–	–	–	–	–	–	–	–	–	–	–	–	–	–	+	3,4-dihydroxy phenylpropionic acid sulfate isomer 5
M186	53.09	$C_9H_{10}O_7S$	261.0062	−4.60	–	–	–	–	–	–	–	–	–	–	–	–	–	–	+	3,4-dihydroxy phenylpropionic acid sulfate isomer 6
M187	44.94	$C_8H_8O_7S$	246.9912	−2.43	–	–	–	–	–	–	–	+	–	–	–	–	–	–	–	3,4-dihydroxy phenylacetic acid sulfate isomer 1

(Continued on following page)

10.3389/fphar.2022.995641

TABLE 1 (*Continued*) Retention times (t_R) molecular formulae, and identities of 10 absorbed compounds and 195 metabolites of PRR and its 14 constituents in mice based on HPLC-ESI-IT-TOF-MS^n.

No.	t_R (min)	Formula	Meas. (Da)	Err (ppm)	P	A	O	B	OB	BO	G	L	ECG	CG	C	EA	DEA	MG	PRR	Identification
M188	49.91	$C_8H_8O_7S$	246.9918	0.00	–	–	–	–	–	–	–	–	+	+	–	–	–	–	–	3,4-dihydroxy phenylacetic acid sulfate isomer 2
M189	44.24	$C_8H_8O_7S$	246.9924	2.43	–	–	–	–	–	–	–	–	–	–	+	–	–	+	–	3,4-dihydroxy phenylacetic acid sulfate isomer 3
M190	51.43	$C_8H_8O_7S$	246.9925	2.83	–	–	–	–	–	–	–	–	+	–	–	–	–	–	–	3,4-dihydroxy phenylacetic acid sulfate isomer 4
M191	41.72	$C_8H_8O_7S$	246.9910	−3.24	–	–	–	–	–	–	–	–	–	–	–	–	–	–	+	3,4-dihydroxy phenylacetic acid sulfate isomer 5
M192	125.83	$C_{12}H_{16}O_8S$	319.0488	−1.57	–	–	–	–	–	–	–	+	–	–	+	–	–	–	–	dihydroxylated methoxylated benzenepentanoic acid sulfate isomer 1
M193	90.36	$C_{12}H_{16}O_8S$	319.0507	4.39	–	–	–	–	–	–	–	–	+	–	–	–	–	–	–	dihydroxylated methoxylated benzenepentanoic acid sulfate isomer 2
M194	126.80	$C_{12}H_{16}O_8S$	319.0490	−0.94	–	–	–	–	–	–	–	–	–	–	+	–	–	–	–	dihydroxylated methoxylated benzenepentanoic acid sulfate isomer 3
M195	124.59	$C_{12}H_{16}O_8S$	319.0495	0.63	–	–	–	–	–	–	–	–	–	–	–	–	–	–	+	dihydroxylated methoxylated benzenepentanoic acid sulfate isomer 4
SUM					23	16	24	17	18	30	27	17	22	17	33	3	8	24	31	

Note: P, paeoniflorin; A, albiflorin; O, oxypaeoniflorin; B, benzoylpaeoniflorin; OB, hydroxybenzoylpaeoniflorin; BO, benzoyloxypaeoniflorin; G, galloylpaeoniflorin; L, lactiflorin; ECG, epicatechin gallate; CG, catechin gallate; C, catechin; EA, ellagic acid; DEA, 3,3′-di-*O*-methylellagic acid; MG, methyl gallate; PRR, Paeoniae Radix Rubra; t_R, retention time; Meas., measured; Err., error.; +, detected; –, undetected; [a], identified by comparison with reference compounds.

3.1.1 Mass spectral features of eight paeoniflorins

The isomers paeoniflorin and albiflorin showed $[M+HCOOH-H]^-$ at *m/z* 525.16 with a molecular formula of $C_{23}H_{28}O_{11}$. The two isomers showed different relative abundances of the characteristic ions at *m/z* 449.14 and 479.15; for paeoniflorin, the relative abundance of the characteristic ion at *m/z* 449.14 was greater than that of the ion at *m/z* 479.15, whereas the opposite was observed for albiflorin. Oxypaeoniflorin showed $[M-H]^-$ at *m/z* 495.15, and its molecular formula was predicted to be $C_{23}H_{28}O_{12}$. The fragment ion at *m/z* 165.05 ($C_9H_{10}O_3$) was formed by the neutral loss of $C_{14}H_{18}O_9$ [150.04 Da ($C_8H_6O_3$) and 180.06 Da ($C_6H_{12}O_6$)].

Benzoylpaeoniflorin showed $[M+HCOOH-H]^-$ at *m/z* 629.18, and its molecular formula was $C_{23}H_{28}O_{12}$. The fragment ion at *m/z* 309.10 was formed by the neutral loss of 122.04 Da ($C_7H_6O_2$, benzoic acid) from the ion at *m/z* 431.13.

The isomers benzoyloxypaeoniflorin and hydroxybenzoylpaeoniflorin showed $[M-H]^-$ at *m/z* 599.17 with a molecular formula of $C_{30}H_{32}O_{13}$. The two isomers showed differences in the relative abundances of the characteristic ions at *m/z* 477.14 and 447.13. For benzoyloxypaeoniflorin, the relative abundance of the characteristic ion at *m/z* 477.14 was higher than that at *m/z* 447.13, whereas the opposite was true for hydroxybenzoylpaeoniflorin.

Galloylpaeoniflorin showed $[M-H]^-$ at *m/z* 631.16 with a molecular formula of $C_{30}H_{32}O_{15}$. The fragment ion at *m/z* 509.12 was formed by a neutral loss of 122.04 Da ($C_7H_6O_2$).

Lactiflorin showed $[M-H]^-$ at *m/z* 461.13 with a molecular formula of $C_{23}H_{26}O_{10}$. The fragment ions at *m/z* 371.11 and 339.11 were formed by neutral losses of 90.03 Da ($C_3H_6O_3$) and 122.04 Da ($C_7H_6O_2$), respectively.

3.1.2 Mass spectral features of three catechins

Epicatechin gallate, catechin gallate, and catechin respectively showed $[M-H]^-$ at *m/z* 441.08, 441.08, and 289.06 with molecular formulae of $C_{22}H_{18}O_{10}$, $C_{22}H_{18}O_{10}$, and $C_{15}H_{14}O_6$. The cleavage pathways for these three catechins are the same as those described previously (Liu et al., 2009).

3.1.3 Mass spectral features of two ellagic acids

Ellagic acid showed $[M-H]^-$ at *m/z* 300.99 with a molecular formula of $C_{14}H_6O_8$. The fragment ion at *m/z* 284.00 was formed by a neutral loss of 17.00 Da (OH•).

3,3′-Di-*O*-methylellagic acid showed $[M-H]^-$ at *m/z* 329.03 with a molecular formula of $C_{16}H_{10}O_8$. The fragment ions at *m/z* 314.01 and 298.98 were formed by two sequential losses of 15.02 Da (CH_3•).

3.1.4 Mass spectral features of one gallate

Methyl gallate showed $[M-H]^-$ at *m/z* 183.03 with a molecular formula of $C_8H_8O_5$. The fragment ions at *m/z* 168.01 and 124.02 were formed by neutral losses of 15.02 Da (CH_3•) and 43.99 Da (CO_2), respectively.

3.2 Identification of the metabolites of eight paeoniflorins (P, A, O, B, OB, BO, G, L).

The metabolic pathways of benzoyloxypaeoniflorin are shown in Figure 1, and the metabolic pathways of other paeoniflorins are shown in Supplementary Figure S3.

3.2.1 Paeonimetabolin II ($C_{10}H_{16}O_4$) and its phase II metabolites (M3–M10 and M50–M54)

According to our previous study, paeonimetabolin II showed $[M-H]^-$ at *m/z* 199.09 with a molecular formula of $C_{10}H_{16}O_4$. M3–M6 showed $[M-H]^-$ at *m/z* 199.09 with a predicted molecular formula of $C_{10}H_{16}O_4$; thus, M3-M6 were tentatively identified as paeonimetabolin II and its isomers (Liang et al., 2013). M7–M10 showed $[M-H]^-$ at *m/z* 279.05 with a predicted molecular formula of $C_{10}H_{16}O_7S$. The fragment ion at *m/z* 96.96 (HSO_4) was observed in the MS^2 spectra of M7, M9, and M10. Therefore, based on the mass spectral features and the literature (Shu et al., 1987; Liang et al., 2013), M7–M10 were tentatively identified as paeonimetabolin II sulfate isomers. M50–M54 showed $[M-H]^-$ at *m/z* 361.15 with a predicted molecular formula of $C_{16}H_{26}O_9$. The characteristic fragment at *m/z* 199.10 ($C_{10}H_{16}O_4$, paeonimetabolin II) was formed by a neutral loss of 162.05 Da in the MS^2 spectra of M54; therefore, M54 was tentatively identified as paeonimetabolin II glucoside. The other compounds, M50–M53, are M54 isomers and were tentatively identified as paeonimetabolin II glucoside isomers.

3.2.2 Phase II metabolites of 2,6-dihydroxycineol ($C_{10}H_{18}O_3$, epomediol or isomer) (M41–M49)

According to our previous identification of 2-hydroxy-1,8-cineol ($C_{10}H_{18}O_2$) and our search of the SciFinder database, $C_{10}H_{18}O_3$ was tentatively identified as 2,6-dihydroxycineol or epomediol. According to the literature (Jose Cuevas et al., 2002; Xu et al., 2022), epomediol reduces cholestasis. M41–M49 showed $[M-H]^-$ at *m/z* 265.07, and the molecular formula was predicted as $C_{10}H_{18}O_6S$. The characteristic fragment ion at *m/z* 183.09 ($C_{10}H_{16}O_3$) was formed by a neutral loss of 81.97 Da (H_2SO_3) in the MS^2 spectra of M45. Therefore, M45 was tentatively identified as 2,6-dihydroxycineol sulfate; M41–M44 and M46–M49 are isomers of M45 and were tentatively identified as 2,6-dihydroxycineol sulfate isomers.

3.2.3 Derivatives of phase II metabolites of 2,6-dihydroxycineol (M55–M62)

M55 and M56 showed $[M-H]^-$ at *m/z* 267.09, and their molecular formula was predicted as $C_{10}H_{20}O_6S$. The characteristic fragment ion at *m/z* 169.09 ($C_{10}H_{17}O_2$) was formed by a neutral loss of 97.99 Da (H_2SO_4) in the MS^2 spectra of M56. Compared to M41–M49, M55 and M66 have two additional H atoms in their molecular formulae; thus, they were tentatively identified as hydrogenated 2,6-dihydroxycineol sulfate isomers.

M57–M62 showed $[M-H]^-$ at *m/z* 359.13, and their molecular formula was predicted as $C_{16}H_{24}O_9$. The characteristic ion at *m/z* 183.10 ($C_{10}H_{16}O_3$) was formed by a neutral loss of 176.03 Da ($C_6H_8O_6$) in the MS^2 spectra of M61; thus, M61 was tentatively identified as dehydrogenated 2,6-dihydroxycineol glucuronide. M57–M60 and M62 are M61 isomers and were thus identified as dehydrogenated 2,6-dihydroxycineol glucuronide isomers.

3.2.4 Lactiflorin-related metabolites (M69–M78)

M69 and M70 showed $[M+HCOOH-H]^-$ at *m/z* 509.16, and their molecular formula was predicted as $C_{23}H_{28}O_{10}$. The characteristic fragment ions at *m/z* 463.16 and 359.15 ($C_{16}H_{24}O_9$) were formed by sequential losses of 46.01 Da (CH_2O_2) and 104.01 Da (C_7H_4O) in the MS^2 spectra of M69. Based on the mass spectral features and origin of M69 (derived from lactiflorin), M69 was predicted as hydrogenated lactiflorin. M70 is an isomer of M69 and was predicted to be a hydrogenated lactiflorin isomer.

M71–M74 showed $[M+HCOOH-H]^-$ at *m/z* 525.15, and their molecular formula was predicted as $C_{23}H_{28}O_{11}$. The fragment ions at *m/z* 479.13 ($C_{23}H_{27}O_{11}$) and 461.13 ($C_{23}H_{25}O_{10}$) were formed by sequential losses of 46.01 Da (CH_2O_2) and 18.01 Da (H_2O) in the MS^2 spectra of M71. The ions at *m/z* 357.10 ($C_{16}H_{21}O_9$) and *m/z* 339.09 ($C_{16}H_{19}O_8$) were formed by sequential losses of 122.04 Da ($C_7H_6O_2$, benzoic acid) and 18.01 Da (H_2O) from the fragment at *m/z* 479.13 ($C_{23}H_{27}O_{11}$). Based on the mass spectral features of M71 and its origin (derived from lactiflorin), M71 was predicted as a metabolite formed by the hydrogenation and hydroxylation of lactiflorin (i.e., M71 is a hydrogenated hydroxylated lactiflorin). M72–M74 are isomers of M71 and were thus predicted to be hydrogenated hydroxylated lactiflorin isomers.

M75–M78 showed $[M-H]^-$ at *m/z* 381.06 with a predicted molecular formula of $C_{17}H_{18}O_8S$. The fragment ions at *m/z* 259.01 ($C_{10}H_{11}O_6S$) and *m/z* 195.07 ($C_{10}H_{11}O_4$) were formed by neutral losses of 122.04 Da ($C_7H_6O_2$) and 186.00 Da [106.04 Da (C_7H_6O) and 79.96 Da (SO_3)] in the MS^2 spectra. The fragment ions at *m/z* 177.03 ($C_{10}H_9O_3$), *m/z* 165.04 ($C_9H_9O_3$), and *m/z* 147.05 ($C_9H_7O_2$) were formed by neutral losses of 18.01 Da (H_2O), 30.01 Da (CH_2O), and 48.02 (H_2O and CH_2O), respectively, from the ion at *m/z* 195.07 ($C_{10}H_{11}O_4$). M75–M78 were all derived from the metabolism of lactiflorin and were thus predicted to be metabolites formed by the hydrogenation, deglycosylation, and sulfation of lactiflorin (i.e., M75–M78 are hydrogenated deglycosylated lactiflorin sulfate isomers).

3.2.5 Other metabolites of paeoniflorins (M1–M2, M11–M40, M63–M68)

M1 and M2 showed $[M+HCOOH-H]^-$ and $[M-H]^-$ at *m/z* 525.16 and 495.15, respectively, and their molecular formulae

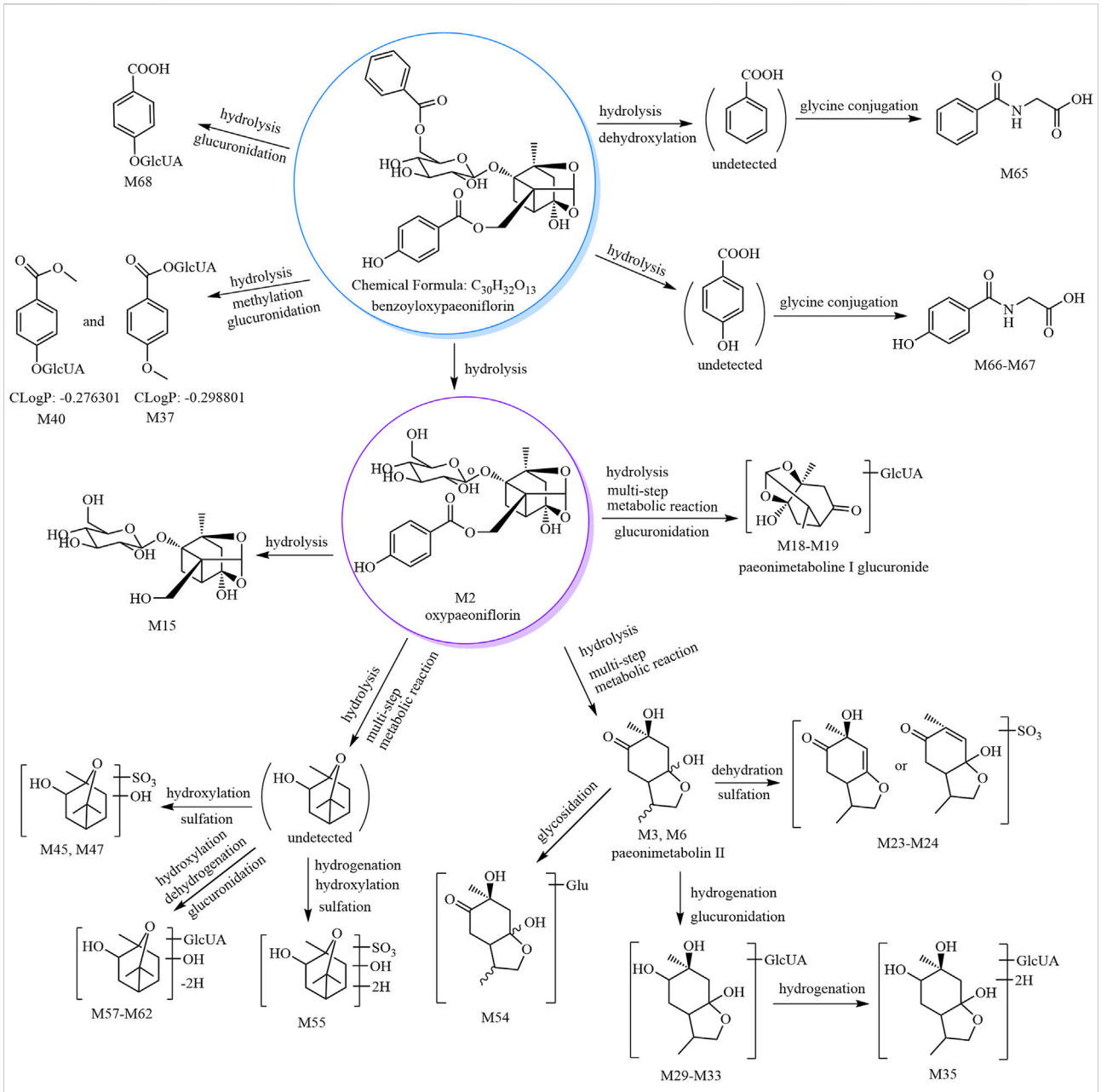

FIGURE 1
The 30 metabolites (all new) and proposed metabolic pathways of benzoyloxypaeoniflorin in mice.

were predicted as $C_{23}H_{28}O_{11}$ and $C_{23}H_{28}O_{12}$, respectively. Their retention time and mass spectral features were consistent with those of the reference substances paeoniflorin and oxypaeoniflorin (see Table 1 and Supplementary Table S1). Thus, M1 and M2 were respectively identified as paeoniflorin and oxypaeoniflorin.

As reported previously (Liang et al., 2013), M11–M13 are isomers of desbenzoylpaeoniflorin ($C_{16}H_{24}O_{10}$) derived from albiflorin. Therefore, we identified M11–M13 as desbenzoyl albiflorin isomers.

According to our previous study (Liang et al., 2013), M14–M15, M16–M17, M23–M28, M35, M36–M40, M63–M64, M65, and M66–M67 were tentatively identified as desbenzoylpaeoniflorin isomers, methyl desbenzoylpaeoniflorin isomers, $C_{10}H_{14}O_3$ sulfate isomers, $C_{10}H_{20}O_4$ glucuronide, $C_8H_8O_3$ glucuronide isomers, gallic acid sulfates, hippuric acid, and hydroxyhipuric acid, respectively.

According to the literature, M18–M22 were tentatively identified as paeonimetabolin I glucuronide isomers (Wang et al., 2017b; Sun et al., 2018); M29–M34 were tentatively

identified as $C_{10}H_{18}O_4$ glucuronide isomers (Liang et al., 2013; Sun et al., 2018), and M68 was tentatively identified as salicylic acid glucuronide (Shen et al., 2015).

3.3 Identification of the metabolites of three catechins (CG, ECG, C)

The metabolic pathway of catechin gallate is shown in Figure 2, and the metabolic pathways of other catechins are shown in Supplementary Figure S4.

3.3.1 Catechin ($C_{15}H_{14}O_6$) and its phase II metabolites (M79–M91)

M79 showed $[M-H]^-$ at *m/z* 289.07, and its molecular formula was predicted as $C_{15}H_{14}O_6$. The retention time and mass spectral data of M79 are consistent with those of catechin's reference substance (see Table 1 and Supplementary Table S1). Therefore, M79 was identified as catechin.

M80–M85 showed $[M-H]^-$ at *m/z* 369.02, and their molecular formula was predicted as $C_{15}H_{14}O_9S$. The fragment ion at *m/z* 289.07 ($C_{15}H_{13}O_6$) was formed by a neutral loss of 79.96 Da in the MS^2 spectra of M80–M85. Therefore, based on the mass spectral features and the literature (Gonzalez-Manzano et al., 2009; Rodriguez-Mateos et al., 2014), M80–M85 were predicted to be (epi)catechin sulfate isomers. In addition, in the MS^2 spectra of M81 and M84, the fragment ion at *m/z* 216.97 ($C_7H_5O_6S$) of the sulfate conjugate of the characteristic fragment ion at *m/z* 137.02 ($C_7H_5O_3$) formed after the RDA cleavage of the C-ring of catechin. Therefore, we presumed that the sulfate group bound to the hydroxyl group at C-5 or C-7. In the MS^2 spectra of M85, the ions at *m/z* 289.06 ($C_{15}H_{13}O_6$) and *m/z* 179.03 ($C_9H_7O_4$) were formed by the sequential losses of 79.96 Da (SO_3) and 110.04 Da ($C_6H_6O_2$) from the ion at *m/z* 369.02; however, no neutral loss of 82 Da (H_2SO_3) was observed. We concluded that the sulfate group did not bind to the hydroxyl group at C-3 due to the energy barrier required for bond breakage. No fragment ion was observed at *m/z* 216.97 ($C_7H_6O_6S$), and we concluded that the sulfate group did not bind to the hydroxyl group at C-5 or C-7. Hence, we assumed that the sulfate group bound to the hydroxyl group at C-3′ or C-4'.

M86–M88 showed $[M-H]^-$ at *m/z* 465.10, and their molecular formula was predicted as $C_{21}H_{22}O_{12}$. The ion at *m/z* 289.06 ($C_{15}H_{13}O_6$) was formed by a neutral loss of 176.03 Da ($C_6H_8O_6$) in the MS^2 spectra. According to the literature (Gonzalez-Manzano et al., 2009; Liang et al., 2013; Rodriguez-Mateos et al., 2014), M86–M88 were predicted to be catechin glucuronide isomers.

M89–M91 showed $[M-H]^-$ at *m/z* 545.06, and their molecular formula was predicted as $C_{21}H_{22}O_{15}S$. The fragment ions at *m/z* 369.02 ($C_{15}H_{13}O_9S$) and 289.05 ($C_{15}H_{13}O_6$) were formed by the sequential losses of 176.03 Da ($C_6H_8O_6$) and 79.96 Da (SO_3) in the MS^2 spectra. Therefore, M89–M91 were predicted to be catechin glucuronide sulfate isomers.

3.3.2 5-(3,4-Dihydroxyphenyl)-valeric acid ($C_{11}H_{14}O_4$) and its phase II metabolites (M97–M100)

M97 showed $[M-H]^-$ at *m/z* 209.08, and its molecular formula was predicted as $C_{11}H_{14}O_4$. The fragment ion at *m/z* 147.07 ($C_{10}H_{11}O$) was formed by a neutral loss of 62.01 Da (CO_2+H_2O) in the MS^2 spectrum. According to the literature (Scheline, 1970), M97 was predicted to be 5-(3,4-dihydroxyphenyl)-valeric acid.

M98–M100 showed $[M-H]^-$ at *m/z* 289.03, and their molecular formula was predicted as $C_{11}H_{14}O_7S$. The fragment ion at *m/z* 209.07 ($C_{11}H_{13}O_4$) was formed by a neutral loss of 79.96 Da (SO_3) in the MS^2 spectra. Therefore, M98–M100 were predicted to be 5-(3,4-dihydroxyphenyl)-valeric acid sulfate isomers.

3.3.3 Phase II metabolites of 5-(3,4-dihydroxyphenyl)-γ-valerolactone ($C_{11}H_{12}O_4$) (M103–M108)

M103–M106 and M107–M108 showed $[M-H]^-$ at *m/z* 287.02 and 383.09, respectively, and their molecular formulae were predicted as $C_{11}H_{12}O_7S$ and $C_{17}H_{20}O_{10}$, respectively. The fragment ion at *m/z* 207.05 ($C_{11}H_{11}O_4$) was formed by a neutral loss of 79.96 Da (SO_3) from the ion at *m/z* 287.02 and a neutral loss of 176.03 Da ($C_6H_8O_6$) from the ion at *m/z* 383.09 in the MS^2 spectra. Based on our previous report (Liang et al., 2013) and a report of 5-(3,4-dihydroxyphenyl)-γ-valerolactone (Kohri et al., 2003), we presumed that M103–M106 were 5-(3,4-dihydroxyphenyl)-γ-valerolactone sulfate isomers, while M107–M108 were 5-(3,4-dihydroxyphenyl)-γ-valerolactone glucuronide isomers.

3.3.4 Identification of methyl catechin gallate (M112)

M112 showed $[M-H]^-$ at *m/z* 455.09, and its molecular formula was predicted as $C_{23}H_{20}O_{10}$. The fragment ion at *m/z* 303.08 ($C_{16}H_{15}O_6$) was formed by a neutral loss of 152.01 Da ($C_7H_4O_4$, galloyl) in the MS^2 spectrum, and the signal at *m/z* 303.08 indicated an additional methyl group compared to catechin ($C_{15}H_{13}O_6$). Thus, M112 was predicted to having a methylcatechin skeleton. In addition, the fragment ion at *m/z* 169.01 ($C_7H_5O_5$, gallic acid group) was observed; thus, its structure was presumed to contain a gallic acid group. Comparison of the molecular formula of M112 ($C_{23}H_{20}O_{10}$) with that of the original constituent (catechin gallate, $C_{22}H_{18}O_{10}$) suggested that M112 was a methylated product of catechin gallate. According to a previous report, M112 was predicted to be methyl catechin gallate (Kohri et al., 2003).

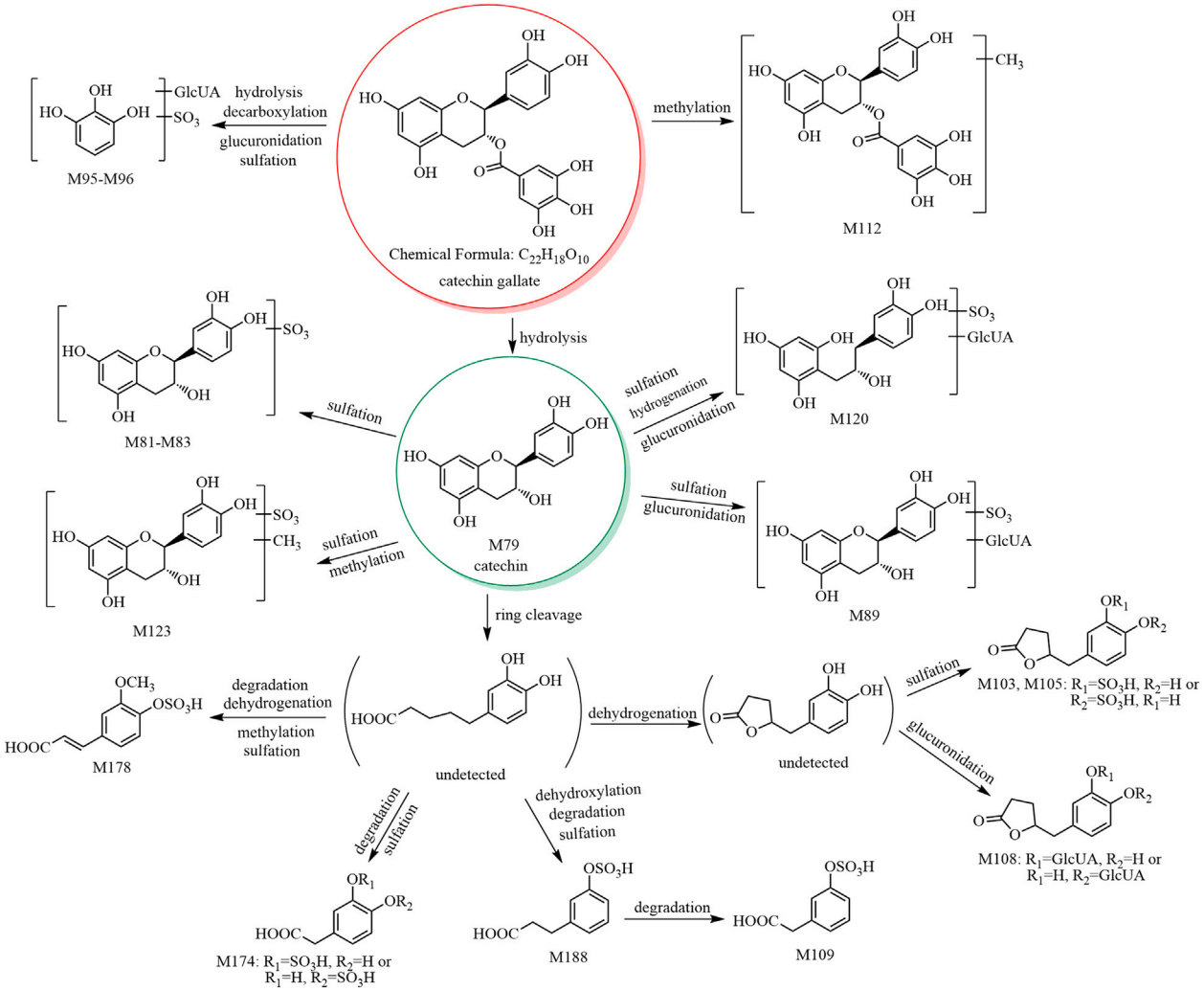

FIGURE 2
The 17 metabolites (all new) and proposed metabolic pathways of catechin gallate in mice.

3.3.5 3,4-DiHPP-2-ol ($C_{15}H_{16}O_6$) and its phase II metabolites (M113–M119, M120)

M113–M119 showed $[M-H]^-$ at *m/z* 291.08, and their molecular formula was predicted as $C_{15}H_{16}O_6$. Based on the literature (Hara-Terawaki et al., 2017) and the origins of the metabolites (M113 was derived from catechin, while M114–M119 were derived from PRR decoction), M113 was tentatively identified as 3,4-diHPP-2-ol, while M114–M119 are isomers of M113 and were thus predicted to be 3,4-diHPP-2-ol isomers.

M120 showed $[M-H]^-$ at *m/z* 547.14, and its molecular formula was predicted as $C_{21}H_{24}O_{15}S$. The characteristic ion at *m/z* 371.11 ($C_{15}H_{15}O_9S$) was formed by a neutral loss of 176.03 Da ($C_6H_8O_6$) in the MS^2 spectrum. Therefore, M120 was tentatively identified as 3,4-diHPP-2-ol glucuronide sulfate.

3.3.6 Phase II metabolites of methyl catechin ($C_{16}H_{16}O_6$) (M122–M126, M127–M129, and M130–M132)

M122–M126 showed $[M-H]^-$ at *m/z* 383.04, and their molecular formula was predicted as $C_{16}H_{16}O_9S$. The ion at *m/z* 303.08 ($C_{16}H_{15}O_6$) of aglycone methylcatechin was formed by a neutral loss of 79.96 Da (SO_3) in the MS^2 spectra. In addition, the fragment ions at *m/z* 216.97 ($C_7H_5O_6S$) and 137.02 ($C_7H_5O_3$) were observed in all these metabolites except M124; hence, we concluded that the sulfate groups of M122, M123, M125, and M126 bind to the hydroxyl group at C-5 or C-7, and the methylation reaction occurs at the hydroxyl group at C-3, C-3′, or C-4′. According to our previous study (Liang et al., 2013), M122–M126 were predicted to be methyl catechin sulfate isomers.

M127–M129 showed $[M-H]^-$ at *m/z* 479.11, and their molecular formula was predicted as $C_{22}H_{24}O_{12}$. The fragment ion at *m/z* 303.08 ($[aglycone-H]^-$, $C_{16}H_{15}O_6$) was formed by a neutral loss of 176.03 Da ($C_6H_8O_6$) in the MS^2 spectra. The fragment ion at *m/z* 313.0573 ($C_{13}H_{13}O_9$) was observed in the MS^2 spectrum of M129, indicating that the glucuronide group binds to the hydroxyl group at C-5 or C-7, and the methylation reaction occurs at the hydroxyl group at C-3, C-3′, or C-4′. According to our previous study (Liang et al., 2013), M127–M129 were predicted to be methyl catechin glucuronide isomers.

M130–M132 showed $[M-H]^-$ at *m/z* 559.07, and its molecular formula was predicted as $C_{22}H_{24}O_{15}S$. The fragment ions at *m/z* 383.04 ($C_{16}H_{15}O_9S$) and 303.08 ($[aglycone-H]^-$, $C_{16}H_{15}O_6$) were formed by sequential losses of 176.03 Da ($C_6H_8O_6$) and 79.96 Da (SO_3) in the MS^2 spectra. Therefore, M130–M132 were predicted to be methyl catechin glucuronide sulfate isomers.

3.3.7 Other metabolites of catechins

M92–M94, M95–M96, M101–M102, M109, M110–M111, M121, M133, and M134–M135 showed $[M-H]^-$ at *m/z* 355.04, 381.01, 305.03, 273.00, 271.02, 531.08, 242.99, and 216.98, respectively, and their molecular formulae were predicted as $C_{15}H_{16}O_8S$, $C_{12}H_{14}O_{12}S$, $C_{11}H_{14}O_8S$, $C_{10}H_{10}O_7S$, $C_{11}H_{12}O_6S$, $C_{21}H_{24}O_{14}S$, $C_9H_8O_6S$, and $C_7H_6O_6$, respectively. According to our previous study (Liang et al., 2013), M92–M94, M95–M96, M101–M102, M109, M110–M111, M121, M133, and M134–M135 were predicted to be 3-HPP-2-ol sulfate isomers, pyrogallol-*O*-glucuronide sulfates, trihydroxy benzenepentanoic acid sulfate isomers, ferulic acid sulfate, 5-(3-hydroxyphenyl)-γ-valerolactone sulfate isomers, 3-HPP-2-ol glucuronide sulfate, *m*-coumaric acid sulfate, and 3/4-hydroxy benzoic acid sulfate isomers, respectively.

3.4 Metabolites of two ellagic acid compounds (EA and DEA)

The metabolic pathway of 3,3′-di-*O*-methylellagic acid is shown in Figure 3, and the metabolic pathway of ellagic acid is shown in Supplementary Figure S5.

M136 and M137 showed $[M-H]^-$ at *m/z* 394.97, and their molecular formula was predicted as $C_{15}H_8O_{11}S$. The fragment ions at *m/z* 315.01 ($C_{15}H_7O_8$) and *m/z* 299.98 ($C_{14}H_4O_8$, ellagic acid) were formed by sequential losses of 79.96 Da (SO_3) and 15.02 Da ($CH_3\bullet$) in the MS^2 spectra. Therefore, M136 and M137 were predicted to be methyl ellagic acid sulfate and isomers.

M138 and M139–M141 showed $[M-H]^-$ at *m/z* 306.99 and *m/z* 290.99, respectively, and their molecular formulae were predicted as $C_{13}H_8O_7S$ and $C_{13}H_8O_6S$, respectively. M138 was predicted to be urolithin A sulfate (Espin et al., 2013), while M139–M141 were predicted as urolithin B sulfate and isomers (Wang et al., 2017a).

Isomer ($C_{16}H_{10}O_8$, M142) and phase II metabolites (M143–M144, M145–M146) of 3,3′-di-*O*-methylellagic acid were tentatively identified as follows. M142 showed $[M-H]^-$ at *m/z* 329.03, and its molecular formula was predicted as $C_{16}H_{10}O_8$. The fragment ions in its MS^2 spectrum were consistent with those of the 3,3′-di-*O*-methylellagic acid reference compound; however, the retention times were different. M142 was therefore predicted to be an isomer of 3,3′-di-*O*-methylellagic acid. M143–M144 showed $[M-H]^-$ at *m/z* 408.98, and their molecular formula was predicted as $C_{16}H_{10}O_{11}S$. The fragment ion at *m/z* 329.02 ($[aglycone-H]^-$, $C_{16}H_9O_8$) was formed by a neutral loss of 79.96 Da (SO_3) in the MS^2 spectra. The ions at *m/z* 314.00 ($C_{15}H_6O_8$) and *m/z* 298.98 ($C_{14}H_3O_8$) were consistent with the 3,3′-di-*O*-methylellagic acid reference compound. Thus, M143–M144 were predicted to be 3,3′-di-*O*-methylellagic acid sulfates. M145–M146 showed $[M-H]^-$ at *m/z* 505.06, and their molecular formula was predicted as $C_{22}H_{18}O_{14}$. The fragment ion at *m/z* 329.03 ($[aglycone-H]^-$, $C_{16}H_9O_8$) was formed by a neutral loss of 176.03 Da ($C_6H_8O_6$) in the MS^2 spectra; hence, M145–M146 were predicted to be 3,3′-di-*O*-methylellagic acid glucuronides.

3.5 Identification of the metabolites of methyl gallate

The metabolic pathway of methyl gallate is shown in Figure 4.

3.5.1 Phase II metabolites of methyl gallate ($C_8H_8O_5$) (M147–M155, M156–M159, M160–M161, M162)

M147–M155 showed $[M-H]^-$ at *m/z* 262.98, and their molecular formula was predicted as $C_8H_8O_8S$. The fragment ion at *m/z* 183.02 ($[aglycone-H]^-$, $C_8H_7O_5$) was formed by a neutral loss of 79.96 Da (SO_3) in the MS^2 spectra. Due to its chemical structure, methyl gallate is unlikely to produce the metabolites of these nine sulfate conjugates. Thus, we speculated that the aglycones of M147–M155 may be methyl gallate and methylgallic acid, which are isomers. These two isomers show different relative abundances of the characteristic ions at *m/z* 168.00 and *m/z* 124.01; for methyl gallate, the relative abundance of the characteristic ion at *m/z* 124.01 is higher than that at *m/z* 168.00, whereas the opposite is true for methylgallic acid. The MS^2 spectra of both M147 and M151 showed higher relative abundances of the characteristic ion at *m/z* 124.01 compared to that at *m/z* 168.00; thus, they were predicted to be methyl gallate sulfates. The other metabolites (M148–M150 and M152–M155) were predicted to be methyl gallate sulfate isomers and potentially originated from the metabolic reactions of methyl gallate (e.g., hydroxylation, dehydroxylation, hydrolysis, methylation, and sulfation).

M156–M159 showed $[M-H]^-$ at *m/z* 359.06, and their molecular formula was predicted as $C_{14}H_{16}O_{11}$. The fragment

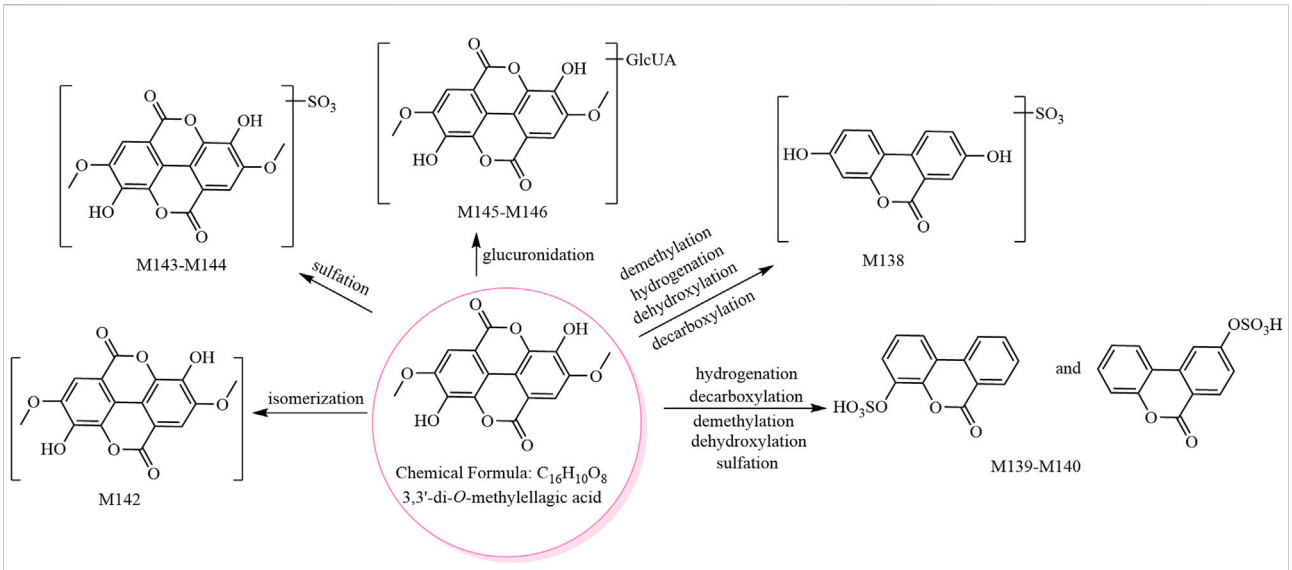

FIGURE 3
The eight metabolites (all new) and proposed metabolic pathways of 3,3′-di-*O*-methylellagic acid in mice.

ion at *m/z* 183.02 ([aglycone–H]$^-$, $C_8H_7O_5$) was formed by a neutral loss of 176.03 Da ($C_6H_8O_6$) in the MS^2 spectra of M156–M158. Thus, M156–M158 were predicted to be methyl gallate glucuronides. M159 was predicted as a methyl gallate glucuronide isomer since it is an isomer of M156–M158. Because of its chemical structure, methyl gallate is unlikely to produce the four glucuronate conjugates. Thus, we speculated that the aglycones of M156–M159 may be methyl gallate and methylgallic acid. In the MS^2 spectrum of M157, the relative abundance of the characteristic ion at *m/z* 124.01 was higher than that at *m/z* 168.00; hence, M157 was tentatively identified as methyl gallate glucuronide, whereas M156, M158, and M159 had insufficient characteristic ions and could only be identified as methyl gallate glucuronide isomers.

M160 and M161 showed [M–H]$^-$ at *m/z* 535.09, and their molecular formula was predicted as $C_{20}H_{24}O_{17}$. The fragment ions at *m/z* 359.06 ($C_{14}H_{15}O_{11}$) and *m/z* 183.02 ([aglycone–H]$^-$, $C_8H_7O_5$) were formed by sequential losses of two 176.03 Da ($C_6H_8O_6$) in the MS^2 spectra. Hence, M160–M161 were predicted to be methyl gallate diglucuronides.

M162 showed [M–H]$^-$ at *m/z* 439.01, and its molecular formula was predicted as $C_{14}H_{16}O_{14}S$. The fragment ions at *m/z* 262.97 ($C_8H_7O_8S$) and *m/z* 183.01 ([aglycone–H]$^-$, $C_8H_7O_5$) were formed by sequential losses of 176.03 Da ($C_6H_8O_6$) and 79.96 Da (SO_3) in the MS^2 spectra. Therefore, M162 was predicted as methyl gallate sulfate glucuronide.

3.5.2 Phase II metabolites of methylated methyl gallate ($C_9H_{10}O_5$) (M163–M165, M166–M168)

M163–M165 showed [M–H]$^-$ at *m/z* 373.07, and their molecular formula was predicted as $C_{15}H_{18}O_{11}$. The fragment ion at *m/z* 175.02 ($C_6H_7O_6$) was observed in the MS^2 spectra of M163–M165, suggesting the aglycone to be $C_9H_{10}O_5$. The fragment ion at *m/z* 183.01 ($C_8H_7O_5$, methyl gallate) was also observed, suggesting the aglycone to be methylated methyl gallate ($C_9H_{10}O_5$).

M166–M168 showed [M–H]$^-$ at *m/z* 277.00, and their molecular formula was predicted as $C_9H_{10}O_8S$. The fragment ion at *m/z* 197.04 ([aglycone–H]$^-$, $C_9H_9O_5$) was formed by a neutral loss of 79.96 Da (SO_3) in the MS^2 spectra.

Therefore, M163–M165 and M166–M168 were predicted as methylated methyl gallate glucuronide isomers and methylated methyl gallate sulfate isomers, respectively.

3.5.3 Phase II metabolite of dimethylated methyl gallate (M169)

M169 showed [M–H]$^-$ at *m/z* 291.01, and its molecular formula was predicted as $C_{10}H_{12}O_8S$. The fragment ions at *m/z* 211.06 ($C_{10}H_{11}O_5$) and 196.03 ($C_9H_8O_5$) were formed by sequential losses of 79.96 Da (SO_3) and 15.02 Da ($CH_3\bullet$) in the MS^2 spectrum. Therefore, M169 was predicted to be dimethylated methyl gallate sulfate.

3.6 Identification of metabolites derived from compounds with different structure types

M171–M176, M177–M180, M181–M186, M187–M191, and M192–M195 showed [M–H]$^-$ at *m/z* 230.99, 245.01, 261.00, 246.99, and 319.04, respectively, and their molecular formulae were predicted as $C_8H_8O_6S$, $C_9H_{10}O_6S$, $C_9H_{10}O_7S$, $C_8H_8O_7S$, and $C_{12}H_{16}O_8S$, respectively.

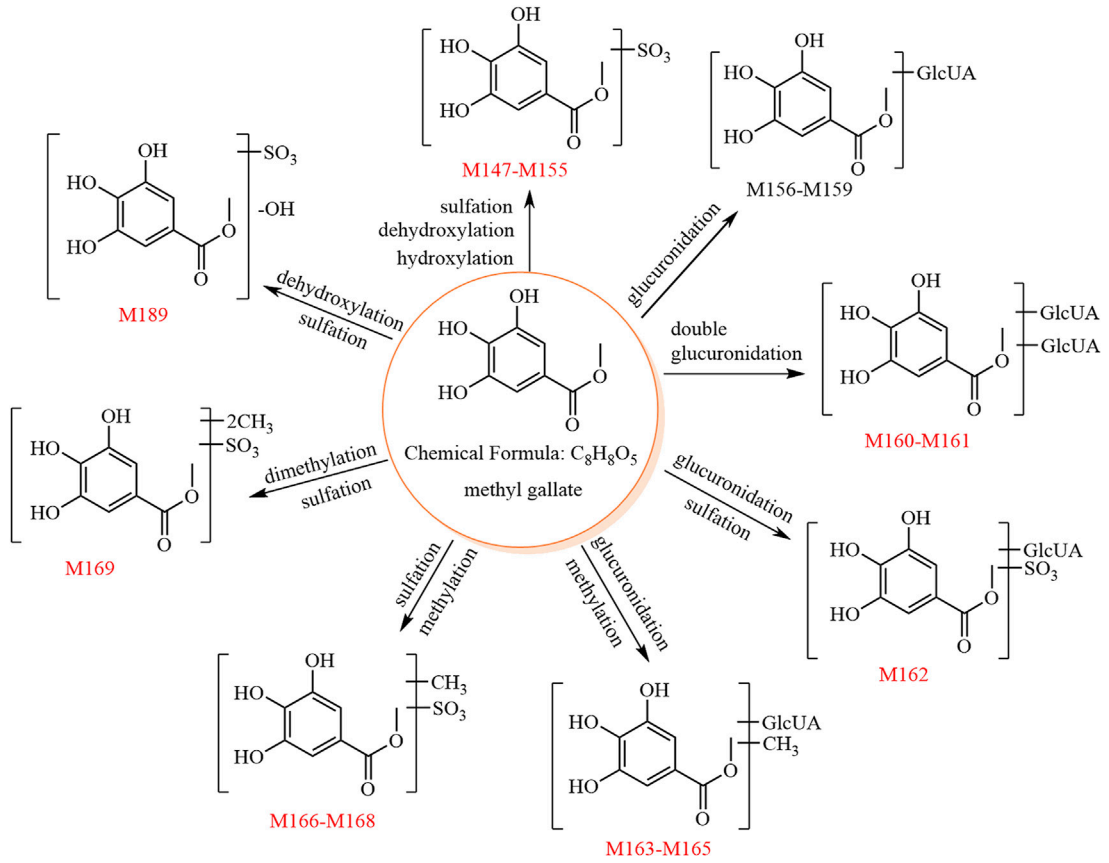

FIGURE 4
The 24 metabolites and proposed metabolic pathways of methyl gallate in mice. The red numbers denote new metabolites.

Based on our previous study (Liang et al., 2013), M171–M176, M177–M180, M181–M186, M187–M191, and M192–M195 were predicted as 3/4-hydroxy phenylacetic acid sulfate and its isomers, 3/4-hydroxy phenylpropionic acid sulfate and its isomers, 3,4-dihydroxy phenylpropionic acid sulfate and its isomers, 3,4-dihydroxy phenylacetic acid sulfate and its isomers, and dihydroxylated methoxylated benzenepentanoic acid sulfate and its isomers, respectively.

M171–M176, M177–M180, M181–M186, and M192–M195 are all derived from paeoniflorins and catechins, while M187–M191 are derived from paeoniflorins, catechins, and gallic acids.

3.7 Identification of the metabolites of PRR

A total of 31 PRR metabolites were identified (Supplementary Figure S6), the analyses of 30 metabolites were consistent with the above (except M170).

M170 showed $[M-H]^-$ at *m/z* 187.00, and its molecular formula was predicted as $C_7H_8O_4S$. The characteristic fragment ion at *m/z* 107.05 (C_7H_7O) was formed by a neutral loss of 79.96 Da (SO_3) in its MS^2 spectrum. Based on a previous report (Liu et al., 2020), M170 was tentatively identified as benzyl alcohol sulfate.

4 Discussion

4.1 Origins of PRR metabolites in mice

A total of 31 metabolites of PRR were identified in mice in this study. The metabolites of 14 PRR constituents were compared, and the relevant literature was analyzed to determine their possible origins. Finally, we identified 13 metabolites derived from catechins (M114–M119, M135, M175–M176, M185–M186, M191, and M195), 14 derived from paeoniflorins (M4–M5, M17, M34, M48–M51, M53, M56, M70, and M72–M74), two derived from ellagic acids (M140–M141), and two derived from other constituents (M65 and M170).

In rats, our previous research (Liang et al., 2013) identified 27, 27, six, 25, and five PRR metabolites derived from catechins,

gallic acids, catechins and gallic acids, paeoniflorins, and other constituents, respectively. In comparison, we identified 20 new metabolites formed by hydroxylation, hydrogenation, glucuronidation, and sulfation in mice: seven catechin-related metabolites (M114–M119, 3,4-diHPP-2-ol isomers; and M195, dihydroxylated methoxylated benzenepentanoic acid sulfate); 10 paeoniflorin-related metabolites (M48–M49, 2,6-dihydroxycineol sulfate isomers; M50, M51, and M53, paeonimetabolin II glucoside isomers; M56, hydrogenated 2,6-dihydroxycineol sulfate; M70, hydrogenated lactiflorin isomer; and M72–M74, hydrogenated hydroxylated lactiflorin isomers); two ellagic acid-related metabolites (M140–M141, urolithin B sulfate isomers); and one other metabolite (M170, benzyl alcohol sulfate).

In our previous research (Liang et al., 2013), the administered dosage in male Sprague–Dawley rats was 9.96 g PRR crude drug/kg rat body weight (equivalent to 18.99 g PRR crude drug/kg of mouse body weight). Pre-experiments revealed that the administration of a high dosage of PRR to ICR mice may lead to diarrhea. Therefore, the administered dosage of PRR in this study was 200 mg crude drug/kg mouse body weight, a much lower dosage than that administered in rats. Due to the lower PRR dose used in this study, we did not expect to discover more metabolites of PRR than that previously reported in rats. In addition, significant species differences have been reported in phase I and phase II metabolism (Qin et al., 2021); hence, the 20 new metabolites of PRR identified in mice might be explained by species differences. PRR produces 11 identical metabolites in rats and mice: paeonimetabolin II and its isomers (M4 and M5); $C_{10}H_{18}O_4$ glucuronide (M34); methyl dibenzoylpaeoniflorin isomer (M17); 3/4-hydroxy phenylacetic acid sulfate isomers (M175–M176); 3,4-dihydroxy phenylpropionic acid sulfate isomers (M185–M186); 3,4-dihydroxy phenylacetic acid sulfate (M191); 3/4-hydroxy benzoic acid sulfate isomer (M135); and hippuric acid (M65).

4.2 New metabolites found in this study

4.2.1 New metabolites of PRR and its 14 constituents in mice

This was the first study on the *in vivo* metabolism of PRR and its 14 major constituents in mice. Thus, all the metabolites identified were newly found in mice.

4.2.2 New metabolites of PRR and each of its 14 constituents in the whole animal kingdom and microorganism

For 14 constituents of PRR, based on comparison with the literature, the following new metabolites were found in this study: eight new metabolites of paeoniflorin (M42–M47, M52, and M55) (Doyle and Griffiths, 1980; Hattori et al., 1985; Shu et al., 1987; Liang et al., 2013; Cao et al., 2015; Zhu et al., 2018); 11 new metabolites of albiflorin (M7, M9–M10, M36–M39, M45, M47, M55, and M65) (Cao et al., 2015; Wang et al., 2017b); 24 new metabolites of oxypaeoniflorin (Ml, M14–M15, M18–M19, M22, M25–M26, M28–M29, M31, M33, M41–M47, M55, M57–M58, and M60–M61) (Hattori et al., 1985); and 17 new metabolites of benzoylpaeoniflorin (Ml, M14–M15, M18–M19, M23–M24, M27, M31, M33, M43–M45, M47, M57–M58, and M61) (Hattori et al., 1985). No metabolites of hydroxybenzoylpaeoniflorin, benzoyloxypaeoniflorin, galloylpaeoniflorin, or lactiflorin had been reported *in vivo* or *in vitro*. Thus, we identified 18, 30, 27, and 17 new metabolites of hydroxybenzoylpaeoniflorin, benzoyloxypaeoniflorin, galloylpaeoniflorin, or lactiflorin, respectively, in this study.

Considering the literature (Kohri et al., 2003), we found 21 new metabolites of epicatechin gallate: M80, M92–M93, M95, M98, M109, M101, M103–M104, M107, M110, M122, M133, M134, M174, M178, M182–M183, M188, M190, and M193. No metabolites of catechin gallate had yet been reported *in vivo* or *in vitro*. Hence, we identified 17 new metabolites of catechin gallate and one new metabolite of catechin (M121) (Liang et al., 2013).

Considering the literature (Doyle and Griffiths, 1980), we found two new metabolites of ellagic acid (M136 and M137). No *in vivo* or *in vitro* metabolites of 3,3′-di-*O*-methylellagic acid had been reported; hence, we identified eight new metabolites of 3,3′-di-*O*-methylellagic acid in this study.

Considering the literature (Jiamboonsri et al., 2016), we found 20 new metabolites of methyl gallate in this study (M147–M155, M160–M169, and M189).

Considering the literature (Liang et al., 2013), 20 new metabolites (M48–M49, M51–M52, M54, M56, M70, M72–M74, M114–M119, M140–M141, and M170) of PRR decoction were found in this study.

4.2.3 New metabolites of paeoniflorins, catechins, ellagic acids, and gallic acids in the whole animal kingdom and microorganism

A total of 26 new metabolites of paeoniflorin-type compounds were found in this study. Specifically, we found eight new metabolites of paeoniflorin, six new metabolites of albiflorin, 13 new metabolites of oxypaeoniflorin, seven new metabolites of benzoylpaeoniflorin, six new metabolites of hydroxybenzoylpaeoniflorin, seven new metabolites of benzoyloxypaeoniflorin, nine new metabolites of galloylpaeoniflorin, and 12 new metabolites of lactiflorin. The 26 new metabolites were hydrogenated 2,6-dihydroxycineol sulfate isomer (M55), 2,6-dihydroxycineol sulfate isomers (M41–M47), paeonimetabolin II sulfate isomers (M7–M10), paeonimetabolin II glucoside isomers (M52 and M54), hydrogenated lactiflorin and its isomer (M69 and M70), hydrogenated hydroxylated lactiflorin isomer (M71), hydrogenated deglycosylated lactiflorin sulfates (M75–M78),

3/4-hydroxy phenylacetic acid sulfate isomers (M171 and M172), 3/4-hydroxy phenylpropionic acid sulfate (M177), 3,4-dihydroxy phenylpropionic acid sulfate (M181), and 3,4-dihydroxy phenylacetic acid sulfate (M187).

One new metabolite of each of catechin gallate and catechin was found, namely, 3,4-diHPP-2-ol glucuronide sulfate (M120) and 3-HPP-2-ol glucuronide sulfate (M121), respectively.

Eight new metabolites of ellagic acids were found in this study. Specifically, we found two new metabolites of ellagic acid [methylellagic acid sulfates (M136 and M137)] and six new metabolites of 3,3′-di-*O*-methylellagic acid [3,3′-di-*O*-methylellagic acid isomer (M142), 3,3′-di-*O*-methylellagic acid sulfates (M143 and M144), and 3,3′-di-*O*-methylellagic acid glucuronides (M145, and M146)].

Eight new metabolites of gallic acids were found in this study: methyl gallate diglucuronides (M160 and M161); methyl gallate sulfate glucuronide (M162); methylated methyl gallate glucuronides (M163–M165); dimethylated methyl gallate sulfate (M169); and 3, 4-dihydroxy phenylacetic acid sulfate isomer (M189).

4.3 Isomer metabolites produced by multiple original constituents of PRR

4.3.1 Isomer metabolites produced by compounds with the same structure type

The eight paeoniflorin constituents all produced desbenzoylpaeoniflorin isomers (M11–M15). Seven paeoniflorin constituents (all except lactiflorin) produced 2,6-dihydroxycineol sulfate isomers (M41–M47). Seven paeoniflorin constituents (all except albiflorin) produced paeonimetabolin I glucuronide isomers (M18–M22) and $C_{10}H_{18}O_4$ glucuronide isomers (M29–M34). Six paeoniflorin constituents (all except albiflorin and lactiflorin) produced $C_{10}H_{14}O_3$ sulfate isomers (M23–M28), hydrogenated 2,6-dihydroxycineol sulfate isomer (M55), and dehydrogenated 2,6-dihydroxycineol glucuronide isomers (M57–M62). Albiflorin, benzoyloxypaeoniflorin, and galloylpaeoniflorin produced $C_8H_8O_3$ glucuronide isomers (M36–M40) and hippuric acid (M65). Paeoniflorin, benzoyloxypaeoniflorin, and galloylpaeoniflorin produced paeonimetabolin II glucoside isomers (M50–M54). Albiflorin, hydroxybenzoylpaeoniflorin, and galloylpaeoniflorin produced paeonimetabolin II sulfate isomers (M7–M10). Albiflorin, benzoylpaeoniflorin, hydroxybenzoylpaeoniflorin, and galloylpaeoniflorin all produced paeoniflorin (M1). Paeoniflorin, hydroxybenzoylpaeoniflorin, and benzoyloxypaeoniflorin all produced oxypaeoniflorin (M2). Both benzoyloxypaeoniflorin and galloylpaeoniflorin produced paeonimetabolin II isomers (M3 and M6).

All three catechin constituents produced (epi)catechin sulfate isomers (M80–M85), 5-(3,4-dihydroxyphenyl)-γ-valerolactone sulfate isomers (M103–M106), and methyl-catechin sulfates (M122–M126). Both catechin gallate and catechin produced catechin glucuronide sulfates (M89–M91). Both epicatechin gallate and catechin produced 3-HPP-2-ol sulfate isomers (M92–M94), 5-(3,4-dihydroxyphenyl)-valeric acid sulfate isomers (M98–M100), trihydroxy-benzenepentanoic acid sulfate isomers (M101–M102), and 5-(3-hydroxyphenyl)-γ-valerolactone sulfate isomers (M110–M111). Both epicatechin gallate and catechin gallate produced pyrogallol-*O*-glucuronide sulfate isomers (M95–M96) and 5-(3,4-dihydroxyphenyl)-γ-valerolactone glucuronide isomers (M107–M108).

Both ellagic acid constituents produced urolithin B sulfate isomers (M139–M141).

4.3.2 Isomer metabolites produced by compounds with different structure types

Lactiflorin and the three catechin constituents produced 3-hydroxy phenylacetic acid sulfate isomers (M171–M176) and 3/4-hydroxy phenylpropionic acid sulfate isomers (M177–M180).

Lactiflorin, epicatechin gallate, and catechin produced 3,4-dihydroxy phenylpropionic acid sulfate isomers (M181–M186) and dihydroxy-methoxyl-benzenepentanoic acid sulfate isomers (M192–M195).

Lactiflorin, epicatechin gallate, catechin gallate, catechin, methyl gallate, and PRR produced 3,4-dihydroxy phenylacetic acid sulfate isomers (M187–M191).

4.4 Origins of the effective forms of PRR

In a previous study, we found 21 effective forms of PRR that account for its effects of clearing away heat, cooling the blood, and dissipating blood stasis (Xu et al., 2022). In this study, we elucidated some possible origins of the 10 known effective forms of PRR and their isomers:

- Desbenzoylpaeoniflorin isomer (C3) can be derived from eight original constituents: paeoniflorin, albiflorin, oxypaeoniflorin, benzoylpaeoniflorin, hydroxybenz oylpaeoniflorin, benzoyloxypaeoniflorin, galloylpae oniflorin, and lactiflorin.
- Paeoniflorin (C1) can be derived from benzoylpaeoniflorin, hydroxybenzoylpaeoniflorin, and galloylpaeoniflorin.
- Oxypaeoniflorin (C2) can be derived from paeoniflorin, hydroxybenzoylpaeoniflorin, and benzoyloxypaeoniflorin.
- 3/4-Hydroxy benzoic acid sulfate (C8) isomer can be derived from epicatechin gallate.
- $C_{10}H_{18}O_4$ glucuronide (C16) isomer can be derived from seven prototype paeoniflorin constituents (all except albiflorin).
- $C_8H_8O_3$ glucuronide isomers (C19 and C20) can be derived from albiflorin, benzoyloxypaeoniflorin, and galloylpa eoniflorin.
- 3′-*O*-methyl (epi)catechin 5-*O*-glucuronide (C5) isomer can be derived from catechin.

- 3-Hydroxy phenylpropionic acid sulfate (C6) isomer can be derived from lactiflorin, epicatechin gallate, catechin gallate, and catechin.
- 3,3′-Di-*O*-methylellagic acid isomer can be isomerized from 3,3′-di-*O*-methylellagic acid.

According to our previous study (Liang et al., 2013), $C_{10}H_{18}O_2$ glucuronides (C9–C15) and $C_{10}H_{14}O_3$ glucuronide (C17), two effective forms of PRR, can be derived from paeoniflorin in rats; however, their origins could not be determined in this study. Other effective forms of PRR including 3-hydroxy-4-methoxy-phenylpropionic acid sulfate (C7), 3-methoxy-4-hydroxy-phenylpropionic acid sulfate (C18), and benzoyl glucuronide (C21) can be derived from catechins in rats (Liang et al., 2013), but their specific origins need further investigation.

4.5 Insights for the quality control of PRR

Seventeen of the effective forms of PRR are metabolites that are not present in PRR and cannot be used for quality control. This study identified some of the precursors of the 10 effective forms of PRR, which can be used as indicators for the quality control of PRR.

5 Conclusion

This was the first study on the *in vivo* metabolism of PRR and its 14 constituents in mice. The metabolites were identified by the HPLC-DAD-ESI-IT-TOF-MS^n. In total, we identified 23, 16, 24, 17, 18, 30, 27, 17, 22, 17, 33, 3, 8, 24, and 31 metabolites of paeoniflorin, albiflorin, oxypaeoniflorin, benzoylpaeoniflorin, hydroxybenzoylpaeoniflorin, benzoyloxypaeoniflorin, galloylpaeoniflorin, lactiflorin, epicatechin gallate, catechin gallate, catechin, ellagic acid, 3,3′-di-*O*-methylellagic acid, methylgallate, and PRR, respectively, in mice. The main metabolic reactions included methylation, hydrogenation, hydrolysis, hydroxylation, glucuronidation, and sulfation. We elucidated the metabolites and metabolic pathways of the 14 constituents of PRR, including paeoniflorins, catechins, ellagic acids, and gallic acids, in mice, and clarified the possible origins of the 10 known effective forms of PRR and their isomers. The findings will facilitate further studies on the effective forms of PRR *in vivo* and are of great significance for exploring the mechanisms of action and quality control of PRR.

Data availability statement

The original contributions presented in the study are included in the article/Supplementary Material, further inquiries can be directed to the corresponding authors.

Ethics statement

The animal study was reviewed and approved by the Biomedical Ethical Committee of Peking University (approval no. LA2019117).

Author contributions

FX and S-QC designed the study. JZ (first author), YL, and JZ (third author) performed the experiment. X-YG, J-JX, P-PW, X-TC, and L-HX participated in animal experiments. JZ (first author) and W-JS analyzed the data. JZ (first author), FX, XW, and S-QC revised the manuscript.

Funding

This study was financially supported by the National Natural Science Foundation of China (Nos. 81973472 and 81573593).

Conflict of interest

The authors declare that the research was conducted in the absence of any commercial or financial relationships that could be construed as a potential conflict of interest.

Publisher's note

Supplementary material

The Supplementary Material for this article can be found online at: https://www.frontiersin.org/articles/10.3389/fphar.2022.995641/full#supplementary-material

References

Cao, W. L., Wang, X. G., Li, H. J., Shi, X. L., Fan, W. C., Zhao, S. H., et al. (2015). Studies on metabolism of total glucosides of paeony from Paeoniae Radix Alba in rats by UPLC-Q-TOF-MS/MS. *Biomed. Chromatogr.* 29 (11), 1769–1779. doi:10.1002/bmc.3493

Doyle, B., and Griffiths, L. A. (1980). The metabolism of ellagic acid in the rat. *Xenobiotica.* 10 (4), 247–256. doi:10.3109/00498258009033752

Espin, J. C., Larrosa, M., Garcia-Conesa, M. T., and Tomas-Barberan, F. (2013). Biological significance of urolithins, the gut microbial ellagic acid-derived metabolites: The evidence so far. *Evid. Based. Complement. Altern. Med.* 2013, 270418. doi:10.1155/2013/270418

Fan, G. H., Zhu, T. Y., Wang, R., and Xiong, J. (2021). Oxypaeoniflorin prevents acute lung injury induced by lipopolysaccharide through the PTEN/AKT pathway in a sirt1-dependent manner. *Oxid. Med. Cell. Longev.* 2021, 6878026. doi:10.1155/2021/6878026

Fang, J. F., Dai, J. H., Ni, M., Cai, Z. Y., and Liao, Y. F. (2018). Catechin protects rat cardiomyocytes from hypoxia-induced injury by regulating microRNA-92a. *Int. J. Clin. Exp. Pathol.* 11 (7), 3257–3266.

Gonzalez-Manzano, S., Gonzalez-Paramas, A., Santos-Buelga, C., and Duenas, M. (2009). Preparation and characterization of catechin sulfates, glucuronides, and methylethers with metabolic interest. *J. Agric. Food Chem.* 57 (4), 1231–1238. doi:10.1021/jf803140h

Hara-Terawaki, A., Takagaki, A., Kobayashi, H., and Nanjo, F. (2017). Inhibitory activity of catechin metabolites produced by intestinal microbiota on proliferation of HeLa cells. *Biol. Pharm. Bull.* 40 (8), 1331–1335. doi:10.1248/bpb.b17-00127

Hatefi-Hesari, F., Heydari, M., Hosseinzadeh, M., Moridi, A., Bahrami, R., Khaledi, M., et al. (2021). Protective effect of ellagic acid on induced liver injury. *Rev. Bras. Farmacogn.* 31 (6), 814–823. doi:10.1007/s43450-021-00220-y

Hattori, M., Shu, Y. Z., Shimizu, M., Hayashi, T., Morita, N., Kobashi, K., et al. (1985). Metabolism of paeoniflorin and related-compounds by human intestinal bacteria. *Chem. Pharm. Bull.* 33 (9), 3838–3846. doi:10.1248/cpb.33.3838

Jiamboonsri, P., Pithayanukul, P., Bavovada, R., Leanpolchareanchai, J., Gao, S., and Hu, M. (2016). *In vitro* glucuronidation of methyl gallate and pentagalloyl glucopyranose by liver microsomes. *Drug Metab. Pharmacokinet.* 31 (4), 292–303. doi:10.1016/j.dmpk.2016.04.003

Jose Cuevas, M., Almar, M., and Gonzalez-Gallego, J. (2002). Effects of epomediol on ethinyloestradiol-induced changes in glutathione homeostasis in the rat. *Pharmacol. Toxicol. Oxf. U. K.)* 90 (3), 121–126. doi:10.1034/j.1600-0773.2002.900302.x

Kadowaki, M., Ootani, E., Sugihara, N., and Furuno, K. (2005). Inhibitory effects of catechin gallates on o-methyltranslation of protocatechuic acid in rat liver cytosolic preparations and cultured hepatocytes. *Biol. Pharm. Bull.* 28 (8), 1509–1513. doi:10.1248/bpb.28.1509

Kohri, T., Suzuki, M., and Nanjo, F. (2003). Identification of metabolites of (-)-epicatechin gallate and their metabolic fate in the rat. *J. Agric. Food Chem.* 51 (18), 5561–5566. doi:10.1021/jf034450x

Kurbitz, C., Heise, D., Redmer, T., Goumas, F., Arlt, A., Lemke, J., et al. (2011). Epicatechin gallate and catechin gallate are superior to epigallocatechin gallate in growth suppression and anti-inflammatory activities in pancreatic tumor cells. *Cancer Sci.* 102 (4), 728–734. doi:10.1111/j.1349-7006.2011.01870.x

Lee, I. S., Jung, S. H., and Kim, J. S. (2018). Polyphenols from Euphorbia pekinensis inhibit AGEs formation *in vitro* and vessel dilation in larval zebrafish *in vivo*. *Planta Med.* 84 (3), 176–181. doi:10.1055/s-0043-120447

Liang, J., Xu, F., Zhang, Y. Z., Huang, S., Zang, X. Y., Zhao, X., et al. (2013). The profiling and identification of the absorbed constituents and metabolites of Paeoniae Radix Rubra decoction in rat plasma and urine by the HPLC-DAD-ESI-IT-TOF-MSn technique: A novel strategy for the systematic screening and identification of absorbed constituents and metabolites from traditional Chinese medicines. *J. Pharm. Biomed. Anal.* 83, 108–121. doi:10.1016/j.jpba.2013.04.029

Liu, G. Q., Dong, J., Wan, H., Wan, L. R., HASHIYukiand Chen, S. Z. (2009). ESI fragmentation studies of four tea catechins. *Chem. J. Chin. Univ.* 30 (08), 1566–1570.

Liu, G. X., Xu, F., Shang, M. Y., Wang, X., and Cai, S. Q. (2020). The Relative Content and Distribution of Absorbed Volatile Organic Compounds in Rats Administered Asari Radix et Rhizoma Are Different between Powder- and Decoction-Treated Groups. *Molecules* 25 (19), E4441. doi:10.3390/molecules25194441

Liu, P., Wang, W., Li, Q., Hu, X., Xu, B. Y., Wu, C., et al. (2021). Methyl gallate improves hyperuricemia nephropathy mice through inhibiting NLRP3 pathway. *Front. Pharmacol.* 12, 759040. doi:10.3389/fphar.2021.759040

Liu, W. J., Xie, G., Yuan, G. X., Xie, D. T., Lian, Z., Lin, Z. H., et al. (2021). 6 '-O-galloylpaeoniflorin attenuates osteoclasto-genesis and relieves ovariectomy-induced osteoporosis by inhibiting reactive oxygen species and MAPKs/c-fos/NFATc1 signaling pathway. *Front. Pharmacol.* 12. doi:10.3389/fphar.2021.641277

Qin, Z.-F., Zhang, B.-B., Xing, H., Wang, P.-L., Yang, J., Zhang, X.-J., et al. (2021). Study on metabolic dynamics, metabolic enzyme phenotype and species difference of hepatic and intestinal microsome of psoralidin. *Zhongguo Zhongyao Zazhi* 46 (13), 3410–3421. doi:10.19540/j.cnki.cjcmm.20210305.201

Rodriguez-Mateos, A., Toro-Funes, N., Cifuentes-Gomez, T., Cortese-Krott, M., Heiss, C., and Spencer, J. P. E. (2014). Uptake and metabolism of (-)-epicatechin in endothelial cells. *Arch. Biochem. Biophys.* 559, 17–23. doi:10.1016/j.abb.2014.03.014

Scheline, R. R. (1970). The metabolism of (+)-catechin to hydroxyphenylvaleric acids by the intestinal microflora. *Biochim. Biophys. Acta* 222 (1), 228–230. doi:10.1016/0304-4165(70)90373-9

Shen, Y. M., Liu, X. W., Yang, Y. J., Li, J. Y., Ma, N., and Li, B. (2015). *In vivo* and *in vitro* metabolism of aspirin eugenol ester in dog by liquid chromatography tandem mass spectrometry. *Biomed. Chromatogr.* 29 (1), 129–137. doi:10.1002/bmc.3249

Shu, Y. Z., Hattori, M., Akao, T., Kobashi, K., Kagei, K., Fukuyama, K., et al. (1987). Metabolism of paeoniflorin and related compounds by human intestinal bacteria. II. Structures of 7S- and 7R-paeonimetabolines I and II formed by Bacteroides fragilis and Lactobacillus brevis. *Chem. Pharm. Bull.* 35 (9), 3726–3733. doi:10.1248/cpb.35.3726

Sun, S. S., Zhu, L. J., Hu, Y. X., and Liu, Y. F. (2018). Studies on the metabolism of paeoniflorin in human intestinal microflora by high performance liquid chromatography/electrospray ionization/Fourier transform ion cyclotron resonance mass spectrometry and quadrupole time-of-flight mass spectrometry. *J. Chromatogr. B Anal. Technol. Biomed. Life Sci.* 1085, 63–71. doi:10.1016/j.jchromb.2018.03.042

Syed Hussein, S. S., Alfarizal Kamarudin, M. N., and Kadir, H. A. (2015). (+)-Catechin attenuates NF-κB activation through regulation of akt, MAPK, and AMPK signaling pathways in LPS-induced BV-2 microglial cells. *Am. J. Chin. Med.* 43, 927–952. doi:10.1142/S0192415X15500548

Tan, Y. Q., Chen, H. W., Li, J., and Wu, Q. J. (2020). Efficacy, chemical constituents, and pharmacological actions of Radix Paeoniae Rubra and Radix Paeoniae alba. *Front. Pharmacol.* 11, 1054. doi:10.3389/fphar.2020.01054

Wang, S. T., Chang, W. C., Hsu, C., and Su, N. W. (2017a). Antimelanogenic effect of urolithin A and urolithin B, the colonic metabolites of ellagic acid, in B16 melanoma cells. *J. Agric. Food Chem.* 65 (32), 6870–6876. doi:10.1021/acs.jafc.7b02442

Wang, Z. G., Tang, S. H., Hattori, M., Zhang, H. L., and Wu, X. H. (2017b). Simultaneous determination of paeonilactone A and paeonilactone B in rat plasma after oral administration of albiflorin by UPLC/TOF/MS following picolinoyl derivatization. *J. Chromatogr. B Anal. Technol. Biomed. Life Sci.* 1061, 327–333. doi:10.1016/j.jchromb.2017.07.047

Xu, J. J., Xu, F., Wang, W., Zhang, Y. F., Hao, B. Q., Shang, M. Y., et al. (2022). Elucidation of the mechanisms and effective substances of Paeoniae Radix Rubra against toxic heat and blood stasis syndrome with a stage-oriented strategy. *Front. Pharmacol.* 13, 842839. doi:10.3389/fphar.2022.842839

Yan, B. J., Shen, M. L., Fang, J. Y., Wei, D. N., and Qin, L. P. (2018). Advancement in the chemical analysis of Paeoniae Radix (shaoyao). *J. Pharm. Biomed. Anal.* 160, 276–288. doi:10.1016/j.jpba.2018.08.009

Zhao, D., Zhang, J., Wang, X., Wang, X., Wang, C., Wang, Y., et al. (2018). Effects of albiflorin and paeoniflorin on monoamine neurotransmitters and cAMP, cGMP in rats of liver depression by chronic immobilization stress. *Shijie Zhongyiyao* 13 (1), 146–150. doi:10.3969/j.issn.1673-7202.2018.01.037

Zhao, Y., Li, X. S., Chu, J. Z., Shao, Y. X., Sun, Y. Z., Zhang, Y. F., et al. (2021). Inhibitory effect of paeoniflorin on IgE-dependent and IgE-independent mast cell degranulation *in vitro* and vivo. *Food Funct.* 12 (16), 7448–7468. doi:10.1039/d1fo01421h

Zhong, W. C., Li, E. C., Hao, R. R., Zhang, J. F., Jin, H. T., and Lin, S. (2021). Anti-anaphylactic potential of benzoylpaeoniflorin through inhibiting HDC and MAPKs from Paeonia lactiflora. *Chin. J. Nat. Med.* 19 (11), 825–835. doi:10.1016/S1875-5364(21)60086-9

Zhu, L. J., Sun, S. S., Hu, Y. X., and Liu, Y. F. (2018). Metabolic study of paeoniflorin and total paeony glucosides from Paeoniae Radix Rubra in rats by high-performance liquid chromatography coupled with sequential mass spectrometry. *Biomed. Chromatogr.* 32 (4), e4141. doi:10.1002/bmc.4141

frontiers | Frontiers in Pharmacology

TYPE Review
PUBLISHED 18 November 2022
DOI 10.3389/fphar.2022.1040154

OPEN ACCESS

EDITED BY
Bingyou Yang,
Heilongjiang University of Chinese Medicine, China

REVIEWED BY
Fangbo Xia,
Southern Medical University, China
Guozheng Huang,
Anhui University of Technology, China

*CORRESPONDENCE
Jianxia Wen,
wenjx32@163.com

†These authors have contributed equally to this work

SPECIALTY SECTION
This article was submitted to Ethnopharmacology, a section of the journal Frontiers in Pharmacology

RECEIVED 09 September 2022
ACCEPTED 03 November 2022
PUBLISHED 18 November 2022

CITATION
Fu S, Liao L, Yang Y, Bai Y, Zeng Y, Wang H and Wen J (2022), The pharmacokinetics profiles, pharmacological properties, and toxicological risks of dehydroevodiamine: A review. *Front. Pharmacol.* 13:1040154. doi: 10.3389/fphar.2022.1040154

The pharmacokinetics profiles, pharmacological properties, and toxicological risks of dehydroevodiamine: A review

Shubin Fu[1†], Liying Liao[1†], Yi Yang[2], Yan Bai[2], Yan Zeng[2], Haoyu Wang[2] and Jianxia Wen[2*]

[1]Jiujiang Inspection and Testing Certification Center, Jiujiang, China, [2]School of Food and Bioengineering, Xihua University, Chengdu, China

Dehydroevodiamine (DHE) is a quinazoline alkaloid isolated from *Evodiae Fructus* (EF, *Wuzhuyu* in Chinese, Rutaceae family), a well-known traditional Chinese medicine (TCM) which is clinically applied to treat headache, abdominal pain, menstrual pain, abdominal distension, vomiting, acid regurgitation, *etc.* Modern research demonstrates that DHE is one of the main components of EF. In recent years, DHE has received extensive attention due to its various pharmacological activities. This review is the first to comprehensively summarize the current studies on pharmacokinetics profiles, pharmacological properties, and toxicological risks of DHE in diverse diseases. Pharmacokinetic studies have shown that DHE has a relatively good oral absorption effect in the mean concentration curves in rat plasma and high absorption in the gastrointestinal tract. In addition, distribution re-absorption and enterohepatic circulation may lead to multiple blood concentration peaks of DHE in rat plasma. DHE possesses a wide spectrum of pharmacological properties in the central nervous system, cardiovascular system, and digestive system. Moreover, DHE has anti-inflammatory effects *via* downregulating pro-inflammatory cytokines and inflammatory mediators. Given the favorable pharmacological activity, DHE is expected to be a potential drug candidate for the treatment of Alzheimer's disease, chronic stress, amnesia, chronic atrophic gastritis, gastric ulcers, and rheumatoid arthritis. In addition, toxicity studies have suggested that DHE has proarrhythmic effects and can impair bile acid homeostasis without causing hepatotoxicity. However, further rigorous and well-designed studies are needed to elucidate the pharmacokinetics, pharmacological effects, potential biological mechanisms, and toxicity of DHE.

KEYWORDS

dehydroevodiamine (DHE), *Evodiae fructus* (EF), pharmacokinetics profiles, pharmacological properties, toxicological risks

Introduction

Dehydroevodiamine (DHE, 14-Methyl-5-oxo-7,8-dihydro-5H-indolo[2′,3’:3,4]pyrido[2,1-b]quinazolin-14-ium-13-ide, Figure 1A), molecular formula: $C_{19}H_{15}N_3O$, PubChem CID: 9817839, CAS NO. 67,909–49–3, relative molecular mass: 301.3 (https://pubchem.ncbi.nlm.nih.gov/compound/9817839), is one of the natural bioactive components derived from a widely used traditional Chinese medicine (TCM), *Evodiae Fructus* (EF, *Wuzhuyu* in Chinese, *Rutaceae* family) (Figure 1B) (Park et al., 1996; Nam et al., 2016; Wang et al., 2021). For thousands of years, EF has been widely used as a central agent in classical Chinese herbal prescriptions (*Wuzhuyu* decoction and *Zuojin* formula) to treat migraine (known as “*Jueyin* headache” in ancient China) as well as other diseases (Sun et al., 2020). Currently, EF is still a commonly used drug in China for the treatment of various diseases, such as headaches, oral ulcers, menstrual discomfort, cardiovascular diseases (CVD), gastrointestinal diseases, and central nervous system diseases (Schramm and Hamburger, 2014; Tian et al., 2019). Alkaloids are traditionally considered to be the primary biologically active compounds in EF, not only because of the isolation of various types of alkaloids from herbal medicines but also because pharmacological and clinical studies have shown that the main chemical constituents in EF are alkaloids (Han et al., 2007; Gong et al., 2009). EF mainly contains chemical components such as indoloquinazoline, quinolone, limonoid alkaloids, and flavonoids (Sugimoto et al., 1998; Huang et al., 2012; Wang et al., 2013).

DHE is a white crystalline powder, which is usually soluble in methanol, ethanol, dimethyl sulfoxide (DMSO), and other organic solvents. Evodiamine (PubChem CID: 442088), rutaecarpine (PubChem CID: 65752), and DHE are the three main biological components derived from EF. All three have the same basic structure as indoloquinazoline alkaloids, with different substituents only at the N-14 atom, which might be the critical factor affecting the three-dimensional conformation change and pharmacological activities of DHE compared with the other two alkaloids (Perkins et al., 2014). In general, DHE is not commercially available. Schramm et al., devised a simple, robust, and scalable procedure to purify DHE at the Gram scale. Simultaneously, the process for the selective removal of DHE from EF extracts was also designed to deal with the drug development and clinical practice of DHE (Schramm and Hamburger, 2014).

Quantitative analysis by liquid chromatography-mass spectrometry (LC-MS) showed that the chloroform extract of 1 g of EF decoction contained 0.60 mg of DHE (Ueng et al., 2002). Due to higher polarity, DHE is the active compound in a higher yield in EF. Chromatographic separations revealed a limit of quantifications of 6.88 ng/ml for DHE in EF (Zhao et al., 2014). Modern researches confirm that DHE exerts extensive pharmacological activities *in vitro* and *in vivo*, such as anti-inflammatory, anti-hypertensive, anti-cancer, anti-thrombotic, anti-obesity, anti-cholinesterase, anti-amnestic, analgesic, neuroprotective, and vasodilatory activities (Yang et al., 1990; Wang et al., 2001; Lim et al., 2004; Zhang Y. N. et al., 2018; Tian et al., 2019; Dai et al., 2022). Thus, the potential therapeutic effects of DHE have been shown on treating Alzheimer’s disease (AD), chronic stress, amnesia, chronic atrophic gastritis (CAG), gastric ulcers, and rheumatoid arthritis (RA) (Loh et al., 2014; Schramm and Hamburger, 2014; Ahmad et al., 2021; Wen et al., 2021; Dai et al., 2022). Based on its broad effectiveness, DHE has attracted much attention as a promising chemical compound and natural product for the prevention and treatment of diverse diseases.

The pharmacokinetics profiles, pharmacological properties, toxicological risks, and biological mechanisms of DHE have been extensively reported in the past decades. However, most of the previous related studies are scattered reports, lacking a systematic and comprehensive summary and induction of DHE. Therefore, this review aims to provide a comprehensive summary and

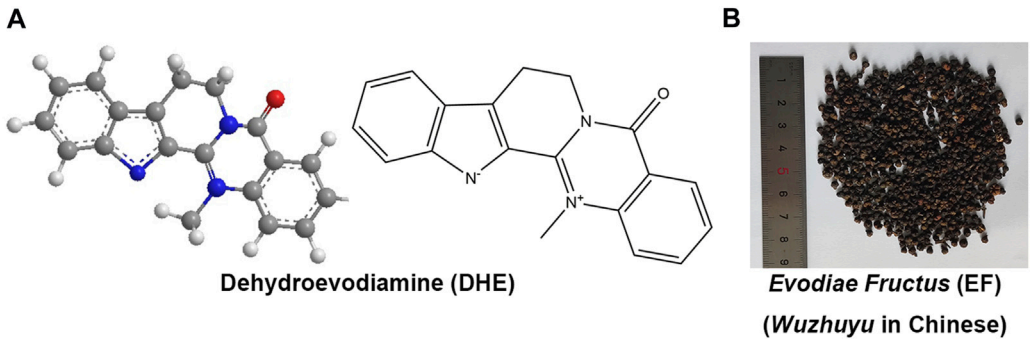

FIGURE 1
The chemical structures of DHE (PubChem CID: 9817839) **(A)** and the prepared slices of EF **(B)**. Notes: DHE, dehydroevodiamine; EF, *Evodiae Fructus*.

discussion of the latest research progress on the pharmacokinetics profiles, pharmacological properties, and toxicological risks of DHE in various diseases, which will be beneficial to the further clinical practice and application of DHE.

Materials and methods

Source material

DHE, a quinazoline alkaloid derived from *Evodiae Fructus* (EF, *Wuzhuyu* in Chinese, Rutaceae family), which is the dry near-ripe fruit of *Evodia rutaecarpa* (Juss.) Benth., *Evodia rutaecarpa* (Juss.) Benth. var. *officinalis* (Dode) Huang or *Evodia rutaecarpa* (Juss.) Benth. var. *bodinieri* (Dode) Huang (Nam et al., 2016; Wang et al., 2021). EF belongs to Rutaceae family, *Tetradium ruticarpum* (A. Juss.) T. G. Hartley [Rutaceae] (http://mpns.kew.org/mpns-portal/; http://www.plantsoftheworldonline.org). The non-scientific name, class of name, and medicinal source of EF are shown in Supplementary Table S1.

Methods

The information of this review was comprehensively searched with resources from multiple literature databases, including PubMed, EMBASE, Web of Science, Wiley Online Library, SinoMed, China National Knowledge Infrastructure (CNKI), VIP medicine information system (VMIS), Wanfang, Chinese Biomedical Database (CBM) and so on. The following search terms were used, including "dehydroevodiamine", "pharmacokinetics", "pharmacology", "toxicology" and so on. Studies concerning the role of DHE in pharmacokinetics profiles, pharmacological properties, and toxicological risks in various diseases were picked out manually. The related studies were downloaded for further evaluation.

Ethics approval and consent to participate

As this study does not involve animal and patient experiments, the ethics approval and consent to participate are not applicable.

Pharmacokinetics profiles of DHE

Studies have investigated the pharmacokinetics of DHE in rats, mice, as well as *in silicon* in recent years. Ahn et al., investigated the distribution kinetics of DHE in the rat brain (Ahn et al., 2004). The time profile of DHE plasma levels decreased in a multi-exponential manner after 15 min of intravenous infusion (at doses of 1–10 mg/kg). Moment analysis indicated that the pharmacokinetics of DHE was linear over the range examined. The concentrations of DHE in cerebrospinal fluid were negligible compared to those in plasma, indicating that the drug is not primarily distributed to the brain through the blood-cerebrospinal fluid barrier. The kinetic analysis indicates that the distribution of DHE inside and outside the brain is regulated by first-order kinetic (Table 1). Xu et al., detected the non-compartmental pharmacokinetic parameters of eight chemical components including DHE in rat plasma (Xu et al., 2013). After oral administration, the plasma concentration of DHE increased rapidly, reaching C_{max} within 1 h, and then decreased sharply in a short period of time. Moreover, the results showed that the pharmacokinetic parameters of DHE were statistically different between normal and headache rats (Table 1). The quaternary ammonium structure of DHE might serve as a suitable substrate for organic cation transporters expressed in the rat gut (Zhang et al., 1998). Therefore, DHE might be actively secreted in the gut, leading to irregular absorption patterns.

Intestinal solubility is a crucial factor affecting the absorption of various components. Zhang et al., calculated the pharmacokinetic parameters of DHE and predicted the physicochemical parameters *in silico* (Zhang Y. et al., 2018). The computer analysis of physicochemical predictions indicated an intrinsic solubility of 0.14 mg/ml for DHE. Male C57BL/6N mice were given DHE at a dose of 80 mg/kg by gavage for 21 days. Calculation of pharmacokinetic parameters showed that the C_{max} values of DHE treatment were 12.8 ± 2.39 μg/ml. Ahmad et al., selected the most active natural compounds from a library of 224, 205 compounds in the ZINC database (Ahmad et al., 2021). According to the pharmacokinetic analysis, DHE has a higher binding free energy to the acetylcholinesterase (AChE) receptor. The energy information obtained by the docking between DHE and AChE is as follows: binding energy: 9.00 kcal/mol; inhibition constant: 4.25 μM; intermolecular energy: 7.50; Van der Waals', 'Hydrogen Bond' and 'Desolvation Energy': 7.46; electrostatic energy: 0.05.

Previous studies have shown that DHE could be used as a representative component reflecting the pharmacokinetic behavior of EF alkaloids after administration of the *Zuojin* formula (*Coptidis Rhizoma*: EF = 6: 1) and *Fan-Zuojin* formula (*Coptidis Rhizoma*: EF = 1: 6). Li et al., analyzed the pharmacokinetic profiles of DHE by developed LC-MS/MS using rat plasma after a single oral administration of an extract mixture of 2 g/kg *Tetradium ruticarpum* fruit (*Wuzhuyu* in Chinese) and 2 g/kg licorice (the root and rhizome of *Glycyrrhiza uralensis* Fisch., *Glycyrrhiza glabra L.,* and *Glycyrrhiza inflata* Batal., *Glycyrrhiza uralensis* Fisch., *Gancao* in Chinese) (Li et al., 2021). The pharmacokinetic parameters of DHE show that the maximum plasma drug concentration is 8.25 ng/ml. The other pharmacokinetic values of DHE are shown in Table 1. Qian et al., performed a comprehensive pharmacokinetic study to compare

TABLE 1 Pharmacokinetic parameters of DHE.

Species	Dose of DHE	Pharmacokinetics parameters
Rats Ahn et al. (2004)	Intravenous infusion of 15 min (1–10 mg kg^{-1})	*Moment Analysis (2.5 mg kg^{-1})* $AUC_{0\to\infty}$: 52,500 ± 19,400 ng min·mL^{-1} $AUMC_{0\to\infty}$: 10,800,000 ± 3,980,000 ng min^2·mL^{-1} $MRT_{apparent}$: 197 ± 6.72 min *CL*: 53.7 ± 25.0 ml min^{-1}·kg^{-1} V_{ss}: 10,200 ± 4680 ml kg^{-1} *Simultaneous Nonlinear Regression Analysis (2.5 mg kg^{-1})* C_1: 2000 ± 1790 ng mL^{-1} C_2: 110 ± 6.94 ng mL^{-1} λ_1: 0.729 ± 0.213 min^{-1} λ_2: 0.00585 ± 0.000223 min^{-1} CL_{influx}: 0.0373 ± 0.0191 ml min^{-1} CL_{efflux}: 0.0431 ± 0.0181 ml min^{-1}
Rats Xu et al. (2013)	Intragastric administration with 6.67 g kg^{-1} *Wuzhuyu* decoction	*Normal Group* $AUC_{0\to t}$: 635.4 ± 282.0 ng h·mL^{-1} $AUC_{0\to\infty}$: 689.1 ± 268.7 ng h·mL^{-1} C_{max}: 432.4 ± 258.9 ng mL^{-1} $T_{1/2}$: 3.81 ± 2.02 h T_{max}: 0.77 ± 0.00 h *Headache Group* $AUC_{0\to t}$: 720.9 ± 220.5 ng h·mL^{-1} $AUC_{0\to\infty}$: 740.9 ± 216.6 ng h·mL^{-1} C_{max}: 564.0 ± 246.2 ng mL^{-1} $T_{1/2}$: 8.79 ± 3.27 h T_{max}: 0.77 ± 0.00 h
C57BL/6N mice Zhang et al. (2018b)	80 mg/kg DHE by gavage	*LogP*: 2.30 Permeability (cm·s^{-1}) (pH = 7.4): 2.00 × 10^{-7} Intrinsic solubility (mg·ml^{-1}) (pH = 7.4): 0.14 Topological polar surface area (Å^2): 39.1 $T_{1/2}$: 64.0 ± 3.45 min T_{max}: 60.0 ± 0.1 min C_{max}: 12.8 ± 2.39 μg ml^{-1} $AUC_{0\sim t}$: 3450 ± 34.6 μg ml^{-1}·min $AUC_{0\sim\infty}$: 4760 ± 36.1 μg ml^{-1}·min
Rats Li et al. (2021)	A single oral administration of an extract mixture of 2 g/kg *Tetradium ruticarpum* fruit and 2 g/kg licorice	C_{max}: 8.25 ± 2.48 ng mL^{-1} T_{max}: 3.77 ± 2.89 h $T_{1/2}$: 2.35 ± 1.27 h $AUC_{0\text{-}t}$: 49.65 ± 12.60 ng h·mL^{-1} $AUC_{0\text{-}C}$: 53.19 ± 12.50 ng h·mL^{-1} MRT: 5.78 ± 0.93 h *k*: 0.34 ± 0.10 h^{-1}

(Continued on following page)

TABLE 1 (*Continued*) Pharmacokinetic parameters of DHE.

Species	Dose of DHE	Pharmacokinetics parameters
Rats Qian et al. (2017)	Orally administered with 12 g/kg *Zuojin formula* (crude drug dose)	$AUC_{0\rightarrow t}$: 532.34 ± 57.78 ng h·mL^{-1} $AUC_{0\rightarrow \infty}$: 537.43 ± 54.97 ng h·mL^{-1}
		$MRT_{0\rightarrow t}$: 260.43 ± 15.40 min
		$MRT_{0\rightarrow \infty}$: 282.90 ± 34.14 min
		$T_{1/2}$: 192.57 ± 135.94 min
		T_{max}: 240 min
		C_{max}: 155.16 ± 27.92 ng mL^{-1}
		T_{sec}: 90 min
		C_{sec}: 117.29 ± 45.45 ng mL^{-1}
	Orally administered with 12 g/kg *Fan-Zuojin* formula (crude drug dose)	$AUC_{0\rightarrow t}$: 274.77 ± 23.19 ng h·mL^{-1}
		$AUC_{0\rightarrow \infty}$: 285.60 ± 24.08 ng h·mL^{-1}
		$MRT_{0\rightarrow t}$: 279.59 ± 56.33 min
		$MRT_{0\rightarrow \infty}$: 357.86 ± 114.71 min
		$T_{1/2}$: 301.96 ± 172.11 min
		T_{max}: 90 min
		C_{max}: 85.27 ± 13.37 ng mL^{-1}
Rats Yan et al. (2012)	Oral gavage with 0.18 g EF and *Zuojin* formula powder/kg body weight	EF
		$AUC_{0\rightarrow t}$: 68,130 ± 17,451 μgH·L^{-1}·h^{-1}
		$AUC_{0\rightarrow \infty}$: 68,134 ± 19,162 μgH·L^{-1}·h^{-1}
		$MRT_{0\rightarrow t}$: 4.6 ± 0.7 h
		$MRT_{0\rightarrow \infty}$: 4.6 ± 5.6 h $t_{1/2z}$: 1.6 ± 6.4 h
		T_{max}: 3.5 ± 3.0 h
		C_{max}: 15,383 ± 7,166 μgH·L^{-1}
		Zuojin Formula
		$AUC_{0\rightarrow t}$: 186,698 ± 46,442 μgH·L^{-1}·h^{-1}
		$AUC_{0\rightarrow \infty}$: 186,715 ± 39,211 μgH·L^{-1}·h^{-1}
		$MRT_{0\rightarrow t}$: 4.9 ± 0.7 h
		$MRT_{0\rightarrow \infty}$: 4.9 ± 3.6 h $t_{1/2z}$: 1.8 ± 5.4 h
		T_{max}: 1.5 ± 1.1 h
		C_{max}: 40,992 ± 21,052 μgH·L^{-1}
In silicon Ahmad et al. (2021)	Not report	With high gastrointestinal absorption
		Log *Kp* (skin permeation): 6.64 cm s^{-1}
		Bioavailability Score: 0.55

Notes: EF, evodiae fructus; AUC, area under concentration-time curve; MRT, mean residence time; CL, clearance.

the pharmacokinetic parameters between the *Zuojin* formula and the *Fan-Zuojin* formula (both are mainly composed of *Coptidis Rhizoma* and EF to illustrate the compatibility dose effect) (Qian et al., 2017). Finally, the pharmacokinetic profiles of 12 alkaloids including DHE after oral administration of the *Zuojin* formula and *Fan-Zuojin* formula were compared *in silico*. The results showed that compared with evodiamine, DHE had a higher level of systemic exposure, regardless of the dose. The C-T curve of DHE is most similar to the comprehensive C-T curve of EF alkaloids, suggesting that DHE can be considered as a representative component reflecting the pharmacokinetic behavior of EF alkaloids. After oral administration of *Wuzhuyu* decoction (6.67 g kg^{-1}) to rats in the control group and headache group. Yan et al., used a rapid LC-MS method to evaluate the comparative pharmacokinetic parameters of DHE in rats' plasma after oral administration of EF and *Coptidis Rhizoma*-EF powders (*Zuojin* formula) combination (Yan et al., 2012). The stability of low and high concentrations of DHE in rat plasma has been comprehensively evaluated under various storage and processing conditions. The stability studies have shown that DHE is stable in plasma for 4 h at room temperature (25°C), after three freeze-thaw cycles, and after the reconstitution at 25°C for 24 h. Taken together, DHE has higher exposure and is well absorbed *in vivo*. The pharmacokinetic parameters of DHE are summarized in Table 1.

TABLE 2 Pharmacological effects of DHE on various central nervous system diseases.

Pharmacological activities	Dose and route of administration	The experimental model of diseases	Mechanisms	References
Restore cognitive and memory deficits				
Reduce AD pathological damage associated with Tau	1 mg/kg, *i.p*	The 5xFAD Tg AD mouse model	Synaptic-related proteins, such as GluN2A-containing NMDARs and PSD-95, Tau protein	Kang et al. (2018)
Restore memory and cognitive impairment				
Anti-oxidation				
Inhibit neurotoxicity				
Decrease intracellular calcium levels	10 mg/kg, *p.o*	Scopolamine-induced amnesia and a $A\beta_{1\text{-}42}$-infused model	ROS, $A\beta_{1\text{-}42}$ peptide, neurotoxicity, intracellular calcium levels	Shin et al. (2017)
Restore memory and cognitive impairment				
Antagonize Aβ deposition	0.5 mg/kg, *i.p*	APP695 transgenic mice	Aβ40, Aβ42, β-secretase	Shin et al. (2016)
Improve memory impairments and depression-like behaviors	10 mg/kg, *p.o*	Immobilization-induced chronic stress in rats	NCAM proteins	Kim et al. (2014)
Anti-oxidative stress	3, 6 mg/kg, *p.o*	D-galactose-induced subacute aging model	SOD	Kang et al. (2010)
Inhibit Tau protein hyperphosphorylation				
Alleviate spatial memory deficit	6.25, 12.5 mg/kg, Tail vein injection	WT/GFX-induced tau hyperphosphorylation and memory impairment rats	GSK-3, Tau protein	Peng et al. (2007)
Decrease inhibitory phosphorylation of PP-2A at Tyr307	10, 100, 200 μM,pre-incubated at 33 °C	Calyculin A-induced AD-like tau hyperphosphorylation	Tyr307-phosphorylated PP-2A, Tau protein	Fang et al. (2007)
Anti-cholinesterase and improve Aβ type amnesia	0.3–12 mg/kg, *i.p*	Scopolamine-and Aβ peptide-(25–35)-induced amnesia in mice	Aβ peptide-(25–35)	Wang et al. (2001)
Improve impaired spatial working memory				
Improve cognitive deficits				
Reduce neuron loss and infarct size	6.25 mg/kg, *i.p*	Scopolamine-induced amnesia model of the rat, the MCA-occluded model, and the electrolytic lesioned model of the entorhinal cortex	Protective effects on cognitive deficits and neuronal loss	Park et al. (2000)
Anti-cholinesterase and anti-amnesic	6.25 mg/kg, *i.p*	Scopolamine-induced amnesia model in rats	Anti-AChE activity	Park et al. (1996)

Notes: AD, Alzheimer's disease; p. o., peros; i. p., intraperitoneal injection; ROS, reactive oxygen species; SOD, superoxide dismutase; AChE, acetylcholinesterase; GSK-3, glycogen synthase kinase-3; Aβ, β-amyloid; WT/GFX, wortmannin and GF-109203X; tg, transgenic; NMDARs, N-methyl-D-aspartate receptors; NCAM, neural cell adhesion molecule; MCA, middle cerebral artery.

Pharmacological effects of DHE

Effects of DHE on the central nervous system

DHE has a clear protective effect on the central nervous system. In recent years, a large number of literatures have reported that DHE has a preventive effect on AD induced by various models, and it exhibits good blood-brain barrier (BBB) permeability. DHE is the main component of EF for neuroprotective effect, and it has a neuroprotective effect on the PC12 cell line damaged by MPP^+ or H_2O_2 (Zhang Y. N. et al., 2018).

AD is a typical and fatal neurodegenerative condition with no available preventive treatments (Kandimalla and Reddy, 2017; Ahmad et al., 2019). Currently, cholinesterase inhibitors (ChEIs) are the treatment of choice for AD based on clinical studies on the effects of drugs on cognition (memory and attention) and behavioral symptoms (apathy and agitation) (Decker, 2005). Also, ChEIs have been officially approved clinically for the symptomatic treatment of AD (Han et al., 2019). Numerous studies claim that DHE has substantially pharmacological effects of anti-AChE and enhances cognitive function in memory-impaired rat models, and thus has the effect of treating AD. DHE exhibits strong anti-amnestic activity *in vivo* and moderate AChE inhibition *in vitro* (Table 2) (Park et al., 1996). Its efficacy

is due in part to AChE inhibition, but also the long-term promotion of synaptic transmission due to the activation of muscarinic and N-methyl-D-aspartate receptors (Park et al., 2003). Lim et al., found that DHE inhibited the uptake and release of glutamate, suggesting that chronic exposure to DHE might alter the characteristics of glutamate release and uptake in granule and glial cells (Lim et al., 2004).

It has been reported that from the comprehensive effect of cerebral blood flow enhancement and AChE inhibition, the natural product-based DHE is less effective on AChE than tacrine, but its anti-amnestic effect is more effective than that of tacrine (Park et al., 1996). The anti-AChE activity of DHE has an IC_{50} value of 37.9 μM in the treatment of AD, which could be used as a positive anti-AD drug in experimental studies (Zhang et al., 2013). Also, Jung et al., reported that the IC_{50} of DHE hydrochloride for inhibitory AChE activity was 37.8 μM (Jung and Park, 2007). Ahmad et al., concentrated on screening natural compounds capable of managing AChE from the ZINC database (224, 205 compounds) (Ahmad et al., 2021). The results indicated that DHE was one of the most potential AChE inhibitors with a free binding energy of -9.00 kcal/mol. Moreover, DHE might cross the BBB and exhibit high levels of intestinal absorption. However, researchers still need to design more experimental studies for using DHE in the treatment of AD.

Changes in compound structure always lead to changes in pharmacokinetics and pharmacological effects. Carboxy-dehydroevodiamine·HCl (cx-DHED) is a derivative of DHED, which increases its solubility in water, enhances its high bioavailability, and is superior to DHE in ameliorating memory impairment. The study by Kang et al., showed that cx-DHED has a clear therapeutic effect on 5xFAD and AD model mice by improving synaptic stability, which could dramatically reduce memory impairment, amyloid plaque numbers, and PHFs-tau, as well as synaptic instability in 5xFAD AD mice (Kang et al., 2018). Thus, these results suggested that cx-DHED could prevent the development and progression of AD pathology as well as memory deficits in 5xFAD mice (Table 2). Also, Kim et al., found that DHEHCl could prevent memory impairment and neuronal cell loss in a rat model of cognitive impairment (Kim et al., 2014). The effects of DHEHCl on stress-induced memory impairment and behavioral abnormalities were investigated. Mechanistic studies showed that DHEHCl treatment significantly restored the stress-induced reduction in neural cell adhesion molecule (NCAM) protein levels as well as cell viability (Table 2). The results suggested that DHEHCl is a potential drug candidate for memory impairment, neuronal death, and stress-induced depression.

In addition, Shin et al., investigated the effects and potential mechanism of DHE on cognitive improving effect in a scopolamine-induced amnesia model and an $A\beta_{1-42}$-infused memory-impaired rat model (Shin et al., 2017). The findings suggest that 10 mg/kg DHE (*p.o.*) has a strong protective effect against cognitive impairment via its anti-oxidant activity, such as a downregulation in ROS production, and inhibition of neurotoxicity as well as intracellular calcium levels. DHE might be a useful therapeutic agent for symptoms of memory impairment such as AD (Table 2). Fang et al., investigated the effect of DHE on the protein phosphatase (PP)-2A and the PP-1 inhibitor calyculin A (CA)-induced AD-like tau hyperphosphorylation, and its involvement in PP-2A content in metabolically competent rat brain slices (Table 2) (Fang et al., 2007). Rat brain sections were pre-incubated for 1 h at 33 °C in the presence or absence of DHE (10, 100, and 200 μM, respectively). Then CA 0.1 μM was added and treated for another 2 h. DHE was found to relieve CA-induced tau hyperphosphorylation at multiple AD-associated sites in metabolically active rat brain slices. The underlying mechanism may involve decreased inhibitory phosphorylation of PP-2 A at Tyr307. Wang et al., examined the protective effects of DHE (0.75–12.0 mg/kg, *i. p.*) on scopolamine-as well as β-amyloid (Aβ) peptide-(25–35)-induced amnesia in mice via a step-through passive avoidance test (Table 2) (Wang et al., 2001). It was found that DHE was more effective in amnesia-induced amnesia than Aβ peptide-(25–35)-induced amnesia. DHE has the effect of anti-cholinesterase, and may also be a new effective ligand for improving Aβ amnesia.

Since DHE readily crosses the BBB, it has been reported to have minimal side effects and doses among cholinesterase inhibitors (Park et al., 1996; Park et al., 2000; Ahn et al., 2004), and in addition to the current findings, it might be a promising candidate for the drug development of AD. Park et al., investigated the pharmacological effects of DHE on a scopolamine-induced amnesia model in rats (Park et al., 2000). A single (20 mg/kg, *p. o.*) and repeated (10 mg/kg, *p. o.*) dosing of DHE significantly reversed the latency of scopolamine (1 mg/kg, *i. p.*) to control levels. Furthermore, DHE dramatically improved the impaired spatial working memory and cognitive deficits in rats, as well as reduced neuronal loss and infarct size (Table 2). These results suggest that DHE might be an effective drug not only for AD types but also for vascular dementia and stroke. Also, Park et al., screened natural products with anti-amnestic activity for their ability to inhibit AChE and reverse scopolamine-induced amnesia. DHE was found to strongly inhibit AChE activity in a dose-dependent and non-competitive manner *in vitro* and exhibited anti-amnestic effects *in vivo*. DHE has an IC_{50} value of 37.8 μM. This potent anti-amnestic effect of DHE is thought to be due to the combined effect of AChE inhibition and the known enhancement of cerebral blood flow. DHE increased cerebral blood flow recorded from the surface of the lateral gyrus of the brain in anesthetized cats. This action reached a maximum 1–4 min after injection and continued for 10 min. However, at the doses examined, the compound had negligible effects on other cardiorespiratory functions (Table 2). These results suggest that DHE selectively increases cerebral blood flow (Haji et al., 1994). Kang et al., discussed the effect of DHE on the learning

and memory ability and anti-oxidant capacity of D-galactose-induced aging model mice, and preliminarily discussed the mechanism of action (Kang et al., 2010). The experimental results show that DHE could improve the learning and memory dysfunction of the aging mouse, which might play an anti-oxidative stress role by regulating the level of superoxide dismutase (SOD) (Table 2).

Effects of DHE on the cardiovascular system

DHE has clear cardiovascular pharmacological activity, which has an anti-arrhythmic effect on guinea pig ventricular myocytes. Yang et al., investigated the cardiovascular effects of DHE *in vivo* and *in vitro* (Yang et al., 1990). The intravenous injection administration of DHE caused a slight decrease in blood pressure *in vivo*, a significant decrease in heart rate, and an increase in ECG cycle length. However, DHE did not alter total peripheral resistance. Except for reduced blood flow to the kidneys and skin, there were no significant changes in blood flow to other organs. Moreover, DHE significantly inhibited spontaneously beating atria in a dose-dependent manner *in vitro*. These findings suggest an important role for DHE in suppressing the heart, which may largely contribute to the anti-hypertensive effects of this alkaloid. However, its vasodilatory effect on hindquarters muscles cannot be ignored.

DHE has been reported to have vasodilatory effects (Chiou et al., 1996b). It could induce vasodilatory effects on rat aorta with intact endothelium through partial endothelium-dependent effects, R1-adrenoceptor blockade, and 5-hydroxytryptamine (5-HT) antagonism (Chiou et al., 1996a). Electrophysiological studies on isolated guinea pig cardiomyocytes indicated that DHE inhibited cardiac ion currents of I_{Na}, $I_{Ca,L}$, and I_K. Simultaneously, it prolonged the duration of action potentials in the ventricle and atrium of the guinea pig (Yang et al., 1990).

DHE reduces arterial blood pressure and prolongs the duration of action potentials in cardiomyocytes in experimental animals. Loh et al., explored the ionic basis of its possible anti-arrhythmic effects (Loh et al., 1992). Studies have shown that DHE might suppress arrhythmias triggered in Ca-overloaded guinea pig cardiomyocytes through its inhibitory effects on I_{Na}, I_{ti}, and to a lesser extent I_{Ca}. DHE also exerts class III anti-arrhythmic effects by reducing the outward K current (I_k) across the sarcolemma. DHE (0.1–0.3 μM) is highly effective in inhibiting cardiac arrhythmias induced in Ca^{2+}-overloaded guinea-pig cardiomyocytes in low K^+ and high Ca^{2+} perfusates in guinea-pig cardiomyocytes. The ionic underlying mechanism of the cardioprotective effect of DHE is mainly due to its inhibitory effect on I_{Na} and I_{Ca} (Loh et al., 1992). Loh et al., investigated the electromechanical effects of DHE in human atrial and ventricular tissue (Loh et al., 2014). In human atrial and ventricular myocardium, DHE (0.1–0.3 μM) reduced slow- and fast-response action potential ascending velocity, action potential amplitude, and contractility. DHE (0.1–1 μM) reversibly and concentration-dependently decreased Na^+ and Ca^{2+} currents in isolated human atrial and ventricular myocytes. In the human ventricular myocardium, strophanthidin-induced triggering activity was attenuated by pretreatment with DHE (0.3 μM). In addition, DHE (0.1–0.3 μM) also memorably increased resting pHi and Na^+-H^+ exchanger (NHE) activity. In the human heart, DHE could antagonize inotrope-induced arrhythmias by generally reducing Na^+ and Ca^{2+} inward currents while increasing resting intracellular pH (pHi) and NHE activity.

DHE has been reported to induce bradycardia in anesthetized rats (Xu et al., 1982; Yang et al., 1990). It inhibits aortic constriction *in vitro* as a calcium antagonist and has been suggested to have calcium-blocking activity on calcium currents in the mammalian heart (Loh et al., 1992). Wong investigated whether DHE could act as a calcium antagonist on chronotropic and inotropic activity in isolated mouse atria (Wong, 1996). The data showed that DHE induced bradycardia, but did not reduce right atrial contraction amplitude. Furthermore, DHE did not attenuate the amplitude of contraction of the electrically driven left atrium, and in the presence of 1×10^{-4} M DHE, the amplitude of contraction of the left atrium increased when the calcium concentration in Krebs solution was further increased. Since calcium antagonists are known to inhibit chronotropic and inotropic activity, it seems unlikely that DHE acts as a calcium antagonist in chronotropic and inotropic activity in isolated mouse atria.

Effects of DHE on the digestive system

In addition to the effects of DHE on cardiovascular and central nervous system cognition, it also has certain pharmacological effects on the digestive system. Wei et al., clarified the pharmacological effects and mechanisms of DHE on indomethacin (IDO)-induced gastric injury (Wei et al., 2021). The study found that DHE attenuated IDO-induced decreased food intake, weight loss, and gastric injury, and normalized gastric pH and mucosal thickness. In addition, DHE down-regulates the expression of myeloperoxidase (MPO), tumor necrosis factor-α (TNF-α), and interleukin-6 (IL-6), and up-regulates the expression of interleukin-10 (IL-10) to reduce inflammation-induced damage and create a healing environment. Furthermore, DHE could significantly inhibit the phosphorylation of extracellular signal-regulated kinase (ERK) and p38 but not c-Jun N-terminal kinase (JNK). Studies have shown that DHE ameliorated IDO-induced dyspepsia, inflammatory infiltration, and tissue damage through the ERK and p38 signaling pathways but not the JNK pathway (Table 3). Wen et al., established a rat CAG model and a GES-1 human gastric epithelial cell injury model using

TABLE 3 Pharmacological activities of DHE in the digestive system.

Effects (Reference)	Animals or cells	Experimental model	Doses of DHE	Pharmacological effects	Pathways
Treatment for CAG Wen et al. (2021)	Rats	170 μg/ml of MNNG-induced CAG	5, 10 mg/kg, *i.g.*	Down-regulate serum inflammatory factor levels Alleviate histological damage of gastric tissue Increase cell proliferation of GES-1 cells Ameliorate MNNG-induced gastric epithelial cell damage and mitochondrial dysfunction Inhibit migration and invasion of GES-1 cells	Regulate inflammation metabolites and energy metabolism-related pathways. Inhibit HIF-1α/VEGF angiogenesis pathway
Treatment for gastric ulcers Wan and Bao, (2020)	Rats	50 μl glacial acetic acid-induced stomach ulcer	6.25, 12.5 mg/kg, *i.g.*	Reduce gastric mucosal ulcers area, serum oxidative stress factor, and serum inflammatory factor levels Increase gastric ulcers inhibition rate, gastric mucosal repair factor levels	Regulate Rho/NF-κB signaling pathway
Treatment for gastric ulcers Wei et al. (2021)	Rats	5 mg/kg IDO-induced gastric ulcers	10, 20, 40 mg/kg, *i.g.*	Relieve gastric injury, restore gastric pH and mucosal thickness. Improves indigestion. Alleviate inflammatory infiltration and tissue damage. Create a healing environment	Regulate the ERK and p38 signaling pathways but not the JNK pathway

Notes: CAG, chronic atrophic gastritis; MNNG, N-methyl-N'-nitro-N-nitrosoguanidine; HIF-1α, hypoxia-inducible factor-1 alpha; VEGF, vascular endothelial growth factor; NF-κb, nuclear factor kappa-B; IDO, indomethacin.

N-methyl-N′-nitro-N-nitrosoguanidine (MNNG) and investigated the therapeutic effect and potential molecular biological mechanism of DHE on CAG (Wen et al., 2021). The results showed that the therapeutic effect of DHE on CAG rats was manifested by down-regulating the levels of serum inflammatory factors and reducing histological damage to gastric histology. In addition, DHE was effective in increasing cell proliferation of GES-1 cells, ameliorating MNNG-induced gastric epithelial cell damage and mitochondrial dysfunction. Molecular biological mechanism studies have shown that DHE has a regulatory effect on tumor angiogenesis, and can play an anti-CAG effect by inhibiting the relative expression of genes and proteins related to the vascular endothelial growth factor (VEGF) signaling pathway mediated by hypoxia-inducible factor-1 alpha (HIF-1α) (Table 3).

In addition, Wan et al., discussed the protective effect and mechanism of DHE on the gastric mucosa of rats with gastric ulcers caused by acetic acid cauterization (Wan and Bao, 2020). The results indicated that DHE has an effect on inhibiting Rho/nuclear factor kappa-B (Rho/NF-κB) signaling, regulating the inflammatory response in gastric ulcer rats, alleviating oxidative stress, and then preventing gastric mucosal damage. Simultaneously, it could promote the release of local trefoil factor family 1 (TFF1) and gastric tissue EGF levels in the stomach and accelerate the repair of the gastric mucosa. It is shown that DHE can significantly improve gastric ulcers in rats through anti-oxidative stress and anti-inflammatory factors, and its potential mechanism may be related to the regulation of the Rho/NF-κB signaling pathway. Therefore, DHE can play a role in the treatment of gastric mucosal ulcers by inhibiting gastric mucosal damage and promoting gastric mucosal repair. The experimental data are provided for the clinical application of DHE against gastric ulcers (Table 3). Overall, the main biological activities and possible molecular mechanisms of DHE on the digestive system were shown in Figure 2.

Anti-inflammatory effects of DHE

The anti-inflammatory effects of DHE have been reported previously (Choi et al., 2006), which could significantly down-regulate pro-inflammatory cytokines and inflammatory mediators. For example, Chiou et al., explored the possible anti-inflammatory effects of DHE by evaluating its effect on nitric oxide (NO) production in the mouse macrophage-like cell line RAW 264.7 (Chiou et al., 1997). The results showed that DHE (10, 50, 100 μM) inhibited interferon-alpha/lipopolysaccharide (IFN-α/LPS)-stimulated NO production in a concentration-dependent manner. However, DHE appears to inhibit NO production by interfering not only with the priming signal elicited by IFN-α but also with inducible nitric oxide synthase (iNOS) protein synthesis.

In recent years, researchers have devoted themselves to finding effective agents for the treatment of RA. It is found that numerous amounts of small molecule compounds derived from natural products have effects on enhancing the therapeutic effects of RA by abating inflammation reactions and inhibiting the abnormal proliferation of fibroblasts. Dai et al., explored the therapeutic effect and feasible mechanism of DHE on RA in complete freund's adjuvant (CFA)-induced adjuvant-induced arthritis (AIA) *in vivo* and *in vitro* (Dai et al., 2022). The results indicated that DHE could substantially improve the symptoms of joint redness and joint swelling in AIA rats. Simultaneously, DHE could inhibit the serum level of pro-inflammatory factors, including TNF-α, interleukin-1 beta (IL-1β), IL-6, and interleukin-17 (IL-17), as well as the relative

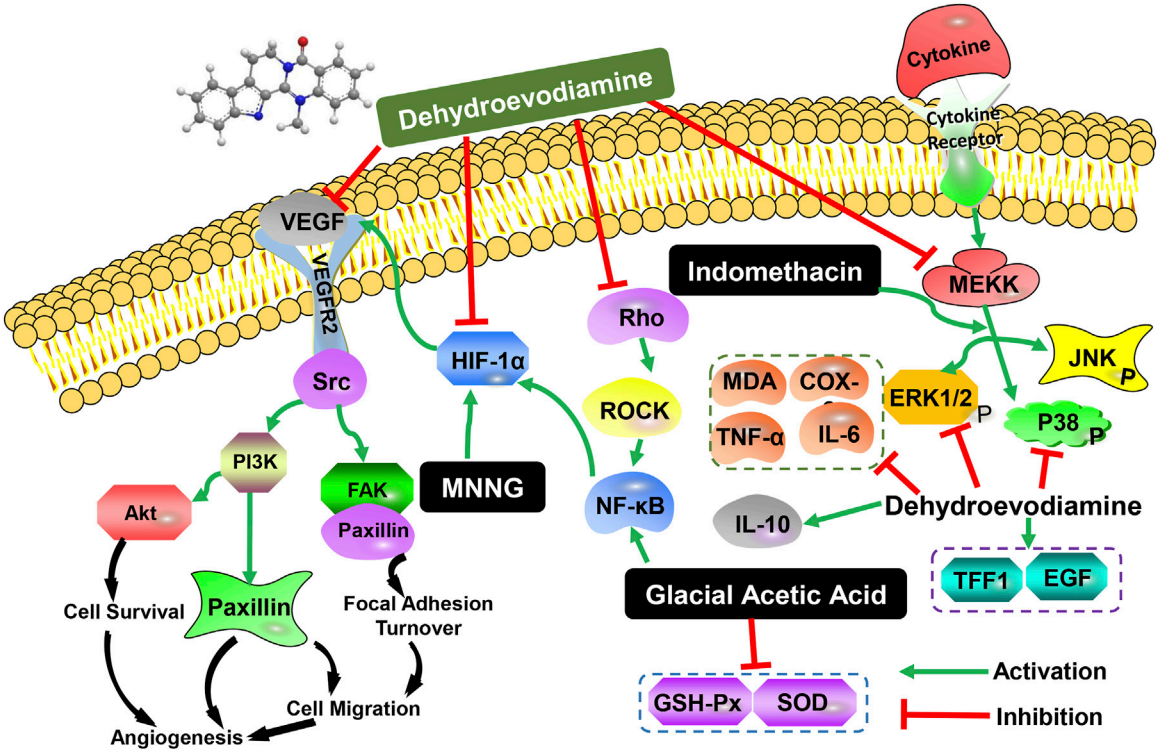

FIGURE 2
The main biological activities and possible molecular mechanisms of DHE on the digestive system.

mRNA expression of matrix metallopeptidase 1 (MMP-1) and matrix metallopeptidase 3 (MMP-3) in MH7A arthritis synovial fibroblasts. DHE plays a role in the treatment of RA by reducing inflammation and inhibiting the abnormal proliferation of fibroblasts. Moreover, the potential mechanism might be related to the regulation of the mitogen-activated protein kinase (MAPK) pathway.

Toxicological risks of DHE

Toxicity and safety should be considered first when evaluating the pharmacological effects of drugs. One of the four classic and the earliest book of TCM *"Shennong's Classic of Materia Medica"* records that EF has mild toxicity in humans and is a relatively safe herbal medicine. For EF, which mainly contains bioactive indoloquinazoline alkaloids, it is necessary to pay attention to its sensitivity to cardiac and liver safety. Although ingestion of EF decoction may induce human hepatic cytochrome P450 family one subfamily A member 1 (CYP1A), DHE does not affect 7-ethoxyresorufin O-deethylation activity (Ueng et al., 2002). The potential toxicological risks of DHE in various diseases are listed as follows according to the previous studies.

DHE has proarrhythmic effects

The quinazoline alkaloid DHE is a potent human ether-a-go-go related gene (hERG) inhibitor in EF extract with an IC_{50} value of 253.2 ± 26.3 nM detected in patch clamp experiments. The hERG channel blocking property of EF decoction is proportional to the content of DHE (Hamburger, 2019). DHE could cause arrhythmias in chronic atrioventricular block dogs (0.33–0.5 mg/5 min) as well as anesthetized rabbits. In 8 chronic atrioventricular block dogs, DHE (0.33 mg/kg/5 min) could increase QT duration by 48 ± 10% and caused Torsade de Pointes (TdP) in 2/4 of these dogs. It is noteworthy that higher doses of DHE did not induce TdP. As for rabbits, DHE significantly increased the QT interval by 12 ± 10% (0.05 mg kg^{-1}.5 min^{-1}) and 60 ± 26% (0.5 mg kg^{-1}.5 min^{-1}) in eight rabbits, and induced TdP arrhythmia(0.5 mg kg^{-1}.5 min^{-1}) in two rabbits. In addition, it could concentration-dependent prolong action potential duration in dog ventricular cardiomyocytes. Early after depolarizations (EADs) were seen in 14, 67, 100, and 67% of dog ventricular cardiomyocytes after 0.01, 0.1, 1, and 10 μM of DHE (Baburin et al., 2018). Therefore, the dose-dependent pro-arrhythmic effect of DHE should raise awareness of the pro-arrhythmic effects of the widely used EF extract.

DHE has no hepatotoxic

Besides, DHE has been reported to be potentially hepatotoxic. Zhang et al., investigated the possibility of hepatotoxicity induced by DHE (Zhang Y. et al., 2018). The livers and serum indices were analyzed in C57BL/6N mice by daily gavage of 80 mg/kg DHE for 3, 12, and 21 days. The results showed that the liver/body weight ratio of the mice did not show a marked difference during the administration period, suggesting that DHE did not cause substantial hepatomegaly. In addition, 80 mg/kg DHE treatment for 21 days did not cause memorably changes in serum alanine aminotransferase (ALT) and aspartate aminotransferase (AST) levels in mice, indicating no apparent hepatotoxicity. These results were also further confirmed by histological analysis, liver/body weight ratio, and serum biochemical analysis.

DHE impairs bile acid homeostasis

DHE was not hepatotoxic at the doses used. However, it disrupted bile acid homeostasis in an aryl hydrocarbon receptor-dependent manner. These findings suggest that the methyl group on the N-14 atom of DHE and its pharmacokinetic behavior were the main determinants of aryl hydrocarbon receptor activation, suggesting that attention should be taken to monitor its effects on bile acid metabolism in the clinical application of EF and DHE (Zhang Y. et al., 2018). Global metabolomics was employed to analyze metabolites in mouse gallbladders. DHE treatment for 21 days could significantly increase the levels of unconjugated bile acids cholic acid, ω-muricholic, taurocholic acid and taurodeoxycholic acid, while slightly increasing α-muricholic, and β-muricholic levels. In addition, DHE could regulate the induction of CYP7A1 or bile salt export pump (BSEP) through the activation of the aryl hydrocarbon receptors.

Conclusion and perspective

Natural products refer to the chemical constituents or their metabolites in animals, plants, and microorganisms. As an important source of drug discovery, natural products have the characteristics of diverse structures and have always been a crucial source of new drug discovery (Shen, 2015; Li, 2016; Ekiert and Szopa, 2022). In recent years, drugs such as artemisinin, ephedrine, vincristine, tripterygium glycosides, and taxol have received increasing attention due to their reliable efficacy and low toxicity (Xu et al., 2020). DHE is a key quinazoline alkaloid isolated from EF and now plays an important role in diseases of the central nervous system, digestive system, cardiovascular system diseases, *etc.* However, there are few comprehensive reports on the pharmacokinetics, pharmacological effects, biological mechanisms, and toxicology risks of DHE. This review provides a comprehensive summary of the chemical properties, pharmacokinetic characteristics, pharmacological activities, biological mechanisms, and toxicity of DHE. Pharmacokinetic studies have shown that DHE has a relatively good oral absorption effect in rats. DHE has a wide spectrum of pharmacological properties in the central nervous system, digestive system, and cardiovascular system, including anti-cholinesterase activity, anti-amnesia, anti-AD, anti-arrhythmic, gastrointestinal protection, and anti-inflammatory effects. In addition, toxicity studies have suggested that DHE has proarrhythmic effects and can impair bile acid homeostasis without hepatotoxic. However, long-term and high-dose toxicity studies in animals are still lacking. This summarized information might be helpful for future research and further development of DHE.

In the aspect of pharmacokinetics profiles, a variety of developed methods are successfully applied to determine the related pharmacokinetic parameters of DHE in rats, and mice, as well as *in silicon* studies. DHE has a relatively good oral absorption effect in the mean concentration curves in rat plasma (Li et al., 2021) and high absorption in the gastrointestinal tract (Ahmad et al., 2021). Also, distributional re-absorption and enterohepatic circulation may lead to multiple blood concentration peaks of DHE in rat plasma (Yan et al., 2012). DHE may be actively secreted in the intestine, resulting in irregular absorption patterns (Xu et al., 2013). In addition, the pharmacokinetic characterization of DHE in the rat brain was also studied. The dynamic distribution of DHE in rat brains showed that the time curve of DHE plasma level decreased exponentially. The clearance rate and steady-state distribution volume were not statistically different from the dose, indicating that the pharmacokinetics of DHE was linear in the range examined. The concentration of DHE in cerebrospinal fluid was negligible compared to that in plasma, suggesting that the drug was not distributed primarily to the brain through the blood-cerebrospinal fluid barrier. This indicates that DHE is transported from systemic circulation to the brain through the BBB. The distribution of DHE into and out of the brain is mediated by first-order kinetics. Consistent with the *in vivo* data, DHE transport across MBEC4 monolayers is all mediated by first-order kinetics (Ahn et al., 2004).

At present, the world has already entered an aging society (Joe et al., 2021). For the elderly, maintaining normal cognitive function is the guarantee of high-quality life. AD is a progressive neurodegenerative disease and the main type of dementia. In the elderly population, the most common diseases that impair the cognitive function are AD and cerebrovascular disease. Both have become diseases that seriously threaten the health of the elderly (Shin et al., 2016; Shin et al., 2017). Epidemiological and pathological data show that AD and cerebrovascular disease have many overlaps in etiology and pathology, and most sporadic AD is also a cerebrovascular disease (Santos et al., 2017). The treatment of cerebrovascular disease can also delay the occurrence and development of AD. It is especially necessary to extract active ingredients from TCM for AD treatment.

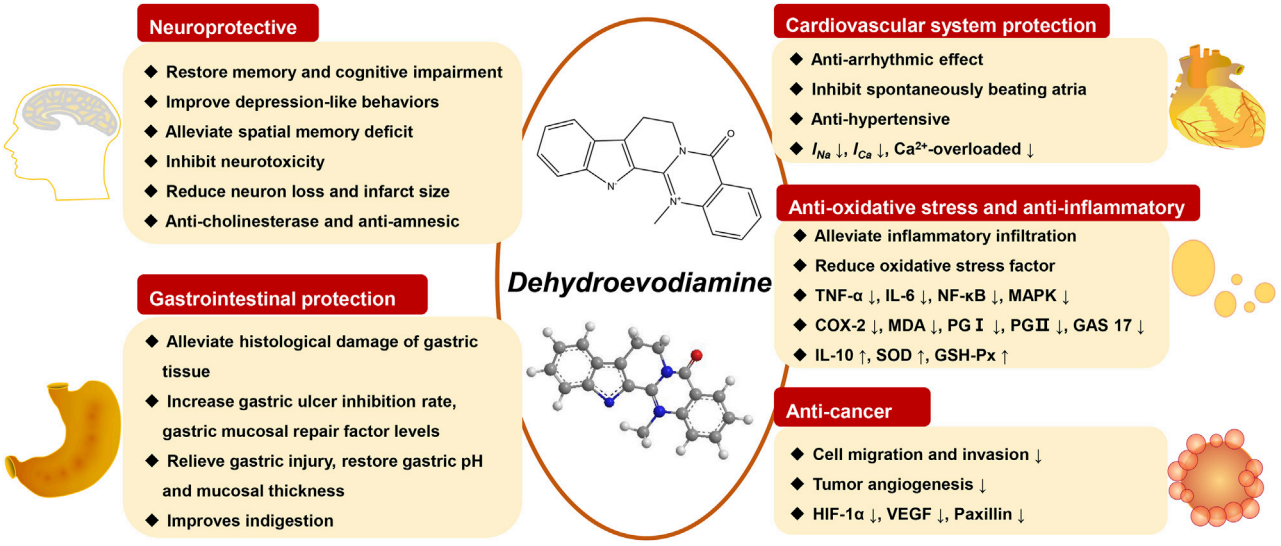

FIGURE 3
The pharmacological properties of DHE and its potential biological mechanisms.

According to the current studies, DHE has a good protective function on the central nervous system and can act on the occurrence and development of AD through multiple pathways. DHE binds strongly to the active site residues of AChE and follows the drug-like properties predicted *in silico*. Further experimental evaluations of DHE may eventually lead to exciting alternative AD therapies (Ahmad et al., 2021). DHE can effectively slow down the occurrence and development of AD through neuroprotective function by repairing memory and cognitive impairment, antagonizing Aβ deposition, inhibiting Tau protein hyperphosphorylation, protecting isolated neurons, inhibiting glial cell activation and inflammatory mediators release, *etc.* Its pharmacological effect on cerebrovascular disease is reflected in the protective effect on ischemic brain injury. Studies have found that DHE can exert anti-AD effects by acting on targets such as ROS, SOD, Aβ40, Aβ42, β-secretase, GSK-3, Tau protein, NCAM proteins, *etc.* Its pharmacological effects include restoring memory and cognitive impairment, antagonizing Aβ deposition, inhibiting Tau protein hyperphosphorylation, restoring cognitive and memory deficits, improving spatial memory impairment, anti-oxidation, inhibiting neurotoxicity, *etc.* (Haji et al., 1994; Park et al., 2000; Fang et al., 2007; Kang et al., 2010; Kim et al., 2014; Shin et al., 2016; Shin et al., 2017; Kang et al., 2018). Although there has been a lot of basic research on DHE, more clinical application experiments are needed based on the existing research to provide a sufficient scientific basis for their future use as effective drugs for AD and cerebrovascular diseases.

Previous work highlighted the role of DHE in the digestive system, which could ameliorate gastric injury in MNNG-induced CAG rats, IDO or glacial acetic acid-induced gastric ulcers (Wan and Bao, 2020; Wei et al., 2021; Wen et al., 2021). The results indicated that the therapeutic effects of DHE on CAG rats were presented in alleviating histological damage of gastric tissue *in vivo*, increasing cell proliferation of GES-1 cells, and ameliorating MNNG-induced gastric epithelial cell damage and mitochondrial dysfunction. In addition, DHE could inhibit MNNG-induced migration and invasion of GES-1 cells. It was found that DHE plays a crucial role in angiogenesis by inhibiting the HIF-1α-mediated VEGF pathway in CAG rats and gastric epithelial cells. Furthermore, DHE ameliorates dyspepsia, inflammatory infiltration, tissue damage, and serum oxidative stress through ERK/p38 and Rho/NF-κB signaling pathways. These studies provide a new promising therapeutic agent for the prevention and treatment of CAG and gastric ulcers. However, more animal studies and clinical trials are necessary to further confirm the protective and therapeutic effect of DHE on the digestive system.

In recent years, studies have found that DHE has cardiovascular and cerebrovascular system effects such as anti-arrhythmia, dilation of blood vessels, lowering blood pressure, slowing heart rate, inhibiting Ca^{2+} inflow, and selectively increasing cerebral blood flow (Schramm and Hamburger, 2014). DHE inhibits calcium overload-induced arrhythmias and works by prolonging the action potential duration in the cardiomyocytes of experimental animals (Baburin et al., 2018). It can reduce the amplitude and contractility of action potentials in human atrial and ventricular myocytes. Simultaneously, DHE (0.1, 0.3 μM) can reversibly and concentration-dependently reduce the influx of Na^+ and Ca^{2+}, and also inhibit atrial delayed depolarization caused by epinephrine and high extracellular Ca^{2+} in isolated human atrial and ventricular myocytes (Loh et al., 2014). Therefore, DHE can produce an anti-arrhythmic effect by reducing the inward current of Na^+ and Ca^{2+},

and increasing the pH value of intracellular fluid and Na^+-H^+ exchange in the resting state (Loh et al., 1992; Loh et al., 2014). In addition, DHE lowers blood pressure while slowing heart rate (Shoji et al., 1986; Yang et al., 1990). The related mechanisms of its anti-hypertensive effect include potassium channel activity (Chiou et al., 1996b).

DHE has a vasodilatory effect, which slows down the heart rate while reducing blood pressure. The lowering effect of diastolic blood pressure was stronger than that of systolic blood pressure, suggesting that DHE has the effect of dilating blood vessels (Loh et al., 1992). This vasodilator effect is related to calcium channel blockade, NO-cGMP system, potassium channel activity, *etc.* (Chiou et al., 1996b). In terms of two-way regulation of blood pressure, DHE has a clear blood pressure-lowering effect and a significant anti-hypertensive effect on diastolic blood pressure, which is manifested as vasodilation. Its vasodilatory mechanism is the inhibition of receptor-mediated Ca^{2+} channels and endothelial activation in vascular smooth muscle (Chiou et al., 1996b). The pharmacological properties of DHE and its potential biological mechanisms are shown in Figure 3.

Although the beneficial effects have been synthetically reported, the potential toxicological risks of DHE as a quinazoline alkaloid still need attention. In the cardiovascular system, studies have found that DHE has a proarrhythmic effect (Baburin et al., 2018; Hamburger, 2019), which can cause arrhythmias in chronic atrioventricular block dogs and in anesthetized rabbits. Specifically, DHE can prolong the QT interval of dogs and rabbits, and dogs can cause TdP. However, higher doses of DHE did not induce TdP. As for the digestive system, DHED was also reported to have potential hepatotoxicity (Lin et al., 2015). However, there was no significant difference in the liver/body weight ratio of mice after intragastric administration of large doses of DHE, suggesting that DHE did not cause significant hepatomegaly. In addition, 80 mg/kg DHE did not cause significant changes in serum liver function indicators ALT and AST levels in mice after 21 days of treatment, indicating that DHE had no significant hepatotoxicity. Moreover, it has also been reported that DHE destroys the homeostasis of bile acids without causing hepatotoxicity by upregulating CYP7A1 or BSEP through a mechanism that is yet to be determined (Zhang Y. et al., 2018). Thus, whether DHE causes hepatotoxicity varies based on experimental conditions and remains controversial. More rigorous and well-designed studies are needed to elucidate the toxicological risks of DHE.

Currently, most of the research on DHE is focused on its pharmacokinetics, chemical constituents, pharmacological effects, and mechanism of action. However, the research is superficial and not in-depth, and the research methods are relatively backward. Therefore, it is necessary to use advanced scientific and technological means to conduct more in-depth research on the chemical constituents and pharmacological mechanism of DHE, especially the pharmacological mechanism of the central nervous system, cardiovascular system, anti-tumor, anti-inflammatory, and other aspects. On the whole, the follow-up research on the chemical constituents and pharmacological activity of DHE should start from the following three aspects: ① The first is to deeply study its pharmacological effects and mechanism of action, and to more comprehensively expound the scientific connotation of the biological activity of DHE, which can provide a strong scientific basis for clinical application; ② The second is to explore the potential pharmacological effects of DHE that have not yet been reported, and expand the application scope of DHE; ③ Thirdly, strengthen the development and utilization of DHE, and enhance its effectiveness and give full play to its medicinal value by modifying the structure of DHE.

Author contributions

SF wrote and amended this manuscript. LL reviewed the drafts and searched the references. YY and YB carefully checked the references. YZ and HW checked crucial information in this manuscript. JW conceived and designed the study. All data were generated in-house, and no paper mill was used. All authors agree to be accountable for all aspects of work ensuring integrity and accuracy.

Acknowledgments

The authors gratefully acknowledge the Xihua University Talent Introduction Project (Z211060).

Conflict of interest

The authors declare that the research was conducted in the absence of any commercial or financial relationships that could be construed as a potential conflict of interest.

Publisher's note

Supplementary material

The Supplementary Material for this article can be found online at: https://www.frontiersin.org/articles/10.3389/fphar.2022.1040154/full#supplementary-material

References

Ahmad, S. S., Khan, H., DanishRizvi, S. M., Ansari, S. A., Ullah, R., Rastrelli, L., et al. (2019). Computational study of natural compounds for the clearance of amyloid-ßeta: A potential therapeutic management strategy for alzheimer's disease. *Molecules* 24, 3233. doi:10.3390/molecules24183233

Ahmad, S. S., Khan, M. B., Ahmad, K., Lim, J. H., Shaikh, S., Lee, E. J., et al. (2021). Biocomputational screening of natural compounds against acetylcholinesterase. *Molecules* 26, 2641. doi:10.3390/molecules26092641

Ahn, S. H., Jeon, S. H., Tsuruo, T., Shim, C. K., and Chung, S. J. (2004). Pharmacokinetic characterization of dehydroevodiamine in the rat brain. *J. Pharm. Sci.* 93, 283–292. doi:10.1002/jps.10546

Baburin, I., Varkevisser, R., Schramm, A., Saxena, P., Beyl, S., Szkokan, P., et al. (2018). Dehydroevodiamine and hortiamine, alkaloids from the traditional Chinese herbal drug Evodia rutaecarpa, are IKr blockers with proarrhythmic effects *in vitro* and *in vivo*. *Pharmacol. Res.* 131, 150–163. doi:10.1016/j.phrs.2018.02.024

Chiou, W. F., Liao, J. F., and Chen, C. F. (1996a). Comparative study of the vasodilatory effects of three quinazoline alkaloids isolated from Evodia rutaecarpa. *J. Nat. Prod.* 59, 374–378. doi:10.1021/np960161+

Chiou, W. F., Liao, J. F., Shum, A. Y., and Chen, C. F. (1996b). Mechanisms of vasorelaxant effect of dehydroevodiamine: A bioactive isoquinazolinocarboline alkaloid of plant origin. *J. Cardiovasc. Pharmacol.* 27, 845–853. doi:10.1097/00005344-199606000-00012

Chiou, W. F., Sung, Y. J., Liao, J. F., Shum, A. Y., and Chen, C. F. (1997). Inhibitory effect of dehydroevodiamine and evodiamine on nitric oxide production in cultured murine macrophages. *J. Nat. Prod.* 60, 708–711. doi:10.1021/np960495z

Choi, Y. H., Shin, E. M., Kim, Y. S., Cai, X. F., Lee, J. J., and Kim, H. P. (2006). Anti-inflammatory principles from the fruits of Evodia rutaecarpa and their cellular action mechanisms. *Arch. Pharm. Res.* 29, 293–297. doi:10.1007/BF02968573

Dai, Y., Sheng, J., He, S., Wu, Q., Wang, Y., and Su, L. (2022). Dehydroevodiamine suppresses inflammatory responses in adjuvant-induced arthritis rats and human fibroblast-like synoviocytes. *Bioengineered* 13, 268–279. doi:10.1080/21655979.2021.1999554

Decker, M. (2005). Novel inhibitors of acetyl- and butyrylcholinesterase derived from the alkaloids dehydroevodiamine and rutaecarpine. *Eur. J. Med. Chem.* 40, 305–313. doi:10.1016/j.ejmech.2004.12.003

Ekiert, H. M., and Szopa, A. (2022). Biological activities of natural products. *Molecules* 27, E5769. doi:10.3390/molecules25235769

Fang, J., Liu, R., Tian, Q., Hong, X. P., Wang, S. H., Cao, F. Y., et al. (2007). Dehydroevodiamine attenuates calyculin A-induced tau hyperphosphorylation in rat brain slices. *Acta Pharmacol. Sin.* 28, 1717–1723. doi:10.1111/j.1745-7254.2007.00655.x

Gong, X., Zhou, X., Cai, Z., Zhang, J., and Zhou, W. (2009). Studies on chemical constituents of Evodia rutaecarpa. *China J. Chin. Materia Medica* 34, 177–179. doi:10.3321/j.issn:1001-5302.2009.02.015

Haji, A., Momose, Y., Takeda, R., Nakanishi, S., Horiuchi, T., and Arisawa, M. (1994). Increased feline cerebral blood flow induced by dehydroevodiamine hydrochloride from Evodia rutaecarpa. *J. Nat. Prod.* 57, 387–389. doi:10.1021/np50105a009

Hamburger, M. (2019). HPLC-based activity profiling for pharmacologically and toxicologically relevant natural products - principles and recent examples. *Pharm. Biol.* 57, 328–334. doi:10.1080/13880209.2019.1606261

Han, J. Y., Besser, L. M., Xiong, C., Kukull, W. A., and Morris, J. C. (2019). Cholinesterase inhibitors may not benefit mild cognitive impairment and mild alzheimer disease dementia. *Alzheimer Dis. Assoc. Disord.* 33, 87–94. doi:10.1097/WAD.0000000000000291

Han, X. H., Hong, S. S., Lee, D., Lee, J. J., Lee, M. S., Moon, D. C., et al. (2007). Quinolone alkaloids from evodiae fructus and their inhibitory effects on monoamine oxidase. *Arch. Pharm. Res.* 30, 397–401. doi:10.1007/BF02980210

Huang, X., Li, W., and Yang, X. W. (2012). New cytotoxic quinolone alkaloids from fruits of Evodia rutaecarpa. *Fitoterapia* 83, 709–714. doi:10.1016/j.fitote.2012.02.009

Joe, S. Y., So, J. H., Hwang, S. H., Cho, B. K., Lee, W. H., Kang, T., et al. (2021). Application of ohmic-vacuum combination heating for the processing of senior-friendly food (multiphase food): Experimental studies and numerical simulation. *Foods* 10, 138. doi:10.3390/foods10010138

Jung, M., and Park, M. (2007). Acetylcholinesterase inhibition by flavonoids from Agrimonia pilosa. *Molecules* 12, 2130–2139. doi:10.3390/12092130

Kandimalla, R., and Reddy, P. H. (2017). Therapeutics of neurotransmitters in alzheimer's disease. *J. Alzheimers Dis.* 57, 1049–1069. doi:10.3233/JAD-161118

Kang, S., Ha, S., Park, H., Nam, E., Suh, W. H., Suh, Y. H., et al. (2018). Effects of a dehydroevodiamine-derivative on synaptic destabilization and memory impairment in the 5xFAD, alzheimer's disease mouse model. *Front. Behav. Neurosci.* 12, 273. doi:10.3389/fnbeh.2018.00273

Kang, W., Liang, B., Li, S., Yang, X., and Hao, X. (2010). Effects of dehydroevodiamine and berberine hydrochloride on learning and memory in aging model mice induced by D-galactose. *J. China Pharm. Univ.* 41, 372–374. doi:10.1016/S1876-3804(11)60004-9

Kim, H. J., Shin, K. Y., Chang, K. A., Ahn, S., Choi, H. S., Kim, H. S., et al. (2014). Dehydroevodiamine.HCl improves stress-induced memory impairments and depression like behavior in rats. *Korean J. Physiol. Pharmacol.* 18, 55–59. doi:10.4196/kjpp.2014.18.1.55

Li, M., Wang, H., Huan, X., Cao, N., Guan, H., Zhang, H., et al. (2021). Simultaneous LC-MS/MS bioanalysis of alkaloids, terpenoids, and flavonoids in rat plasma through salting-out-assisted liquid-liquid extraction after oral administration of extract from Tetradium ruticarpum and Glycyrrhiza uralensis: A sample preparation strategy to broaden analyte coverage of herbal medicines. *Anal. Bioanal. Chem.* 413, 5871–5884. doi:10.1007/s00216-021-03568-1

Li, R. (2016). Natural product-based drug discovery. *Med. Res. Rev.* 36, 3. doi:10.1002/med.21380

Lim, D. K., Lee, Y. B., and Kim, H. S. (2004). Effects of dehydroevodiamine exposure on glutamate release and uptake in the cultured cerebellar cells. *Neurochem. Res.* 29, 407–411. doi:10.1023/b:nere.0000013745.17014.a3

Lin, S., Ren, L., and Sun, A. (2015). Acute toxicity study on evodiamine, rutacarpine and evodia total alkaloids in mice. *J. Zunyi Med. Univ.* 38, 146–149. doi:10.14169/j.cnki.zunyixuebao.2015.0033

Loh, S. H., Lee, A. R., Huang, W. H., and Lin, C. I. (1992). Ionic mechanisms responsible for the antiarrhythmic action of dehydroevodiamine in Guinea-pig isolated cardiomyocytes. *Br. J. Pharmacol.* 106, 517–523. doi:10.1111/j.1476-5381.1992.tb14368.x

Loh, S. H., Tsai, Y. T., Lee, C. Y., Chang, C. Y., Tsai, C. S., Cheng, T. H., et al. (2014). Antiarrhythmic effects of dehydroevodiamine in isolated human myocardium and cardiomyocytes. *J. Ethnopharmacol.* 153, 753–762. doi:10.1016/j.jep.2014.03.043

Nam, E. Y., Kim, S. A., Kim, H., Kim, S. H., Han, J. H., Lee, J. H., et al. (2016). Akt activation by Evodiae Fructus extract protects ovary against 4-vinylcyclohexene diepoxide-induced ovotoxicity. *J. Ethnopharmacol.* 194, 733–739. doi:10.1016/j.jep.2016.10.048

Park, C. H., Kim, S. H., Choi, W., Lee, Y. J., Kim, J. S., Kang, S. S., et al. (1996). Novel anticholinesterase and antiamnesic activities of dehydroevodiamine, a constituent of Evodia rutaecarpa. *Planta Med.* 62, 405–409. doi:10.1055/s-2006-957926

Park, C. H., Lee, Y. J., Lee, S. H., Choi, S. H., Kim, H. S., Jeong, S. J., et al. (2000). Dehydroevodiamine.HCl prevents impairment of learning and memory and neuronal loss in rat models of cognitive disturbance. *J. Neurochem.* 74, 244–253. doi:10.1046/j.1471-4159.2000.0740244.x

Park, E. J., Suh, Y. H., Kim, J. Y., Choi, S., and Lee, C. J. (2003). Long-lasting facilitation by dehydroevodiamine. HClof synaptic responses evoked in the CA1 region of rat hippocampal slices. *Neuroreport* 14, 399–403. doi:10.1097/00001756-200303030-00020

Peng, J. H., Zhang, C. E., Wei, W., Hong, X. P., Pan, X. P., and Wang, J. Z. (2007). Dehydroevodiamine attenuates tau hyperphosphorylation and spatial memory deficit induced by activation of glycogen synthase kinase-3 in rats. *Neuropharmacology* 52, 1521–1527. doi:10.1016/j.neuropharm.2007.02.008

Perkins, A., Phillips, J. L., Kerkvliet, N. I., Tanguay, R. L., Perdew, G. H., Kolluri, S. K., et al. (2014). A structural switch between agonist and antagonist bound conformations for a ligand-optimized model of the human aryl hydrocarbon receptor ligand binding domain. *Biol. (Basel)* 3, 645–669. doi:10.3390/biology3040645

Qian, P., Zhang, Y. B., Yang, Y. F., Xu, W., and Yang, X. W. (2017). Pharmacokinetics studies of 12 alkaloids in rat plasma after oral administration of Zuojin and fan-zuojin formulas. *Molecules* 22, 214. doi:10.3390/molecules22020214

Santos, C. Y., Snyder, P. J., Wu, W. C., Zhang, M., Echeverria, A., and Alber, J. (2017). Pathophysiologic relationship between alzheimer's disease, cerebrovascular disease, and cardiovascular risk: A review and synthesis. *Alzheimers Dement. (Amst).* 7, 69–87. doi:10.1016/j.dadm.2017.01.005

Schramm, A., and Hamburger, M. (2014). Gram-scale purification of dehydroevodiamine from Evodia rutaecarpa fruits, and a procedure for selective removal of quaternary indoloquinazoline alkaloids from Evodia extracts. *Fitoterapia* 94, 127–133. doi:10.1016/j.fitote.2014.02.005

Shen, B. (2015). A new golden age of natural products drug discovery. *Cell.* 163, 1297–1300. doi:10.1016/j.cell.2015.11.031

Shin, K. Y., Noh, S. J., Park, C. H., Jeong, Y. H., Chang, K. A., Yoo, J., et al. (2016). Dehydroevodiamine●HCl protects against memory impairment and cerebral amyloid-β production in Tg2576 mice by acting as a β-secretase inhibitor. *CNS Neurol. Disord. Drug Targets* 15, 935–944. doi:10.2174/1871527315666160815163723

Shin, K. Y., Kim, K. Y., and Suh, Y. H. (2017). Dehydroevodiamine.HCl enhances cognitive function in memory-impaired rat models. *Korean J. Physiol. Pharmacol.* 21, 55–64. doi:10.4196/kjpp.2017.21.1.55

Shoji, N., Umeyama, A., Takemoto, T., Kajiwara, A., Ohizumi, Y., and KajiwArA, A. (1986). Isolation of evodiamine, a powerful cardiotonic principle, from Evodia rutaecarpa Bentham (Rutaceae). *J. Pharm. Sci.* 75, 612–613. doi:10.1002/jps.2600750619

Sugimoto, T., Miyase, T., Kuroyanagi, M., and Ueno, A. (1988). Limonoids and quinolone alkaloids from Evodia rutaecarpa Bentham. *Chem. Pharm. Bull.* 36, 4453–4461. doi:10.1248/cpb.36.4453

Sun, Q., Xie, L., Song, J., and Li, X. (2020). Evodiamine: A review of its pharmacology, toxicity, pharmacokinetics and preparation researches. *J. Ethnopharmacol.* 262, 113164. doi:10.1016/j.jep.2020.113164

Tian, K. M., Li, J. J., and Xu, S. W. (2019). Rutaecarpine: A promising cardiovascular protective alkaloid from evodia rutaecarpa (Wu zhu yu). *Pharmacol. Res.* 141, 541–550. doi:10.1016/j.phrs.2018.12.019

Ueng, Y. F., Don, M. J., Peng, H. C., Wang, S. Y., Wang, J. J., and Chen, C. F. (2002). Effects of Wu-chu-yu-tang and its component herbs on drug-metabolizing enzymes. *Jpn. J. Pharmacol.* 89, 267–273. doi:10.1254/jjp.89.267

Wan, J., and Bao, Q. (2020). Protective effect of dehydroevodiamine on gastric mucosa of rats with experimental gastric ulcer and its mechanism. *Chin. Traditional Herb. Drugs* 51, 4698–4703. doi:10.7501/j.issn.0253-2670.2020.18.013

Wang, H. H., Chou, C. J., Liao, J. F., and Chen, C. F. (2001). Dehydroevodiamine attenuates beta-amyloid peptide-induced amnesia in mice. *Eur. J. Pharmacol.* 413 (2-3), 221–225. doi:10.1016/s0014-2999(00)00913-4

Wang, M., Zhou, B., Cong, W., Zhang, M., Li, Z., Li, Y., et al. (2021). Amelioration of AOM/DSS-Induced murine colitis-associated cancer by evodiamine intervention is primarily associated with gut microbiota-metabolism-inflammatory signaling Axis. *Front. Pharmacol.* 12, 797605. doi:10.3389/fphar.2021.797605

Wang, X. X., Zan, K., Shi, S. P., Zeng, K. W., Jiang, Y., Guan, Y., et al. (2013). Quinolone alkaloids with antibacterial and cytotoxic activities from the fruits of Evodia rutaecarpa. *Fitoterapia* 89, 1–7. doi:10.1016/j.fitote.2013.04.007

Wei, Y., Ren, S., Wang, J., Wang, Y., Cui, Y., Tian, M., et al. (2021). Dehydroevodiamine ameliorates indomethacin-induced gastric injury via inhibition of ERK and p38 signaling pathway. *Phytomedicine.* 93, 153764. doi:10.1016/j.phymed.2021.153764

Wen, J. X., Tong, Y. L., Ma, X., Wang, R. L., Li, R. S., Song, H. T., et al. (2021). Therapeutic effects and potential mechanism of dehydroevodiamine on N-methyl-N'-nitro-N-nitrosoguanidine-induced chronic atrophic gastritis. *Phytomedicine.* 91, 153619. doi:10.1016/j.phymed.2021.153619

Wong, K. K. (1996). Lack of calcium-antagonizing activity of dehydroevodiamine on the chronotropic and inotropic activities of mouse isolated atria. *Planta Med.* 62, 246–249. doi:10.1055/s-2006-957869

Xu, H., Li, Q., Yin, Y., Lv, C., Sun, W., He, B., et al. (2013). Simultaneous determination of three alkaloids, four ginsenosides and limonin in the plasma of normal and headache rats after oral administration of Wu-Zhu-Yu decoction by a novel ultra fast liquid chromatography-tandem mass spectrometry method: Application to a comparative pharmacokinetics and ethological study. *J. Mass Spectrom.* 48, 519–532. doi:10.1002/jms.3183

Xu, S. B., Huang, Y. M., Lau, C. N., Wat, C. K., and Kong, Y. C. (1982). Hypotensive effect of dehydroevodiamine from evodiae fructus. *Am. J. Chin. Med.* 10 (1-4), 75–85. doi:10.1142/S0192415X82000130

Xu, T., Kuang, T., Du, H., Li, Q., Feng, T., Zhang, Y., et al. (2020). Magnoflorine: A review of its pharmacology, pharmacokinetics and toxicity. *Pharmacol. Res.* 152, 104632. doi:10.1016/j.phrs.2020.104632

Yan, R., Wang, Y., Shen, W., Zhao, X., and Zhang, X. (2012). Relative determination of dehydroevodiamine in rat plasma by LC-MS and study on its pharmacokinetics. *J. Chromatogr. Sci.* 50, 582–585. doi:10.1093/chromsci/bms050

Yang, M. C., Wu, S. L., Kuo, J. S., and Chen, C. F. (1990). The hypotensive and negative chronotropic effects of dehydroevodiamine. *Eur. J. Pharmacol.* 182, 537–542. doi:10.1016/0014-2999(90)90052-8

Zhang, L., Brett, C. M., and Giacomini, K. M. (1998). Role of organic cation transporters in drug absorption and elimination. *Annu. Rev. Pharmacol. Toxicol.* 38, 431–460. doi:10.1146/annurev.pharmtox.38.1.431

Zhang, X., Oh, M., Kim, S., Kim, J., Kim, H., Kim, S., et al. (2013). Epimediphine, a novel alkaloid from Epimedium koreanum inhibits acetylcholinesterase. *Nat. Prod. Res.* 27, 1067–1074. doi:10.1080/14786419.2012.708660

Zhang, Y. N., Yang, Y. F., and Yang, X. W. (2018a). Blood-brain barrier permeability and neuroprotective effects of three main alkaloids from the fruits of Euodia rutaecarpa with MDCK-pHaMDR cell monolayer and PC12 cell line. *Biomed. Pharmacother.* 98, 82–87. doi:10.1016/j.biopha.2017.12.017

Zhang, Y., Yan, T., Sun, D., Xie, C., Zheng, Y., Zhang, L., et al. (2018b). Structure-activity relationships of the main bioactive constituents of euodia rutaecarpa on aryl hydrocarbon receptor activation and associated bile acid homeostasis. *Drug Metab. Dispos.* 46, 1030–1040. doi:10.1124/dmd.117.080176

Zhao, Y., Zhao, Y., Zhou, X., and Gong, X. (2014). Development and validation of an UPLC-ESI-MS/MS method for determination of dehydroevodiamine, limonin, evodiamine, and rutaecarpine in Evodiae Fructus. *Pharmacogn. Mag.* 10, 374–383. doi:10.4103/0973-1296.137381

Glossary

DHE Dehydroevodiamine
TCM Traditional Chinese medicine
EF *Evodiae Fructus*
CVD Cardiovascular diseases
LC-MS Liquid chromatography-mass spectrometry
AD Alzheimer's disease
CAG Chronic atrophic gastritis
RA Rheumatoid arthritis
DMSO Dimethyl sulfoxide
AChE Acetylcholinesterase
AUC Area under concentration-time curve
MRT Mean residence time
CL Clearance
BBB Blood-brain barrier
ChEIs Cholinesterase inhibitors
cx-DHED Carboxy-dehydroevodiamine·HCl
NCAM Neural cell adhesion molecule
CA Calyculin A
PP Protein phosphatase
Aβ β-amyloid
SOD Superoxide dismutase
p.o Peros
i.p. Intraperitoneal injection
ROS Reactive oxygen species
GSK-3 Glycogen synthase kinase-3
WT/GFX Wortmannin and GF-109203X
Tg Transgenic
NMDARs N-methyl-D-aspartate receptors
MCA Middle cerebral artery
5-HT 5-Hydroxytryptamine
NHE Na^+-H^+ exchanger
IDO Indomethacin
MPO Myeloperoxidase
TNF-α Tumor necrosis factor-α
IL-6 Interleukin-6
IL-10 Interleukin-10
ERK Extracellular signal-regulated kinase
JNK c-Jun N-terminal kinase
MNNG N-methyl-N′-nitro-N-nitrosoguanidine
VEGF Vascular endothelial growth factor
HIF-1α Hypoxia-inducible factor-1 alpha
NF-κb Nuclear factor kappa-B
TFF1 Trefoil factor family one
EGF Epidermal growth factor
NO Nitric oxide
IFN-α Interferon alpha
LPS Lipopolysaccharide
iNOS Inducible nitric oxide synthase
CFA Complete freund's adjuvant
AIA Adjuvant-induced arthritis
IL-1β Interleukin-1 beta
IL-17 Interleukin-17
MMP-1 Matrix metallopeptidase 1
MMP-3 Matrix metallopeptidase 3
MAPK Mitogen-activated protein kinase
CYP1A Cytochrome P450 family 1 subfamily A member 1
hERG Human ether-a-go-go related gene
TdP Torsade de Pointes
EADs Early after depolarizations
ALT Alanine aminotransferase
AST Aspartate aminotransferase
BSEP Bile salt export pump

Frontiers in Pharmacology

Explores the interactions between chemicals and living beings

The most cited journal in its field, which advances access to pharmacological discoveries to prevent and treat human disease.

Discover the latest Research Topics

See more →

Frontiers

Avenue du Tribunal-Fédéral 34
1005 Lausanne, Switzerland
frontiersin.org

Contact us

+41 (0)21 510 17 00
frontiersin.org/about/contact